

SEISMICALLY RESILIENT BRIDGE COLUMNS WITH POLYURETHANE-
ENHANCED DAMAGE-RESISTANT (DR) JOINTS AND REPLACEABLE
ENERGY DISSIPATING (ED) LINKS

A Dissertation

by

MOHAMMAD TAGHI NIKOUKALAM MOFAKHAM

Submitted to the Office of Graduate and Professional Studies of
Texas A&M University
in partial fulfillment of the requirements for the degree of

DOCTOR OF PHILOSOPHY

Chair of Committee,	Petros Sideris
Committee Members,	Joseph Bracci
	Mary Beth Hueste
	Anastasia Muliana
Head of Department,	Robin Autenrieth

December 2019

Major Subject: Civil Engineering

Copyright 2019 Mohammad Taghi Nikoukalam Mofakham

ABSTRACT

In this dissertation, the concept of seismically resilient bridge columns with polyurethane (PU)-enhanced damage-resistant (DR) joints and replaceable energy dissipating (ED) links is proposed. The proposed system introduces the component of explicit damage control and accelerated low cost post-earthquake retrofit/repair in the design of bridges for moderate to high seismicity regions; hence, expanding the focus of the bridge engineering community from ABC to ABC&AR, where AR stands for “accelerated retrofit/repair”. PU-enhanced column with ED links offer: (i) explicit damage control through PU damage-resistant end segments (ii) self-centering through internal unbonded post-tensioning, (iii) energy dissipation and flexural stiffness/strength through external replaceable ED links.

The mechanical properties of selected PU materials with various compositions, was characterized through a comprehensive experimental program accounting for environmental conditions, loading conditions, and long term effects.

The performance of the proposed system was assessed through three-dimensional finite element analysis for various PU segment geometries and various ED link properties in terms of strength, stiffness, ductility capacity, energy dissipation properties, self-centering capabilities, and damage resistance.

Novel uniaxial visco-elastic/plastic constitutive models were developed capable of capturing the salient response features of the selected PU materials. The constitutive

models were calibrated using the test data. The developed constitutive models are implemented in the OpenSEES structural analysis software.

Seismic performance of the proposed system was assessed through numerical models of the proposed system generated in OpenSEES structural analysis software. The monotonic and cyclic response of the proposed system was investigated and compared with the response of a conventional reinforced concrete (RC) monolithic and rocking column. Moreover, the seismic performance of the proposed system was investigated via fragility analysis accounting for various damage states.

The performance of the proposed system was experimentally evaluated and compared to a conventional RC rocking column through large scale ($\sim 1:1.25$) quasi-static cyclic tests. Finally, the performance of the numerical models was validating with the test data. In summary, the proposed column design demonstrated a high ductility capacity associated with the damage in the replaceable ED links and the minor or no damage in other components of the system, and high re-centering capacity upon releasing/removing the ED links.

DEDICATION

In memory of my father and my son.

To my mother, and my wife, Hoda.

"...وَكَفَى بِالْمَرْءِ جَهْلًا أَلَّا يَعْرِفَ قَدْرَهُ..."

"... و همین بس برای جهل آدمی که قدر خود را نشناسد ..."

- امیرالمومنین علی (علیه السلام)
(نهج البلاغه، خطبه 102)

"...and this ignorance is enough for mankind that it does not know his value..."

- Imam Ali (600-661 A.D.)
(*Nahj al-balagha*, Sermon 102)

ACKNOWLEDGEMENTS

I would like to express my deepest gratitude to my supervisor, Dr. Petros Sideris, for his guidance, support, and patience over the course of the past five years. I benefitted significantly from his vast knowledge and experience in the field of Structural Engineering and Mechanics. Thanks also go to other members of my dissertation committee, Dr. Joseph Bracci, Dr. Mary Beth Hueste, and Dr. Anastasia Muliana for their feedback and encouragement.

The success of this research is in large part due to the invaluable support from BASF Company by donating polyurethane (PU) solutions and samples. I should single out Mr. Patrick Webster for being such a wonderful mentor by sharing his vast knowledge in the field of polymeric materials and providing guidance in the preparation of PU specimens.

I would also like to thank the staff at Structural and Material Testing Laboratory (SMTL) at University of Colorado-Boulder for providing the equipment for preparing and testing PU samples. I am especially thankful to Derek Carpenter for his assistance and his patience with my inexperience with tools and equipment. Furthermore, I wish to thank the personnel at Center for Infrastructure Renewal (CIR) of Texas A&M University, particularly Dr. Peter Keating and Charles Droddy, for their assistance and guidance during execution of my experimental work at CIR.

Thanks also go to my friends and colleagues and the department faculty and staff for making my time in University of Colorado-Boulder and Texas A&M University a great

experience. Special thanks go to Mohammad Aramfard, a true friend who never failed to cheer me up, for his kindness, generosity, and support, especially during difficult days when I needed words of encouragement.

I would also like to thank my beloved parents for being an endless source of peace and inspiration throughout my life. Nothing could be achieved without their sacrifice, advice, and prayers. I wish to extend my warmest thanks to my beloved wife, Hoda, for her continuous encouragement, patience, and support over the course of my studies and to my son, Mahdi, who, with his short presence in my life, taught me invaluable lessons and reminded me of what is most important in the life.

Above all, I would like to thank God, the Compassionate and the Merciful, for all of His blessings. All my accomplishments in my life has been due to His gracious kindness, and all thanks go to Him.

CONTRIBUTORS AND FUNDING SOURCES

Contributors

This work was supervised by a dissertation committee consisting of Dr. Petros Sideris (chair) and Dr. Joseph Bracci and Dr. Mary Beth Hueste of the Zachry Department of Civil and Environmental Engineering and Dr. Anastasia Muliana of the Department of Mechanical Engineering.

Funding Sources

This work was made possible in by funding provided by the Texas A&M University and the University of Colorado at Boulder, as well as support by the BASF company in terms of polymeric materials and expertise in polymer processing. Its contents are solely the responsibility of the authors and do not necessarily represent the official views of the sponsors.

TABLE OF CONTENTS

	Page
ABSTRACT	ii
DEDICATION	iv
ACKNOWLEDGEMENTS	v
CONTRIBUTORS AND FUNDING SOURCES.....	vii
TABLE OF CONTENTS	viii
LIST OF FIGURES.....	xii
LIST OF TABLES	xxxii
1. INTRODUCTION.....	1
1.1. Background and Problem Statement.....	1
1.2. Research Objectives and Scope.....	12
1.3. Dissertation Organization.....	15
2. PU-ENHANCED COLUMNS WITH ENERGY DISSIPATION LINKS: SYSTEM DEVELOPMENT AND DESIGN CONCEPTS.....	17
2.1. Introduction	17
2.2. Description of PU-enhanced Columns with Energy Dissipation Links.....	18
2.2.1. Mechanics of PU-enhanced Columns with ED Links: Simplified Analytical Model.....	21
2.3. Seismic Design Concepts for PU-enhanced Columns with Energy Dissipation Links.....	31
2.3.1. Displacement-based Seismic Design of PU-enhanced Columns with ED Links.....	31
2.4. Summary and Findings	36
3. CHARACTERIZATION OF THE MECHANICAL PROPERTIES OF POLYURETHANE MATERIALS	37
3.1. Introduction.....	37
3.2. Scope and Objectives	39
3.3. Experimental Program.....	39
3.3.1. Phase 1 – Exploration of Various PUs under Compressive Loading.....	39

3.3.2. Phase 2 – Compression Testing of Selected PUs	44
3.3.3. Phase 3 – Multi-test Program on ECast and ECore.....	52
3.4. Summary and Findings	111
4. FINITE ELEMENT SIMULATION OF PU-ENHANCED COLUMNS WITH ENERGY DISSIPATION LINKS	113
4.1. Scope and Objectives	113
4.2. Model Calibration for PU Specimens	113
4.2.1. Constitutive Relations	113
4.2.2. Model Validation for PU Test Specimen	118
4.3. Performance Assessment of Rocking Columns with PU End Segments	120
4.3.1. Reference Column	120
4.3.2. Finite Element Modeling.....	122
4.3.3. Parametric Study	125
4.4. Energy Dissipating Links.....	133
4.4.1. Design Concepts.....	133
4.4.2. Rocking Columns with PU DR Segments and ED Links	135
4.5. Summary and Findings	139
5. UNIAXIAL VISCOELASTIC SOFTENING VISCOPLASTIC MODEL FOR POLYURETHANE.....	142
5.1. Introduction	142
5.2. Scope and Objectives	146
5.3. Simplified Model.....	147
5.3.1. Model Description.....	147
5.3.2. Model Validation and Calibration.....	149
5.4. Advanced Model	152
5.4.1. Model Description.....	152
5.4.2. Constitutive Equations	154
5.4.3. Computational Implementation.....	162
5.4.4. Model Parameter Calibration Procedure	162
5.5. Summary and Findings	174
6. SEISMIC PERFORMANCE ASSESSMENT OF BRIDGE COLUMNS WITH POLYURETHANE-ENHANCED DAMAGE-RESISTANT END JOINTS AND ENERGY DISSIPATION LINKS	176
6.1. Scope and Objectives	176
6.2. Bridge Column Designs	176
6.2.1. Reference Conventional RC Column.....	176
6.2.2. RC Rocking Column	177
6.2.3. PU-enhanced Rocking Column with ED Links	178
6.3. Structural Modeling.....	180

6.3.1. Conventional Monolithic RC Column Modeling.....	180
6.3.2. RC Rocking Column Modeling.....	185
6.3.3. Modeling of PU-enhanced Rocking Column	188
6.3.4. Modeling of PU-enhanced Rocking Column with ED Links.....	189
6.4. Pushover Analysis.....	190
6.5. Cyclic Analysis	191
6.6. Seismic Fragility Assessment.....	195
6.6.1. Selected Damage States.....	196
6.6.2. Fragility Assessment	199
6.7. Summary and Findings	206

7. EXPERIMENTAL VALIDATION OF THE PERFORMANCE OF PRECAST CONCRETE ROCKING COLUMNS WITH POLYURETHANE END SEGMENTS 209

7.1. Scope and Objectives	209
7.2. Design of Specimens.....	209
7.2.1. Prototype Structure.....	209
7.2.2. Laboratory Test Specimens	210
7.3. Performance Assessment through CSM.....	216
7.4. Detailing of Test Specimens	219
7.4.1. Reinforced Concrete Elements.....	219
7.4.2. PU Segments	222
7.4.3. ED Links.....	223
7.4.4. Footing and Cap Beam	224
7.4.5. PT Anchorage Block	224
7.5. Test Setup.....	225
7.6. Instrumentation.....	228
7.7. Data Acquisition and Control System.....	239
7.7.1. Data Acquisition System	239
7.7.2. Control System	240
7.8. Data Processing.....	241
7.9. Construction Procedure	241
7.9.1. Specimens.....	241
7.9.2. Test Setup Assembly	252
7.10. Material Properties	256
7.10.1. Concrete.....	256
7.10.2. Reinforcing Steel.....	257
7.10.3. Post-tensioning Strands	258
7.10.4. PU Material	258
7.10.5. Energy Dissipation (ED) Links	260
7.10.6. Steel Collar and Attachments	260
7.11. Loading Sequence	260
7.11.1. RC Rocking Column	260
7.11.2. PU Rocking Column with Bi-layered PU Segment and ED Links	262

7.11.3. PU Rocking Column with Solid PU Segment.....	267
7.12. Test Results	270
7.12.1. RC Rocking Specimen	270
7.12.2. PUED-1 Specimen	289
7.12.3. PUED-2 Specimen	305
7.12.4. PU Specimen	338
7.13. Summary and Findings	352
8. VALIDATION OF THE NUMERICAL MODEL WITH TEST DATA	356
8.1. Scope and Objectives	356
8.2. Pre-test Blind Prediction	356
8.2.1. Finite Element Modeling.....	356
8.2.2. Simulation Results.....	359
8.3. Post-test Validation	371
8.3.1. Revised Finite Element Model.....	373
8.3.2. Simulation Results.....	374
8.4. Summary and Findings	386
9. SUMMARY, CONCLUSIONS, AND RECOMMENDATIONS FOR FUTURE RESEARCH	388
9.1. Summary	388
9.2. Major Conclusions	393
9.3. Original Contribution	399
9.4. Recommendations for Future Research	403
REFERENCES	408
APPENDIX A	424
APPENDIX B CAD DRAWINGS OF SPECIMENS	427

LIST OF FIGURES

	Page
Figure 1.1. Emulative column-to-footing socket connection proposed by Haraldsson et al. (2013).....	2
Figure 1.2. Emulative column connections: (a) grouted foundation socket connection (Reprinted from Lehman and Roeder (2012)); (b) pocket connection (Reprinted from Mehrsoroush (2014)).	3
Figure 1.3. Grouted duct column connection: (a) Restrepo et al. (2011); (b) Tazarv and Saiid Saiidi (2015)).....	3
Figure 1.4. Bar coupler column connections proposed by Haber et al. (2014): (a) connection details; (b) connection region before closure grouting (Reprinted from Haber et al. (2014)).....	4
Figure 1.5. Segmental concrete bridge columns with steel reinforcing bars as energy dissipation bars and internal unbonded posttensioning (Reprinted from Ou et al. 2010).	5
Figure 1.6. Precast columns and cap beam connection with partially unbonded prestressing strands (Reprinted from Thonstad et al. 2016).	6
Figure 1.7. Post-tensioned, precast concrete-filled tube (CFT) segmental bridge columns (Reprinted from Chou and Chen 2006).....	7
Figure 1.8. Posttensioned non-emulative column-footing connections with FRP wrap (Reprinted from White and Palermo 2016).	7
Figure 1.9. Segmental bridge columns with elastomeric bearing pad: (a) Elastomeric bearing pad; (b) base segment with elastomeric bearing pad (Reprinted from Motaref et al. 2013).	8
Figure 1.10. Non-emulative rocking connections with supplemental energy dissipation: (a) precast segmental unbonded posttensioned concrete bridge columns with internal partially unbonded bars (Reprinted from Ou et al. 2009); (b) post-tensioned, precast concrete-filled tube (CFT) segmental bridge columns with external energy-dissipating devices (Reprinted from Chou and Chen 2006); (c) posttensioned column-footing connections with external energy dissipation links (Reprinted from White and Palermo 2016). 10	10

Figure 1.11. Non-emulative rocking column connection with friction links (Reprinted from Morgen and Kurama 2004).	11
Figure 1.12. Hybrid sliding-rocking columns, introduced by Sideris (2012).	11
Figure 2.1. Schematic representation of the PU-enhanced column system with ED links: (a) system with solid PU segment; (b) system with bi-layered PU segment; (c) isometric view of the system in the vicinity of the PU segment; (d) details of the ED link.	20
Figure 2.2. (a) Typical PUED reference model; (b) cross section view; (c) strain distribution; (d) stress diagram for PU layer; (e) stress diagram for concrete layer (Not all ED links are shown for clarity purposes).	22
Figure 2.3. Capacity spectrum method flow-chart.	33
Figure 2.4. Graphical computation of F_{peak}^+ , F_{peak}^- , u_{peak}^+ and u_{peak}^- and K_{sec} at a given cycle.	35
Figure 3.1. Stress versus strain curve and deformed shape at 20% and 40%: (a) ECast; (b) ECore; (c) EShore.	44
Figure 3.2. Applied strain history for ECore and ECast.	47
Figure 3.3. Details of the test setup.	48
Figure 3.4. (a) Engineering stress vs. strain curves; (b) Strain recovery history of specimens at the end of loading application.	51
Figure 3.5. (a) Geometry of dog-bone specimens; (b) test setup for cylindrical specimens; (c) test setup for dog-bone specimens.	54
Figure 3.6. Test setup for tests at various temperatures.	55
Figure 3.7. (a) Vic-2d camera; (b) speckle pattern on a dog-bone specimen.	57
Figure 3.8. Toe compensation for material with Hookean region.	59
Figure 3.9. Multi-step relaxation test results: (a) stress-strain curves; (b) stress-time curves.	62
Figure 3.10. Stress relaxation ratio at each holding segment: (a) ECore; (b) ECast.	63
Figure 3.11. Stress-strain curves at various strain rates in compression: (a) ECore; (b) ECast.	67

Figure 3.12. Stress-strain curves from monotonic tensile tests at various strain rates: (a) ECore; (b) ECast.	67
Figure 3.13. Variation of compression overstress with strain rate at various strain levels: (a) ECore; (b) ECast.	68
Figure 3.14. Variation of compressive elastic modulus with strain rate: (a) ECore; (b) ECast.	69
Figure 3.15. Variation of tensile elastic modulus with strain rate at various strain levels: (a) ECore; (b) ECast.	70
Figure 3.16. Variation of response parameters under compression and tension with strain rate for ECast: (a) elastic modulus; (b) peak stress; (c) strain at peak stress.	71
Figure 3.17. Deformed shape of ECore specimens under monotonic compressive load at various strain rates: (a) un-deformed state; (b) peak compressive strain (~10%); (c) after unloading.	72
Figure 3.18. Deformed shape of ECast specimens under monotonic compressive load at various strain rates: (a) un-deformed state; (b) peak compressive strain (~10%); (c) after unloading.	73
Figure 3.19. Deformed shape of ECore specimens at the end of monotonic tensile load at strain rate of: (a) 0.001 /s; (b) 0.01 /s; (c) 0.05 /s.	73
Figure 3.20. Deformed shape of ECast specimens at the end of monotonic tensile load at strain rate of: (a) 0.001 /s; (b) 0.01 /s; (c) 0.05 /s.	74
Figure 3.21. Comparison of stress-strain results for monotonic compressive and compression-only cyclic loading at a strain rate of: (a) 0.001 /s; (b) 0.01 /s; (c) 0.05 /s.	77
Figure 3.22. Comparison of stress-strain results for monotonic tensile and tension- only cyclic loading at a strain rate of: (a) 0.001 /s; (b) 0.01 /s; (c) 0.05 /s (Early rupture occurred in specimen at the bottom grip).	78
Figure 3.23. Deformed shape of specimens at the end of cyclic tensile load at strain rate of 0.001 /s: (a) ECast; (b) ECore.	79
Figure 3.24. Loading protocol of combined cyclic compression-tension tests: (a) ECore; (b) ECast.	81

Figure 3.25. Cyclic compression-tension stress-strain curves at various strain rates: (a) ECore; (b) ECast.	82
Figure 3.26. Comparison of cyclic compression-tension and monotonic stress-strain curves for 0.001 /s strain rate: (a) ECore; (b) ECast.....	83
Figure 3.27. Effect of the loading-direction sequence on the response of ECast at 0.001 /s strain rate.....	83
Figure 3.28. Deformed shape of ECore and ECast specimens at different states of the reversed cyclic load at strain rate of 0.01 /s: (a), (d) peak tension; (b), (e) peak compression; (c), (f) end of the test [T: Tension; C: Compression].	84
Figure 3.29. (a) Creep strain-time curves from creep test at various stress levels; (b) creep compliance-time curves from creep test at various stress.....	87
Figure 3.30. Stress-time curves from relaxation test: (a) ECore; (b) ECast.....	88
Figure 3.31. Stress-strain curves of ECast at various strain rates and temperatures compared to room temperature: (a) +80 °C; (b) +60 °C; (c) +40 °C; (d) 0 °C; (e) -15 °C; (f) -20 °C.	91
Figure 3.32. Stress-strain curves of ECore at various strain rates and temperatures compared to room temperature: (a) +80 °C; (b) +40 °C; (c) 0 °C; (d) -15 °C.	92
Figure 3.33. Stress-strain curves at various temperatures for each strain rate: (a) 0.001 /s; (b) 0.01 /s; (c) 0.05 /s.	92
Figure 3.34. Variation of elastic modulus with strain rate at various temperatures: (a) ECore; (b) ECast.....	93
Figure 3.35. Variation of strength with strain rate at various temperatures: (a) ECore; (b) ECast.	93
Figure 3.36. Variation of elastic modulus with temperature for various strain rates: (a) ECore; (b) ECast.....	94
Figure 3.37. Variation of strength with temperature for various strain rates: (a) ECore; (b) ECast.	94
Figure 3.38. Layout of five virtual extensometers on the specimen surface.....	96
Figure 3.39. Strain measurements: clip-on extensometer versus DIC system from monotonic tensile test on ECore at various strain rates: (a) 0.001 /s; (b) 0.01 /s; (c) 0.05 /s.	97

Figure 3.40. Strain measurements: clip-on extensometer versus DIC system from monotonic tensile test on ECast at various strain rates: (a) 0.001 /s; (b) 0.01 /s; (c) 0.05 /s.	97
Figure 3.41. Location of lines of interest over the width of the area of interest.	98
Figure 3.42. Stress vs. strain curve of ECore at 0.01 /s strain rate determined using the clip-on extensometer, indicating the points taken for strain contour and strain distributions shown in Figure 3.43 and Figure 3.44, respectively.	99
Figure 3.43. Monotonic tensile test on ECore at 0.01 /s strain rate: strain field at various global strain levels in three dimensional (top row) and two dimensional (bottom row) space.	100
Figure 3.44. ECore under monotonic tensile load at 0.01 /s strain rate: local tensile strain distribution along three lines of interest at various global strain levels: (a) left line; (b) center line; (c) right line.	101
Figure 3.45. Stress vs. strain curve of ECast at 0.001 /s strain rate determined using the clip-on extensometer, indicating the points taken for strain contour and strain distributions shown in Figure 3.46 and Figure 3.47, respectively.	102
Figure 3.46. Monotonic tensile test on ECast at 0.001 /s strain rate: strain field at various global strain levels in three dimensional (top row) and two dimensional space (bottom row).	103
Figure 3.47. ECast under monotonic tensile load at 0.001 /s strain rate: local tensile strain distribution along three lines of interest at various global strain levels: (a) left line; (b) center line; (c) right line.	104
Figure 3.48. (a) Strain measurements time history: clip-on extensometer versus DIC system from monotonic compressive test on ECore at 0.001 /s strain rate; (b) relative strain error time history.	105
Figure 3.49. (a) Strain measurements time history: clip-on extensometer versus DIC system from monotonic compressive test on ECast at 0.001 /s strain rate; (b) relative strain error time history.	106
Figure 3.50. Stress vs. strain curve of ECore under monotonic compression load at 0.001 /s strain rate determined using the clip-on extensometer, indicating the points taken for strain contour and strain distributions shown in Figure 3.51 and Figure 3.52, respectively.	107

Figure 3.51. Monotonic compression test on ECore at 0.001 /s strain rate: strain field at various global strain levels (indicated in Figure 3.50) in three dimensional (top row) and two dimensional (bottom row) space.	107
Figure 3.52. ECore under monotonic compression load at 0.001 /s strain rate: local compressive strain distribution along three lines of interest at various global strain levels: (a) left line; (b) center line; (c) right line.....	108
Figure 3.53. Stress vs. strain curve of ECast under monotonic compression load at 0.001 /s strain rate determined using the clip-on extensometer, indicating the points taken for strain contour and strain distributions shown in Figure 3.54 and Figure 3.55, respectively.....	109
Figure 3.54. Monotonic compression test on ECast at 0.001 /s strain rate: strain field at various global strain levels (indicated in Figure 3.53) in three dimensional (top row) and two dimensional (bottom row) space.	110
Figure 3.55. ECast under monotonic compression load at 0.001 /s strain rate: local compressive strain distribution along three lines of interest at various global strain levels: (a) left line; (b) center line; (c) right line.....	111
Figure 4.1. Rheological representation of constitutive models for elastomers.	117
Figure 4.2. ABAQUS model of PU specimen.	119
Figure 4.3. Predicted and measured uniaxial compressive stress vs. strain response at different strain rates: (a) 0.001 s ⁻¹ ; (b) 0.01 s ⁻¹ ; (c) 0.05 s ⁻¹	120
Figure 4.4. Predicted and measured stress-strain and strain recovery relationships at different strain rates: (a) 0.001 s ⁻¹ ; (b) 0.01 s ⁻¹ ; (c) 0.05 s ⁻¹	120
Figure 4.5. Monolithic reference segmental column, reprinted from Motaref et al. (2013).....	122
Figure 4.6. Benchmark column verification results – comparison of lateral force versus drift ratio.	124
Figure 4.7. Nominal strain (NE33) on deformed shape of columns with PU segments at 15% drift ratio.	128
Figure 4.8. Lateral force versus drift ratio for various h_j/D_c ratios.	128
Figure 4.9. Variation of elastic stiffness with D_j/D_c and h_j/D_c	129
Figure 4.10. Column with PU segments: peak axial compressive strain for lateral drift ratios of 5% and 10% for: (a) concrete material; (b) PU segment.....	129

Figure 4.11. Cyclic behavior of columns with PU segments: (a) $D_j/D_c = 0.875$; (b) $D_j/D_c = 0.825$	131
Figure 4.12. (a) Cumulative dissipated energy (CDE); (b) relative self-centering efficiency (RSE).	132
Figure 4.13. Lateral force versus drift ratio for various loading rates.....	133
Figure 4.14. Details of ED link setup.....	135
Figure 4.15. Hysteretic response of columns with PU segments and ED links as function of λ_C parameter.	138
Figure 4.16. Column with PU segments and ED links: (a) cumulative dissipated energy; (b) relative self-centering efficiency.....	138
Figure 4.17. Recovery of residual drift after sequential removal of ED links.	138
Figure 5.1. (a) Rheological representation of constitutive model; (b) variation of damage reduction factor, R_n , with strain.....	149
Figure 5.2. Predicted and measured uniaxial compressive stress vs. strain response at different strain rates: (a) 0.001 /sec; (b) 0.01 /sec; (c) 0.05 /sec.....	151
Figure 5.3. Predicted and measured cyclic compressive stress vs. strain response at different strain rates: (a) 0.001 /sec; (b) 0.01 /sec; (c) 0.05 /sec.....	151
Figure 5.4. Rheological structure of the advanced model.	153
Figure 5.5. (a) Approximate fit of the response with a minimal set of material parameters per Step 1; (b) fitting of Weibull function of damage factor of Eq. (5.13) to test data; (c) approximate fit of the response including the damage in the yield surface per Step 2.	165
Figure 5.6. Fit of rate-dependent Weibull function for viscosity, Eq. (5.18), to test data.....	166
Figure 5.7. Fit of the model with minimal set of parameters, per Step 3, to the monotonic compression tests on cylindrical specimens at various strain rates: (a) 0.001 /s; (b) 0.01 /s; (c) 0.05 /s.....	166
Figure 5.8. Fit of the model with damage to the overstress to the monotonic compression tests on cylindrical specimens at various strain rates: (a) 0.001 /s; (b) 0.01 /s; (c) 0.05 /s.....	167

Figure 5.9. Fit of the model with damage to the overstress and yield strength to the monotonic tension tests on dog-bone specimens at various strain rates: (a) 0.001 /s; (b) 0.01 /s; (c) 0.05 /s.....	168
Figure 5.10. Schematic representation of the effect of viscoelastic elements on the response.	170
Figure 5.11. Fit of the model to the cyclic compression-tension test on dog-bone specimen at 0.001 /s strain rate.....	171
Figure 5.12. Fit of the full model to the equilibrium path stress-strain relationship.....	171
Figure 5.13. Fit of the full model to the monotonic compression tests on cylindrical specimens at various strain rates: (a) 0.001 /s; (b) 0.01 /s; (c) 0.05 /s.....	172
Figure 5.14. Fit of the full model to the monotonic tension tests on dog-bone specimens at various strain rates: (a) 0.001 /s; (b) 0.01 /s; (c) 0.05 /s.....	172
Figure 5.15. Fit of the model to: (a) 48-hours relaxation test data; (b) 5-days creep test data at various stress levels.....	173
Figure 6.1. (a) Elevation view of the Jack Tone Road overcrossing Kaviani et al. 2014; (b) cross-section of the column.	177
Figure 6.2. Schematic representation of the FE model of the columns: (a) RC monolithic, (b) RC rocking, (c) PU rocking, (d) PU with ED links; (e) cross- section of the monolithic RC reference column; (f) cross-section of the RC segment of rocking columns.....	180
Figure 6.3. Comparison of lateral load-drift ratio curve between the FE model and the cyclic test for BC specimen by Nikoukalam and Sideris (2016a): (a) without bond-slip; (b) with bond-slip.	184
Figure 6.4. Uniaxial elastic multilinear response of the zero-length gap element.	186
Figure 6.5. Comparison of model prediction to test results for (a) JH1 specimen, and (b) JH2 specimen: (I) predicted cyclic lateral load versus drift ratio compared to the backbone of the cyclic test result; (II) cyclic test result (Hewes and Priestley 2002); (III) predicted strain increase in PT system-drift ratio compared to the test data (Hewes and Priestley 2002).....	188
Figure 6.6. Monotonic response of different column systems and various damage states.	191

Figure 6.7. Cyclic response of columns: (a) RC monolithic vs. RC rocking vs. PU column; (b) PUED column with $\lambda_C = 0.25$ vs. PU column; (c) PUED column with $\lambda_C = 0.5$ vs. PU column.	192
Figure 6.8. Graphical computation of F_{peak}^+ , F_{peak}^- , u_{peak}^+ and u_{peak}^- and K_{sec} at a given cycle.	194
Figure 6.9. (a) Equivalent viscous damping ratio vs. peak column drift ratio; (b) residual drift ratio vs. peak column drift ratio.	195
Figure 6.10. Fragility curves for the DSs of: (a) system demolition/replacement, and (b) structural collapse; (c) median capacities for system demolition/replacement and structural collapse.	202
Figure 6.11. Fragility curves, using IM definition based on fundamental periods for each individual column system, for the DSs of: (a) system demolition/replacement, and (b) structural collapse; (c) median capacities for system demolition/replacement and structural collapse.	202
Figure 6.12. Fragility curves for the DSs of: (a) cover spalling, and (b) core crushing; (c) median capacities for cover spalling and core crushing.	203
Figure 6.13. (a) Fragility curves for the DS of PU proportionality limit; (b) median capacities.	204
Figure 6.14. Fragility curves for the DSs of: (a) PT bar yielding, and (b) PT bar rupture; (c) median capacities for PT bar yielding and rupture.	205
Figure 6.15. Fragility curves, using IM definition based on fundamental periods for each individual column system, for the DSs of: (a) PT bar yielding, and (b) PT bar rupture; (c) median capacities for PT bar yielding and rupture.	205
Figure 6.16. Fragility curves for the two PUED columns for the DSs of: (a) ED link yielding, and (b) ED link rupture; (c) median capacities for ED link yielding and rupture.	206
Figure 7.1. Lateral force versus drift ratio for rocking column with bi-layered PU segment with various concrete core diameter.	215
Figure 7.2. Schematic view of test specimens: (a) RC rocking column; (b) rocking column with solid PU end segment; (c) rocking column with bi-layered PU end segment; (d) rocking column with bi-layered PU end segment and ED Links (All dimensions are in inches. Section views are for the base section at the foundation level. ED links are not shown in section view).	216

Figure 7.3. Response spectrum in prototype and model domain: (a) DE; (b) MCE.....	218
Figure 7.4. Performance point at various hazard levels: (a) RC rocking column; (b) PU enhanced column; (c) PUED column.	218
Figure 7.5. RC rocking column: geometry and reinforcement details.	220
Figure 7.6. RC segment with steel collar: geometry and reinforcement details.	221
Figure 7.7. Steel collar: geometry details.....	222
Figure 7.8. Bi-layered PU segment: geometry and reinforcement details.	223
Figure 7.9. Details of the ED link setup.	224
Figure 7.10. PT anchorage block: geometry and reinforcement details (Note: Details of the multi-plane anchor are not shown.).....	225
Figure 7.11. Schematic representation of test setup for RC rocking column: (a) east- west elevation (looking south); (b) south-north elevation (looking west) (support wall not shown) (Note: Instrumentation not shown.).....	227
Figure 7.12. Schematic representation of instrumentation for RC rocking specimen: (a) south-north elevation (looking west); (b) east-west elevation (looking south).	231
Figure 7.13. RC rocking column test setup.....	232
Figure 7.14. Schematic representation of instrumentation for PUED rocking specimen: (a) south-north elevation (looking west); (b) east-west elevation (looking south); (c) ED link elongation string potentiometers (Note: ED links not shown.).....	234
Figure 7.15. PUED column test setup.	235
Figure 7.16. Schematic representation of instrumentation for PU rocking specimen: (a) south-north elevation (looking west); (b) east-west elevation (looking south) (Note: ED links not shown.).....	237
Figure 7.17. PU enhanced column test setup.	238
Figure 7.18. Components of the PT anchorage system.....	242
Figure 7.19. Reinforcement cages: (a) RC rocking column; (b) PT anchorage block; (c) central core of PU bi-layered segment; (d) RC segment with steel collar; (e) cap beam.....	242

Figure 7.20. (a) Foundation rebar cage in formwork; (b) ED link end anchor setup.....	243
Figure 7.21. (a) Lowering the rebar cage of RC rocking column to formwork; (b) central PVC pipe secured and sealed.....	244
Figure 7.22. Construction steps for RC segment with steel collar: (a) steel collar and central steel pipe; (b) plan view of steel collar and central steel pipe; (c) central pipe assembled; (d) details of the central pipe assembly.....	246
Figure 7.23. Construction steps for PT anchorage block: (a) embedded components of the PT system; (b) top view of the final assembly; (c) isometric view of the final assembly.	247
Figure 7.24. Cap beam reinforcement cage in the formwork: final assembly.	248
Figure 7.25. RC elements in the formwork prior to casting.....	249
Figure 7.26. Casting: (a) first batch (morning); (b) second batch (afternoon).....	250
Figure 7.27. (a) Surface air voids were observed on the top surface of the foundation block; (b) surface patched with non-shrink grout.....	250
Figure 7.28. Casting of PU sleeve: (a) mold shells bolted to the base plate; (b) sealing the top interface; (c) heating the silicone sealant; (d) bolting the top lid; (e) sealing bolted connections; (f) final mold assembly prior to casting; (g) injecting the PU material solution; (h) PU sleeve after demolding.	252
Figure 7.29. Test setup assembly steps for RC rocking specimen: (a) foundation blocked to pass the strands; (b) lowering the foundation block; (c) lowering segment(s); (d) lowering cap-beam-actuators assembly; (e) placing load cells in position; (f) lowering PT anchorage block; (g) post-tensioning.	255
Figure 7.30. Test setup assembly for PU-enhanced column with bi-layered PU segment: (a) moving bi-layered PU segment; (b) lowering the RC segment with steel collar in place; (c) passing the pipe sticking out of the RC segment through the PU segment.	255
Figure 7.31. Location of enlarged slotted holes on mounting eyes of the steel collar (the cut is shown in red).....	256
Figure 7.32. Test setup for compression test on cylindrical specimens.....	259
Figure 7.33. Compressive stress-strain curves at various strain rates.....	259

Figure 7.34. Comparison of compressive stress-strain curves for specimens tested at CIR and SMTL at various strain rates: (a) 0.001 /sec; (b) 0.01 /sec; (c) 0.05 /sec.	260
Figure 7.35 . Damage in RC rocking column at various drift ratios.	275
Figure 7.36. Damage in RC rocking column: hoops exposed at 3.7% drift ratio: (a) east side; (b) west side.	277
Figure 7.37. Damage in RC rocking column at 5.54% drift ratio: (a) crack in the core concrete on east side; (b) hoops exposed on the west side.	278
Figure 7.38. Damage in RC rocking column at 7.39% drift ratio: (a) vertical crack in the core concrete and extensive concrete crushing on east side; (b) extensive concrete crushing on the west side; (c) grout delamination on foundation block surface.	278
Figure 7.39. Damage in RC rocking column at 11.09% drift ratio: opening of vertical crack in the core concrete on east side.	278
Figure 7.40. Damage in RC rocking column at 12.93% drift ratio: exposure of longitudinal rebar.	279
Figure 7.41. Damage inspection of RC column after loose concrete was removed.	280
Figure 7.42. Visual inspection of the damage state in the vicinity of the rocking joint.	281
Figure 7.43. Longitudinal rebar buckling/bending in RC rocking column.	281
Figure 7.44. Damage in the foundation at the location of longitudinal rebar of the RC rocking column.	282
Figure 7.45. Lateral load vs. drift ratio hysteresis curve for the RC rocking column.	283
Figure 7.46. (a) Post-tensioning load vs. peak drift ratio for the RC rocking column; (b) post-tensioning load at the end of each cycle vs. peak drift ratio.	284
Figure 7.47. Average curvature at the base of the RC rocking column vs. drift ratio.	285
Figure 7.48. RC rocking column: (a) cumulative dissipated energy versus drift ratio; (b) equivalent viscous damping versus drift ratio.	287
Figure 7.49. RC rocking column: (a) relative self-centering efficiency (RSE); (b) residual drift ratio.	289

Figure 7.50. Connection loosened in ED links in PUED rocking column at 0.4×DE level: (a) location of ED links with loosened connection (orange circles); (b) ED-5 with hammer wrench on for retightening.....	290
Figure 7.51. Washers deformed in top connection of ED links in PUED rocking column at 1.2×DE: (a) location of ED links with deformed washers (brown circles); (b) ED-1; (c) ED-6; (d) ED-8.	291
Figure 7.52. Slight local buckling at top connection of ED links in PUED rocking column at 1.2×DE: (a) location of damaged ED links (brown circles); (b) ED-5 and ED-6; (c) ED-8.	292
Figure 7.53. Cracks in concrete in PUED rocking column at 1.8×DE: (a) east side; (b) west side.....	293
Figure 7.54. Damage in top connection of ED links in PUED rocking column at 1.8×DE: (a) location of damaged links (red circles); (b) damage in ED-6; (c) damage in ED-8.	293
Figure 7.55. Minor grout delamination at PU-foundation interface in PUED-1 rocking column at 1.8×DE.....	294
Figure 7.56. Cutting damaged ED links with hand band-saw.....	295
Figure 7.57. PUED-1 specimen: extracted view of ED links.....	295
Figure 7.58. Lateral load vs. drift ratio hysteresis curve for the PUED-1 rocking column at different hazard levels.....	297
Figure 7.59. Lateral load vs. drift ratio hysteresis curve: PUED-1 vs. RC rocking column.	298
Figure 7.60. (a) Post-tensioning load vs. peak drift ratio for the PUED-1 column; (b) post-tensioning load at the end of each cycle vs. peak drift ratio.....	300
Figure 7.61. Average curvature at the base of the bi-layered PU segment vs. drift ratio.....	301
Figure 7.62. PUED-1 column vs. RC rocking column: (a) cumulative dissipated energy; (b) equivalent viscous damping.	302
Figure 7.63. PUED-1 column vs. RC rocking column: (a) relative self-centering efficiency (RSE); (b) residual drift ratio.....	303
Figure 7.64. Normalized axial deformation in ED links versus drift ratio.....	304

Figure 7.65. 3/8” thick plate washers at the top connection of ED links.	306
Figure 7.66. Damage state in PUED-2 column at 1.8×DE (1.2×MCE): (a) cracks in concrete on east side; (b) cracks in concrete on west side; (c) location of fractured ED links (red circles).....	308
Figure 7.67. Damage state in PUED-2 column at 1.8×DE (1.2×MCE) at the loading rate of 2.71 in/sec (0.025 drift ratio/sec): (a) cover concrete spalling on east side; (b) cover concrete spalling on west side; (c) location of fractured ED link (red circle).	309
Figure 7.68. Location of ED links removed from PUED-2 specimen (gray circles) at the end of Phase 2.3 of the testing program.....	310
Figure 7.69. Damage state in PUED-2 column at 7.39% drift ratio at the loading rate of 1.08 in/sec (0.01 drift ratio/sec): (a) southeast side; (b) west side.	311
Figure 7.70. Damage state in PUED-2 column at 9.24% drift ratio at the loading rate of 1.08 in/sec (0.01 drift ratio/sec): (a) long crack in PU on northeast side; (b) short cracks in PU on east side; (c) grout delamination and cracks in PU.	312
Figure 7.71. Damage state in PUED-2 column at 9.24% drift ratio at the loading rate of 2.71 in/sec (0.025 drift ratio/sec): (a) PU complete fracture on east side; (b) crack in PU on northeast side.....	313
Figure 7.72. Visual inspection of the damage state at the top and bottom surfaces of the bi-layered PU segment.....	314
Figure 7.73. PUED-2 specimen: extracted view of ED links.....	315
Figure 7.74. Damage in ED-1.	316
Figure 7.75. Damage in ED-5.	317
Figure 7.76. Damage in ED-6.	318
Figure 7.77. Lateral load vs. drift ratio hysteresis curve for the PUED-2 column at different hazard levels, per Phase 2.1.	319
Figure 7.78. PUED-2 column response history over ED link release and retightening: (a) lateral load time history; (b) lateral displacement time history.....	321
Figure 7.79. Lateral load vs. drift ratio hysteresis curve for the PUED-2 column at different hazard levels before (PUED-2.1) and after (PUED-2.2) recovery.	322

Figure 7.80. Lateral load vs. drift ratio hysteresis curve for the PUED-2 column: (a) comparison to PUED-1 specimen at 1.8×DE (1.2×MCE) hazard level; (b) all hazard levels (0.4×DE, 0.6×DE, 1.2×DE, and 1.8×DE (1.2×MCE)).	323
Figure 7.81. Lateral load vs. drift ratio hysteresis curve for the PUED-2 column at different hazard levels and loading rates.	325
Figure 7.82. Lateral load vs. drift ratio hysteresis curve for the PUED-2 column up to 8" (7.39% drift ratio) lateral displacement at various loading rates.	327
Figure 7.83. Lateral load vs. drift ratio hysteresis curve for the PUED-2.4 column up to 10 in. (Phase 2.4) lateral displacement (9.24% drift ratio) at 0.01 /sec loading rates.	328
Figure 7.84. Lateral load vs. drift ratio hysteresis curve: PUED-2.4 with two ED links vs. RC rocking column.	329
Figure 7.85. PUED-2 column: (a) post-tensioning load vs. peak drift ratio; (b) post-tensioning load at the end of each cycle vs. peak drift ratio.	331
Figure 7.86. Curvature at the base of the bi-layered PU segment vs. drift ratio: PUED-2 vs. PUED-1 and RC rocking column.	332
Figure 7.87. PUED-2 column vs. RC rocking column: (a) cumulative dissipated energy; (b) equivalent viscous damping.	333
Figure 7.88. PUED-2 column vs. PUED-1 and RC rocking columns: (a) relative self-centering efficiency (RSE); (b) residual drift ratio.	335
Figure 7.89. Normalized axial deformation in ED links versus drift ratio: PUED-2, Phase 2.1 and 2.2.	336
Figure 7.90. Normalized axial deformation in ED links versus drift ratio: PUED-2, Phase 2.3.	337
Figure 7.91. Normalized axial deformation in ED links versus drift ratio: PUED-2, Phase 2.4.	337
Figure 7.92. Damage state in PU column at 1.2×DE: (a) grout delamination at the loading rate of 0.11 in/sec; (b) crack in concrete at the loading rate of 5.41 in/sec.	339
Figure 7.93. PU column at 1.8×DE (1.2×MCE) at the loading rate of 0.11 in/sec: gap at the PU-foundation interface.	340

Figure 7.94. PU column at $1.8 \times DE$ ($1.2 \times MCE$) at the loading rate of 0.11 in/sec: crack in cover concrete.	341
Figure 7.95. PU column at $1.8 \times DE$ ($1.2 \times MCE$) at the loading rate of 1.08 in/sec: (a) and (b): gap size increased on east and west sides; (c) crack in cover concrete.....	341
Figure 7.96. Lateral load vs. drift ratio hysteresis curve for the PU column at different hazard levels and loading rates.	343
Figure 7.97. Lateral load vs. drift ratio hysteresis curve: PU column vs. PUED-2.4 column with two ED links, PUED-1, and RC rocking column.	345
Figure 7.98. Post-tensioning load vs. peak drift ratio for PU column at the hazard levels.	346
Figure 7.99. Post-tensioning load at the end of each cycle vs. peak drift ratio for PU column at various hazard levels.....	347
Figure 7.100. (a) Curvature at the top and bottom interface of the PU segment vs. drift ratio; (b) curvature at the bottom PU interface: PU column vs. PUED-2.2 and PUED-2.4.....	348
Figure 7.101. PU column vs. PUED and RC rocking columns: (a) cumulative dissipated energy; (b) equivalent viscous damping.	349
Figure 7.102. PU column vs. PUED and RC rocking columns: (a) relative self- centering efficiency (RSE); (b) residual drift ratio.....	350
Figure 8.1. Schematic representation of the FE model of the PUED specimen.....	359
Figure 8.2. Comparison of experimental and predicted response of RC rocking column from the original model: (a) lateral load vs. drift ratio; (b) post- tensioning load vs. drift ratio.	360
Figure 8.3. Comparison of experimental and predicted response of RC rocking column from the original model: (a) peak post-tensioning load vs. drift ratio; (b) final post-tensioning load vs. drift ratio.....	361
Figure 8.4. Comparison of experimental and predicted response of RC rocking column from the original model: (a) average residual drift ratio vs. drift ratio; (b) equivalent viscous damping vs. drift ratio.....	362

Figure 8.5. Comparison of experimental and predicted response of PUED-2 column from the original model: (a) lateral load vs. drift ratio; (b) post-tensioning load vs. drift ratio.....	364
Figure 8.6. Comparison of experimental and predicted response of PUED-2 column from the original model: (a) peak post-tensioning load vs. drift ratio; (b) final post-tensioning load vs. drift ratio.....	366
Figure 8.7. Comparison of experimental and predicted response of PUED-2 column from the original model: (a) average residual drift ratio vs. drift ratio; (b) equivalent viscous damping vs. drift ratio.....	368
Figure 8.8. Comparison of experimental and predicted response of PU column from the original model: (a) lateral load vs. drift ratio; (b) post-tensioning load vs. drift ratio.....	369
Figure 8.9. Comparison of experimental and predicted response of PU column from the original model: (a) peak post-tensioning load vs. drift ratio; (b) final post-tensioning load vs. drift ratio.....	370
Figure 8.10. Comparison of experimental and predicted response of PU column from the original model: (a) average residual drift ratio vs. drift ratio; (b) equivalent viscous damping vs. drift ratio.....	371
Figure 8.11. Comparison of experimental and predicted response of RC rocking column from the revised model: (a) lateral load vs. drift ratio; (b) post-tensioning load vs. drift ratio.....	375
Figure 8.12. Comparison of experimental and predicted response of RC rocking column from the original and revised model: (a) peak post-tensioning load vs. drift ratio; (b) final post-tensioning load vs. drift ratio.....	376
Figure 8.13. Comparison of experimental and predicted response of RC rocking column from the original and revised model: (a) average residual drift ratio vs. drift ratio; (b) equivalent viscous damping vs. drift ratio.....	377
Figure 8.14. Comparison of experimental and predicted response of PUED-2 column from the revised model: (a) lateral load vs. drift ratio; (b) post-tensioning load vs. drift ratio.....	378
Figure 8.15. Comparison of experimental and predicted response of RC rocking column from the revised model (2): (a) lateral load vs. drift ratio; (b) post-tensioning load vs. drift ratio.....	380

Figure 8.16. Comparison of experimental and predicted response of PUED-2 column from the original and revised models: (a) peak post-tensioning load vs. drift ratio; (b) final post-tensioning load vs. drift ratio.....	381
Figure 8.17. Comparison of experimental and predicted response of PUED-2 column from the original and revised model: (a) average residual drift ratio vs. drift ratio; (b) equivalent viscous damping vs. drift ratio.....	383
Figure 8.18. Comparison of experimental and predicted response of PU column from the revised model (1): (a) lateral load vs. drift ratio; (b) post-tensioning load vs. drift ratio.....	384
Figure 8.19. Comparison of experimental and predicted response of PU column from the original and revised model: (a) peak post-tensioning load vs. drift ratio; (b) final post-tensioning load vs. drift ratio.	385
Figure 8.20. Comparison of experimental and predicted response of PU column from the original and revised model: (a) average residual drift ratio vs. drift ratio; (b) equivalent viscous damping vs. drift ratio.	386
Figure A.1. Reproducibility of ECore response: Monotonic compression test at various strain rates.	424
Figure A.2. Reproducibility of ECast response: Monotonic compression test at various strain rates.	424
Figure A.3. Reproducibility of cyclic compression-only response at 0.001 /s strain rate: (a) ECore, (b) ECast.	425
Figure A.4. Heat flow versus temperature for ECore.	425
Figure A.5. Heat flow versus temperature for ECast.	426
Figure B.1. General notes and abbreviations.	428
Figure B.2. Geometry details: RC segments.	429
Figure B.3. Reinforcement layout: RC segments.....	430
Figure B.4. Details of reinforcement: RC segments.	431
Figure B.5. Geometry details: cap beam.	432
Figure B.6. Reinforcement layout: cap beam.....	433

Figure B.7. Details of reinforcement: cap beam.	434
Figure B.8. Geometry details: foundation block.	435
Figure B.9. Reinforcement layout: foundation block.....	436
Figure B.10. Details of reinforcement: foundation block.	437
Figure B.11. Details of solid PU segment.	438
Figure B.12. Details of PU sleeve.	439
Figure B.13. Details of steel collar.....	440
Figure B.14. Details of ED link.....	441
Figure B.15. Details of load cell assembly.....	442
Figure B.16. Details of load cell body.	443
Figure B.17. Details of load cell end plates.	444

LIST OF TABLES

	Page
Table 3.1. Main chemical components of polyurethanes.....	40
Table 3.2. Summary of mechanical properties for ECore.....	51
Table 3.3. Summary of mechanical properties for ECast.	51
Table 3.4. Summary of strain recovery response.	52
Table 3.5. Multi-step relaxation test: summary of test procedure parameters.	61
Table 3.6. Monotonic compression test: summary of test procedure parameters.	65
Table 3.7. Monotonic tension test: summary of test procedure parameters.....	65
Table 3.8. Elastic modulus in tension and compression at various strain rates.	70
Table 3.9. Cyclic compression-only test: summary of test procedure parameters.....	76
Table 3.10. Cyclic tension-only test: summary of test procedure parameters.	76
Table 3.11. Fracture srtarin of ECast under tensile monotonic and cyclic load.	78
Table 3.12. Combined compressio-tension cyclic test: summary of test procedure parameters.....	80
Table 3.13. Summary of relaxation testing procedure.	86
Table 3.14. Summary of relaxation test results.	88
Table 4.1. Constitutive model parameters.....	118
Table 5.1. Calibrated model parameters.....	151
Table 6.1. Reference column structural and geometric parameters.	177
Table 6.2. Design details of the monolithic and rocking columns.	178
Table 6.3. Damage states definition matrix.....	199
Table 7.1. Scale factors for monolithic column specimen.	211

Table 7.2. Summary of design details of the reinforced concrete monolithic and rocking columns.....	213
Table 7.3. Performance point at various hazard levels for various test specimens.....	219
Table 7.4. Instrumentation list for RC rocking column.	233
Table 7.5. Instrumentation list for PUED-1 and PUED-2 columns.	236
Table 7.6. Instrumentation list for PU column.....	239
Table 7.7. Concrete compression strength.	257
Table 7.8. Mechanical properties of the reinforcing steel.	257
Table 7.9. Displacement-controlled loading sequence for RC rocking column.	262
Table 7.10. Displacement-controlled loading sequence for PUED-1 rocking column. .	264
Table 7.11. Displacement-controlled loading sequence for PUED-2 rocking column. .	266
Table 7.12. PT load and PT loss at different states.	268
Table 7.13. Displacement-controlled loading sequence for PU rocking column.....	269
Table 7.14. RC rocking column: equivalent viscous damping, RSE, and RDR at various hazard levels.....	289
Table 7.15. Summary of peak lateral strength in positive and negative direction at various hazard levels: PUED-1 specimen.....	298
Table 7.16. PUED-1 column vs RC rocking column: equivalent viscous damping, RSE, and RDR at various hazard levels.	303
Table 7.17. Summary of peak lateral strength in positive and negative direction at various hazard levels: PUED-2 specimen, Phase 2.1 and 2.2.	323
Table 7.18. Summary of peak lateral strength in positive and negative direction at various hazard levels and loading rates: PUED-2 specimen, Phase 2.3.....	326
Table 7.19. Summary of peak lateral strength in positive and negative direction at various hazard levels and loading rates: PU specimen.....	343
Table 7.20. Equivalent viscous damping at various hazard levels for all specimens. ...	351

Table 7.21. Relative self-centering efficiency (RSE) at various hazard levels for all specimens.....	351
Table 7.22. Average residual drift ratio (RDR) at various hazard levels for all specimens.....	351
Table 8.1. Comparison of experimental and predicted peak lateral strength for PUED-2 column in Phase 2.2 from the original model in positive and negative direction at various hazard levels.	365
Table 8.2. Comparison of experimental and predicted peak lateral strength for PUED-2 column in Phase 2.3 from the original model in positive and negative direction at various hazard levels.	365
Table 8.3. Comparison of experimental and predicted peak lateral strength for PUED-2 column in Phase 2.4 from the original model in positive and negative direction at various peak drift ratios.	365
Table 8.4. Comparison of experimental and predicted peak lateral strength for PU column from the original model in positive and negative direction at various hazard levels.	370
Table 8.5. Comparison of experimental and predicted peak lateral strength for PUED-2 column in Phase 2.2 from the revised model (1) in positive and negative direction at various hazard levels.	379
Table 8.6. Comparison of experimental and predicted peak lateral strength for PUED-2 column in Phase 2.3 from the revised model (1) in positive and negative direction at various hazard levels.	379
Table 8.7. Comparison of experimental and predicted peak lateral strength for PUED-2 column in Phase 2.4 from the revised model (1) in positive and negative direction at various peak drift ratios.	379
Table 8.8. Comparison of experimental and predicted peak lateral strength for PU column from the revised model in positive and negative direction at various hazard levels.	385

1. INTRODUCTION

1.1. Background and Problem Statement

In the U.S., a vast number of bridges, several of which are located in regions of moderate and high seismicity, have been classified as structurally deficient and/or functionally obsolete (ASCE's Report Card for America's Infrastructure (2017)). These bridges are in need of immediate replacement or retrofit in order to meet performance objectives stated in the current design codes (e.g., AASHTO LRFD Bridge Design Specifications (2014)). To perform bridge replacement in seismic regions with minor service disruption, several efforts have been made over the last decade to develop systems that combine construction rapidity and improved seismic performance.

Segmental precast concrete bridge superstructures have long been used as a means of accelerating construction. However, precast substructure systems have rarely been used in the regions of moderate or high seismicity, due to concerns about their seismic performance, primarily originating from lack of sufficiently proven seismically resistant connection details and available design specifications.

To address this challenge, research efforts over the past two decades have developed and investigated several seismically resistant column connection details. These connections can be broadly categorized into *emulative* (or monolithic) and *non-emulative*. The most common types of emulative connections are the socket or pocket connections (Figure 1.1 and 1.2) (Haraldsson et al. 2009; Lehman and Roeder 2012; Haraldsson et al. 2013; Mehrsoroush 2014), grouted duct connections (Figure 1.3) (Brenes et al. 2006;

Matsumoto et al. 2008; Steuck et al. 2009; Pang et al. 2010; Restrepo et al. 2011; Pantelides et al. 2014; Tazarv and Saiid Saiidi 2015; Tazarv and Saiidi 2015), and bar coupler connections (Figure 1.4) (Haber et al. 2014; Pantelides et al. 2014; Tazarv and Saiidi 2016). Although these connections can ensure life safety and collapse prevention, they sustain significant damage in the form of concrete cover spalling and core crushing, rebar yielding and rupture, and large residual deformations, often requiring system demolition and replacement.



Figure 1.1. Emulative column-to-footing socket connection proposed by Haraldsson et al. (2013).

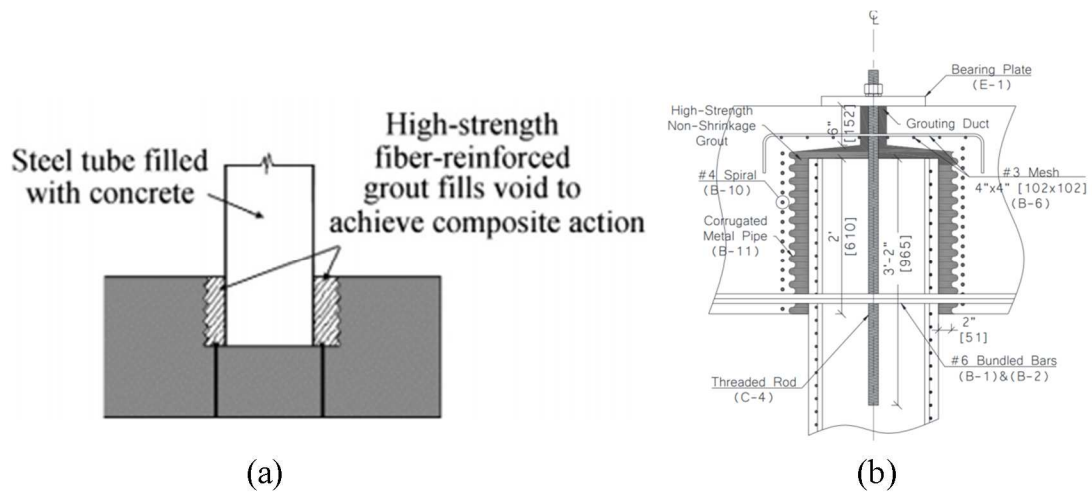
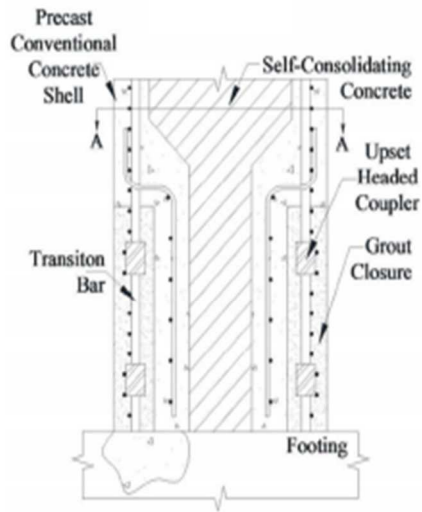


Figure 1.2. Emulative column connections: (a) grouted foundation socket connection (Reprinted from Lehman and Roeder (2012)); (b) pocket connection (Reprinted from Mehrsoroush (2014)).



Figure 1.3. Grouted duct column connection: (a) Restrepo et al. (2011); (b) Tazary and Saiid Saiidi (2015)).



(a)



(b)

Figure 1.4. Bar coupler column connections proposed by Haber et al. (2014): (a) connection details; (b) connection region before closure grouting (Reprinted from Haber et al. (2014)).

To address the limitations of emulative systems, building on early work by Mander and Cheng (1997), precast columns with rocking end joints/connections, internal unbonded posttensioning, and hysteretic energy dissipation (ED) links at the joints (Figure 1.5) (Hewes and Priestley 2002; Chou and Chen 2006; Hewes 2007; Yamashita and Sanders 2009; Ou et al. 2010; Restrepo et al. 2011; ElGawady and Dawood 2012) have been explored as a means of reducing peak and residual displacement demands. More recently, columns with pre-tensioned unbonded strands in socket footings or bent-caps (Figure 1.6) (Davis 2011; Finnsson 2013; Thonstad et al. 2016; Davis et al. 2017) have been explored with the objective of further reducing on-site construction times by eliminating the need for on-site post-tensioning application. Other studies have investigated use of shape memory alloy rebar at the joints (Nakashoji 2014; Varela and

Saiidi 2014; Varela and Saiidi 2017) as a means of reducing residual deformations. Rather than non-emulative systems, the posttensioning system has been used in emulative base connections with posttensioned precast segments above the base segment (Ou et al. 2013).

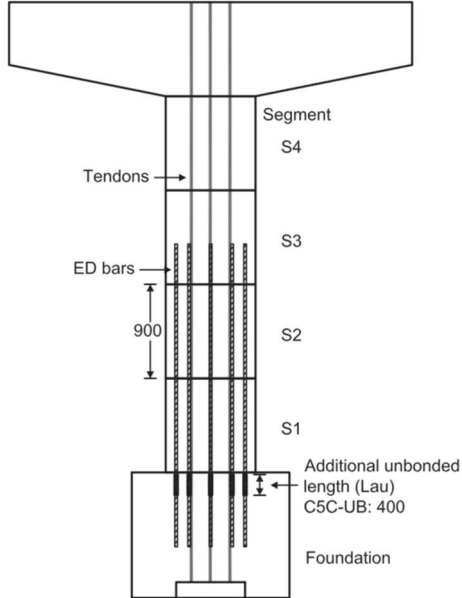


Figure 1.5. Segmental concrete bridge columns with steel reinforcing bars as energy dissipation bars and internal unbonded posttensioning (Reprinted from Ou et al. 2010).

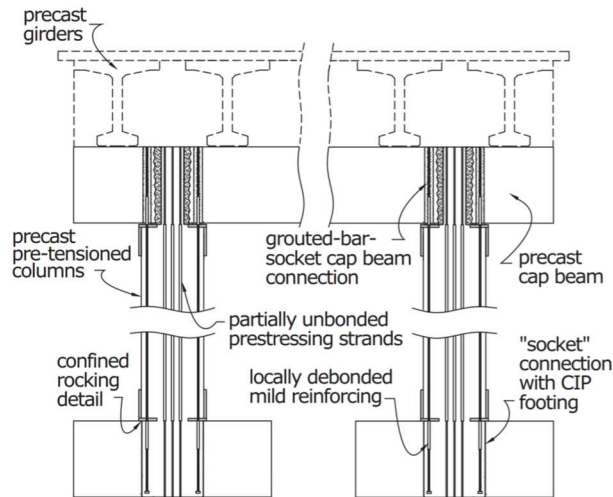


Figure 1.6. Precast columns and cap beam connection with partially unbonded prestressing strands (Reprinted from Thonstad et al. 2016).

Although (non-emulative) rocking connections improve the seismic performance of the precast column systems by eliminating tensile damage in concrete and reducing residual deformations, concrete compressive damage is still sustained. Concrete compressive damage can be partially reduced using high performance cementitious materials (Billington and Yoon 2004; Motaref et al. 2013; Trono et al. 2014; Ichikawa et al. 2016; Moustafa et al. 2017), and various types of confinement, such as steel jacketing (Figure 1.7) (Chou and Chen 2006; Hewes 2007), fiber reinforced polymers (FRP) jacketing (Figure 1.8) (ElGawady and Dawood 2012; White and Palermo 2016), or a combination of steel and FRP jacketing (Abdelkarim et al. 2016; White and Palermo 2016). Alternatively, shimmed elastomeric bearings with yielding rebar have been used as flexural joints (Figure 1.9) (Motaref et al. 2013; Varela and Saiidi 2017).

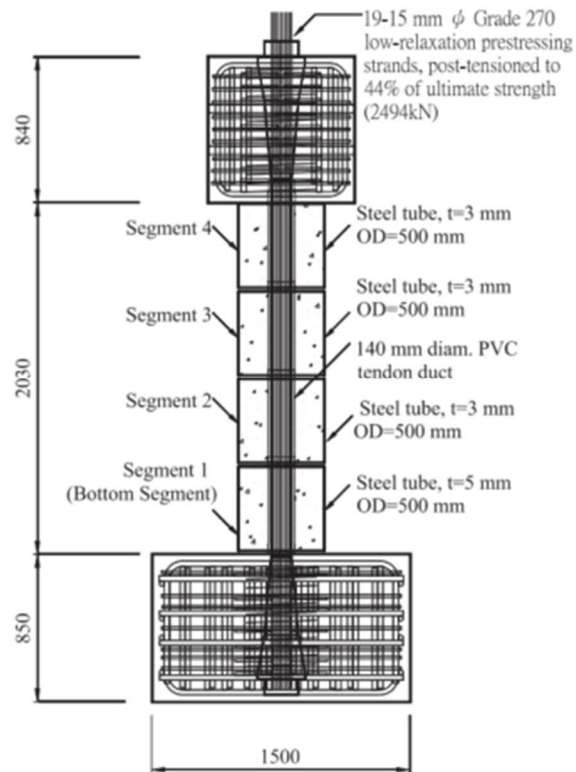


Figure 1.7. Post-tensioned, precast concrete-filled tube (CFT) segmental bridge columns (Reprinted from Chou and Chen 2006).



Figure 1.8. Posttensioned non-emulative column-footing connections with FRP wrap (Reprinted from White and Palermo 2016).

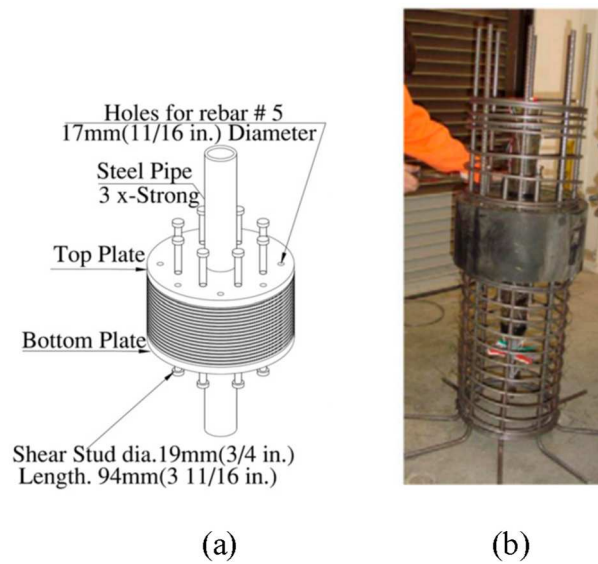
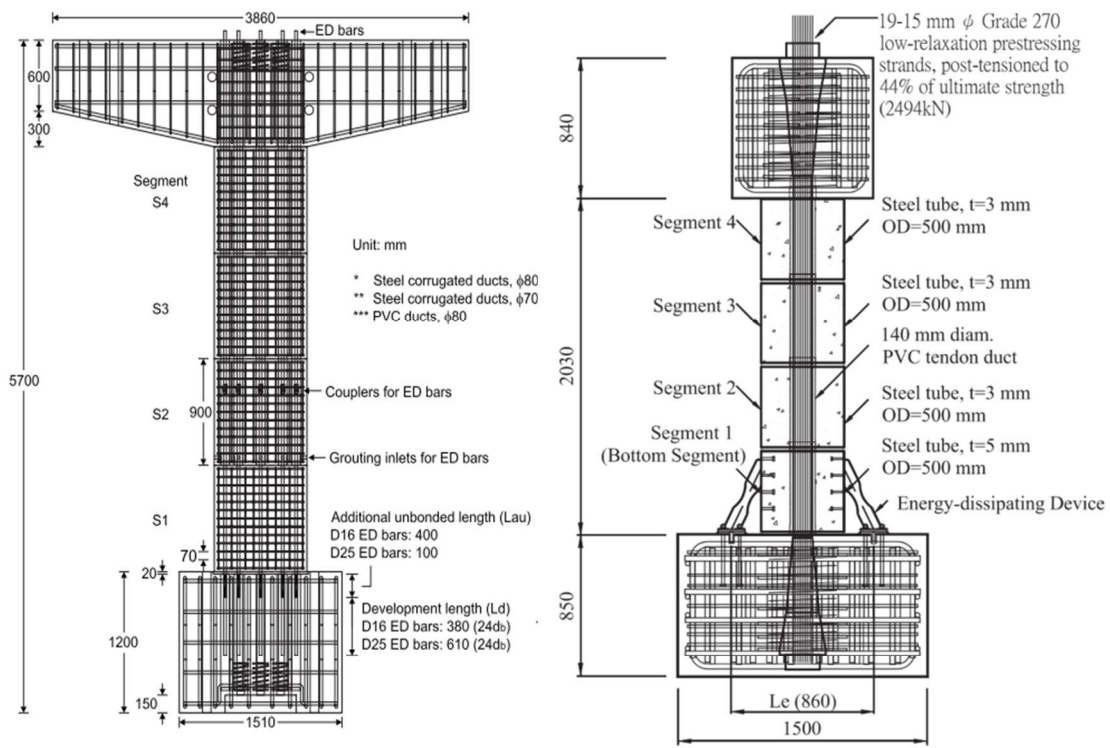


Figure 1.9. Segmental bridge columns with elastomeric bearing pad: (a) Elastomeric bearing pad; (b) base segment with elastomeric bearing pad (Reprinted from Motaref et al. 2013).

Energy dissipation capacity of non-emulative rocking connections can be enhanced through supplemental energy dissipation from different mechanisms including yielding of *internal* partially unbonded bars made of high performance steel or shape memory alloys crossing the joints (Figure 1.10(a)) (Ou et al. 2007; Wang et al. 2008; Ou et al. 2009; Ou et al. 2010; Roh and Reinhorn 2010; Motaref et al. 2013), yielding of externally attached links (Figure 1.10(b) and (c)) (Chou and Chen 2006; Marriott et al. 2009; Guerrini et al. 2014; White and Palermo 2016; Moustafa and ElGawady 2017), friction links (Figure 1.11) (Morgen and Kurama 2004), and viscous damping elements (Marriott 2009). An alternative energy dissipation mechanism using joint friction has been considered in the hybrid sliding-rocking columns, introduced by Sideris (2012) (Figure 1.12) and Sideris et al. (2014b; 2015), and further explored by Salehi et al. (2017). The

hybrid sliding-rocking columns incorporates internal unbonded post-tensioning, end rocking joints, and intermediate sliding joints distributed over the column height.



(a)

(b)



(c)

Figure 1.10. Non-emulative rocking connections with supplemental energy dissipation: (a) precast segmental unbonded posttensioned concrete bridge columns with internal partially unbonded bars (Reprinted from Ou et al. 2009); (b) post-tensioned, precast concrete-filled tube (CFT) segmental bridge columns with external energy-dissipating devices (Reprinted from Chou and Chen 2006); (c) posttensioned column-footing connections with external energy dissipation links (Reprinted from White and Palermo 2016).



Figure 1.11. Non-emulative rocking column connection with friction links (Reprinted from Morgen and Kurama 2004).

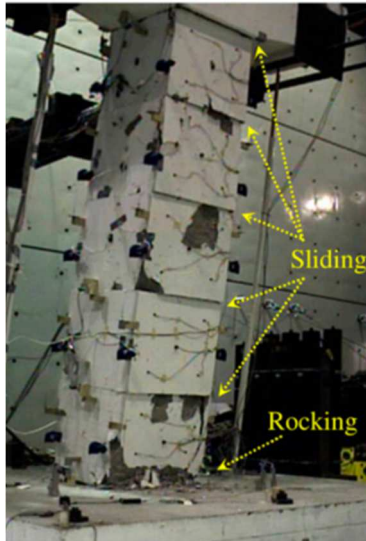


Figure 1.12. Hybrid sliding-rocking columns, introduced by Sideris (2012).

Although the aforementioned column designs combine construction rapidity with improved seismic performance (compared to monolithic systems), they still sustain considerable concrete damage at the rocking joints under large seismic hazards, which reduces their ultimate strength, ductility capacity and self-centering capabilities, and often requires major post-earthquake repairs.

1.2. Research Objectives and Scope

This research primarily aims at introducing the component of explicit damage control and combine it with the concept of accelerated low cost post-earthquake retrofit/repair in the design of bridges for moderate to high seismicity regions; hence, expanding the focus of the bridge engineering community from ABC to ABC&AR, where AR stands for “accelerated retrofit/repair”. This will be done by developing the novel system of bridge columns with damage resistant (DR) joints and replaceable energy dissipation (ED) links. This system will combine construction rapidity, enhanced seismic performance, superior damage control and accelerated low cost post-earthquake retrofit. Specific objectives of this research include:

- Development of the seismically resilient bridge columns with PU-enhanced damage-resistant (DR) joints and replaceable ED links, for applications in moderate and high seismicity areas. This study introduces the concept of the PU-enhanced column with ED links which offers: (i) explicit damage control through polyurethane (PU) damage-resistant end segments (ii) self-centering through internal unbonded post-tensioning, (iii) energy dissipation and flexural stiffness/strength through external replaceable energy dissipating (ED) links in the form of buckling restrained yielding steel bars. Due to the high deformability of the PU material compared to concrete, large induced deformations on the column system are sustained with limited or no permanent damage. Supplemental energy dissipation and the required flexural stiffness and strength is provided by external energy dissipating links. The

replaceability of ED links offers low cost rapid post-earthquake retrofit without operation disruptions.

- Identification and characterization of the mechanical properties of PU materials potentially suitable for structural applications. From the analysis and design perspective, a proper design of a structural system incorporating polymeric materials necessitates the development of numerical constitutive models that are capable of capturing the salient features of the material response. Considering the complex response of polymeric materials, calibrating the numerical constitutive model parameters requires an extensive set of test data, covering all the desired features for the intended application. The objective of this study is to thoroughly characterize the properties of selected polyurethanes (PU) with various compositions that has been found to be potentially suitable for structural applications via a comprehensive experimental program accounting for environmental conditions (e.g. temperature), loading conditions (e.g. cyclic vs. monotonic loading, loading path and rate), and long term effects (e.g. relaxation and creep).
- Investigation of the performance of the proposed column design for various design parameters. Attention should be paid to the performance assessment of the proposed column design for various PU segment geometries and various ED link properties through three-dimensional finite element analysis.

- Development of uniaxial visco-elasto viscoplastic model for PU materials. Attention should be paid to the development of novel uniaxial visco-elastic/plastic constitutive models capable of capturing the salient response features of the selected PU materials, such as rate dependency, hysteresis and damage (softening), and long term effects (creep, relaxation, and recovery). The proposed models should be computationally efficient and suitable for structural engineering applications, which include numerous analyses with several ground motions.
- Evaluation of the seismic performance of the proposed system of PU-enhanced rocking columns with ED links. Specifically, attention should be paid to investigation of the monotonic and cyclic response of the proposed column design with respect to the properties of the ED links. Moreover, the seismic performance of the proposed column design should be investigated through incremental dynamic analyses, and a comprehensive quantitative comparison should be provided against conventional RC column systems (i.e. monolithic and rocking) via fragility analysis accounting for various damage states.
- Validation of the performance of the proposed system through large-scale testing. Attention should be paid to experimentally evaluating the performance of bridge columns with polyurethane-enhanced DR joints and ED links, and validating the proposed replacement strategy for ED links. Moreover, the experimental study aimed at providing the data for calibration of finite element models presented in previous sections.

1.3. Dissertation Organization

This dissertation consists of nine sections and two appendices. Following this introductory section, Section 2 presents the development of the concept of PU-enhanced damage resistant columns with energy dissipation links for seismic applications in bridges. In this section, the mathematics and mechanics of PU-enhanced columns with ED links are presented, followed by illustration of a displacement-based seismic design approach. Section 3 presents a three-phase experimental program characterizing the mechanical properties of selected polyurethanes (PUs) with various compositions that have been found to be potentially suitable for the proposed system. Section 4 studies the performance of the proposed column design for various PU segment geometries and various ED link properties through three-dimensional finite element analysis. In Section 5, two novel uniaxial visco-elastic/plastic constitutive models capable of capturing the PU material response observed in the experiments presented in Section 3. In this section, the constitutive models are calibrated using the test data presented in Section 3. These models were used to study the seismic performance of bridge systems incorporating the proposed column design. Section 6 assesses the seismic performance of the PUEC columns. Specifically, the monotonic and cyclic response of the proposed column design is investigated with respect to the properties of the ED links and is compared with the response of a *reference* conventional reinforced concrete (RC) monolithic column and a RC rocking column. Moreover, the seismic performance of the proposed column design is investigated through incremental dynamic analyses with a suite of far-field ground motions, and provides a comprehensive quantitative comparison against the reference

conventional RC monolithic column and the RC rocking column via fragility analysis accounting for various damage states. Section 7 presents an experimental study investigating the performance of large-scale ($\sim 1:2.5$) column systems including an RC rocking column as the reference, a PU-enhanced column with a bi-layered axisymmetric PU-concrete segment with ED links, and a PU-enhanced column with a solid PU segment. The specimens were subjected to displacement-controlled quasi-static cyclic loading with progressively increasing amplitude. In Section 8, the numerical modeling approach presented in Section 6 is validated in two stages for selected test results (from Section 7). In the first stage, responses predicted by models of the test specimen developed following the modeling approach presented in Section 6 are compared to the test results (blind predictions). In the second stage, based on the test data, recommendations are made which lead to a revised model, which is capable to provide more accurate response predictions. Section 9 presents a summary of the performed research, major conclusions, and original contributions of this study, followed by recommendations for future research.

The dissertation is complemented by two appendices. Appendix A is associated with the PU material testing program. Appendix B presents the CAD drawings of the large-scale test specimens.

2. PU-ENHANCED COLUMNS WITH ENERGY DISSIPATION LINKS: SYSTEM DEVELOPMENT AND DESIGN CONCEPTS

2.1. Introduction

Bridge substructures designed and constructed based on traditional seismic design methodologies provide energy dissipation capabilities through formation of ductile plastic hinges at the column ends under major earthquake events. Although this traditional design philosophy ensures collapse prevention, the bridge typically sustains excessive physical damage, which results in high repair costs and downtime. Additionally, traditional construction methods require long construction times and large construction footprints, which lead to major direct and indirect socioeconomic impacts. In this section, a novel segmental bridge substructure system is proposed in the framework of accelerated bridge construction, which is intended for moderate and high seismicity areas. The proposed system is herein referred as seismically resilient post-tensioned bridge columns with polyurethane-enhanced damage-resistant (DR) joints and external energy dissipation links (or PU-enhanced columns with ED links, or PUED columns in short). In the following sections, the proposed system is discussed in detail and a simplified analytical model is presented to describe the response of the proposed system. Finally, seismic design concepts for the proposed system, in the framework of a displacement-based design method, are presented.

2.2. Description of PU-enhanced Columns with Energy Dissipation Links

The PU-enhanced column with Energy Dissipation (ED) links offers: (i) *explicit damage control* through polyurethane (PU) damage-resistant end segments (ii) *self-centering* through internal unbonded post-tensioning, (iii) *energy dissipation* and *flexural stiffness/strength* through external replaceable energy dissipating (ED) links in the form of buckling restrained yielding steel bars (Figure 2.1).

Because polyurethane is a highly deformable material compared to concrete, large induced deformations on the column system can be sustained with limited or no permanent damage. As a result, during strong earthquakes, the proposed PU damage-resistant end segments can sustain large strains with minor or no damage, preventing damage from propagating to the column length (Figure 2.1(a)). However, it is well-known that the polymeric materials may sustain significant deformation under constant load (creep) over the time. Creep (and relaxation) can negatively affect the performance of structural systems. In bridge systems, such as the one proposed herein, creep under constant loads (e.g. gravity and post-tensioning) can significantly impair the serviceability of the system. Cases of complete structural failure under service loads have also been observed due to large concrete creep deformations and the resulting stress redistribution over the structure (Bažant et al. 2012). To provide the required long term performance against creep under service loads, a bi-layered (BL) axisymmetric segment design is proposed (Figure 2.1(b)), which combines an internal concrete core with an exterior PU layer (sleeve). The interior concrete core, being stiffer is used to sustain the permanent service (loads), whereas the

exterior PU layer is used to provide resistance, with no or minimum damage, against flexure generated from lateral loading.

Supplemental energy dissipation and the required additional flexural stiffness and strength is provided by external energy dissipating links. The ED link setup (Figure 2.1(c) and (d)) includes a stiff steel collar, which is mounted to the face of the concrete segment right above the PU segment, and the ED links, which are bolted to the steel collar and the footing. ED links are usually steel circular rods with their end portions having larger diameter (unmilled parts), so that they remain elastic and un-deformed compared to the *yielding length* (milled part), which covers the middle portion and has smaller diameter. ED links are typically encased in thick steel tubes (Marriott et al. 2009) to prevent buckling, and can be easily obtained from mild steel reinforcing bars by milling the middle portion to provide a target (equivalent) diameter over the yielding length. The *replaceability* of ED links offers *low cost rapid post-earthquake retrofit* without operation disruptions.

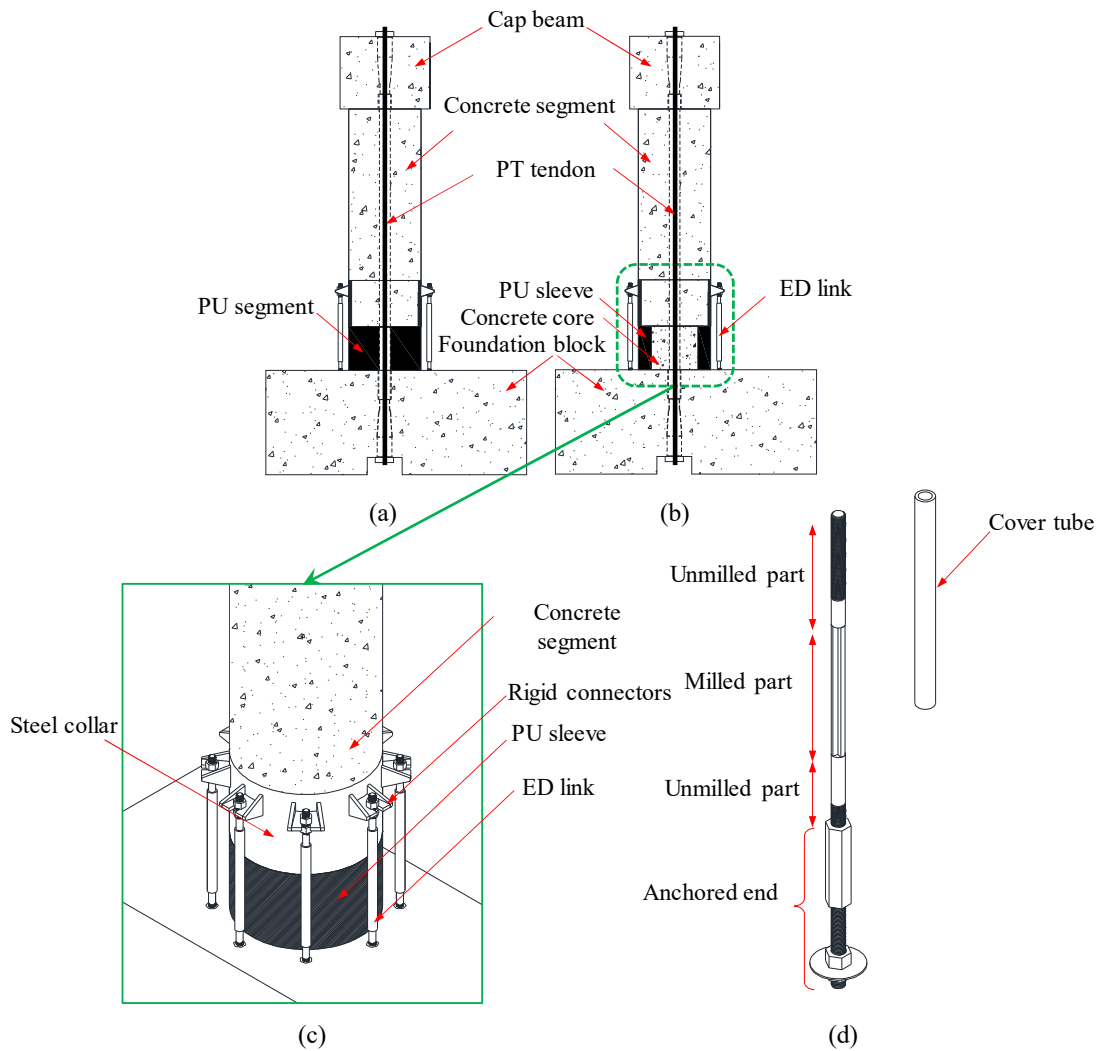


Figure 2.1. Schematic representation of the PU-enhanced column system with ED links: (a) system with solid PU segment; (b) system with bi-layered PU segment; (c) isometric view of the system in the vicinity of the PU segment; (d) details of the ED link.

2.2.1. Mechanics of PU-enhanced Columns with ED Links: Simplified Analytical

Model

In this section, a simplified analytical model is proposed to predict the response of PU-enhanced columns with ED links under a constant vertical load and monotonically increasing lateral load. Using the proposed analytical model, discrete points of the pushover curve are computed based on the peak strain in PU material ($\epsilon_{PU,max}$) at the base rocking interface (Figure 2.2(c)) as the control input parameter which determines the state of deformation in the system.

At each state of deformation, the lateral force and displacement of the system can be defined using a set of equilibrium (force and moment) and compatibility equations. The neutral axis depth, c , in the section corresponding to each state of deformation is determined so that the force equilibrium in the vertical direction is satisfied at the base rocking section as below:

$$N_{PT} + P_v - (N_{PU} + N_{ED} + N_c) = 0 \quad (2.1)$$

where N_{PT} is the total force in the PT bar considering the rocking effect, P_v is the constant applied vertical load (gravity load), N_{PU} is the resultant vertical force in the PU material, N_c is the resultant vertical force in the concrete, and N_{ED} is the resultant axial force in ED links considering the rocking effect.

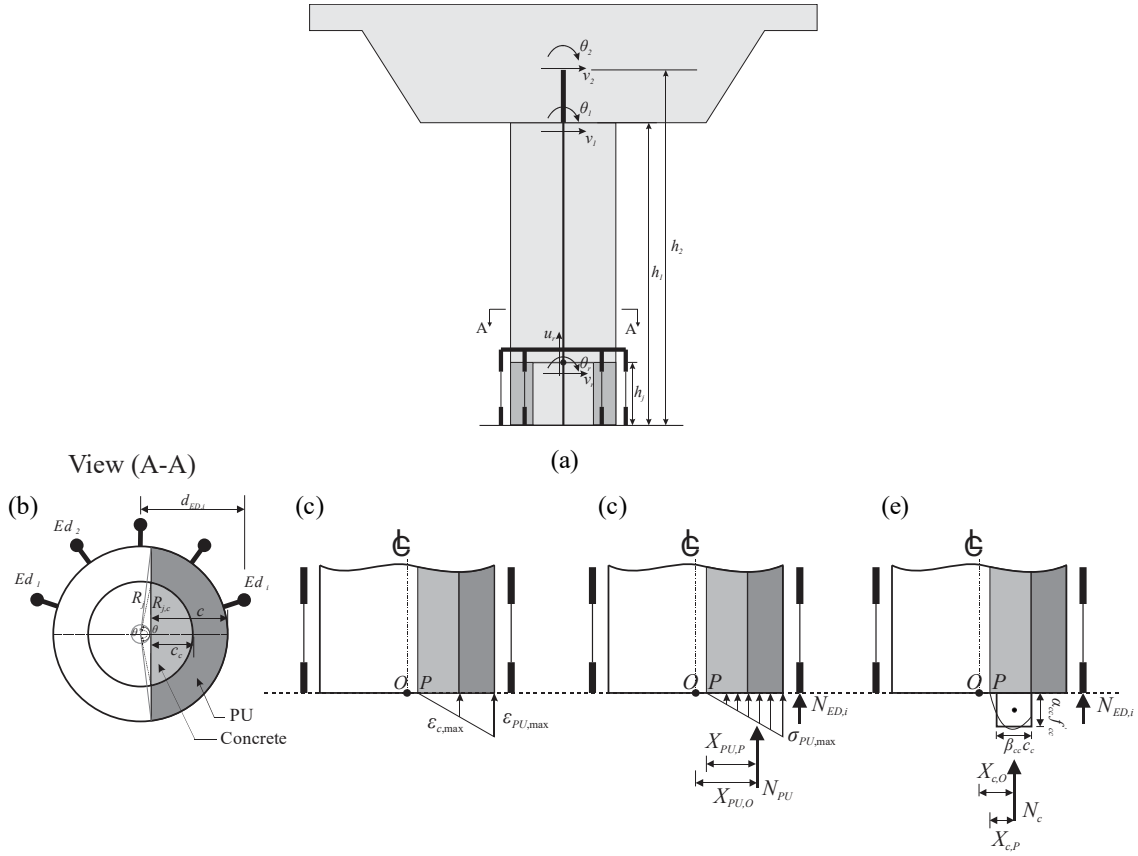


Figure 2.2. (a) Typical PUED reference model; (b) cross section view; (c) strain distribution; (d) stress diagram for PU layer; (e) stress diagram for concrete layer (Not all ED links are shown for clarity purposes).

In the proposed model, a linear strain distribution is assumed in the depth of the section. Using the equivalent stress block for the compressive concrete in the section, the resultant vertical force in the concrete, N_c , is defined as:

$$N_c = \alpha_{cc} f'_{cc} A_{c,eq} \quad (2.2)$$

where $A_{c,eq}$ is the area of the compressive concrete layer with a thickness equal to the depth of the equivalent stress block, which depending on the location of the neutral axis of the section, c , and neglecting the area of the central duct, is defined as:

$$A_{c,eq} = \begin{cases} 0 & c \leq (D_j - D_{jc})/2 \\ \frac{(D_{jc})^2}{8} (\theta - \sin(\theta)) & (D_j - D_{jc})/2 < c \leq (D_j + D_{jc})/2 \\ \pi D_{jc}^2 / 4 & (D_j + D_{jc})/2 < c \leq D_j \end{cases} \quad (2.3)$$

$$\text{With } \begin{cases} \theta = 2 \cos^{-1} \left(1 - \frac{2a_c}{D_{jc}} \right) \\ a_c = \beta_{cc} c_c \end{cases}$$

where D_j is the diameter of the PU segment, D_{jc} is the diameter of the central concrete core, c_c is the depth of the compressive concrete layer, and θ is the central angle as shown in Figure 2.2(b). In Eq. (2.2) and (2.3), α_{cc} and β_{cc} are equivalent stress block parameters defined based on the work by Karthik and Mander (2010) for the confined concrete with confinement ratio $K = f'_{cc} / f'_c$, where f'_{cc} and f'_c is the confined and unconfined concrete compressive strength, respectively. For maximum concrete stress smaller than $0.5f'_c$, instead of using the equivalent stress block method, a linear stress distribution over the compressive concrete can be assumed with the resultant concrete force computed as:

$$N_c = \int_{A_c} \sigma_c(x) dA \quad (2.4)$$

where $\sigma_c(x)$ is the concrete stress at distance x from the reference axis.

The total axial compressive PT force, N_{PT} , is defined as:

$$N_{PT} = \sigma_{PT} A_{PT} \quad (2.5)$$

where σ_{PT} and A_{PT} is the stress level in the PT tendon and the cross-section area of the PT tendon, respectively. Assuming a bilinear response for the PT tendon steel with a post-yield stiffness expressed as a fraction b of the initial elastic modulus of the steel material, E_s , the stress level in the PT tendon can be defined as:

$$\sigma_{PT} = \begin{cases} E_s \varepsilon_{PT} & \varepsilon_{PT} < \varepsilon_y \\ f_y + (\varepsilon_{PT} - \varepsilon_y) b E_s & \varepsilon_{PT} \geq \varepsilon_y \end{cases} \quad (2.6)$$

where f_y is the minimum yield strength of the steel material, ε_{PT} is the total axial strain in the PT tendon considering the extra strain in the PT bar due to rocking (as defined later in Eq. (2.23)), and ε_y is the yield strain of the steel material.

The resultant vertical force in the PU material is defined as:

$$N_{PU} = \int_A \sigma_{PU}(x) dA - \int_{A_c} \sigma_{PU}(x) dA \quad (2.7)$$

where $\sigma_{PU}(x)$ is the PU stress at distance x from the reference axis, A is the total contact area, and A_c is the area of the compressive concrete defined by Eq.(2.3) by putting $\beta_\alpha = 1$. Generally, $\sigma_{PU}(x)$ is defined using the constitutive material model of the PU material, such as the models presented in Section 5. Assuming that the PU material is in the linear range of the response ($\varepsilon_{PU,max} < 0.05$), the resultant vertical force in the PU material can be defined as:

$$N_{PU} = \frac{\sigma_{PU,max}}{c} \left(\int_A x dA - \int_{A_c} x dA \right) = \frac{\sigma_{PU,max}}{c} (I - I') \quad (2.8)$$

where $\sigma_{PU,max}$ is the maximum stress in PU material given as:

$$\sigma_{PU,max} = E_{PU} \varepsilon_{PU,max} \quad (2.9)$$

where E_{PU} is the elastic modulus of the PU material. The other parameters of Eq.(2.8) are defined as:

$$\begin{cases} I = A e \\ I' = A' e' \end{cases}, \text{ with } \begin{cases} e = X - (D_j / 2 - c) \\ e' = X'_c - (D_j / 2 - c) \end{cases} \quad (2.10)$$

where X is the distance from the centroid of the total compressive segment to the center of the section (O), and X'_c is the centroid of the compressive concrete part of the section from the center of the section (O) defined as:

$$\begin{cases} X = \frac{2D_j \sin^3(\theta/2)}{3(\theta - \sin(\theta))} \\ X'_c = \frac{2D_{j,c} \sin^3(\theta'/2)}{3(\theta' - \sin(\theta'))} \end{cases}, \text{ with } \begin{cases} \theta = 2 \cos^{-1} \left(1 - \frac{2c}{D_j} \right) \\ \theta' = 2 \cos^{-1} \left(\frac{D_j - 2c}{D_{j,c}} \right) \end{cases} \quad (2.11)$$

Area of the compression part of the section is defined as:

$$A = \frac{D_j^2}{8} (\theta - \sin(\theta)) \quad (2.12)$$

The resultant axial force in ED links is found as below:

$$N_{ED} = \sum_{i=1}^{n_{ED}} N_{ED,i} = \sum_{i=1}^{n_{ED}} \sigma_{ED,i} A_{ED,i} \quad (2.13)$$

where $\sigma_{ED,i}$, $A_{ED,i}$, and $N_{ED,i}$ is the stress, cross-section are, and axial force in i -th ED link, and n_{ED} is the number of ED links. Assuming a bilinear response with a post-yield

stiffness expressed as a fraction b of the initial elastic modulus of the steel (E_s), $\sigma_{ED,i}$ can be defined as below:

$$\sigma_{ED,i} = \begin{cases} E_s \varepsilon_{ED,i} & \varepsilon_{ED,i} < \varepsilon_y \\ f_y + (\varepsilon_{ED,i} - \varepsilon_y) b E_s & \varepsilon_{ED,i} \geq \varepsilon_y \end{cases} \quad (2.14)$$

where f_y is the minimum yield strength of the ED link steel material, $\varepsilon_{ED,i}$ is the axial strain in the i -th ED link, and ε_y is the yield strain of the ED link steel material.

Assuming a rigid body motion for the RC element above the PU segment and no rocking between the PU segment and the above RC element, the rocking effect is considered by defining the rotation due to rocking, θ_r , and the extension due to rocking, u_r , at top of the PU segment (Figure 2.2(b)). The rotation at the top of the PU segment, θ_r , due to rocking at the bottom can be expressed as the integration of curvature, φ , over the height of the PU segment, h_j , as below:

$$\theta_r = \int_0^{h_j} \varphi dh \quad (2.15)$$

According to the observations from the preliminary finite element analysis results from the numerical models presented in Section 6.3, the variation of curvature over the height of the PU segment was found as below:

$$\begin{aligned} \varphi_m &= 0.5\varphi_b \\ \varphi_t &= 0.25\varphi_b \end{aligned} \quad (2.16)$$

where $\varphi_b, \varphi_m, \varphi_t$ is the curvature at the bottom, middle, and top section of the PU segment, respectively. Assuming a linear strain distribution in the depth of the section, the curvature at the base section can be defined for a given $\varepsilon_{PU,\max}$ and c as:

$$\varphi_b = \frac{\varepsilon_{PU,\max}}{c} \quad (2.17)$$

From Eq.(2.16), θ_r can be simplified as:

$$\theta_r = \left(\frac{\varphi_t + \varphi_b}{2} \right) h_j = \left(\frac{0.25\varphi_b + \varphi_b}{2} \right) h_j = 0.625\varphi_b h_j \quad (2.18)$$

The extension due to rocking can be expressed as below:

$$u_r = \int_0^{h_j} \varepsilon_0 dh - u_0 \quad (2.19)$$

where u_0 is the deformation at top of the PU segment due to the initial total vertical load including PT and gravity load, and ε_0 is the total axial strain at the center of each section over the height of the PU segment. Assuming a linear distribution for ε_0 along the PU segment, Eq.(2.19) can be simplified as:

$$u_r = \left(\frac{\varepsilon_{0,b} + \varepsilon_{0,t}}{2} \right) h_j - u_0 \quad (2.20)$$

where $\varepsilon_{0,b}$ is the strain at center of the base section of the PU segment defined as:

$$\varepsilon_{0,b} = (D_j / 2 - c) \varphi_b \quad (2.21)$$

Given the extension due to rocking, the total extension in the PT tendon at a specific state of deformation is defined as:

$$u_{PT} = u_{PT,0} + u_r \quad (2.22)$$

where $u_{PT,0}$ is the extension in the PT bar due to initial Post-tensioning.

The extra strain in the PT bar due to rocking ($\varepsilon_{PT,r}$) can be defined as:

$$\varepsilon_{PT,r} = \frac{u_{PT,r}}{L_{PT}} \quad (2.23)$$

where L_{PT} is the initial length of the PT bar.

Given the extension and rotation due to rocking, the total deformation in the i -th ED link at a specific state of deformation is defined as:

$$u_{ED,i} = u_r + d_{ED,i} \theta_r \quad (2.24)$$

where $d_{ED,i}$ is the distance of the i -th ED link from the mid-section. The total strain in the ED links is given as:

$$\varepsilon_{ED,i} = \frac{u_{ED,i}}{L_{ED,Y}} \quad (2.25)$$

where $L_{ED,Y}$ is the length of the milled (yielding) part of the ED links, which is assumed to be identical for all ED links.

The lateral strength of the system, p_h , considering the second order effects (the so called large P-Delta effect) can be defined using the moment equilibrium equation at the base taken about the center of the section (O) as:

$$p_h h_2 = M_{PU} + M_c + M_{ED} - p_v \Delta_h$$

$$\left\{ \begin{array}{l} M_{PU} = N_{PU} X_{PU} \\ M_c = N_c X_c \\ M_{ED} = \sum_{i=1}^{n_{ED}} N_{ED,i} X_{ED,i} \end{array} \right. \quad (2.26)$$

with:

where M_{PU} is the moment resistance due to PU, M_c is the moment resistance due to concrete, M_{ED} is the moment resistance due to the ED links, p_h is the lateral (horizontal) force applied at a height h_2 , Δ_h (v_2 in Figure 2.2(a)) is the lateral displacement at a height h_2 , where h_2 (Figure 2.2(a)) is the center of mass of the superstructure, and X_{PU} , X_c , and $X_{ED,i}$ is the distance of the N_{PU} , N_c , and $N_{ED,i}$ to the center of the section (point O).

X_{PU} and X_c are defined as below:

$$X_{PU} = X_{PU,P} + D_j / 2 - c \quad (2.27)$$

$$X_c = \frac{D_{jc} - a_c}{2} \quad (2.28)$$

where $X_{PU,P}$ is the distance of N_{PU} to the neutral axis (P) defined as:

$$X_{PU,P} = \frac{I_p - I'_p}{I - I'}, \text{ with } \left\{ \begin{array}{l} I_p = (I_o - AX^2) + Ae^2 \\ I'_p = (I'_o - A_c (X'_c)^2) + A_c e'^2 \end{array} \right. \quad (2.29)$$

where I_0 and I'_o are the second moment of inertia of the total compressive part and the compressive concrete part of section, respectively, defined as:

$$\begin{cases} I_o = \frac{D_j^4}{128} (\theta - \sin(\theta) + 2 \sin(\theta) \sin^2(\theta/2)) \\ I_o' = \frac{D_{j,c}^4}{128} (\theta' - \sin(\theta') + 2 \sin(\theta') \sin^2(\theta'/2)) \end{cases} \quad (2.30)$$

At a given deformation stage, the corresponding lateral displacement of the centroid of the deck is given as:

$$v_2 = v_1 + \theta_1 (h_2 - h_1) \quad (2.31)$$

where h_1 and h_2 is the distance from the base to top of the column and deck centroid, respectively (Figure 2.2(a)), and v_1 and θ_1 is the lateral displacement and rotation at top of the column, respectively, defined as:

$$v_1 = \underbrace{v_r + \theta_r (h_1 - h_j)}_{\text{Displacement due to rigid body motion}} + \underbrace{\frac{p_h (h_1 - h_j)^3}{3EI} + \frac{p_h (h_2 - h_1)(h_1 - h_j)^2}{2EI}}_{\text{Displacement due to lateral load}} \quad (2.32)$$

$$\theta_1 = \theta_r + \frac{p_h (h_1 - h_j)^2}{2EI} + \frac{p_h (h_2 - h_1)(h_1 - h_j)}{EI} \quad (2.33)$$

where v_r is the lateral displacement at top of the PU segment given as below:

$$v_r = \theta|_{h_j/2} (h_j/2) \quad (2.34)$$

In Eq.(2.32) and (2.33), \overline{EI} is the weighted flexural rigidity of the nonhomogeneous section at the base consisting of PU, concrete, and ED links, which is computed as:

$$\overline{EI} = E_{PU} I_{PU} + E_c I_c + E_{ED} \sum_{i=1}^{n_{ED}} I_{ED,i} \quad (2.35)$$

where E_c is the Young's modulus of the concrete, I_{PU} and I_c is the moment of inertia of PU and concrete parts about the neutral axis, respectively, $I_{ED,i}$ is the moment of inertia of

the i -th ED link about the neutral axis, and E_{ED} is the Young's modulus of the ED links, which is assumed to be the same for all ED links.

2.3. Seismic Design Concepts for PU-enhanced Columns with Energy Dissipation

Links

2.3.1. Displacement-based Seismic Design of PU-enhanced Columns with ED Links

The direct displacement design (DDBD) is a seismic design methodology that uses displacements as the basis for the design procedure. The basic goal of the DDBD is to achieve a structure, which will experience a predetermined deformation state when subjected to a given seismic hazard intensity (e.g., design earthquake, maximum considered earthquake). The development of displacement-based seismic design and assessment methods has been driven for a long time by research on reinforced concrete building structures (Moehle 1992; Priestley 1996; Chopra and Goel 2001), steel structures (Mazzolani and Piluso 1997; Medhekar and Kennedy 2000), and reinforced concrete bridges (Kowalsky et al. 1995; Kowalsky 2002; Dwairi and Kowalsky 2006; Pinho et al. 2007; Cardone et al. 2009; Adhikari et al. 2010). The growing interest in the DDBD methods has mainly stemmed from the recognition that structural damage is related directly to the displacement demands. Displacement-based design methods have shown to yield more realistic and less conservative results than force-based design methods. Moreover, the displacement-based design provides the ability to control explicitly the displacement demand in each component of the structure, as opposed to the force based design where a single response modification factor (R) is assigned to the entire structure to modify the design forces (Calvi and Kingsley 1995). On the other hand, force based

design methods, which indirectly account for the energy dissipation properties and ductility capacity of the system through R-factors, cannot be used for new systems due to lack of such R-factors. For new systems, R factors can be estimated by using the procedure given in Kowalsky (2002) and validated using FEMA P695 (Federal Emergency Management Agency 2009). However, the methodology mainly focusses on building structures.

Capacity spectrum methods (CSMs) are equivalent to the DDBD methods, and provide prediction of response variables for given hazard and a set of trial design/system parameters. In this section, a capacity spectrum design methodology is adopted to assess and compare the performance of columns with various designs with respect to the peak displacement demand. The methodology is discussed in detail in the following section. The methodology is applied later on to various column systems designed for the large scale testing presented in Section 7.3 to estimate the performance point of the columns for a given level of hazard (e.g. DE, MCE, $2\times$ MCE ...).

2.3.1.1. Design Methodology

A general flowchart of the capacity spectrum method is shown in Figure 2.3.

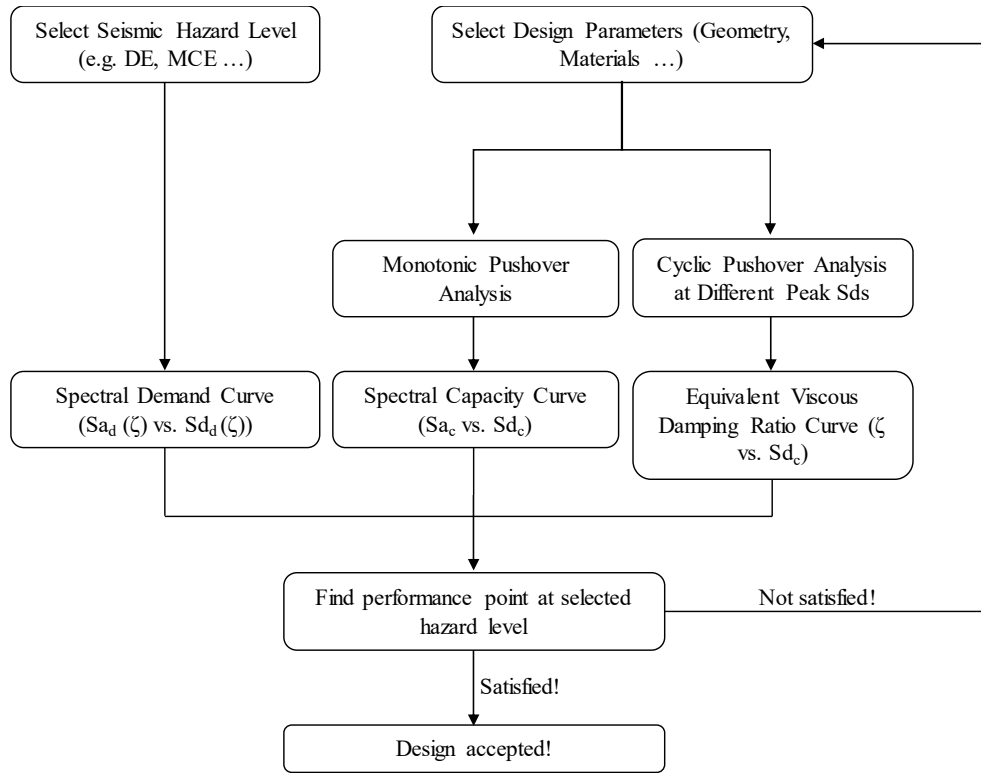


Figure 2.3. Capacity spectrum method flow-chart.

In the CSM, the nonlinear force versus displacement pushover curve is converted to the so-called spectral *capacity* curve, which is expressed as spectral acceleration versus spectral displacement using relations, which for a single degree of freedom system are given below:

$$S_a = \frac{P}{m} \quad (2.36)$$

$$S_d = u \quad (2.37)$$

where, P is the lateral load obtained from pushover analysis, m is the mass of the structure and u is the lateral displacement of the column.

The seismic *demand* curve at the desired hazard level is generated from the design response spectrum scaled to account for hysteretic damping effects. The five-percent-damped design response spectrum is computed per AASHTO LRFD Bridge design Specifications (2014). The corresponding parameters of the design spectrum at the location of the bridge can be obtained from the USGS Seismic Design Maps (2018).

To scale the 5%-damped design response spectrum for any given value of damping, the equation given in European Committee for Standardization (1994) is used:

$$S_{a,\xi_{eq}} = \sqrt{\frac{0.07}{0.02 + \xi_{eq}}} S_a \quad (2.38)$$

where, ξ_{eq} is the total equivalent damping in the system which for any given displacement u can be estimated as below:

$$\xi_{eq}(u) = \xi_0 + \xi_{hyst}(u) \quad (2.39)$$

where ξ_0 is the inherent damping in the system ($\sim 3\text{-}5\%$), and $\xi_{hyst}(u)$ is the damping ratio due to hysteretic response defined as:

$$\xi_{hyst} = \frac{E_d}{2\pi K_{sec} u_0^2} \quad (2.40)$$

where E_d is the total energy dissipated per cycle, K_{sec} is the secant stiffness, and u_0 is the displacement amplitude of the cycle. For a given amplitude, K_{sec} is calculated as:

$$K_{sec} = \frac{F_{peak}^+ - F_{peak}^-}{u_{peak}^+ - u_{peak}^-} \quad (2.41)$$

and u_0 is calculated as:

$$u_0 = \frac{u_{peak}^+ - u_{peak}^-}{2} \quad (2.42)$$

where F_{peak}^+ and F_{peak}^- are the peak positive and negative force values, respectively, and

u_{peak}^+ and u_{peak}^- are the peak positive and negative displacement values, respectively.

Calculation of F_{peak}^+ , F_{peak}^- , u_{peak}^+ and u_{peak}^- is graphically demonstrated in Figure 2.4.

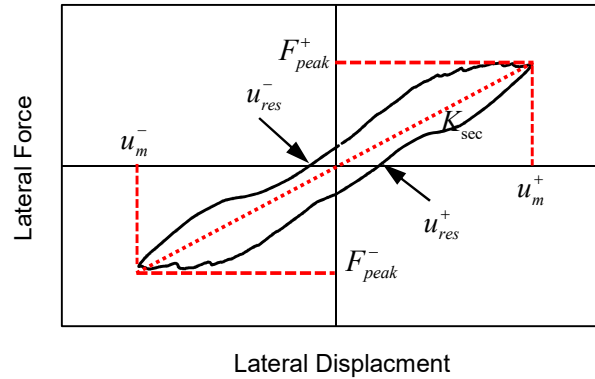


Figure 2.4. Graphical computation of F_{peak}^+ , F_{peak}^- , u_{peak}^+ and u_{peak}^- and K_{sec} at a given cycle.

The variation of the equivalent viscous damping with lateral displacement (damping curve) is obtained by conducting a set of cyclic analyses at various amplitudes. In this study, each set includes two cycles of the same amplitude.

The intersection of the capacity and demand curve, which is termed the *performance point*, is determined using a bisection algorithm. It should be noted that the performance assessment through CSM is only based on the peak deformation demand,

while other response parameters, such as residual deformations and residual strength are not considered.

2.4. Summary and Findings

In the section, the PU-enhanced columns with energy dissipation links are discussed in detail and a simplified analytical model was presented to describe the response of the proposed system. Finally, seismic design concepts for the proposed system, in the framework of a displacement-based design method, were presented.

3. CHARACTERIZATION OF THE MECHANICAL PROPERTIES OF POLYURETHANE MATERIALS*

3.1. Introduction

The application of polymeric materials in different fields has been significantly increased over the past 30 years. Polymeric materials are used in different structures and systems such as automobiles, load bearing elements, jet engines, etc. Specifically, in the field of civil engineering, polymeric materials has been used in both structural e.g., roof systems, structural insulated panel systems) and non-structural components (i.e. thermal insulations, waterproofing and protection, cladding and facades, floorings, etc). Particularly, soft rubbery materials have also been used in bridge and building seismic isolation bearings to protect the system from earthquakes (Roeder and Stanton 1983; Mokha et al. 1990; Kelly 1993). Recently, a sandwich plate systems (SPS) (BASF 1993) with polyurethane core has been developed and used in different structural systems such as offshore platforms, high-rise building slabs, bridges' deck, metro rail track beds, etc. Compared to conventional construction materials (i.e. concrete, steel, etc), SPS offers a higher stability, better vibration isolation, weight reduction, and lower costs compared to conventional component parts.

* Part of the data reported in this section is reprinted with permission from “Experimental characterization and constitutive modeling of polyurethanes for structural applications, accounting for damage, hysteresis, loading rate and long term effects” by Nikoukalam, M. T., & Sideris, P., 2019. *Engineering Structures*, 198, 109462, Copyright 2019 by Elsevier.

With the fast growing application of polymers in different fields, such as structural engineering, the material response under various loading conditions are of great importance concerning the specific desired performance (Bardenhagen et al. 1997; Khan and Lopez-Pamies 2002). The stress-strain behavior of polyurethane polymers shows strong hysteresis, rate dependence, cyclic softening, and temperature dependency.

The *energy dissipation* capacity of some polymeric materials has been used for the design and development of energy absorbing systems mainly for crash and impact loading. On the other hand, the *rate dependency* of the deformation response, which is known as the source of creep and relaxation phenomena, can greatly affect the performance of a structural system. Moreover, the *cyclic hardening/softening* is another important feature, especially for systems subjected to reversed loading conditions (e.g. structures under earthquake-induced loading). Environmental conditions (e.g. temperature, humidity, UV radiation...) are another set of parameters that can highly affect the performance of the systems with polymeric materials.

From an analysis and design perspective, a proper design of a structural system incorporating polymeric materials necessitates the development of numerical constitutive models that are capable of capturing the salient features of the material response, including but not being limited to abovementioned features. A constitutive model includes a set of parameters known as material constants which represent the actual material response qualitatively. These material constants must be identified through proper experimental data. To this end, a well-detailed knowledge of the material response under various processes, such as monotonic and cyclic loading, creep and relaxation, and the effects of

other parameters, such as temperature and loading rate, is essential. Moreover, considering the complex response of polymeric materials, calibrating the constitutive model parameters requires an extensive set of test data, covering all the desired features for the intended application.

3.2. Scope and Objectives

The objective of this Section is to thoroughly characterize the properties of polyurethanes (PUs) of selected compositions that have been found to be potentially suitable for structural applications via a comprehensive experimental program accounting for environmental conditions (e.g. temperature), loading conditions (e.g. tension vs. compression, cyclic vs. monotonic loading, loading path and rate), and long term effects (e.g. relaxation and creep). The experimental program included three phases which are explained in detail in the following sections.

3.3. Experimental Program

3.3.1. Phase 1 – Exploration of Various PUs under Compressive Loading

The objective of Phase 1 was to explore the mechanical properties of three selected PUs, which would then be used to assess potential applicability of those PUs in the PU-enhanced column design developed in this dissertation.

3.3.1.1. Test Specimens and Testing Program

Three different types of elastomers available from BASF (2016) as Elastocore (ECore), Elastocast (ECast), and Elastoshore (EShore), with chemical compositions as listed in Table 3.1, were considered as to be potentially suitable for the column design

proposed in this study. All elastomers were produced and tested in the Structures and Materials Testing Laboratory (SMTL) of the University of Colorado – Boulder. The resin and isocyanate were mixed at 1160 rpm for 30 seconds in a mixer. The resulting mixture was poured into cylindrical molds of length of 4 in and diameter of 2 in. The samples were cured at room temperature (~ 73 °F [23°C]) for 2 days, and were then tested under uniaxial compression loading at a crush rate of 0.05 in/min based on ASTM D695 (2010). The top and bottom loading plates were lubricated with silicone to reduce frictional confining effects on the compression response. All tests were performed at room temperature (~ 73 °F [23°C]) under normal humidity conditions (40% - 50%). These tests allowed a preliminary characterization of the mechanical properties of the polyurethanes selected for this study.

Table 3.1. Main chemical components of polyurethanes

	Liquid Components		Mix Ratio (by weight)	
	Resin	Isocyanate	Resin	Isocyanate
ELASTOCORE	9010/100R	9010T	100	83
ELASTOCAST	72610R	P1001U	100	80.1
ELASTOSHORE	10036R	5070T	100	133

3.3.1.2. Test Setup and Instrumentation

Tests were conducted via a uniaxial servo-hydraulic MTS-810 system with 110 kips loading capacity and a total stroke of 6 in. (± 3 in.). The control system was an MTS FlexTest 60 digital controller. The force and displacement were measured using the built-in load cell and linear variable differential transformer (LVDT) of the loading frame.

Because the total reaction force of the 2”×4” samples was small, compared to the force capacity of the system, the effect of the flexibility of the loading frame on the measured strain was considered small, while, because this was a preliminary study, potential (small) discrepancies in the deformation measurements due to this flexibility effect were considered acceptable.

3.3.1.3. Data Post-processing

For both the strain and stress, the engineering values were calculated and reported. The engineering strain was obtained by dividing the deformation by the initial height of the specimen at the undeformed state. The engineering stress was obtained by dividing the force by the initial cross-section area of the specimen at the undeformed state. A second order low-pass Butterworth zero-phase filter with a corner frequency of 1Hz was used to filter out the noise from the recorded signals from the loading frame load cell and LVDT.

3.3.1.4. Results and Observations

The deformation of the specimens at 20% and 40% strain with the stress-strain plots from the experiment is shown in Figure 3.1. According to Figure 3.1(a), ECore showed a linear response up to about 0.4 ksi, followed by a nonlinear response with hardening up to 60% strain. A rubber-like nonlinear stiffening was observed, particularly at large compressive strains (>35%), which is attributed to the alignment of the macromolecular network of the entangled polymer chains (Bardenhagen et al. 1997). During the loading process, a homogenous deformation state was observed over the height of the specimen. However, ribs were formed locally on the surface of the specimen which

was attributed to the local internal damages occurred close to the exterior surface due to the air entrapped in the mix over the casting process.

According to Figure 3.1(b), ECast showed a linear response up to about 7 ksi, followed by a nonlinear response with hardening up to the peak stress of about 8.5 ksi. Following the peak strength, a mild post-peak softening is observed up to about 11% strain, followed by a plateau up to 14% strain. At compressive strains exceeding 14%, the material stiffened again up (rubber-like nonlinear stiffening) to a compressive strength of 13.8 ksi at 50% strain. During the loading process, a nonhomogeneous deformation state (indicated by barreling of the specimen) was observed over the height of the ECast, with maximum lateral deformation in the vicinity of the mid-height of the specimen which decreased towards to ends of the specimen.

According to Figure 3.1(c), EShore's response clearly resembled the response of a neo-Hookean rubber-like material (Ogden 2013). The response was initially linear. No clear plateau was observed during the loading process. At 40% strain, nonlinear stiffening was observed up to the peak compressive strain of 60%. Similar to ECore, uniform barreling was observed over the height of the EShore during the loading process. Moreover, ribs were formed locally on the surface of the specimen which was attributed to the local internal damages occurred close to the exterior surface due to the air entrapped in the mix over the casting process.

The elastic modulus of ECore, ECast, and EShore was defined as 17 ksi, 273 ksi, and 2 ksi, respectively, which also include the contribution of the flexibility of the loading

frame and will be refined later. Given the relatively low mechanical properties of the EShore compared to ECore and ECast, it was found unsuitable for the proposed application. It is worth noting that the lower mechanical properties of ECore, compared to ECast, was primarily attributed to the air entrapped in the material during mixing. Generally, the density and subsequently the mechanical response of polymers can significantly change by the mix quality, especially the entrapped-air content. The density and mechanical properties of polymers decrease with the amount of entrapped-air content. The entrapped-air content can be minimized if both the resin and isocyanate are degassed in a vacuum chamber prior to use.

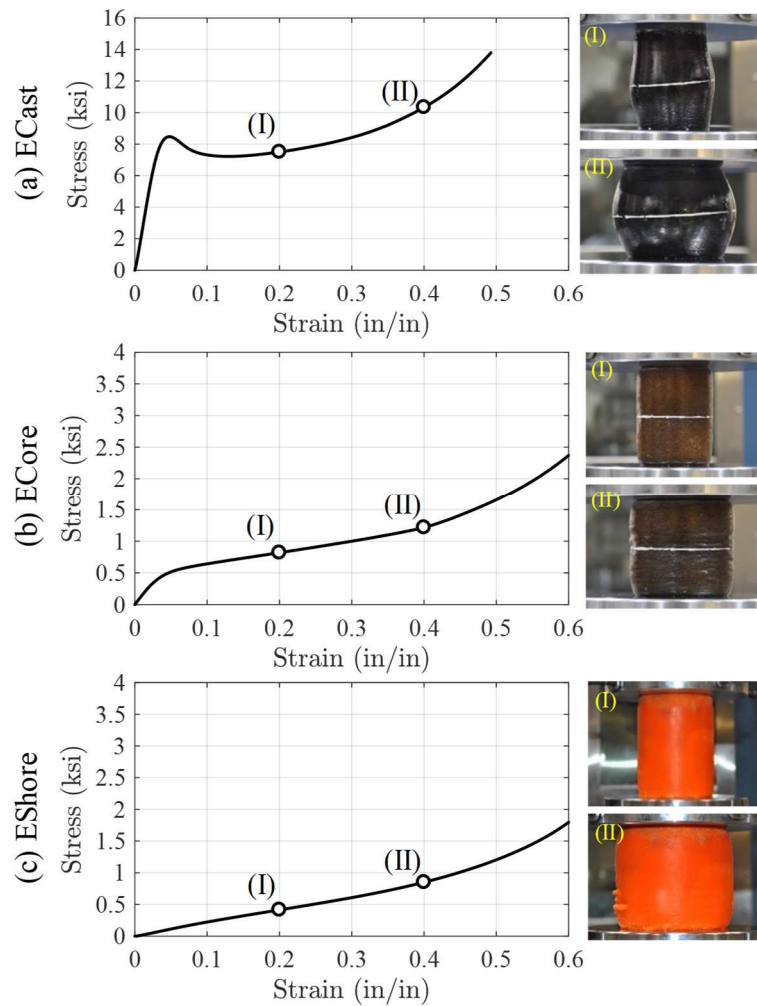


Figure 3.1. Stress versus strain curve and deformed shape at 20% and 40%: (a) ECast; (b) ECore; (c) EShore.

3.3.2. Phase 2 – Compression Testing of Selected PUs

According to the findings of Phase 1 of the testing program, among the three PU materials considered in this study, EShore was found unsuitable for the proposed application, primarily due to its low mechanical properties. Phase 2 was aimed at further

investigation of the response of ECore and ECast, particularly focusing on its response in compression, including monotonic loading, relaxation segments and unloading.

3.3.2.1. Test Specimens

Both ECast and ECore are classified as highly cross-linked polyether polyol-based thermoset polymers. ECast specimens were casted in the Structures and Materials Testing Laboratory (SMTL) at University of Colorado (CU) – Boulder. For the preparation of the ECast, the resin, which is a liquid, is first re-homogenized through shaking and stirring, because it includes solid materials, which settle and agglomerate over time and act as moisture scavengers. Subsequently, the isocyanate, which is also a liquid, is added to the resin and mixed with a spatula for 30 seconds. The prepared solution is then poured into cylindrical molds of length of 4 in. and diameter of 2 in., corresponding to specimens with aspect ratio equal to 2, in accordance with ASTM D695 (2010). The specimens are then cured at room temperature (~ 73 °F [23°C]) for 2 days. On the contrary, ECore specimens were casted in BASF's facilities, because both the resin and isocyanate needed to be degassed in a vacuum chamber prior to their use to minimize the air entrapped in the mixture. After degassing, the resin and isocyanate were mixed at 2000 rpm for 36 seconds in a centrifugal mixer connected to a vacuum system. The resulting mixture is poured into 2×4 in² cylindrical molds in an angle to minimize air bubbles. ECast specimens prepared in SMTL and BASF's facilities were compared in terms of their mechanical properties to ensure consistency.

3.3.2.2. Testing Program and Loading Protocols

Each PU specimen was subjected to a uniaxial compression strain-controlled half-cycle under a constant engineering strain rate using the test setup shown in Figure 3.3. Because PU materials demonstrate rate-dependent properties, a number of hold periods during which the applied strain was held constant was inserted into the loading strain history (Figure 3.2(a) and (b)) to assess the stress relaxation properties of the material. Additionally, at the end of the loading half-cycle, when contact between the specimen and the loading piston was lost, the (unloaded) specimen was left to recover for a period of 4 hours. Both the stress relaxation and deformation recovery histories generated by the selected loading protocol are fundamental to the calibration of the viscous components of the material models.

The ECore and ECast specimens were loaded to a peak nominal strain of 20% and 10%, respectively, while tests were conducted for three different compression strain rates, i.e. 0.001 s^{-1} , 0.01 s^{-1} , and 0.05 s^{-1} . For both the ECore and ECast specimens, the hold period was 125 s in between strain increments of 0.025 for the strain rate of 0.001 s^{-1} , 12.5 s in between strain increments of 0.025 for a strain rate of 0.01 s^{-1} , and 5 s in between strain increments of 0.05 for a strain rate of 0.05 s^{-1} . All tests were performed at room temperature ($\sim 73 \text{ }^\circ\text{F}$ [23°C]) and under normal humidity conditions (40% - 50%).

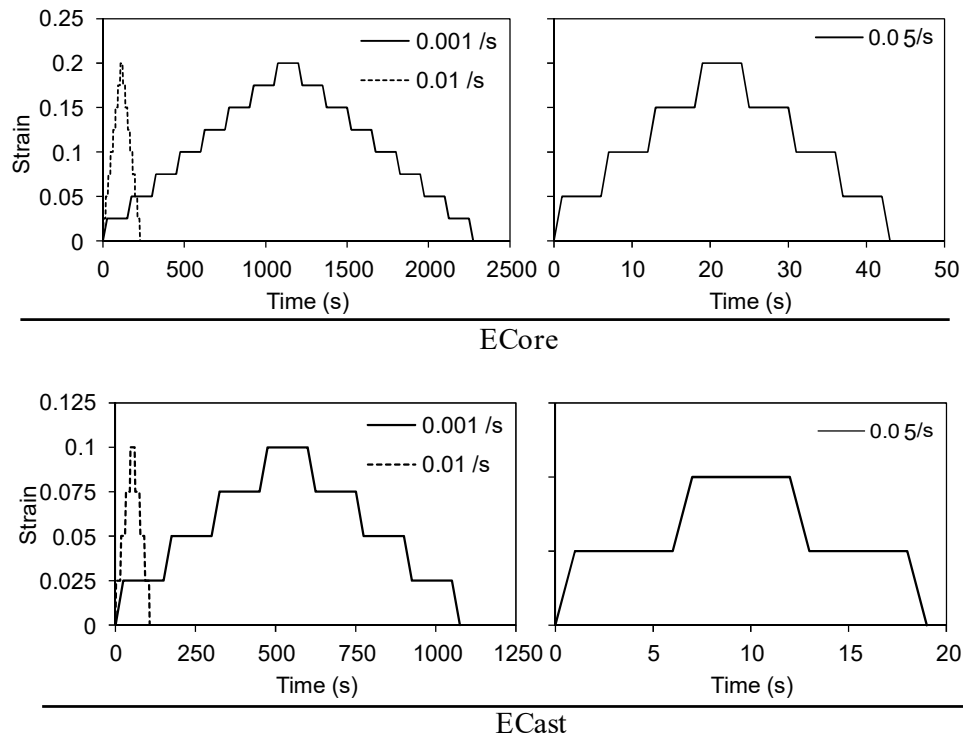


Figure 3.2. Applied strain history for ECore and ECast.

3.3.2.3. Test Setup and Instrumentation

Tests were conducted via a uniaxial servo-hydraulic MTS-810 system with 110 kips loading capacity and a total stroke of 6 in. (± 3 in.). The control system was an MTS FlexTest 60 digital controller.

Figure 3.3 shows the test setup. To get the actual deformation of the specimen excluding the deformation of the machine, the axial deformation of the specimens was directly measured by two external linear variable differential transformer (LVDTs) with a total stroke of 2 in. (± 1 in.) placed between the top and bottom platen. LVDTs were attached to an aluminum plate resting on top of the specimen, as the reference. Both the

upper and lower aluminum contact plates of the test setup (Figure 3.3) were lubricated with silicone oil to minimize friction that would prevent lateral expansion at the specimen ends. The axial force was measured by the load cell of the testing machine.

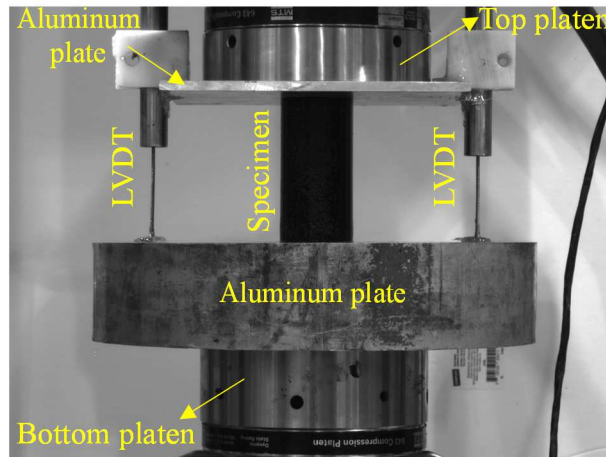


Figure 3.3. Details of the test setup.

3.3.2.4. Data Post-processing

Engineering strain and stress values were calculated and reported for all tests. The engineering strain was obtained by dividing the deformation by the initial height of the specimen at the undeformed state. The engineering stress was obtained by dividing the force by the initial cross-section area of the specimen at the undeformed state. A second order low-pass zero-phase Butterworth filter with a corner frequency of 1Hz was used to filter out the noise from the recorded signals from the loading frame load cell and LVDTs.

3.3.2.5. Results and Observations

Engineering stress vs. strain curves for ECore and ECast specimens are presented in Figure 3.4(a) for tests with the three strain rates, i.e. 0.001 s^{-1} , 0.01 s^{-1} , and 0.05 s^{-1} . Both materials demonstrated visco-plastic properties, according to which, in the elastic range, the dependence of the response on the strain rate was small, whereas, in the inelastic range, the response is significantly affected by the strain rate. Consistent with observations made in Phase 1, ECore exhibited lower stiffness and strength than those of ECast, while, for both materials, the stiffness and strength increased with the strain rate. It is worth noting that compared to response obtained in Phase 1 for ECore, the mechanical properties of ECore have significantly increased by degassing the resin and isocyanate prior to use. As shown in Table 3.2 and 3.3, the peak compressive strength (over the entire applied strain history) increases by 22% and 44%, for ECore and ECast, respectively, as the strain rate increases from 0.001 s^{-1} to 0.05 s^{-1} . However, the elastic modulus, which is less dependent on the strain rate, increases only by 6% and 20%, for ECore and ECast, respectively, as the strain rate increases from 0.001 s^{-1} to 0.05 s^{-1} . ECore exhibited hardening post-elastic response, and for this reason, the peak strength was observed at the peak strain. On the contrary, ECast exhibited mild softening properties, and the peak strength was observed at a strain of approximately 7% (for all strain rates), which was smaller than the peak applied strain. The unloading branches are nearly identical, for different strain rate tests, since they are controlled by the elastic properties of the material, which are less dependent on the strain rate.

During the constant strain periods, the observed *stress relaxation* was primarily dependent on the duration of the hold period, rather than the strain amplitude or rate. For both PU materials, stress relaxation was larger in the loading branch (where it appears as stress reduction) than the unloading branch (where it appears as stress increase). During each hold period, about 85% of the stress relaxation occurred in the first 2 to 5 seconds, irrespectively of the loading rate. This overall time-dependent behavior is characteristic of conventional elastomeric materials (Haward and Thackray 1968; ASTM-D695 2010; Ogden 2013).

Following the end of the half-cycle, the *strain recovery* of the (unloaded) specimen was measured (Figure 3.4(b)). For all tests and PU materials, the rate of recovery is initially large, but it reduces over time. The residual strains (at all time instants) decrease with the rate of loading, implying that plastic traveling is smaller at higher strain rates, which is consistent with the fundamentals of visco-plasticity. According to Table 3.4, for ECore, the residual strain is 38% of the total peak strain of 0.2 applied at a strain rate of 0.001 s^{-1} , whereas it reduces to 26% of the total peak strain of 0.2 applied at a strain rate of 0.05 s^{-1} . For ECast, the residual strain is 50 % of the total peak strain of 0.1 applied at a strain rate of 0.001 s^{-1} , whereas it reduces to 32% of the total peak strain of 0.1 applied at a strain rate of 0.05 s^{-1} . Moreover, the rate of recovery is higher for the tests conducted at larger strain rates. Specifically, for the ECore, 68% and 89% of the total recovery is achieved in the first 10 minutes for the tests conducted at strain rates of 0.001 s^{-1} and 0.05 s^{-1} , respectively. For the ECast, 72% and 94% of the total recovery is achieved in the first 10 minutes for the tests conducted at strain rates of 0.001 s^{-1} and 0.05 s^{-1} , respectively.

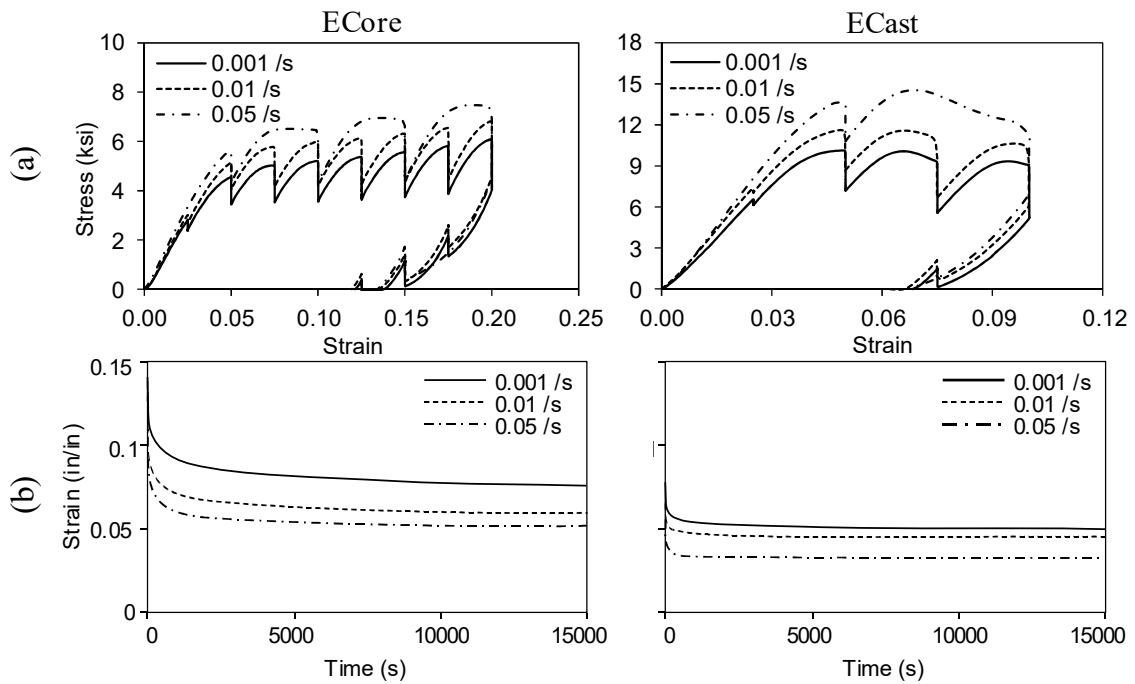


Figure 3.4. (a) Engineering stress vs. strain curves; (b) Strain recovery history of specimens at the end of loading application.

Table 3.2. Summary of mechanical properties for ECore.

	Strain Rate (s^{-1})		
	0.001	0.01	0.05
E (ksi)	130 (0.036)	138 (0.038)	146 (0.040)
f_c (ksi)	6.1 (1.22)	6.83 (1.37)	7.47 (1.49)

Note: Numbers inside parantheses are parameters normalized to normal weight concrete with nominal compressive strength of 5 ksi.

Table 3.3. Summary of mechanical properties for ECast.

	Strain Rate (s^{-1})		
	0.001	0.01	0.05
E (ksi)	287 (0.07)	314.5 (0.08)	350 (0.09)
f_c (ksi)	10.1 (2.02)	11.6 (2.32)	14.5 (2.90)

Note: Numbers inside parantheses are parameters normalized to normal weight concrete with nominal compressive strength of 5 ksi.

Table 3.4. Summary of strain recovery response.

	ECore			ECast		
	Strain Rate (s ⁻¹)			Strain Rate (s ⁻¹)		
	0.001	0.01	0.05	0.001	0.01	0.05
Residual strain: after test	0.121	0.120	0.134	0.070	0.066	0.066
Residual strain: 4 hr after test	0.075	0.058	0.052	0.050	0.045	0.032
Total recovery (%)	46	58	61	29	32	52
90% Recovery duration (min)	106	52	13	60	41	3
Residual strain after 10 min	0.096	0.072	0.061	0.055	0.048	0.034
% of total recovery after 10 min	68	82	89	72	86	94

3.3.3. Phase 3 – Multi-test Program on ECast and ECore

In this phase, an extensive set of uniaxial tests are conducted to further characterize the main features of two selected polyurethanes (PUs) studied in Phase 2. The wide variety of the selected tests is intended to allow for potential “decoupling” of different features of the response (e.g. rate-dependent and rate-independent parts) and support the systematic calibration of a numerical constitutive model proposed later in this study.

3.3.3.1. Test Specimens

Specimens were casted in BASF’s facilities, because both the resin and isocyanate need to be degassed in a vacuum chamber prior to use. After degassing, the resin and isocyanate were mixed at 2000 rpm for 36 seconds in a centrifugal mixer connected to a vacuum system. The resulting mixture was poured into 2×4 in² cylindrical molds corresponding to specimens with aspect ratio equal to 2, in accordance with ASTM D695 (2010). The mixture was poured in the molds in an angle to minimize air bubbles. The specimens were then cured at room temperature (~ 73 °F [23°C]) for 2 days.

For testing procedures including tension (monotonic tensile, cyclic tensile, cyclic compression-tension), dog-bone specimens were milled out of the cast cylinders with the

geometry details shown in Figure 3.5(a). The gauge length and the reduced section diameter of specimens was 1 in. and 0.65 in., respectively.

3.3.3.2. Testing Program and Loading Protocols

The testing program included multi-step compression relaxation tests, monotonic compression and tension tests, compression-only and tension-only cyclic tests, cyclic combined tension-compression tests, and creep and relaxation tests. To investigate the effect of temperature on the mechanical properties of the selected PUs, uniaxial monotonic (in compression) and reversed cyclic loading tests were conducted at various temperatures. The variability and reproducibility of the obtained responses was investigated for the monotonic compression tests at various strain rates by repeating several of those tests under the same loading conditions. However, the *test-to-test variability was found to be very small*, particularly for low strain rates, and, for this reason (and limitations in available resources), repetitions were not performed for all tests. However, for several tests over the testing program, repetitions were performed just to check that the reproducibility remained high.

3.3.3.3. Test Setup and Instrumentation

Tests were conducted via a uniaxial servo-hydraulic MTS-810 system with 110 kips loading capacity and a total stroke of 6 in. (± 3 in.). The control system was an MTS FlexTest 60 digital controller.

Figure 3.5(b) shows the compression-only test setup for cylindrical specimens. The test setup and instrumentation were similar to the ones used in Phase 2 of the testing program.

Dog-bone specimens were tested using the setup shown in Figure 3.5(c). An MTS 634.31E-24 extensometer with the total stroke of 0.3 in. was used to measure the deformation over the gage length. The extensometer was fixed to the specimen using rubber bands (Figure 3.5(c)).

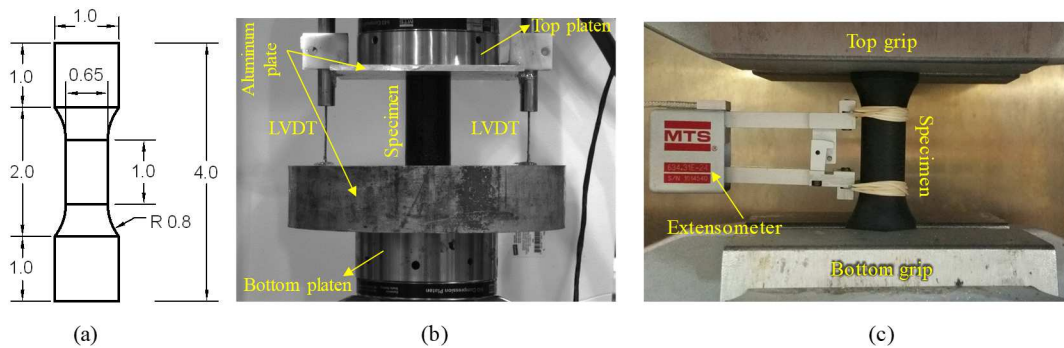


Figure 3.5. (a) Geometry of dog-bone specimens; (b) test setup for cylindrical specimens; (c) test setup for dog-bone specimens.

For the tests at various temperatures beyond the room temperature, an environmental chamber was used to hold the temperature constant at the target value during a test (Figure 3.6). The specimens were conditioned in the chamber prior to testing for one day to ensure a uniform temperature over their volume.



Figure 3.6. Test setup for tests at various temperatures.

Non-contact strain measurement devices, specifically optical devices, have been widely used recently to characterize the mechanical properties of various materials (Parsons et al. 2004; Parsons et al. 2005; Addiego et al. 2006; Fang et al. 2006; De Almeida et al. 2008). Optical measurement devices are particularly desirable for soft materials, since local stress concentrations at the attachment points of mechanical devices (e.g. extensometers) are totally avoided (Jerabek et al. 2010). Moreover, emergence of numerical material models based on nonlocal and gradient theories requires more advanced measurement techniques to get the required data for model calibration purposes (i.e. strain distributions over an area/length of interest). As a result, strain measurement in the form of contours over an area of interest is more desirable than measuring over a so-called gage length and calculating an average strain. Measuring strain over an area using conventional strain measuring instruments (i.e. strain gage, extensometer, LVDTs, etc.) would be very expensive or impractical.

In principle, optical strain measurement devices can be categorized in two groups: (1) devices with a fixed gage length which measure strain between two marks on the test specimen (known as video extensometers (Fauster et al. 2005)), (2) full-field strain measurement devices, commonly known as digital image correlation (DIC) (Jerabek et al. 2010). A comprehensive literature review on the history of DIC systems can be found in Schreier et al. (2009).

In this study, a digital image correlation (DIC) system known as Vic-2d (Correlated Solutions 2017) was used to measure the strain contour over an area of the interest. In DIC, a mathematical correlation analysis is conducted on the images taken from the specimen over the test to get the desired measurement data. The Vic-2d system consists of a digital camera with specific lens and resolution (Figure 3.7(a)) and a software package for capturing and processing images. Using Vic-2d, two-dimensional displacement and strain maps can be generated. The DIC technique relies on a contrasting, non-repetitive (random), and isotropic pattern on the surface of the specimen. The speckles should be of an optimal size (neither too small nor too large) to get excellent results. Thus, the resolution and accuracy of measurements of a DIC system depends on the entire system including objective, camera, light system, and speckle pattern (Jerabek et al. 2010). Herein, a white rubbery paint is used to create a speckle pattern over the gage length of the dog-bone specimens (Figure 3.7(b)). In principle, any DIC system overlays a grid of *subsets* on the random gray value intensity distribution of the pattern produced on the object (Jerabek et al. 2010). The subset size is equivalent to the minimum local gage length (Jerabek et al. 2010). During a test, as the specimen is deformed, the pattern is deformed

accordingly. In the recorded images, the subsets can be detected in each frame based on the intensity distribution determined in the reference image (un-deformed state) (Jerabek et al. 2010). As the specimen is strained, the strain field on the specimen surface is calculated by analyzing the speckle pattern and the deformed subsets.

It should be noted that the DIC technique was used only for selected tests conducted on dog-bone specimens at room temperature. Images were recorded simultaneously with the acquisition of the analog inputs (e.g., force and displacement signal) from the test machine. The camera was mounted on a tripod located at about 4 ft. from the specimen. The photo shooting speed was limited to maximum 8 frames per second by the camera.

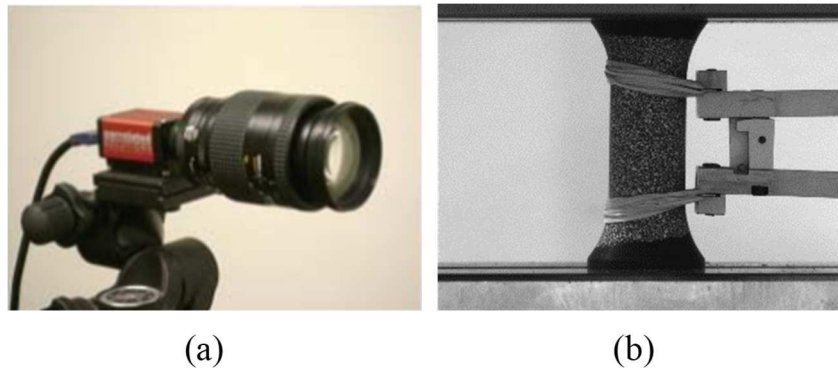


Figure 3.7. (a) Vic-2d camera; (b) speckle pattern on a dog-bone specimen.

3.3.3.4. Data Post-processing

For all tests, engineering strains and stresses were calculated and reported. The engineering strain was obtained by dividing the extension/contraction by the initial height

of the specimen at the undeformed state. The engineering stress was obtained by dividing the force by the initial cross-section area of the specimen at the undeformed state.

The size of the subsets (equivalent to the minimum gage length) is known to be the most critical software specific adjustable parameter of a DIC system, affecting the accuracy of the calculated results (Pan et al. 2008; Jerabek et al. 2010). It should be noted that there is no systematic method to define the proper subset size and is based on the operator experience and judgment (Jerabek et al. 2010). In this study, square subsets with a size of 21 pixels and a step of 5 pixels between the two subsets were used.

Looking at the stress-strain curves from the LVDTs, a toe segment was observed in the early stage of the test, which is known as a typical artifact originated from a take-up of slack, and alignment or seating of the specimen (ASTM D695 2010). To get correct values for parameters such as strain and modulus, this artifact must be corrected to get the actual zero point of the strain axis. In this study, the method suggested in ASTM D695 (2010) for materials with Hookean (linear) region is used for toe compensation. In this method, the zero-strain point (B) is obtained by continuation of the linear segment (CD) of the curve through the zero-stress axis (strain-axis). All strains are measured from the corrected zero-strain point (B).

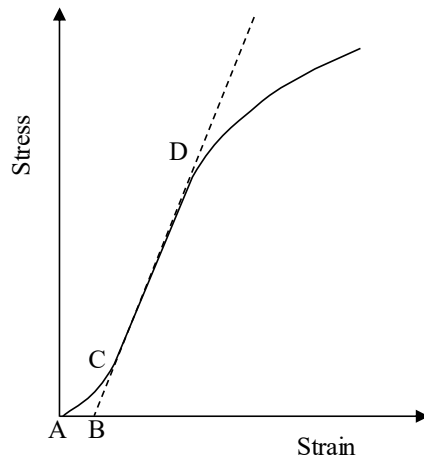


Figure 3.8. Toe compensation for material with Hookean region.

A second order zero-phase low-pass Butterworth filter with a corner frequency of 1Hz was used to filter out the noise from the recorded test measurements from the loading frame load cell and two external LVDTs. No filtering was applied to the data measured by the DIC system.

3.3.3.5. Test Results

3.3.3.5.1. Multi-step Compression Relaxation Testing

3.3.3.5.1.1. Objective

The main objective of this test is to characterize the rate independent part of the response, known as equilibrium path, which consists of a set of equilibrium points obtained by stress relaxation segments (i.e. constant strain holding periods) at the different strains. Additionally, the intermittent relaxation segments allow to get an insight into the relaxation response of the material at various strain/stress levels during both loading and unloading.

Theoretically, the equilibrium path can be determined through a continuous monotonic test at a nearly-zero strain rate. Because load application at a nearly-zero strain rate could be impractical, the equilibrium path is often obtained by tests at higher, yet low, strain rates with intermediate constant strain holding periods, which allow for stress relaxation. A “sufficiently” low strain rate is dependent on the viscoelastic and viscoplastic properties of a material. For example, for stainless steel, Haupt and Lion (1995) showed that the stress vs. strain curves obtained from very low strain rate tests were very close to the equilibrium path composed of discrete equilibrium points obtained from tests at higher strain rates, but with intermediate stress relaxation segments. On the contrary, considering the much more dominant viscous properties of polyurethanes and the practical limitations in loading application in a laboratory environment, a monotonic test at low strain rate would not be slow enough to predict their equilibrium path.

It should be noted that herein, the equilibrium path was characterized for the compression response only, which is of primary importance for applications to PU-enhanced columns.

3.3.3.5.1.2. Details of the Testing Procedure

In this study, each specimen was subjected to a uniaxial compression strain-controlled monotonic loading at various strain rates and up to a strain of 0.2 and 0.1 for ECore and ECast (Table 3.5), respectively, using the test setup shown in Figure 3.5(b). A number of holding periods during which the applied strain was held constant was inserted into the loading and unloading branch at strain increments of 0.025 and 0.01 in ECore and ECast, respectively.

According to observations from relaxation tests (presented later in Section 3.3.3.5.5), stress relaxation significantly slows down in about 48 hr with stress rates becoming lower than 10^{-6} ksi/s. Because a monotonic test with several 48 hr holding periods would be impractical, holding periods of reduced duration (~36 min and ~70 min for ECore and ECast, respectively) were selected. The reduced durations were found to result in about 80% of the stress relaxation observed in a 48 hr relaxation test.

The details of the testing procedure is summarized in Table 3.5.

Table 3.5. Multi-step relaxation test: summary of test procedure parameters.

Parameter	ECore	ECast
Target peak strain (in/in) (ϵ_{\max})	0.2	0.1
Strain increment (in/in) ($\Delta\epsilon$)	0.025	0.01
Holding period (min) (t_h)	36	70
Strain rates (/s)	0.001, 0.01, 0.05	0.001*

*The test data at 0.01 /s and 0.05 /s strain rates were corrupted.

3.3.3.5.1.3. Results and Observations

An approximation of the theoretical (zero stress rate) equilibrium path – indicated as “Eq. path” in Figure 3.9 – was obtained by connecting the discrete terminal points at the end of each intermediate relaxation segment (Figure 3.9(a)). Based on the stress time history of Figure 3.9(b), it is reasonable to expect that the actual equilibrium path may have slightly lower values in the plastic range, for which the stress rate at the end of the relaxation segments was slightly larger than the corresponding stress rate in the elastic loading and the unloading branches. A significant hysteretic response is observed for the equilibrium path since the terminal points of loading and unloading at each strain level do

not coincide. It is noteworthy that the equilibrium paths obtained for ECore from tests at various strain rates coincide (Figure 3.9 (a)).

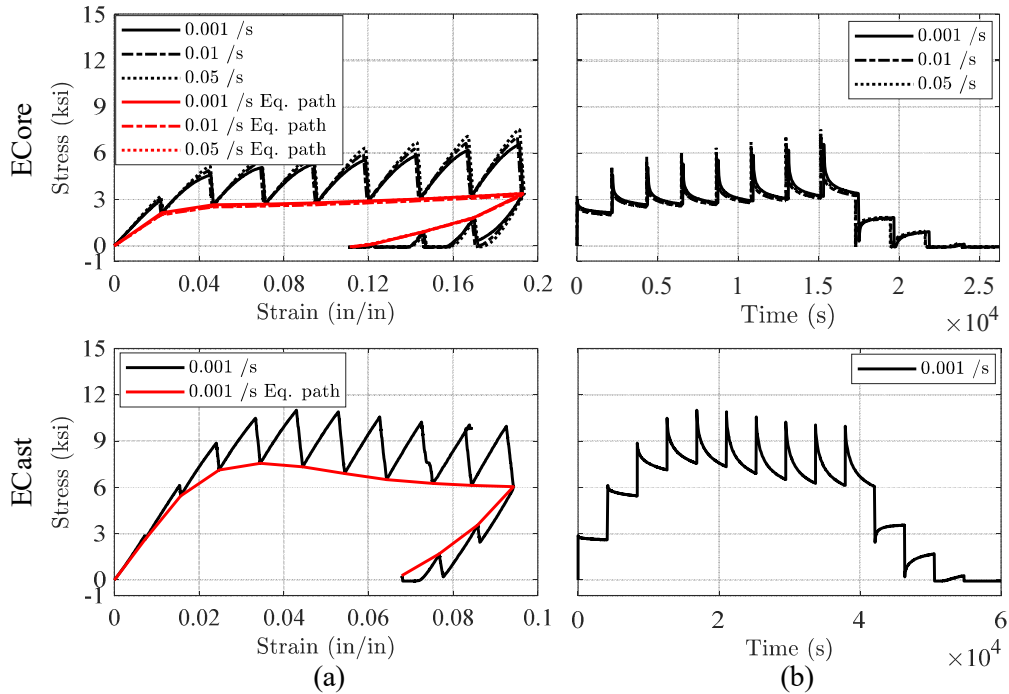


Figure 3.9. Multi-step relaxation test results: (a) stress-strain curves; (b) stress-time curves.

Figure 3.10 shows the stress relaxation ratio (defined as the ratio of stress at the end of each relaxation segment to the initial stress). Smaller values of this ratio represent higher relaxation. According to Figure 3.10, relaxation response was different at various strain/stress levels. Specifically, for both ECore and ECast, the stress relaxation ratio decreased with the strain amplitude up to about 0.07 strain, indicating that the total stress relaxation increased up to about 0.07. For higher strain values, the stress relaxation ratio

remained unchanged. Moreover, at the same strain magnitude, higher relaxation was observed in ECore than ECast.

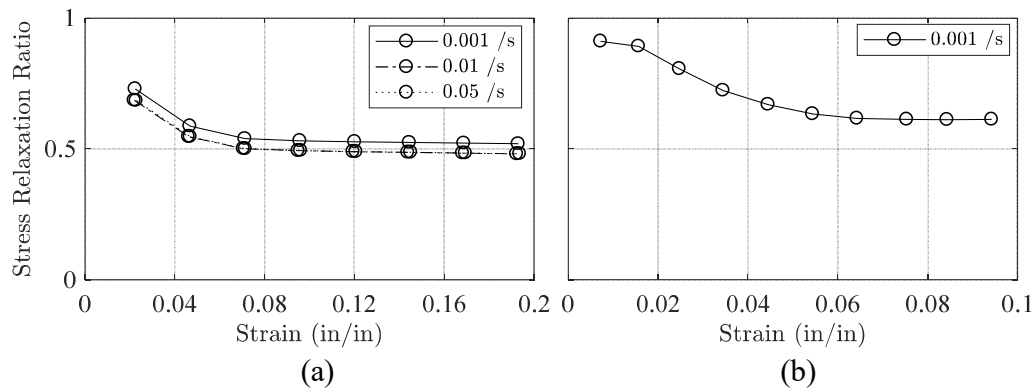


Figure 3.10. Stress relaxation ratio at each holding segment: (a) ECore; (b) ECast.

3.3.3.5.2. Monotonic Compression and Tension Tests at Various Strain Rates

3.3.3.5.2.1. Objective

If the stress-strain curve obtained from experiments conducted at different strain rates differ from each other, the material behavior is rate-dependent. The difference between the stress measured in an experiment at a nonzero strain rate and the equilibrium stress is called *overstress*.

The objective of this set of tests was to characterize the dependence of the compressive and tensile response of the selected polyurethane on the loading rate. Moreover, unloading to the zero stress will give further insights into the hysteretic

response of the material, which is further investigated later on through various cyclic loading protocols.

3.3.3.5.2.2. Details of the Testing Procedure

Compression testing included cylindrical specimens subjected, via the setup of Figure 3.5(b), to strain-controlled monotonic loading up to a peak nominal strain of about 0.2 and 0.1 for ECore and ECast, respectively (based on expected peak strains on bridge columns from early computational investigations, presented in Section 4 (Nikoukalam and Sideris 2017) followed by unloading to zero stress. Tests were conducted under a set of constant engineering strain rates (Table 3.6). The strain rate was increased from test to test until there was no significant change in the response, thereby, reaching the so-called *instantaneous response*.

Tension testing considered dog-bone specimens subjected to monotonic loading, with a set of constant engineering strain rates presented in Table 3.7, up to fracture (or peak stroke of the extensometer, whichever occurred first) using the test setup shown in Figure 3.5(c). Failure was not investigated in compression tests, because the selected polyurethane can accommodate strains up to 0.4-0.5, before failure is observed (Nikoukalam and Sideris 2016b) (see Section 3.3.1.4). Two specimens were tested at each strain rate in compression. The test data showed very good reproducibility with negligible difference in the measured response (see Figure A.1 for ECore and Figure A.2 for ECast).

Table 3.6. Monotonic compression test: summary of test procedure parameters.

	ECore	ECast
Target peak strain (in/in)	0.2	0.1
Strain rates (/s)	0.001, 0.01, 0.05, 0.1, 0.15, 0.2	0.001, 0.01, 0.05, 0.1

Table 3.7. Monotonic tension test: summary of test procedure parameters.

	ECore	ECast
Target peak strain (in/in)	Variable*	Variable**
Strain rates (/s)	0.001, 0.01, 0.05	0.001, 0.01, 0.05

* 0.27 in test at 0.001 /s strain rate (The travelling length of extensometer in compression (0.1 in.) was not used in tension); 0.33 in tests at 0.01 /s and 0.05 /s strain rate.

** Up to fracture or maximum stroke of the extensometer, whichever occurs earlier.

3.3.3.5.2.3. Results and Observations

The stress vs. strain responses of ECore and ECast in compression are presented in Figure 3.11(a) and (b), respectively, and in tension in Figure 3.12(a) and (b), respectively.

According to Figure 3.11 and Figure 3.12, as the strain rate increases, a clear non-proportional increase in the stress level is observed at all strain magnitudes and for both ECore and ECast, thereby approaching the *instantaneous* response. Moreover, the stress in ECast is substantially higher than ECore. Following the peak strength in compression, a mild post-peak softening is observed at all strain rates for ECast (Figure 3.11(b)), whereas no softening was observed for ECore. Prior testing of ECast (see Figure 3.1) indicated that, at larger compressive strains, the material stiffens again (Nikoukalam and Sideris 2016b). However, the post-peak response of ECast in tension is followed by fracture upon further straining (Figure 3.12(b)). The tensile fracture strain decreases as the strain rate increases. Specifically, the specimens fractured at a peak tensile strain of 0.153,

0.112, and 0.1 for nominal strain rates of 0.001 /s, 0.01 /s, and 0.05 /s, respectively. No post-peak softening was observed in the compressive and tensile response of ECore (Figure 3.11(a) and Figure 3.12(a)). For ECore, tension tests were terminated prior to reaching their fracture strain, which appears to be larger than 25% to 35%.

By accounting for the difference in the achieved peak strain for various strain rates, it can be concluded that the unloading branches of compressive response are nearly identical, for tests conducted at different strain rates, because unloading is controlled by the elastic properties of the PU, which are less dependent on the strain rate. It should be noted that the achieved strain levels (calculated using data from external LVDTs) are smaller than the target strain values. This is due to the fact that part of the applied deformation goes to the deformable parts of the machine and test setup.

For ECast, compression tests at 0.001 /s strain rate with cylindrical specimens predicted a compressive strength almost identical to the tensile strength from dog-bone specimens. At 0.01 /s and 0.05 /s strain rates, the compressive strength was found to be larger than the tensile strength by 0.69 ksi and 0.78 ksi, respectively. However, it should be noted that the tensile and compressive specimens are of different shapes and also have different boundary conditions during the test. To account for the effects of specimen shape and boundary conditions, a dog-bone ECast specimen was also tested under monotonic compressive loading up to ~ 0.1 strain at 0.001 /s strain rate, where it showed a compressive strength of 1.2 ksi smaller than the tensile strength under the same strain rate. Given that, the larger compressive strength of the cylindrical specimens was considered

fictional and can be attributed, in part, to confinement effects at the ends of cylindrical compression specimens due to friction between the cylindrical specimens and the plates.

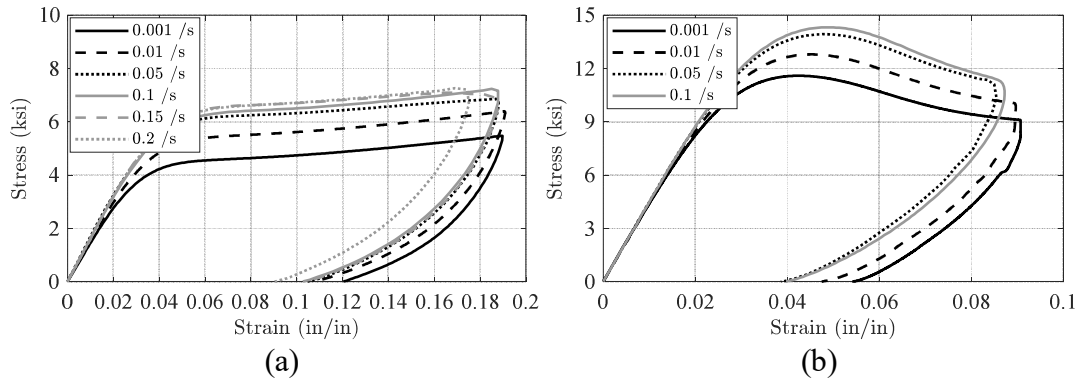


Figure 3.11. Stress-strain curves at various strain rates in compression: (a) ECore; (b) ECast.

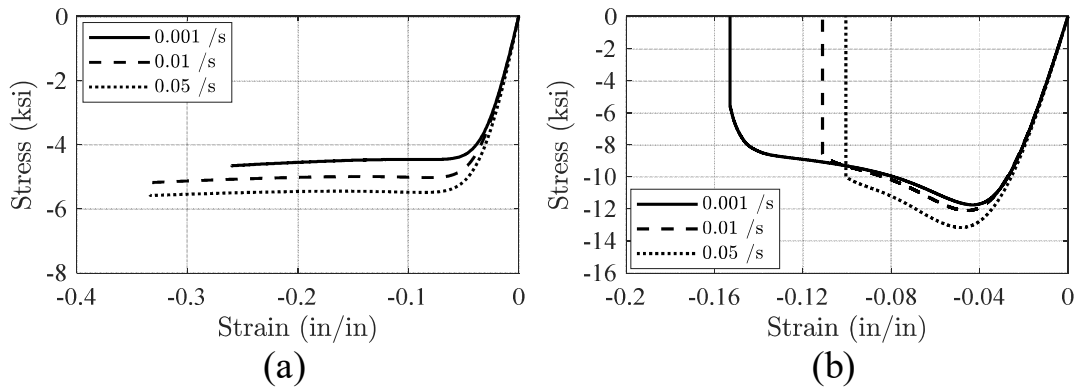


Figure 3.12. Stress-strain curves from monotonic tensile tests at various strain rates: (a) ECore; (b) ECast.

To get a better insight into the rate dependency of the compressive response in terms of strength, the variation of overstress with strain rate is presented in Figure 3.13.

Overstress is defined at various strain levels as the difference in the stress in equilibrium path obtained from the multi-step compression relaxation tests (see Section 3.3.3.5.1), and the total stress at each selected strain level. It can be seen that overstress is significantly larger in the plastic range of the response where the viscoplastic component is activated. Compared to the equilibrium state, for strains exceeding 2%, the overstress increased up to 4 ksi at 10% strain level (150% increase relative to the equilibrium state) and 7 ksi at 8% strain (110% increase relative to the equilibrium state) in ECore and ECast, respectively. At 2% strain, the overstress is limited to 1.7 ksi (65% increase relative to the equilibrium state) and 2.2 ksi (40% increase relative to the equilibrium state) in ECore and ECast, respectively. For large enough strain levels where the viscoplastic component is fully activated, the variation of overstress with strain rate is similar for various strain levels. Moreover, it can be seen that the overstress does not change significantly with the strain rate beyond 0.15 /s and 0.05/s for ECore and ECast, respectively.

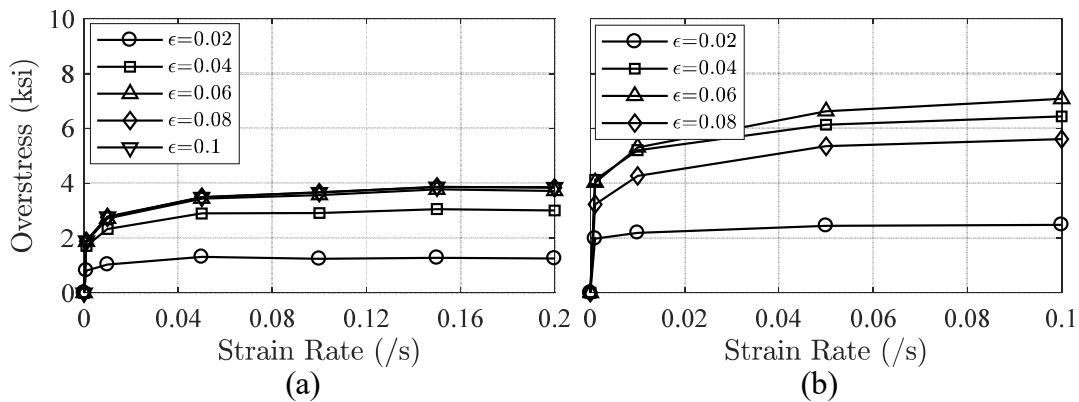


Figure 3.13. Variation of compression overstress with strain rate at various strain levels: (a) ECore; (b) ECast.

The variation of the compressive and tensile elastic modulus with the strain rate is shown in Figure 3.14 and Figure 3.15, respectively. It should be noted the elastic modulus from the equilibrium path was also included in Figure 3.14. From the equilibrium path, the elastic modulus was determined as 96 ksi and 363 ksi for ECore and ECast, respectively. As the strain rate increases to 0.001 /s, the elastic modulus increases by 52% and 25% for ECore and ECast, respectively, compared to the elastic modulus of the equilibrium path. However, as the strain rate further increases, the elastic modulus remained nearly constant in both ECore and ECast.

The elastic modulus was found to be the same in tension and compression for ECast (Figure 3.16(a) and Table 3.8), especially at strain rates exceeding 0.001 /s. The elastic modulus of ECore was found to be ~16% higher in compression than tension (Table 3.8).

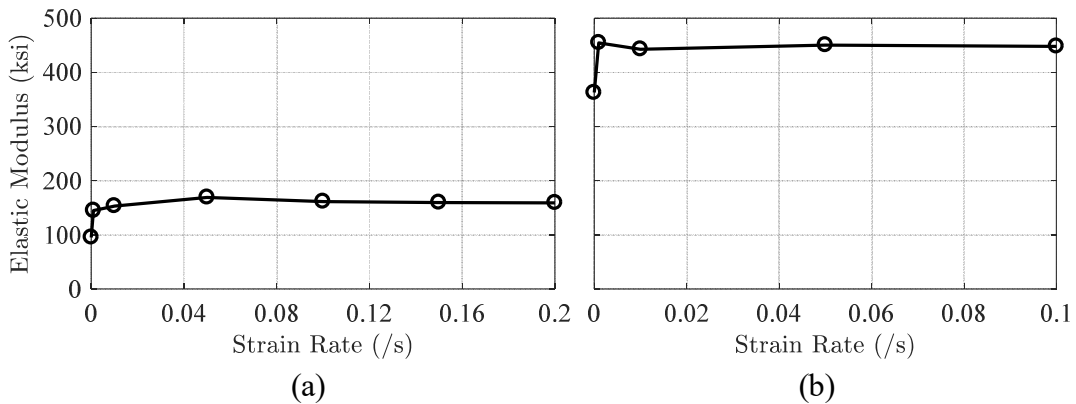


Figure 3.14. Variation of compressive elastic modulus with strain rate: (a) ECore; (b) ECast.

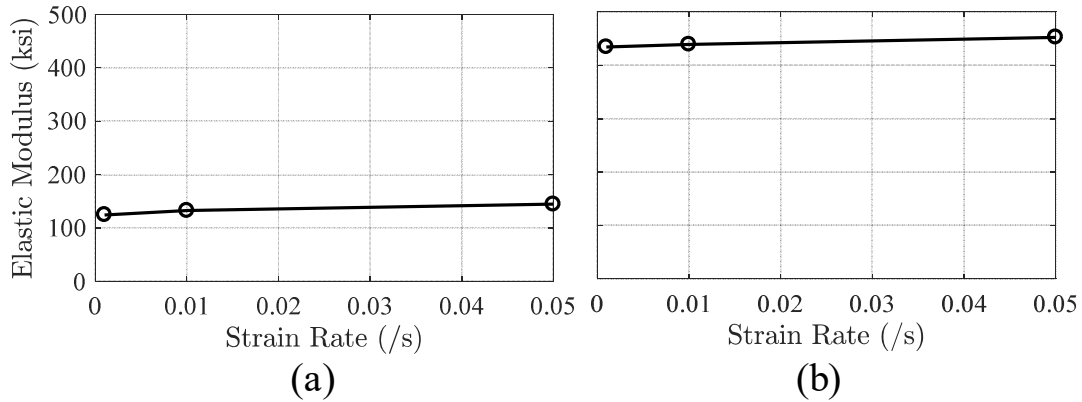


Figure 3.15. Variation of tensile elastic modulus with strain rate at various strain levels: (a) ECore; (b) ECast.

Table 3.8. Elastic modulus in tension and compression at various strain rates.

Strain rate (/s)	Elastic modulus (ksi)			
	ECore		ECast	
	Tension	Compression	Tension	Compression
0.001	125	145	434	455
0.01	133	153	439	443
0.05	145	169	453	451
0.1	-	154	-	450

As the strain rate increased from 0.001 /s to 0.01 /s and, then, to 0.05 /s, the compressive peak stress of ECast increased by 10% and 20% respectively, while the tensile peak stress increased by 3% and 12%, respectively (Figure 3.16(b)). Under both tension and compression, the strain at the peak stress increased by 5% and 12% as the strain rate increased from 0.001 /s to 0.01 /s and 0.05 /s, respectively (Figure 3.16(c)). Similar comparison of response parameters in tension and compression could not be made for ECore, since the response did not show a clear peak.

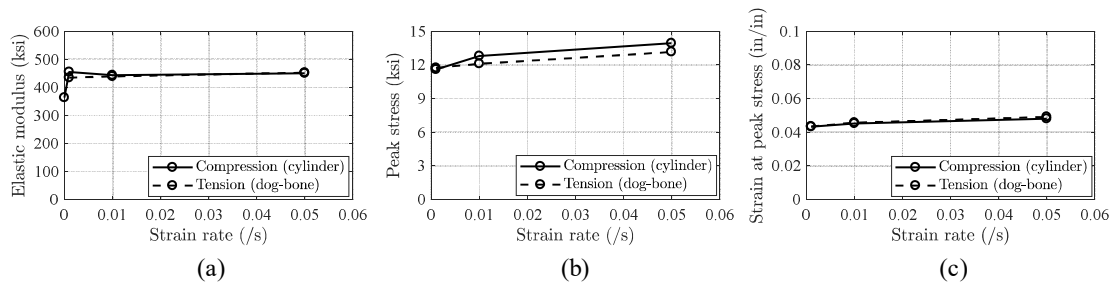


Figure 3.16. Variation of response parameters under compression and tension with strain rate for ECast: (a) elastic modulus; (b) peak stress; (c) strain at peak stress.

The un-deformed and deformed shape of the ECore and ECast at the peak compressive strain and after unloading at various strain rates is shown in Figure 3.17 and Figure 3.18, respectively. In both ECore and ECast, an inclined potential failure surface was observed over the test at large compressive strains at all strain rates. It is noteworthy that the inclination of the ECore specimen at the peak compressive strain at 0.01 /s strain rate is towards back which is not visible the front elevation shown in Figure 3.17.

The deformed shape of the ECore and ECast at the peak tensile strain at various strain rates is shown in Figure 3.19 and Figure 3.20, respectively. It should be noted that for ECast, the presented deformed shape is one frame prior to fracture. As shown in Figure 3.19, no sign of damage was observed in the ECore up to the end of the test at various strain rates. In ECast, a highly strained neck region was observed in the vicinity of the mid-gauge length where horizontal cracks were formed, which is an indication of response ductility. The size of the highly strained neck region decreased with the loading rate, indicating ductility reduction with loading rate, which was also reflected in the tensile strain at peak strength and the tensile fracture strain reduced with the strain rate.

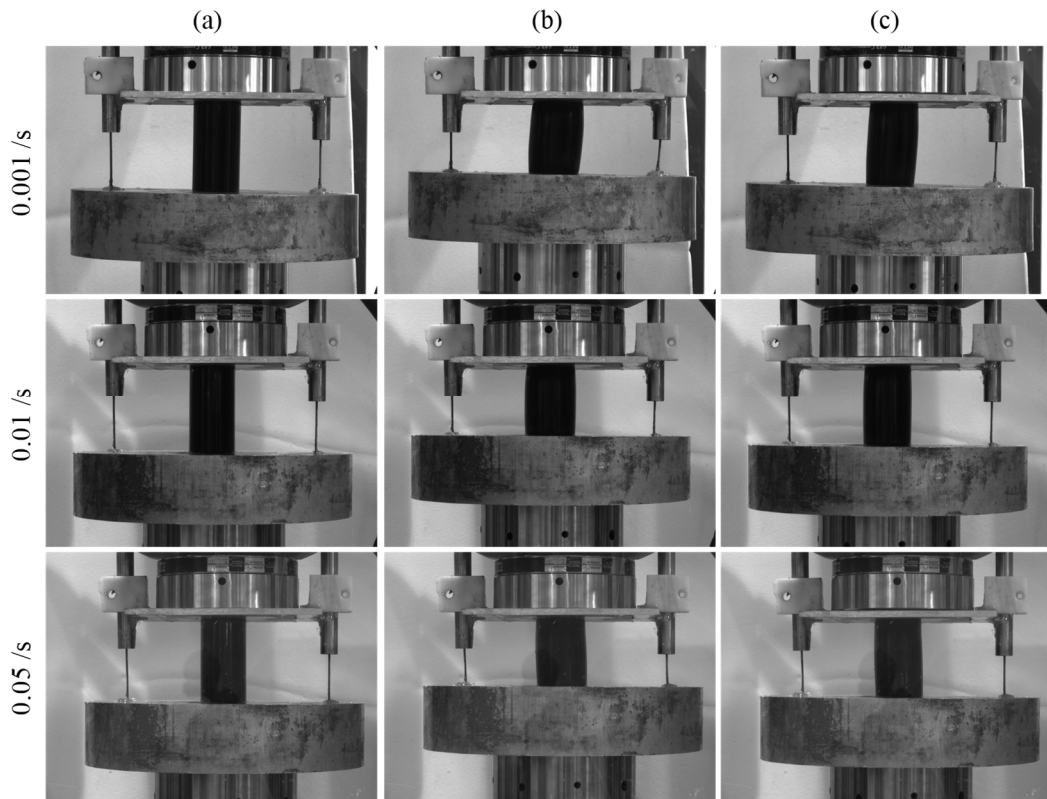


Figure 3.17. Deformed shape of ECore specimens under monotonic compressive load at various strain rates: (a) un-deformed state; (b) peak compressive strain (~10%); (c) after unloading.

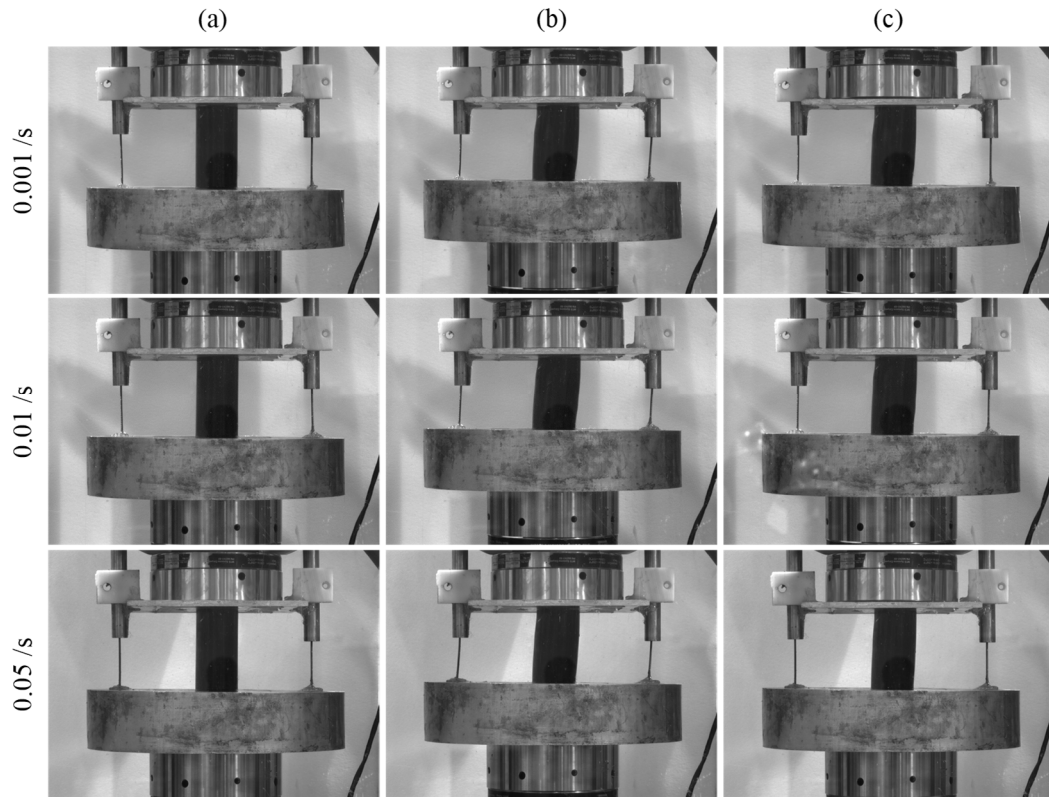


Figure 3.18. Deformed shape of ECast specimens under monotonic compressive load at various strain rates: (a) un-deformed state; (b) peak compressive strain (~10%); (c) after unloading.

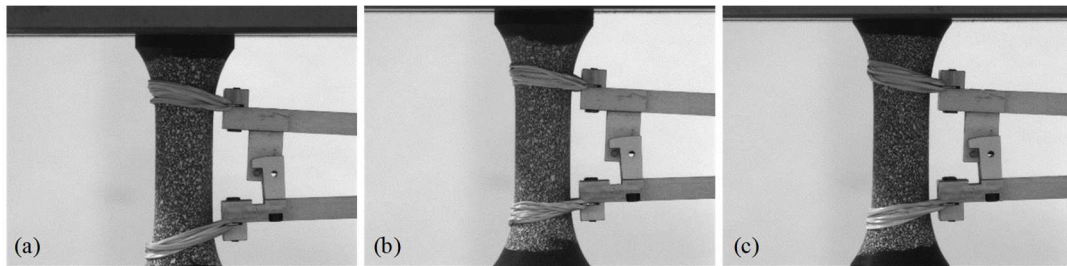


Figure 3.19. Deformed shape of ECore specimens at the end of monotonic tensile load at strain rate of: (a) 0.001 /s; (b) 0.01 /s; (c) 0.05 /s.

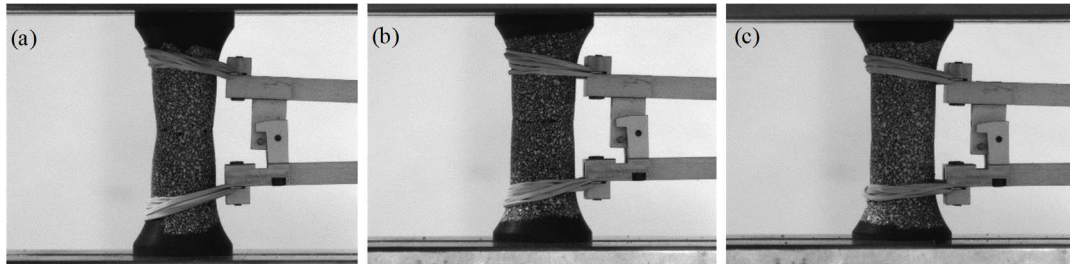


Figure 3.20. Deformed shape of ECast specimens at the end of monotonic tensile load at strain rate of: (a) 0.001 /s; (b) 0.01 /s; (c) 0.05 /s.

3.3.3.5.3. Cyclic Compression-only and Tension-only Tests at Various Strain Rates

3.3.3.5.3.1. Objective

Cyclic loading with increasing strain amplitude and repeated cycles at each strain amplitude provides information on cyclic damage and in-cycle damage, associated with cumulative and peak compressive/tensile plastic strains, respectively. It was reported by researchers that rubbery materials show a significant *softening* after experiencing the first cycle of loading in tension. This phenomenon was extensively investigated by Mullins (1948), and is often referred after his name as “Mullins effect”. The Mullins effect can be described as below:

- Some rubbery materials show softening (strain softening) under repeated cycles at a constant strain level. Most of the softening occurs in the first cycle and after a few cycles, the material response tends to stabilize to a fixed path.
- As the strain level exceeds the maximum previously experienced strain level, the material response quickly reaches that of a virgin sample loaded monotonically (strain hardening)

Except for uniaxial tension, the Mullins effect is also observed in other deformation states such as uniaxial compression (Amin et al. 2002), simple shear (Mars and Fatemi 2004), and equi-biaxial tension (Johnson and Beatty 1995; Mars and Fatemi 2004; Németh et al. 2005; Li et al. 2008). After more than six decades of research, the Mullins effect is still recognized as a major challenge in the response of rubbery materials (Diani et al. 2009).

3.3.3.5.3.2. Details of the Testing Procedure

Cylindrical and dog-bone specimens were subjected to uniaxial compression-only and tension-only strain-controlled cyclic load using the test setups of Figure 3.5(b) and (c), respectively. Testing was conducted at a various strain rates: 0.001 /s, 0.1 /s, and 0.05 /s (Table 3.9 and Table 3.10).

The loading protocol included sets of cycles at individual strain amplitudes shown in Table 3.9 and Table 3.10 for compression-only and tension-only tests, respectively. Each set included 5 and 10 cycles for ECore and ECast, respectively. For ECast, the amplitude increased up to a peak strain of 0.1 and 0.12 in compression and tension, respectively, while for ECore the amplitude increased up to a peak strain of 0.2 and 0.26 in compression and tension, respectively

To avoid detachment of the top platen from the cylindrical specimens, the unloading was limited to the strain level corresponding to 1 ksi stress in compression. Two specimens were tested at 0.001 /s strain rate in compression. The test data showed very good reproducibility with negligible difference in the measured response (see Figure A.3).

Table 3.9. Cyclic compression-only test: summary of test procedure parameters.

	ECore	ECast
Target peak strain (in/in)	0.2	0.1
Strain amplitudes (in/in)	0.025, 0.05, 0.1, 0.15, 0.2	0.02, 0.04, 0.06, 0.08, 0.1
Number of cycles at each amplitude	5	10
Strain rates (/s)	0.001, 0.01, 0.05	0.001, 0.01, 0.05

Table 3.10. Cyclic tension-only test: summary of test procedure parameters.

	ECore	ECast
Target peak strain (in/in)	0.26*	0.12
Strain increment (in/in)	0.02	0.02
Number of cycles at each amplitude	5	10
Strain rates (/s)	0.001, 0.01, 0.05	0.001, 0.01, 0.05**

* Limited by the maximum stroke of the extensometer.

** Rupture occurred in the bottom grip.

3.3.3.5.3.3. Results and Observations

Recorded stress-strain curves from compression and tension tests are shown in Figure 3.21 and Figure 3.22, respectively, over-plotted with stress-strain curves from monotonic tests with the same strain rate (i.e. 0.001 /s). As shown, for both compression-only and tension-only tests, cyclic damage/softening due to repeated cycles at the same peak strain level progressively saturates/stabilizes with the number of cycles, resulting in progressively smaller hysteretic energy dissipation. For compression-only tests on ECast (Figure 3.21(II)) and strains below 0.05, the envelope of the cyclic curve matches the monotonic compressive curve. However, for compressive strains exceeding 0.05, the envelope of the cyclic curve exceeds the monotonic compressive curve. For compression-only tests on ECore (Figure 3.21(I)), for compressive strains exceeding 0.14, the envelope of the cyclic curve slightly exceeds the monotonic compressive curve. The residual strains under monotonic compressive loading and subsequent unloading are much smaller than

those obtained after unloading following several loading cycles, which is attributed to the accumulated cyclic damage (and cumulative plastic strains).

For tension-only tests on ECast (Figure 3.22(II)), the envelope of the cyclic curve is much lower than the monotonic curve, demonstrating that cyclic damage, associated with cumulative plastic strains is much larger in tension compared to compression. This is further manifested by the fact that the rupture strain under tensile cyclic loading reduces by 42% and 12% compared to the corresponding rupture strain under tensile monotonic loading (Table 3.11). For tension-only tests on ECore (Figure 3.22(I)), the monotonic curve is higher than the envelope of the cyclic curve. Further research is needed to establish a plausible explanation for this observation.

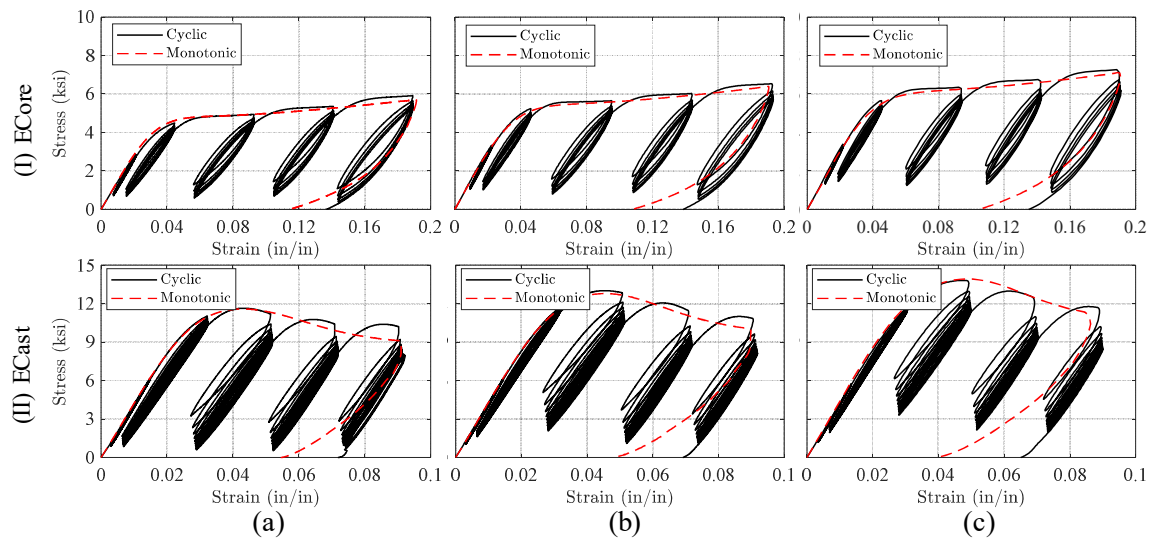


Figure 3.21. Comparison of stress-strain results for monotonic compressive and compression-only cyclic loading at a strain rate of: (a) 0.001 /s; (b) 0.01 /s; (c) 0.05 /s.

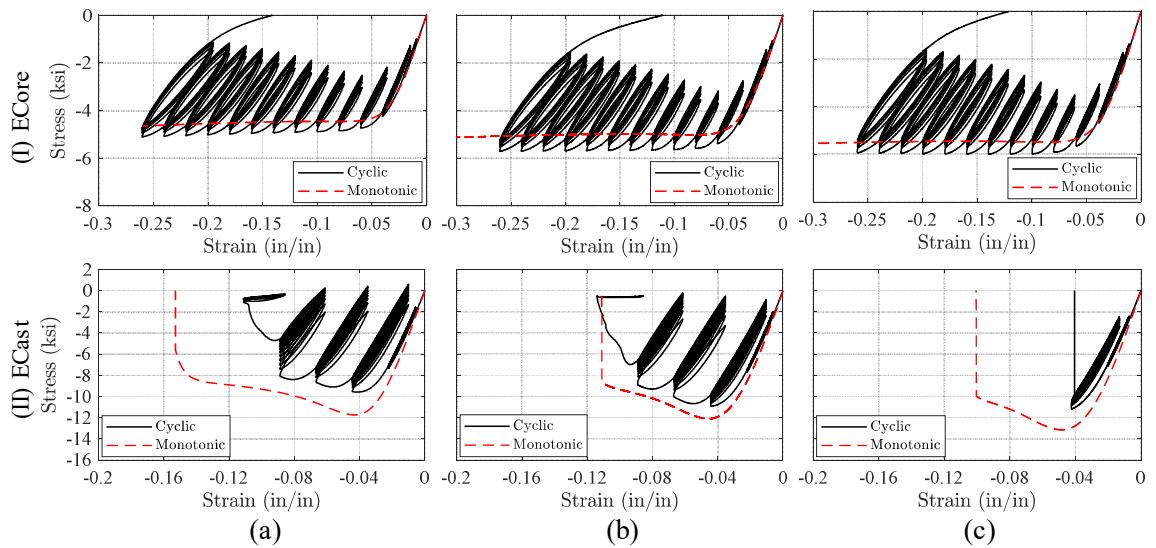


Figure 3.22. Comparison of stress-strain results for monotonic tensile and tension-only cyclic loading at a strain rate of: (a) 0.001 /s; (b) 0.01 /s; (c) 0.05 /s (Early rupture occurred in specimen at the bottom grip).

Table 3.11. Fracture strain of ECast under tensile monotonic and cyclic load.

Strain rate (/s)	Fracture strain		
	Monotonic	Cyclic	Reduction (%)
0.001	0.153	0.108	42
0.01	0.112	0.10	12
0.05	0.10	(End failure)	-

It should be noted that at 0.001 /s strain rate, similar to the monotonic loading, a ductile failure occurred in ECast under the cyclic process (Figure 3.23(a)). However, a clearer necking was observed under monotonic than cyclic loading. At 0.01 /s strain rate, a brittle failure was observed under the monotonic loading while a ductile failure was observed under the cyclic loading. No damage was observed in ECore specimens up to 26% strain at all strain rates (Figure 3.23(b)).

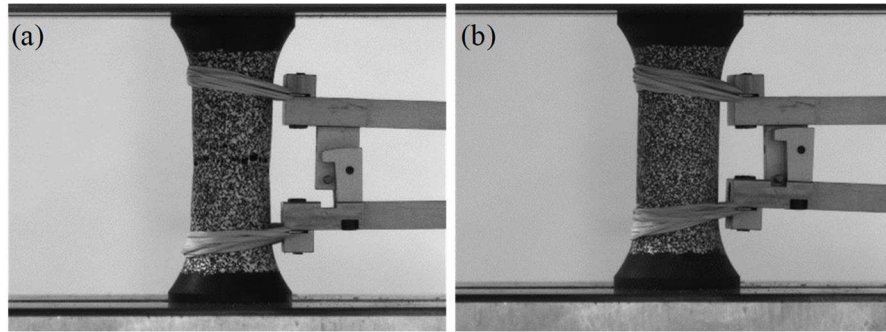


Figure 3.23. Deformed shape of specimens at the end of cyclic tensile load at strain rate of 0.001 /s: (a) ECast; (b) ECore.

3.3.3.5.4. Combined Compression-Tension Cyclic Tests

3.3.3.5.4.1. Objective

The main objective of this set of tests was to investigate the hysteretic response of the selected polyurethane under combined tension-compression cyclic loading and investigate the coupling between tensile and compressive damage/softening.

3.3.3.5.4.2. Details of the Testing Procedure

All tests were conducted with dog-bone specimens using the test setup shown in Figure 3.5(c). The loading protocol (Figure 3.24) included strain-controlled asymmetric cycles (always starting with compression) of increasing amplitude, with one cycle per amplitude and various loading rates (Table 3.12).

The strain amplitude increased by a strain increment of 0.018 and 0.009 increments for ECore and ECast, respectively, in both compression and tension (Table 3.12). The peak compressive strain was 0.18 and 0.11 for ECore and ECast, respectively (Table 3.12). To ensure that early fracture of ECast specimens at low tensile strains is avoided, the peak

strain amplitude in tension was limited to 0.027 for compression strains below 0.09 and it was increased up to 0.054 for compressive strains beyond 0.09. For ECore, the peak tensile strain was limited to 0.09, based on the maximum travelling length of the extensometer in tension (0.1 in.).

To investigate the effect of the loading direction sequence on the response, one ECast specimen was also tested at 0.001 /s strain rate under the same loading protocol starting in tension.

Table 3.12. Combined compressio-tension cyclic test: summary of test procedure parameters.

Parameter	ECore	ECast
Peak strain in compression	0.18	0.11
Strain increment in compression	0.018	0.009
Peak strain in tension	0.1	0.06
Strain increment in tension	0.018	0.009
Number of cycles at each amplitude	1	1
Strain rates (/s)	0.001, 0.01, 0.025	0.001, 0.01, 0.025

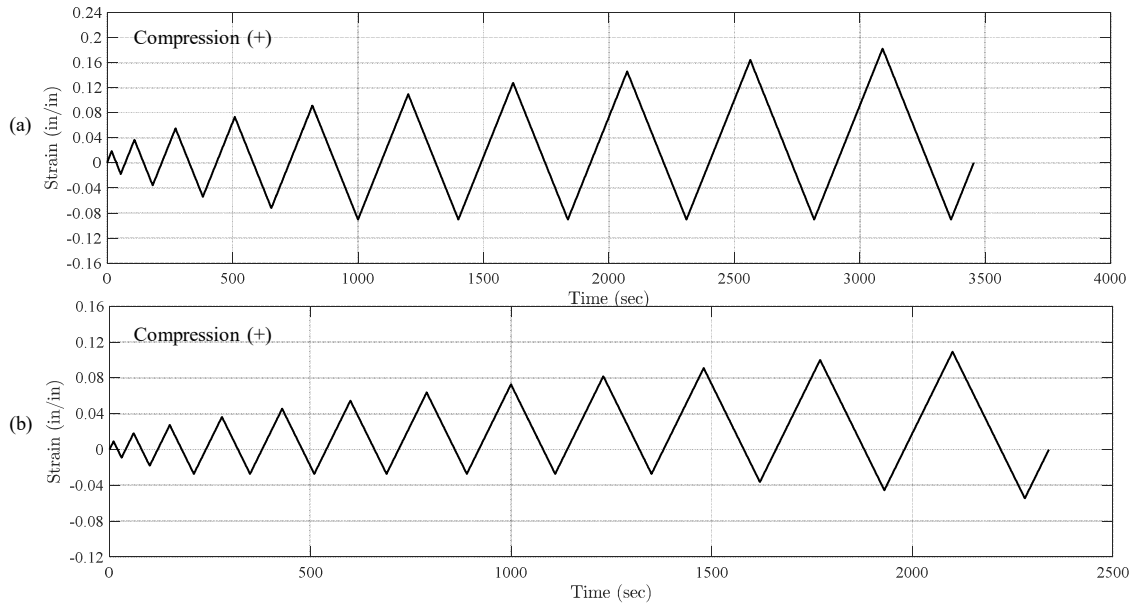


Figure 3.24. Loading protocol of combined cyclic compression-tension tests: (a) ECore; (b) ECast.

3.3.3.5.4.3. Results and Observations

The stress vs. strain curves at various strain rates are shown in Figure 3.25(a) and (b) for ECore and ECast respectively. Regarding the loading rate effect, similar observations to those for the monotonic loading results can be made from Figure 3.25 for the reversed cyclic loading.

The stress vs. strain curve from a cyclic test is overlaid in Figure 3.26 with stress vs. strain curves from monotonic tensile and compressive tests, both conducted with the same strain rate (i.e. 0.001 /s,) and same specimen type (i.e. dog-bone specimens). Based on Figure 3.26 (and in comparison with Figure 3.21 and Figure 3.22), clear coupling between tension and compression damage is observed in the response, i.e. the

damage/softening in compression is affected by inelastic traveling in both tension and compression, while this is also the case for tension damage/softening. According to Figure 3.25(b), coupling between tension and compression damage increases with the loading rate for ECast, but, this is not the case for ECore. Tension damage seems to be more dependent on compressive inelastic traveling than compression damage is on tensile inelastic traveling. Comparing the unloading branches of monotonic and cyclic curves in compression, it was concluded that unloading response is fairly independent of the loading history.

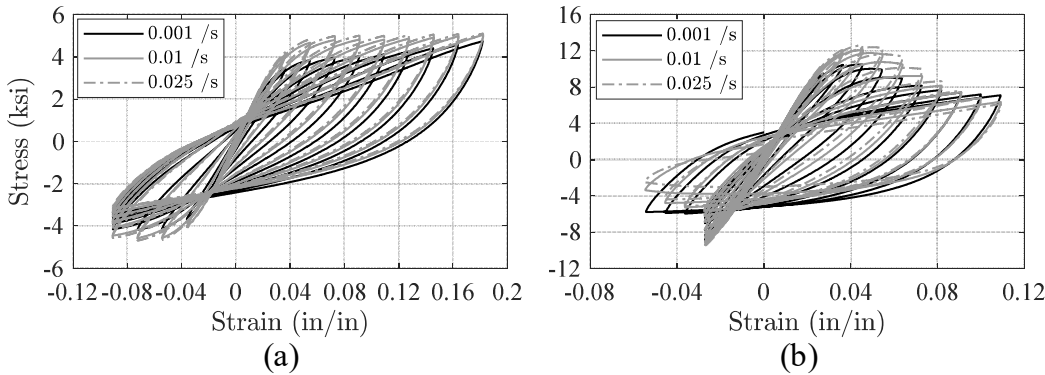


Figure 3.25. Cyclic compression-tension stress-strain curves at various strain rates: (a) ECore; (b) ECast.

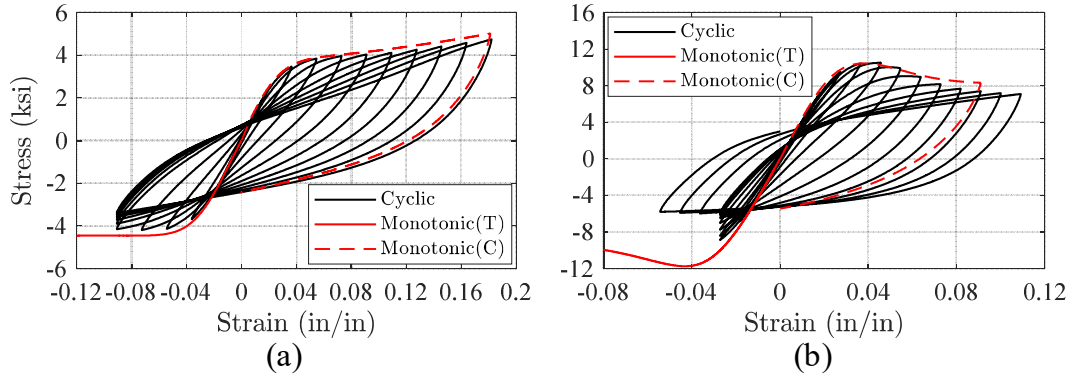


Figure 3.26. Comparison of cyclic compression-tension and monotonic stress-strain curves for 0.001 /s strain rate: (a) ECore; (b) ECast.

As shown in Figure 3.27, it was concluded that the loading direction sequence has no effect on the response of ECast at 0.001 /s strain rate under the applied loading protocol (Table 3.12).

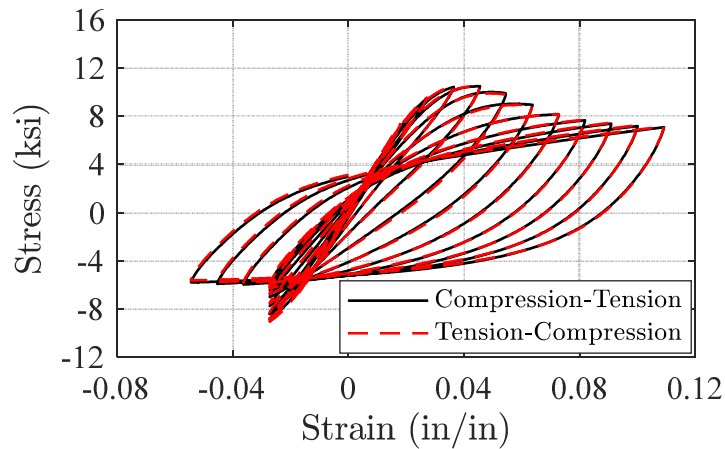


Figure 3.27. Effect of the loading-direction sequence on the response of ECast at 0.001 /s strain rate.

Figure 3.28 shows the deformation of ECore and ECast at the peak tensile and compressive strain and also at the end of the test (zero strain). It is noteworthy that no visible damage (e.g. cracks) was identified in ECore. However, in both ECore and ECast, an inclined potential failure surface was observed over the test at large compressive strains. Damage in the form of small voids was observed at the ends of this plane in ECast.

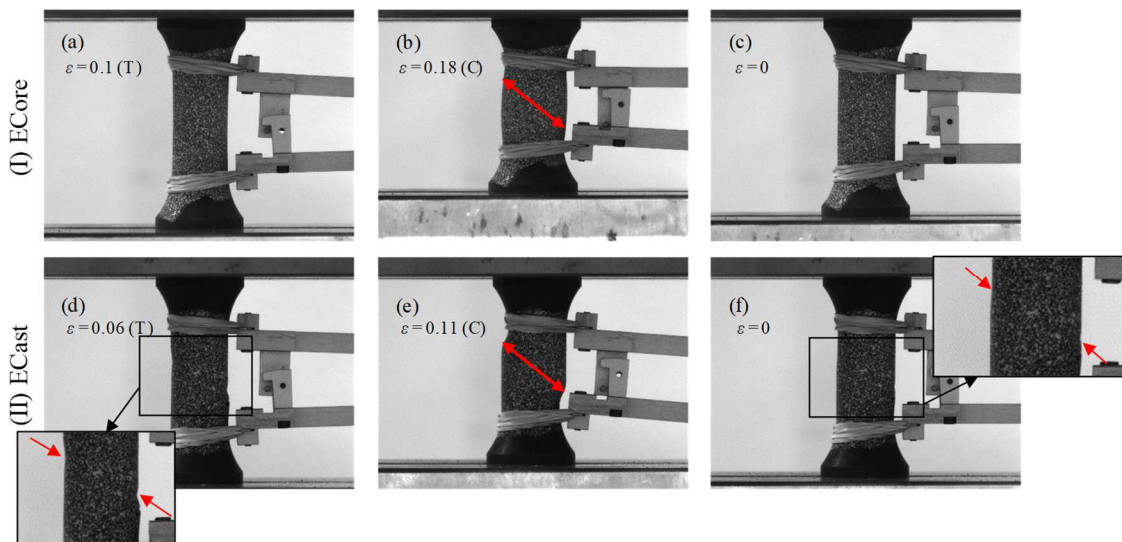


Figure 3.28. Deformed shape of ECore and ECast specimens at different states of the reversed cyclic load at strain rate of 0.01 /s: (a), (d) peak tension; (b), (e) peak compression; (c), (f) end of the test [T: Tension; C: Compression].

3.3.3.5.5. Creep and Relaxation Compression Tests

3.3.3.5.5.1. Objective

In bridge systems, such as the one proposed in this study (Nikoukalam and Sideris 2016b; Nikoukalam and Sideris 2017), creep under permanent loads (e.g. gravity and post-tensioning) can significantly impair the serviceability of the system and its overall

performance under extreme events (e.g., earthquakes), while cases of complete structural failure under service loads have also been observed due to large concrete creep deformations and the resulting stress redistribution over the structure (Bažant et al. 2012).

Data from creep and relaxation tests are essential to characterizing the time-dependent material response, before and after yielding. The main objective of these tests is to characterize the long-term response of the selected PUs under constant strain (relaxation) and constant load (creep).

3.3.3.5.5.2. Details of the Testing Procedure

In this study, all tests were conducted on ECast in compression (Figure 3.5(b)), which is the dominant permanent stress state for the structural applications of interest to this study. Creep tests were conducted in load control and at three stress levels, 1 and 3 ksi, to provide information on the time-dependent response in the elastic range and at stresses levels associated with serviceability conditions in structural systems. In all tests, loading was applied at a constant rate of 1.5 kips/s (~0.48 ksi/s) up to the target peak stress (1 or 3 ksi) and remained constant for 5 days.

Relaxation tests were conducted in the inelastic range (for which load control testing would result in instabilities) and, apart from providing information on the time dependent properties of the material after yielding, also supported decisions on the constant strain hold period of the multi-step compression relaxation testing program discussed earlier. In relaxation tests, loading was applied in displacement-control at a

constant strain rate of 0.01 /s up to a peak strain of 0.1 and 0.05 (i.e. in the post-peak range) in ECore and ECast, respectively, and remained constant for 48 hours (Table 3.13).

Table 3.13. Summary of relaxation testing procedure.

Parameter	ECore	ECast
Peak strain (%)	10%	5%
Relaxation time (hr)	48	48
Strain rate (/s)	0.01	0.01

3.3.3.5.5.3. Results and Observations

According to the creep test data (Figure 3.29(a)), the total creep strain (defined as the total strain over the entire loading period minus the initial *instantaneous* strain at the target stress) was found to be 0.00088 and 0.00280 for 1 and 3 ksi, respectively. The rate of the creep strain increases with the applied stress, but decreases progressively over time for both stress levels. The creep compliances for both stress levels are nearly identical (Figure 3.29(b)), which confirms the linearity of the response in the considered stress range (up to 3 ksi).

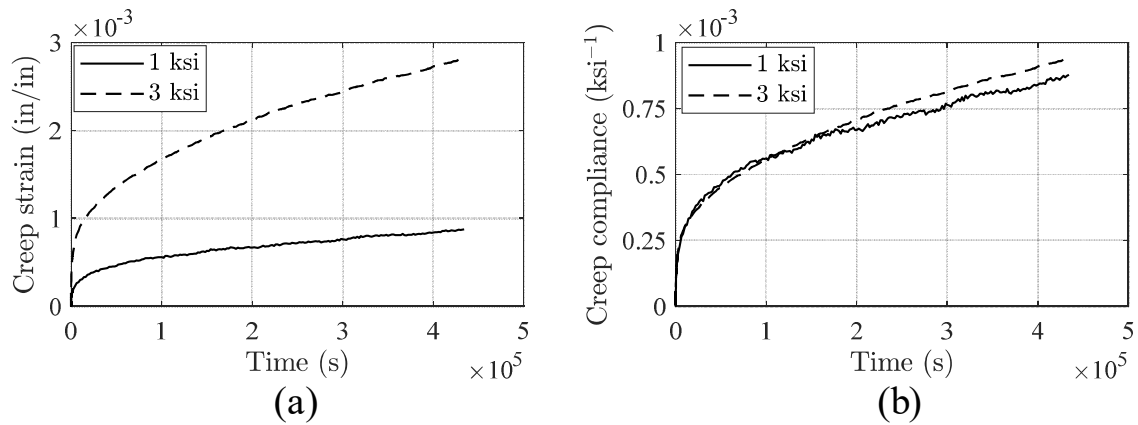


Figure 3.29. (a) Creep strain-time curves from creep test at various stress levels; (b) creep compliance-time curves from creep test at various stress.

Based on the relaxation test data (e.g., Figure 3.30 and Table 3.14), the total stress relaxation (defined as the stress at the target strain of 0.1 (ECore) and 0.05 (ECast) minus the stress at the end of the test) was 4.4 ksi and 8.6 ksi in ECore and ECast, respectively. Approximately 80% of this relaxation occurred in the first ~36 minutes and ~70 minutes in ECore and ECast, respectively (which is the selected holding period for the multi-step compression relaxation testing program described earlier). The rate of stress relaxation decreases with time.

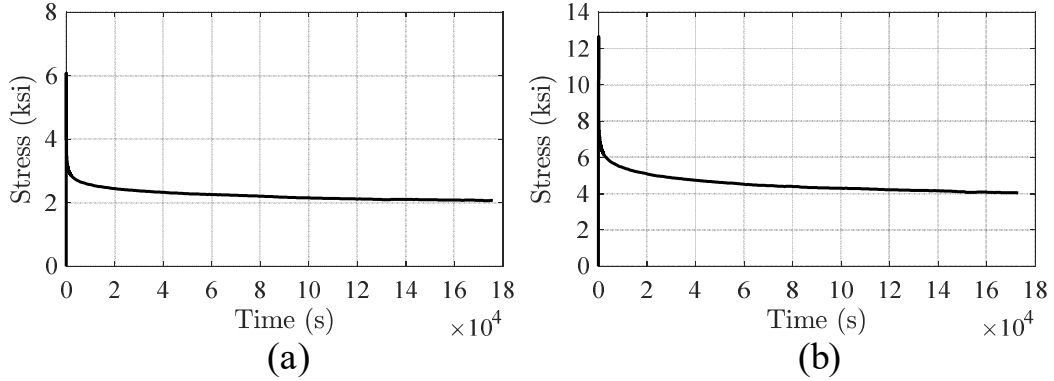


Figure 3.30. Stress-time curves from relaxation test: (a) ECore; (b) ECast.

Table 3.14. Summary of relaxation test results.

Parameter	ECore	ECast
Stress at peak strain (ksi)	6.6	12.6
Residual stress (ksi)	2.3	4.0
Total relaxed stress (ksi)	4.4	8.6
Total relaxation (%)	66	68
time at 80% relaxation (min)	36	67
time at 85% relaxation (min)	104	206
time at 90% relaxation (min)	314	481

3.3.3.5.6. *Temperature Effect*

3.3.3.5.6.1. *Objective*

It is well-known that the material properties of polymers are highly temperature dependent. The main objective of this set of tests was to investigate the effect of temperature on the response of the selected PUs under uniaxial monotonic compressive loading.

3.3.3.5.6.2. Details of the Testing Procedure

Compression testing included cylindrical specimens subjected, via the setup of Figure 3.5(b), to strain-controlled monotonic loading with various strain rates (0.001 /s, 0.01/s, and 0.05 /s) up to a peak nominal strain of about 0.2 and 0.1 for ECore and ECast, respectively. ECast specimens were tested under +80 °C (176 °F), +60 °C (140 °F), +40 °C (104 °F), 0 °C (32 °F), -15 °C (5 °F), and -20 °C (-4 °F), while ECore specimens were tested at +80 °C (176 °F), +40 °C (104 °F), 0 °C (32 °F), -15 °C (5 °F), covering temperatures below and above the glass transition temperature, reported by BASF (2016) as 45 °C (113 °F) and 57 °C (134.6 °F) for ECore and ECast, respectively (see Figure A.4 and A.5).

The target temperature was achieved using a (heating-cooling) environmental chamber shown in Figure 3.6. The specimens were conditioned for 24 hours to reach the thermal equilibrium state.

3.3.3.5.6.3. Results and Observations

The stress vs. strain curves at various strain rates and temperatures are compared to room temperature in Figure 3.31 and Figure 3.32 for ECore and ECast, respectively. Also, the stress vs. strain curves at various temperatures for each strain rate is shown Figure 3.33(I) and (II) for ECore and ECast, respectively. It was clearly seen that the material response significantly changes with the temperature. To get a better insight into how different mechanical parameters are affected by temperature, the variation of elastic modulus and strength (peak strength for ECast and strength at 0.05 strain for ECore) with the strain rate at various temperatures is shown in Figure 3.34 and Figure 3.35,

respectively. Moreover, the variation of the elastic modulus and strength (peak strength for ECast and strength at 0.05 strain for ECore) with temperature for various strain rates are presented in Figure 3.36 and Figure 3.37, respectively. Comparing the slopes of the lines in Figure 3.34, the rate sensitivity of both peak strength and elastic modulus was lower at low temperatures for ECast. This was also reflected in Figure 3.36, where the deviation of three curves (corresponding to various strain rates) increased for temperatures above $\sim +20$ °C (68 °F).

In ECore, the elastic modulus and strength at 0.05 strain reduced linearly with temperature at all strain rates. No significant change was observed in mechanical properties of ECore at temperatures above the glass transition temperature (~ 57 °C (134.6 °F))

The elastic modulus of ECast reduced linearly (with a slow rate) as the temperature increases from -20 °C (-4 °F) to $+20$ °C (68 °F), beyond which the elastic modulus decreases with a higher rate compared to the temperatures below $+20$ °C (68 °F) (Figure 3.36(b)). The elastic modulus of ECast significantly reduces at temperatures above $\sim +40$ °C (104 °F) indicating a transition from “glassy” to “rubbery” phase. The peak strength of ECast reduced linearly with temperature with similar rate at all strain rates up to the temperature of $\sim +40$ °C (104 °F), beyond which the strength reduced with a higher rate.

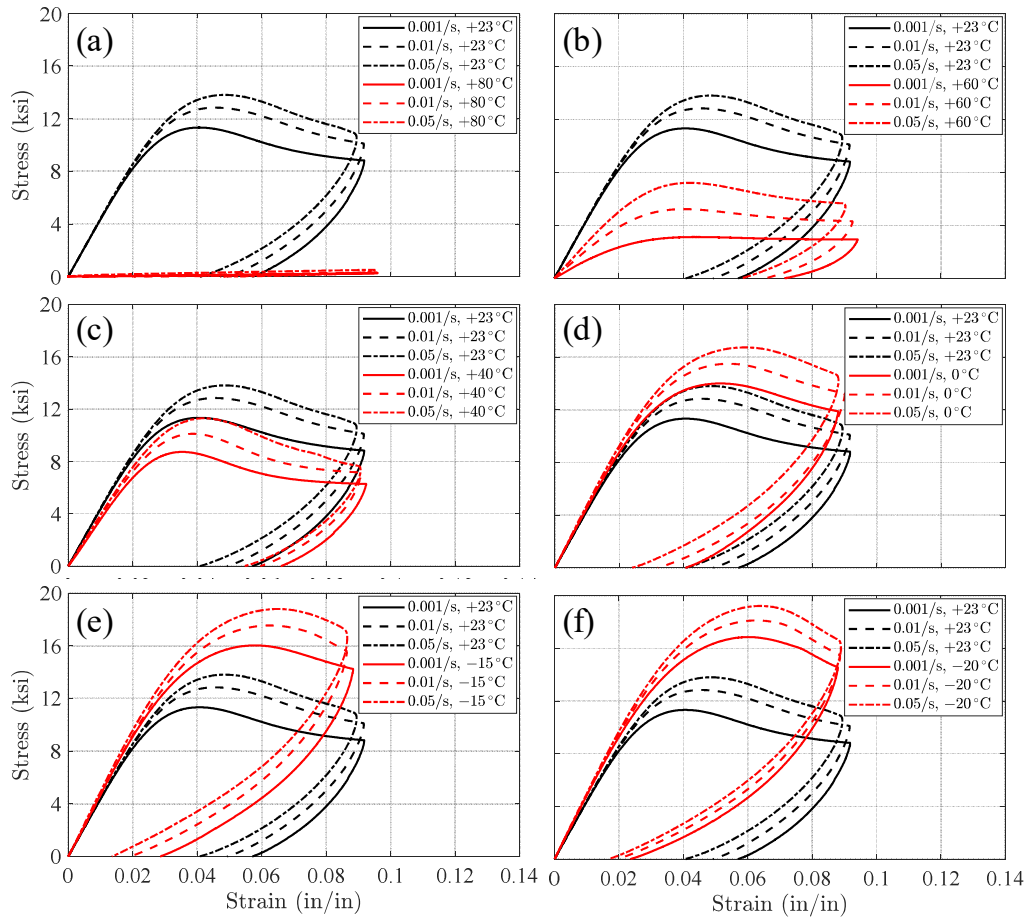


Figure 3.31. Stress-strain curves of ECast at various strain rates and temperatures compared to room temperature: (a) +80 °C; (b) +60 °C; (c) +40 °C; (d) 0 °C; (e) -15 °C; (f) -20 °C.

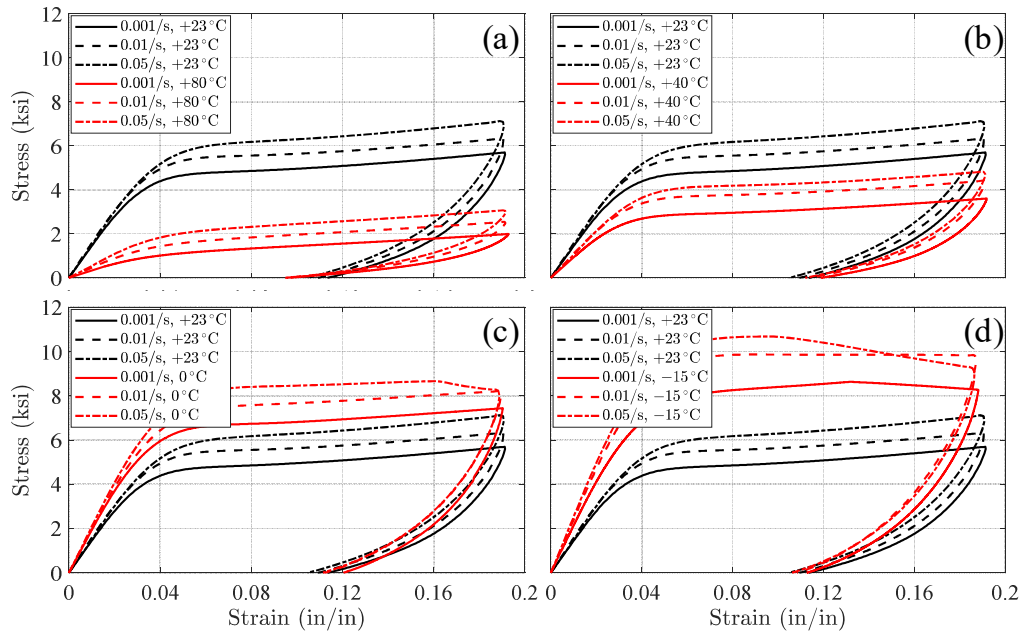


Figure 3.32. Stress-strain curves of ECore at various strain rates and temperatures compared to room temperature: (a) +80 °C; (b) +40 °C; (c) 0 °C; (d) -15 °C.

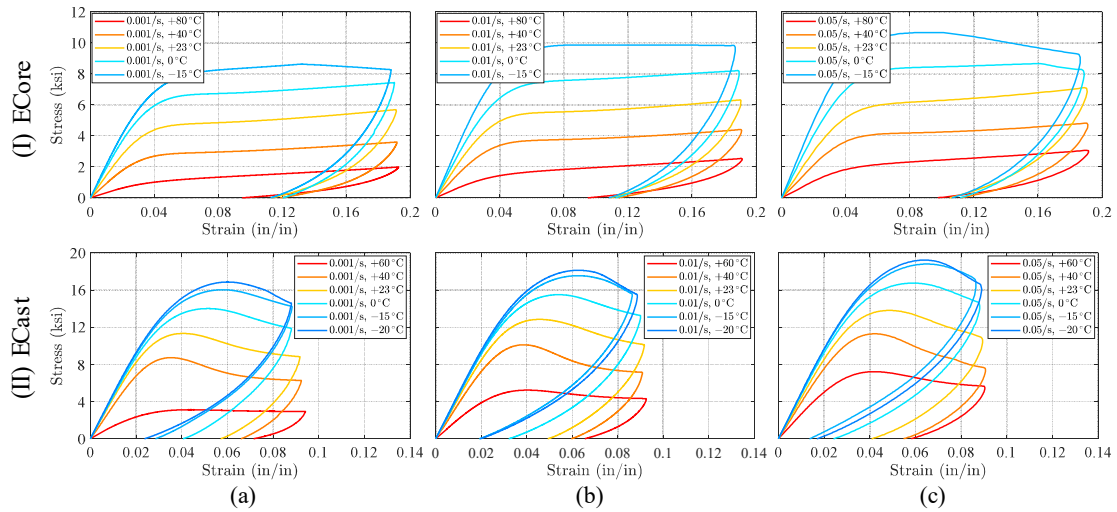


Figure 3.33. Stress-strain curves at various temperatures for each strain rate: (a) 0.001 /s; (b) 0.01 /s; (c) 0.05 /s.

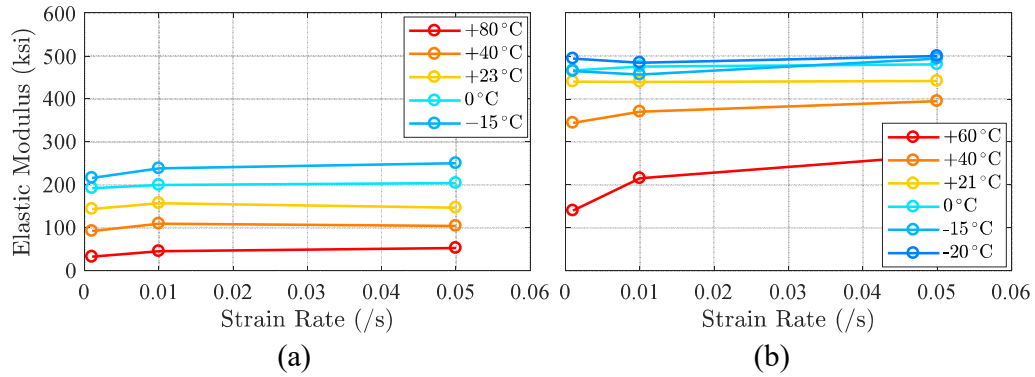


Figure 3.34. Variation of elastic modulus with strain rate at various temperatures: (a) ECore; (b) ECast.

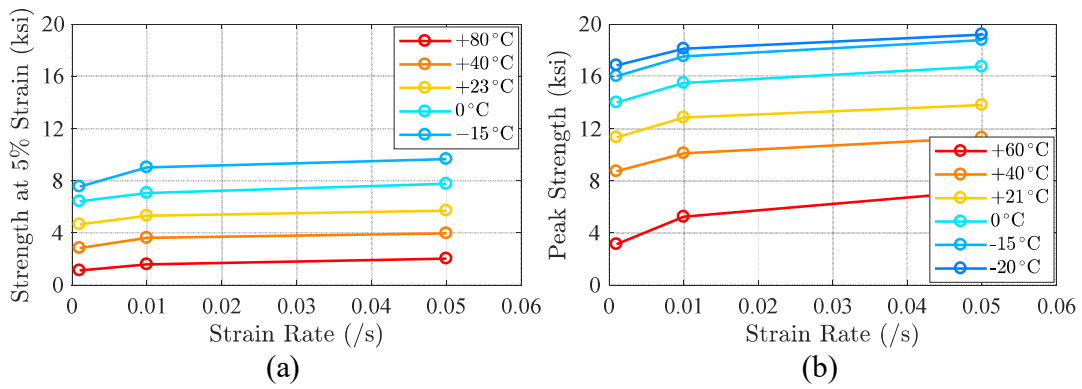


Figure 3.35. Variation of strength with strain rate at various temperatures: (a) ECore; (b) ECast.

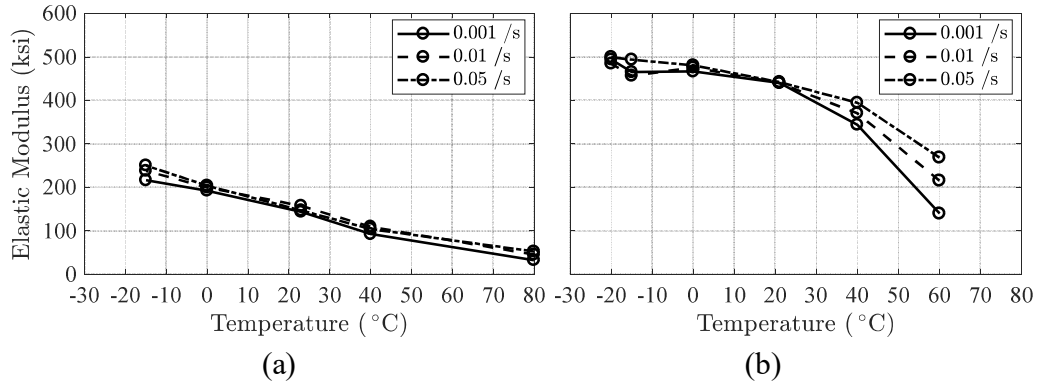


Figure 3.36. Variation of elastic modulus with temperature for various strain rates: (a) ECore; (b) ECast.

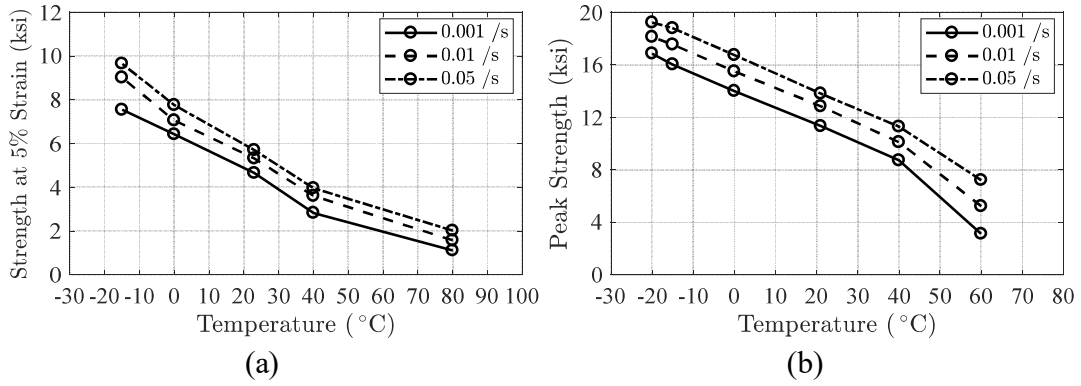


Figure 3.37. Variation of strength with temperature for various strain rates: (a) ECore; (b) ECast.

3.3.3.5.7. Strain Measurements from Digital Image Correlation (DIC) System

3.3.3.5.7.1. Monotonic Tension

The mechanical clip-on extensometer measures the relative displacement between the two extensometer ends (knife edges), which is then used to calculate the average strain over the gage length by dividing the relative displacement with the gage length (initial gage length for engineering strain measure or current gage length for true strain measure). The DIC system measures the absolute displacement values for each subset on the specimen. Strain measures are calculated by post-processing of the measured data, either for any defined gage length (like a virtual extensometer) on the specimen surface, or for any defined area (defined as Area of Interest (AOI) in the DIC system).

The accuracy of strain measures from DIC system is evaluated through comparing the results obtained from DIC system with the results from mechanical clip-on extensometer. To this end, a rectangular AOI ($\sim 0.55 \times 0.8$ in²) is defined inside the gage length (Figure 3.38), covering the maximum clear area between the connection points of the external extensometer. Using DIC, the longitudinal strain field is obtained over the defined AOI. Moreover, using the acquired strain field, five virtual extensometers with a gage length of 0.8 in. (=height of the AOI) are defined in the AOI over the width of the AOI (Figure 3.38). The strain measurements from the five DIC extensometers are compared to the measurements from the clip-on extensometer for ECore and ECast under monotonic tensile loading at various strain rates in the top row of Figure 3.39 and Figure 3.40, respectively. To get a better insight into the accuracy of the DIC system measurements, the relative strain error of the average of the five DIC extensometers with

respect to the clip-on extensometer is plotted in the bottom row of Figure 3.39 and Figure 3.40 for ECore and ECast, respectively. Overall, as expected, good agreement was observed between the strain measurements from the clip-on extensometer and the average of the five DIC extensometers. In both ECore and ECast, the strain error is larger in the lower strain levels and decreases with the strain level. In ECore, the maximum error was 4%, 30%, and 50%, at strain rates of 0.001 /s, 0.01 /s, and 0.05 /s, respectively, occurred at a strain of about 0.01, while in ECast, the maximum error was 2%, 22%, and 35%, at strain rates of 0.001 /s, 0.01 /s, and 0.05 /s occurred at a strain of about 0.005, 0.01, and 0.02, respectively. The error observed was primarily attributed to using a two-dimensional DIC system (one camera) for a three-dimensional curved surface on the specimen.

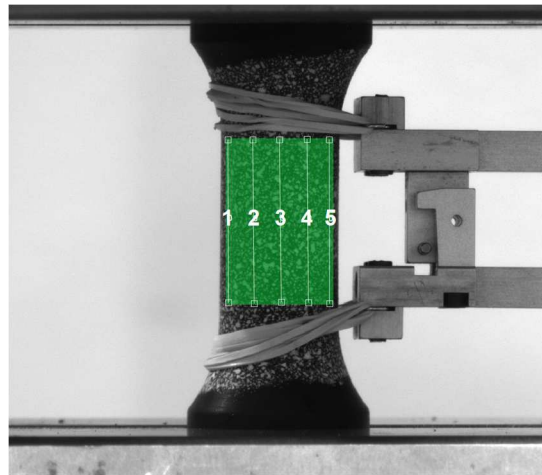


Figure 3.38. Layout of five virtual extensometers on the specimen surface.

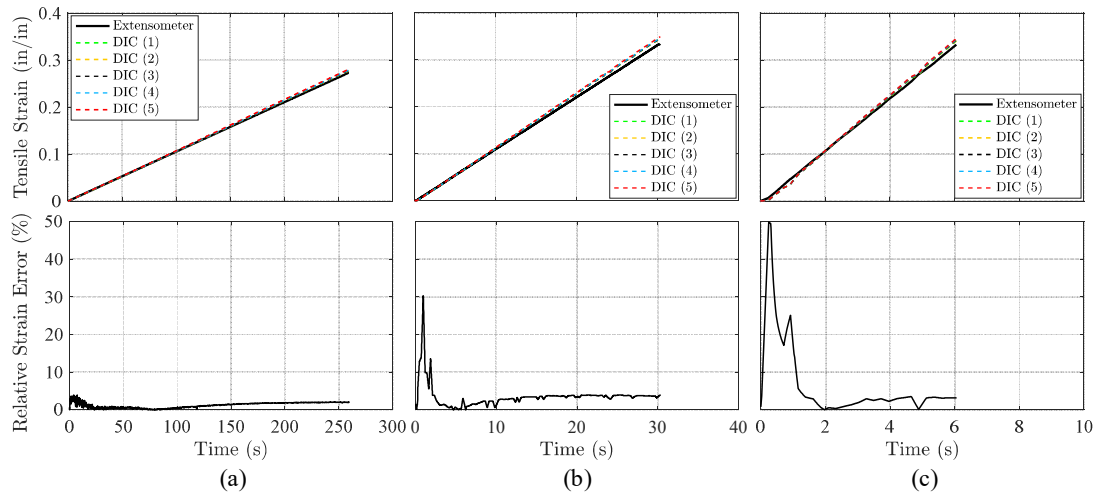


Figure 3.39. Strain measurements: clip-on extensometer versus DIC system from monotonic tensile test on ECore at various strain rates: (a) 0.001 /s; (b) 0.01 /s; (c) 0.05 /s.

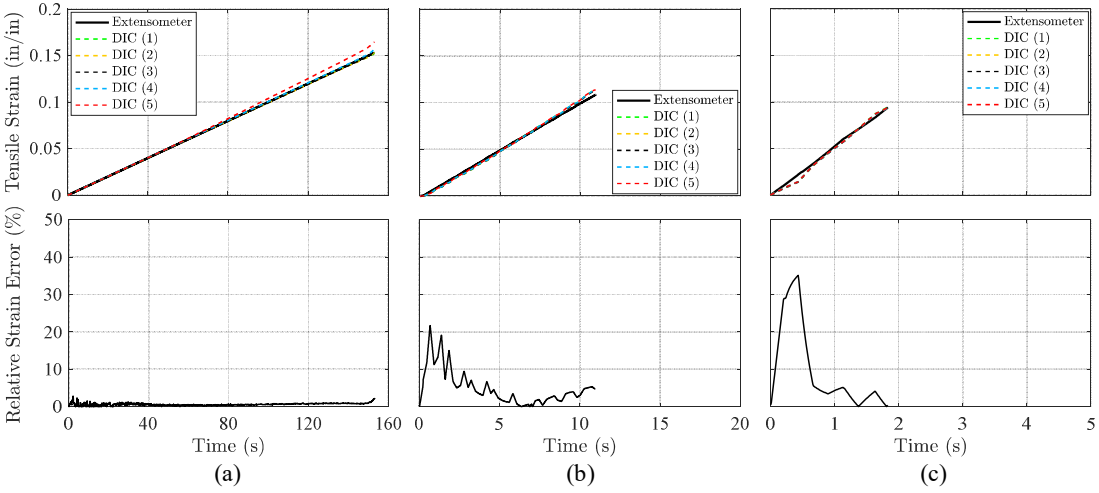


Figure 3.40. Strain measurements: clip-on extensometer versus DIC system from monotonic tensile test on ECast at various strain rates: (a) 0.001 /s; (b) 0.01 /s; (c) 0.05 /s.

The stress-strain (measured by the clip-on extensometer) curve of ECore at 0.01 /s strain rate is depicted in Figure 3.42. The longitudinal local strain contours corresponding to points (a) to (e) are shown in Figure 3.43. Figure 3.44 shows the local longitudinal strain profile versus the normalized position on the area of interest along three locations over the width of the AOI as indicated in Figure 3.41. In a uniaxial tensile or compressive test, a constant strain is expected along the gage length as long as the deformation is homogenous. It can be seen that the strain distribution along the area of interest is uniform at 5% strain. However, at 10% strain, a slight gradient was observed along the area of interest with higher strains at the mid-height of the specimen. The strain gradient is an indication of the location of necking at larger strains. Although a clear necking was not observed in the ECore up to 33.37% global tensile strain, according to the observed strain gradient, the necking is expected to occur in the vicinity of the mid-height of the specimen where the maximum strain was observed.

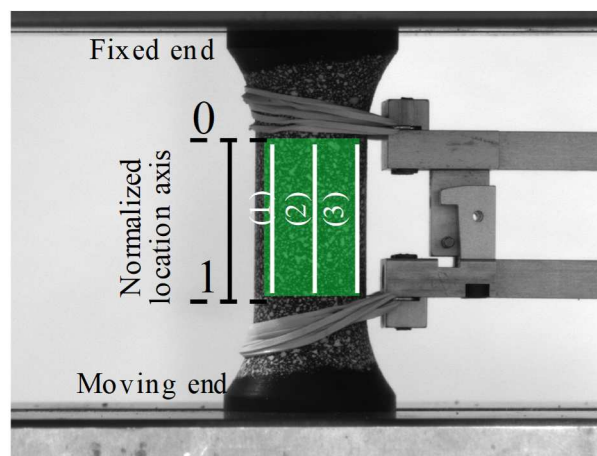


Figure 3.41. Location of lines of interest over the width of the area of interest.

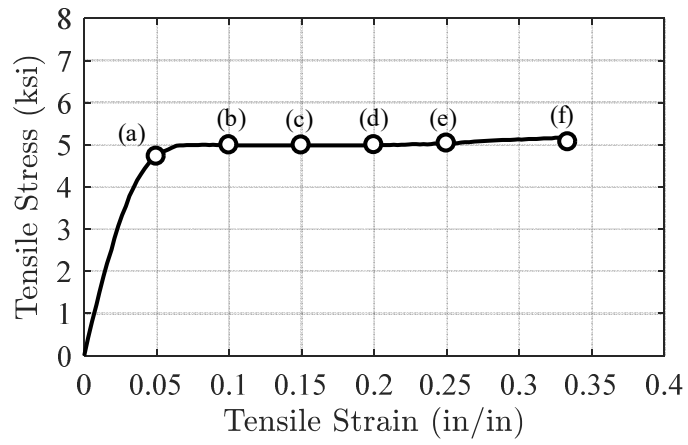


Figure 3.42. Stress vs. strain curve of ECore at 0.01 /s strain rate determined using the clip-on extensometer, indicating the points taken for strain contour and strain distributions shown in Figure 3.43 and Figure 3.44, respectively.

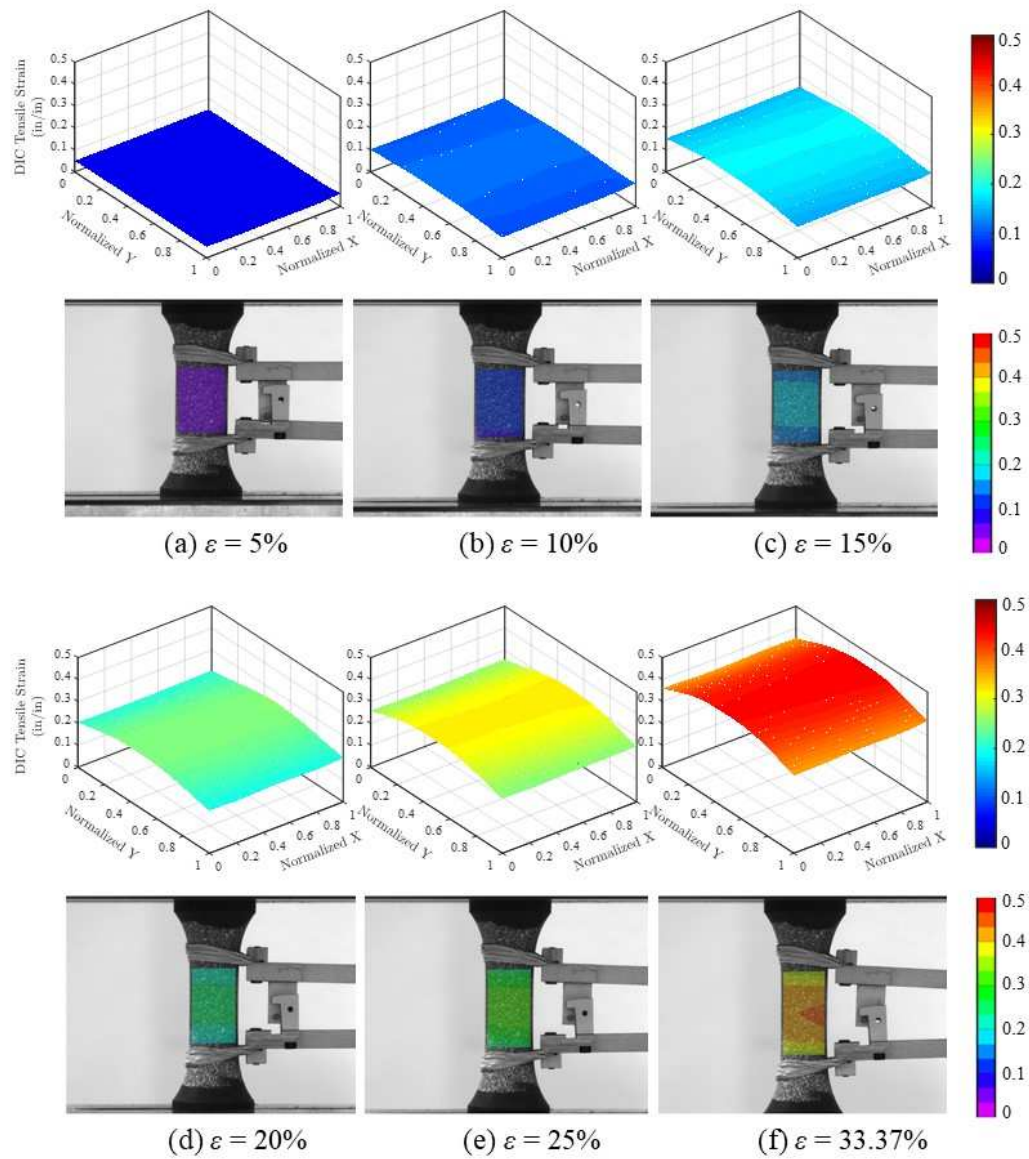


Figure 3.43. Monotonic tensile test on ECore at 0.01 /s strain rate: strain field at various global strain levels in three dimensional (top row) and two dimensional (bottom row) space.

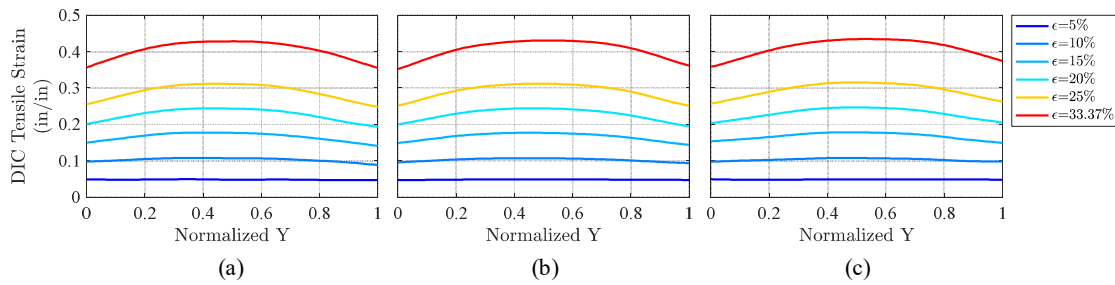


Figure 3.44. ECore under monotonic tensile load at 0.01 /s strain rate: local tensile strain distribution along three lines of interest at various global strain levels: (a) left line; (b) center line; (c) right line.

The stress-strain (measured by the clip-on extensometer) curve of ECast at 0.001 /s strain rate is depicted in Figure 3.45. The longitudinal strain contours corresponding to points (a) to (e) are shown in Figure 3.46. Figure 3.47 shows the longitudinal strain profile versus the normalized position on the area of interest along three locations over the width of the AOI as indicated in Figure 3.41. It can be seen that the strain distribution along the area of interest is uniform at 2% strain. However, at 4% strain, a slight gradient was observed along the area of interest with higher strains at the mid-height of the specimen. The strain gradient is an indication of the location of necking at larger strains, which was clearly visible at 10% strain (Figure 3.46(c)). The strain gradient increased by the global strain up to the fracture strain (15.3%). A discontinuity was observed in the local strain contour (Figure 3.46) and local strain distributions (Figure 3.47) at 15.3% strain which was due to the loss of correlation in the vicinity of fracture region. Moreover, for global strains (measured by clip-on extensometer) exceeding $\sim 5\%$ where the material is in the softening range of the response, while the local strain increases at the highly strained neck region, the adjacent regions (in the vicinity of the two ends of the AOI) experience

unloading. This was clearly reflected in the local strain distributions shown in Figure 3.47, where the local strain distributions at a higher global strain level crossed the distribution at lower strain levels. For instance, at the onset of fracture (15.3% global strain), unloading occurs in the material over the normalized position 0-0.4 and 0.65-1 (Figure 3.47(b)).

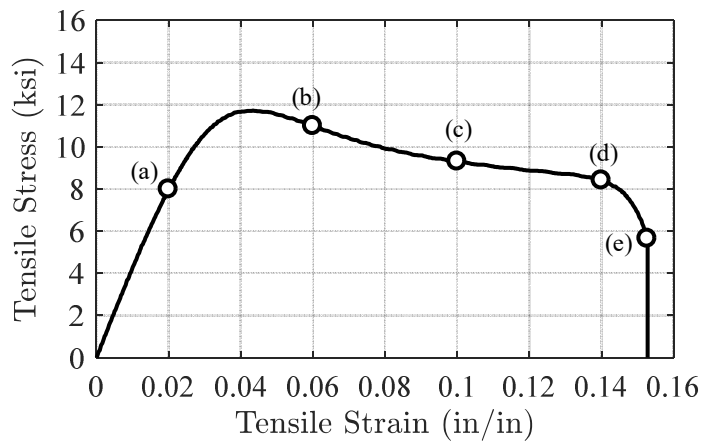


Figure 3.45. Stress vs. strain curve of ECast at 0.001 /s strain rate determined using the clip-on extensometer, indicating the points taken for strain contour and strain distributions shown in Figure 3.46 and Figure 3.47, respectively.

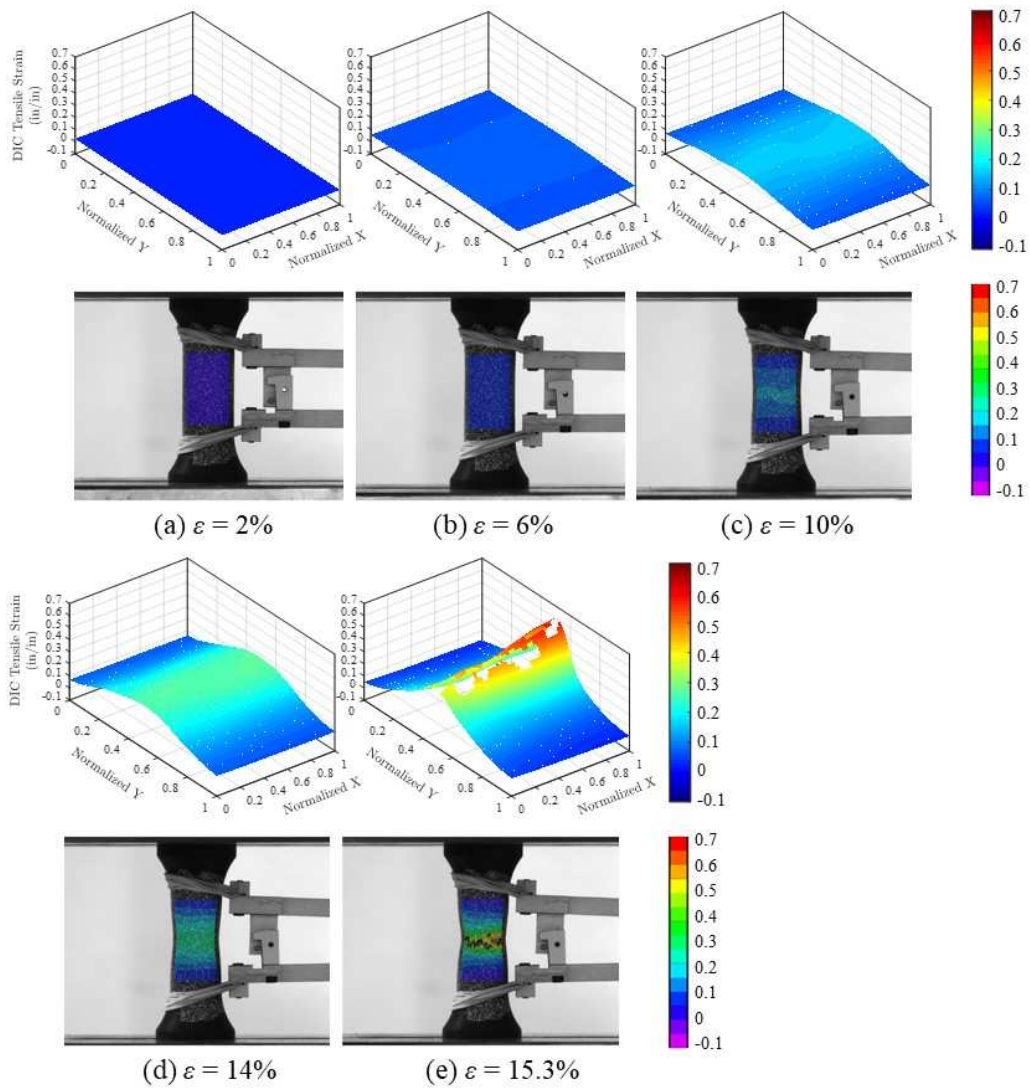


Figure 3.46. Monotonic tensile test on ECast at 0.001 /s strain rate: strain field at various global strain levels in three dimensional (top row) and two dimensional space (bottom row).

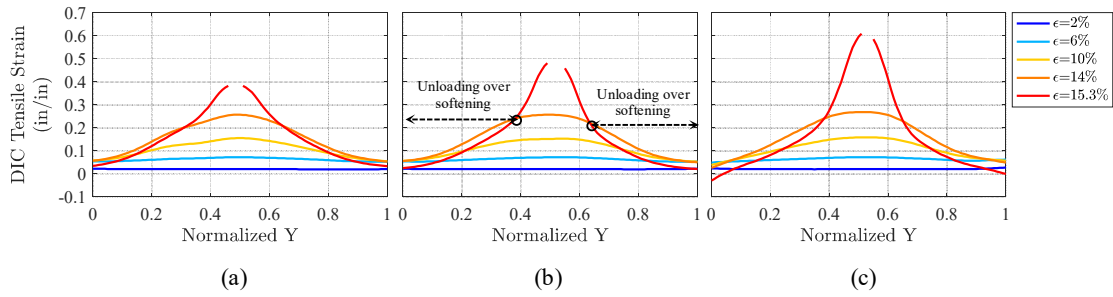


Figure 3.47. ECast under monotonic tensile load at 0.001 /s strain rate: local tensile strain distribution along three lines of interest at various global strain levels: (a) left line; (b) center line; (c) right line.

3.3.3.5.7.2. Monotonic Compression

Similar to tensile tests, the accuracy of strain measures from the DIC system is evaluated by comparing the results obtained from the DIC system with the results from the mechanical clip-on extensometer. To this end, a rectangular AOI ($\sim 0.55 \times 0.8$ in²) is defined inside the gage length (Figure 3.38), covering the maximum clear area between the connection points of the clip-on extensometer. Using DIC, the longitudinal strain field is obtained over the defined AOI. Moreover, using the acquired strain field, five virtual extensometers with a gage length of 0.8 in. (=height of the AOI) are defined in the AOI over the width of the AOI (Figure 3.38). The strain measurements from the five DIC extensometers are compared to the measurements from the clip-on extensometer for ECore and ECast under monotonic compressive loading at 0.001 /s strain rate in Figure 3.48(a) and Figure 3.49(a), respectively. The relative strain error of the average of the five DIC extensometers with respect to the clip-on extensometer is plotted Figure 3.48(b) and Figure 3.49(b) for ECore and ECast, respectively. Overall, as expected, good agreement

was observed between the strain measurements from the clip-on extensometer and the DIC system. The maximum observed error for ECore and ECast was about 6% and 60% occurred at a strain of 0.02 over loading and 0.015 over unloading, respectively. The error observed was primarily attributed to using a two-dimensional DIC system (one camera) for a three-dimensional curved surface on the specimen.

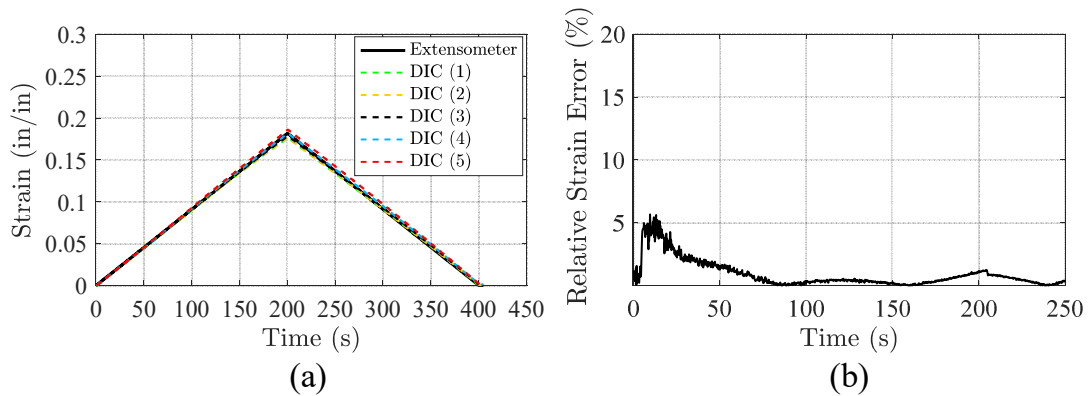


Figure 3.48. (a) Strain measurements time history: clip-on extensometer versus DIC system from monotonic compressive test on ECore at 0.001 /s strain rate; (b) relative strain error time history.

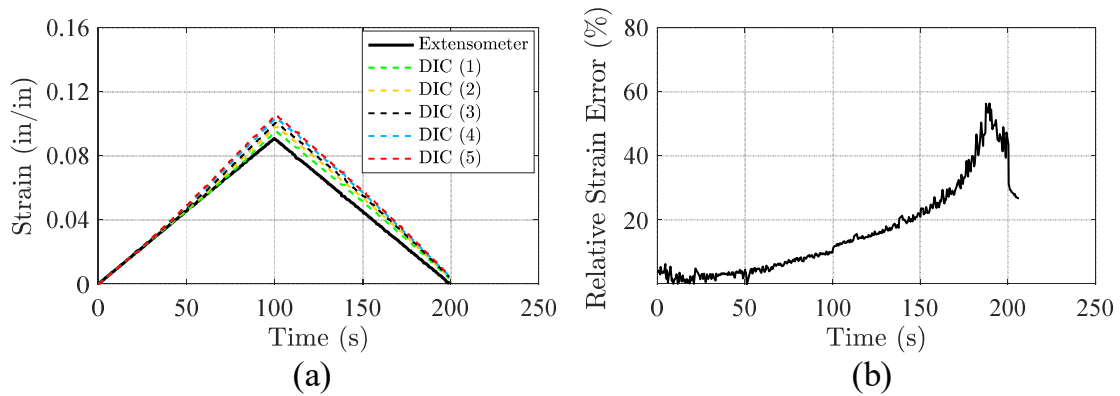


Figure 3.49. (a) Strain measurements time history: clip-on extensometer versus DIC system from monotonic compressive test on ECast at 0.001 /s strain rate; (b) relative strain error time history.

The stress-strain (measured by the clip-on extensometer) curve of ECore under monotonic compression load at 0.001 /s strain rate is depicted in Figure 3.50. The longitudinal local strain contours corresponding to points (a) to (i) are shown in Figure 3.51. Figure 3.52 shows the local longitudinal strain profile versus the normalized position on the area of interest along three locations over the width of the AOI as indicated in Figure 3.41. In a uniaxial tensile or compressive test, a constant strain is expected along the gage length as long as the deformation is homogenous. It can be seen that the compressive local strain distribution along the area of interest is uniform at 2% strain over the loading process. However, at 10% strain, a slight gradient was observed along the area of interest. The strain gradient is an indication of the location of strain localization at higher strains. According to the local strain contours, the strain was localized in a diagonal region, with the width decreasing with strain up to the peak compressive strain.

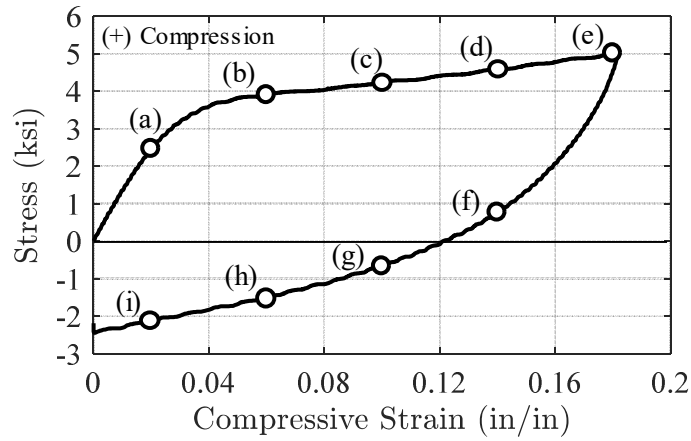


Figure 3.50. Stress vs. strain curve of ECore under monotonic compression load at 0.001 /s strain rate determined using the clip-on extensometer, indicating the points taken for strain contour and strain distributions shown in Figure 3.51 and Figure 3.52, respectively.

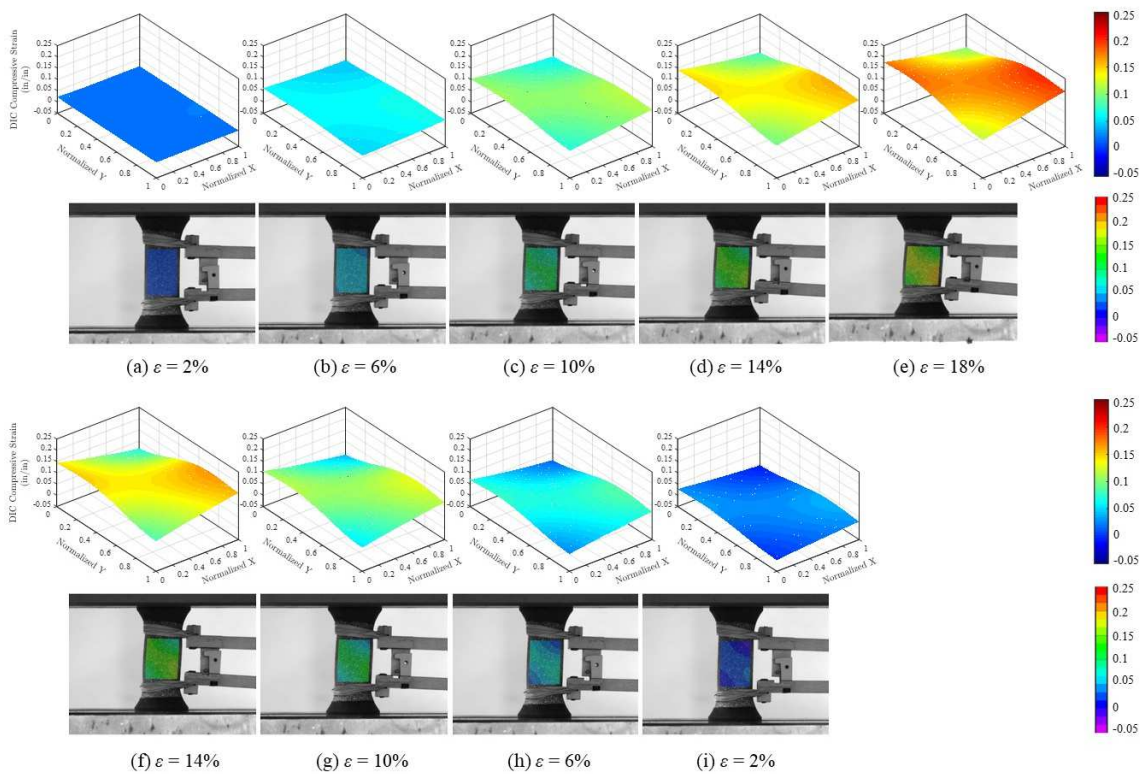


Figure 3.51. Monotonic compression test on ECore at 0.001 /s strain rate: strain field at various global strain levels (indicated in Figure 3.50) in three dimensional (top row) and two dimensional (bottom row) space.

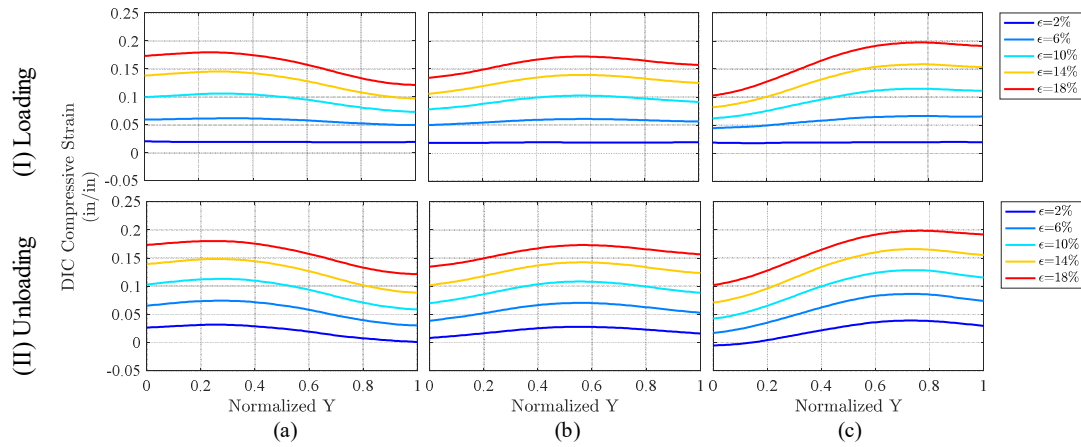


Figure 3.52. ECore under monotonic compression load at 0.001 /s strain rate: local compressive strain distribution along three lines of interest at various global strain levels: (a) left line; (b) center line; (c) right line.

The stress-strain (measured by the clip-on extensometer) curve of ECast under monotonic compression load at 0.001 /s strain rate is shown in Figure 3.53. The longitudinal local strain contours corresponding to points (a) to (i) are shown in Figure 3.54. Figure 3.55 shows the local longitudinal strain profile versus the normalized position on the area of interest along three locations over the width of the AOI as indicated in Figure 3.41. It can be seen that the compressive local strain distribution along the area of interest is uniform at 2% strain over the loading process. However, at 4% strain, a slight gradient was observed along the area of interest which indicates the location of strain localization at higher strains. According to the local strain contours, similar to ECore, the strain was localized in a diagonal region, with the width decreasing with strain up to the peak compressive strain. Moreover, for global strains (measured by clip-on extensometer) exceeding ~4% where the material is in the softening range of the response, while the local strain increased at the highly strained diagonal region, the adjacent regions (in the vicinity

of the two ends of the AOI) experience unloading. This was clearly reflected in the local strain distributions shown in Figure 3.55, where the local strain distributions at a higher global strain level crossed the distribution at lower strain levels. For instance, at the onset of fracture (15.3% global strain), unloading occurs in the material over the normalized position 0-0.4 and 0.65-1 (Figure 3.47(b)).

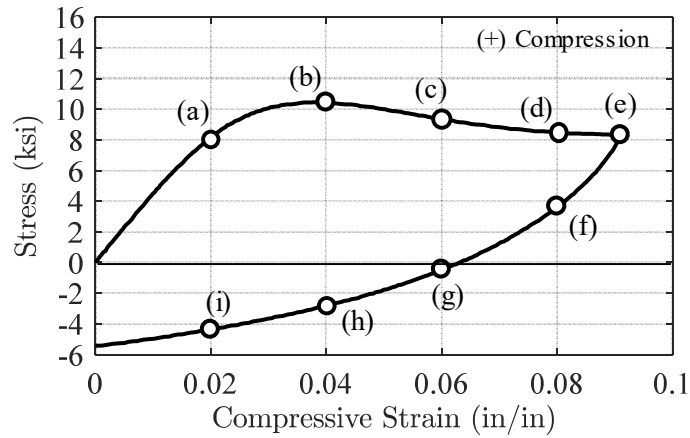


Figure 3.53. Stress vs. strain curve of ECast under monotonic compression load at 0.001 /s strain rate determined using the clip-on extensometer, indicating the points taken for strain contour and strain distributions shown in Figure 3.54 and Figure 3.55, respectively.

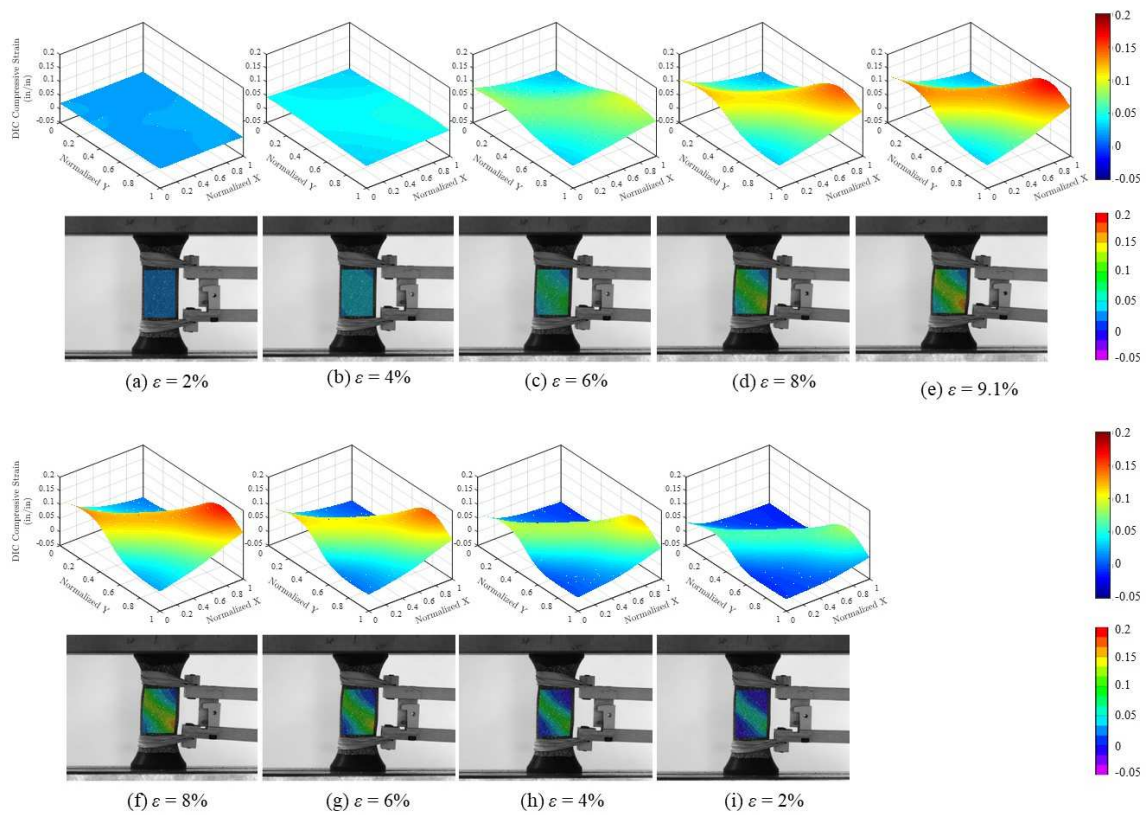


Figure 3.54. Monotonic compression test on ECast at 0.001 /s strain rate: strain field at various global strain levels (indicated in Figure 3.53) in three dimensional (top row) and two dimensional (bottom row) space.

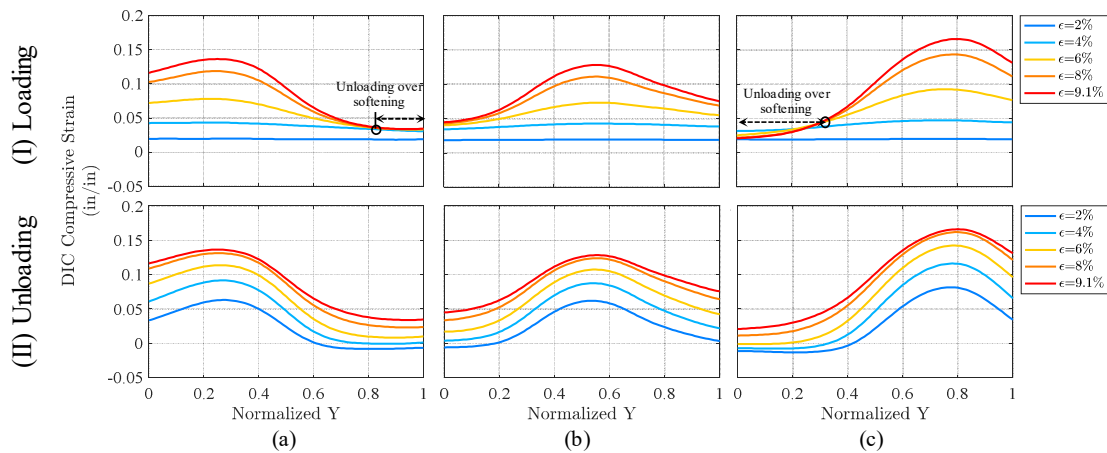


Figure 3.55. ECast under monotonic compression load at 0.001 /s strain rate: local compressive strain distribution along three lines of interest at various global strain levels: (a) left line; (b) center line; (c) right line.

3.4. Summary and Findings

Polymers are highly customizable materials, and, thus, attractive for structural engineering applications. Three different types of elastomers available from BASF (2016) as Elastocore (ECore), Elastocast (ECast), and Elastoshore (EShore) were considered with potential application in seismically resilient bridges and other infrastructure systems. Through monotonic compression tests at constant strain rate (Phase 1 of experimental program), EShore was found unsuitable for the proposed application primarily due to relatively low mechanical properties compared to ECore and ECast.

ECore and ECast, which are known as highly cross-linked amorphous thermosetting polyether polyol-based polyurethanes, were investigated thoroughly in Phase 2 and Phase 3 of the experimental program through a set of tests, including multi-step compression relaxation tests, monotonic compression and tension tests, compression-

only and tension-only cyclic tests, cyclic combined tension-compression tests, and creep and relaxation tests. Based on the test data, the selected polyurethanes exhibit strain-rate dependent properties in the elastic and inelastic range, highly nonlinear equilibrium hysteresis with a Bauschinger-type reverse yielding, and damage/softening with tension-compression coupling. Moreover, it was shown that the response of the selected PUs is highly temperature dependent; the mechanical properties (stiffness and strength) decreased with temperature in both ECore and ECast.

4. FINITE ELEMENT SIMULATION OF PU-ENHANCED COLUMNS WITH ENERGY DISSIPATION LINKS*

4.1. Scope and Objectives

The *objective* of this study was to investigate the performance of the proposed column design for various PU segment geometries and various ED link properties through three-dimensional finite element analysis. To this end, a cantilever bridge column with a PU (ECast) segment of various geometries and various ED link properties was subjected to monotonic and cyclic pushover loading at various loading rates and amplitudes. The performance of the proposed column design was assessed in terms of strength, stiffness, ductility capacity, energy dissipation properties, self-centering capabilities, and damage resistance. The numerical study was conducted using the general-purpose finite element code ABAQUS (SIMULIA 2013).

4.2. Model Calibration for PU Specimens

4.2.1. Constitutive Relations

As shown in Section 3 (see Figure 3.4, for instance), the response of the ECast exhibited mild visco-elastic and strong visco-plastic properties with hysteretic and

* Reprinted with permission from “Resilient bridge rocking columns with polyurethane damage-resistant end segments and replaceable energy-dissipating links” by Nikoukalam, M. T., & Sideris, P., 2017. *Journal of Bridge Engineering*, 22(10), 04017064, Copyright 2019 by American Society of Civil Engineers (This material may be found at [https://doi.org/10.1061/\(ASCE\)BE.1943-5592.0001069](https://doi.org/10.1061/(ASCE)BE.1943-5592.0001069). This material may be downloaded for personal use only. Any other use requires prior permission of the American Society of Civil Engineers.).

softening characteristics. This response can be captured by elasto-visco-plastic models that typically include sets of parallel networks usually combining an *elastic equilibrium network* with several *time-dependent networks*. The rheological representation of this family of constitutive models is shown in Figure 4.1. Early versions of these models (Bergström and Boyce 1998; 2000; Qi and Boyce 2004; 2005) included a nonlinear elastic network (denoted as Network A in Figure 4.1) and a single time-dependent network (denoted as Network B₁, without Networks B₂, B₃, etc., in Figure 4.1). The elastic equilibrium network is often described using the eight-chain hyper-elastic model, originally proposed by Arruda and Boyce (1993) on the basis of molecular and microstructural considerations. Each time-dependent network usually includes an elastic component in series with a visco-plastic component. More recent studies (Bergstrom and Bischoff 2010; Bergstrom 2012) have generalized this family of models to include any number of elastic and time-dependent networks (similarly to visco-elasticity), while several advancements have been included in the individual components of these models.

In this study, the selected PU was modeled using an elastic (A) and two time-dependent (B₁ and B₂) networks. The total Cauchy stress tensor, $\boldsymbol{\sigma}$, was obtained as: $\boldsymbol{\sigma} = \boldsymbol{\sigma}_A + \boldsymbol{\sigma}_{B_1} + \boldsymbol{\sigma}_{B_2}$, where $\boldsymbol{\sigma}_A$ is the stress of the elastic equilibrium network, and $\boldsymbol{\sigma}_{B_1}$ and $\boldsymbol{\sigma}_{B_2}$ are the stress tensors for the first and second time-dependent networks. Deformation compatibility requires that the deformation gradient \mathbf{F} is identical for all networks, i.e. $\mathbf{F} = \mathbf{F}_A = \mathbf{F}_{B_1} = \mathbf{F}_{B_2}$. The response of the elastic network was obtained by the modified

eight-chain model (Bergstrom and Bischoff 2010), which includes both I_1 and I_2 dependence and is given by:

$$\boldsymbol{\sigma}_A = \frac{1}{1+q} \left\{ \begin{array}{l} \frac{\mu_A}{J\bar{\lambda}^*} \frac{L^{-1}(\bar{\lambda}^*/\lambda_L)}{L^{-1}(1/\lambda_L)} \text{dev}[\mathbf{b}^*] + \kappa_A (J-1) \mathbf{1} + \dots \\ \dots + q \frac{\mu_A}{J} \left[I_1^* \mathbf{b}^* - \frac{2I_2^*}{3} \mathbf{1} - (\mathbf{b}^*)^2 \right] \end{array} \right\} \quad (4.1)$$

where $J = \det[\mathbf{F}]$, μ_A is the shear modulus, $\mathbf{b}^* = J^{-2/3} \mathbf{F}(\mathbf{F})^T$ is the Cauchy-Green deformation tensor, and $\bar{\lambda}^* = (\text{tr}[\mathbf{b}^*]/3)^{1/2}$ is the effective chain stretch based on the eight-chain topology assumption (Arruda and Boyce 1993), λ_L is the chain locking stretch, $L^{-1}(x)$ is the inverse Langevin function, where $L(x) = \coth(x) - 1/x$, κ_A is the bulk modulus, $I_1^* = \text{tr}[\mathbf{b}^*]$ and $I_2^* = (\text{tr}[\mathbf{b}^*]^2 - \text{tr}[(\mathbf{b}^*)^2])/2$ are the first and second invariants of the Cauchy-Green deformation tensor, and q is the relative contribution of I_2^* .

For the time-dependent (B_1 and B_2) networks, the deformation gradient for each network was multiplicatively decomposed into elastic and visco-plastic components, as $\mathbf{F}_{B_i} = \mathbf{F}_{B_i}^e \mathbf{F}_{B_i}^v$, with $i = 1, 2$; and $\mathbf{F}_{B_i}^e$ and $\mathbf{F}_{B_i}^v$ being the elastic and visco-plastic deformation gradients, respectively. The response of the elastic component was also obtained by the same eight-chain hyper-elastic model, as:

$$\boldsymbol{\sigma}_{B_i} = \frac{1}{1+q_{B_i}} \left\{ \begin{array}{l} \frac{\mu_{B_i}}{J_{B_i}^e \bar{\lambda}_{B_i}^{e*}} \frac{L^{-1}(\bar{\lambda}_{B_i}^{e*}/\lambda_{L,B_i})}{L^{-1}(1/\lambda_{L,B_i})} \text{dev}[\mathbf{b}_{B_i}^{e*}] + \kappa_{B_i} (J_{B_i}^e - 1) \mathbf{1} + \dots \\ \dots + q \frac{\mu_A}{J} \left[I_{1,B_i}^{e*} \mathbf{b}_{B_i}^{e*} - \frac{2I_{2,B_i}^{e*}}{3} \mathbf{1} - (\mathbf{b}_{B_i}^{e*})^2 \right] \end{array} \right\}, \text{ for } i = 1, 2 \quad (4.2)$$

where $J_{B_i}^e = \det(\mathbf{F}_{B_i}^e)$, μ_{B_i} is the effective shear modulus, κ_{B_i} is the bulk modulus,

$\mathbf{b}^{e*} = \left(J_{B_i}^e\right)^{-2/3} \mathbf{F}_{B_i}^e \left(\mathbf{F}_{B_i}^e\right)^T$ is the Cauchy-Green deformation tensor, and $\bar{\lambda}_{B_i}^{e*} = \left(\text{tr}(\mathbf{b}_{B_i}^{e*})/3\right)^{1/2}$

is the effective chain stretch. Also, $I_{1,B_i}^{e*} = \text{tr}(\mathbf{b}_{B_i}^{e*})$ and $I_{2,B_i}^{e*} = \left\{ \text{tr}(\mathbf{b}_{B_i}^{e*})^2 - \text{tr}\left((\mathbf{b}_{B_i}^{e*})^2\right) \right\} / 2$,

while q_{B_i} is the relative contribution of I_{2,B_i}^{e*} . The strain rate gradient of the visco-elastic flow is given by:

$$\dot{\mathbf{F}}_{B_i}^v = \dot{\gamma}_{B_i} \left(\mathbf{F}_{B_i}^e\right)^{-1} \frac{\text{dev}[\boldsymbol{\sigma}_{B_i}]}{\tau_{B_i}} \mathbf{F}_{B_i} \quad (4.3)$$

where $\tau_{B_i} = \left\| \text{dev}[\boldsymbol{\sigma}_{B_i}] \right\|_F$ with $\left\| \cdot \right\|_F$ denoting the Frobenius norm, and $\dot{\gamma}_{B_i}$ is the effective deviatoric flow rate given by a power flow equation (Bergstrom and Bischoff 2010; Bergstrom 2012) as:

$$\dot{\gamma}_{B_i} = \dot{\gamma}_{0,B_i} \left(\frac{\tau_{B_i}}{f_{\varepsilon_p,B_i} \hat{\tau}_{B_i}} \right)^{m_{B_i}} \quad (4.4)$$

In this equation, $\dot{\gamma}_{0,B_i}$ ($\equiv 1/\text{s}$) is a constant introduced for dimensional consistency, $\hat{\tau}_{B_i}$ is the shear flow resistance (yield stress), m_{B_i} is the constant exponent of the model, and f_{ε_p,B_i} is the flow evolution factor considered to account for the strain softening response. The flow evolution factor was herein selected to follow a double exponential evolution as:

$$f_{\varepsilon_p, B_i} = \frac{1}{2} \left\{ f_{1, B_i} + (1 - f_{1, B_i}) \exp \left[\frac{-\varepsilon_{p, B_i}}{e_{1, B_i}} \right] + f_{2, B_i} + (1 - f_{2, B_i}) \exp \left[\frac{-\varepsilon_{p, B_i}}{e_{2, B_i}} \right] \right\} \quad (4.5)$$

where ε_{p, B_i} is the effective Mises plastic strain, f_{1, B_i} and f_{2, B_i} are the final values of the first and second exponential contribution, respectively, and e_{1, B_i} and e_{2, B_i} are characteristic transition strains for the first and second exponential contribution, respectively.

Because this constitutive model was not available in ABAQUS, the material library of the *PolyUMod* software by Bergstrom (2012) was used. The *PolyUMod* software included a calibration tool to determine all model parameters based on the experimental data, and also generated a UMAT subroutine for the calibrated constitutive model that was implemented in ABAQUS. Calibrated model parameters are presented in Table 4.1.

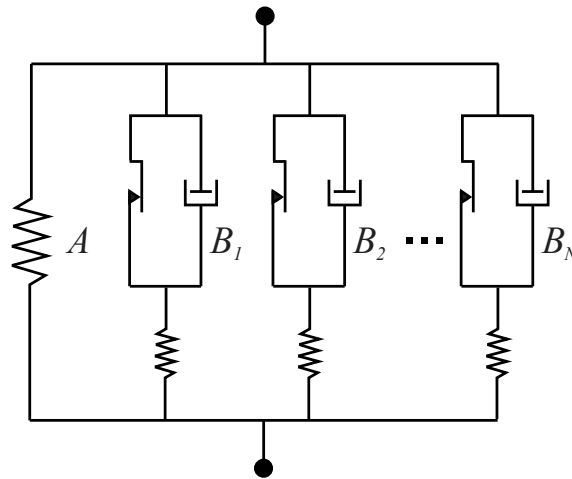


Figure 4.1. Rheological representation of constitutive models for elastomers.

Table 4.1. Constitutive model parameters.

Symbol	Unit	Description	Value		
			Network A	Network B ₁	Network B ₂
μ	psi	Shear modulus of network	6720	6000	76000
λ_L	-	Chain locking stretch	1	1	1
κ	psi	Bulk modulus	1.50E+07	1.50E+07	1.50E+07
q	-	Relative contribution of I_2	0.1	0.1	0.1
$\hat{\tau}$	psi	Flow resistance of network	-	8500	18600
m	-	Shear flow exponent	-	7	7
f_1	-	Final value of f_{ep} for exponential 1	-	2.5	3.7
e_1	-	Characteristic transition strain for exponential 1	-	0.005	0.43
f_2	-	Final value of f_{ep} for exponential 2	-	-0.8	-3
e_2	-	Characteristic transition strain for exponential 2	-	0.1	0.14

4.2.2. Model Validation for PU Test Specimen

The calibration was validated through modeling of the cylindrical PU specimens using solid continuum elements (Figure 4.2). Since most polymers have very little compressibility compared to their shear flexibility, the Poisson's ratio was selected to be 0.50. As recommended in the ABAQUS user's manual (SIMULIA 2013), solid continuum hybrid elements (C3D8H) were used to avoid potential convergence problems for incompressible hyper-elastic materials with Poisson's ratio greater than 0.495. The top and bottom platens were modeled using shell elements (S4R) and an elastic steel material with elastic modulus of 29000 ksi and Poisson's ratio of 0.3. Successive mesh refinements were applied to determine a fine enough mesh to reach convergence of the computational predictions. Fixed support boundary conditions were selected for the bottom platen. For the platen-to-specimen contact, Coulomb friction with a small coefficient of friction of 0.01 was considered in the parallel direction, and hard contact was considered in the

normal direction. Displacement-controlled loading was applied to the top platen in the axial direction. The simulations were performed using static analysis.

Computationally predicted vs. experimentally measured engineering stress-strain responses and computationally predicted vs. experimentally measured strain recovery responses are presented in Figure 4.3 and 4.4, respectively, at all considered strain rates; demonstrating good agreement between measured and predicted responses. The predictions of elastic stiffness, peak strength, stress relaxation during holding times, unloading response, and residual strains also compare favorably with the test results.

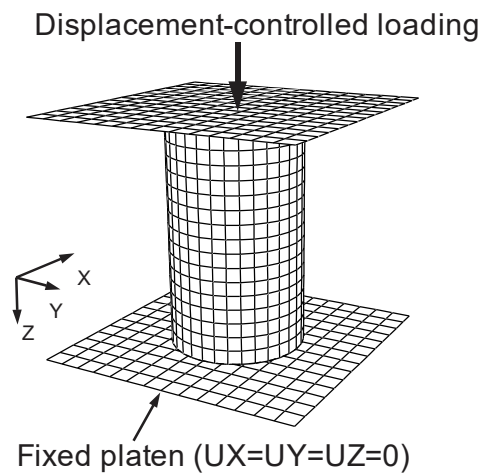


Figure 4.2. ABAQUS model of PU specimen.

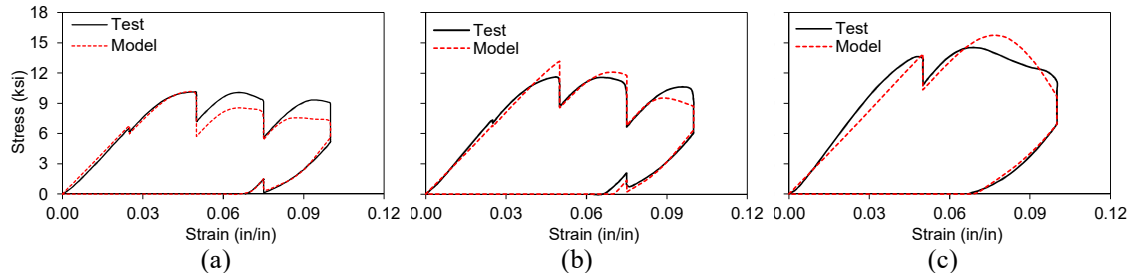


Figure 4.3. Predicted and measured uniaxial compressive stress vs. strain response at different strain rates: (a) 0.001 s^{-1} ; (b) 0.01 s^{-1} ; (c) 0.05 s^{-1} .

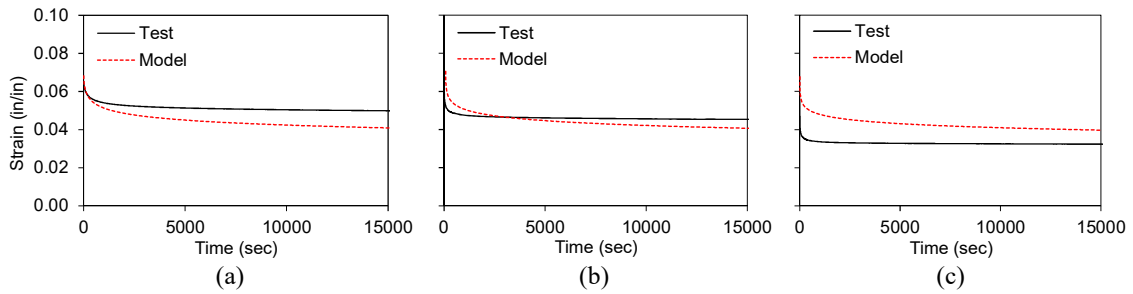


Figure 4.4. Predicted and measured stress-strain and strain recovery relationships at different strain rates: (a) 0.001 s^{-1} ; (b) 0.01 s^{-1} ; (c) 0.05 s^{-1} .

4.3. Performance Assessment of Rocking Columns with PU End Segments

4.3.1. Reference Column

The rocking column design with the DR end segments was obtained via modification of a selected reference column. The reference column was a segmental concrete column (specimen SC-2) tested by Motaref et al. (2013). The geometry and reinforcement details of the reference column are shown in Figure 4.5. The diameter of the column was 16 in. and the height was 72 in., leading to an aspect ratio of 4.5. The bottom segment of the column was monolithically connected to the footing through longitudinal steel reinforcement in a single pouring. Unbonded post-tensioning was

provided by a 1-5/8 in. diameter high strength steel bar passing through a 2.5 in. diameter PVC pipe placed at the centerline of the column. The total axial load on the column included a gravity load of 80 kips and the (initial) post-tensioning load of 110 kips, corresponding to an axial load index (ALI) of 0.20. ALI is defined as the ratio of the axial load to the product of the gross cross-section area with the nominal concrete compressive strength. The longitudinal steel reinforcement ratio was 1% in the bottom segment in accordance with the minimum amount required by CALTRANS (2006). Because, the bottom segment is monolithically connected to the foundation, a second reference column was also considered obtained by cutting the longitudinal steel reinforcement at the segment-to-foundation interface and allowing free rocking/opening at this joint. The resulting rocking reference column will demonstrate response differences with respect to the original monolithic reference column and will provide baseline responses for comparison with the proposed rocking column with PU end segments.

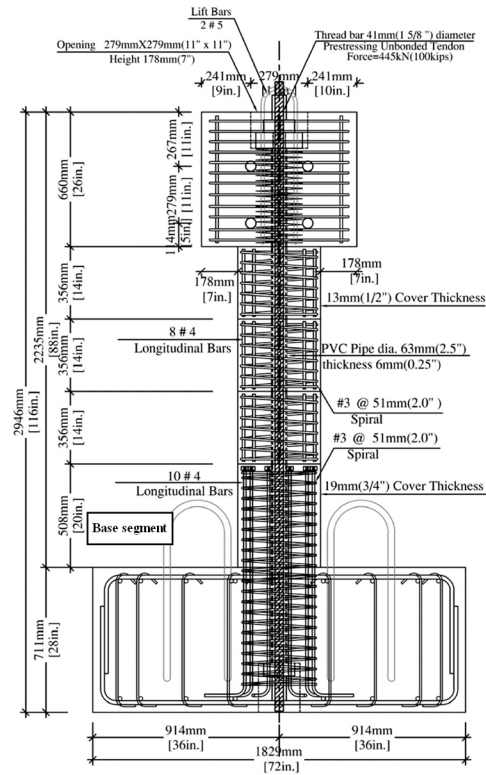


Figure 4.5. Monolithic reference segmental column, reprinted from Motaref et al. (2013).

4.3.2. Finite Element Modeling

The reference columns were modeled using the general purpose finite element software, ABAQUS/Implicit (SIMULIA 2013). The concrete segments and foundation were modeled using three-dimensional eight-node solid elements (C3D8R). The longitudinal and transverse reinforcement bars were modeled as two-node truss elements (T3D2) embedded into the concrete material. The post-tensioning bar was modeled by beam elements (B31) pinned at the top and bottom ends to the column top and foundation, respectively. All contact interactions were traced using the *general contact algorithm* and implemented using a penalty method. Particularly for segment-to-segment contact,

Coulomb friction with a coefficient of friction of 0.5 was considered in the parallel direction, and hard contact was considered in the normal direction. Hard contact in the normal direction and frictionless contact in the parallel direction was used to simulate the interaction between the post-tensioning bar and the duct.

The concrete damaged plasticity (CDP) model was used to describe the concrete material behavior. The CDP model incorporates two failure (or yielding) mechanisms – tensile cracking and compressive crushing – and adopts the yield surface proposed by Lubliner et al. (1989) with the modifications by Lee and Fenves (1998a). It also considers non-associated potential plastic flow with the flow potential being given by the Drucker-Prager hyperbolic function. In accordance with the values recommended by SIMULIA (2013), for the flow potential, the dilation angle, ψ , and the eccentricity, ε , were assumed to be $\psi = 15^\circ$ and $\varepsilon = 0.1$. For the yield surface, the ratio of the equi-biaxial compressive yield stress to the uni-axial compressive yield stress, f_{bo}/f_{co} , and the ratio of the second stress invariant on the tensile meridian to that on the compressive meridian, K_c , were assumed to be: $f_{bo}/f_{co} = 1.16$ and $K_c = 2/3$, while the viscosity parameter, μ , was set to zero. The compressive strength was considered to be 6.5 ksi according to the average measured strength on the test day (Motaref et al. 2013), while Young's modulus and Poisson's ratio were assumed to be 4500 ksi and 0.2, respectively. Steel material response was described by a uniaxial plasticity model with isotropic hardening and a strain hardening ratio of 1%. The yield stress of the longitudinal and transverse reinforcement was 64 ksi and 69.5 ksi, respectively (Motaref et al. 2013). The yield stress of the post-tensioning bar was 137 ksi.

To reduce the computational effort, only half of the column was modeled, and symmetry boundary conditions were enforced on the symmetry plane. First, the post-tensioning load was applied followed by application of the gravity load as a uniform pressure at the top surface of the column. A linearly increasing lateral displacement was, subsequently, applied to the top surface of the column up to a 10% drift ratio. The lateral force versus drift ratio response obtained from the test and analysis is shown in Figure 4.6. The predicted response by the *monolithic reference column* model is in good agreement with the experimental data, while the response from the *rocking reference column* model shows a slightly lower strength, because the mild steel reinforcement does not cross the column-to-foundation interface. The response of the rocking reference column will be used, in the sections to follow, for comparison with responses obtained for various designs of the rocking column with PU segments.

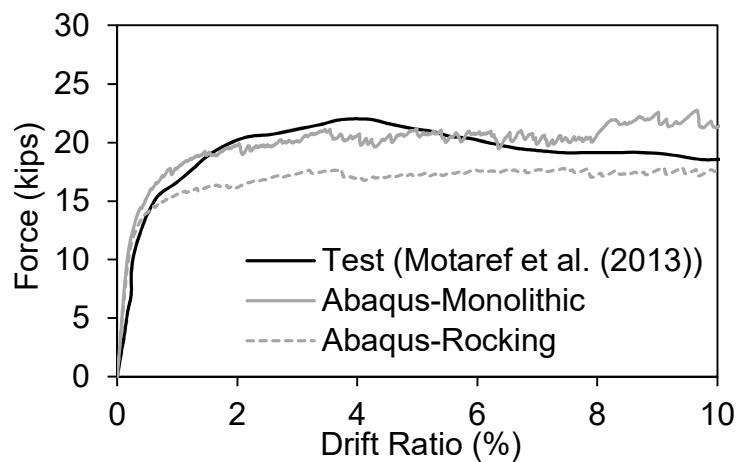


Figure 4.6. Benchmark column verification results – comparison of lateral force versus drift ratio.

4.3.3. Parametric Study

A rocking column with a DR segment was obtained by replacing the bottom concrete segment – height of 20 in. and diameter of 16 in. – of the *rocking reference column* with a PU segment. Parametric studies were conducted by varying the PU segment height, h_j , and diameter, D_j , while maintaining the same total column height. The height of the PU segment was varied from 8 to 20 in. with an increment of 4 in. resulting in h_j/D_c ratios (D_c : column diameter) ranging from 0.5 to 1.25. The diameter of the PU segment was varied from 12 to 18 in. with increments ranging between 1 and 2 in., resulting in D_j/D_c ratios ranging from 0.75 to 1.125. All column designs were subjected to monotonic pushover loading with a low drift ratio rate (0.015 s^{-1}), while selected designs were further subjected to cyclic pushover loading with the same loading rate. The performance of the various designs was assessed in terms of elastic stiffness, strength, peak compressive strain in concrete and PU, energy dissipation, and self-centering capabilities.

4.3.3.1. Monotonic Analysis

Monotonic analyses were conducted up to a peak lateral drift ratio of 15%. Contours of the axial strain for columns with PU segments of various h_j/D_c and D_j/D_c ratios at the peak lateral drift ratio of 15% are shown in Figure 4.7. The deformation mechanism combines flexure and rocking. For $D_j/D_c \leq 1$, the response always starts with rocking at the bottom. However, at larger deformations and for $h_j/D_c \leq 0.75$, the rocking at the bottom joint closes and the rocking at the joint above the PU segments, which was originally small, starts increasing with the applied drift ratio. This is because, in the

deformed shape, the inclination of the concrete column is larger than the inclination of the PU segment and, as a result, the compressive force of the concrete column (caused by the PT tendons) closes the gap at the bottom joint and increases the gap at the joint above the PU segment.

For $h_j/D_c \geq 1$ (and $D_j/D_c \leq 1$), the joint above the PU segment is “further away” from the bottom and is subjected to lower moment demands. As a result, under lateral loading, the rocking at the bottom joint becomes large, before the rocking at the joint above the PU segment, which would change the alignment between the concrete column and the PU segment, increases sufficiently. As a result, the PU segment and the concrete column above remain well aligned at larger deformations. Rocking at the bottom (as opposed to the joint above the PU segment) reduces the spreading and intensity of concrete compression damage (peak strains), by transferring (localized) deformations only to the PU segment (Figure 4.7).

For $D_j/D_c > 1$, the flexural strength of the bottom joint is always larger than the flexural strength of the joint above and, as a result, rocking at the bottom remains always small, compared to the rocking at the joint above the PU segment.

Lateral force vs. drift ratio curves for various h_j/D_c and D_j/D_c ratios are presented in Figure 4.8. The strength (at larger drift ratios, ~10%) and elastic stiffness increase with the D_j/D_c ratio. On the contrary, the elastic stiffness decreases with the h_j/D_c ratio, while strength only slightly increases with the h_j/D_c ratio. The lateral elastic column stiffness is quantified in Figure 4.9 with respect to the h_j/D_c and D_j/D_c ratios.

Peak axial compressive strains in the concrete material and the PU segment are presented for two lateral drift ratios, 5% and 10%, in Figure 4.10. The peak compressive strains in the concrete decrease as the D_j/D_c ratio decreases, because stresses from the PU segment are solely transferred to the confined concrete core and stress concentrations at the concrete cover are avoided. Similarly, peak compressive strains in the concrete decrease as the h_j/D_c ratio increases, because the PU segment-to-concrete interface is moved further away from the bottom, larger flexural demands are enforced. Peak compressive strains in the PU segments are practically unaffected by the D_j/D_c ratio, but decrease with the h_j/D_c ratio.

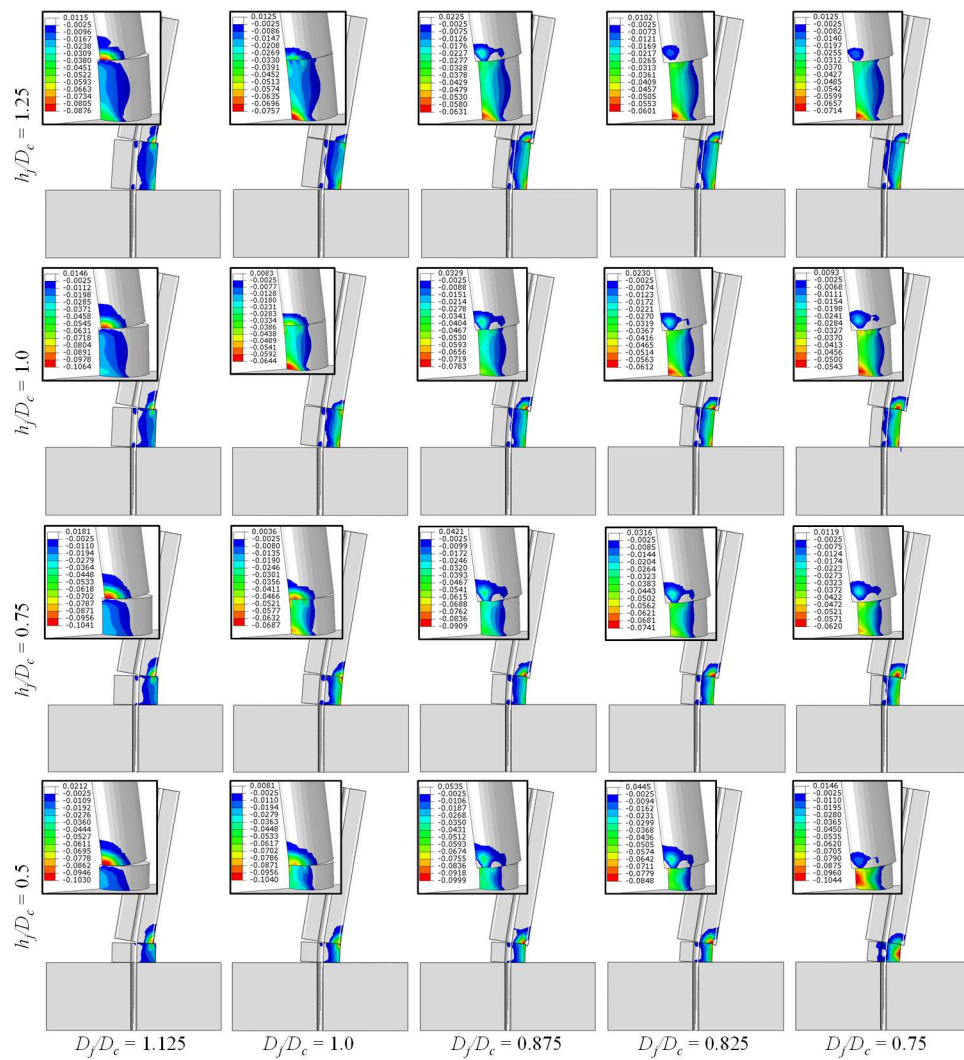


Figure 4.7. Nominal strain (NE33) on deformed shape of columns with PU segments at 15% drift ratio.

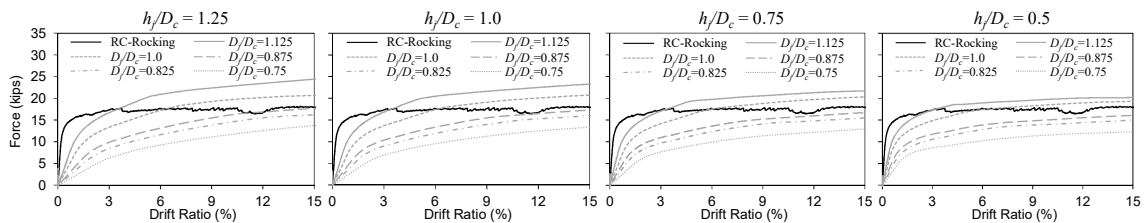


Figure 4.8. Lateral force versus drift ratio for various h_j/D_c ratios.

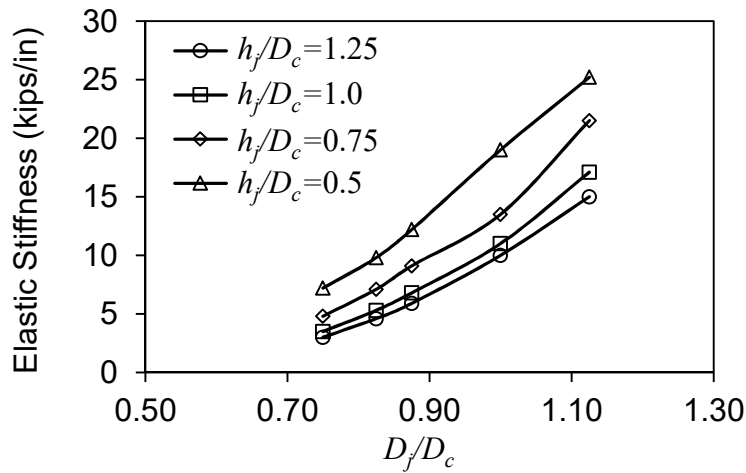


Figure 4.9. Variation of elastic stiffness with D_j/D_c and h_j/D_c .

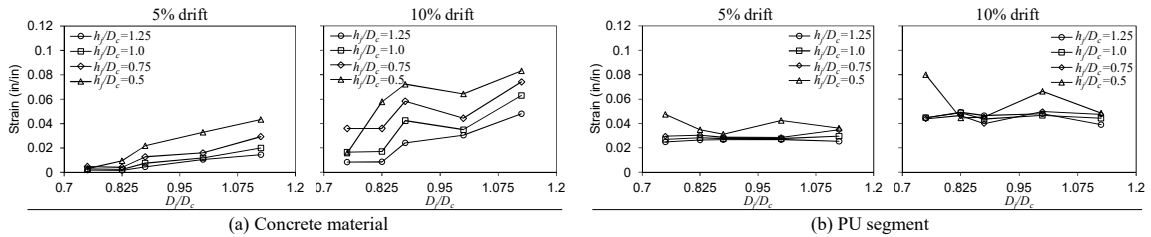


Figure 4.10. Column with PU segments: peak axial compressive strain for lateral drift ratios of 5% and 10% for: (a) concrete material; (b) PU segment.

4.3.3.2. Cyclic Analysis

According to the monotonic analysis results and with the objective of minimizing damage (i.e., peak strains), the PU segment height, h_j , and diameter, D_j , should satisfy $h_j/D_c \geq 1$ and $D_j/D_c \leq 1$ to ensure that rocking will occur at the bottom joint. Furthermore, D_j should be small enough, so that larger stresses are solely transferred to the confined concrete core. Very small values of D_j should be avoided, because they result in small lateral stiffness and strength. Large values of the h_j should also be avoided, because they

result in small lateral stiffness, with only minor increase in strength. Thus, reasonable geometric properties for the PU segment are: $h_j/D_c = 1$ and $D_j/D_c = 0.8$ to 0.9 . In reference to the ratios considered earlier, cyclic analyses were conducted for $h_j/D_c = 1$ and $D_j/D_c = 0.825$ and 0.875 . The loading protocol included single displacement-controlled cycles at peak drift ratios of 0.25%, 0.5%, 0.75%, 1%, 1.5%, and 2 % increased up to 10% with increments of 1%, and followed by two final cycles at 11.5% and 13%, respectively. In accordance with the monotonic loading, the drift ratio rate was 0.015 s^{-1} .

The lateral force vs. drift ratio hysteretic response of the columns with PU segments is compared to the response of the *rocking reference* column in Figure 4.11. The columns with PU segments exhibit a stable hysteretic response. Unlike the rocking reference column, which shows significant strength and stiffness degradation beyond a 3% drift ratio, the columns with PU segments maintain hardening response for the entire loading history and show larger strength compared to the rocking reference column at drift ratios exceeding 9%.

Energy dissipation capabilities were quantified through the cumulative dissipated energy (CDE) computed at the end of each test cycle, accounting for the current and all previous cycles. Self-centering capabilities were quantified through the relative self-centering efficiency (RSE) (Sideris et al. 2014b), which expresses the portion of the peak deformations that are recoverable, and is defined as:

$$\text{RSE} = 1 - \frac{u_{res}^+ - u_{res}^-}{u_m^+ - u_m^-} \quad (4.6)$$

where u_{res}^+ and u_{res}^- are the positive and negative residual displacements, respectively, and u_m^+ and u_m^- are the positive and negative peak displacements, respectively, as graphically indicated in Figure 2.4. An RSE value of unity corresponds to perfectly self-centering systems (i.e., systems with zero residual deformations), whereas a RSE value of zero corresponds to systems without any re-centering capabilities (e.g., Coulomb friction springs). The CDE and RSE as function of the drift ratio are shown in Figure 4.12. The columns with PU segments provide reduced energy dissipation compared to the rocking reference column, because of the small strains sustained by the PU segments, which only slightly exceeded the yield strain of the selected PU. As a result, the self-centering capabilities of the columns with PU segments achieve an RSE of 100% up to a drift ratio of 9%, which progressively decreases to 95% at the peak drift ratio of 13%. The effect of D_j/D_c in the computed responses was minor.

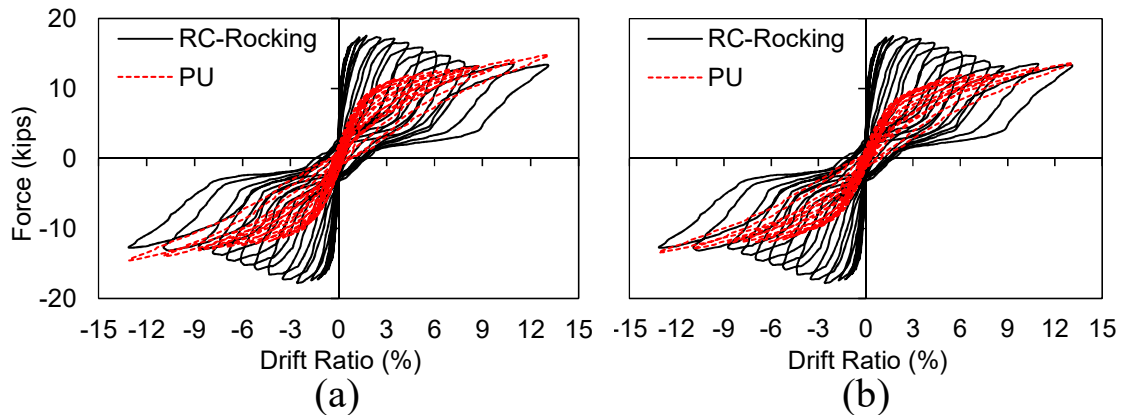


Figure 4.11. Cyclic behavior of columns with PU segments: (a) $D_j/D_c = 0.875$; (b) $D_j/D_c = 0.825$.

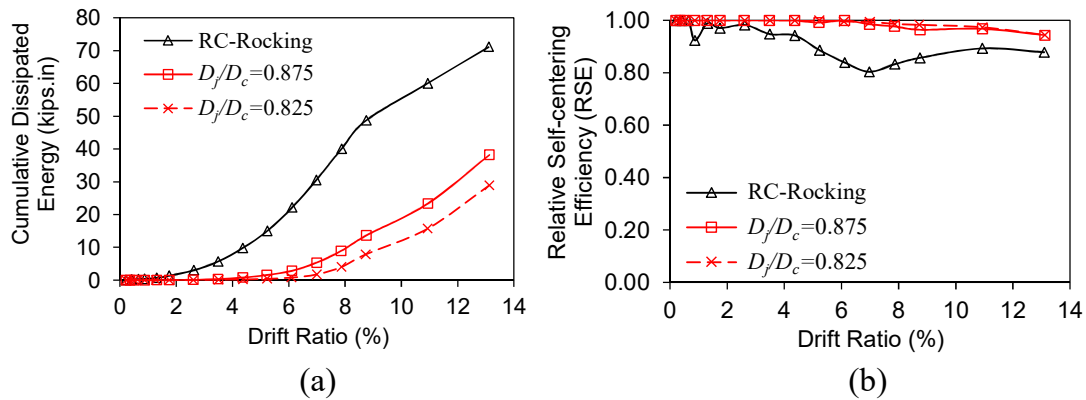


Figure 4.12. (a) Cumulative dissipated energy (CDE); (b) relative self-centering efficiency (RSE).

4.3.3.3. Effect of Rate of Loading

The effect of the rate of loading was examined by subjecting the columns with PU segments to a monotonic displacement-controlled lateral load up to a drift ratio of 15%, at three drift ratio rates, namely, 0.001, 0.01, 0.1 s^{-1} , followed by unloading to zero force. As shown in Figure 4.13, the strength slightly increases and the residual deformations significantly decrease with the drift ratio rate. This strength increase is much smaller than the strength increase observed in the uniaxial compression tests, because, for the proposed design, only a small portion of the cross-section actually experiences large strains, for which rate effects are significant. Rate effects in those portions (due to the dashpots in the rheological representation of Figure 4.1) reduce the contribution of plastic strains in the total strains, resulting in smaller (total) residual deformations with the strain rate.

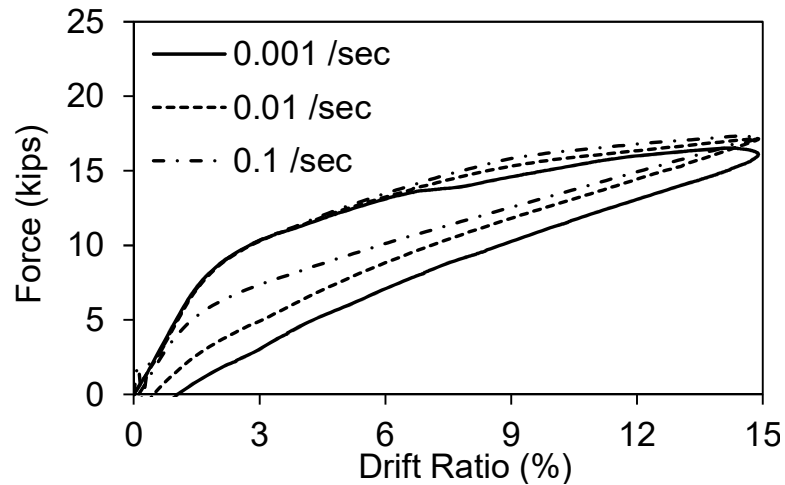


Figure 4.13. Lateral force versus drift ratio for various loading rates.

4.4. Energy Dissipating Links

While damage prevention in rocking columns is highly desirable, the low energy dissipation capabilities together with the moderate lateral stiffness could result in high lateral displacement demands. Supplemental (hysteretic) damping and flexural stiffness/strength can be provided in the vicinity of the PU segment through external energy dissipating (ED) links, which, herein, have the form of buckling-restrained yielding bars made of high performance steel. External ED links allow for easy inspection and rapid replacement upon damage.

4.4.1. Design Concepts

The ED link setup (Figure 4.14) includes a stiff steel collar, which is mounted to the face of the column right above the PU segment, and the ED links, which are bolted to the steel collar and the footing. ED links are usually steel circular rods with their end portions having larger diameter, so that they remain elastic and undeformed compared to

the *yielding length*, $L_{ED,y}$, which covers the middle portion and has smaller diameter. ED links are typically encased in thick steel tubes (Marriott et al. 2009) to prevent buckling, and can be easily obtained from mild steel reinforcing bars by milling the middle portion to provide a target diameter over the yielding length. ED links are attached to the column after the post-tensioning and dead load have been applied.

Various design criteria have been proposed for the design of ED links in rocking columns (e.g. Standards New Zealand 2006; Marriott et al. 2009; Guerrini et al. 2014), two of which have been adopted herein. The first criterion requires that self-centering, which can be compromised by the ED links, is maintained, and is expressed through a self-centering coefficient, λ_C , which is herein defined as:

$$\lambda_C = \frac{M_{ED}}{M_{P_v} + M_{PT}} \leq 1 \quad (4.7)$$

where M_{PT} is moment of the post-tensioning tendons/bars, M_{P_v} is moment of the external vertical axial load, and M_{ED} is the moment of the ED links. All moments are computed at the target design column drift ratio and refer to the location of the resultant PU compressive force at the bottom cross-section. To account for uncertainties, a smaller upper bound may be considered, e.g., $\lambda_C \leq 0.85$ (Standards New Zealand 2006). It is noted that λ_C is also a *flexural strength ratio* representing the additional flexural strength provided by the ED links over the total flexural strength without the contribution of the ED links.

The second criterion requires that fracture of the ED links is avoided at column drift ratios below the target design drift ratio. Accounting for low-cycle fatigue, Guerrini et al. (2014)

proposed that, at the target column drift ratio, the tensile strain, ε_{ED} , over the milled length, $L_{ED,Y}$, should not exceed half of the strain at the nominal tensile strength, $\varepsilon_{s,u}$, of the link:

$$\max \{ \varepsilon_{ED} \} \leq \varepsilon_{s,u} / 2 \quad (4.8)$$

which results in the following condition for $L_{ED,Y}$:

$$L_{ED,Y} \geq \frac{\max \{ u_{ED} \}}{\varepsilon_{s,u} / 2} \quad (4.9)$$

where u_{ED} is the extension of the milled length.

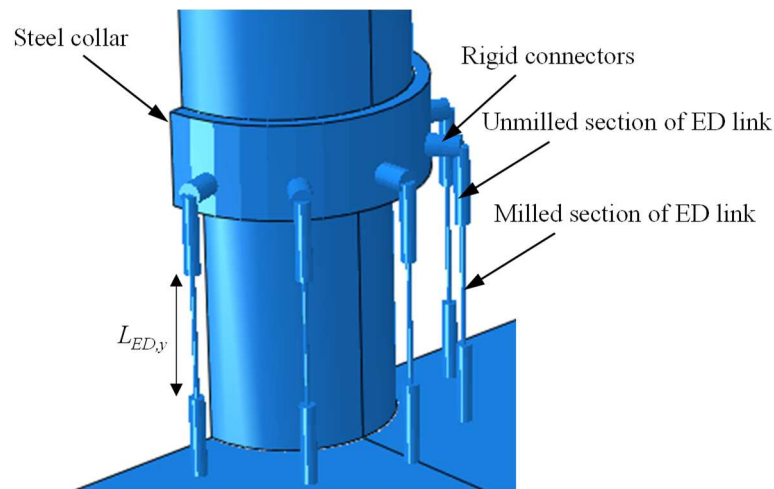


Figure 4.14. Details of ED link setup.

4.4.2. Rocking Columns with PU DR Segments and ED Links

ED links were considered for the columns with $h_j/D_c = 1$ and $D_j/D_c = 0.825$. Each column included ten radially distributed equally spaced ED links (Figure 4.14), which were offset by 3 in. from the face of the column and were assumed to be buckling-restrained. The ED links were designed for a target drift ratio of 5% and two values of λ_C ,

namely, 0.25 and 0.5. The steel material conformed to Grade 60 per ASTM A706 (ASTM A706/A706M-16 2016) with a nominal yield strength of 64 ksi and a strain hardening ratio of 0.8%. The yielding length, $L_{ED,y}$, was computed to be 8 in., per Eq. (4.9). The diameter of the rod over the yielding length was 0.24 in. and 0.34 in. for λ_C equal to 0.25 and 0.5, respectively, whereas, the diameter of the elastic end portions was 1.0 in. It was observed that the diameter of these elastic portions should be selected such that the stiffness of these portions is always much larger (by a factor of 10 or higher) than the stiffness of the yielding length, so that all induced deformations are transferred to the yielding length. For the same reason, the steel collar was designed to be stiff and remain elastic. The steel collar had a width/height of 5 in. and thickness of 1 in. and its material properties conformed to Grade 50 high strength steel per ASTM A572 (ASTM A572/A572M-15 2015).

4.4.2.1. Cyclic Analysis

Analyses were conducted with the cyclic loading protocol used earlier. The ED links were fixed to the footing, after application of the gravity loads and initial post-tensioning, to ensure that they are stress-free at the beginning of application of the lateral load. According to the computed lateral force vs. drift ratio hysteretic response (Figure 4.15), columns with ED links exhibit significantly higher elastic lateral stiffness and peak lateral strength compared to columns without ED links. Both strength and stiffness increase with λ_C , which represents the contribution of the ED links to the total flexural stiffness and strength. The ED links also offer major energy dissipation capabilities (Figure 4.16(a)) compared to those of columns without ED links and the rocking reference

column. No damage is observed in the concrete cover and core, due to the confinement provided by the steel collar. The peak axial strain in the ED links at the target column drift ratio of 5% is approximately 7 % for both values of λ_C , while the peak axial strain in the ED links at the peak column drift ratio of 13% is approximately 20 % for both values of λ_C . Mild yielding of the post-tensioning bar is observed at a lateral drift ratio of 8.2% and 7.0% for Λ_C equal to 0.25 and 0.5, respectively.

At the end of the loading protocol, the column with $\lambda_C = 0.25$ exhibits large self-centering capabilities (RSE ≈ 90 %), while moderate self-centering capabilities (RSE ≈ 50 %) are exhibited for $\lambda_C = 0.5$, as shown in Figure 4.16 (b). Because residual deformations mainly result from residual strains in the ED links, their largest portion is recoverable upon replacement of the ED links. This is demonstrated in Figure 4.17, which shows the lateral drift ratio for both columns during sequential removal of the ED links, after completion of the loading protocol. The ED links were removed in three steps with a difference of 1 hour. After removal of all ED links, negligible residual deformations (RSE $> 99.5\%$) are reached almost immediately, for both values of λ_C .

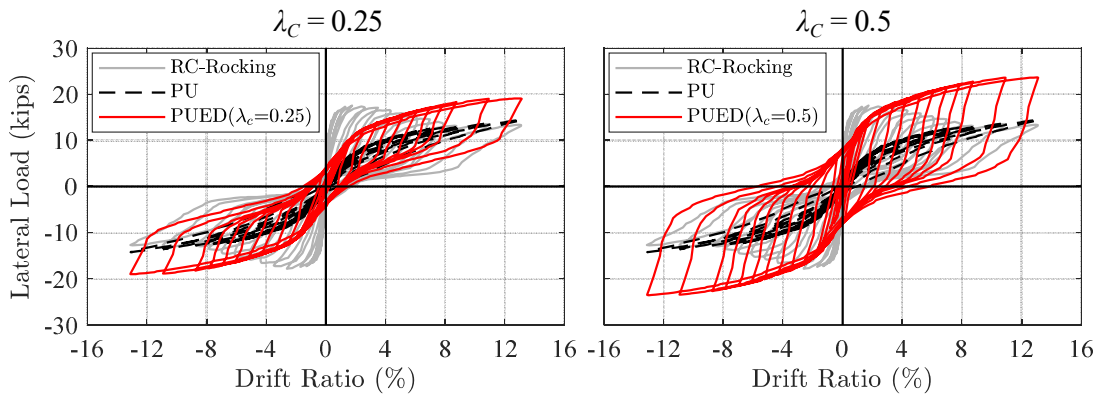


Figure 4.15. Hysteretic response of columns with PU segments and ED links as function of λ_c parameter.

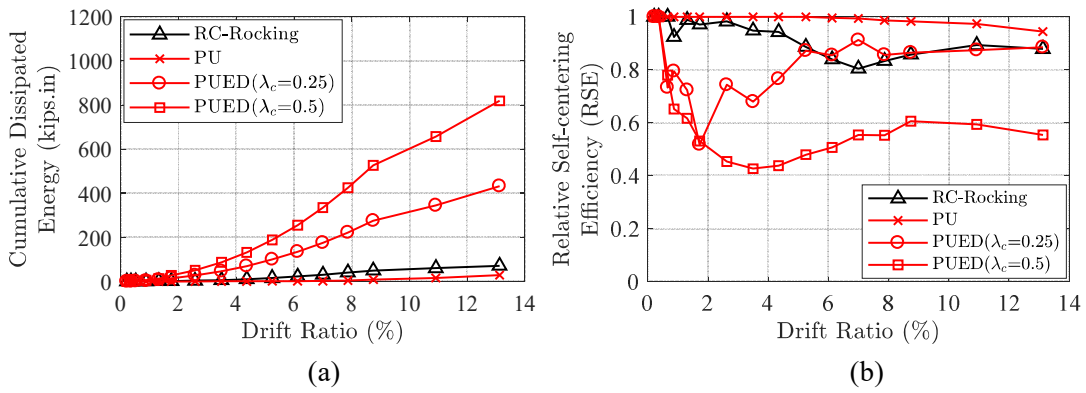


Figure 4.16. Column with PU segments and ED links: (a) cumulative dissipated energy; (b) relative self-centering efficiency.

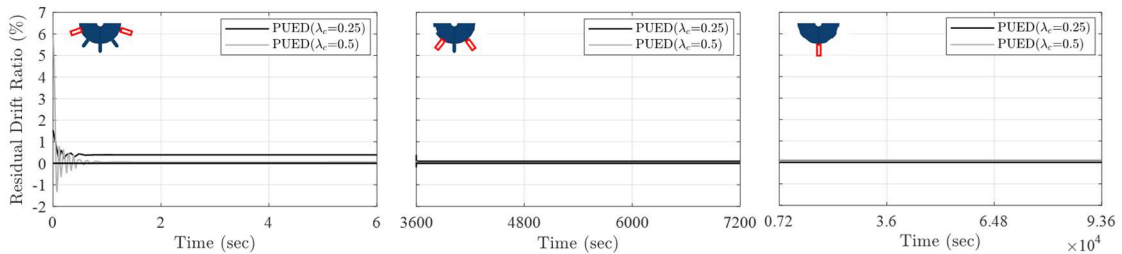


Figure 4.17. Recovery of residual drift after sequential removal of ED links.

4.5. Summary and Findings

In this section, the performance of the proposed column design was investigated for various PU segment geometries and various ED link properties through three-dimensional finite element analysis. To this end, elasto-visco-plastic constitutive relations were investigated and calibrated to the test data obtained in Phase 2 of the material characterization testing program for ECast (see Section 3.3.2). Parametric studies were subsequently conducted via three dimensional finite element modeling of a bridge column to assess the performance of the proposed column design in terms of the PU segment geometry and the properties of the ED links. Major findings include:

- Post-tensioned rocking columns with PU end segments and external ED links can provide low damage, large deformation capacity and rapid retrofit capabilities. In the absence of ED links, columns with PU end segments provide moderate stiffness and strength, low energy dissipation capacity and large self-centering capabilities. Incorporation of ED links increases the stiffness, strength and energy dissipation capabilities of the proposed column designs. Stiffness, strength and residual deformations increase with λ_C (i.e., the contribution of ED links).
- Because of the large elastic deformation capacity and the visco-plastic properties of the selected PU, permanent deformations are small. Specifically, the large elastic deformability permits large deformations without damage, while the visco-plastic properties limit the contribution of the plastic strains in the total strains. As a result, removal of the ED links after large induced lateral drift ratios ($\sim 13\%$),

eliminated all column residual deformations (RSE > 99.5%) indicating that the PU segments remained nearly undamaged.

- Rate effects were found to be small on the peak strength of the column, because only a small portion of the PU segment is actually subjected to large strains, for which strain rate effects are significant. However, the residual deformations significantly decreased with the loading rate, indicating that locally induced plastic strains were alleviated, because of the viscous contributions during plastic traveling.
- The geometric properties of the PU segment – height, h_j , and diameter, D_j – strongly affect the observed damage, and lateral stiffness and strength of the column. Specifically, the lateral stiffness and strength increase with D_j/D_c , where D_c is the column diameter. However, the lateral stiffness decreases with h_j/D_c , while the lateral strength only slightly increases with h_j/D_c . On the other hand, the PU segment height should satisfy $h_j/D_c \geq 1$ to ensure that rocking will occur at the bottom joint, while the PU segment diameter should be small enough ($D_j/D_c = 0.8$ to 0.9), so that large (concentrated) stresses are solely transferred to the confined concrete core.

From a design perspective, the proposed column design is expected to be easily deployable onsite and can reach the stiffness and strength of conventional monolithic columns through the use of ED links. Compared to conventional columns, the proposed design provides significantly larger deformation capabilities and significantly smaller

residual deformations. Unlike conventional monolithic columns, the proposed design also offers a path to rapid and cost-effective post-earthquake retrofit, because damage is mostly concentrated in the ED links, which can be quickly replaced, following a strong earthquake.

5. UNIAXIAL VISCOELASTIC SOFTENING VISCOPLASTIC MODEL FOR POLYURETHANE*

5.1. Introduction

To ensure the desired safety and longevity of infrastructure systems incorporating polymeric components, such as the system proposed in this study, the mechanical behavior of such materials needs to be characterized through properly designed and executed experiments. Depending on the loading conditions and temperature, the mechanical behavior of polymers can vary widely from brittle to ductile. For analysis and design purposes, a comprehensive constitutive model is subsequently required, capable of capturing the salient features of the material response, such as nonlinear strain rate dependency, nonlinear unloading, hysteresis, softening/damage, and creep and relaxation.

To this extent, a wide range of constitutive models have been developed. Models based on classical linear viscoelasticity (Christensen 2012; Tschoegl 2012), although capable of capturing loading rate dependency, creep, and relaxation in the elastic range, have limited predictive capabilities, because polymeric materials often exhibit nonlinear viscoelastic response even at relatively small strains. To address the usually large number of model parameters of linear visco-elastic models, models of fractional viscoelasticity

* Part of the data reported in this section is reprinted with permission from “Experimental characterization and constitutive modeling of polyurethanes for structural applications, accounting for damage, hysteresis, loading rate and long term effects” by Nikoukalam, M. T., & Sideris, P., 2019. *Engineering Structures*, 198, 109462, Copyright 2019 by Elsevier.

(Bagley and Torvik 1983; Müller et al. 2011) have been developed and have been shown capable of describing the rate dependent behavior with less parameters, a trade-off that comes with a higher computational cost. To capture the nonlinear viscoelastic response of polymers, Green and Rivlin (1957) proposed a general multi-integral nonlinear viscoelastic model, which, because of its complexity and the large number of experimental data required for calibration of its parameter, has found very limited application. More applicable nonlinear viscoelastic models have been presented by Findley and Onaran (1968), McGuirt and Lianis (1970), Smart and Williams (1972), and Reese and Govindjee (1998), amongst others.

Considering that polymeric materials also experience plastic deformations, especially at relatively large strains, viscoplastic constitutive models have also been developed. Krempl (1996) proposed a unified state variable viscoplasticity theory for metals and alloys based on the concept of overstress, usually termed *viscoplasticity based on overstress* (VBO) theory. The VBO theory was later extended to polymers, resulting in the so-called *viscoplasticity based on overstress for polymers* (VBOP) theory (Krempl and Ho 2000; Ho and Krempl 2002). The VBOP theory consists of two tensor valued state variables, namely, the equilibrium stress and the kinematic stress, and two scalar valued state variables, namely, the isotropic stress and drag stress. The isotropic stress, which is a rate-independent contribution to the stress, is responsible for modeling hardening and softening (Krempl and Ho 2000). The kinematic stress, which is similar to the backstress in the classical plasticity theories, is used to model the final hardening rate of the stress–strain curve and the Bauschinger effect. This model was used to capture the *tensile*

response of Nylon 66 under *monotonic* loading-unloading at various strain rates, and the completely *reversed cyclic* response at a constant strain. Ho and Krempl (2002) introduced a decreasing and subsequently increasing augmentation function into the equilibrium stress evolution equation to model the rate dependent strain softening and hardening. This model was used to capture the *monotonic* response of polymethyl methacrylate (PMMA) under *tension* and *compression*. Modified versions of this model have been used by Colak (2005; 2008) to reproduce the *monotonic tensile* response of polyphenylene oxide with a focus on the nonlinear rate-dependent and nonlinear unloading, *creep* at different stresses above and below the yield point, and *recovery*.

To capture the viscoplastic response of polymers, models have been also developed based on the kinetic theory of polymer chains and other micromechanical considerations (Boyce et al. 1988; Arruda and Boyce 1993; Heinrich and Kaliske 1997; Drozdov 1998; Bergström and Hilbert 2005). Of particular relevance to the behavior of amorphous polymers in the small-to-moderate strain regime ($< 15\%$), i.e. the range relevant to structural applications, is the study of Hasan (1994) and Hasan and Boyce (1995), which proposes a physically motivated constitutive framework to describe the glassy state of amorphous polymers based on the distributed nature of microstructural disorder. Hasan and Boyce (1995) proposed a *one-dimensional* constitutive model in which they consider a *distribution in the activation energy barrier* to capture deformation as part of a *thermally activated* process. In their model, *hardening* is modeled through evolution of a *backstress* and *softening* is modeled through reduction of the activation energy. Hasan and Boyce (1995) showed the capability of their model to capture the response of PMMA under

monotonic compression at various strain rates and *compressive creep* at various stress levels.

Building upon basic concepts presented in models by Parks, Argon, Boyce, Arruda and their co-workers (Boyce et al. 1988; Arruda and Boyce 1993; Hasan and Boyce 1995), a general elasto-visco-plastic constitutive model was developed by Anand and Gurtin (2003) for amorphous polymers and later refined by Anand and Ames (2006) to reproduce the experimentally measured indentation load vs. depth response of PMMA. This model captured the highly nonlinear behavior of glassy polymers through the evolution of the *local free volume*, a microstructural state variable distributed non-homogeneously throughout the material (Hasan and Boyce 1995). The hardening and softening response was modeled through the evolution of a *backstress* (resistance to plastic flow). The model was used to capture major features of the mechanical response of PMMA at ambient temperature with the focus on *monotonic compression* loading-unloading and *creep* at various stress levels.

Building on the work of Tanaka and Edwards (1992), Drozdov and Lejre (2009) derived a constitutive model combining the Eyring concept of inelastic processes (viscoplasticity) with the concept of transient networks for viscoelastic processes. In their model, the polymer network is thought as heterogeneous and composed of meso-domains with various activation energies for re-arrangement of polymer chains. The model was used to reproduce the response of polypropylene/clay nanocomposites from *tensile* tests with various strain rates, *relaxation* tests at various strains, and *creep* tests under various stresses at room temperature.

In the spirit of the model proposed by Drozdov and Lejre (2009), Kontou and Spathis (2014) developed a three-dimensional model, which simulated the viscoelastic response via transient networks (Tanaka and Edwards 1992) and the viscoplastic response via the kinematic formulation developed by Rubin (1994) combined with a functional form of the rate of plastic deformation. This model successfully described the *monotonic* loading (nonlinear, strain-dependent) and all main stages of *creep*, including tertiary creep of polypropylene as a semi-crystalline polymer. Kontou (2016) further modified this model to capture the nonlinear unloading response observed in the *cyclic* viscoplastic response of an amorphous glassy polymer.

5.2. Scope and Objectives

The majority of the models mentioned in the previous section are three-dimensional, computationally expensive, and tailored to specific polymers. This often makes them unsuitable for structural engineering applications, which include numerous analyses with several ground motions. The primary objective of this section is to address this challenge by developing novel uniaxial visco-elastic/plastic constitutive models capable of capturing the salient response features of the selected polyurethane (primarily, ECast), such as rate dependency, hysteresis and damage (softening), and long term effects (creep, relaxation, and recovery). To this end, in this first stage (Section 5.3), the present study develops a simplified uniaxial visco-elastic softening visco-plastic constitutive model that is capable of capturing major response properties of the selected polyurethane (ECast), and requires significantly less computational time. The constitutive model was calibrated using the test data obtained in Phase 2 of the experimental material characterization

program presented in Section 3.3.2. The proposed simplified model was implemented in the OpenSees structural analysis software and was later used to study the seismic performance of bridge systems incorporating the proposed column design (see Section 6). In the second stage (Section 5.4), a more versatile uniaxial model is proposed which is capable of capturing the response of the selected PU at room temperature under all loading sequences presented in Phase 3 of the experimental material characterization program presented in Section 0.

5.3. Simplified Model

5.3.1. Model Description

The proposed simplified constitutive model consists of a linear elastic spring A in parallel with a set of visco-elastic/plastic networks B_n , with $n = 1, 2, \dots$, as shown in Figure 5.1 (a). Each network B_n consists of an elastic spring in series with a softening elasto-plastic element that is in parallel with a nonlinear viscous dashpot. The elastic spring has a different elastic modulus in tension and compression, which has been found to provide reasonably accurate predictions on the unloading branch of the stress vs. strain response. The response of the elastic spring of network B_n is given as:

$$\sigma_{B,n} = \begin{cases} E_{B,n} (\varepsilon_n - \varepsilon_{r,n}) & , \varepsilon_n - \varepsilon_{r,n} \leq 0 \\ \beta_n E_{B,n} (\varepsilon_n - \varepsilon_{r,n}) & , \varepsilon_n - \varepsilon_{r,n} > 0 \end{cases} \quad (5.1)$$

where $E_{B,n}$ is the initial elastic modulus of the network B_n , ε_n is the total applied strain, $\varepsilon_{r,n}$ is the strain in the nonlinear viscous damper, and β_n is the ratio of the elastic modulus in tension to the elastic modulus in compression.

The stress vs. strain response of the softening elasto-plastic element is given in incremental/rate form as:

$$\begin{aligned} \dot{\sigma}_{ep,n} &= R_n E_{ep,n} \dot{\varepsilon}_{r,n} \\ \text{with } \begin{cases} \sigma_{ep,n} \leq \sigma_{n,UP} = R_n \left(f_{y,n} + r_{y,n} E_{ep,n} \left(\varepsilon_{r,n} - \frac{f_{y,n}}{E_{ep,n}} \right) \right) \\ \sigma_{ep,n} \geq \sigma_{n,LO} = R_n \left(f_{y,n} + r_{y,n} E_{ep,n} \left(\varepsilon_{r,n} + \frac{f_{y,n}}{E_{ep,n}} \right) \right) \end{cases} \end{aligned} \quad (5.2)$$

where $\sigma_{ep,n}$, $E_{ep,n}$, $f_{y,n}$, and $r_{y,n}$ are the stress, initial elastic stiffness, yield stress, and hardening ratio of the softening elasto-plastic element of network B_n . The inequalities represent upper and lower *bounding* surfaces that represent yielding. The description of Eq. (5.2) is equivalent to classical plasticity with linear kinematic hardening, yet more computationally efficient, because it does not require iterations. Also, R_n is the damage reduction factor of the network B_n , which is a function of the peak absolute strain of the elasto-plastic element over the entire loading history, $\varepsilon_{r,n,peak}$, and is given as:

$$R_n = \begin{cases} 1 & , \varepsilon_{r,n,peak} \leq \varepsilon_{1,n} \\ 1 - \frac{1 - R_{\min,n}}{\varepsilon_{2,n} - \varepsilon_{1,n}} (\varepsilon_{r,n,peak} - \varepsilon_{1,n}) & , \varepsilon_{1,n} < \varepsilon_{r,n,peak} < \varepsilon_{2,n} \\ R_{\min,n} & , \varepsilon_{r,n,peak} \geq \varepsilon_{2,n} \end{cases} \quad (5.3)$$

with $\varepsilon_{r,n,peak} = \max_t (|\varepsilon_{r,n}(t)|)$

where R_n varies linearly from unity at $\varepsilon_{1,n}$ to a residual value ($R_{\min,n}$) at $\varepsilon_{2,n}$ (Figure 5.1(b)).

The stress in the nonlinear viscous damper, $\sigma_{D,n}$, of network B_n is given as:

$$\sigma_{D,n} = \frac{\eta_n}{a_n} \left(1 - e^{-a_n |\dot{\epsilon}_{r,n}|}\right) \text{sgn}(\dot{\epsilon}_{r,n}) \quad (5.4)$$

where η_n is the initial viscosity of the dashpot, a_n is the exponent power coefficient which has units of time and represents how fast the damping stress reaches its peak value, η_n/a_n . Also, $\dot{\epsilon}_{r,n}$ is the strain rate, and $\text{sgn}(\cdot)$ is the sign function. Note that that for high yield stress and small strain rates, each network B_n is essentially a “linear” solid model. Thus, each network B_n can capture both visco-elastic and visco-plastic response.

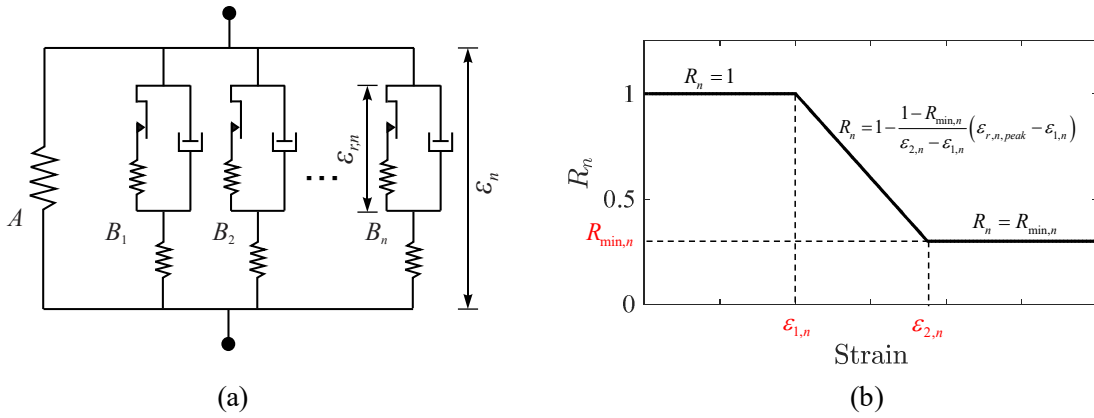


Figure 5.1. (a) Rheological representation of constitutive model; (b) variation of damage reduction factor, R_n , with strain.

5.3.2. Model Validation and Calibration

For the selected PU material, two B networks were found to be capable of simulating the experimentally measured material response. The proposed model was calibrated to the test data from the uniaxial compression strain-controlled half-cycle test under a constant engineering strain rate (presented in Section 3.3.2.5) via minimization of

an error norm representing the difference between experimentally measured stresses and stresses predicted from the proposed simplified model. This minimization was performed using a constraint minimization algorithm from MATLAB (2016) and introducing suitable constraints for all model parameters. The optimized/calibrated model parameters are presented in Table 5.1. Computationally predicted vs. experimentally measured engineering stress vs. engineering strain responses from multi-step compression relaxation tests and cyclic compression-only tests are presented in Figure 5.2 and 5.3, respectively, for all considered strain rates, demonstrating good agreement between measured and predicted responses. The predictions of elastic stiffness, peak strength, stress relaxation during holding times, unloading and reloading response, cyclic damage/softening, and residual strains also compare favorably with the test results especially for the medium (0.01 /sec) and high (0.05 /sec) strain rates, which are of interest in this study. The discrepancies observed in the fit of the model to the test data at low strain rate are mainly attributed to the constant initial viscosity of the dashpot. A better fit of the model to the test data (finer control over the response) can be achieved by defining the initial viscosity as a function of the strain rate, which would be at the cost of introducing more parameters to the model, and for this reason is not considered herein.

Table 5.1. Calibrated model parameters.

Symbol	Description	Value		
		Network A	Network B ₁	Network B ₂
E_A or E_B	elastic stiffness of elastic springs (ksi)	4.93	300	300
β	tension to compression stiffness ratio	-	0.01	0.67
E_{ep}	elastic stiffness of elasto-plastic element (ksi)	-	300	300
f_y	yield strength of elasto-plastic element (ksi)	-	4.43	3.78
b	strain-hardening ratio of elasto-plastic element	-	0.08	0.05
ϵ_1	strain at which deterioration starts	-	4.7	2.1
ϵ_2	strain at which deterioration ends	-	5	7
R_{min}	minimum strength deterioration factor	-	0.84	0.05
η	initial viscosity of the dashpot (ksi-s)	-	1182	91
a	nonlinear viscous dashpot exponent power coefficient (s)	-	198	91

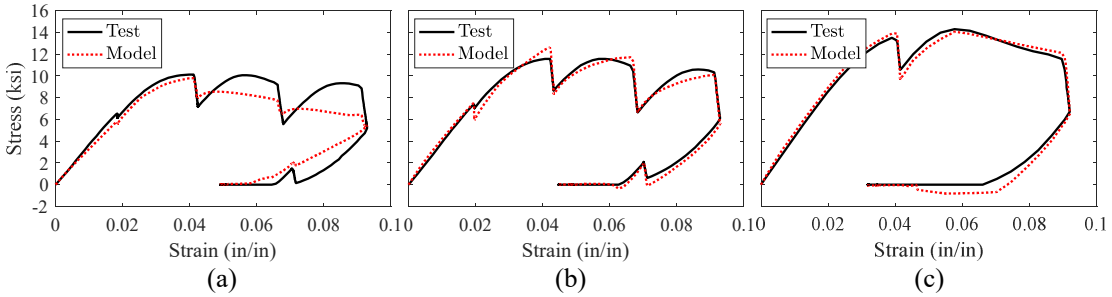


Figure 5.2. Predicted and measured uniaxial compressive stress vs. strain response at different strain rates: (a) 0.001 /sec; (b) 0.01 /sec; (c) 0.05 /sec.

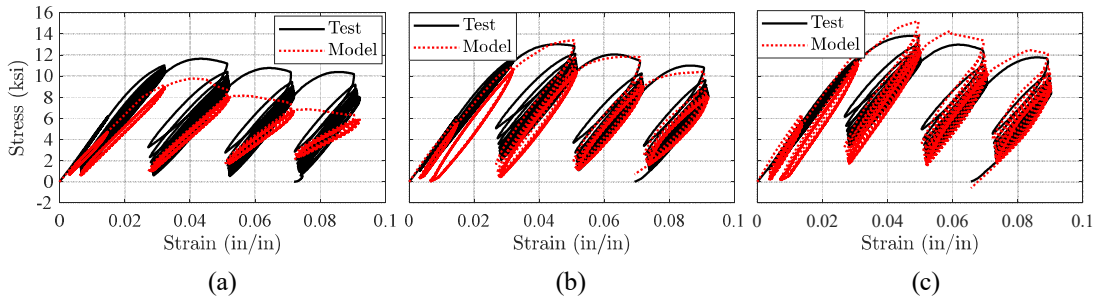


Figure 5.3. Predicted and measured cyclic compressive stress vs. strain response at different strain rates: (a) 0.001 /sec; (b) 0.01 /sec; (c) 0.05 /sec.

5.4. Advanced Model

The simplified model presented in Section 5.3, although very versatile, was not able to capture the response of the selected PU under more complicated loading conditions, such as cyclic compression-tension (see Section 3.3.3.5.4). In this section, a more versatile uniaxial model is proposed, which is capable of capturing the response of the selected PU at room temperature under all loading sequences presented in Phase 3 of the experimental material characterization program (see Section 0), specifically the cyclic compression-tension process.

5.4.1. Model Description

Under applied strain, the response of amorphous polymers includes an *instantaneous* (time-independent) component, due to bond stretching, i.e. the intermolecular interaction between polymer chains, and a *viscous* (time-dependent) component due to conformational uncoiling of the polymer chains (Ward and Sweeney 2004; Halary et al. 2011). At larger strains, yielding and softening occurs, mostly due to motion of atom clusters of strong bonds within a weaker, lower density, matrix (Fortunelli and Ortiz 2007; Halary et al. 2011; Bergstrom 2015). Particularly at large compressive strains, rubber-like nonlinear stiffening is observed due to the alignment of the macromolecular network of the entangled polymer chains (Haward and Thackray 1968). Damage and failure is manifested usually in the form of shear bands, which are observed in both compressive and tensile tests, and crazes (cracks with fibrils), which exclusively occur under tension (Halary et al. 2011).

To simulate the complex mechanical response of the selected polyurethane (ECast), and, by extension the response of amorphous polymers of similar properties, a constitutive model, following the rheological representation of Figure 5.4, is proposed. The proposed model includes an elasto-visco-plastic component in series with two generalized Kelvin-Voigt networks. The first Kelvin-Voigt network includes nonlinear viscoelastic elements and is intended to capture the nonlinear viscoelastic response at short time scales. The second Kelvin-Voigt network includes linear viscoelastic elements and is intended to capture the long-term creep response. Damage effects are considered in the elasto-visco-plastic component as well as the nonlinear generalized Kelvin-Voigt network. Damage is taken to be a function of peak and cumulative plastic strains, thereby, introducing a coupling between elastic and inelastic responses. A nonlinear stiffening spring is further introduced, in parallel with this network, to describe the rubber-like nonlinear stiffening behavior at large compressive strains.

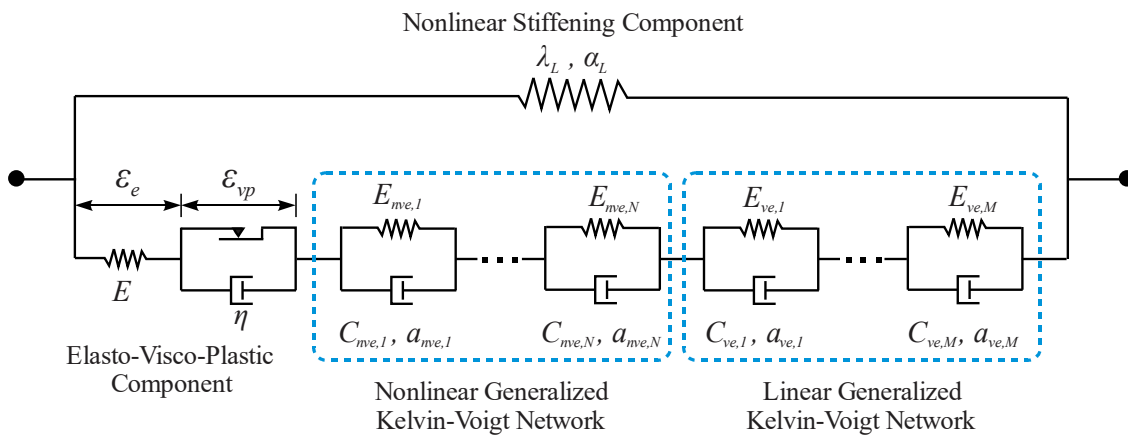


Figure 5.4. Rheological structure of the advanced model.

5.4.2. Constitutive Equations

The mathematical structure of the constitutive equations for the proposed model is derived by the constitutive relations of the individual components and the connectivity amongst them. In the formulation presented herein, compression is assumed negative.

5.4.2.1. Compatibility and Equilibrium Equation

Strain compatibility between the elasto-visco-plastic component and the two generalized Kelvin-Voigt networks, requires that:

$$\boldsymbol{\varepsilon} = \boldsymbol{\varepsilon}_e + \boldsymbol{\varepsilon}_{vp} + \sum_{j=1}^N \boldsymbol{\varepsilon}_{nve,j} + \sum_{i=1}^M \boldsymbol{\varepsilon}_{ve,i} \quad (5.5)$$

where $\boldsymbol{\varepsilon}$ is the total applied strain, $\boldsymbol{\varepsilon}_e$ is the elastic strain, $\boldsymbol{\varepsilon}_{vp}$ is the viscoplastic strain, $\boldsymbol{\varepsilon}_{nve,j}$ is the strain of the j -th nonlinear viscoelastic component, $\boldsymbol{\varepsilon}_{ve,i}$ is the strain of the i -th linear viscoelastic component, and N and M is the total number of nonlinear and linear viscoelastic components, respectively. Equilibrium requires that the total stress of the model is given as:

$$\boldsymbol{\sigma} = \boldsymbol{\sigma}_s + \boldsymbol{\sigma}_e \quad (5.6)$$

where $\boldsymbol{\sigma}_s$ and $\boldsymbol{\sigma}_e$ are the stresses in the nonlinear stiffening spring and the elastic spring, respectively. Equilibrium further requires that $\boldsymbol{\sigma}_e = \boldsymbol{\sigma}_{vp} = \boldsymbol{\sigma}_{nve,j} = \boldsymbol{\sigma}_{ve,i}$, where $\boldsymbol{\sigma}_{vp}$ is the stress in the viscoplastic component, and $\boldsymbol{\sigma}_{nve,j}$ and $\boldsymbol{\sigma}_{ve,i}$ are the stresses in the corresponding nonlinear and linear viscoelastic components.

5.4.2.2. Nonlinear Stiffening Component

The nonlinear stiffening component represents the compressive stiffening response of glassy polymers at large strains and is herein given as:

$$\sigma_s = \alpha_L L^{-1}(\bar{\varepsilon}) H(-\varepsilon), \quad \text{with } \bar{\varepsilon} = \frac{\varepsilon}{\lambda_L} \quad (5.7)$$

where λ_L is the locking strain, α_L is the stress factor, and L^{-1} is the inverse of the Langevin function, which, in lack of a closed form, is herein approximated as (Cohen 1991):

$$L^{-1}(\bar{\varepsilon}) \approx \bar{\varepsilon} \left(\frac{3 - \bar{\varepsilon}^2}{1 - \bar{\varepsilon}^2} \right) \quad (5.8)$$

Also, a Heaviside function is introduced to ensure zero tensile response. Although no test data are available for compressive strains that are large enough to exhibit stiffening during Phase, the nonlinear response of the selected material has been confirmed in Phase 1 of the material characterization program (see Section 3.3.1.4), and for this reason, the stiffening component is introduced for completeness.

5.4.2.3. Elasto-Visco-Plastic Component

The elastic stress is given as:

$$\sigma_e = E \varepsilon_e \quad (5.9)$$

where E is the modulus of the elastic spring. This stress represents the intermolecular resistance of the material, or, equivalently, the resistance against deformation of a chain imposed by its surrounding chains (Boyce et al. 1988).

The *yield/loading function* is defined as:

$$f = |\xi| - R_f R_{fr} f_y \quad (5.10)$$

with

$$\xi = \sigma - q \quad (5.11)$$

where q is the *backstress* obtained from a kinematic *hardening* model described below, f_y is the yield strength (identical in tension and compression). The yield strength, f_y , represents the stress at which inelastic response – motion of chain segments – initiates, while the backstress represents the resistance of surrounding polymer matrix to the motion of chain segments, which results in the observed hardening response. Hardening continuously increases until the peak strength– often termed *macro-yield strength* – is reached. Further straining results in new defects, which cause a decrease in the macroscopic material resistance and result in the observed softening response (Hasan and Boyce 1995). In this study, softening is simulated through R_f , which is a damage factor to the yield strength, with $R_f \in [0,1]$, and R_η , which is a damage factor to the plastic viscosity (described later), with $R_\eta \in [0,1]$. Also, $R_f = 1$ (and $R_\eta = 1$) represents no damage and $R_f = 0$ (and $R_\eta = 0$) represents complete loss of strength. The damage factor R_f is multiplicatively decomposed into a monotonic, R_f^{mono} , and cyclic, R_f^{cyc} , damage factor, following a Weibull function, which was herein found to match the experimental data, of the peak absolute and accumulated viscoplastic strains, respectively, as:

$$R_f = R_f^{mono} R_f^{cyc} \quad (5.12)$$

with

$$\begin{cases} R_f^{mono}(\varepsilon_{vp,max}) = 1 - (1 - R_{f,min}^{mono}) \exp\left(-c_f^{mono} |\varepsilon_{vp,max}|^{-d_f^{mono}}\right) \\ R_f^{cyc}(\varepsilon_{vp,cum}^T) = 1 - (1 - R_{f,min}^{cyc}) \exp\left(-c_f^{cyc} |\varepsilon_{vp,cum}^T|^{-d_f^{cyc}}\right) \end{cases} \quad (5.13)$$

and

$$\begin{cases} \varepsilon_{vp,max} = \max_t \{|\varepsilon_{vp}|\} \\ \dot{\varepsilon}_{vp,cum}^T = |\dot{\varepsilon}_{vp}| H(\dot{\varepsilon}_{vp}) H(\sigma_e) \end{cases} \quad (5.14)$$

where $\varepsilon_{vp,max}$ is the peak absolute viscoplastic strain over the entire history of loading, $\varepsilon_{vp,cum}^T$ is the cumulative viscoplastic strain during tensile response. Also, c_f^{mono} , c_f^{cyc} , d_f^{mono} , and d_f^{cyc} are positive material constants. Both R_f^{mono} and R_f^{cyc} decrease from unity to the minimum value of $R_{f,min}^{mono}$ and $R_{f,min}^{cyc}$, respectively, following a Weibull function, which was found to match the experimental data of this study (for example, see Figure 5.5).

Tensile fracture is simulated by the damage factor, R_{fr} (with $R_{fr} \in [0,1]$), which is included in the yield criterion (Eq. (5.10)), the flow rule (Eq. (5.17)) and the hardening law (Eq. (5.20)), and is given by:

$$R_{fr} = \frac{1}{2} \left(1 - \tanh \left(a_{fr} \max_t \{ \varepsilon - \varepsilon_{fr}(\dot{\varepsilon}) \} \right) \right) \quad (5.15)$$

where a_{fr} is a material constant which controls the rate of damage/fracture progression and the vicinity around ε_{fr} over which deterioration initiates and is completed. Based on the data from the monotonic tensile tests, the tensile fracture strain, ε_{fr} (> 0), is selected to

vary with the total strain rate via a Weibull type function, which was found to match the experimental data:

$$\varepsilon_{fr}(\dot{\varepsilon}) = \varepsilon_{fr,\max} - (\varepsilon_{fr,\max} - \varepsilon_{fr,\min}) \exp\left(-|c_{fr} \dot{\varepsilon}|^{-d_{fr}}\right) \quad (5.16)$$

where $\varepsilon_{fr,\min}$ is the minimum fracture strain obtained at larger strain rates, and $\varepsilon_{fr,\max}$ is the maximum fracture strain obtained at smaller strain rates. Also, c_{fr} and d_{fr} are positive material constants. The continuous transition to zero stress achieved by the continuous form of R_{fr} ensures computational stability of the numerical solution algorithm. It is further noted that R_f and R_{fr} are not damage factors, as typically described in the framework of damage mechanics, since they are not applied to the elastic stiffness. They rather constitute the *isotropic hardening/softening* component of the yield function and are intended to capture strain-driven strength deterioration and tensile fracture. Also, the multiplicative decomposition considered for R_f , despite being a convenient approach for holistically integrating different sources/types of damage and has often been considered in damage mechanics, such as the widely used concrete damage plasticity model by Lee and Fenves (Lee and Fenves 1998a; Lee and Fenves 1998b), it is not capable of capturing the stress recovery in compression of a material cracked in tension. Yet, based on the experimental data of this study, this phenomenon was not found to be dominant, which makes this approach suitable for this study, as shown later via comparisons of experimental data with model predictions.

The **flow rule**, which controls the evolution of the viscoplastic strain during yielding, representing the motion of chain segments into the polymer matrix, is given by the following of Perzyna type viscoplastic constitutive equation (Perzyna 1966):

$$\dot{\varepsilon}_{vp} = \frac{\langle f(\xi) \rangle}{\max\{R_{fr} R_{\eta} \eta(\dot{\varepsilon}), \eta_m\}} \text{sign}(\xi) \quad (5.17)$$

where the McCauley brackets $\langle \cdot \rangle$ ensure that $\dot{\varepsilon}_{vp} = 0$ when $f < 0$. The so-called *overstresses*, σ_{os} , is given as: $\sigma_{os} = \langle f(\xi) \rangle \text{sign}(\xi)$. Also, $\eta_m (=1.0\text{e-}6)$ is the minimum value of the denominator, utilized when $R_{fr} = 0$, i.e. when tensile fracture occurs, in order to avoid computational instabilities. Based on data from monotonic tests at various strain rates (e.g. see Figure 5.6, which is discussed later), the viscosity function, η , is selected to vary with the total strain rate, $\dot{\varepsilon}$, between the minimum value η_{\min} and the maximum value of η_{\max} via a Weibull type function, which was found to match the experimental data:

$$\eta(\dot{\varepsilon}) = \eta_{\max} - (\eta_{\max} - \eta_{\min}) \exp\left(-|c_{\eta} \dot{\varepsilon}|^{-d_{\eta}}\right) \quad (5.18)$$

where c_{η} and d_{η} are positive material constants. The damage reduction factor R_{η} is given by $R_{\eta} = R_{\eta}^{mono} R_{\eta}^{cyc}$ with:

$$\begin{aligned} R_{\eta}^{mono}(\varepsilon_{vp,\max}) &= 1 - (1 - R_{\eta,\min}^{mono}) \exp\left(-c_{\eta}^{mono} |\varepsilon_{vp,\max}|^{-d_{\eta}^{mono}}\right) \\ R_{\eta}^{cyc}(\varepsilon_{vp,\text{cum}}^T) &= 1 - (1 - R_{\eta,\min}^{cyc}) \exp\left(-c_{\eta}^{cyc} |\varepsilon_{vp,\text{cum}}^T|^{-d_{\eta}^{cyc}}\right) \end{aligned} \quad (5.19)$$

where c_{η}^{mono} , c_{η}^{cyc} , d_{η}^{mono} , and d_{η}^{cyc} are positive material constants. Both R_{η}^{mono} and R_{η}^{cyc} decrease from unity to the minimum value of $R_{\eta,\min}^{mono}$ and $R_{\eta,\min}^{cyc}$, respectively. Variation

of the viscosity with the strain rate has been previously considered in modeling of metallic materials by Haupt and Lion (1995) and for polymeric materials by Lion (1996) and Kästner et al. (2012).

The backstress, q , is given by a *kinematic hardening law* obtained by modifying the Armstrong and Frederick model (Armstrong 1966) to introduce the maximum backstress, q_{max} , and the fracture damage factor, R_{fr} , as:

$$\dot{q} = R_{fr} q_{max} \gamma \dot{\epsilon}_{vp} - \gamma q |\dot{\epsilon}_{vp}| \quad (5.20)$$

where γ is a positive constant controlling the rate of variation of q with respect to the viscoplastic strain rate. Both q_{max} and γ are material parameters.

5.4.2.4. Nonlinear Generalized Kelvin-Voigt Network

Each component of this network consists of a nonlinear viscous dashpot and a linear damaged spring. The stress of the j -th component is given as:

$$\sigma_{mve,j} = R_{E,j} E_{mve,j} \epsilon_{mve,j} + C_{mve,j} \left(1 - e^{-a_{mve,j} |\dot{\epsilon}_{mve,j}|} \right) \text{sgn}(\dot{\epsilon}_{mve,j}) \quad (5.21)$$

where $E_{mve,j}$ is the elastic modulus, $R_{E,j}$ is a damage factor to the elastic modulus, $C_{mve,j}$ is the *resistance* or *activation stress* (Anand and Ames 2006), which represents the peak resistance of the dashpot, $a_{mve,j}$ is the *strain-rate sensitivity* parameter, $\dot{\epsilon}_{mve,j}$ is the strain rate, and $\text{sgn}(\cdot)$ is the signum function. The damage factor $R_{E,j}$ controls the evolution of the elastic modulus, which has been found to be responsible for the highly nonlinear unloading response that is indicative of a strain recovery capacity of the selected polyurethane. The damage factor is herein selected to vary with the peak viscoplastic strain

following a Weibull function, which was found to match the experimental data, as shown below (Eq. (5.22)), thereby introducing coupling between the nonlinear generalized Kelvin-Voigt network and the elasto-visco-plastic component.

$$R_{E,j}(\varepsilon_{vp,\max}) = 1 - (1 - R_{E,j,\min}) \exp\left(-c_{E,j} |\varepsilon_{vp,\max}|^{-d_{E,j}}\right) \quad (5.22)$$

The parameters $c_{E,j}$ and $d_{E,j}$ are positive material constants. It is noted that, unlike traditional damage and plastic-damage models, where a damage factor is applied to the elastic stiffness, in this study, damage factors, $R_{E,j}$, are applied to the elastic components of all nonlinear Generalized Kelvin-Voigt viscoelastic elements, because this approach was found to provide more accurate predictions of the experimentally observed responses.

5.4.2.5. Linear Generalized Kelvin-Voigt Network

Each component of this network consists of a linear viscous dashpot and a linear spring:

$$\sigma_{ve,i} = E_{ve,i} \varepsilon_{ve,i} + C_{ve,i} \dot{\varepsilon}_{ve,i} \quad (5.23)$$

where $E_{ve,i}$ is the elastic modulus, $C_{ve,i}$ is the linear viscosity, and, $\dot{\varepsilon}_{ve,i}$ is the strain rate. This network is primarily intended to capture long-term creep in the elastic range, and refers to much larger time scales compared to those of the nonlinear generalized Kelvin-Voigt network, which primarily focuses on relaxation phenomena in the inelastic range and the highly nonlinear unloading response.

5.4.3. Computational Implementation

The developed constitutive relations are discretized in time and solved using an implicit solution algorithm to compute the material state (i.e. stresses and strains at all component) for any arbitrary time history of the total strain, ε . The developed constitutive relations have also been implemented in the OpenSEES structural analysis software (McKenna and Fenves 2001), which is widely used for the nonlinear dynamic analysis of structures in various structural engineering applications.

5.4.4. Model Parameter Calibration Procedure

Calibrating the parameters of the developed constitutive relations to a set of test data is challenging, because: (i) the proposed relations introduce a large number of parameters, which are difficult to calibrate through a brute-force error minimization approach due to the large analysis/calibration times required and the potential for several solutions leading to comparably minimal errors (solution multiplicity), and (ii) the number of model parameters is not *a priori* known, because the number of components within the linear and nonlinear Kelvin-Voigt networks is not known ahead of time, and should be determined during the calibration based on the properties of the response. To address this challenge, a *structured step-by-step calibration methodology* is adopted, which attempts to partially “decouple” different material responses (associated with different components of the rheological model of Figure 5.4) through selected types of material testing, and progressively/sequentially introduce the different components of the model within the calibration process. The most major advantage of this approach is that it can be conducted *manually* by trial and error, allowing the user to select physically meaningful values for

the model parameters, as opposed to brute-force optimization approaches that select values from a vast solution space. It is noted that, because in the compressive tests, the peak applied strain remained low, the rubber-like nonlinear stiffening is not present in the test data, and, for this reason, the parameters of the nonlinear stiffening component are not calibrated below. However, it is reminded that because the nonlinear stiffening response of the selected material at large strains has been confirmed in Phase 1 of the material characterization program (see Section 3.3.1.4), the nonlinear stiffening component is maintained for completeness of the proposed constitutive relations.

5.4.4.1. Step-by-Step Calibration Methodology

The proposed calibration methodology is applied to the available test data through the following steps.

5.4.4.1.1. Step 1: Calibrate Undamaged Rate-independent Plastic Response

This step is focused on estimating the parameters controlling the macro-yield response of the material which is represented by the equilibrium path (obtained from the multi-step compression relaxation testing) and is controlled by the rate-independent properties of the viscoplastic component of the proposed model (Figure 5.4). For this calibration, the viscoelastic networks are not considered (i.e. $N = M = 0$, see Eq. (5.5)), no damage is considered (i.e. all damage reduction factors equal unity), and plastic viscosity is neglected (i.e. η is set to $\eta_m = 1.0e-6$ /s). These assumptions reduce the number of parameters to be calibrated to the yield strength of the cylindrical specimen in compression, f_y ; and the kinematic hardening parameters, q_{\max} and λ . Additionally, the

elastic modulus, E , of the elasto-visco-plastic component, which represents the *instantaneous* modulus of the material, is explicitly obtained from the data from the monotonic test with the highest strain rate, presented in the following steps. A few iterations for these parameters, i.e. f_y , q_{\max} and λ , result in an approximate fit to the equilibrium path stress-strain relationship shown in Figure 5.5(a). The identified parameters used for producing this fit are:

$$\{E = 475 \text{ ksi}, f_y = 5.5 \text{ ksi}, q_{\max} = 2.0 \text{ ksi}, \gamma = 600$$

5.4.4.1.2. Step 2: Calibrate Compression Damage in Rate-independent Plastic

Response

To capture the post-peak softening response of the equilibrium path relationship (rate-independent softening), the damage factor of the yield strength, R_f^{mono} , is activated in the model, which adds three additional parameters, $R_{f,\min}^{mono}$, c_f^{mono} , and d_f^{mono} . In this step, the fracture damage factor, R_{fi} , is taken as unity (no fracture).

The damage factor at discrete strain levels is extracted from the equilibrium path relationship by taking the ratio of stress at the corresponding strain level to the peak stress. A Weibull function is then fitted to the obtained $(\varepsilon_{vp,\max}, R_f^{mono})$ data points, as shown in Figure 5.5 (b). A few trials for $R_{f,\min}^{mono}$, c_f^{mono} , and d_f^{mono} gives the fit shown in Figure 5.5 (c). The identified parameters from this fitting are:

$$\{R_{f,\min}^{mono} = 0.65, c_f^{mono} = 0.00579, d_f^{mono} = 1.297$$

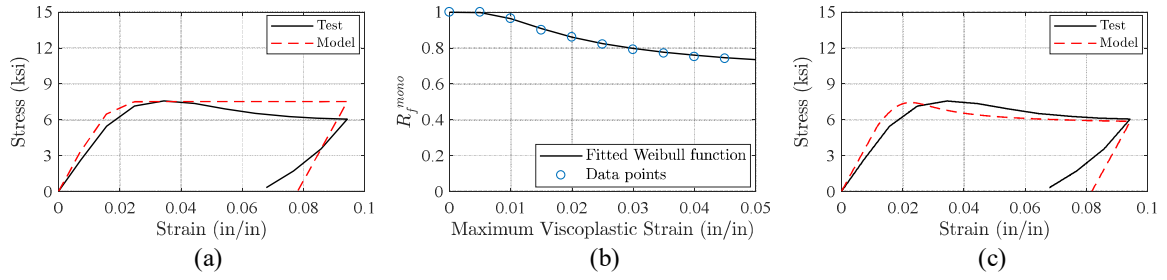


Figure 5.5. (a) Approximate fit of the response with a minimal set of material parameters per Step 1; (b) fitting of Weibull function of damage factor of Eq. (5.13) to test data; (c) approximate fit of the response including the damage in the yield surface per Step 2.

5.4.4.1.3. Step 3: Calibrate Rate-Dependency of Plastic Response

In this step, the parameters of the plastic viscosity of the viscoplastic component are quantified (calibrated) using the data from monotonic compression tests at the following strain rates: 0.001 /s, 0.01 /s, and 0.05 /s. The additional parameters introduced in this step are η_{max} , η_{min} , c_η , and d_η . The viscosity function is initially taken to be constant by setting $\eta_{max} = \eta_{min}$. Then, η is identified for each test data set with various strain rates to capture the peak strength including the rate-dependent overstress, resulting to a set of discrete $(\dot{\epsilon}, \eta)$ data points. Finally, the Weibull function parameters are identified by fitting to the obtained data points, as shown in Figure 5.6. A few trials give the fit shown in Figure 5.7 with the identified parameters from this fitting procedure listed below:

$$\{\eta_{max} = 4800 \text{ ksi-s}, \eta_{min} = 124 \text{ ksi-s}, c_\eta = 313.396 \text{ s}, d_\eta = 1.916$$

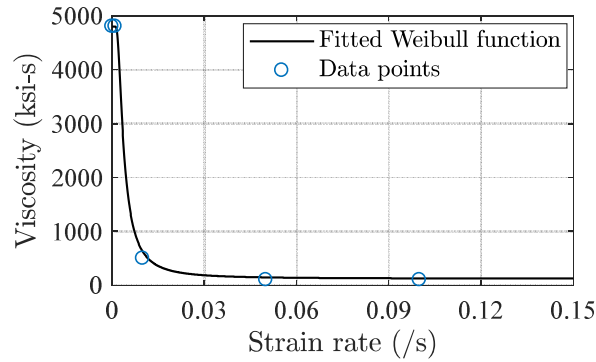


Figure 5.6. Fit of rate-dependent Weibull function for viscosity, Eq. (5.18), to test data.

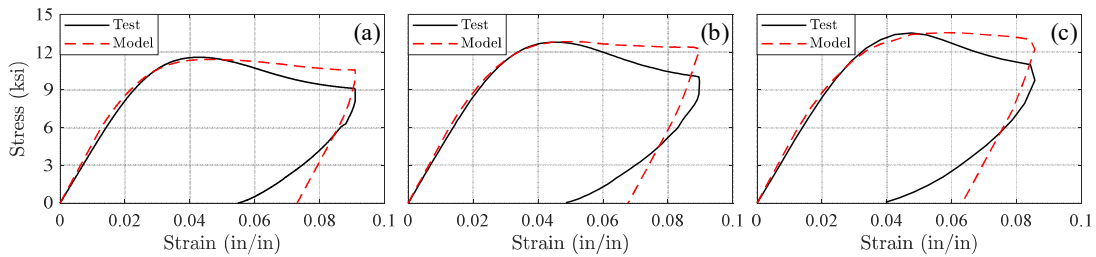


Figure 5.7. Fit of the model with minimal set of parameters, per Step 3, to the monotonic compression tests on cylindrical specimens at various strain rates: (a) 0.001 /s; (b) 0.01 /s; (c) 0.05 /s.

5.4.4.1.4. Step 4: Calibrate Compression Damage to the Plastic Viscosity of Overstress Model

In this step, compression damage is introduced to the plastic viscosity of the flow rule (or overstress model) to capture the post peak softening response corresponding to the rate dependent overstress. This introduces three additional parameters: $R_{\eta, \min}^{mono}$, c_{η}^{mono} , and d_{η}^{mono} . Similar to step 2, the damage factor is extracted from the test at 0.001 /s strain rate at discrete strain levels by taking the ratio of stress at the corresponding strain level

to the peak stress. A Weibull function is then fitted to the obtained $(\varepsilon_{vp,max}, R_{\eta}^{mono})$ data points. A few trials for $R_{\eta,min}^{mono}$, c_{η}^{mono} , and d_{η}^{mono} gives the fit shown in Figure 5.8. The identified parameters from this fitting are:

$$\{R_{\eta,min}^{mono} = 0.65, c_{\eta}^{mono} = 1.012E - 6, d_{\eta}^{mono} = 4.3$$

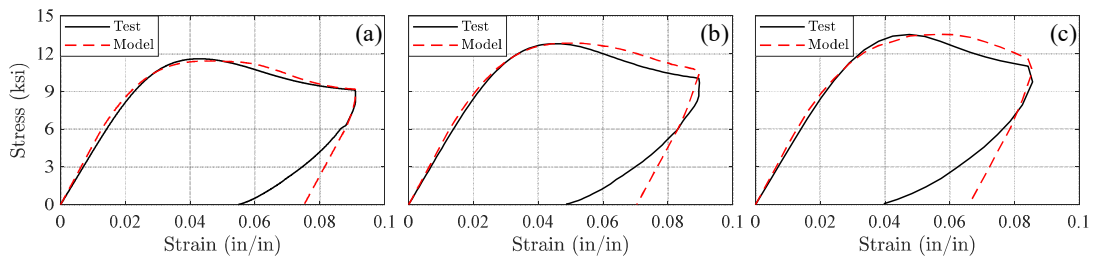


Figure 5.8. Fit of the model with damage to the overstress to the monotonic compression tests on cylindrical specimens at various strain rates: (a) 0.001 /s; (b) 0.01 /s; (c) 0.05 /s.

5.4.4.1.5. Step 5: Calibrate Overall Tensile Viscoplastic Response, including Tensile Fracture

In this step, the parameters governing the tensile response of the material are quantified using monotonic tension test data up to rupture at various strain rates (0.001 /s, 0.01 /s, and 0.05/s). It should be noted that due to lack of test data regarding the equilibrium path relationship in tension, material parameters controlling both the rate independent and rate dependent responses are calibrated simultaneously. The parameters calibrated in this step include the tensile damage parameters, $R_{f,min}^T$, c_f^T , d_f^T , damage

parameters for the plastic viscosity, $R_{\eta,\min}^{cyc}$, c_{η}^{cyc} , and d_{η}^{cyc} , and fracture damage parameters, a_{fr} , $\varepsilon_{fr,\min}$, $\varepsilon_{fr,\max}$, c_{fr} and d_{fr} . The fracture damage parameters, $\varepsilon_{fr,\min}$, $\varepsilon_{fr,\max}$, c_{fr} and d_{fr} , are determined by fitting a Weibull type function to $(\varepsilon_{fr}, \dot{\varepsilon})$ data points extracted from the monotonic tensile tests at the fracture point. It is assumed that the maximum tensile fracture strain, $\varepsilon_{fr,\max}$, is equal to the ε_{fr} at 0.001 /s strain rate (0.152) and is constant for strain rates lower than 0.001 /s. A few iterations using a procedure similar to that presented in step 2 gives the fit shown in Figure 5.9, with the identified parameters listed below:

$$\begin{cases} R_{f,\min}^T = 0.85, c_f^T = 0.00469, d_f^T = 1.682 \\ R_{\eta,\min}^{cyc} = 0.85, c_{\eta}^{cyc} = 0.00469, d_{\eta}^{cyc} = 1.682 \\ \varepsilon_{fr,\min} = 0.091, \varepsilon_{fr,\max} = 0.152, c_{fr} = 242.623s, d_{fr} = 1.1, a_{fr} = 5000 \end{cases}$$

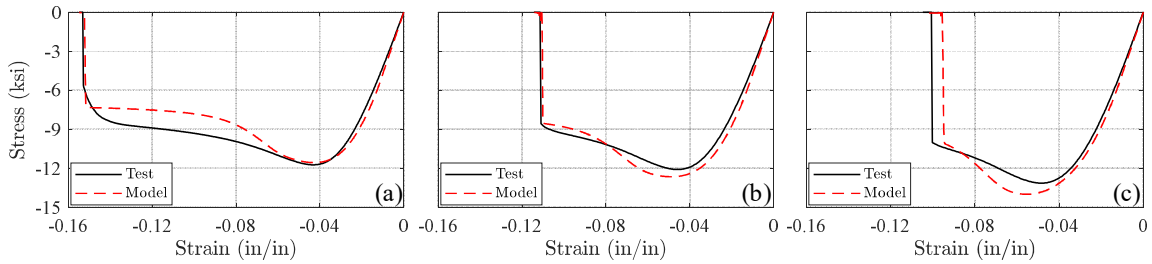


Figure 5.9. Fit of the model with damage to the overstress and yield strength to the monotonic tension tests on dog-bone specimens at various strain rates: (a) 0.001 /s; (b) 0.01 /s; (c) 0.05 /s.

5.4.4.1.6. Step 6: Calibrate Nonlinear Viscoelastic Response

In this step, three nonlinear viscoelastic elements are incorporated in the model to primarily capture the nonlinear unloading response. It is noted that a finer control over the response can be achieved by introducing more viscoelastic elements, at the cost of more model parameters. For the purposes of this study, three nonlinear viscoelastic elements were found to provide sufficient accuracy.

Figure 5.10 schematically shows how the three viscoelastic elements affect the material response under compression over the loading and unloading processes. The points labeled as $x^{(j)}$ indicate where each j -th viscoelastic element is approximately activated. The activation stress level of the j -th element is represented by $C_{nve,j}$. Thus, each element is activated at $-2C_{nve,j}$ over unloading, measured relative to the stress at the onset of unloading.

Over the loading process, the slope connecting the origin to $x^{(1)}$ is controlled by E . The slope connecting every two consecutive $x^{(j)}$ is governed by the equivalent modulus of all activated elements up to that point. For instance, the slope connecting $x^{(1)}$ and $x^{(2)}$ is governed by the equivalent modulus of E and $E_{nve,1}$ in series. According to the equilibrium path (Figure 5.5), the $C_{nve,j}$ should be below ~ 5 ksi and satisfy $C_{nve,1} < C_{nve,2} < C_{nve,3}$. Furthermore, the value of modulus $E_{nve,j}$ for each j -th element is taken as:

$$E_{nve,j} = \frac{\alpha_{j-1}\alpha_j}{\alpha_{j-1} - \alpha_j} E \quad (5.24)$$

where $\alpha_j = \left(\frac{E_{eq}^{(j)}}{E} \right)$, with $\alpha_0 = 1$, is the ratio of the target total equivalent tangent elastic modulus, $E_{eq}^{(j)}$, after activation of j -th element to the initial elastic modulus, which is controlled by E . Herein, the values 0.95, 0.9, and 0.8 were used for α_1 , α_2 , and α_3 , respectively, resulting in the response shown in Figure 5.10.

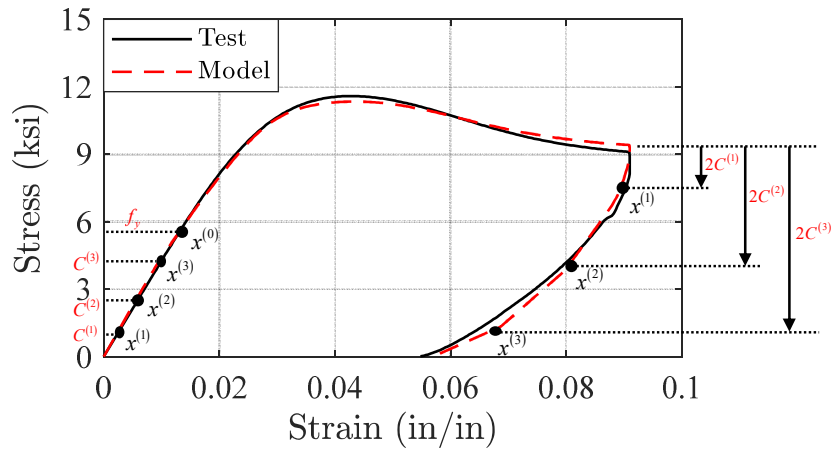


Figure 5.10. Schematic representation of the effect of viscoelastic elements on the response.

Given the guidelines above and using the cyclic compression-tension test data, the model parameters introduced in this step, i.e. $C_{nve,j}$, $a_{nve,j}$, $R_{E,j,\min}$, $c_{E,j}$, and $d_{E,j}$, were calibrated after a few iterations. The obtained parameters provide a model fitting to the cyclic compression-tension test data as shown in Figure 5.11 and to previous test data as shown in Figures Figure 5.12 – 5.14. It is noted that, in this step, the viscosity function parameters and the corresponding damage parameters, i.e. η_{\max} , η_{\min} , $R_{\eta,\min}^{mono}$, and $R_{\eta,\min}^{cyc}$, are re-calibrated, because the evolution of all $E_{nve,j}$, results in changes in the strain rate of

the viscoplastic element, which is the control response parameter for the overstress and also all of the damage functions.

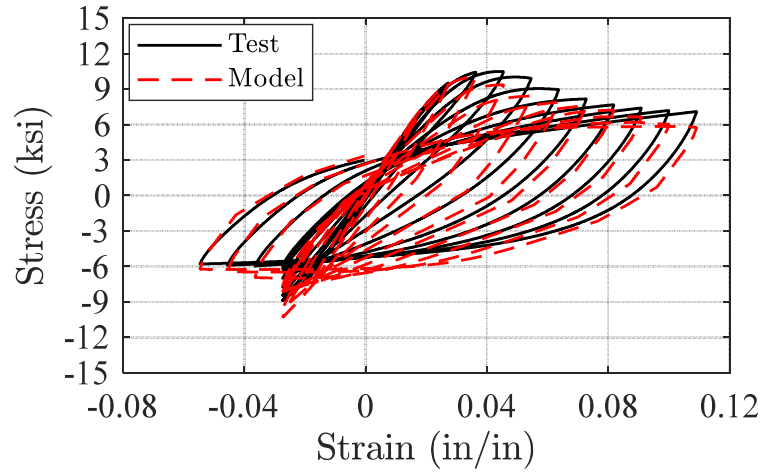


Figure 5.11. Fit of the model to the cyclic compression-tension test on dog-bone specimen at 0.001 /s strain rate.

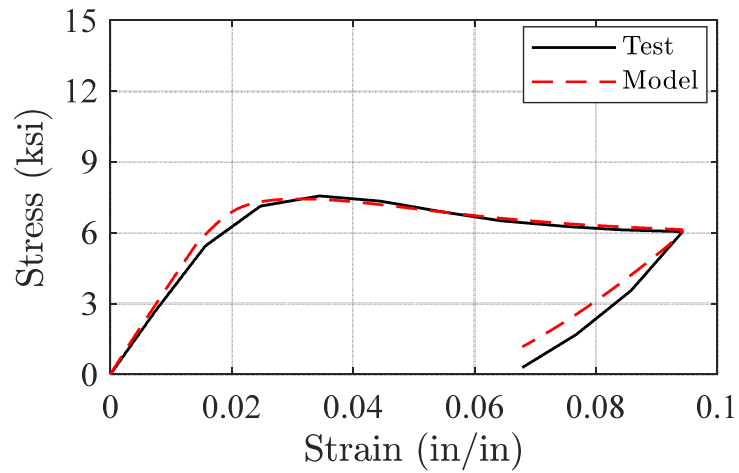


Figure 5.12. Fit of the full model to the equilibrium path stress-strain relationship.

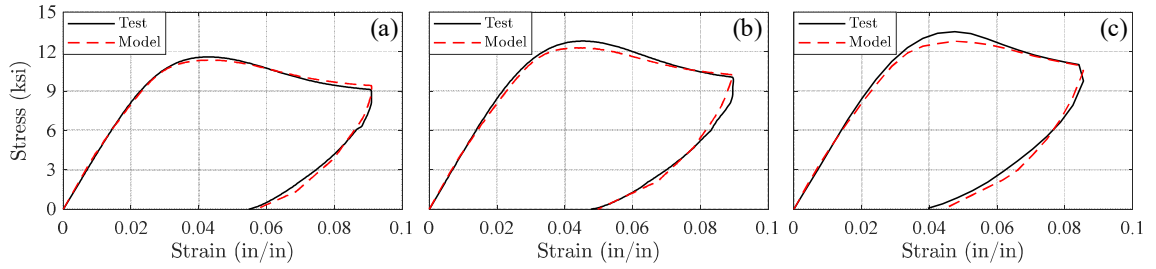


Figure 5.13. Fit of the full model to the monotonic compression tests on cylindrical specimens at various strain rates: (a) 0.001 /s; (b) 0.01 /s; (c) 0.05 /s.

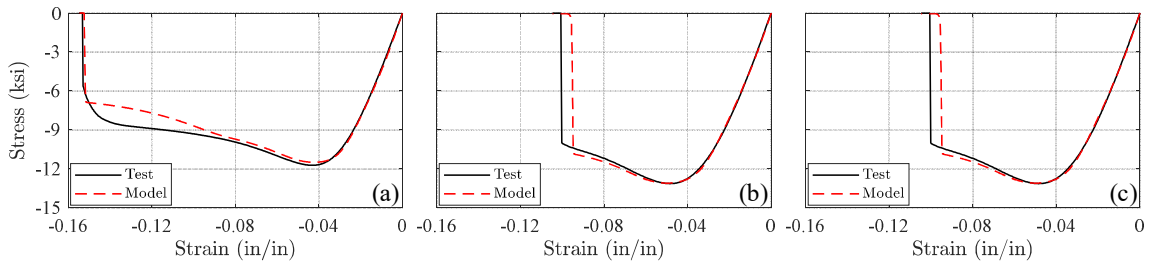


Figure 5.14. Fit of the full model to the monotonic tension tests on dog-bone specimens at various strain rates: (a) 0.001 /s; (b) 0.01 /s; (c) 0.05 /s.

5.4.4.1.7. Step 7: Calibrate Linear Viscoelastic Response for Creep and Refine

Selected Nonlinear Viscoelastic Parameters for Relaxation

In this step, the estimated *strain-rate sensitivity* parameters, $a_{nve,j}$, of the nonlinear viscoelastic networks are further refined to fit the results of the relaxation test data. However, without the contribution of the linear viscoelastic network, the model is not capable of capturing the creep response in the elastic range, i.e. at stress levels below the macro-yield, because the retardation times, $\tau^{(j)} = E_{nve,j} / (a_{nve,j} C_{nve,j}) < 1$, of the nonlinear viscoelastic elements are short, and do not properly cover the 5-day test duration. To capture the creep response at stress levels below the macro-yield, one linear viscoelastic

element with a retardation time of 5E+5 seconds led to acceptable results for the purpose of this study. It is noted that the creep response could be reproduced more accurately by including more linear viscoelastic elements at the cost of introducing more model parameters.

The optimal fits after a few trials are shown in Figure 5.15 (a) for the relaxation test and Figure 5.15 (b) for the creep tests. The following parameters were updated/calibrated in this step:

$$\{a_{nve,3} = 2E+6 \text{ s}^{-1}, \quad C_{ve,1} = 5E+8 \text{ ksi-s}, \quad E_{ve,1} = 1000 \text{ ksi}$$

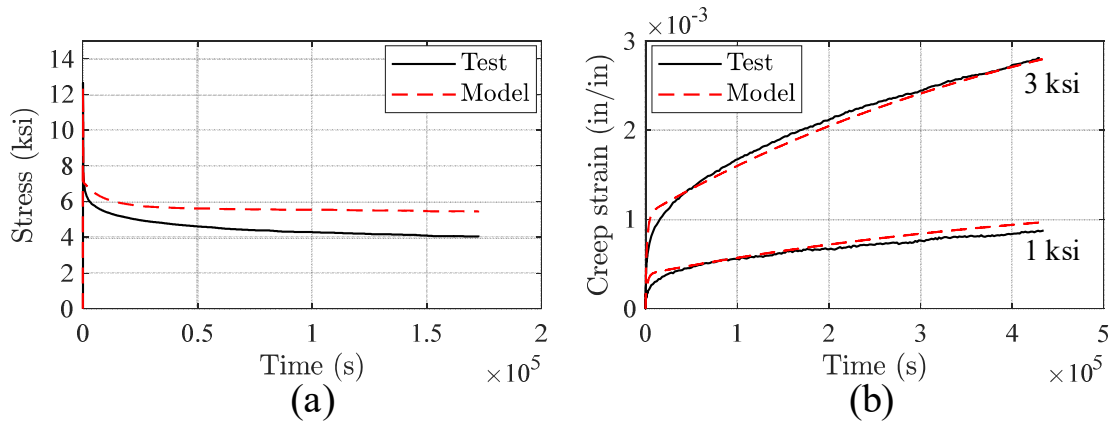


Figure 5.15. Fit of the model to: (a) 48-hours relaxation test data; (b) 5-days creep test data at various stress levels.

5.4.4.2. Summary of Calibrated Parameters

Based on the above procedure, the final calibrated parameters are:

- *Nonlinear Generalized Kelvin-Voigt Network*

$$\{C_{ve,1} = 5E+8 \text{ ksi-s}, \quad E_{ve,1} = 1000 \text{ ksi}$$

- *Nonlinear Generalized Kelvin-Voigt Network*

$$\left\{ \begin{array}{lll} C_{mve,1} = 1.0 \text{ ksi} & C_{mve,2} = 2.5 \text{ ksi} & C_{mve,3} = 4.0 \text{ ksi} \\ a_{mve,1} = 1.0E+5 \text{ s}^{-1} & a_{mve,2} = 1.0E+5 \text{ s}^{-1} & a_{mve,3} = 2E+6 \text{ s}^{-1} \\ E_{mve,1} = 9025 \text{ ksi} & E_{mve,2} = 8123 \text{ ksi} & E_{mve,3} = 3416 \text{ ksi} \\ R_{E,1,\min} = 0.13 & R_{E,2,\min} = 0 & R_{E,3,\min} = 0.063 \\ c_{E,1} = 8.53E-5 & c_{E,2} = 2.05E-3 & c_{E,3} = 4.71E-6 \\ d_{E,1} = 1.821 & d_{E,2} = 1.08 & d_{E,3} = 2.076 \end{array} \right.$$

- *Elasto-Visco-Plastic Network*

$$\left\{ \begin{array}{l} E = 475 \text{ ksi}, f_y = 5.5 \text{ ksi}, q_{\max} = 2.0 \text{ ksi}, \quad \gamma = 600 \\ R_{f,\min}^{mono} = 0.65, \quad c_f^{mono} = 0.00579, \quad d_f^{mono} = 1.297 \\ R_{f,\min}^{cyc} = 0.85, \quad c_f^{cyc} = 0.00469, \quad d_f^{cyc} = 1.682 \\ \varepsilon_{fr,\min} = 0.091, \quad \varepsilon_{fr,\max} = 0.152, \quad c_{fr} = 242.623 \text{ s}, \quad d_{fr} = 1.1, \quad a_{fr} = 5000 \\ \eta_{\max} = 1.6E+6 \text{ ksi-s}, \quad \eta_{\min} = 414 \text{ ksi-s}, \quad c_{\eta} = 313.396 \text{ s}, \quad d_{\eta} = 1.916 \\ R_{\eta,\min}^{mono} = 0.25, \quad c_{\eta}^{mono} = 1.017E-6, \quad d_{\eta}^{mono} = 2.87 \\ R_{\eta,\min}^{cyc} = 0.44, \quad c_{\eta}^{cyc} = 0.00469, \quad d_{\eta}^{cyc} = 1.682 \end{array} \right.$$

It is noted that the calibrated parameters are applicable at least up to the peak strain rates considered in the tests, i.e. 0.1 /s. However, from the monotonic compression test results (Figure 3.11), it was observed that the *instantaneous response* is achieved at a strain rate of ~0.05 /s, which implies that the calibrated model parameters are valid for even higher strain rates.

5.5. Summary and Findings

In this section, first, a simplified visco-elastic softening visco-plastic model was developed capable of capturing major response properties of the selected PU (ECast) observed in Phase 2 of the experimental material characterization program (see Section

3.3.2). The proposed simplified model allowed the use of structural analysis software OpenSees (McKenna and Fenves 2001), as opposed to prohibitively time consuming continuous solid finite element analysis software, to study the dynamic response of columns with PU end segments (see Section 6).

In the second stage, a versatile uniaxial softening viscoelastic viscoplastic constitutive model was developed combining the *classical viscoplasticity* with *linear and nonlinear generalized viscoelastic Kelvin-Voigt* networks. Damage was considered in both the elastic and inelastic components via damage factors that account for both tensile and compressive plastic traveling, thereby introducing tension-compression and elastic-inelastic coupling. The developed constitutive model was calibrated to the large set of data from the aforementioned tests via a proposed structured calibration methodology that avoids brute-force curve fitting approaches by calibrating individual model components via properly designed tests.

The presented work particularly addresses the lack of constitutive models for this type of glassy polymers from the point of view of structural applications focusing on the small-to-moderate strain range ($< 15\%$), accounting for various loading conditions, and simultaneously offering computational simplicity compared to three-dimensional constitutive relations. Building on this work, future research should address the effect of temperature variations on the observed mechanical properties as well as long term effects over a periods of time longer than 5 days (i.e. the duration of creep tests in this study), both in terms of material mechanical testing and constitutive modeling.

6. SEISMIC PERFORMANCE ASSESSMENT OF BRIDGE COLUMNS WITH POLYURETHANE-ENHANCED DAMAGE-RESISTANT END JOINTS AND ENERGY DISSIPATION LINKS

6.1. Scope and Objectives

This section computationally assesses the seismic performance of the PU-enhanced rocking columns with ED links. Specifically, the monotonic and cyclic response of the proposed column design is investigated with respect to the properties of the ED links and compared with the response of a *reference* conventional reinforced concrete (RC) monolithic column and an RC rocking column. Moreover, the seismic performance of the proposed column design is investigated through incremental dynamic analyses with a suite of far-field ground motions, and a comprehensive quantitative comparison is provided against the reference conventional RC *monolithic* column and the RC *rocking* column via fragility analysis accounting for various damage states.

6.2. Bridge Column Designs

6.2.1. Reference Conventional RC Column

The reference column considered in this study (Figure 6.1) is that of the single-column substructure of the Jack Tone Road Overcrossing, located in the city of Ripon, California, at the intersection of Route 99 and Jack Tone Road with identification number 10-SJ-099-2.34-RIP (Kaviani et al. 2014). Built in 2001, this bridge has two spans of 108.58 ft and 111.82 ft, respectively, reaching a total length of 220.4 ft. The superstructure of the bridge consists of a three-cell continuous pre-stressed, reinforced-concrete box

girder. The cap-beam is integral with the superstructure and a monolithic reinforced-concrete circular column with a height of 19.68 ft. and diameter of 5.51 ft. The column's longitudinal reinforcement ratio is approximately 2%. Key structural and geometric properties of the reference column are summarized in Table 6.1, while further details may be found in Kaviani et al. (2014).

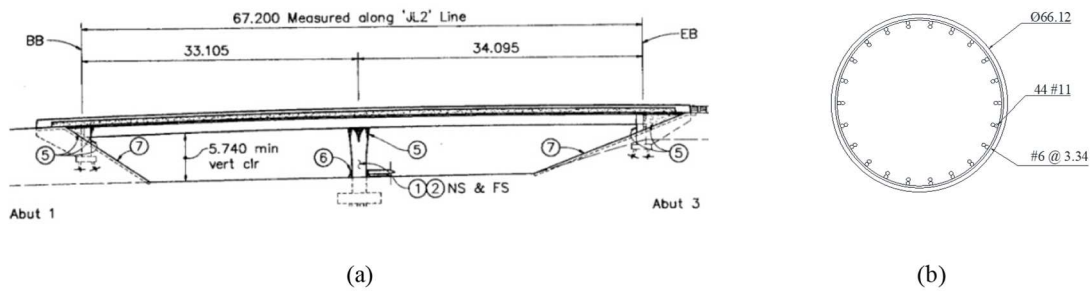


Figure 6.1. (a) Elevation view of the Jack Tone Road overcrossing Kaviani et al. 2014; (b) cross-section of the column.

Table 6.1. Reference column structural and geometric parameters.

Parameter	Value/Description
Column diameter (D_c)	5.51 ft
Deck centroid ($D_{c.g.}$)	2.48 ft
Concrete material properties (f'_c)	5 ksi
Steel reinforcement yield strength (f_y)	68 ksi
Longitudinal reinforcement details	44#11 (bundles of 2), $\rho_l=2\%$
Transverse reinforcement details	Spiral, #6 @3.34 in.

6.2.2. RC Rocking Column

A rocking column is obtained by cutting the mild longitudinal reinforcement at the interface between the column and the footing, and adding a post-tensioning bar in a duct passing at the center of the cross-section. Because the design objective herein is to have a

rocking column with lateral strength similar to that of the conventional monolithic reference column, the cross-section diameter is increased by about 18%. By increasing the diameter, the elastic stiffness slightly increased compared to the monolithic column. The axial load index – ratio of total applied axial loading, including post-tensioning, to the concrete cross-section strength – of the rocking column is 0.15, which is larger compared to the monolithic column, due to the presence of post-tensioning load. The design details of the monolithic and rocking columns are summarized in Table 6.2 with the cross-sections shown in Figure 6.2(e) and (f).

Table 6.2. Design details of the monolithic and rocking columns.

Parameter	Monolithic (Reference)	Rocking
Column diameter (in)	66.12	78
Duct diameter (in)	-	8
Longitudinal reinforcing steel	44#11	44#11
Transverse reinforcing steel	#6@3.34 in.	#7@2.0 in.
Transverse volumetric reinforcing ratio (%)	0.8	1.6
Yield stress of longitudinal and transverse reinforcement (ksi)	68	68
Post-tensioning steel diameter (Equivalent single bar) (in)	-	6.2
Post-tensioning steel area (in ²)	-	30.2
PT load (kips)	-	1812
PT stress (ksi)	-	60
Yield stress of PT bar steel (ksi)	-	135
Longitudinal reinforcing ratio including PT steel (%)	2	2.2
Unconfined compressive strength (ksi)	5	5
Confined compressive strength (ksi)	6.72	8.02
Axial load index (ALI)	0.1	0.15

6.2.3. PU-enhanced Rocking Column with ED Links

The PU-enhanced rocking column design is obtained by replacing part of the bottom of the rocking column (Figure 6.2(b)) with a PU segment. In accordance with the findings of Section 4.3.3, who showed that damage (i.e., peak strains in both concrete and

PU) is minimized for $h_j/D_c \geq 0.75$ and $D_j/D_c \leq 1$, in the present study, the PU segment height, h_j , and diameter, D_j , are selected to be $D_j/D_c=1.0$ and $h_j/D_c=1.0$, where D_c is the cross-section diameter of the rocking column.

As mentioned before (see Section 4.4), supplemental energy dissipation and the additional required flexural stiffness and strength is provided by external energy dissipating links in the form of buckling restrained yielding bars made of high performance steel and implemented in the vicinity of the PU segment. It is assumed that the links are attached to the column after application of the initial post-tensioning and gravity loads. Following the two design criteria for ED links explained in Section 4.4.1, two columns with re-centering ratios, λ_C , of 0.25 and 0.5 were designed for a target drift ratio of 3%. Each column included ten radially distributed equally spaced ED links (Figure 2.1(c)), which were offset by 3 in. from the face of the column through rigid connectors. The rigid connectors are attached to a steel collar of height of 15 in. mounted to the face of the column right above the PU segment. The milled length, $L_{ED,Y}$, of the ED links for both columns was found to be 20 in. for the selected target drift ratio. The cross-section area of the ED links was 2 in² and 4 in² for λ_C of 0.25 and 0.5, respectively. The steel material conformed to ASTM A706– Gr. 60 (ASTM A706/A706M-16 2016). In accordance with the findings of Nikoukalam and Sideris (2017) (see Section 4.4), the diameter of the unmilled length of the link was selected to be 4 times larger than that of the milled length, so that the stiffness of these elastic portions is always much larger (by a factor of 10 or higher) than the stiffness of the yielding length, and, thereby, all induced deformations are transferred to the yielding length.

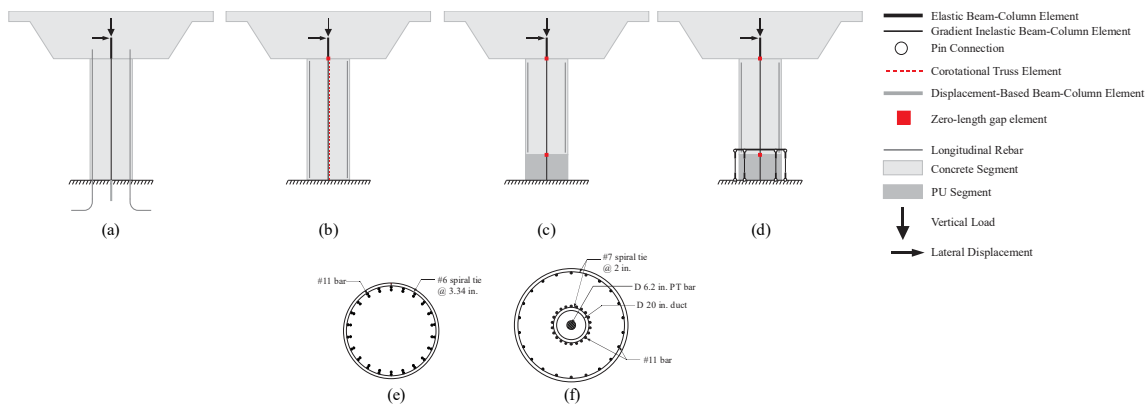


Figure 6.2. Schematic representation of the FE model of the columns: (a) RC monolithic, (b) RC rocking, (c) PU rocking, (d) PU with ED links; (e) cross-section of the monolithic RC reference column; (f) cross-section of the RC segment of rocking columns.

6.3. Structural Modeling

All column models were generated using the open-source structural analysis software OpenSees (McKenna and Fenves 2001).

6.3.1. Conventional Monolithic RC Column Modeling

The RC column (Figure 6.2(a)) was simulated using gradient inelastic force-based fiber elements (Sideris and Salehi 2016; Salehi and Sideris 2017), which eliminate strain localization and achieve response objectivity (i.e. convergence with the number of integration points) using a characteristic (or plastic hinge) length, l_c , that controls damage spreading. Analyses considered l_c to be equal to the cross-section diameter, and seven integration points, so that the requirement of $l_c/\Delta x > 1.5$ for discretization convergence (Sideris and Salehi 2016; Salehi and Sideris 2017) is satisfied.

The cover concrete had an (unconfined) compressive strength of 5 ksi. For the core concrete based on the material and geometric properties and the transverse reinforcement (spiral #6@3.34 in., A706 steel Gr. 60), the confined-to-unconfined compressive strength ratio, K , was taken as 1.34 and 1.30 for monolithic and rocking column sections, respectively (Mander et al. 1988). The strain at the peak compressive strength, ϵ_{co} , was taken as 0.0025 for unconfined concrete, and 0.0068 and 0.0062 for confined concrete in monolithic and rocking column (Mander et al. 1988), respectively. The ultimate/crushing strain, ϵ_{cu} , was taken as 0.0085 (Mander et al. 1988) and 0.02 (Paulay and Priestley 1992) for unconfined and confined concrete, respectively. The residual strength at the ultimate strain was defined as $0.2Kf'_c$ (for the unconfined concrete, $K = 1$) based on the Kent and Park model (Scott et al. 1982). The concrete cover of all column systems and the core confined concrete of all rocking columns was modeled using the Kent and Park model (Scott et al. 1982) available in OpenSees as *Concrete01*, while the same model, as modified by (Lee and Billington (2009)) – available in OpenSees as *ConcreteWithSITC* – to better capture residual deformations, was used for the core confined concrete of the monolithic column. It should be noted that Lee and Billington (2009) have shown that the reduction in pinching introduced by using *ConcreteWithSITC* model improves the prediction of the residual deformations in monolithic columns, while it is not desired in rocking systems with unbonded PT system, and therefore the model is not recommended for such systems. Elastic shear deformations were considered through an area shape reduction factor of 0.9 (compensating for the circular area), with the concrete shear modulus being obtained for a Poisson's ratio of 0.2. The steel reinforcement behavior was

simulated using the model by Menegotto and Pinto (1973) with a modification to account for strain softening and fracture via a reduction factor R varying linearly from unity at ε_{f1} to a residual value at ε_{f2} (similar to Eq.(5.3)). The yield stress, f_y , and elastic modulus, E_s , were 68 ksi (per CALTRANS (2006) recommendations for Gr. 60 A706 steel) and 29000 ksi. The strain-hardening ratio was assumed to be 1% (Barbosa et al. 2015). The values of $\varepsilon_{f1} = 14\%$ and $\varepsilon_{f2} = 25\%$, corresponding to the strain at peak strength and fracture strain of the steel material, respectively, were selected from the tensile monotonic stress-strain response for typical reinforcing bar (A706 Grade 60), e.g. Barbosa et al. 2015. For the residual value of the reduction factor, R_{min} , a small nonzero value (0.001) was selected to simulate the fracture of the rebar, while avoiding any numerical instabilities. Geometric nonlinearities were considered using the Corotational Transformation (CorotCrdTransf) available in OpenSees.

Strain penetration effects in the vicinity of the column-to-foundation interface were captured by a displacement-based fiber element added to the column lower end and into the foundation. This element had the same cross section geometry with the column and length equal to the minimum anchorage length, $l_{a,min}$, of the steel bars in the foundation. The minimum anchorage length, $l_{a,min}$, was obtained by equating the rebar yield reaction force with the bond reaction force over $l_{a,min}$ assuming an average bond stress of $21\sqrt{f'_c}$ (psi) (Eligehausen et al. 1983), which resulted in:

$$l_{a,min} \text{ (in)} = \frac{1}{84} \frac{f_y \text{ (psi)}}{\sqrt{f'_c} \text{ (psi)}} d_b \text{ (in)} \quad (6.1)$$

where d_b is rebar diameter, f_y is the yield strength of reinforcement steel, f'_c is concrete compressive strength. Confined concrete material response was assumed for the entire cross-section, with a confinement factor 1.5 times larger than the confinement factor of the column above the foundation, to account for the additional confinement provided by the foundation reinforcement and prevent unrealistic compressive concrete damage within the foundation. The stress vs. strain response for the steel rebar was obtained from the model of Zhao and Sritharan (2007) – available in OpenSees (McKenna and Fenves 2001) as *Bond_SP01* – which accounts for both the steel material properties and bond-slip. This model is expressed in terms of stress vs. slip, with yield and ultimate strength those of the steel rebar (i.e. 68 ksi and 90 ksi, respectively), and *slip at yield stress*, S_y , given as:

$$S_y \text{ (in)} = 0.1 \left(\frac{d_b \text{ (in)}}{4000} \frac{f_y \text{ (psi)}}{\sqrt{f'_c \text{ (psi)}}} (2\alpha + 1) \right)^{1/\alpha} + 0.013 \text{ (in)} \quad (6.2)$$

where α is a parameter that can be taken as 0.4 per CEB-FIP Model Code (2010). To express this model in terms of stresses vs. strains, the bar slip is divided by the minimum anchorage length, $l_{a,min}$. This modeling approach was validated against quasi-static cyclic testing of a monolithic column, identified as BC, tested by Nikoukalam and Sideris (2016a). The specimen was a nearly full-scale ($\sim 1:1.14$ or $\sim 88\%$) model of the first-story column of a four-story four-bay special moment resisting RC frame. More details regarding the design, material properties, and test setup can be found in Nikoukalam and Sideris (2016a). A model of the BC specimen was developed in OpenSees following the modeling approach described above. Figure 6.3 compares the lateral load versus drift ratio curve between the OpenSees model and the test. To better show the effect of the bond-

slip on the response, the results from the model without considering the bond-slip effect (Figure 6.3(a)) are presented beside the results from the model including the bond-slip effect (Figure 6.3(b)). As shown, the model with the bond-slip effect predicts well the elastic stiffness, strength, and stiffness degradation, whereas the model without bond-slip overestimates the stiffness and underestimates the stiffness degradation.

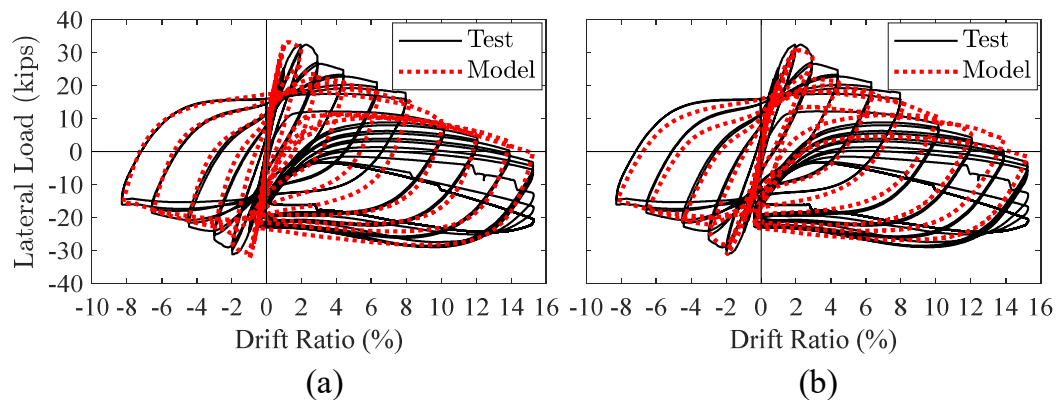


Figure 6.3. Comparison of lateral load-drift ratio curve between the FE model and the cyclic test for BC specimen by Nikoukalam and Sideris (2016a): (a) without bond-slip; (b) with bond-slip.

The embedded portion of the column within the superstructure was modeled by a stiff linear elastic beam element connecting the top of the column to the centroid of the superstructure cross-section. Translational ($4 \text{ kip}\cdot\text{sec}^2/\text{in}$) and rotational tributary mass ($35376 \text{ kip}\cdot\text{sec}^2\cdot\text{in}$) from the superstructure and the columns was lumped at the centroid. Soil-structure–foundation interaction was not considered and the column was assumed fixed at the base. Geometric nonlinearities were considered using the co-rotational formulation.

6.3.2. RC Rocking Column Modeling

Similarly to the conventional monolithic RC column, the rocking column (Figure 6.2(b)) was modeled by a gradient inelastic fiber element. At the rocking interface (column bottom), a steel material model with no tension was used for the mild longitudinal reinforcement by using the steel model described earlier in series with an elastic compression-only material model of high compressive stiffness. The PT bar was modeled by a co-rotational truss element with material response given by the model of Menegotto and Pinto (1973) including the reduction factor described earlier to simulate strain softening and fracture. The yield strength and elastic modulus were 135 ksi and 29000, respectively. The strain-hardening ratio was assumed to be 2%. The softening of the PT steel material was described by $R_{min} = 0.001$, $\varepsilon_{f1} = 5\%$, and $\varepsilon_{f2} = 8\%$, with these strain values being obtained by the manufacturer (Structural Technologies 2016). The initial post-tensioning load in the PT bar was applied in the form of initial strain. An automated iterative procedure was implemented to adjust the value of this strain accounting for immediate losses due to elastic shortening, so that the target post-tensioning load is achieved with acceptable accuracy. To simulate the gap between the PT bar and the interior wall of the central duct, a zero-length element was defined at the top node of the column (between the top node of the column and an intermediate node defined over the height of the PT element at the location of column top-end node), with a uniaxial elastic multilinear material model. The response of the elastic multilinear material model consists of a multi-linear curve that is defined by a set of points (Figure 6.4), which despite being nonlinear, it's elastic. This means that the material loads and unloads along the same curve,

and no energy is dissipated (McKenna and Fenves 2001). Herein, as shown in Figure 6.4, the response of the gap element in both positive and negative direction is defined with a tri-linear elastic material model with increasing stiffness (0.1, 1000, and 10,000 kips/in).

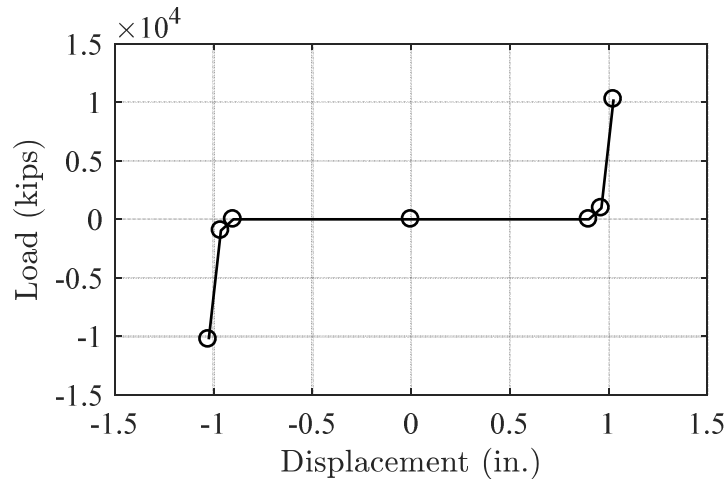


Figure 6.4. Uniaxial elastic multilinear response of the zero-length gap element.

Furthermore, the method for modeling the RC rocking column was validated against quasi-static cyclic testing of two segmental rocking columns, named as JH1 and JH2, studied by Hewes and Priestley (2002). For both columns, a base segment and another three segments are connected by an unbonded pre-stressed tendon at the center of the column. All the segments have a circular cross section with a diameter of 610 mm (24 in.). To minimize the damage of the concrete segments, the base segments of JH1 and JH2 are confined by with A36 steel jackets with the thickness of 6 mm (0.24 in.) and 2.8 mm (0.11 in.), respectively. No steel bars are placed in the base segments. The upper segments are transversely confined by Grade 60 #3 bar spiral spaced at 75 mm (2.95 in.). Eight

Grade 60 #4 longitudinal steel bars with a diameter of 12.7 mm (0.5 in.) are also placed around the section evenly in the upper segments. The tendons used in the columns are ASTM A779 Grade 270 pre-stressing strands. The total cross section area of the tendons for each column is 2665 mm² (4.13 in.²). A constant axial compressive load of 890 kN (200 kips) was applied to the column by a transfer beam and a pair of 35 mm (1.38 in.) diameter high-strength steel posttensioning bars.

Two-dimensional models of the column JH1 and JH2 was developed in OpenSees following the modeling approach used in this study. Figure 6.5(I) compares the lateral load versus drift ratio curve between the OpenSees model and the backbone of the test results for both specimens. Moreover, the cyclic test results are presented in Figure 6.5 (II) for comparison purposes. It can be seen that the predicted force vs. drift ratio responses for both JH1 and JH2 specimens are in good agreement with the test data. A comparison between the predicted and experimental tendon strain increase due to opening of the crack at the column base is shown in Figure 6.5(III). The experimental curve is constructed using the readings from the strain gages mounted on the tendon strands (Hewes and Priestley 2002); a measuring approach that involves high uncertainty. It can be seen that the tendon strain increase is over-predicted by the model except at low drift levels. In light of the uncertainty regarding the strain gage readings and the good agreement between force-displacement curves, it can be expected that the actual differences between predicted and actual tendons strains are smaller. It is also worth noting that the error in measuring tendon strains using strain gauges increases with the tendon extension (i.e. at larger tendon strains), which explains why the error in tendon strain predictions increases with the

column deformation, yet the error in lateral force predictions is unaffected by the column deformations.

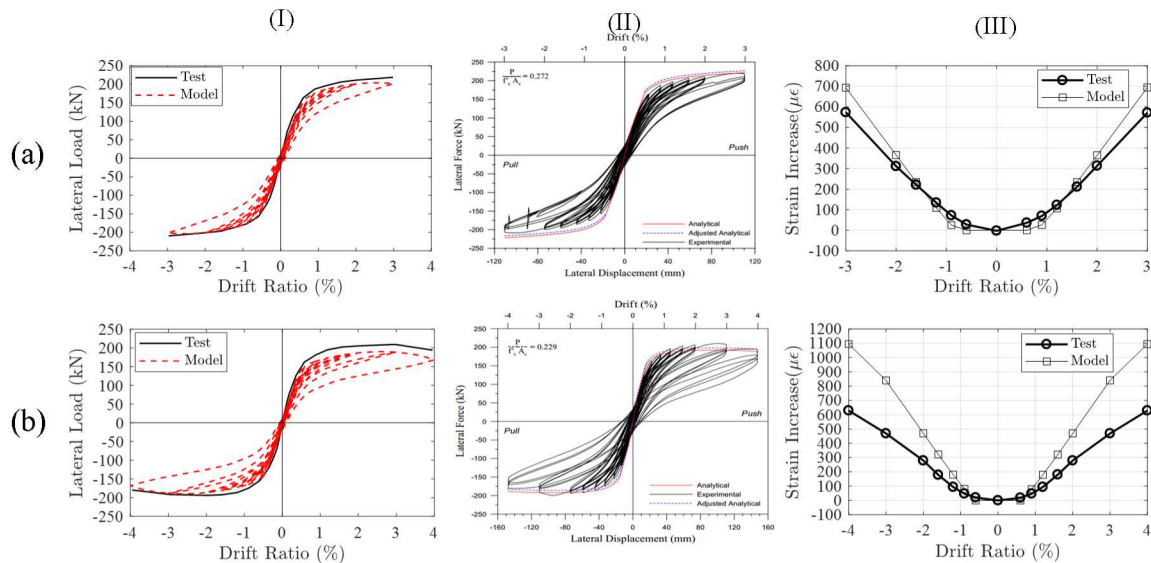


Figure 6.5. Comparison of model prediction to test results for (a) JH1 specimen, and (b) JH2 specimen: (I) predicted cyclic lateral load versus drift ratio compared to the backbone of the cyclic test result; (II) cyclic test result (Hewes and Priestley 2002); (III) predicted strain increase in PT system-drift ratio compared to the test data (Hewes and Priestley 2002).

6.3.3. Modeling of PU-enhanced Rocking Column

For the PU-enhanced rocking column, the reinforced concrete element and the PT bar were modeled as above. The PU segment was modeled using a gradient inelastic element with three integration points (Figure 6.2(c)). The characteristic length, l_c , was assumed to be equal to the cross-section diameter. Similar to the RC rocking column, the gap between the PT bar and the interior wall of the central duct was simulated with zero-length elements with the response similar to Figure 6.4, defined at the top node of the PU

segment as well as the top node of the RC segment above the PU segment (Figure 6.2(c)). The PU material behavior was simulated using the simplified visco-elastic softening visco-plastic material model developed herein (Section 5.3) and implemented in the OpenSees. Elastic shear deformations were considered through an area shape reduction factor of 0.9 (compensating for the circular area), with the PU material shear modulus being defined using the elastic modulus obtained from the test data and a Poisson's ratio of 0.49, assuming the PU material is nearly incompressible, a common assumption for polymers. Post-tensioning was applied as in the case of the rocking column.

6.3.4. Modeling of PU-enhanced Rocking Column with ED Links

For the PU-enhanced rocking column with ED links, the reinforced concrete element/component, the PT bar, the PU segment, and the gap between the PT bar and the interior wall of the central duct were modeled as described in the previous section. The two unmilled portions of the ED links and the connectors between the ED links and the steel collar were modeled by elastic beam elements (Figure 6.2(d)). The milled length of the links was modeled with a gradient inelastic fiber element with three integration points. The characteristic length, l_c , was assumed to be equal to the length of the milled (yielding) length, $L_{ED,Y}$. The steel material, which conformed to ASTM A706 – Gr. 60 (ASTM A706/A706M-16 2016), was modeled using the Menegotto-Pinto model (Menegotto and Pinto 1973) with the reduction factor described earlier, using the expected yield strength of 68 ksi and a strain hardening ratio of 0.5%. The residual value of the reduction factor was $R_{min} = 0.001$ with $\epsilon_{f1} = 14\%$ and $\epsilon_{f2} = 25\%$. To account for the confinement effect of the steel collar, confined concrete properties were assigned to both the concrete cover and

core over the height covered by the steel collar. Possible composite action of the steel collar and concrete was not considered.

The ED link setup, i.e. connectors and link elements, was incorporated to the model after application of post-tensioning and gravity loads. The connection of the ED links to the steel collar and the foundation was pinned, and was realized via zero-length elements of small rotational stiffness.

6.4. Pushover Analysis

Monotonic analyses were conducted with a low drift ratio rate (0.0004 s^{-1}) up to the drift ratio corresponding to the zero lateral force. Figure 6.6 presents the lateral force vs. drift ratio response for all column designs. In accordance with the aforementioned design objective, the monolithic and rocking columns exhibit similar strength. However, the monolithic column has lower stiffness, whereas the rocking column exhibits faster post-peak deterioration. This faster post-peak deterioration of the RC rocking column, compared to the monolithic column, results from: (i) the lack of mild reinforcement crossing the rocking interface and the resulting larger concrete compression stress/strain demands (indicated by the early concrete spalling, at a drift ratio of less than 1%), and (ii) the yielding of the PT bar. For the RC rocking column, yielding of the PT bar occurs at a drift ratio of 2%, which is when the post-peak response initiates. Steel or FRP jacketing at the rocking joint can limit the contribution of compression crushing to this deterioration, but PT bar yielding will eventually control. The PU-enhanced rocking column achieves similar strength with the RC monolithic and rocking columns, but much lower stiffness.

Addition of the ED links increases the stiffness and strength of PU-enhanced columns, which when having ED links are termed *PUED columns* herein. For both values of λ_C , 0.25 and 0.5, the strength of the PUED columns exceeds the strength of the other column designs, while, for $\lambda_C = 0.5$, the stiffness of the PUED column becomes similar to that of the rocking column. For both values of λ_C , ED links yield at column drift ratios not exceeding 1%, while the first and second link fracture at drift ratios of about 6.5% and 8.5%, respectively. Yielding of the post-tensioning bar of the PU and PUED columns starts at a column drift ratio of about 4%. A quantitative definition of these damage states is discussed later and is summarized in Table 6.3.

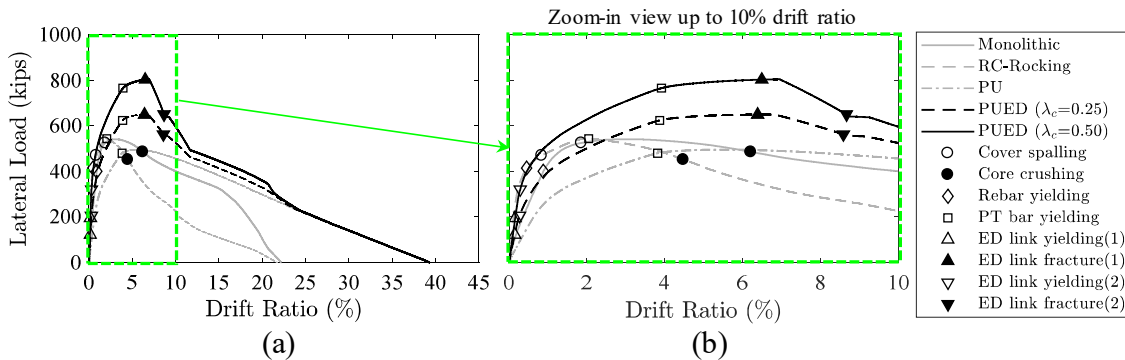


Figure 6.6. Monotonic response of different column systems and various damage states.

6.5. Cyclic Analysis

Similarly to the monotonic loading, cyclic loading is applied at a peak drift ratio rate not exceeding 0.0004 s^{-1} . The lateral force vs. drift ratio response for all columns is presented in Figure 6.7. The RC monolithic column and the PU-enhanced column show a

stable hysteretic response and mild post-peak strength degradation, which becomes more evident only at drift ratios exceeding 10% (Figure 6.7 (a)). On the other hand, the RC rocking column exhibits significant strength and stiffness degradation beyond a 2-3% drift ratio. In accordance with the discussion above, this rapid post-peak degradation results from the yielding of the PT bar, and the large concrete compression damage at the bottom/rocking section, which results from the lack of mild longitudinal reinforcements crossing the column-foundation interface that leads to larger compressive stress/strain demands to the concrete material. The PUED columns also show stable hysteresis, and, compared to PU columns without ED links, they exhibit significantly higher stiffness, strength and energy dissipation, which increases with λ_C (Figure 6.7 (b) and (c)). Following fracture of the ED links, the response of the PUED columns reduces to that of the PU-enhanced columns without ED links (Figure 6.7 (b) and (c)).

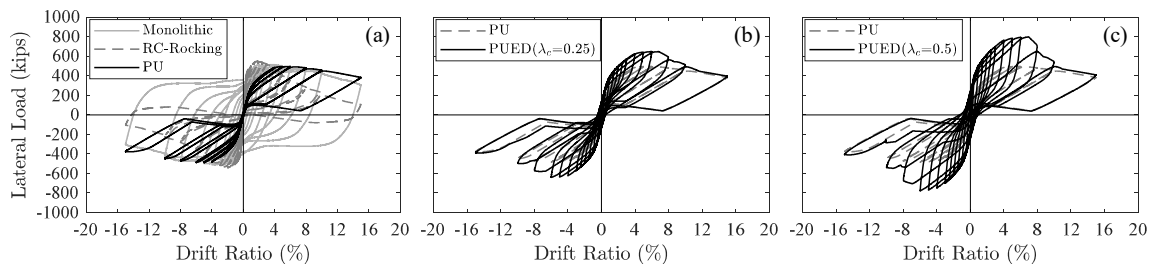


Figure 6.7. Cyclic response of columns: (a) RC monolithic vs. RC rocking vs. PU column; (b) PUED column with $\lambda_C = 0.25$ vs. PU column; (c) PUED column with $\lambda_C = 0.5$ vs. PU column.

Energy dissipation in PUED columns was provided primarily by the ED links and the PU material, while some contributions were also provided by the post-tensioning bar,

which yielded at a drift ratio of 4%, but did not exceed a peak strain of 1.2% at the peak drift ratio of 15%. Energy dissipation in the RC rocking column was provided by concrete spalling and core crushing and by yielding of the post-tensioning bar, which initiated at a drift ratio of about 2%, but did not exceed a peak strain of 0.9% at the peak drift ratio of 15%. The energy dissipation capabilities of all columns were evaluated, for each loading cycle, through their equivalent viscous damping ratios, ζ_{eq} , calculated as (Filiatrault et al. 2013):

$$\zeta_{eq} = \frac{E_d}{2\pi K_{sec} u_0^2} \quad (6.3)$$

where E_d is the total energy dissipated per cycle, K_{sec} is the secant stiffness, and u_0 is the displacement amplitude of the cycle. For a given test, E_d is computed as the average energy dissipation of the two cycles, while K_{sec} is calculated as:

$$K_{sec} = \frac{F_{peak}^+ - F_{peak}^-}{u_{peak}^+ - u_{peak}^-} \quad (6.4)$$

and u_0 is calculated as:

$$u_0 = \frac{u_{peak}^+ - u_{peak}^-}{2} \quad (6.5)$$

where F_{peak}^+ and F_{peak}^- are the peak positive and negative force values, respectively, and

u_{peak}^+ and u_{peak}^- are the peak positive and negative displacement values, respectively.

Calculation of F_{peak}^+ , F_{peak}^- , u_{peak}^+ and u_{peak}^- is graphically demonstrated in Figure 2.4.

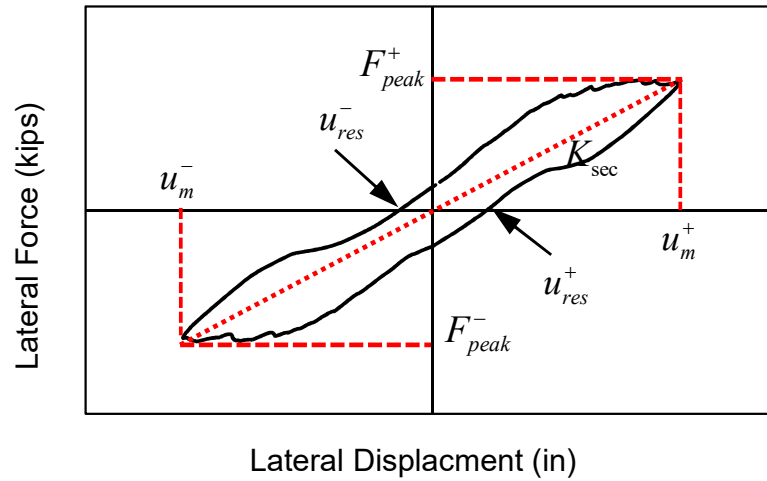


Figure 6.8. Graphical computation of F_{peak}^+ , F_{peak}^- , u_{peak}^+ and u_{peak}^- and K_{sec} at a given cycle.

As shown in Figure 6.9 (a), for $\lambda_C = 0.25$ and 0.5 , the PUED columns provide a damping ratio of 10%-15% and 15%-20%, respectively, up to a drift ratio of 8%. The RC rocking provides higher damping ratios than the PUED columns for lateral column drift ratios exceeding 9%, i.e. after fracture of the ED links in the PUED columns. The RC monolithic column provides small damping ratios at column drift ratios below 2% or 3%, but exhibits large damping ratios as damage progresses, reaching a damping ratio of almost 45% at a drift ratio of 15%.

A comparison of the self-centering capabilities of all columns is presented in Figure 6.9 (b) in terms of residual drift ratios (at each loading cycle) vs. the peak drift ratio of the cycle. As shown, the RC monolithic column exhibits residual deformations that increase with the peak drift ratio, reaching almost 14% at the peak drift ratio of 15%. Residual deformations in the RC rocking column remain small, except for the last cycle

at a drift ratio of 15% for which concrete crushing has become excessively large (see also Figure 6.7 (a)). Residual deformations in PUED columns slightly increase with λ_c , but always remain below 1%. However, because residual deformations mainly result from residual strains in the ED links, their largest portion is recoverable upon replacement of the ED links (see Section 4.4.2.1).

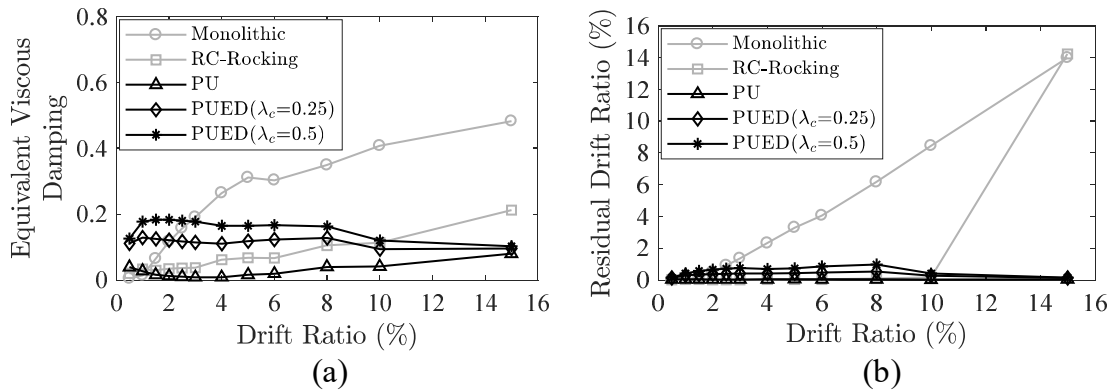


Figure 6.9. (a) Equivalent viscous damping ratio vs. peak column drift ratio; (b) residual drift ratio vs. peak column drift ratio.

6.6. Seismic Fragility Assessment

Fragility assessment is performed through incremental dynamic analysis (IDA) (Luco and Cornell 2000; Vamvatsikos and Cornell 2002) using the 22 motions of the far-field ground motion (GM) ensemble of FEMA P695 (Federal Emergency Management Agency 2009) normalized as described in FEMA P695. Each horizontal component of these motions is used individually, resulting in a total number of 44 ground motions. Scaling is performed with respect to the 5% damped geometric mean spectral acceleration

of all GMs at the mean of the fundamental periods of all column systems, which is the intensity measure (IM) suggested by FEMA P695. The first mode period of the RC monolithic, RC rocking, PU-enhanced rocking, PUED with $\lambda_C = 0.25$, and PUED with $\lambda_C = 0.5$ was found to be 0.8 s, 0.54 s, 1.07 s, 0.75 s, and 0.63 s, respectively, with an average of 0.76 s.

For all systems, Rayleigh damping with a 2% damping ratio assigned to the first two modes was considered. For the PUED columns, because most of the residual deformations are due to the residual strains in the ED links, whereas the PU material has the capability to recover a portion of its initial residual strains (see Figure 3.4) upon removal of the ED links, the column residual deformations are expected to significantly decrease during replacement of damaged ED links (as also observed in Section 4.4.2.1). To quantify this phenomenon, at the end of each analysis, the ED links were removed one-by-one, as part of the analysis. After each ED link removal, the analysis continued (free vibration) for an hour over which part of the residual deformation in the PU segment was recovered resulting in a smaller residual drift of the column system.

Boundary conditions/effects due to the abutments are not considered. In that sense, the generated models are representative of the response of a long bridge in the transverse direction and away from the abutments (e.g. the Hanshin Expressway that collapsed sideways during the 1995 Kobe earthquake).

6.6.1. Selected Damage States

Damage states (DSs) represent states of actual structural damage and are quantified by *limits* (termed *limit states*, LSs) on a set of *engineering demand parameters* (EDPs). For highway bridges, EDPs have been categorized by Mackie and Stojadinović (2005) into three groups: (1) *global* EDPs, which describe the overall performance of the bridge system, such as peak column displacement and residual displacements, (2) *intermediate* EDPs, which describe the performance of the bridge in terms of the response of its structural components, such as maximum moment and curvature in columns, and (3) *local* EDPs, which describe bridge performance in terms of material response, such as strains and stresses in concrete and steel. The damage states adopted herein include global and local EDPs and are presented in Table 6.3 together with their corresponding LSs.

Two DSs are used in terms of the residual drift ratio (RDR): (a) *catastrophic/actual structural collapse*, and (b) *system demolition/replacement*. The LS corresponding to the DS of catastrophic/actual collapse is defined for each column design individually as the residual drift ratio being equal to the drift ratio at which the pushover curve crosses the zero-force axis (see Figure 6.6), which implies that the column becomes unstable, thereby, experiencing catastrophic collapse. For the DS of *system demolition/replacement*, a LS value of 1.5% was used for the residual drift ratio, based on the newly adopted Japanese code for highway bridge design (Japan Road Association 2006), beyond which the bridge would be considered unusable regardless of the state of the other bridge components.

Two DSs are defined based on the peak strain in the concrete cover and core: (i) *cover spalling*, corresponding to a peak strain of 0.004 and (ii) *core crushing*, corresponding to a peak strain of 0.02 (Mander et al. 1988).

For the PU material, a single DS is considered to express that the proportionality limit has been reached (i.e. transition from the linear to nonlinear response). The corresponding LS is the strain at the proportionality limit, which is approximately 4% (see Figure 3.4(a)). It is clarified that exceeding the proportionality limit does not necessarily represent damage, due to the viscoelastic properties of the PU material.

Two DSs are adopted for the PT bar based on the peak strain in the steel material: (1) *yielding* at a strain of $\underline{\varepsilon}_y = 0.0047$, defined as $f_y/E_s = 135 \text{ ksi}/29000 \text{ ksi}$, and (2) *rupture* at a strain of $\varepsilon_u = 0.05$, provided by the manufacturer (Structural Technologies 2016).

For the ED links, two DSs are defined based on the peak strain in the steel material: (I) *yielding* at a strain of $\varepsilon_y = 0.0023$, defined as $f_y/E_s = 68 \text{ ksi}/29000 \text{ ksi}$, and (II) *rupture* at a strain of $\varepsilon_u = 0.14$, per ASTM A706 – Gr. 60 (ASTM A706/A706M-16 2016) steel.

Table 6.3. Damage states definition matrix.

Physical Damage – Damage State	Related EDP	LS	Reference
Catastrophic structural collapse	Residual drift ratio – RDR	22% for monolithic RC 21.5 % for rocking RC 39% for PU 39.3% for PUED ($\lambda_C = 0.25$) 39.3% for PUED ($\lambda_C = 0.5$)	From pushover curve
System demolition/replacement	RDR	1.5%	Japan Road Association (2006)
Core concrete crushing	$\mathcal{E}_{c,core,peak}$	0.02	Mander et al. (1988)
Cover concrete spalling	$\mathcal{E}_{c,cover,peak}$	0.004	-
PU proportionality limit	$\mathcal{E}_{PU,peak}$	0.04	-
PT bar yielding	$\mathcal{E}_{PT,peak}$	0.0047	-
PT bar rupture	$\mathcal{E}_{PT,peak}$	0.05	Manufacturer: Structural Technologies (2016)
ED link yielding	$\mathcal{E}_{ED,peak}$	0.0023	-
ED link rupture	$\mathcal{E}_{ED,peak}$	0.14	ASTM A706/A706M-16 (2016)

6.6.2. Fragility Assessment

Fragility curves are generated for different DSs via the *occurrence ratio* of each DS as function of the IM. The occurrence ratio is defined as the number of motions, n , for which a DS is reached, under given IM, over the total number of motions, N ($= 44$). A DS is reached when the corresponding EDP exceeds the associated LS, as defined in Table 6.3. For the i -th DS, the fragility can be expressed as:

$$P(DS_i | IM) = P(EDP_i > LS_i | IM) = \frac{n_i}{N} \quad (6.6)$$

A lognormal cumulative distribution function (CDF) is fitted to the data obtained from Eq. (6.6) by minimizing the sum of squared errors (SSE) (Baker 2015) between observed (from Eq. (6.6)) and predicted (from the CDF) probabilities, as:

$$\{\hat{\mu}_i, \hat{\beta}_i\} = \arg \min_{\mu, \beta} \sum_{j=1}^m \left(\frac{n_{i,j}}{N} - \Phi \left(\frac{\ln(IM_j) - \mu_i}{\beta_i} \right) \right)^2 \quad (6.7)$$

where the index i refers to the i -th DS, index j refers to the j -th data point, m is the total number of data points of the fragility curve, $\Phi(\cdot)$ is the lognormal CDF with mean and standard deviation of μ and β , respectively, and $\hat{\mu}_i$ and $\hat{\beta}_i$ are the optimal mean and dispersion of the CDF. Following this procedure, fragility curves were developed for the five column designs and all the DSs listed in Table 6.3. Median capacities, defined as the value of IM at $P(DS_i|IM)=50\%$, were also determined for all DSs to allow for a more direct assessment.

Fragility curves for the DSs of system demolition/replacement and catastrophic structural collapse, per Table 6.3, are compared in Figure 6.10 (a) and (b). As shown, the PUED columns have higher capacity against demolition/replacement and catastrophic collapse, compared to the conventional and rocking RC columns and the PU-enhanced column (without ED links). This capacity increases with λ_C . This is further illustrated in Figure 6.10 (c), which shows the median capacities of all column designs against these two DSs. In fact, the median capacity against catastrophic collapse from the RC monolithic column to the PUED column increases by 7% and 17% for λ_C of 0.25 and 0.5, respectively. Similarly, the median capacity against replacement/demolition from the RC

monolithic column to the PUED column increases by 107% and 125% for λ_C of 0.25 and 0.5, respectively. It is further observed that the median capacity of the PU column (without ED links) against demolition/replacement is larger than that of the monolithic and rocking RC columns, while the median capacity of the PU column against catastrophic collapse is larger than that of the RC rocking column, but not the monolithic column. The RC rocking column exhibits lower capacity against the DS of catastrophic collapse, compared to the RC monolithic column. This lower capacity against catastrophic collapse is associated with the fact that the LS for this DS refers to large drift ratios, for which the RC rocking column exhibits more rapid (post-peak) deterioration (Figure 6.7(a)) and much lower energy dissipation capabilities (Figure 6.9 (a)), compared to the RC monolithic column. However, the observed lower capacity of the RC rocking column, compared to the monolithic column, against the DS of system demolition/replacement (Figure 6.10 (c)) is unexpected, because the LS for this DS is associated with small drift ratios (1.5%), for which the RC rocking column exhibits lower residual deformations (Figure 6.7(a)) and similar energy dissipation capabilities (Figure 6.9 (a)) with the RC monolithic column. Further investigation of this response revealed sensitivity of this particular finding on the definition of the IM. For the case that the IM for each column system is defined as the *5%-damped spectral acceleration at its own/individual fundamental period*, the median capacity of the RC rocking column against system demolition is found to be larger than that of the RC monolithic column and the PU column (Figure 6.11), which seems more reasonable. It is noted that, with this alternative IM definition, the PUED columns still outperform all other column designs.

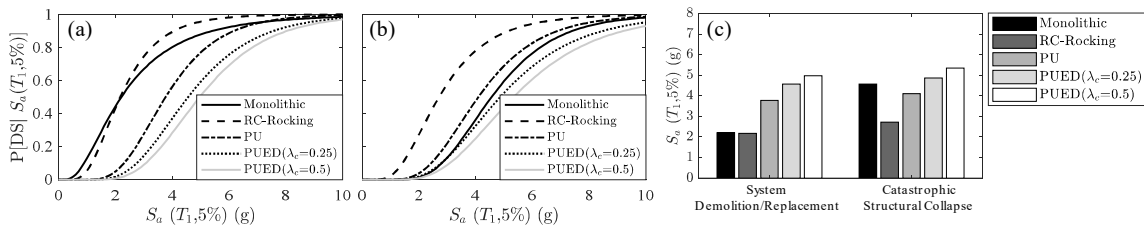


Figure 6.10. Fragility curves for the DSs of: (a) system demolition/replacement, and (b) structural collapse; (c) median capacities for system demolition/replacement and structural collapse.

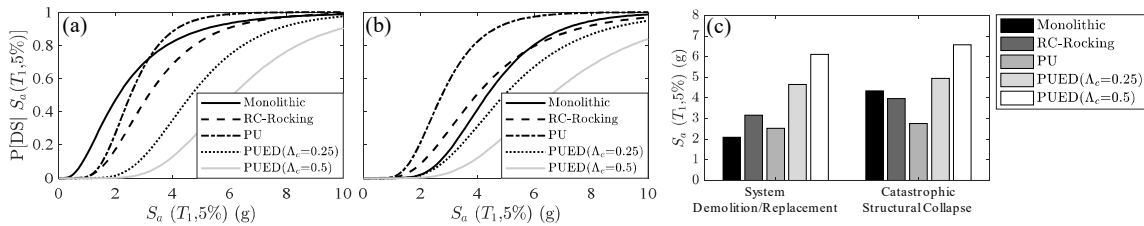


Figure 6.11. Fragility curves, using IM definition based on fundamental periods for each individual column system, for the DSs of: (a) system demolition/replacement, and (b) structural collapse; (c) median capacities for system demolition/replacement and structural collapse.

Evaluation of the fragility curves for the DSs of concrete cover spalling and core crushing, shown in Figure 6.12, indicates that for both DSs, the capacity against damage in concrete is significantly higher in columns with PU segment, especially in PUEd columns, compared to the conventional and rocking RC columns. Moreover, this capacity increases with λ_c . According to Figure 6.12(c), the median capacity against cover spalling from the RC monolithic column to the PUEd column increases by 274% and 317% for λ_c of 0.25 and 0.5, respectively. Similarly, the median capacity against core crushing from the RC monolithic column to the PUEd column increases by 85% and 107% for λ_c of 0.25 and 0.5, respectively. The RC rocking column exhibits the lowest capacity against

spalling, which is in agreement with observations from monotonic analyses (Figure 6.6), and also holds true for both IM definitions.

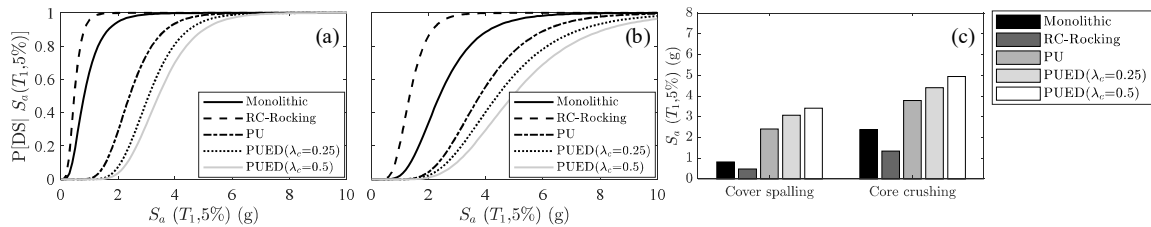


Figure 6.12. Fragility curves for the DSs of: (a) cover spalling, and (b) core crushing; (c) median capacities for cover spalling and core crushing.

Fragility curves for the DS of the PU proportionality limit, per Table 6.3, are shown in Figure 6.13(a). As shown, the PUED columns exhibit higher capacity against exceeding this limit compared to PU columns without ED links. This higher capacity results from the presence of the ED links, which reduce the deformation demands on the PU segment, and increases with λ_C . Specifically, the median capacity regarding the PU proportionality limit from the PU column to the PUED columns increases by 23% and 39% for λ_C of 0.25 and 0.5, respectively (Figure 6.13(b)). These observations qualitatively hold true for both IM definitions.

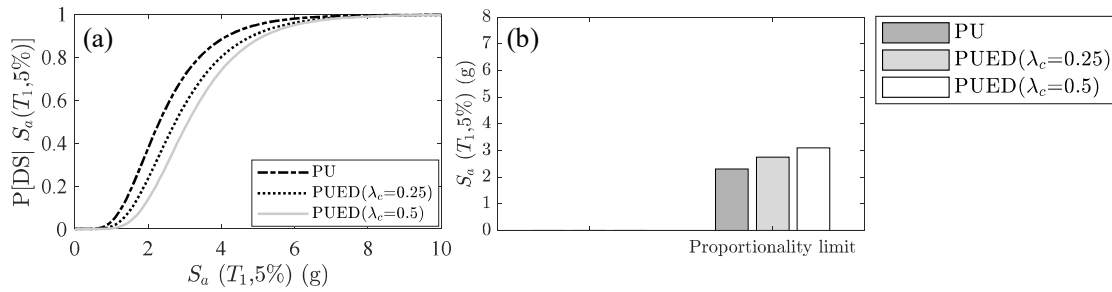


Figure 6.13. (a) Fragility curves for the DS of PU proportionality limit; (b) median capacities.

Fragility curves for the DSs of PT bar yielding and rupture, per Table 6.3, are shown in Figure 6.14(a) and (b). As shown, the PUED columns provide higher capacity against PT bar yielding and rupture compared to the PU rocking column (without ED links), and this capacity increases with λ_C . This is because the ED links reduce the deformation demands due to the higher strength and energy dissipation that they offer. In fact, per Figure 6.14(c), the median capacity against PT bar yielding from the PU to the PUED columns increases by 42% and 69% for λ_C of 0.25 and 0.5, respectively. Similarly, the median capacity against PT bar rupture from the PU to the PUED columns increases by 19% and 30% for λ_C of 0.25 and 0.5, respectively. The RC rocking column exhibits the lowest capacity against PT bar yielding and fracture (Figure 6.14). However, if the alternative IM definition is considered (Figure 6.15), the RC rocking column exhibits larger capacity against PT yielding and fracture, compared to the PU column, which is reasonable, because the RC column has larger stiffness and strength. On the other hand, the PUED columns outperform all other columns irrespectively of the selected IM definition.

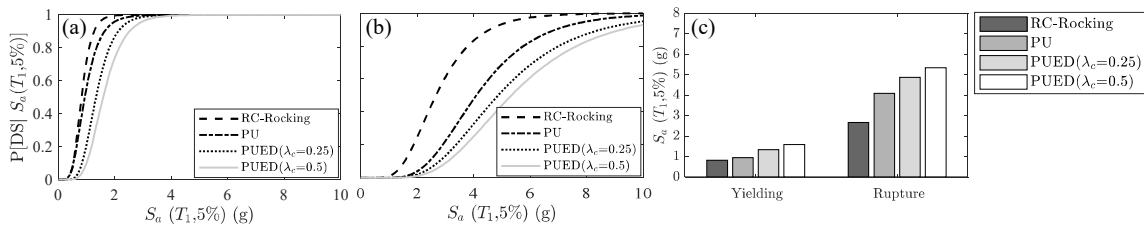


Figure 6.14. Fragility curves for the DSs of: (a) PT bar yielding, and (b) PT bar rupture; (c) median capacities for PT bar yielding and rupture.

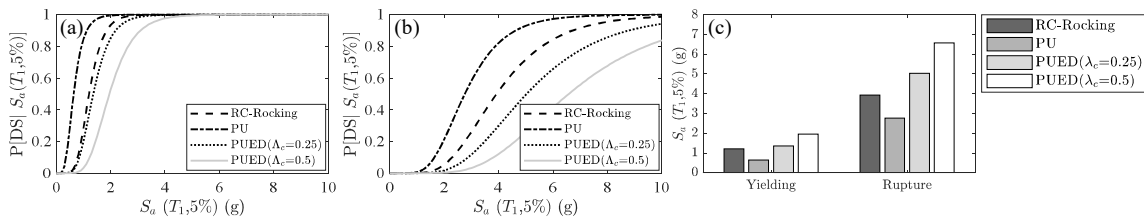


Figure 6.15. Fragility curves, using IM definition based on fundamental periods for each individual column system, for the DSs of: (a) PT bar yielding, and (b) PT bar rupture; (c) median capacities for PT bar yielding and rupture.

The fragility curves for the DSs of ED link yielding and rupture in the PUED columns are compared in Figure 6.16(a) and (b). As shown, both columns show similar capacity against ED link yielding, while the capacity against ED link rupture increases with λ_c , since the strength and energy dissipation capacity of the system increases, resulting in lower deformation demands. According to Figure 6.16(c), the median capacity against ED link rupture increases by 16% as λ_c increases from 0.25 to 0.5. These observations qualitatively hold true for both IM definitions.

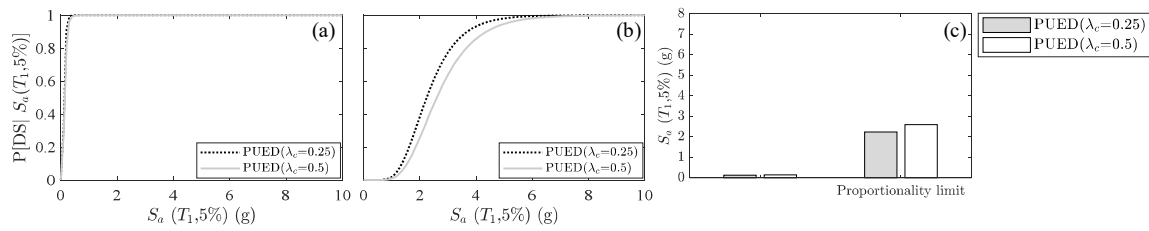


Figure 6.16. Fragility curves for the two PUED columns for the DSs of: (a) ED link yielding, and (b) ED link rupture; (c) median capacities for ED link yielding and rupture.

Overall, all findings, at least from a qualitative perspective, appear to be independent of the selected IM, except for the DSs of (i) system demolition/replacement, for which, using the alternative IM, the RC rocking column is shown to outperform the RC monolithic and PU columns, and (ii) the DSs of PT bar yielding and rupture, for which, using the alternative IM, the RC rocking column is shown to outperform the PU-enhanced column (without ED links).

6.7. Summary and Findings

In this section, the seismic performance of the proposed column system was computationally investigated and compared to that of conventional reinforced concrete monolithic and rocking columns. The proposed column design offers explicit damage control via damage resistant end segments made of polyurethane, energy dissipation and flexural strength/stiffness through energy dissipation links, and self-centering through internal unbonded post-tensioning. The response of the proposed designs was first investigated under monotonic and cyclic loading and compared to the response of conventional and rocking RC columns. Fragility analysis was subsequently conducted via

incremental dynamic analyses to assess the seismic performance of the proposed column design compared to conventional and rocking RC columns. Major findings include:

- PU-enhanced columns were capable of accommodating large deformations with minor or repairable damage. Specifically, the studied column designs accommodated lateral drift ratios up to 5% without damage and lateral drift ratios up to 15% with damage at the ED links, which are easily replaceable, and minor yielding at the post-tensioning rebar. Moreover, columns with PU segments demonstrated mild post-peak strength deterioration, contrary to rocking RC columns which demonstrated rapid post-peak deterioration, particularly at large drift ratios ($> 5\%$).
- PU-enhanced columns with ED links exhibited much higher median capacity against post-event demolition, which increased with the contribution of the ED links, becoming up to 125% larger (for $\lambda_C = 0.5$) than that of the conventional cast-in-place column. Similarly, the capacity against structural collapse increased by 17% (for $\lambda_C = 0.5$) with respect to the median capacity of the conventional RC column.
- The performance of the RC rocking column was found to be sensitive on the selection of the intensity measure, IM. Two intensity measures were considered: (i) the 5% damped spectral acceleration at the mean of the fundamental periods of all column designs, and (ii) the 5% damped spectral acceleration at the individual fundamental period of each column design. The second/alternative IM resulted in

the RC rocking column outperforming the RC monolithic column for the DS of system demolition/replacement, and also outperforming the PU-enhanced column (without ED links) against the DSs of system demolition/replacement and PT bar yielding and rupture. All other findings were found to be independent of the selected IM, at least, from a qualitative perspective.

- PU-enhanced columns with ED links demonstrated major resistance against structural damage, in terms of: (i) concrete spalling and crushing, because concrete in the vicinity of the bottom joint has been replaced by PU, and (ii) post-tensioning bar yielding and fracture. Specifically, the median capacity against yielding and fracture increased by 94% and 100% respectively, with respect to that of the rocking RC column (with respect to the first IM) or by 206% and 138% respectively, with respect to that of the PU column (with respect to the second IM).
- Peak strains in the PU decreased with the contribution of ED links, further showing the capability of ED links to prevent damage in other components of the column.

7. EXPERIMENTAL VALIDATION OF THE PERFORMANCE OF PRECAST CONCRETE ROCKING COLUMNS WITH POLYURETHANE END SEGMENTS

7.1. Scope and Objectives

This section describes the execution of a quasi-static testing program on bridge columns with polyurethane end joints and ED links. The main objective of this program was to experimentally evaluate the performance of this bridge column design, validate the replacement strategy proposed for ED links, and assess the performance of the “repaired” PU-enhanced columns, i.e. after replacement of the yielded ED links. Moreover, the experimental study aimed at providing the data for calibration of finite element models developed previously (Section 6.3).

7.2. Design of Specimens

7.2.1. Prototype Structure

The prototype structure considered in this study was the reference column introduced in Section 6.2.1 (Figure 6.1). It is reminded that the reference column was that of the single-column substructure of the Jack Tone Road Overcrossing, located in the city of Ripon, California, at the intersection of Route 99 and Jack Tone Road with identification number 10-SJ-099-2.34-RIP (Kaviani et al. 2014). Key structural and geometric properties of the reference column have been summarized in Table 6.1, while further details may be found in Kaviani et al. (2014).

7.2.2. Laboratory Test Specimens

7.2.2.1. Similitude Analysis

A scale-down model of the prototype column was achieved through similitude analysis; a mathematical framework that establishes relationships between the measured quantities in a prototype structure and a smaller scale model. The main objective of similitude analysis is to define scale factors between all the parameters contributing in mathematical rules which explain the behavior of a prototype system. These scale factors are defined as:

$$S_X = \frac{X_P}{X_M} \quad (7.1)$$

where S_X is the scale factor for the physical parameter X , while P and M refer to prototype and model structure, respectively. Since there are three fundamental dimensions (measures) in structural dynamics (Length (L), Force (F), and Time (T)) (without considering temperature effects), the number of scale factors that can be chosen arbitrarily is limited to three (Harris and Sabnis 1999).

In this study, the selected independent scale factors were those referring to the length (S_L), stress (S_σ), and material mass density (S_ρ). The scale factor S_L was selected to be 2.543 to meet the size and facilities limitations. The scale factors S_σ and S_ρ were selected to be 1.0, assuming that the prototype and the model structures are made of the same material. Other scale factors can be expressed in terms of the three independent prescribed factors (Table 7.1).

Table 7.1. Scale factors for monolithic column specimen.

Parameter	Scale Factor	Value
Length (selected)	S_L	2.543
Stress (selected)	S_σ	1
Mass density (selected)	S_ρ	1
Displacement	S_D	2.543
Area	S_A	6.467
Volume	S_V	16.447
Force	S_F	6.467
Mass	S_m	16.447
Acceleration	S_a	0.393
Gravitational Acceleration	S_g	0.393
Weight	S_W	6.467
Time	S_T	2.543

7.2.2.2. Design of Test Specimens

7.2.2.2.1. Monolithic Column

The monolithic column was detailed in the model space based on the AASHTO LRFD Bridge Design Specifications (AASHTO LRFD Bridge Design Specifications 2014) and Caltrans Seismic Design Criteria (CALTRANS 2006). The design details of the monolithic column are summarized in Table 7.2. It should be noted that the monolithic column model was designed only as a reference for the design of the reinforced concrete rocking column.

7.2.2.2.2. Reinforced Rocking Column

A rocking column was obtained by cutting the mild longitudinal reinforcement at the interface of the column and footing and adding post-tensioning strands in a duct at the center of the cross-section (Figure 7.2(a)). The design objective was to have a rocking column with lateral strength similar to that of the conventional monolithic reference column and maintain the axial load index (ALI) of the rocking column as close to that of the monolithic column as possible. These objectives could be technically achieved by the following approaches: (i) increase the cross-section diameter, (ii) use concrete of higher strength and provide more confinement. Herein, the second approach was adopted to achieve the prescribed design objectives. The last column on the right of Table 7.2 shows the target and final achieved dimensions of the RC-rocking column after considering the constraints due to attachment holes pattern on the support wall.

Table 7.2. Summary of design details of the reinforced concrete monolithic and rocking columns.

Parameter	Monolithic: Prototype	Monolithic: Model	RC-Rocking: Target/Achieved*
Column diameter (in)	66	26	26
Column height (in)	236	93	93/96.5
Duct inner diameter (in)	-	-	4
Longitudinal reinforcing steel	44#11	14#8	14#8
Transverse reinforcing steel	#6@3.34 in. (spiral)	#3@2.25 in. (spiral)	#4@2.5 in. (hoop)/
Transverse volumetric reinforcing ratio (%)	0.8	0.9	1.36
Post-tensioning steel	-	-	12 × 0.6" Strands
PT load (kips)	-	-	475
Yield stress of PT bar steel (ksi)	-	-	243
Longitudinal reinforcing ratio including PT steel (%)	2.00	2.0	2.3
Unconfined compressive strength (ksi)	5	5	8
Confined compressive strength (ksi)	6.72	6.80	10.76
Axial load index (ALI)	0.10	0.10	0.17

* Achieved design parameters are depicted only for those different than target.

7.2.2.2.3. Rocking column with solid PU end segment

The proposed rocking column design with a PU end segment is obtained by replacing part of the bottom of the rocking column (Figure 7.2(b)) with a PU segment. In accordance with the findings of Section 4.3.3, where it was shown that damage (i.e., peak strains in both concrete and PU) is minimized for $h_j/D_c \geq 0.75$ and $D_j/D_c \leq 1$, and considering the limitations of the PU casting facilities, in the present study, the PU segment height, h_j , and diameter, D_j , were selected such that $D_j/D_c = 1.0$, while $h_j/D_c = 0.6$, which, despite being smaller than 0.75, does not result in additional concrete damage, because of the steel collar that will be used for the attachment of the ED links, and will

confine the enclosed concrete. Also, D_c is the cross-section diameter of the rocking column.

7.2.2.2.4. Rocking Column with Bi-layered PU End Segment and ED Links

The height and diameter of the bi-layered PU segment was selected to be the same as the solid PU segment. Given that, the only new geometric parameter in the design of the bi-layered PU segment was the diameter of the central reinforced concrete core, $D_{j,c}$, which was expressed through the ratio of $D_{j,c}$ over D_j , defined herein as $\beta = D_{j,c}/D_j$. The value of β was determined by the design objective of having a system with lateral strength and post-peak response similar to that of the rocking column with solid PU segment, while keeping the axial load index (ALI) in the concrete core below 0.4. Parametric studies were conducted by varying the concrete core diameter, $D_{j,c}$, from 14" to 20" with an increment of 1 in. up to 18" and 2" for the last increment. According to the analysis results of the models developed in OpenSees (McKenna and Fenves 2001), it was shown that the prescribed design objectives could be achieved with $\beta=0.6$ to 0.8 ($D_{j,c} = 15.6-21$) (Figure 7.1), resulting to an ALI of 0.4-0.25. The value of $D_{j,c}$ was selected to be 17" ($\beta=0.65$), resulting to an ALI of 0.34, which was closer to the lower bound of the optimal range of β , so that the concrete core is protected by the stress concentrations towards the edges of the cross-section under lateral load.

A schematic view of the rocking column with bi-layered PU end segment is shown in Figure 7.2(c).

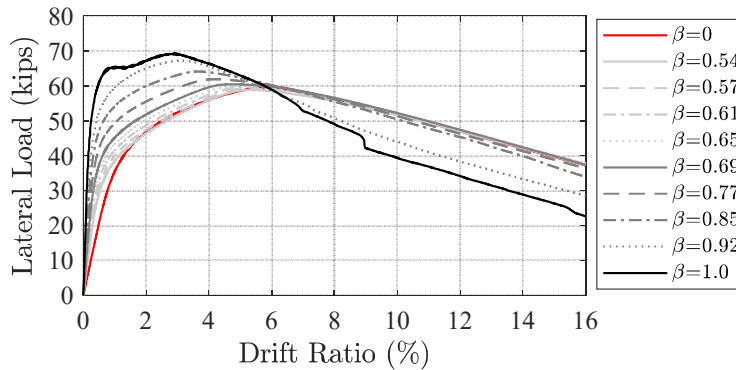


Figure 7.1. Lateral force versus drift ratio for rocking column with bi-layered PU segment with various concrete core diameter.

As mentioned earlier (Section 4.4), supplemental energy dissipation and the required flexural stiffness and strength is provided by external energy dissipating links in the form of buckling restrained yielding bars made of mild steel and implemented in the vicinity of the PU segment. It was assumed that the links are attached to the column after the initial post-tensioning and gravity loads are applied. Following the two design criteria for ED links explained in Section 4.4.1, a column with the re-centering ratios, λ_C , of 0.25 was designed for a target drift ratio of 3%. The column included eight radially distributed equally spaced ED links. The milled (fuse) length, $L_{ED,Y}$, and cross-section area, $A_{ED,Y}$, of the ED links was determined to be 14 in. and 0.7 in² for the selected target drift ratio.

The rocking column with bi-layered PU end segment and ED links is shown in Figure 7.2(d).

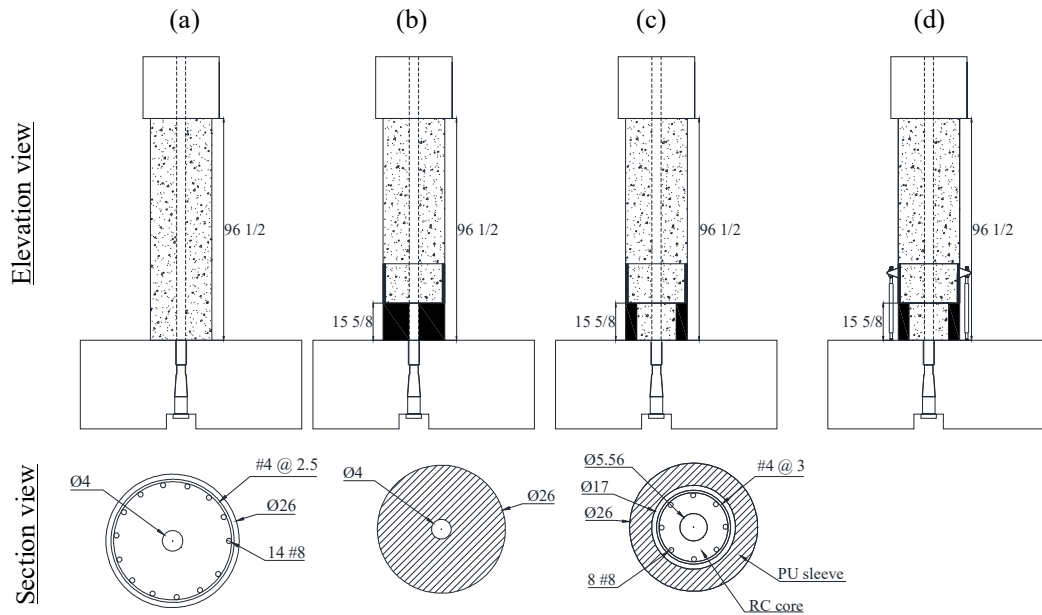


Figure 7.2. Schematic view of test specimens: (a) RC rocking column; (b) rocking column with solid PU end segment; (c) rocking column with bi-layered PU end segment; (d) rocking column with bi-layered PU end segment and ED Links (All dimensions are in inches. Section views are for the base section at the foundation level. ED links are not shown in section view).

7.3. Performance Assessment through CSM

The performance point (which represents the peak response) of the designed test specimens for various levels of hazard including $0.4 \times DE$, $0.6 \times DE$, $1.2 \times DE$, and $1.8 \times DE$ (equivalent to $1.2 \times MCE$) was evaluated following the CSM methodology described in Section 2.3.1.1. It is worth noting that the design earthquake (DE) is defined as 7% probability of exceedance in 75 years (i.e. a return period of about 1000 years); and maximum considered earthquake (MCE) is defined as 3% probability of exceedance in 75

years (i.e. a return period of about 2500 years). The corresponding parameters of the design spectrum at the location of the bridge was obtained from the USGS Seismic Design Maps (2018). The site class was assumed to be D. The short-period (S_s) and 1-sec period (S_1) spectral acceleration coefficient were determined as 0.631 and 0.230, respectively. The response spectrum for MCE hazard level was obtained by scaling the DE response spectrum by a factor of 1.5. All response spectra were further scaled in accordance with the similitude analysis (Figure 7.3).

To this end, following the procedure of Section 2.3.1.1, the variation of the equivalent viscous damping with lateral displacement (damping curve) was obtained for each specimen by conducting a set of cyclic analyses up to a 15 in. lateral displacement with an increment of 1 in. Each set included two cycles of the same amplitude. The performance point, which is defined as the intersection of the capacity and damped demand curve, was computationally determined using the bisection method (Figure 7.4). The spectral displacement, S_d , at the performance point and the corresponding drift ratio is listed in Table 7.3 for various specimens at four hazard levels considered in this study.

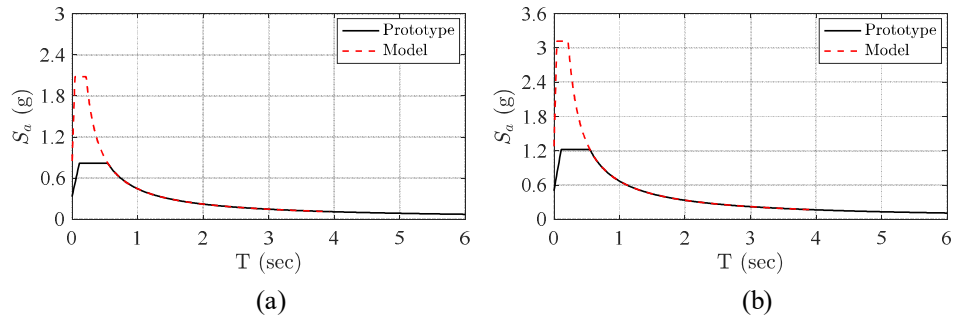


Figure 7.3. Response spectrum in prototype and model domain: (a) DE; (b) MCE.

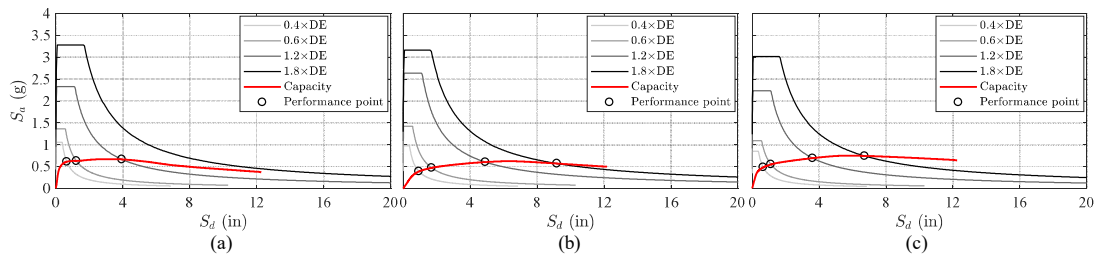


Figure 7.4. Performance point at various hazard levels: (a) RC rocking column; (b) PU enhanced column; (c) PUED column.

Table 7.3. Performance point at various hazard levels for various test specimens.

Specimen	Hazard level	S_a at performance point (in)	Drift ratio at performance point (%)
RC	0.4×DE	0.64	0.59
	0.6×DE	1.22	1.13
	1.2×DE	3.9	3.60
	1.8×DE (1.2×MCE)	-	-
PUED (bi-layered)	0.4×DE	0.65	0.60
	0.6×DE	1.1	1.02
	1.2×DE	3.5	3.23
	1.8×DE (1.2×MCE)	6.7	6.19
PU	0.4×DE	0.92	0.85
	0.6×DE	1.65	1.52
	1.2×DE	4.79	4.42
	1.8×DE (1.2×MCE)	9.17	8.47

7.4. Detailing of Test Specimens

7.4.1. Reinforced Concrete Elements

Two reinforced concrete elements were casted. The first element was the RC-rocking column with an overall height of 8'-1/2" and a diameter of 26" and a 4" schedule 40 PVC pipe at the center to enclose the post-tensioning strands. Details of the longitudinal and transverse reinforcement are shown in Figure 7.5 and summarized in Table 7.2 (see Figure B.2 for more details).

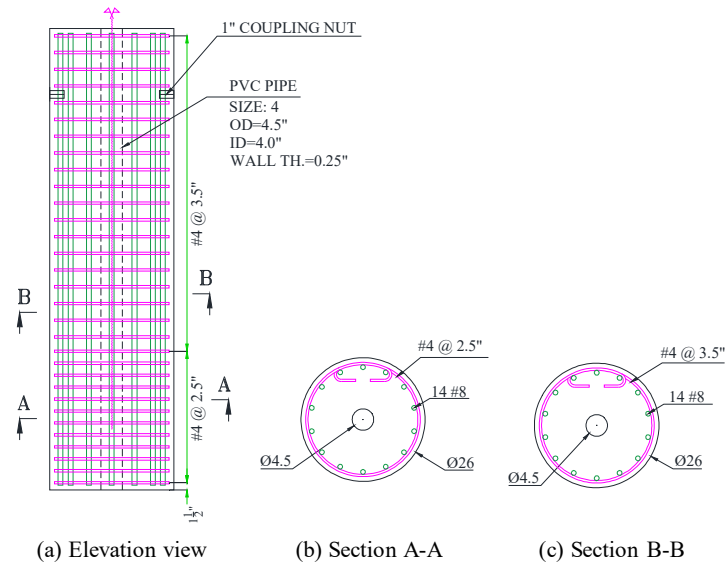


Figure 7.5. RC rocking column: geometry and reinforcement details.

The second reinforced concrete element was the top segment of PU and PUED columns with an overall height of 6'-8 7/8" and a diameter of 26". Towards its lower end, the duct was a 29" long steel pipe with a 4" inside diameter, and with its lower end sticking out of the segment by 13" to serve as a shear key. This steel pipe was connected to a 4" diameter schedule 40 PVC pipe with a 4" steel coupling and 4" PVC male adapter (Figure 7.6, see Figure 7.22 and Figure B.2 for more details). This PVC pipe extended all the way to the top end of the concrete element. This concrete element further included a cylindrical steel collar (mounting collar for ED links) at its lower end, which was made out of a steel pipe with an outer diameter of 26", wall thickness of 1", and cut to have an overall height of 16" (Figure 7.7). Eight radially distributed equally spaced mounting eyes/adapters were

welded to the outer surface of the steel tube at 1'-5/16" from the bottom. To eliminate any relative movement between the collar and the surrounding concrete, two sets of eight radially distributed equally spaced shear studs were welded to the inner face of the tube at 3" and 1'-5/16" from the bottom to provide interlock between the steel collar and the concrete (see Figure 7.7 and Figure B.13 for more details of steel collar).

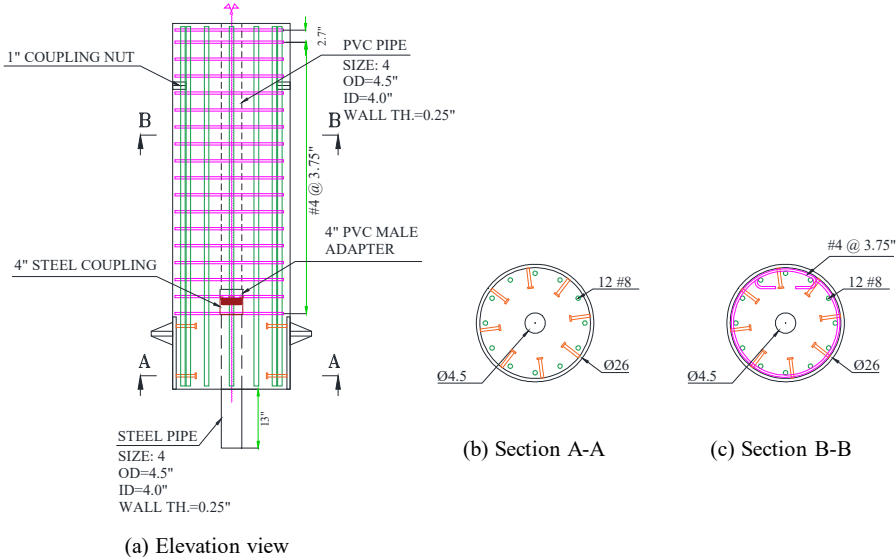


Figure 7.6. RC segment with steel collar: geometry and reinforcement details.

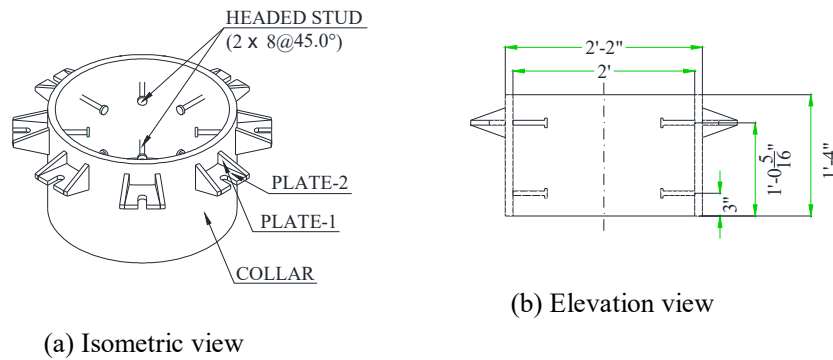


Figure 7.7. Steel collar: geometry details.

7.4.2. PU Segments

Three PU segments including a solid PU segment and two sleeves were casted at a PU casting facility and shipped to the laboratory. All three segments had an overall height of 1'-3 5/8" and diameter of 26". The solid PU segment was hollow with a 5" diameter hole at the center to enclose the post-tensioning strands (see Figure B.11). The PU sleeves had a wall thickness of 4 1/2" (see Figure B.12). The 17" diameter central hollow core of PU sleeves was filled with a reinforced concrete segment with 8 # 8 longitudinal reinforcement and #4 @ 3" hoops transverse reinforcement. A 5" steel pipe (OD = 5.56" and ID=4.81") was placed at the center of the segment to serve as duct for the post-tensioning strands and accommodate the shear key (steel pipe) protruding from the bottom of the RC segment with steel collar (Figure 7.8).

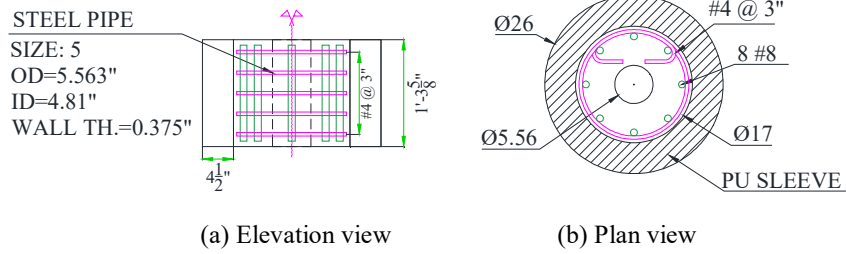


Figure 7.8. Bi-layered PU segment: geometry and reinforcement details.

7.4.3. ED Links

ED links were fabricated using 1.5 in. diameter, Grade A36 ($f_y = 36$ ksi and $f_u = 58-80$ ksi per ASTM A36 (ASTM A36/A36M-19 2019)) steel rods. The cross-section of the rod was reduced over a 14 in. fuse length to a smaller cross-section area of 0.679 in^2 (vs. the original area of 1.767 in^2) by milling three grooves parallel to the axis of the rod at 120° interval, as shown in Figure 7.9. A buckling restraining steel tube of outside diameter of 2.375 in. and wall thickness of 0.375 in., thus, resulting in a gap of 0.0625 in. between the rod and the buckling restraining (Figure 7.9 (c)), was used.

the cap beam (Section 7.5). The PT anchorage system including the multiplane anchor wedge, trumpet, and anchor spiral (#5 @ 2.25") were encase in a circular reinforce concrete block with a diameter of 26" with 14 # 8 longitudinal reinforcement and #4 @ 2.75" hoops transverse reinforcement (Figure 7.10). Detailed drawings of the anchorage block are presented in Appendix B (see Figure B.2-B.4).

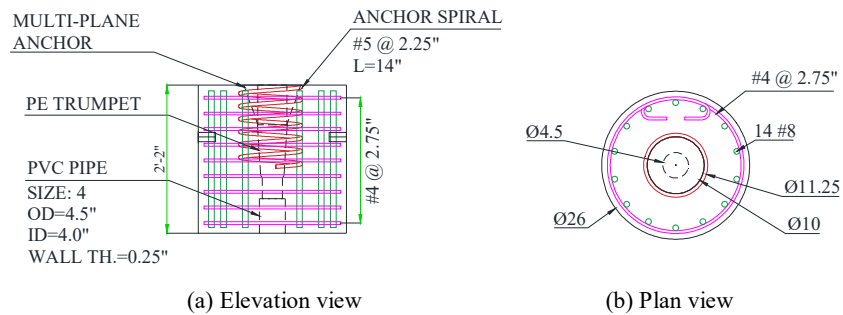
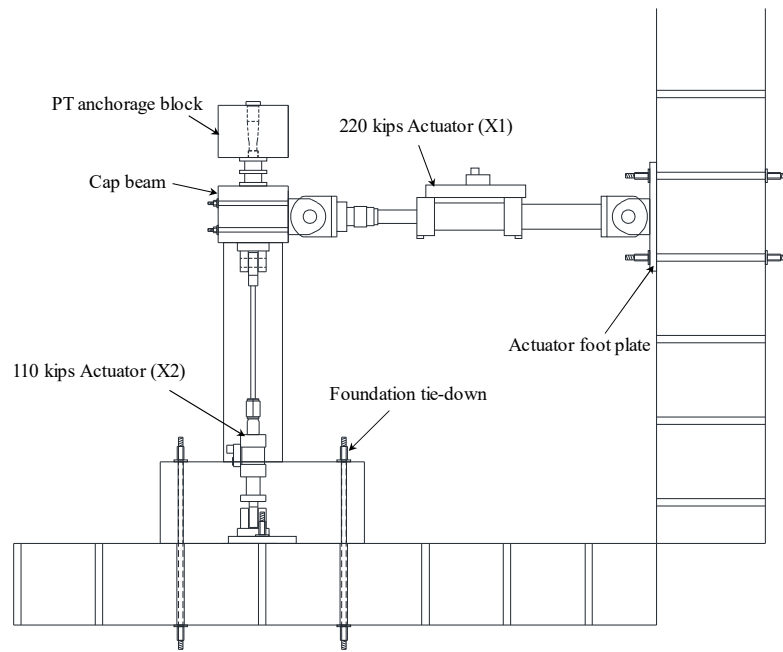


Figure 7.10. PT anchorage block: geometry and reinforcement details (Note: Details of the multi-plane anchor are not shown.).

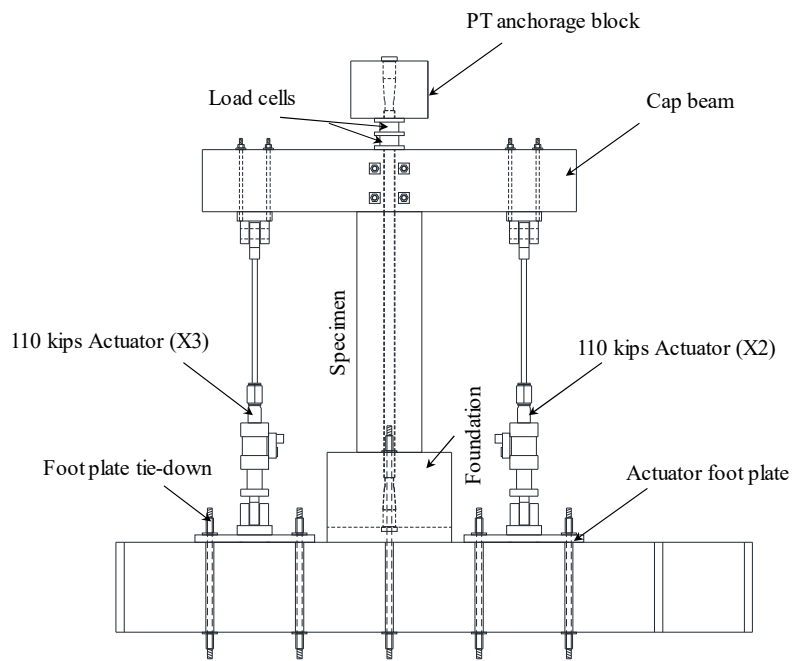
7.5. Test Setup

A schematic representation of the test setup for the RC rocking column is shown in Figure 7.11. The setup for PU rocking columns was similar to that of the RC rocking column. The foundation block was tied down to the laboratory strong floor with two high strength 2.5" post-tensioning bars. A total vertical load of 218 (= 2×109) kips representing the gravity load on the column was applied by two servo-controlled hydraulic actuators with a capacity of 110 kips and a 6 in (±3.0 in) stroke. The top swivel of vertical actuators

was tied to the bottom face of the cap beam with four 1” all thread rods and the bottom swivel was screwed to a 3” thick steel foot plate. The foot plates were tied down to the laboratory strong floor with two high strength 2.5” post-tensioning bars. The cyclic lateral displacement was applied to the specimen by a servo-controlled hydraulic actuators with a capacity of 220 kips and a 30 in (± 15.0) stroke. The 220 kips actuator was tied to the cap beam with four 1.5” all thread rods and was reacting off the laboratory strong support wall.



(a)



(b)

Figure 7.11. Schematic representation of test setup for RC rocking column: (a) east-west elevation (looking south); (b) south-north elevation (looking west) (support wall not shown) (Note: Instrumentation not shown).

7.6. Instrumentation

In all tests, the applied vertical and lateral loads were obtained from the actuator load cells. Horizontal displacements were measured using three string potentiometers over the height of the specimen, including the location of the applied lateral load (indicated as SP-1, SP-2, and SP-3 in Figure 7.12). String potentiometers were attached to a supporting reference frame that was tied-down to the laboratory strong floor.

The post-tensioning load was obtained from two custom-made 1000 kips load cells, stacked between the cap beam and the PT anchorage block. One of the load cells included two independent circuits, thus providing two independent readings of the axial load; thus, resulting in a total of three readings, indicated as LC-1, and LC-2, 3 in Figure 7.12.

In the RC rocking column (Figure 7.13), the curvature was measured in the vicinity of the column end (where the damage is expected to occur) by two string potentiometers attached to the foundation on the east and west sides, measuring the vertical displacement at a height of 18” from the column-foundation interface.

Two horizontal string potentiometers were connected to the north and south side of each end of the column to measure potential sliding at the column-foundation (identified as SP-8 and SP-9 in Figure 7.12) and column-cap beam interface (identified as SP-6 and SP-7 in Figure 7.12).

Two vertical string potentiometers (identified as SP-12 and SP-13 in Figure 7.12) were connected to the west and east side of the footing to measure potential uplift, while two string potentiometers (identified as SP-14 and SP-15 in Figure 7.12) were connected horizontally on the north and south side of the footing to measure potential sliding of the foundation block.

Besides the string pot measuring the lateral displacement at the location of the applied lateral load, three other string potentiometers were used to measure the lateral displacement of the cap beam in the loading direction at different heights (identified as SP-3, SP-4, and SP-5 in Figure 7.12). The measurements from these string potentiometers was used to calculate the cap beam rotation.

In the PUED column (Figure 7.15), eight string potentiometers (identified as SP-18 to SP-25 in Figure 7.14(c)) were used to measure the axial deformation of the ED links over the length measured from the footing to the center of the flat mounting plate. The curvature over the height of the bi-layered PU segment was measured by four string potentiometers attached to the foundation on the east and west sides (two string potentiometers at each side (identified as SP-10, SP-11, SP-16, and SP-17 in Figure 7.14(a) and (b))), measuring the vertical displacement at the top of the PU segment. Two horizontal linear variable differential transformer (LVDTs) (identified as LVDT-1 and LVDT-2 in Figure 7.14(a) and (b)) were connected to the top of the PU segment to measure potential sliding at the top PU interface.

In the PU rocking column with solid PU segment (Figure 7.17), two vertical string potentiometers (identified as SP-16 and SP-17 in Figure 7.16) were connected to the west and east side of the PU segment to measure potential uplift at the top PU interface. The curvature over the height of the solid PU segment was measured by two string potentiometers attached to the foundation on the east and west sides (identified as SP-10 and SP-11 in Figure 7.16), measuring the vertical displacement at top of the PU segment.

A list of instrumentation including their identification number, type, stroke, purpose, and location on the setup is presented in Table 7.4, Table 7.5, and Table 7.6 for the RC rocking, PUED, and PU column, respectively.

To better identify the locations of damage in the concrete, all concrete surfaces were painted white. In the RC rocking column, a grid pattern was drawn with black markers on the specimen prior to the test to help visually quantify the extent of cracking and spanning. The horizontal and vertical grid lines were spaced at 6 in. and 5.5 in., respectively.

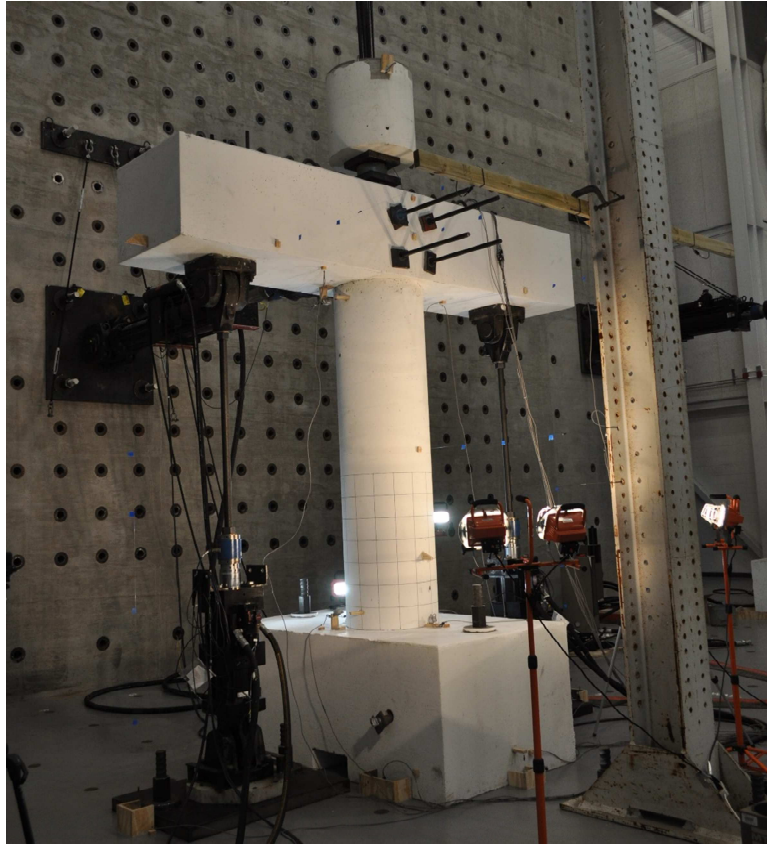


Figure 7.13. RC rocking column test setup.

Table 7.4. Instrumentation list for RC rocking column.

Sensor ID	Type	Stroke (in)	Purpose	Location
SP-1	String Potentiometer	50 (± 25)	Lateral displacement	Lateral load center line on east side of cap-beam
SP-2				Mid-height of column on east side
SP-3				11.5" above SP-1 on cap-beam
SP-4				Southeast side of cap-beam
SP-5		24 (± 12)		Northeast side of cap-beam
SP-6		4 (± 2)	Column sliding	Top-south side of column
SP-7				Top-north side of column
SP-8				Bottom-south side of column
SP-9				Bottom-north side of column
SP-10		12 (± 6)	Joint opening (for curvature calculations)	East side of column
SP-11				West side of column
SP-12		4 (± 2)	Foundation uplift	East side of foundation
SP-13				West side of foundation
SP-14			Foundation sliding	South side of foundation
SP-15				North side of foundation

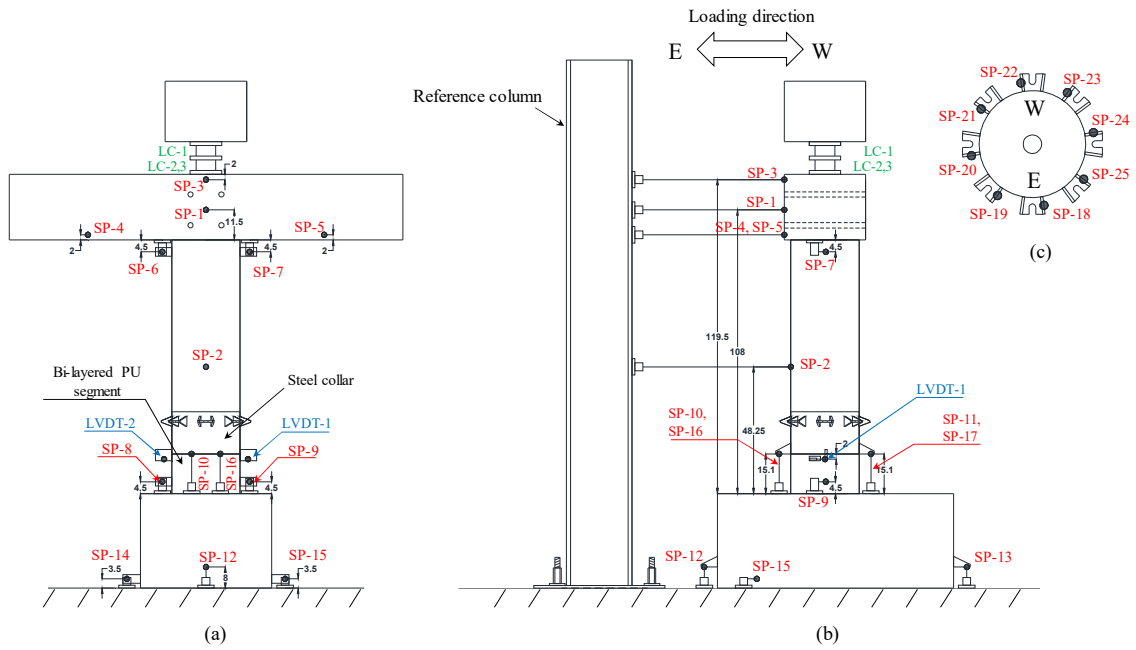


Figure 7.14. Schematic representation of instrumentation for PUED rocking specimen: (a) south-north elevation (looking west); (b) east-west elevation (looking south); (c) ED link elongation string potentiometers (Note: ED links not shown).



Figure 7.15. PUEd column test setup.

Table 7.5. Instrumentation list for PUED-1 and PUED-2 columns.

Sensor ID	Type	Stroke (in)	Purpose	Location	
SP-1	String Potentiometer	50 (±25)	Lateral displacement	Lateral load center line on east side of cap-beam	
SP-2				Mid-height of column on east side	
SP-3				11.5" above SP-1 on cap-beam	
SP-4				Southeast side of cap-beam	
SP-5		24 (±12)	Northeast side of cap-beam		
SP-6		4 (±2)	Column sliding	Top-south side of column	
SP-7				Top-north side of column	
SP-8				Bottom-south side of column	
SP-9				Bottom-north side of column	
SP-10		12 (±6)	Joint opening (for curvature calculations)	East side of steel collar-bottom	
SP-16				East side of steel collar-bottom	
SP-11				West side of steel collar-bottom	
SP-17				West side of steel collar-bottom	
SP-12		4 (±2)	Foundation uplift	East side of foundation	
SP-13				West side of foundation	
SP-14			Foundation sliding	South side of foundation	
SP-15				North side of foundation	
SP-18		12 (±6)	ED link deformation	East side of steel collar-top	
SP-19				Southeast side of steel collar-top	
SP-20		4 (±2)		South side of steel collar-top	
SP-21		12 (±6)		Southwest side of steel collar-top	
SP-22				West side of steel collar-top	
SP-23				Northwest side of steel collar-top	
SP-24		4 (±2)		North side of steel collar-top	
SP-25		12 (±6)		Northeast side of steel collar-top	
LVDT -1	Linear Variable Differential Transformer	0.5 (±25)		Sliding at the top joint of PU segment	North side of PU segment-top
LVDT -2					South side of PU segment-top

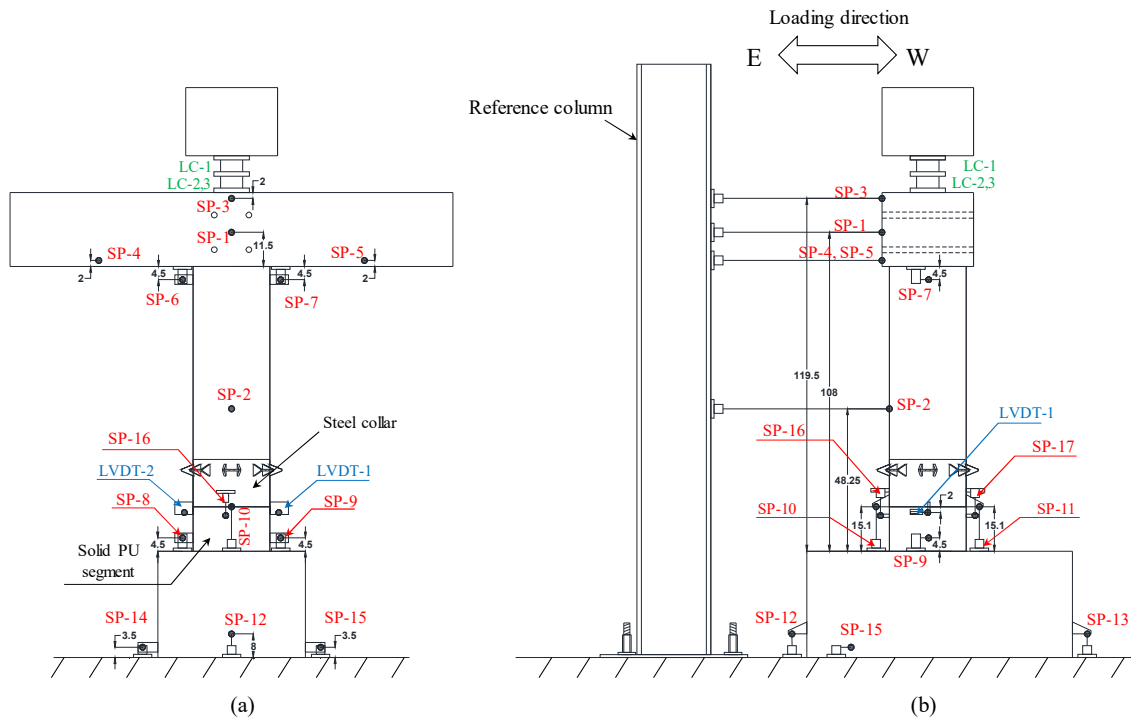


Figure 7.16. Schematic representation of instrumentation for PU rocking specimen: (a) south-north elevation (looking west); (b) east-west elevation (looking south) (Note: ED links not shown.).

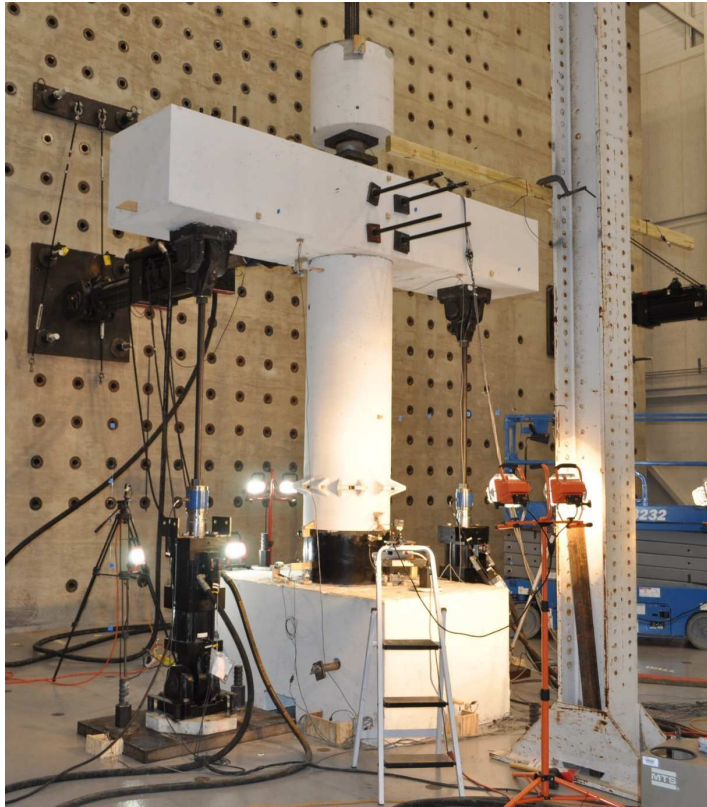


Figure 7.17. PU enhanced column test setup.

Table 7.6. Instrumentation list for PU column.

Sensor ID	Type	Stroke (in)	Purpose	Location
SP-1	String Potentiometer	50 (±25)	Lateral displacement	Lateral load center line on east side of cap-beam
SP-2				Mid-height of column on east side
SP-3				11.5" above SP-1 on cap-beam
SP-4				Southeast side of cap-beam
SP-5				Northeast side of cap-beam
SP-6		4 (±2)	Column sliding	Top-south side of column
SP-7				Top-north side of column
SP-8				Bottom-south side of column
SP-9				Bottom-north side of column
SP-10		12 (±6)	Joint opening (for curvature calculations)	East side of PU segment-Bottom
SP-11				West side of PU segment-Bottom
SP-12		4 (±2)	Foundation uplift	East side of foundation
SP-13				West side of foundation
SP-14			Foundation sliding	South side of foundation
SP-15				North side of foundation
SP-16		4 (±2)	Joint opening (for curvature calculations)	East side of PU segment-Top
SP-17				West side of PU segment-Top
LVDT-1	Linear Variable Differential Transformer	0.5 (±25)	Sliding at the top joint of PU segment	North side of PU segment-top
LVDT-2				South side of PU segment-top

7.7. Data Acquisition and Control System

7.7.1. Data Acquisition System

The data acquisition system included two National Instrument (NI) SCXI 1001 chassis with an input frequency range of 47 Hz-73 Hz, which were used to acquire analogue signals from the instrumentation channels and convert them into a digital format. Each chassis was loaded with 12 SCXI modules of different types, including SCXI-1315

(for LVDTs), and SCXI-1314 (for load cells and string potentiometers). Both chassis were synchronized to record simultaneously. A sampling rate of 64 readings per second was used to provide sufficient accuracy during quasi-static testing at a loading rate of approximately 0.1 in/sec, while for tests at higher loading rate (1.08-5.4 in/sec), a sampling rate of 512 readings per second was adopted.

In addition to the abovementioned recorded signals, digital videos were taken with five cameras during each tests to record the global and local behavior of the specimens. Four cameras were zoomed on the specimen in the vicinity of the column-footing joint from northeast, northwest, southeast, and southwest. One camera recorded the entire setup from southeast. Moreover, to document localized damage in different components of each specimen, digital photos and notes were taken before and after each loading step. Also, concrete cracks occurred during each loading step were traced with colored markers in the intervals between the loading steps.

7.7.2. Control System

Each column specimen was loaded in the vertical direction by two MTS 204-12 actuators with a stroke of 6" (± 3 ") and standard rated force capacity of 110 kips in tension and compression. The lateral load was applied by an MTS 244-51S actuator with a static and dynamic stroke of 31.25" (± 15.625 ") and 30" (± 15 "), respectively, and standard rated force capacity of 220 kips in tension and compression.

7.8. Data Processing

The measured test data were filtered by a second order zero-phase Butterworth low-pass filter with a corner frequency of 1 Hz, which was found adequate to remove the noise from the recorded test data without any major distortion.

7.9. Construction Procedure

7.9.1. Specimens

The test specimens were constructed at Texas A&M University's Center for Infrastructure Renewal (CIR) at Rellis campus. Reinforcement cages for all RC segments were assembled at CIR's high-bay lab (Figure 7.19).

The post-tensioning system was a single unbonded tendon comprised of 12 0.6" diameter Grade 270 seven-wire low relaxation strands compliant to ASTM A-416. The PT anchorage system was a two-part multiplane anchor, which is primarily used for longitudinal tendons in bridges. The system consists of a compact conical body with three load transfer planes and a wedge plate (Figure 7.18). The separation of anchor body and wedge plate allows to insert strands after casting the concrete. A polyethylene (PE) trumpet deviates the strands into the central circular duct (4" PVC pipe herein). A #5 @ 2 ¼" Grade 60 anchor spiral provides the required confinement at the local anchor zone.

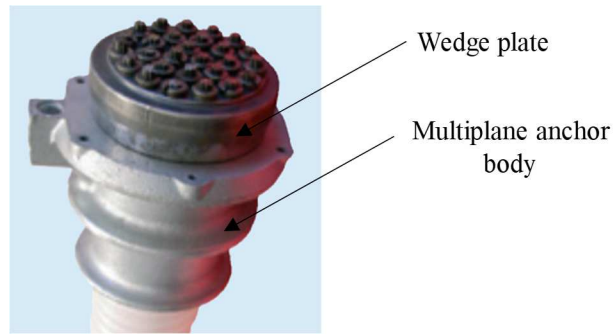


Figure 7.18. Components of the PT anchorage system.



Figure 7.19. Reinforcement cages: (a) RC rocking column; (b) PT anchorage block; (c) central core of PU bi-layered segment; (d) RC segment with steel collar; (e) cap beam.

The embedded components of the PT system including the multiplane conical body, PE trumpet, and PVC pipe (tendon duct), were assembled and held in place at the base of the foundation formwork and secured in place with four bolts. The anchor spiral was placed in the form around the multiplane conical body. To prevent concrete from

entering the embedded components, all the holes and edges of contact surfaces were sealed using a fast curing silicone sealant. The rebar cage was lowered into the formwork. Two 3" PVC pipes for passing the lifting rods were placed in position horizontally and were secured in place by passing through the holes in the formwork side walls. Two 3" PVC pipes were placed in position vertically for inserting the tie-down bars. The pipes were secured in place by passing through a hole at the casting bed. Holes were cut-out from a 1/2" plywood sheet matching the pattern of ED links in plan. The coupling setups for ED links (end anchor setup) including the coupling nut and the all-thread rod (Figure 7.20(b)) were aligned with the holes on the plywood sheet and secured to the plywood with a customized bolt (made of a piece of an all-thread rod with a nut welded to one end). The plywood sheet with the ED links' end anchor setups was moved in place in the rebar cage and centered as precise as possible. The plywood sheet was secured in place by staples. Finally, the end anchor washer and nuts were attached in place.



Figure 7.20. (a) Foundation rebar cage in formwork; (b) ED link end anchor setup.

For all RC elements, cardboard forming tubes, termed “sonotubes” per the name of the corresponding manufacturer, of inner diameter of 26” were used as the formwork. For the RC rocking column, the central 4” PVC pipe was attached to the base of the formwork. To prevent concrete from entering the pipe, the pipe was sealed using a fast curing silicone sealant. The cardboard forming tube was braced laterally to avoid any lateral instability during casting of the concrete. Then, the rebar cage was lowered into the formwork. Two 1” lifting nuts were placed in the formwork and secured in place with temporary bolts. Finally, the PVC pipe was centered and secured in place with #3 rebars. To prevent concrete from entering the PVC pipe, the top end of the pipe was sealed using duct tape.

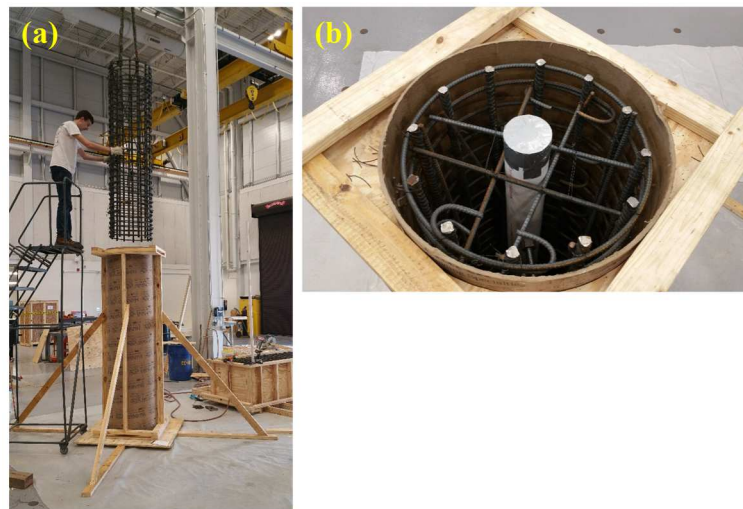


Figure 7.21. (a) Lowering the rebar cage of RC rocking column to formwork; (b) central PVC pipe secured and sealed.

The steel collar was fabricated from a steel pipe of outside diameter of 26" with a wall thickness of 0.75". The mounting eyes for the ED links, including the horizontal plate with the slotted hole and side stiffeners, were fabricated from 1" steel plates.

For the RC element with the steel collar, the base of the formwork was elevated for the insert pipe sticking out from the bottom of the segment. First, the 4" (inner) diameter steel pipe was positioned and sealed to prevent any leakage. Then, the steel collar was lowered in place and sealed. The central pipe system including the adapters and the PVC pipe was assembled. The cardboard forming tube was placed in position and braced for lateral stability. The rebar cage was lowered into the formwork. Two 1" lifting nuts were placed in the formwork and secured in place with temporary bolts. The central PVC pipe was centered and secured in place with #3 rebars. To prevent concrete from entering the PVC pipe, the top end of the pipe was sealed using duct tape.

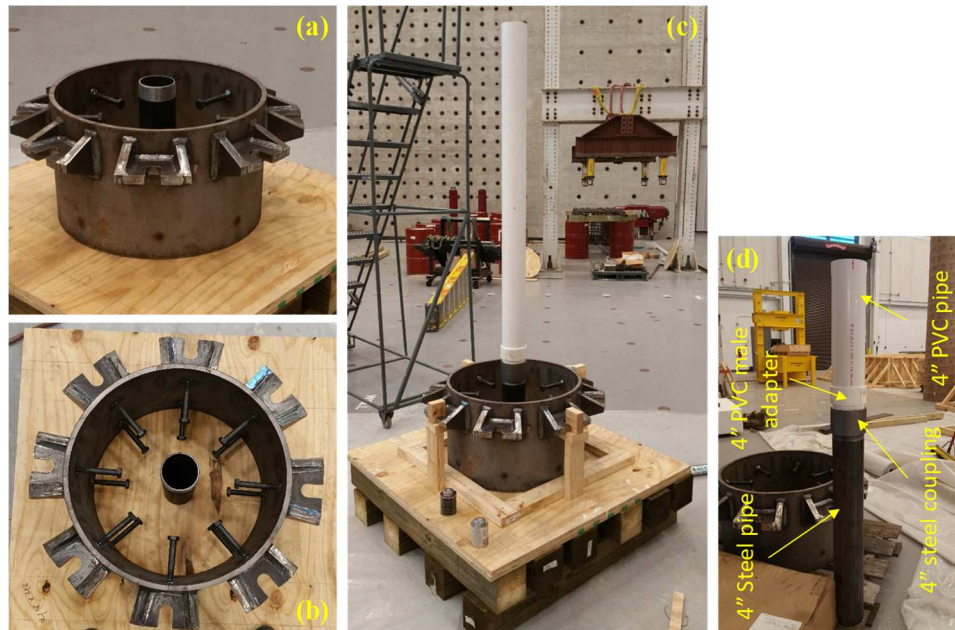


Figure 7.22. Construction steps for RC segment with steel collar: (a) steel collar and central steel pipe; (b) plan view of steel collar and central steel pipe; (c) central pipe assembled; (d) details of the central pipe assembly.

For the PT anchorage block, similar to the foundation block, the embedded components of the PT system including the multiplane conical body (Figure 7.18), PE (polyethylene) trumpet, and PVC pipe were assembled and held in place at the base of the formwork and secured in place with four bolts. Finally, the anchor spiral was placed in the formwork around the multiplane conical body. To prevent concrete from entering the embedded components, all the holes and edges of contact surfaces were sealed using a fast curing silicone sealant. The cardboard forming tube was placed and sealed to avoid any leakage. The rebar cage was lowered into the formwork. Two 1" lifting nuts were placed in the formwork and secured in place with temporary bolts. Finally, the PVC pipe was

centered and secured in place with #3 rebar. To prevent concrete from entering the PVC pipe, the top end of the pipe was sealed using duct tape.



Figure 7.23. Construction steps for PT anchorage block: (a) embedded components of the PT system; (b) top view of the final assembly; (c) isometric view of the final assembly.

For the cap beam, first the rebar cage lowered into the formwork. The central 4” PVC pipe, which serves as the tendon duct, was placed in position and secured by passing through holes at the casting bed and tied to the reinforcement cage with tie wires at the top. Four 1.5” PVC pipes were placed in position at each end with the pattern matching with the attachment holes on the vertical actuators’ swivel. The pipes were secured in place by passing through holes at the casting bed and with #3 bars tied to the reinforcement cage rebar on top. Also, four 2” PVC pipes were placed in position at the center of the cap beam with the pattern matching with the attachment holes on the horizontal actuator’s swivel. The pipes were secured in place by passing through the holes in the formwork side walls. Four lifting hooks were placed in position and secured to the reinforcement cage

with tie wire. To prevent concrete from entering the PVC pipe, the top end of the pipe was sealed using duct tape.



Figure 7.24. Cap beam reinforcement cage in the formwork: final assembly.

For the bi-layered PU segment, the PU sleeve was used as the formwork for casting the central reinforced concrete core. The PU sleeve was placed on a plywood sheet as the casting bed. The edges were carefully sealed to prevent any concrete leakage. The central steel pipe of 5.5" (outside) diameter was placed in position and centered. To prevent concrete from entering the pipe, the pipe was carefully sealed with a silicone sealant at the bottom and the top end was sealed with duct tape.

Figure 7.25 shows all elements (except for the bi-layered PU segment) in the formwork prior to casting. All the RC elements except for the central core of the bi-layered

PU segment were cast on the same day. The RC column, PT anchorage block, and cap beam were cast in the morning (Figure 7.26(a)) and RC element with steel collar and foundation block were cast in the afternoon using a different concrete batch (Figure 7.26(b)). The central cores of the bi-layered PU segments were cast in another day using a different concrete batch.

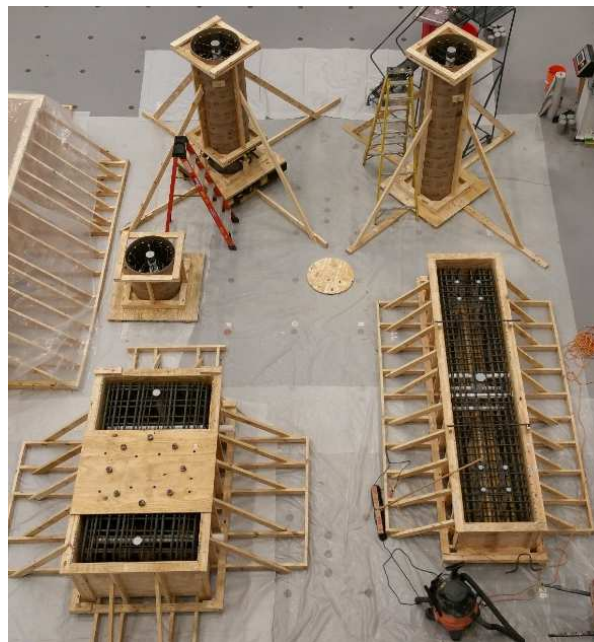


Figure 7.25. RC elements in the formwork prior to casting.

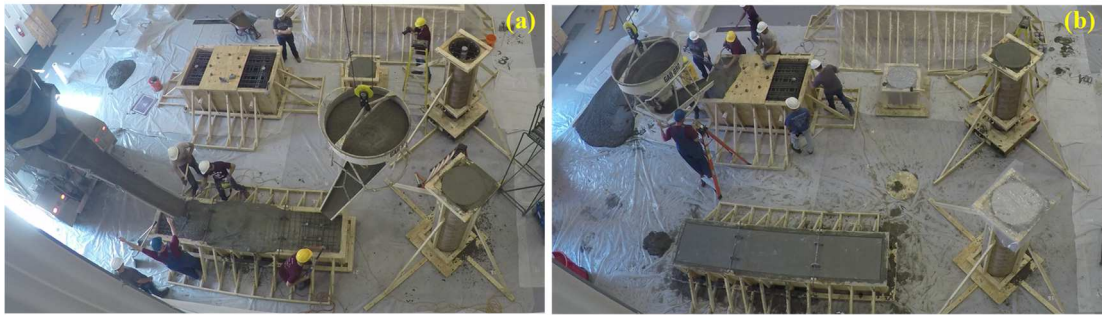


Figure 7.26. Casting: (a) first batch (morning); (b) second batch (afternoon).

After demolding the specimens, surface air voids were observed on the top surface of the foundation block due to the entrapment of air bubbles in the surface of the top plywood sheet used to hold the end anchor setup for ED links in place (Figure 7.27(a)). The surface was patched with a non-shrink grout compliant with ASTM C-1107 that can achieve up to 14 ksi compression strength at 28 days (Figure 7.27(b)).

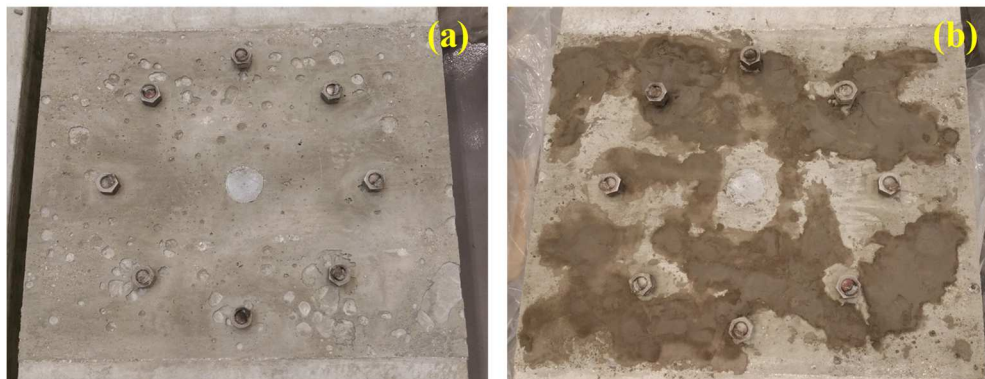


Figure 7.27. (a) Surface air voids were observed on the top surface of the foundation block; (b) surface patched with non-shrink grout.

The PU segments including the sleeve and solid segment were cast at the facilities of an outside contractor. The mold for the hollow core PU sleeve consists of a base plate, two steel cylindrical shells, with PU material cast in between, and the top lid. The inner shell was a three-part steel cylinder while the outer shell was a two-part steel cylinder. Both the inner and outer shells were bolted to the base plate. To prevent the PU leaking from the mold, the contact surface was sealed with a rubber strip attached to the bottom side of the shells with a silicone sealant. The top lid was bolted to the inner and outer shells and sealed similar to the bottom end. For additional protection against leakage, all the bolted connections were sealed with the silicone sealant. The silicone sealant was heated with a heat gun to expedite the curing. The mixed solution of the PU material was injected into the mold from the bottom through a plastic pipe connected to the inlet placed on the outer shell. To prevent air entrapping in the material, an outlet was fabricated on the top lid to allow the air flowing out of the mold while casting. The solid PU segment was cast in a similar way with the difference that the inner steel shell was replaced with a 5" PVC pipe. The PU material was allowed to cure for 24 hours before demolding.



Figure 7.28. Casting of PU sleeve: (a) mold shells bolted to the base plate; (b) sealing the top interface; (c) heating the silicone sealant; (d) bolting the top lid; (e) sealing bolted connections; (f) final mold assembly prior to casting; (g) injecting the PU material solution; (h) PU sleeve after demolding.

7.9.2. Test Setup Assembly

Assembly of test specimens was very straightforward, and in agreement with the objectives of accelerated bridge construction (ABC), the total assembly time for each specimen was approximately 1.5-3 hours. According to the erection procedure followed (Figure 7.29 and Figure 7.30):

- The foundation block was first placed on two steel beams, and then the bottom end wedge plate was secured in place (Figure 7.29(a)).
- Mono-strands were passed through the central duct of the foundation block from the top to the bottom (Figure 7.29(a)).
- A three-piece wedge-anchor was mounted on each mono-strand from the bottom end.
- Mono-strands were bundled together as a single tendon using duct tape at several locations over the length of mono-strands.
- The foundation block was lowered in place on the strong floor and tied down with two #18 Dywidag bars.
- The concrete elements (i.e. columns and solid or bi-layered PU segment) were lifted and lowered in place by passing through the tendon with the primary crane while the tendon was held up straight with a secondary crane (Figure 7.29(c) and Figure 7.30).
- The foot plates of the two vertical actuators were placed in position on the floor and tied down with Dywidag bars.
- The cap beam assembly (including the cap-beam and the two vertical actuators) was lifted and lowered in place by passing through the tendon. The

cap beam assembly was supported by the fork lift prior to applications of the post-tensioning load (Figure 7.29(d) and (e)).

- Load cells were passed through the tendon and placed in position (Figure 7.29(e)).
- The last component to be placed was the PT anchorage block, which was lifted and lowered in place, with the tendon passing through (Figure 7.29(f)).
- After placing the top wedge plate and wedge-anchors, the post-tensioning load was applied monostrand after monostrand in 2 or three cycles using a monostrand post-tensioning jack (Figure 7.29(g)).
- Each vertical actuator was attached to the foot plate with four 1” bolts.

The surface of ED bars was lubricated with an all-purpose grease to reduce the friction between the bar and confining tube. The ED links were assembled and installed on the specimen prior to the test, while the top connection was tightened after the vertical load was applied. It should be noted that due to accumulated construction discrepancies, while installing ED links on the PUEC column, four ED links (ED-1, ED-7, ED-8, and ED-6 as shown in Figure 7.31) did not fit in the slotted hole of the mounting eye on the steel collar with enough clearance, which would be necessary for removing and replacing (if needed) ED links after a test. To provide the required clearance, the slotted holes of the abovementioned ED links were further enlarged by approximately ¼” with an oxy-fuel cut.



Figure 7.29. Test setup assembly steps for RC rocking specimen: (a) foundation blocked to pass the strands; (b) lowering the foundation block; (c) lowering segment(s); (d) lowering cap-beam-actuators assembly; (e) placing load cells in position; (f) lowering PT anchorage block; (g) post-tensioning.

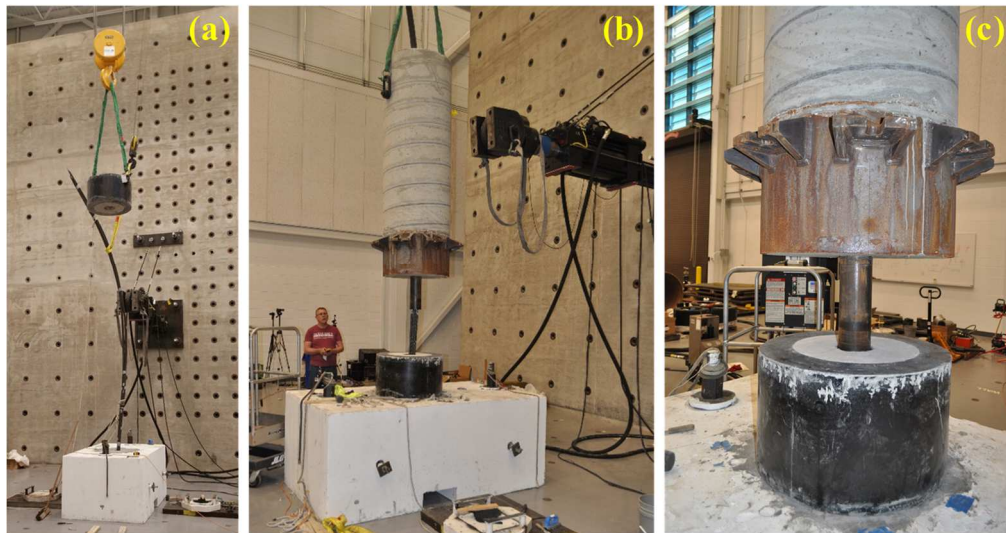


Figure 7.30. Test setup assembly for PU-enhanced column with bi-layered PU segment: (a) moving bi-layered PU segment; (b) lowering the RC segment with steel collar in place; (c) passing the pipe sticking out of the RC segment through the PU segment.

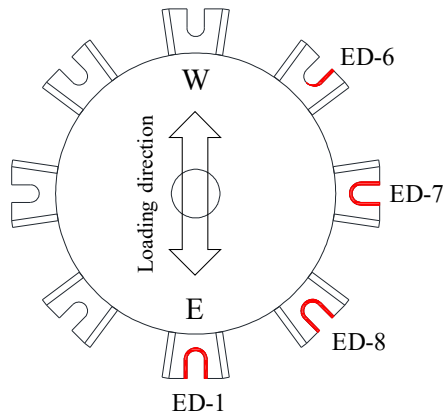


Figure 7.31. Location of enlarged slotted holes on mounting eyes of the steel collar (the cut is shown in red).

7.10. Material Properties

7.10.1. Concrete

The specified compressive strength of the concrete in all segments was 8 ksi with a maximum aggregate size of 3/8". Due to the high congestion of reinforcement in the specimens, especially the foundation, concrete with a higher slump was used for all specimens. The slump for the concrete batch poured in the morning (RC rocking column, PT anchorage block, and cap beam) and afternoon (RC segment with steel collar and foundation) was 8.5" and 7", respectively.

The compression strength of the concrete material used in casting the specimens was determined through testing 4"×8" cylindrical samples collected during the pour. The compression strength of concrete was measured at 28 days and on each test day. The results are summarized in Table 7.7.

Table 7.7. Concrete compression strength.

Batch ¹	Age	Average Strength ²
	(days)	(ksi)
A	28	6.77
	248*	8.28
	304**	8.52
B	28	7.71
	304**	9.03
	321+	9.14
C	28	8.04
	256**	10.14

1 – Batch A: RC rocking column, PT anchorage block, and cap beam

– Batch B: RC segment with steel collar and foundation block

– Batch C: central core of bi-layered PU segment.

2 – Average of three samples.

* RC rocking specimen test day.

** PUEd-1 specimen test day.

+ PU specimen test day.

7.10.2. Reinforcing Steel

All the reinforcing steel was specified as ASTM 615 Gr. 60 (2018) deformed bar.

The measured mechanical properties of rebar per the mill test certificates provided by the rebar supplier are summarized in Table 7.8.

Table 7.8. Mechanical properties of the reinforcing steel.

Rebar Size	Yield Strength	Tensile Strength	Elongation	Elongation Gage Length
	(ksi)	(ksi)	(%)	(in)
# 4	70.5	100.4	13.1	8
# 5	66.7	105.3	13	8
# 8	67.4	104.8	15	8

7.10.3. Post-tensioning Strands

The post tensioning strands were specified as Grade 270 seven-wire low relaxation strands compliant to ASTM A416 (2018) with nominal diameter of 0.6", minimum yield strength $f_y=243$ ksi, tensile strength $f_u= 270$ ksi, and elastic modulus $E=28000$ ksi.

7.10.4. PU Material

Three 2"×4" cylindrical samples complying to ASTM D695 (2010) were taken from each PU batch used in casting PU segments. The cylindrical samples were subjected, via the setup of Figure 7.32, to strain-controlled monotonic compression loading up to a peak nominal strain of about 0.1 followed by unloading to zero stress. Tests were conducted with the following strain rates: 0.001, 0.01, and 0.05 /sec. The stress vs. strain responses from various tests for the PU sleeve are presented in Figure 7.33. The overall response at various strain rates is similar to the response of samples tested at SMTL at the University of Colorado – Boulder presented in Section 3. According to Figure 7.34, the material used in casting the PU sleeve (tested at CIR) shows slightly higher peak strength, especially at 0.05 /sec strain rate, compared to the material tested at SMTL for material characterization purposes. The difference in the observed response of samples tested at CIR and SMTL is not only be attributed to small differences in the material properties of the two batches from which the samples were cast, but it also accounts for facility-to-facility driven variations in the test executions and measurements, because the specimens were tested at two different facilities using different loading frames and instrumentation.

It should be noted that the sudden drop observed in the unloading branch of the test at 0.001 /sec performed at CIR was due to operator error (Figure 7.33 and Figure 7.34), which resulted in halting the loading for a few seconds.

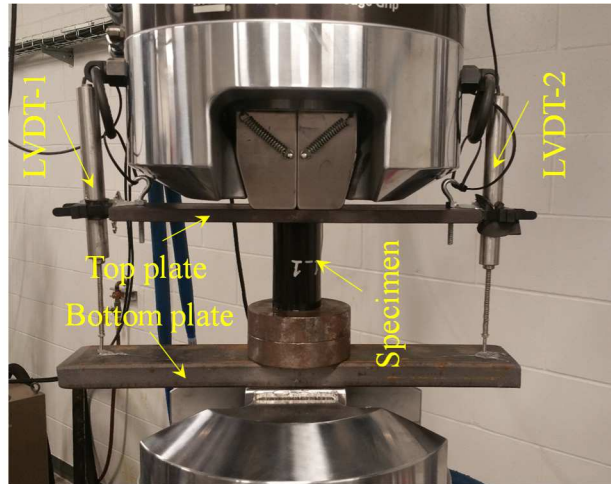


Figure 7.32. Test setup for compression test on cylindrical specimens.

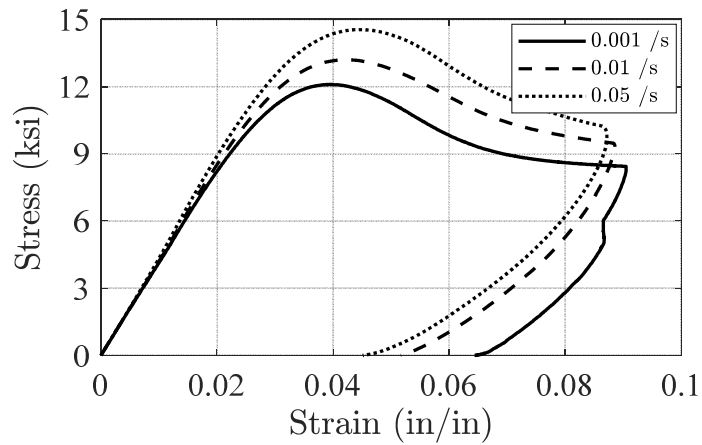


Figure 7.33. Compressive stress-strain curves at various strain rates.

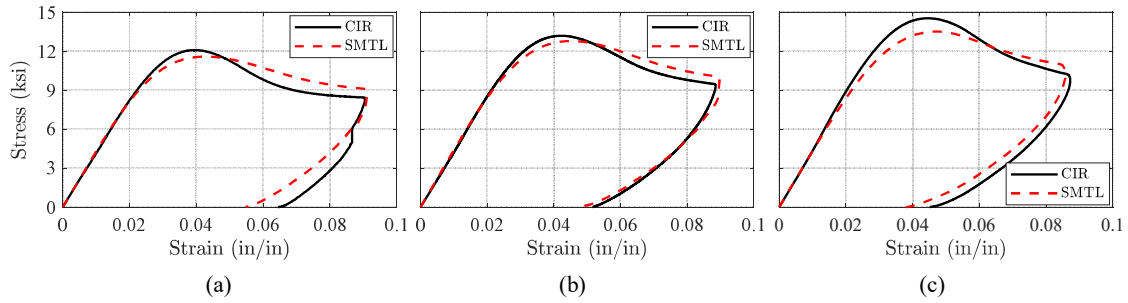


Figure 7.34. Comparison of compressive stress-strain curves for specimens tested at CIR and SMTL at various strain rates: (a) 0.001 /sec; (b) 0.01 /sec; (c) 0.05 /sec.

7.10.5. Energy Dissipation (ED) Links

The ED links were specified as Grade 36 steel compliant with ASTM A36 (2019) with a minimum yield strength of $f_y=36$ ksi and tensile strength of $f_u=58-80$ ksi.

7.10.6. Steel Collar and Attachments

The steel collar and attachment eyes were specified by the provider as Grade 50 steel compliant with ASTM A572 (2015).

7.11. Loading Sequence

7.11.1. RC Rocking Column

First, the specimen was post-tensioned monostrand-by-monostrand using a hydraulic jack. The total target initial post-tensioning load was 475 kips. The post-tensioning load was monitored during the stressing using two load cells stacked between the cap beam and the PT anchorage block. Strands were tensioned sequentially in two

stages. The initially achieved PT load in the tendon was 458 kips. The post-tensioning load was 432 kips after 78 days at test day, corresponding to 5.68% loss.

Second, the vertical gravity load of 218 kips was slowly (0.5-1.0 kips/sec) applied by the two vertical actuators (X2 and X3 in Figure 7.11). Displacement-controlled sinusoidal reversed cyclic loading was subsequently applied following the loading protocol summarized in Table 7.9. The selected loading protocol consisted of sets of symmetric cycles of increasing amplitude up to the maximum working stroke of the horizontal actuator (X1 in Figure 7.11), which was 14.5 in. resulting in a peak drift ratio of 13.39%. Each set included two cycles of the same amplitude. Displacement amplitudes and the corresponding drift ratios applied are shown in Table 7.9. The drift ratio was defined as the ratio of the lateral displacement at the location of lateral load application to the height of that location from the footing (108.25 in.). The loading was applied at a rate of 0.1-0.3 in/sec (Table 7.9) corresponding to a drift ratio rate of 0.001-0.0028 /sec.

Table 7.9. Displacement-controlled loading sequence for RC rocking column.

Cycle No.	Displacement	Drift Ratio	Number of cycles	Frequency	Displacement Rate	Drift Ratio Rate
	(in)	(%)		(Hz)	(in/sec)	/sec
1	0.5	0.46	2	0.050000	0.1	0.0009
2	1	0.92	2	0.025000	0.1	0.0009
3	2	1.85	2	0.012500	0.1	0.0009
4	4	3.70	2	0.006250	0.1	0.0009
5	6	5.54	2	0.004167	0.1	0.0009
6	8	7.39	2	0.003125	0.1	0.0009
7	10	9.24	2	0.002500	0.1	0.0009
8	12	11.09	2	0.002083	0.1	0.0009
9	14	12.93	2	0.001786	0.1	0.0009
10	14.5	13.39	2	0.005172	0.3	0.0028

7.11.2. PU Rocking Column with Bi-layered PU Segment and ED Links

7.11.2.1. Phase 1 – PUED-1 Specimen

Similar to the RC rocking column, first, the specimen was post-tensioned monostrand-by-monostrand using a hydraulic jack. The target initial post-tensioning load was 475 kips. The post-tensioning load was monitored during the stressing using two load cells stacked between the cap beam and the PT anchorage block. Strands were tensioned sequentially in two stages. The final achieved load in the tendon was 451.3 kips. The post-

tensioning load was 443.7 kips on the test day, which was after 15 days later, corresponding to a loss of 1.7%.

Second, the axial gravity load of 218 kips was slowly (0.5-1.0 kips/sec) applied by the two vertical actuators (X2 and X3 in Figure 7.11)

The measured PT load decreased to 437.7 kips after the vertical load was applied, corresponding to 1.37% loss relative to the value before the vertical load was applied. Displacement-controlled sinusoidal reversed cyclic loading was subsequently applied following the loading protocol summarized in Table 7.10. The selected loading protocol consisted of sets of symmetric cycles at amplitudes corresponding to various hazard levels including $0.4 \times DE$, $0.6 \times DE$, $1.2 \times DE$, and $1.8 \times DE$ ($1.2 \times MCE$). The displacement demand corresponding to various hazard levels was defined following the CSM procedure (see Table 7.3). Each set included two cycles of the same amplitude. Displacement amplitudes and the corresponding drift ratios applied are shown in Table 7.10. The loading was applied at a rate of 0.1 in/sec corresponding to a drift ratio rate of 0.001 /sec.

Table 7.10. Displacement-controlled loading sequence for PUED-1 rocking column.

Test ID	Hazard Level	Displacement	Drift Ratio	Number of cycles	Frequency	Displacement Rate	Drift Ratio Rate
		(in)	(%)		(Hz)	(in/sec)	/sec
PUED1_0.4DE	0.4×DE	0.65	0.60	2	0.042308	0.1	0.0010
PUED1_0.6DE	0.6×DE	1.1	1.02	2	0.025000	0.1	0.0010
PUED1_1.2DE	1.2×DE	3.5	3.23	2	0.007857	0.1	0.0010
PUED1_1.8DE	1.8×DE (1.2×MCE)	6.7	6.19	2	0.004104	0.1	0.0010

7.11.2.2. Phase 2 – PUED-2 Specimen (ED links Replaced)

At the end of the PUED-1 test, all the ED links were replaced with new links. After replacement, the axial gravity load of 218 kips was slowly (0.5-1.0 kips/sec) applied by the two vertical actuators (X2 and X3 in Figure 7.11). Displacement-controlled sinusoidal reversed cyclic loading was subsequently applied in four phases following the loading protocol summarized in Table 7.11.

In the first phase (Phase 2.1), the selected loading protocol consisted of sets of symmetric cycles at amplitudes corresponding to various hazard levels including 0.4×DE, 0.6×DE, and 1.2×DE. Each set included two cycles of the same amplitude. The loading was applied at a rate of 0.1 in/sec corresponding to a drift rate of 0.001 /sec.

At this point, to evaluate the re-centering capacity of the system upon releasing the ED links, all the ED links were released, allowing the system to re-center, and then re-

tightened. Next, displacement-controlled sinusoidal reversed cyclic loading was subsequently applied in the second phase (Phase 2.2), consisted of sets of symmetric cycles at amplitudes corresponding to various hazard levels including $0.4 \times DE$, $0.6 \times DE$, $1.2 \times DE$, and $1.8 \times DE$ ($1.2 \times MCE$). Each set included two cycles of the same amplitude. The loading was applied at a rate of 0.1 in/sec corresponding to a drift rate of 0.001 /sec.

At the end of the Phase 2.2, the fractured ED links (ED-1 and ED-5) were removed. Subsequently, in the third phase (Phase 2.3), displacement-controlled sinusoidal reversed cyclic loading was applied, which consisted of symmetric cycles at amplitudes corresponding to various hazard levels including $0.4 \times DE$, $0.6 \times DE$, $1.2 \times DE$, and $1.8 \times DE$ ($1.2 \times MCE$). Each set included two cycles of the same amplitude. For each hazard level, the loading was applied at increasing rates, including 0.1, 1.08, 2.71, and 5.41 in/sec corresponding to a drift rate of 0.001, 0.01, 0.025, and 0.05 /sec (Table 7.11). The objective of Phase 2.3 was to assess the remaining capacity of the system after failure of the two links.

At the end of the Phase 2.3, the damaged ED links (ED-2, 4, 6 and 8) were removed. Finally, in the fourth phase (Phase 2.4), displacement-controlled sinusoidal reversed cyclic loading was applied, consisted of symmetric cycles at amplitudes of 8 in. and 10 in. Each set included two cycles of the same amplitude. For each amplitude, the loading was applied at various rates including 1.08 and 2.71 in/sec corresponding to a drift ratio rate of 0.01 and 0.025 /sec (Table 7.11). The objective of Phase 2.4 was to investigate the ultimate failure and potential collapse of the PU-enhanced column design.

Table 7.11. Displacement-controlled loading sequence for PUEd-2 rocking column.

Phase	Test ID	Hazard Level	Drift Ratio		Number of cycles	Frequency (Hz)	Displacement Rate (in/sec)	Drift Ratio /sec
			Displacement (in)	(%)				
Phase 2.1	PUEd2_R1_0.4DE	0.4×DE	0.65	0.60	2	0.0423	0.11	0.0010
	PUEd2_R1_0.6DE_1	0.6×DE	1.1	1.02	2	0.0250	0.11	0.0010
	PUEd2_R1_1.2DE_2	1.2×DE	3.5	3.23	2	0.0079	0.11	0.0010
ED links released and retightened								
Phase 2.2	PUEd2_R1_0.4DE_2	0.4×DE	0.65	0.60	2	0.0423	0.11	0.0010
	PUEd2_R1_0.6DE_2	0.6×DE	1.1	1.02	2	0.0250	0.11	0.0010
	PUEd2_R1_1.2DE_2	1.2×DE	3.5	3.23	2	0.0079	0.11	0.0010
	PUEd2_R1_1.8DE_1	1.8×DE (1.2×MCE)	6.7	6.19	2	0.0041	0.11	0.0010
Two fractured ED links removed								
Phase 2.3	PUEd2_Rvar_0.4DE_3	0.4×DE	0.65	0.60	2	0.0423	0.11	0.0010
					2	0.4163	1.08	0.0100
					2	1.0409	2.71	0.0250
	PUEd2_Rvar_0.6DE_3	0.6×DE	1.1	1.1	2	2.0817	5.41	0.0500
					2	0.0250	0.11	0.0010
					2	0.2460	1.08	0.0100
					2	0.6151	2.71	0.0250
	PUEd2_Rvar_1.2DE_3	1.2×DE	3.5	3.23	2	1.2301	5.41	0.0500
					2	0.0079	0.11	0.0010
					2	0.0773	1.08	0.0100
PUEd2_R2_1.8DE_2	1.8×DE (1.2×MCE)	6.7	6.19	2	0.1933	2.71	0.0250	
				2	0.0404	1.08	0.0100	
Four ED links removed								
Phase 2.4	PUEd2_Rvar_8in	-	8	7.39	2	0.0338	1.08	0.0100
					2	0.0846	2.71	0.0250
					2	0.0271	1.08	0.0100
	PUEd2_Rvar_10in	-	10	9.24	1	0.0271	1.08	0.0100

7.11.3. PU Rocking Column with Solid PU Segment

Similar to the other specimens, first, the specimen was post-tensioned monostrand-by-monostrand using a hydraulic jack. The target initial post-tensioning load was 475 kips. The post-tensioning load was monitored during the stressing using two load cells stacked between the cap beam and the PT anchorage block. Strands were tensioned sequentially in two stages. The final achieved load in the tendon was 447 kips. Then, the vertical gravity load of 218 kips was slowly (0.5-1.0 kips/sec) applied by the two vertical actuators (X2 and X3 in Figure 7.11). The measured PT load decreased to 432 kips after the vertical load was applied, corresponding to 3.36% loss relative to the initial PT load. The post-tensioning load was 422 kips on the test day, which was 5 days later, corresponding to a 2.3% loss relative to the PT load after the gravity load was applied. After the gravity load was removed and reapplied at test day, the measured PT load was 429.2, corresponding to a total loss of 3.98% relative to the initial PT load (Table 7.12).

Table 7.12. PT load and PT loss at different states.

	Initial	After Gravity	After 5 days	After Gravity on test day
PT load (kips)	447	432	422	429.2
PT loss¹ (%)	-	3.36	5.59	3.98

1 – Relative to the initial PT load.

Displacement-controlled sinusoidal reversed cyclic loading was subsequently applied following the loading protocol summarized in Table 7.13. The selected loading protocol consisted of sets of symmetric cycles at amplitudes corresponding to various hazard levels including $0.4 \times DE$, $0.6 \times DE$, $1.2 \times DE$, and $1.8 \times DE$ ($1.2 \times MCE$). Each set included two cycles of the same amplitude. Displacement amplitudes and the corresponding drift ratios applied are shown in Table 7.13. The loading was applied at various rates including 0.1, 1.08, 2.71, and 5.41 in/sec corresponding to a drift rate of 0.001, 0.01, 0.025, and 0.05 /sec, respectively (Table 7.13).

Table 7.13. Displacement-controlled loading sequence for PU rocking column.

Test ID	Hazard Level	Displacement	Drift Ratio	Number of cycles	Frequency	Displacement Rate	Drift Ratio Rate
		(in)	(%)				
PU_R1_0.4DE	0.4×DE	0.92	0.85	2	0.029891	0.11	0.0010
PU_R2_0.4DE				2	0.294158	1.08	0.0100
PU_R3_0.4DE				2	0.735394	2.71	0.0250
PU_R4_0.4DE				2	1.470788	5.41	0.0500
PU_R1_0.6DE	0.6×DE	1.65	1.52	2	0.016667	0.11	0.0010
PU_R2_0.6DE				2	0.164015	1.08	0.0100
PU_R3_0.6DE				2	0.410038	2.71	0.0250
PU_R4_0.6DE				2	0.820076	5.41	0.0500
PU_R1_1.2DE	1.2×DE	4.79	4.42	2	0.005741	0.11	0.0010
PU_R2_1.2DE				2	0.056498	1.08	0.0100
PU_R3_1.2DE				2	0.141245	2.71	0.0250
PU_R4_1.2DE				2	0.282490	5.41	0.0500
PU_R1_1.8DE	1.8×DE (1.2×MCE)	9.17	8.47	2	0.002999	0.11	0.0010
PU_R2_1.8DE				2	0.029512	1.08	0.0100

7.12. Test Results

7.12.1. RC Rocking Specimen

7.12.1.1. Observations

The observed response of the RC rocking specimen under repeated cyclic loading with increasing amplitude is described at each amplitude and supported with photo illustrations. The specimen was pulled to the west and pushed to the east. The test started with pulling the specimen.

7.12.1.1.1. Amplitude 1: ± 0.5 in. ($\pm 0.46\%$ drift ratio)

A minor hairline crack was observed on the east side extending up to about 2” from the column-foundation interface (Figure 7.35(a)). No damage was observed on the west side.

7.12.1.1.2. Amplitude 2: ± 1 in. ($\pm 0.92\%$ drift ratio)

On the east side, opening of the crack formed during the previous step was observed as well as formation of more compression cracks (Figure 7.35(b)). Two vertical cracks observed in the northwest side, extending up to about 3” from the column-foundation interface.

7.12.1.1.3. Amplitude 3: ± 2 in. ($\pm 1.85\%$ drift ratio)

On the east side: (i) cover spalling was observed up to about 3” from the column-foundation interface; (ii) more vertical cracks were formed extending up to about 10” from

the column-foundation interface. On the west side: (i) cover spalling was observed up to about 2” from the column-foundation interface; (ii) more flexural and vertical cracks were formed extending up to about 10” from the column-foundation interface (Figure 7.35(c)).

7.12.1.1.4. Amplitude 4: ± 4 in. ($\pm 3.7\%$ drift ratio)

On the east side: (i) cover spalling extended up to about 10” from the column-foundation interface (Figure 7.35(d)). The first two transverse reinforcement ties from the bottom of the column were exposed (Figure 7.36(a)); (ii) more flexural and vertical cracks were formed extending up to about 13” from the column-foundation interface; (iii) initiation of concrete crushing at the confined core was observed in the vicinity of the column-foundation interface. On the west side: (i) cover spalling extended up to about 6” from the column-foundation interface. The second transverse reinforcement tie from the bottom of the column was exposed (Figure 7.36(b)); (ii) vertical cracks were formed extending up to about 18” from the column-foundation interface; (iii) initiation of concrete crushing at the confined core was observed in the vicinity of the column-foundation interface.

7.12.1.1.5. Amplitude 5: ± 6 in. ($\pm 5.54\%$ drift ratio)

On the east side: (i) cover spalling extended to the southeast and northeast and up to about 13” from the column-foundation interface (Figure 7.35(e)); (ii) more flexural hairline cracks were formed extending up to about 18” from the column-foundation interface (Figure 7.35(e)); (iii) vertical cracks were observed in the core extending up to

about 8” from column-foundation interface (Figure 7.37(a)); (iv) extensive concrete crushing was observed in the vicinity of the column-foundation interface. On the west side: (i) cover spalling extended to the southwest up to about 18” from the column-foundation interface. The first four transverse reinforcement ties from the bottom of the column were exposed (Figure 7.37(b)); (ii) flexural cracks extended up to about 18” from the column-foundation interface; (iii) extensive core concrete crushing was observed in the vicinity of the column-foundation interface (Figure 7.35(e)).

7.12.1.1.6. Amplitude 6: ± 8 in. ($\pm 7.39\%$ drift ratio)

On the east side: (i) more flexural and vertical hairline cracks were formed extending up to about 19” from the column-foundation interface (Figure 7.35(f)); (ii) a vertical crack was observed in the core extending up to about 9” from column-foundation interface (Figure 7.38(a)); (iii) cover spalling extended further to the northeast. On the west side, opening of the flexural and vertical crack formed during the previous step was observed as well as formation of more flexural cracks (Figure 7.35(f)). Also, an increased amount of core concrete crushing at the column-foundation interface was observed (Figure 7.38(b)). Grout delamination was observed on the northwest side of the foundation surface due to longitudinal rebar punching into to foundation (Figure 7.38(c)).

7.12.1.1.7. Amplitude 7: ± 10 in. ($\pm 9.24\%$ drift ratio)

On the east side, vertical crack observed in the core over the previous steps extended up to about 10” from the column-foundation interface (Figure 7.35(g)). On the

west side: (i) cover spalling extended to the southwest and up to about 21” from the column-foundation interface (Figure 7.35(g)); (ii) an increased amount of core concrete crushing at the column-foundation interface was observed.

7.12.1.1.8. Amplitude 8: ± 12 in. ($\pm 11.09\%$ drift ratio)

On the east side: (i) more flexural and vertical cracks were formed extending up to about 22” from the column-foundation interface (Figure 7.35(h)); (ii) opening of the cracks formed in the core over the previous steps was observed extending up to about 12” from the column-foundation interface (Figure 7.39). On the west side: (i) opening of the flexural and vertical cracks formed during the previous step was observed (Figure 7.35(h)); (ii) cover spalling extended to the northwest and up to about 15” from the column-foundation interface (Figure 7.35(h)); (iii) vertical cracks were observed in the core concrete extending up to about 9” from the column-foundation interface (Figure 7.35(h)).

7.12.1.1.9. Amplitude 9: ± 14 in. ($\pm 12.93\%$ drift ratio)

On the east side: (i) cover spalling extended to the southeast and northeast and up to about 18” from the column-foundation interface (Figure 7.35(i)); (ii) vertical cracks formed in the core over the previous steps were observed extending up to about 15” from the column-foundation interface (Figure 7.35(i)); (iii) longitudinal rebar was exposed upon extensive crushing of concrete in the vicinity of the column-foundation interface (Figure 7.40). On the west side: (i) opening of the flexural and vertical cracks formed during the previous step was observed (Figure 7.35(i)); (ii) cover spalling extended to the northwest and up to about 15” from the column-foundation interface (Figure 7.35(i)); (iii) core concrete crushing in the vicinity of the column-foundation extended further to the northwest.

7.12.1.1.10. Amplitude 10: ± 14.5 in. ($\pm 13.39\%$ drift ratio)

No further damage was observed.

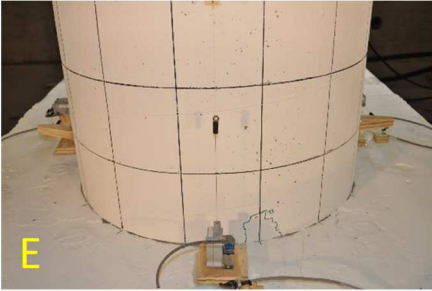
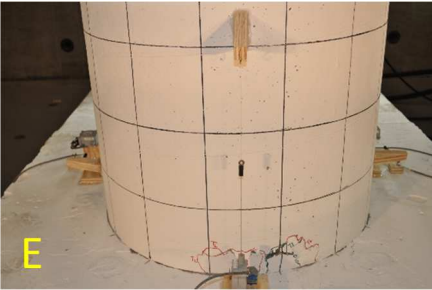
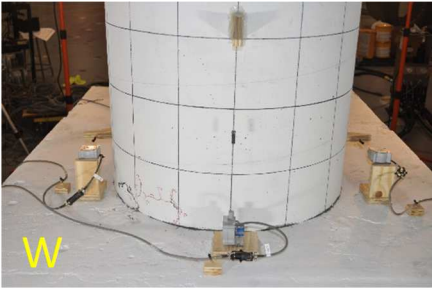
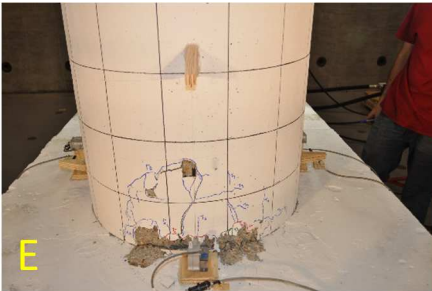

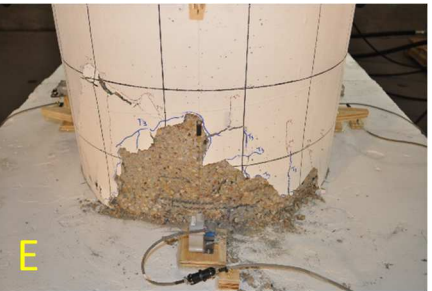

	East Side	West Side
(a) 0.46% drift ratio		No damage
(b) 0.92% drift ratio		
(c) 1.85% drift ratio		
(d) 3.7% drift ratio		

Figure 7.35 . Damage in RC rocking column at various drift ratios.



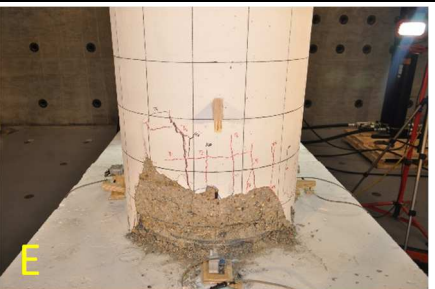

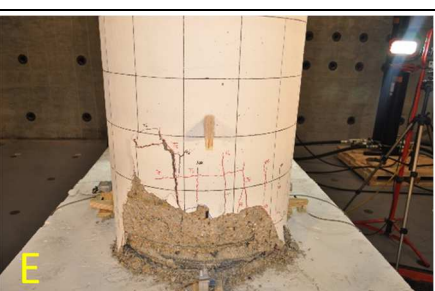

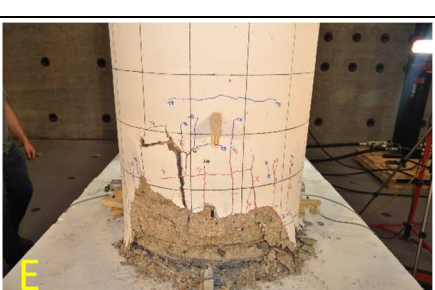

(e) 5.54% drift ratio		
(f) 7.39% drift ratio		
(g) 9.24% drift ratio		
(h) 11.09% drift ratio		

Figure 7.35 (Continued).

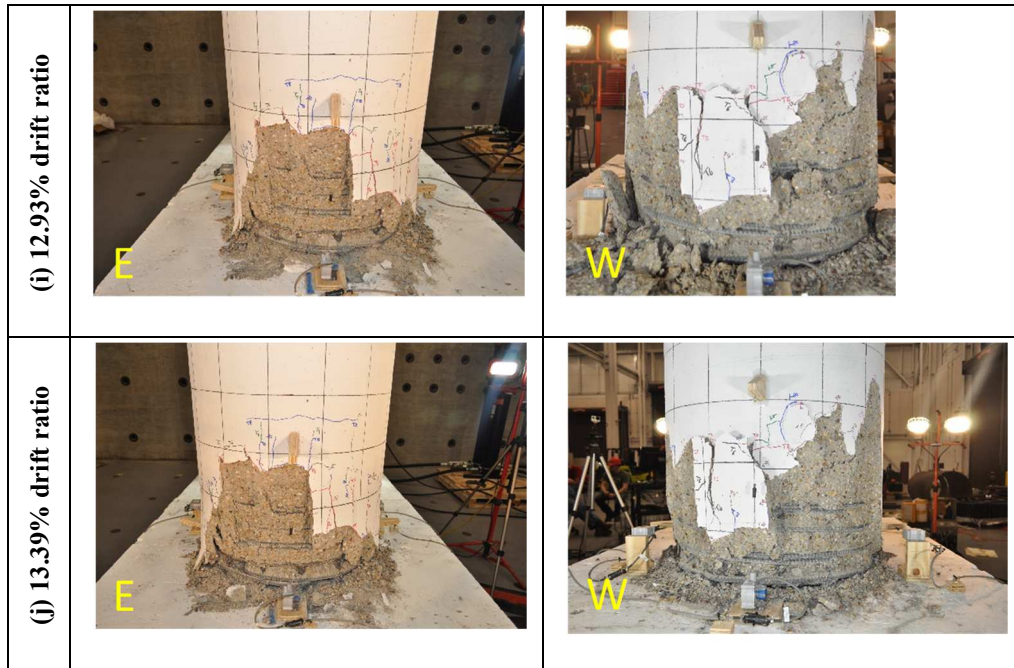


Figure 7.35 (Continued).

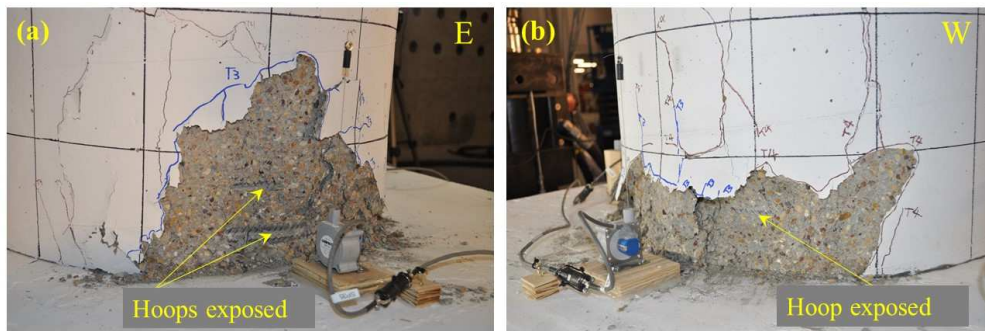


Figure 7.36. Damage in RC rocking column: hoops exposed at 3.7% drift ratio: (a) east side; (b) west side.

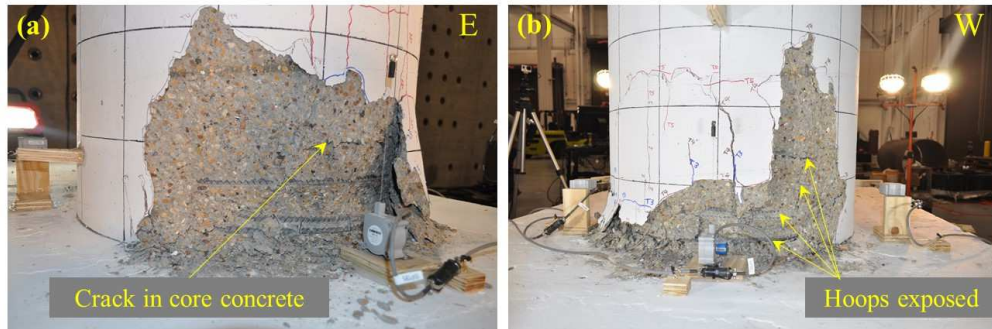


Figure 7.37. Damage in RC rocking column at 5.54% drift ratio: (a) crack in the core concrete on east side; (b) hoops exposed on the west side.

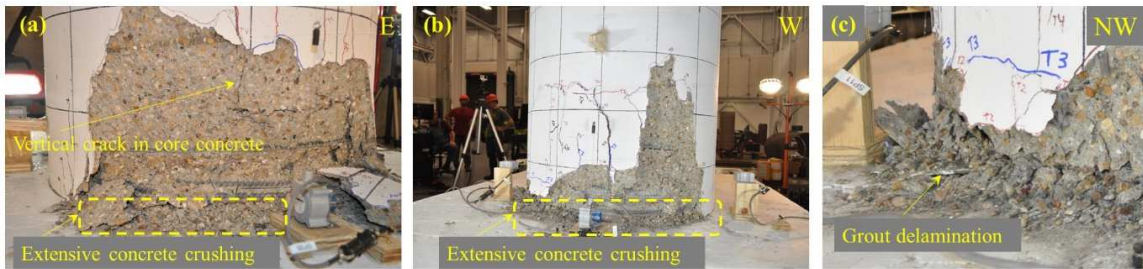


Figure 7.38. Damage in RC rocking column at 7.39% drift ratio: (a) vertical crack in the core concrete and extensive concrete crushing on east side; (b) extensive concrete crushing on the west side; (c) grout delamination on foundation block surface.



Figure 7.39. Damage in RC rocking column at 11.09% drift ratio: opening of vertical crack in the core concrete on east side.

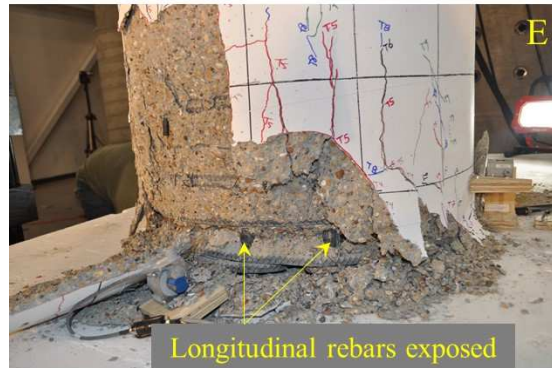


Figure 7.40. Damage in RC rocking column at 12.93% drift ratio: exposure of longitudinal rebar.

7.12.1.2. Post-test Inspection of the Segments and PT System

At the end of the test, before disassembling the specimen, the loose concrete in the damaged region was removed to provide a clearer picture of the damage in the system (Figure 7.41 and Figure 7.42). According to Figure 7.41, significant cover spalling occurred on the east and west sides extended up to about 19” and 21” on east and west side, respectfully. Significant core concrete crushing occurred in the vicinity of the rocking joint on both east and west side, extended up to approximately 8” from the joint.

Local damage was observed in the foundation due to the longitudinal rebar punching into the foundation (Figure 7.42(a) and Figure 7.37), followed by local bucking/bending in the longitudinal bar on the east and west side (Figure 7.43). Moreover, permanent gap formed at the rocking joint (Figure 7.42(b) and (c)), attributed to the high moment demands at the joint over the test.

No damage was observed in the cap beam and the tendon over inspection after disassembling the setup.

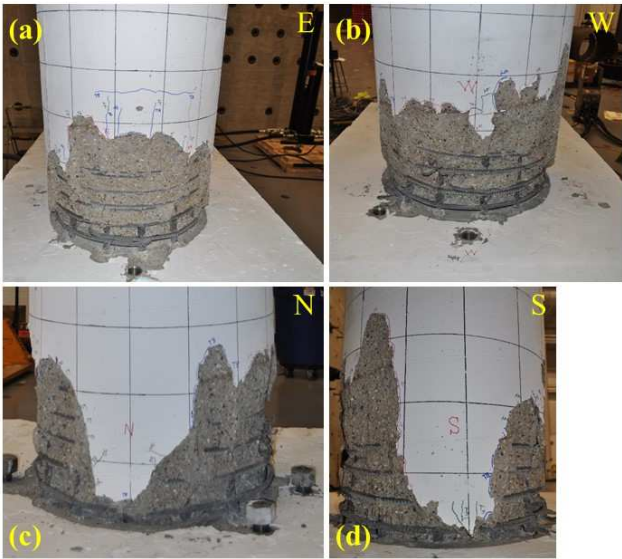


Figure 7.41. Damage inspection of RC column after loose concrete was removed.

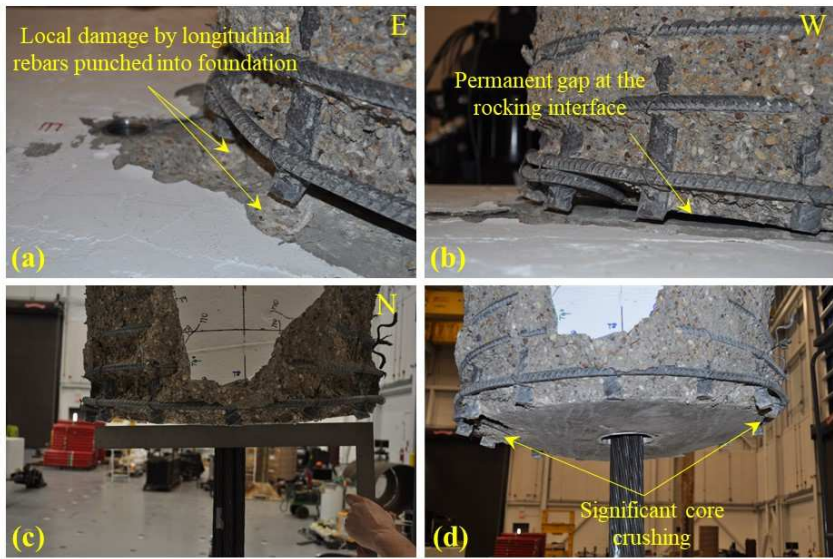


Figure 7.42. Visual inspection of the damage state in the vicinity of the rocking joint.

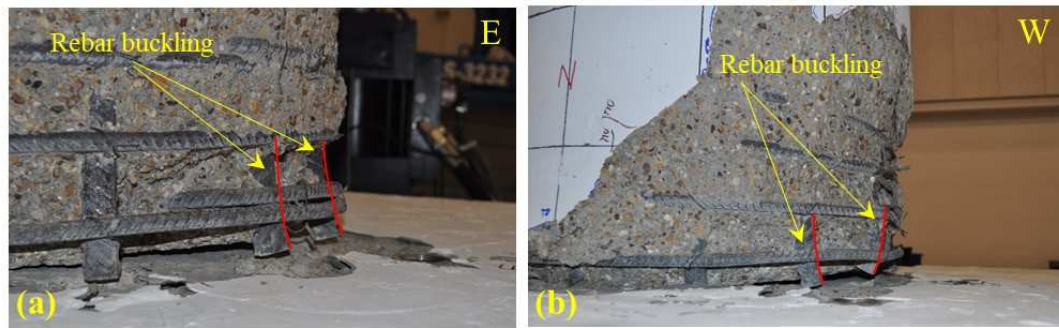


Figure 7.43. Longitudinal rebar buckling/bending in RC rocking column.

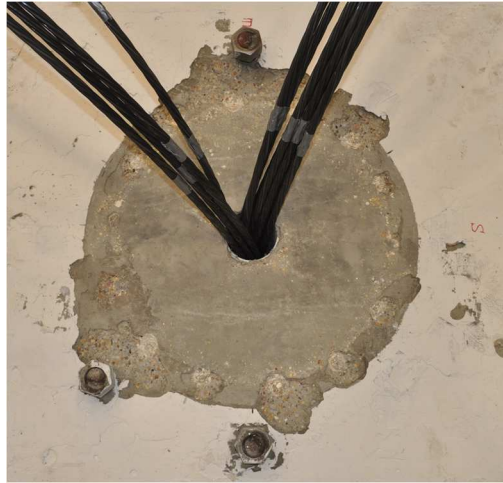


Figure 7.44. Damage in the foundation at the location of longitudinal rebar of the RC rocking column.

7.12.1.3. Lateral Load-Drift Response

Lateral load vs. drift ratio hysteresis curve for the RC rocking specimen is shown in Figure 7.45. The lateral and vertical forces have been corrected for the inclination of the vertical actuators in the deformed configuration. A stable response is observed up to about 3% drift ratio. Column peak lateral strength was 54.3 kips and -59.2 kips, in the positive and negative direction, respectively, and was observed at 1.85% drift ratio. Significant softening was observed in the form of stiffness and strength degradation for drift ratios exceeding 3% with a rate increasing with the drift ratio. This post-peak degradation results from the large concrete compression damage at the bottom/rocking section, which results from the lack of mild longitudinal reinforcements crossing the column-foundation interface that leads to larger compressive stress/strain demands to the concrete material. A slight hardening following a short plateau was observed in the

response when pushing or pulling the specimen to the peak amplitude, for drift ratios beyond about 6%. This is attributed to the over-strength due to the longitudinal rebar punching into the foundation.

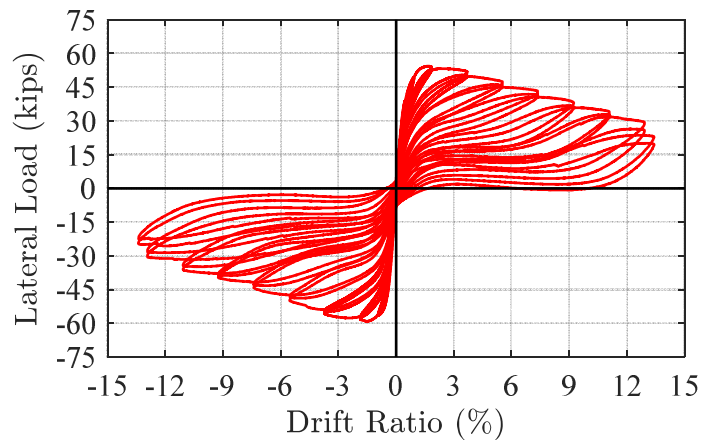


Figure 7.45. Lateral load vs. drift ratio hysteresis curve for the RC rocking column.

7.12.1.4. Post-tensioning Load History

The variation of the PT load with drift ratio is shown in Figure 7.46(a). The initial PT load level (434 kips) is shown with the dashed red line. It should be noted that readings from LC1 as the only calibrated load cell was used as the measured PT load. Due to the opening at the rocking interface (column-foundation interface), the PT load increases as the column is loaded from the rest position (zero displacement) to the peak displacement in positive or negative direction.

The post-tensioning load at the end of each set of cycles versus the peak drift ratio is shown in Figure 7.46(b). The PT load at the end of each set of cycles decreases with the peak drift ratio for drift ratios beyond 3.7% due to column shortening as a result of concrete crushing in the vicinity of the rocking interface (Figure 7.46(b)). The PT load measured at the end of the test was 409.3 kips, which corresponds to a total loss of 5.6% relative to the initial PT load (434 kips). The maximum observed PT load in the tendon during the entire loading history was 591 kips which was below the nominal yield load (632.7 kips), defined using the nominal yield strength of strands (243 ksi).

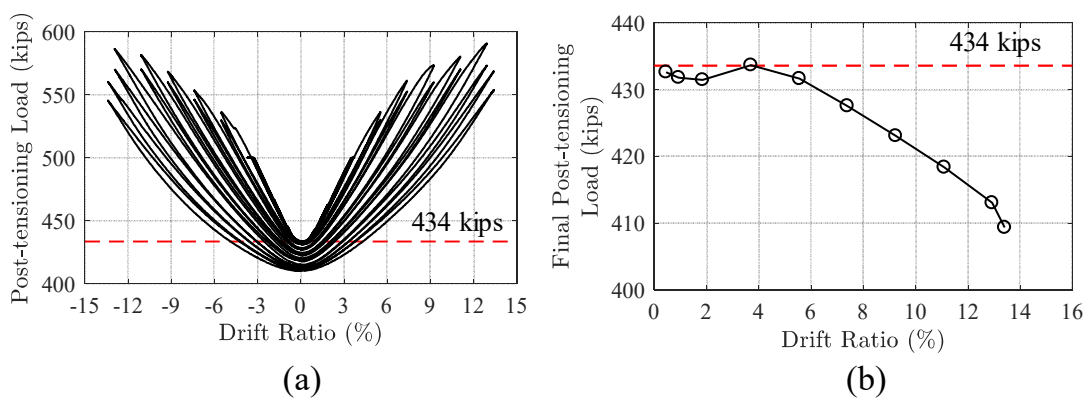


Figure 7.46. (a) Post-tensioning load vs. peak drift ratio for the RC rocking column; (b) post-tensioning load at the end of each cycle vs. peak drift ratio.

7.12.1.5. Curvature

The average curvature was computed over a gage length of 18” using the data from the string potentiometers attached to the foundation on the east and west side of the

specimen (Figure 7.12). The string potentiometers were located at 2.4” from the column face. Average curvature was calculated using Eq. (7.2):

$$\varphi = \frac{\Delta \theta}{H} \quad (7.2)$$

where φ is the average curvature over the gage length, H , and $\Delta\theta$ is the rotation calculated using Eq. (7.3):

$$\Delta\theta = \frac{\delta_W - \delta_E}{L} \quad (7.3)$$

where δ_W and δ_E are the extension (or contraction) measured by the west and east string potentiometers, respectively, and L is the horizontal distance between the west and east string potentiometers. The computed average curvature versus drift ratio is shown in Figure 7.47.

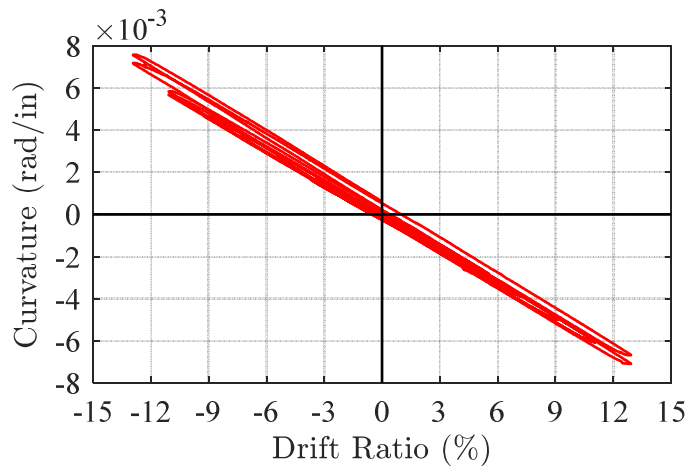


Figure 7.47. Average curvature at the base of the RC rocking column vs. drift ratio.

7.12.1.6. Energy Dissipation and Equivalent Viscous Damping

Energy dissipation capabilities are quantified through the cumulative energy dissipation (CED) computed at the end of each test cycle, accounting for the current and all previous cycles. The energy dissipation capabilities of the tested columns were further evaluated through their equivalent viscous damping ratios, ζ_{eq} , for each set of loading cycles at a given amplitude. The equivalent viscous damping ratio is calculated using Eq. (6.3).

The cumulative dissipated energy and equivalent viscous damping versus drift ratio is presented in Figure 7.48, where the drift ratio corresponding to various hazard levels (0.4×DE, 0.6×DE, DE, MCE) is identified with vertical red lines. The CDE increased with the drift ratio in RC rocking column (Figure 7.48(a)) resulting from the spreading of concrete damage over the height of the column. This is also reflected in the equivalent viscous damping which slightly decreases at the very beginning and then increases with the drift ratio. The equivalent viscous damping corresponding to various hazard levels is shown in Table 7.14.

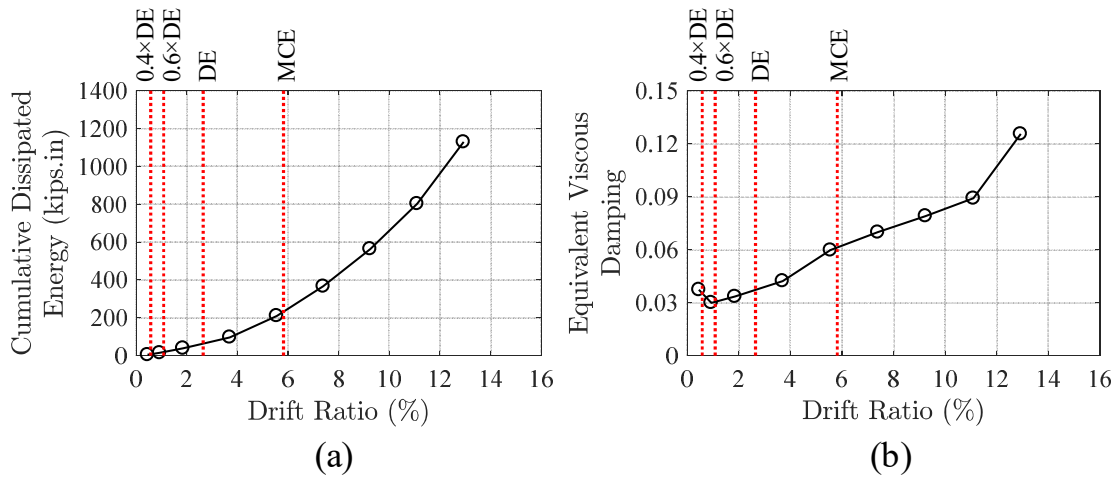


Figure 7.48. RC rocking column: (a) cumulative dissipated energy versus drift ratio; (b) equivalent viscous damping versus drift ratio.

7.12.1.7. Self-centering Efficiency

The self-centering capabilities of the specimens were assessed using the relative self-centering efficiency (RSE) (Sideris et al. 2014b), which quantifies the ability of a system to self-center when subjected to cyclic loading. The RSE expresses the portion of the peak deformations that are recoverable and is defined using Eq.(4.6). It is reminded that an RSE value of unity corresponds to perfectly self-centering systems (i.e., systems with zero residual deformations), whereas a RSE value of zero corresponds to systems without any re-centering capabilities (e.g., Coulomb friction springs).

The self-centering capabilities of the specimens were further assessed through the average residual drift ratio (RDR) defined at each cycle as:

$$\bar{D}_{res} = \frac{|u_{res}^+| + |u_{res}^-|}{2h_{tot}} \times 100 \quad (7.4)$$

where h_{tot} is the height measured from the lateral loading center to the column-foundation interface.

The RSE and residual drift ratio versus the peak drift ratio of each cycle is presented in Figure 7.49, where the drift ratio corresponding to various hazard levels (0.4×DE, 0.6×DE, DE, MCE) is identified with vertical red lines. RSE increases from 0.93 to 0.98 as the drift ratio increases from 0.46% to 3.7%, and remains approximately constant up to 9.24% drift ratio (Figure 7.49(a)). For drift ratios exceeding 9.24%, the RSE decreases with drift ratio. The residual drift ratio increases with the peak drift ratio with a constant rate up to 9.24% drift ratio, beyond which it increases with drift ratio with an increasing rate (Figure 7.49(b)). The values of RSE and average RDR corresponding to various hazard levels is shown in Table 7.14.

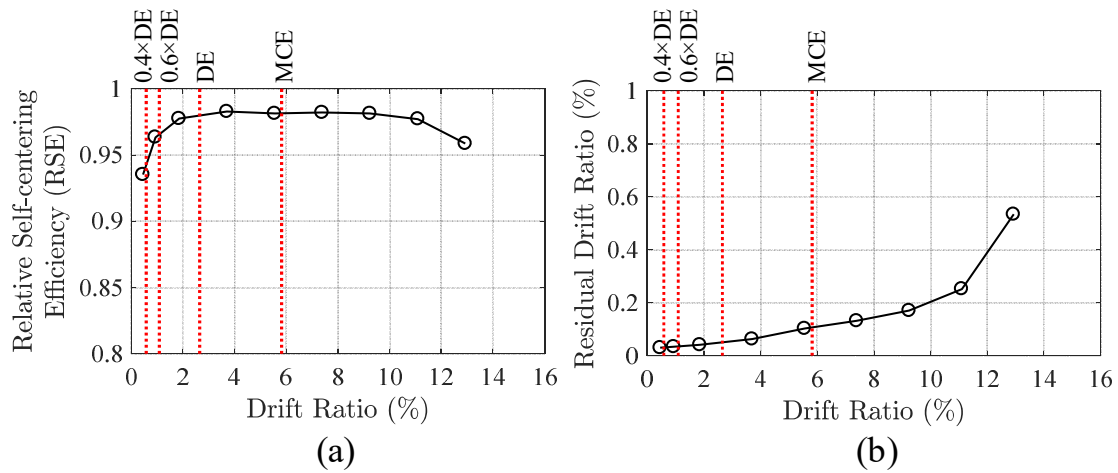


Figure 7.49. RC rocking column: (a) relative self-centering efficiency (RSE); (b) residual drift ratio.

Table 7.14. RC rocking column: equivalent viscous damping, RSE, and RDR at various hazard levels.

Hazard Level	Peak Drift Ratio (%)	Equivalent Viscous Damping	RSE	Average RDR (%)
0.4xDE	0.58	0.035	0.94	0.031
0.6xDE	1.13	0.031	0.97	0.035
DE	2.66	0.037	0.98	0.051
MCE	5.82	0.061	0.98	0.107

7.12.2. PUED-1 Specimen

The observed response of PUED-1 specimen under the loading sequence presented in Table 7.10 is described at each amplitude and supported with photo illustrations. The specimen was pulled to the west (positive direction) and pushed to the east (negative direction). The test started with pulling the specimen.

It should be noted that the damage in the foundation from the previous test due to longitudinal rebar punching into the foundation was fixed by patching the damaged areas with a non-shrink grout compliant with ASTM C-1107 that can achieve up to 14 ksi compression strength for plastic consistency at 28 days.

In reference to Section 7.11.2.1, the study with the PUED-1 specimen is termed *Phase 1*.

7.12.2.1. Observations

7.12.2.1.1. Amplitude 1 – $0.4 \times DE$: ± 0.65 in. ($\pm 0.6\%$ drift ratio)

The top nut at the top ED link connection was loosened in ED-5 (Figure 7.50). The loosened nut was retightened before starting the next test.

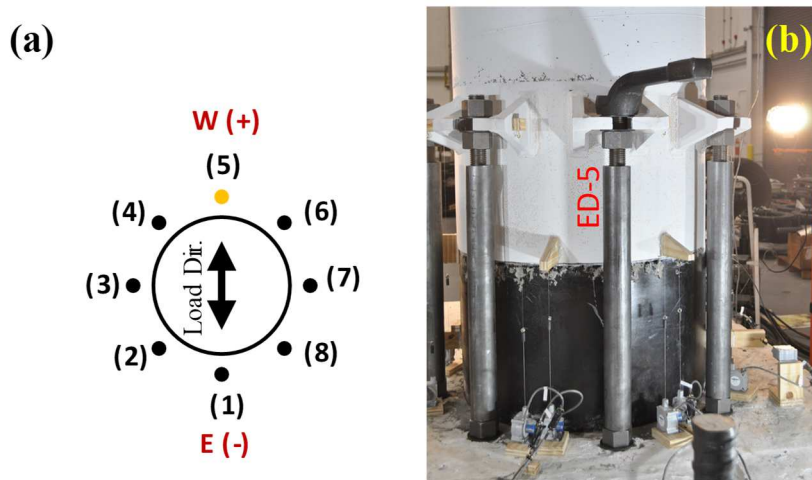


Figure 7.50. Connection loosened in ED links in PUED rocking column at $0.4 \times DE$ level: (a) location of ED links with loosened connection (orange circles); (b) ED-5 with hammer wrench on for retightening.

7.12.2.1.2. Amplitude 2 – $0.6 \times DE$: ± 1.1 in. ($\pm 1.02\%$ drift ratio)

The top nut at the top ED link connection was loosened in ED-1, ED-4, and ED-6. The loosened nuts were retightened before starting the next test.

7.12.2.1.3. Amplitude 3 – $1.2 \times DE$: ± 3.5 in. ($\pm 3.23\%$ drift ratio)

Bending was observed in washers at the top ED link connection in ED-1, ED-6, and ED-8 (Figure 7.51). Also, slight local buckling of the link over the unconfined length at its top end was observed for ED-5, ED-6, and ED-8 (Figure 7.52).



Figure 7.51. Washers deformed in top connection of ED links in PUED rocking column at $1.2 \times DE$: (a) location of ED links with deformed washers (brown circles); (b) ED-1; (c) ED-6; (d) ED-8.

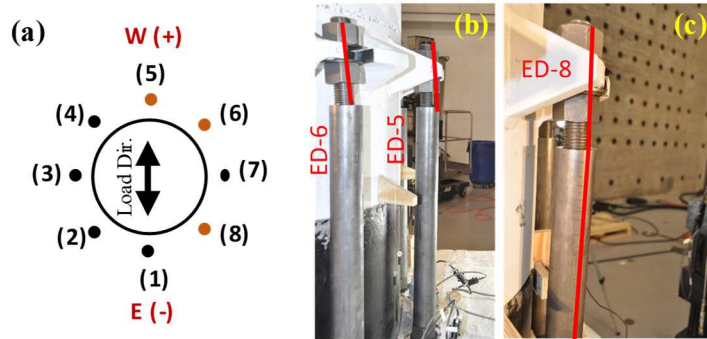


Figure 7.52. Slight local buckling at top connection of ED links in PUED rocking column at $1.2 \times DE$: (a) location of damaged ED links (brown circles); (b) ED-5 and ED-6; (c) ED-8.

7.12.2.1.4. Amplitude 4 – $1.8 \times DE$ ($1.2 \times MCE$): ± 6.7 in. ($\pm 6.19\%$ drift ratio)

Minor damage in the form of hairline cracks was observed in the concrete above the steel collar due to stress concentration at the steel-to-concrete interface. On the east side, vertical hairline cracks were observed in the vicinity of the concrete cover-steel collar joint (at top of the steel collar) extending up to about 5” from the joint (Figure 7.53(a)). Moreover, flexural cracks were observed at concrete-steel collar joint and 8”, 20”, and 35” above the concrete-steel collar joint (Figure 7.53(a)).

On the west side, vertical hairline cracks were observed in the vicinity of the concrete cover-steel collar joint (at top of the steel collar) extending up to about 6” from the joint (Figure 7.53(b)). Two flexural cracks were observed at about 6” and 10” above the concrete-steel collar joint (Figure 7.53(b)).

Extensive damage was observed at the top connection of ED-6 and ED-8. The damage was in the form of extensive flexural deformation of the washers at the top ED link connections followed by local buckling of the link over the unconfined length at the

top of the link (Figure 7.54). The observed damage is attributed to the reduced flexural stiffness of the washers due to the enlarged slots on the horizontal mounting plate as mentioned in Section 7.9.2.

Moreover, on the west side, minor damage was observed at the foundation surface in the form of grout delamination (Figure 7.55).

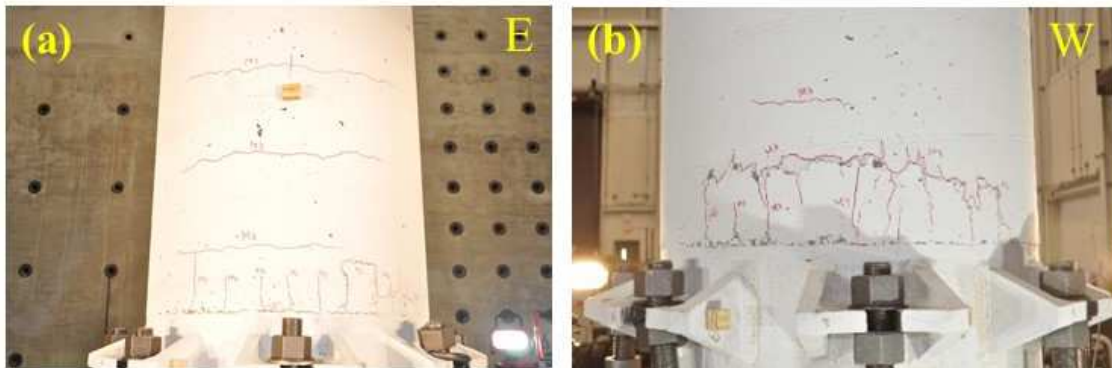


Figure 7.53. Cracks in concrete in PUED rocking column at $1.8 \times DE$: (a) east side; (b) west side.

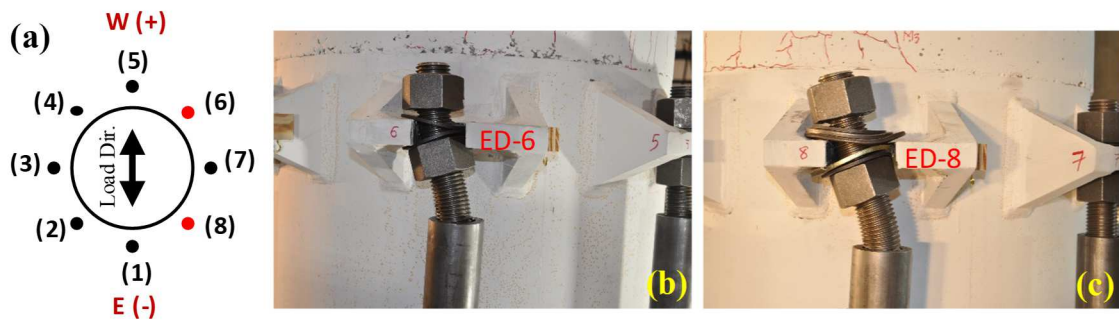


Figure 7.54. Damage in top connection of ED links in PUED rocking column at $1.8 \times DE$: (a) location of damaged links (red circles); (b) damage in ED-6; (c) damage in ED-8.

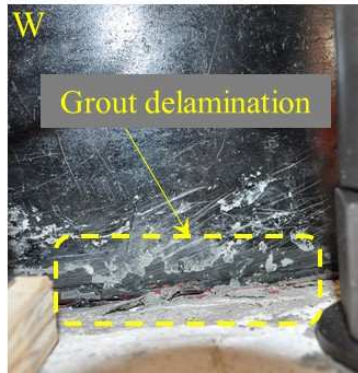


Figure 7.55. Minor grout delamination at PU-foundation interface in PUED-1 rocking column at 1.8×DE.

7.12.2.2. Post-test Inspection of Segments and ED Links

At the end of the test, the ED links were removed from the setup for further inspection. Three ED links (ED-5, ED-6, and ED-8) were removed by cutting the link at the top connection with a hand band-saw (Figure 7.56). The other links were easily removed by unscrewing the top and bottom connections.

The ED bars are arranged radially at their location on a plan view of the ED links setup in Figure 7.57. Buckling is observed in all eight links. It can be seen that the two outermost links in the west (ED-5) and east (ED-1) side have experienced more damage compared to the other links, as expected.

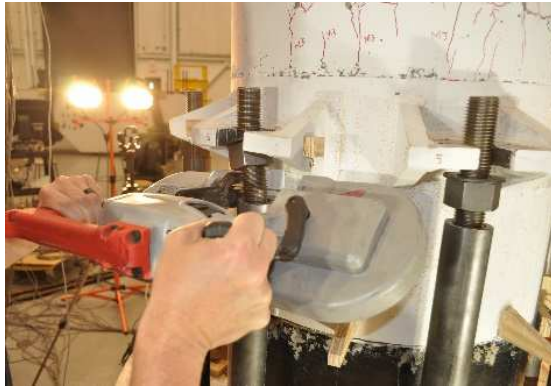


Figure 7.56. Cutting damaged ED links with hand band-saw.



Figure 7.57. PUED-1 specimen: extracted view of ED links.

7.12.2.3. Lateral Load-Drift Response

Lateral load vs. drift ratio hysteresis curve for the PUED-1 rocking specimen corresponding to various hazard levels is shown in Figure 7.58. Vertical and horizontal forces have been corrected for the inclination of the vertical actuators in the deformed configuration. The peak lateral load in positive (pull) and negative (push) direction at various hazard levels is summarized in Table 7.15. A stable response without any softening is observed up to 6.2% drift ratio, corresponding to $1.8\times DE$ ($1.2\times MCE$) hazard level. An elastic response was observed up to 0.6% drift ratio corresponding to the $0.4\times DE$ hazard level (Figure 7.58(a)). Minor hysteresis was observed in the response up to 1.02% drift ratio corresponding to $0.6\times DE$ hazard level (Figure 7.58(b)). This nonlinear response is attributed to yielding at ED-1 and ED-5. Clear nonlinear response was observed in the curves corresponding to $1.2\times DE$ and $1.8\times DE$ ($1.2\times MCE$) hazard levels which is attributed not only to the yielding of ED links, but also to the nonlinear response of the PU material in the vicinity of the PU-to-foundation interface. Column peak lateral strength was 98.8 kips and -95.2 kips, in the positive and negative direction, respectively, observed at 6.2% drift ratio (Table 7.15).

The lateral load vs. drift ratio hysteretic response of the PUED-1 column at all hazard levels is compared to the hysteretic response of the RC rocking column in Figure 7.59. The PUED-1 column clearly shows higher lateral strength compared to the RC rocking column due to the contribution of ED links. The initial elastic stiffness of the

PUED-1 column is comparable to that of the RC rocking column as shown in Figure 7.59(b).

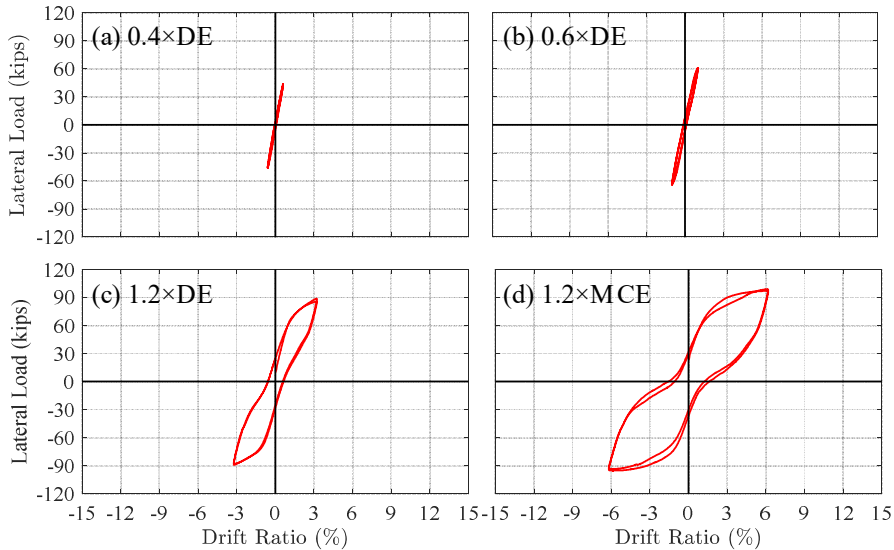


Figure 7.58. Lateral load vs. drift ratio hysteresis curve for the PUED-1 rocking column at different hazard levels.

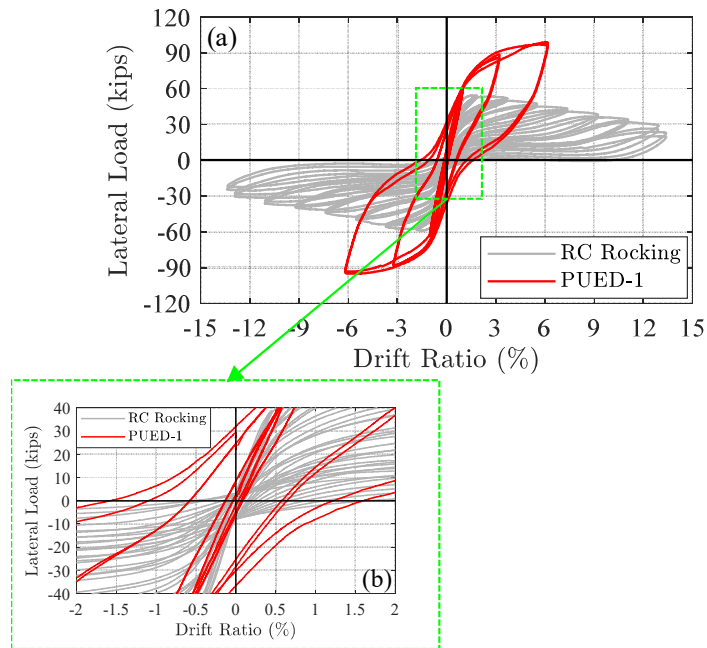


Figure 7.59. Lateral load vs. drift ratio hysteresis curve: PUED-1 vs. RC rocking column.

Table 7.15. Summary of peak lateral strength in positive and negative direction at various hazard levels: PUED-1 specimen.

Hazard Level	Peak Drift Ratio	F_{peak}^+	F_{peak}^-
	(%)	(kips)	(kips)
0.4×DE	0.60	44.0	-46.0
0.6×DE	1.02	61.2	-63.8
1.2×DE	3.23	88.8	-89.0
1.8×DE (1.2×MCE)	6.19	98.8	-95.2

7.12.2.4. Post-tensioning Load History

The variation of the PT load with drift ratio is shown in Figure 7.60(a). The initial PT load level (438 kips) is shown with the dashed red line. Due to the opening at the rocking interface (PU-to-foundation interface), the PT load increases as the column is loaded from the rest position (zero displacement) to the peak displacement in positive or negative direction.

The post-tensioning load at the end of each set of cycles versus the corresponding peak drift ratio is shown in Figure 7.60(b). Minor loss was observed in PT load at the end of each set of cycles. The PT load measured at the end of the test was 431.8 kips, which corresponds to a total loss of 1.3% relative to the initial PT load (438 kips). The maximum observed PT load in the tendon during the entire loading history was 528.6 kips which was below the nominal yield load (632.7 kips), defined using the nominal yield strength of strands (243 ksi).

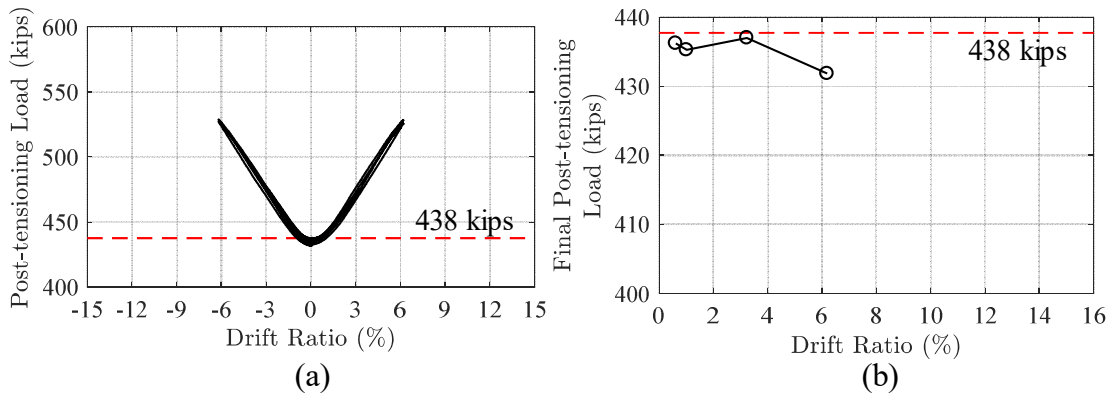


Figure 7.60. (a) Post-tensioning load vs. peak drift ratio for the PUED-1 column; (b) post-tensioning load at the end of each cycle vs. peak drift ratio.

7.12.2.5. Curvature

The average curvature was computed over a gage length of 15.625” (height of the bi-layered PU segment) using the data from the string potentiometers attached to the foundation on the east and west side of the specimen (Figure 7.14). The string potentiometers were located at 2.4” from the column face. Average curvature was calculated using the procedure explained in Section 7.12.1.5.

The computed average curvature over the height of the bi-layered PU segment versus drift ratio is shown in Figure 7.61. Since the rocking mechanism at top interface of the bi-layered PU segment was locked by the central steel pipe, no opening was observed at the top of the bi-layered segment (i.e. at the concrete-to-PU interface). Thus, the measured lateral displacement at the loading center was only due to the rotation of the column about its compression toe at the PU-foundation interface.

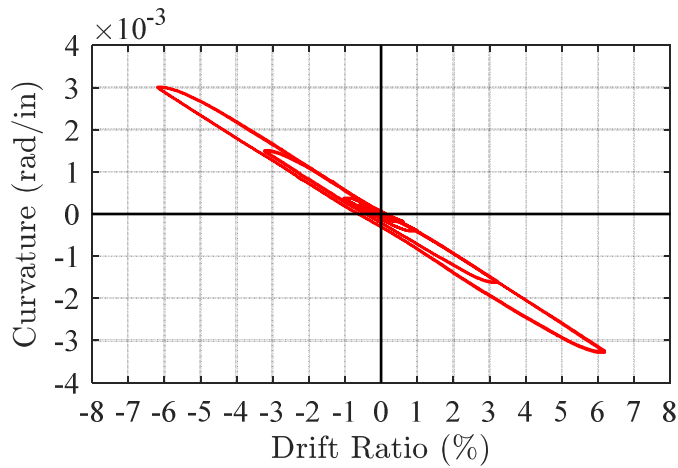


Figure 7.61. Average curvature at the base of the bi-layered PU segment vs. drift ratio.

7.12.2.6. Energy Dissipation and Equivalent Viscous Damping

The CDE and equivalent viscous damping versus drift ratio (calculated as described previously in Section 7.12.1.6) is presented in Figure 7.48 for the PUED-1 and RC rocking specimen, where the drift ratio demand on PUED-1 column corresponding to various hazard levels (0.4×DE, 0.6×DE, DE, MCE) is identified with vertical red lines. The CDE and, accordingly, the equivalent viscous damping ratio increased with the drift ratio in PUED-1 rocking column (Figure 7.48(a) and (b) and Table 7.16). Energy dissipation in PUED-1 column was provided primarily by the ED links and the PU material. As shown in Figure 7.62, the PUED-1 column provides higher energy dissipation capacity compared to the RC rocking column, especially at drift ratios exceeding 1%.

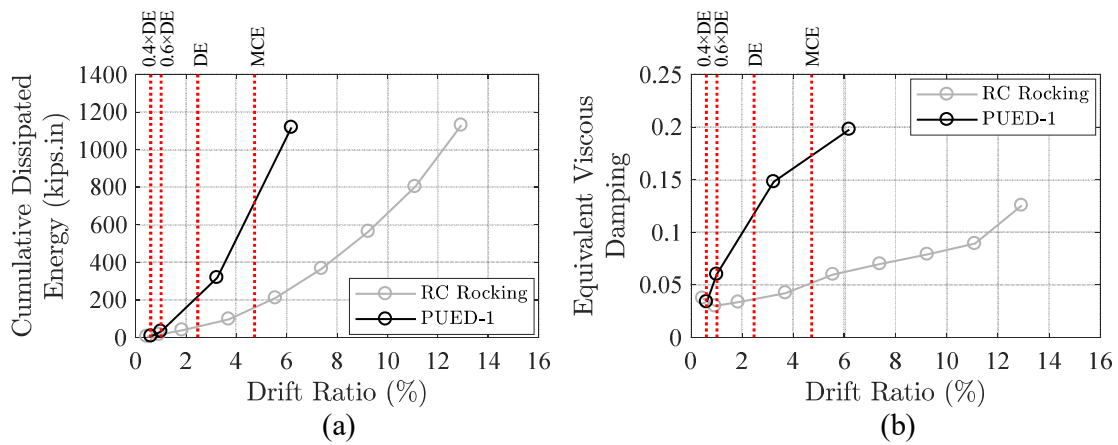


Figure 7.62. PUED-1 column vs. RC rocking column: (a) cumulative dissipated energy; (b) equivalent viscous damping.

7.12.2.7. Self-centering Efficiency

A comparison of the self-centering capabilities of PUED-1 and RC rocking column is presented in Figure 7.63 in terms of RSE (Figure 7.63(a)) and residual drift ratios (at each loading cycle) (Figure 7.63(b)) vs. the peak drift ratio of the cycle. The drift ratio demand on PUED-1 column corresponding to various hazard levels (0.4xDE, 0.6xDE, DE, MCE) is identified with vertical red lines. As shown, the re-centering capability of the PUED-1 column decreases with the peak drift ratio, as is reflected in Figure 7.63(a) and (b) by RSE and residual drift ratio decreasing and increasing with peak drift ratio, respectively. However, since residual deformations in PUED-1 column mainly result from residual deformations in the ED links, it is shown later on (see Section 7.12.3.3) their largest portion is recoverable upon releasing and retightening (or replacement) of the ED

links. The values of RSE and average RDR for PUED-1 and RC rocking columns corresponding to various hazard levels are presented in Table 7.16.

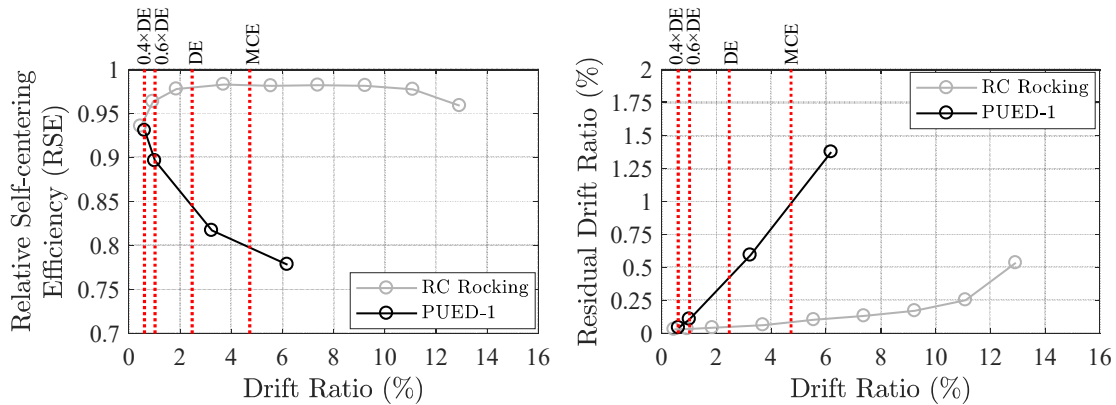


Figure 7.63. PUED-1 column vs. RC rocking column: (a) relative self-centering efficiency (RSE); (b) residual drift ratio.

Table 7.16. PUED-1 column vs RC rocking column: equivalent viscous damping, RSE, and RDR at various hazard levels.

Hazard Level	Equivalent Viscous Damping		RSE		Average RDR (%)	
	RC rocking	PUED-1	RC rocking	PUED-1	RC rocking	PUED-1
0.4×DE	0.035	0.034	0.94	0.93	0.031	0.041
0.6×DE	0.031	0.060	0.97	0.89	0.035	0.107
DE	0.037	0.117	0.98	0.84	0.051	0.420
MCE	0.061	0.173	0.98	0.79	0.107	0.980

7.12.2.8. Deformation of ED Link

The normalized axial deformation ($\Delta L/L_0$, where ΔL is the axial deformation and L_0 is the gage length (~12'')) of ED links versus drift ratio for all ED links is shown in

Figure 7.64. As expected, the ED-1 and ED-5 with the maximum distance from the neutral axis experienced the maximum deformation among the others. In all ED links, the measured tensile deformation was larger than the compressive deformation due to the larger distance of the ED links from the neutral axis in tension than compression. Theoretically, in a fully symmetric system, identical response is expected in ED links with the same distance from the mid-plane of the column (e.g. ED-1 and ED-5, ED-4 and ED-6, ED-2 and ED-8, ED-3 and ED-7). However, as shown in Figure 7.64, the expected response symmetry is not observed, indicating that the setup was not fully symmetric.

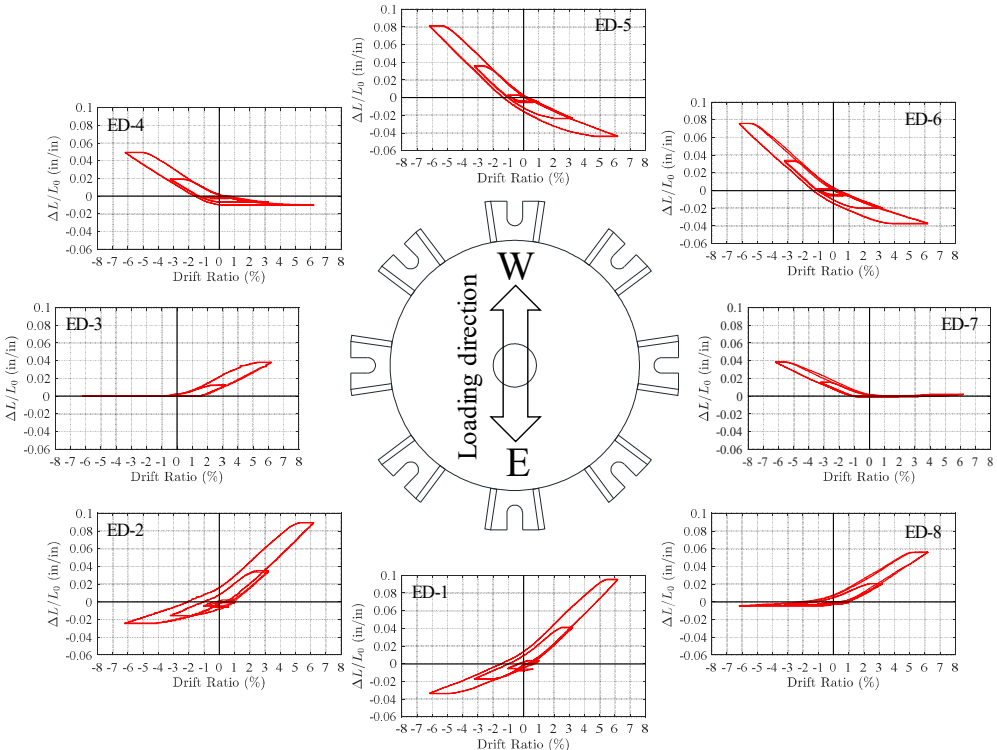


Figure 7.64. Normalized axial deformation in ED links versus drift ratio.

7.12.3. PUED-2 Specimen

The observed response of PUED-2 specimen under the loading sequence presented in Table 7.11 is described at each amplitude and supported with photo illustrations. The specimen was pulled to the west (positive direction) and pushed to the east (negative direction). The test started with pulling the specimen.

It is reminded that all eight ED links damaged over the previous test (specimen PUED-1) were replaced with a new set of links. Since no damage was observed in the steel confining tubes from the previous test, they were reused in this test. To prevent premature damage in the top connection of the ED links, the top connection flat washers were replaced with thick plate washers, custom made out of an existing 3/8" thick steel plate in the lab. The material properties of the steel plate was not known, but as it will be shown later, the plates remained undamaged. In this phase, the top nut at the top connection of the ED links were tightened with a torque wrench up to the 450 lb-ft torque corresponding to 20 kips clamp load.

In reference to Section 7.11.2.2, the study with the PUED-2 specimen is termed *Phase 2*, and it is separated into four sub-phases, Phase 2.1, Phase 2.2, Phase 2.3 and 2.4, per Table 7.11.

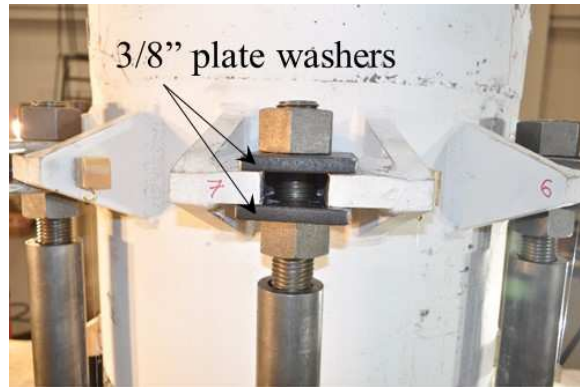


Figure 7.65. 3/8" thick plate washers at the top connection of ED links.

7.12.3.1. Observations

7.12.3.1.1. Phase 2.1

7.12.3.1.1.1. Amplitude 1 – $0.4 \times DE$: ± 0.65 in. ($\pm 0.6\%$ drift ratio)

No damage was observed.

7.12.3.1.1.2. Amplitude 2 – $0.6 \times DE$: ± 1.1 in. ($\pm 1.02\%$ drift ratio)

No damage was observed.

7.12.3.1.1.3. Amplitude 3 – $1.2 \times DE$: ± 3.5 in. ($\pm 3.23\%$ drift ratio)

In ED-5 and ED-6, at the top link connection, the top nut was loosened and the bottom nut was loosened in ED-1 and ED-8. The loosened nuts were retightened prior to the next test.

7.12.3.1.2. Phase 2.2

Before starting this phase of the test, all the ED links were released and retightened to evaluate the re-centering capacity of the system upon removal of ED links. This process is described subsequently in Section 7.12.3.3, where the re-centering capabilities are demonstrated and quantified.

7.12.3.1.2.1. Amplitude 1 – $0.4 \times DE$: ± 0.65 in. ($\pm 0.6\%$ drift ratio)

No damage was observed.

7.12.3.1.2.2. Amplitude 2 – $0.6 \times DE$: ± 1.1 in. ($\pm 1.02\%$ drift ratio)

No damage was observed.

7.12.3.1.2.3. Amplitude 3 – $1.2 \times DE$: ± 3.5 in. ($\pm 3.23\%$ drift ratio)

No damage was observed.

7.12.3.1.2.4. Amplitude 4 – $1.8 \times DE$ ($1.2 \times MCE$): ± 6.7 in. ($\pm 6.19\%$ drift ratio)

On the east side, the flexural and vertical cracks in the concrete above the steel collar formed during the previous test (PUED-1) extended to the southeast and northeast. Moreover, formation of more hairline flexural cracks (Figure 7.66(a)) was observed. On the west side, the flexural and vertical cracks in the concrete above the steel collar formed during the previous test (PUED-1) extended to the southwest and northwest. Moreover, formation of one more vertical hairline crack was observed in the vicinity of the concrete cover-to-steel collar joint (at top of the steel collar) extending up to about 5" from the joint (Figure 7.66(b)).

Moreover, ED-1 and ED-5 fractured at 6.19% drift ratio during the second pull and second push loading cycle, respectively (Figure 7.66(c)).

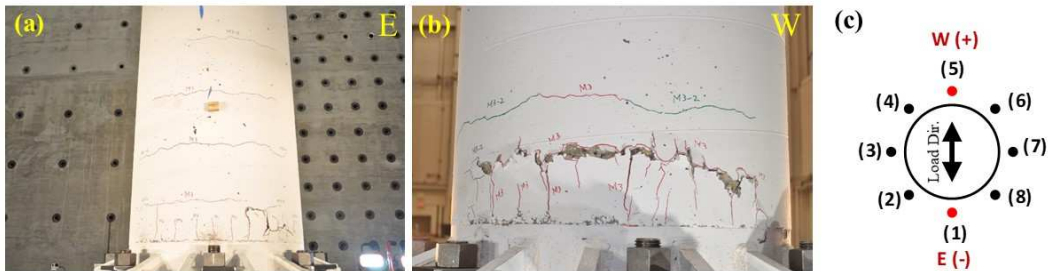


Figure 7.66. Damage state in PUED-2 column at $1.8 \times DE$ ($1.2 \times MCE$): (a) cracks in concrete on east side; (b) cracks in concrete on west side; (c) location of fractured ED links (red circles).

7.12.3.1.3. Phase 2.3

Before starting this phase, the ED links fractured in the previous phase (ED-1 and ED-5 as shown in Figure 7.66(c)) were removed from the test setup.

7.12.3.1.3.1. Amplitude 1 – $0.4 \times DE$: ± 0.65 in. ($\pm 0.6\%$ drift ratio)

No damage was observed.

7.12.3.1.3.2. Amplitude 2 – $0.6 \times DE$: ± 1.1 in. ($\pm 1.02\%$ drift ratio)

No damage was observed.

7.12.3.1.3.3. Amplitude 3 – $1.2 \times DE$: ± 3.5 in. ($\pm 3.23\%$ drift ratio)

No damage was observed.

7.12.3.1.3.4. Amplitude 4 – 1.8×DE (1.2×MCE): ±6.7 in. (±6.19% drift ratio)

No damage was observed over the test at the loading rate of 1.08 in/sec (0.01 drift ratio/sec). At the loading rate of 2.71 in/sec (0.025 drift ratio/sec), cover concrete spalling was observed above the steel collar-concrete joint on both east and west side (Figure 7.67(a) and (b)). Moreover, ED-6 fractured during the second push loading cycle (Figure 7.67(c)) about the peak drift ratio (6.19%).



Figure 7.67. Damage state in PUED-2 column at 1.8×DE (1.2×MCE) at the loading rate of 2.71 in/sec (0.025 drift ratio/sec): (a) cover concrete spalling on east side; (b) cover concrete spalling on west side; (c) location of fractured ED link (red circle).

7.12.3.1.4. Phase 2.4

Before starting this phase of the testing program, all ED links except for ED-3 and ED-7 were removed from the test setup (Figure 7.68).

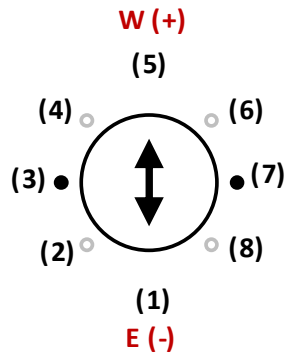


Figure 7.68. Location of ED links removed from PUED-2 specimen (gray circles) at the end of Phase 2.3 of the testing program.

7.12.3.1.4.1. Amplitude 1: ± 8 in. ($\pm 7.39\%$ drift ratio)

At the loading rate of 1.08 in/sec (0.01 drift ratio/sec), more vertical cracks were formed on the southeast side in the vicinity of the concrete cover-steel collar joint (at top of the steel collar) extending up to about 3” from the joint (Figure 7.69(a)).

On the west side, more cover concrete spalling was observed as well as formation of more vertical cracks on the southwest and northwest sides in the vicinity of the concrete cover-steel collar joint (at top of the steel collar) extending up to about 3” from the joint (Figure 7.69(b)).

No further damage was observed during testing with the loading rate of 2.71 in/sec (0.025 drift ratio/sec).

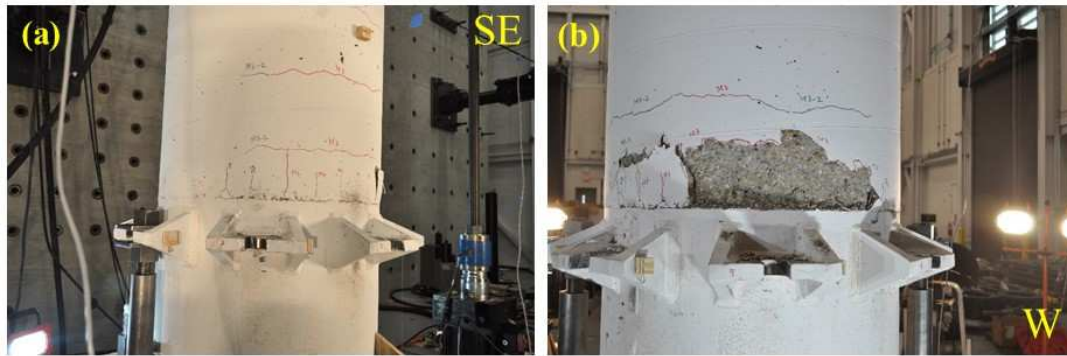


Figure 7.69. Damage state in PUED-2 column at 7.39% drift ratio at the loading rate of 1.08 in/sec (0.01 drift ratio/sec): (a) southeast side; (b) west side.

7.12.3.1.4.2. Amplitude 2: ± 10 in. ($\pm 9.24\%$ drift ratio)

At the loading rate of 1.08 in/sec (0.01 drift ratio/sec), after the first two repeated loading cycles, multiple vertical cracks were observed in the PU on the east and northeast side (Figure 7.70). Moreover, minor grout delamination was observed on the surface of the foundation block in contact with the PU (Figure 7.70(c)).

The specimen was not tested at a higher rate due to safety concerns associated with the unexpected cracks observed in the PU material. However, the performance of the system at this damaged state was assessed by repeating the loading cycle with the peak displacement of 10" (9.24% drift ratio) and the loading rate of 1.08 in/sec (0.01 drift ratio/sec) for the third time. In the push loading cycle, crack opening was observed in the PU material followed by an extensive damage occurred in the PU material on the east side in the form of complete fracture in a large area indicated with white marks in Figure 7.71(a) and detachment of a piece of PU material. Moreover, a crack extending over the

entire height of the PU segment was observed on the northeast side (Figure 7.71(b)). The cause of this unexpected failure is still unknown, as it was not observed during testing of material samples, and needs to be further investigated. However, potential causes may include imperfections within the volume/mass of the PU material, stress concentration due to imperfections at the PU-to-foundation or PU-to-concrete column interface, or the triaxial state of the material, which may be different than that generated by uniaxial testing of PU cylindrical samples.

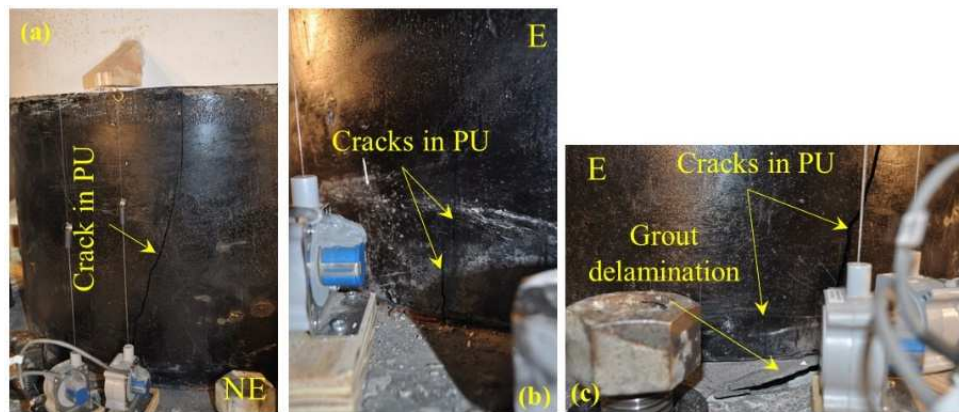


Figure 7.70. Damage state in PUED-2 column at 9.24% drift ratio at the loading rate of 1.08 in/sec (0.01 drift ratio/sec): (a) long crack in PU on northeast side; (b) short cracks in PU on east side; (c) grout delamination and cracks in PU.



Figure 7.71. Damage state in PUED-2 column at 9.24% drift ratio at the loading rate of 2.71 in/sec (0.025 drift ratio/sec): (a) PU complete fracture on east side; (b) crack in PU on northeast side.

7.12.3.2. Post-test Inspection of Segments and ED Links

After the specimen was disassembled, the segments were visually inspected to identify further damage, especially at contact surfaces. No damage was observed at the bottom surface of the RC rocking element with steel collar. As shown in Figure 7.72, minor damage was observed in the concrete core of the bi-layered PU segment in the top and bottom surfaces, mainly in the form of hairline cracks. Minor local crushing was observed in the concrete core on the west side at the top surface, most probably from stress concentrations due to imperfections at the contact interface when the vertical load (post-tensioning and gravity) was applied. On the east side of the top and bottom surfaces (where the PU rupture occurred over the last loading cycle), cracks were observed in the PU material through the entire thickness of the PU sleeve.

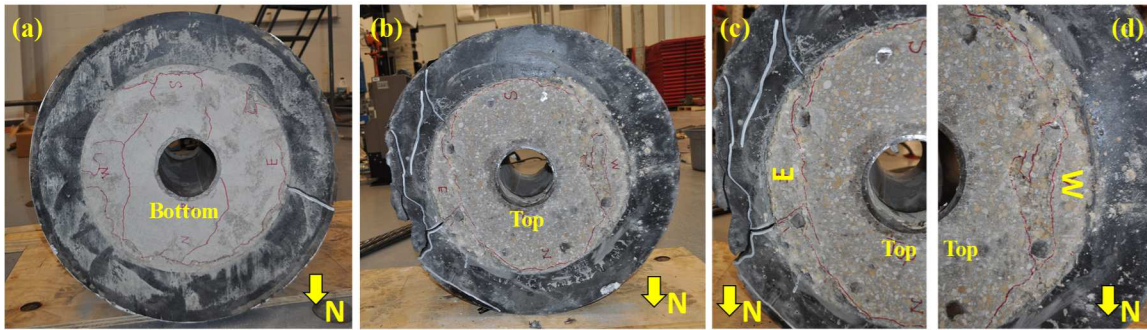


Figure 7.72. Visual inspection of the damage state at the top and bottom surfaces of the bi-layered PU segment.

At the end of the test, the ED links were disassembled and visually inspected to identify the damage states. The ED bars are arranged radially at their location on a plan view of the ED links setup in Figure 7.73. High-mode buckling was observed in all eight links, confirming the essential role of the confining tube in preventing low buckling modes and ensuring yielding in both tension and compression, thereby providing stable energy dissipation capabilities.



Figure 7.73. PUED-2 specimen: extracted view of ED links.

As mentioned earlier, ED-1 fractured in tension during the second pull loading cycle about the peak drift ratio of 6.19% (Figure 7.74(a)). As expected, fracture occurred around the middle of the yielding length with reduced cross-section area. Upon the load reversal, bearing mechanism was activated at the fracture surfaces, when the two broken piece of the link came in compressive contact (Figure 7.74(b) and (d)), causing bearing damage as shown in Figure 7.74(f) and (g).

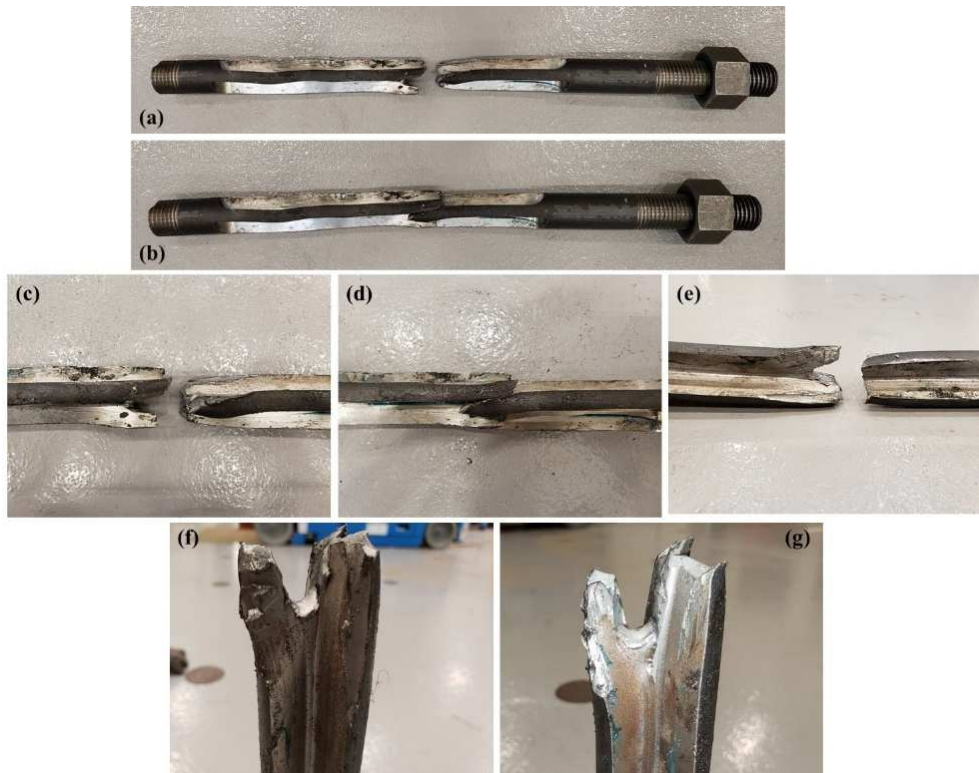


Figure 7.74. Damage in ED-1.

ED-5 fractured in tension during the second push loading cycle about the peak drift ratio of 6.19% (Figure 7.75(a)). Similar to ED-1, fracture occurred around the middle of the yielding length with reduced cross-section area, as expected. Upon the load reversal, although the system was pulled to the initial position (zero displacement), the top and bottom pieces of the broken link came in contact, thus, activating a bearing mechanism (Figure 7.75(b) and (d)), that caused bearing damage as shown in Figure 7.75(f) and (g).

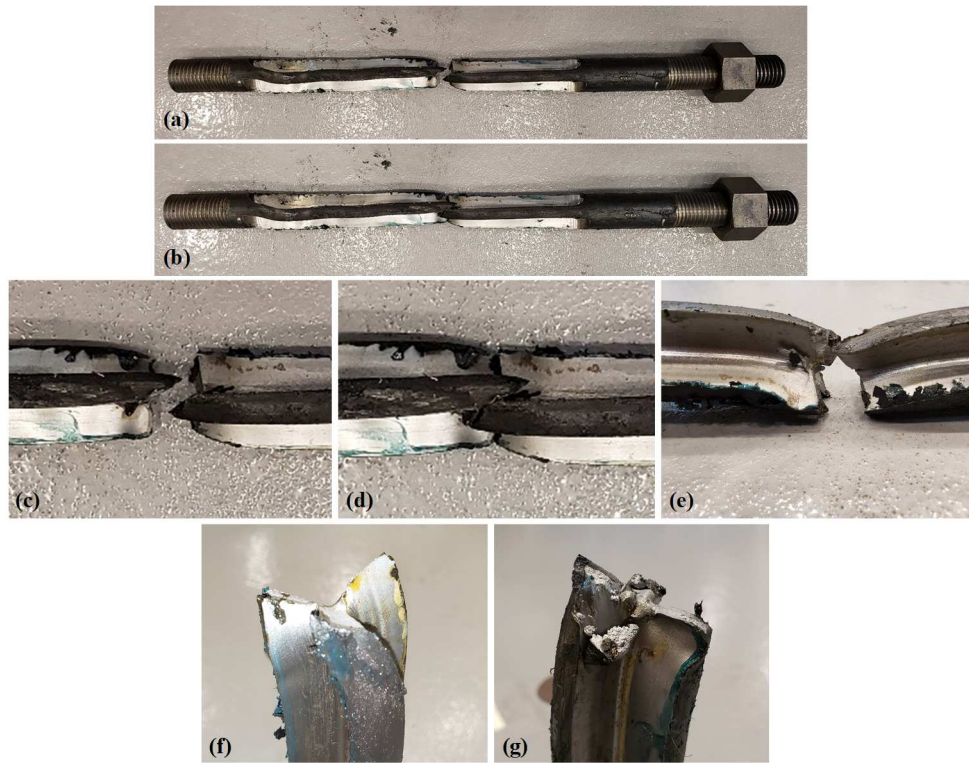


Figure 7.75. Damage in ED-5.

ED-6 fractured in tension during the second push loading cycle about the peak drift ratio of 6.19% (Figure 7.76). Similar to ED-1 and ED-5, fracture occurred around the middle of the yielding length with reduced cross-section area, as expected. No sign of damage was observed at the fracture surfaces in the form of bearing crush, indicating that the bearing mechanism was not activated in ED-6.

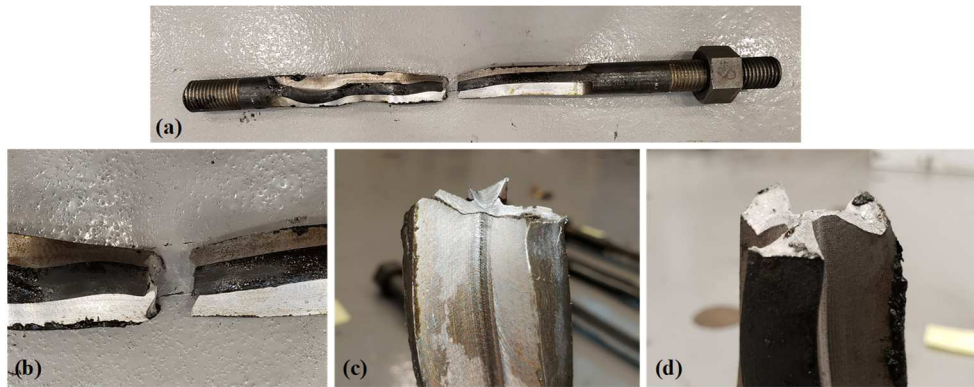


Figure 7.76. Damage in ED-6.

7.12.3.3. Lateral Load-Drift Response

7.12.3.3.1. Phase 2.1

Lateral load vs. drift ratio hysteretic response of the PUED-2 specimen in Phase 2.1 is compared to PUED-1 specimen at various hazard levels ($0.4\times DE$, $0.6\times DE$, $1.2\times DE$) in Figure 7.77. Forces have been corrected for the contribution of the vertical actuators in the deformed configuration. The peak lateral load in positive (pull) and negative (push) direction at various hazard levels is summarized in Table 7.17. Similar to the PUED-1 column, the PUED-2 column exhibited a stable response without any softening up to a 3.23% drift ratio, corresponding to $1.2\times DE$ hazard level. The identical response of PUED-1 and PUED-2 columns further supports the response stability/reliability of the PUED system, and furthermore, it indicates that the bi-layered PU segment and the top RC element have not experienced any major damage over the previous tests (tests on PUED-1).

An elastic response was observed up to 0.6% drift ratio corresponding to the 0.4×DE hazard level (Figure 7.77(a)). Minor hysteretic response was observed in the curve corresponding to 0.6×DE hazard level (Figure 7.77 (b)). Nonlinear response initiated at about 60 kips lateral load. It is believed that the nonlinear response originated from the yielding at ED-1 and ED-5. Clear nonlinear response was observed in the curves corresponding to 1.2×DE hazard levels which is believed to be not only due to the yielding of ED links, but also the nonlinear response of the PU material in the vicinity of the PU-foundation interface. The peak lateral strength was 98.7 kips and -95.2 kips, in the positive and negative direction, respectively, and was observed at a 6.2% drift ratio.

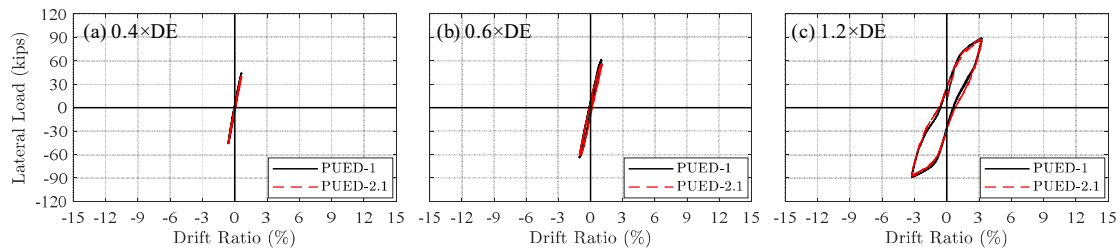


Figure 7.77. Lateral load vs. drift ratio hysteresis curve for the PUED-2 column at different hazard levels, per Phase 2.1.

7.12.3.3.2. Recovery (ED links released and retightened)

Before moving on to the Phase 2.2 of the test plan, the re-centering capacity of the system was assessed by releasing and retightening the ED links in the order of 5-1-2-8-6-4-7-3. Since the specimen was loaded in displacement-controlled mode, at the end of each

test, a residual load was measured by the horizontal actuator (about 22 kips here). The residual load corresponds to the load required to hold the specimen at zero displacement state, while the specimen tends to achieve its natural stable equilibrium state under gravity loads which may not be the zero displacement state, depending on the damage experienced by the specimen.

To remove the ED links, the residual load in the horizontal actuator was first removed manually, by pulling or pushing the specimen to positive or negative direction (Figure 7.78(a)). Every time an ED link was removed, the reaction force in the horizontal actuator was released (to zero). After releasing all the ED links (and simultaneously and continuously setting the force of the horizontal actuator to zero, Figure 7.78(a)), that lateral displacement also landed at zero (Figure 7.78(b)), which corresponds to full recovery of the system.

The ED links were then retightened following the same order they were released, for Phase 2.2 to begin.

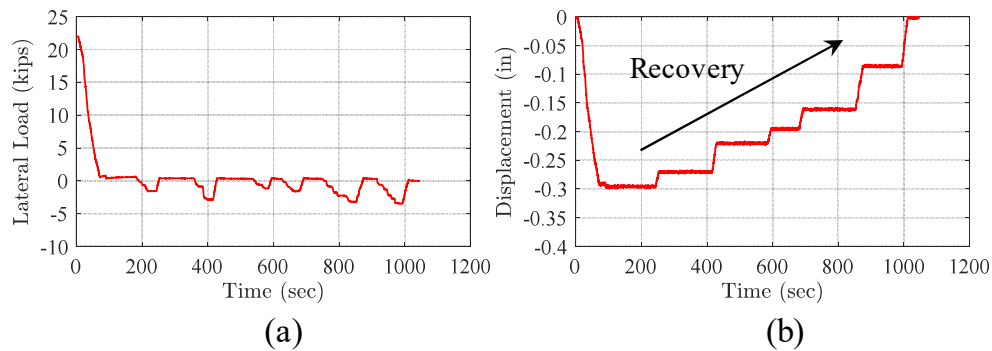


Figure 7.78. PUED-2 column response history over ED link release and retightening: (a) lateral load time history; (b) lateral displacement time history.

7.12.3.3.3. Phase 2.2

Lateral load vs. drift ratio hysteretic response of the PUED-2 specimen before (Phase 2.1) and after (Phase 2.2) recovery at various hazard levels ($0.4 \times DE$, $0.6 \times DE$, $1.2 \times DE$) is compared in Figure 7.79. The peak lateral load in positive (pull) and negative (push) direction at various hazard levels is summarized in Table 7.17. The hysteretic response of the PUED-2 column at all hazard levels is also shown in Figure 7.80(b). Forces have been corrected for the contribution of the vertical actuators in the deformed configuration. The specimen response before and after the recovery were identical, which ensures the performance stability of the system under repeated loading, at least up to a drift ratio corresponding to $1.2 \times DE$ hazard level.

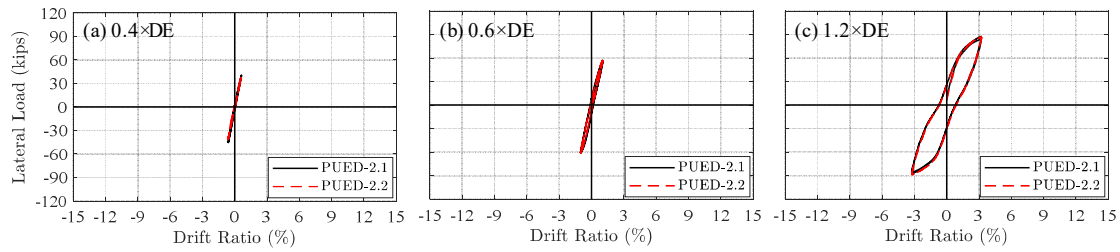


Figure 7.79. Lateral load vs. drift ratio hysteresis curve for the PUED-2 column at different hazard levels before (PUED-2.1) and after (PUED-2.2) recovery.

The performance stability of the system at higher drift ratios corresponding to $1.8\times DE$ hazard level was confirmed by comparing the hysteresis response of the response of the PUED-2 specimen after recovery with the response of the PUED-1 specimen (Figure 7.80(a)). As shown, the two specimens exhibited identical response, except for the fracture of two ED links (ED-1 and ED-5) which occurred in PUED-2 specimen during the second pull and push loading cycle at 6.19% drift ratio, respectively (Figure 7.80(a)). The lateral load dropped by 11.7 kips and 11 kips upon fracture of ED-1 and ED-5, respectively. However, the hysteretic response remained stable.

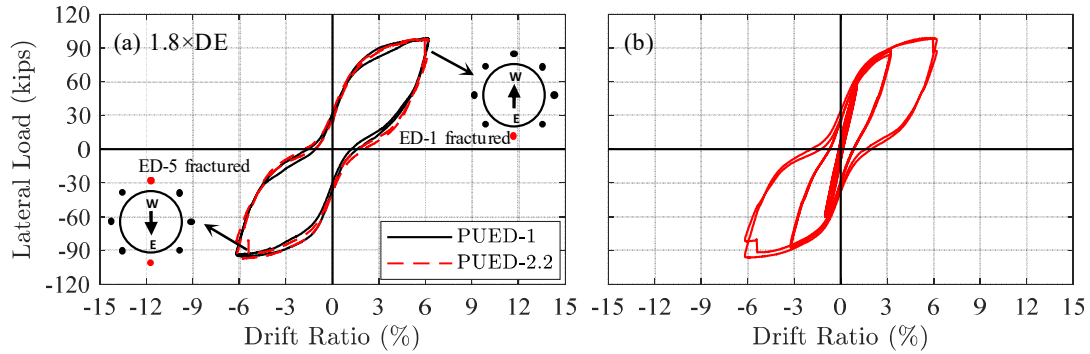


Figure 7.80. Lateral load vs. drift ratio hysteresis curve for the PUED-2 column: (a) comparison to PUED-1 specimen at 1.8×DE (1.2×MCE) hazard level; (b) all hazard levels (0.4×DE, 0.6×DE, 1.2×DE, and 1.8×DE (1.2×MCE)).

Table 7.17. Summary of peak lateral strength in positive and negative direction at various hazard levels: PUED-2 specimen, Phase 2.1 and 2.2.

Hazard Level	Peak Drift Ratio (%)	F_{peak}^+		F_{peak}^-	
		Phase 2.1	Phase 2.2	Phase 2.1	Phase 2.2
0.4×DE	0.60	39.3	39.3	-40.7	-40.7
0.6×DE	1.02	56.8	56.8	-60.9	-60.9
1.2×DE	3.23	87.4	87.6	-88.7	-88.7
1.8×DE (1.2×MCE)	6.19	-	98.6	-	-97.2

7.12.3.3.4. Phase 2.3

After removing the fractured ED links (ED-1 and ED-5), Phase 2.3 started, which included cyclic displacement-controlled sinusoidal reversed loading applied at amplitudes corresponding to selected hazard levels, namely 0.4×DE, 0.6×DE, 1.2×DE, and 1.8×DE (1.2×MCE). For each hazard level, the loading was applied at various rates including 0.1,

1.08, 2.71, and 5.41 in/sec corresponding to a drift ratio rate of 0.001, 0.01, 0.025, and 0.05 /sec, respectively (Table 7.11).

Lateral load vs. drift ratio hysteretic responses of the PUED-2 specimen at three hazard levels ($0.4 \times DE$, $0.6 \times DE$, and $1.2 \times DE$) and four loading rates are shown in Figure 7.81. Forces have been corrected for the contribution of the vertical actuators in the deformed configuration.

It should be noted that the tests at 0.001 drift ratio/sec were not performed for amplitudes corresponding to $1.2 \times DE$, and $1.8 \times DE$ ($1.2 \times MCE$) hazard levels due to time limitations. Moreover, the test at 0.05 drift ratio/sec was not performed for amplitude corresponding to $1.8 \times DE$ ($1.2 \times MCE$) hazard level due to concerns for potential specimen instability.

In all loading cycles, the specimen showed higher strength (up to about 11 kips) in the push direction (negative direction) of the loading compared to the pull direction (positive direction) (Table 7.18). This can be attributed to the eccentricity of the post-tensioning tendon which is reflected in Figure 7.85(c) as asymmetric post-tensioning load response with higher values in the push direction (negative direction) of the loading.

Overall, no significant rate effect was observed in the response of the system at various hazard levels up to the maximum achieved loading rate of 5.41 in/sec. This was further verified by comparing the peak lateral strength in pull and push direction for various hazard levels at different loading rates (Table 7.18). The peak strength either did

not change or decreased with the loading rate. The reduction in the peak strength with the loading rate is attributed to the incapability of the lateral actuator in capturing the target peak displacements at 0.025 /sec and 0.05 /sec loading rates.

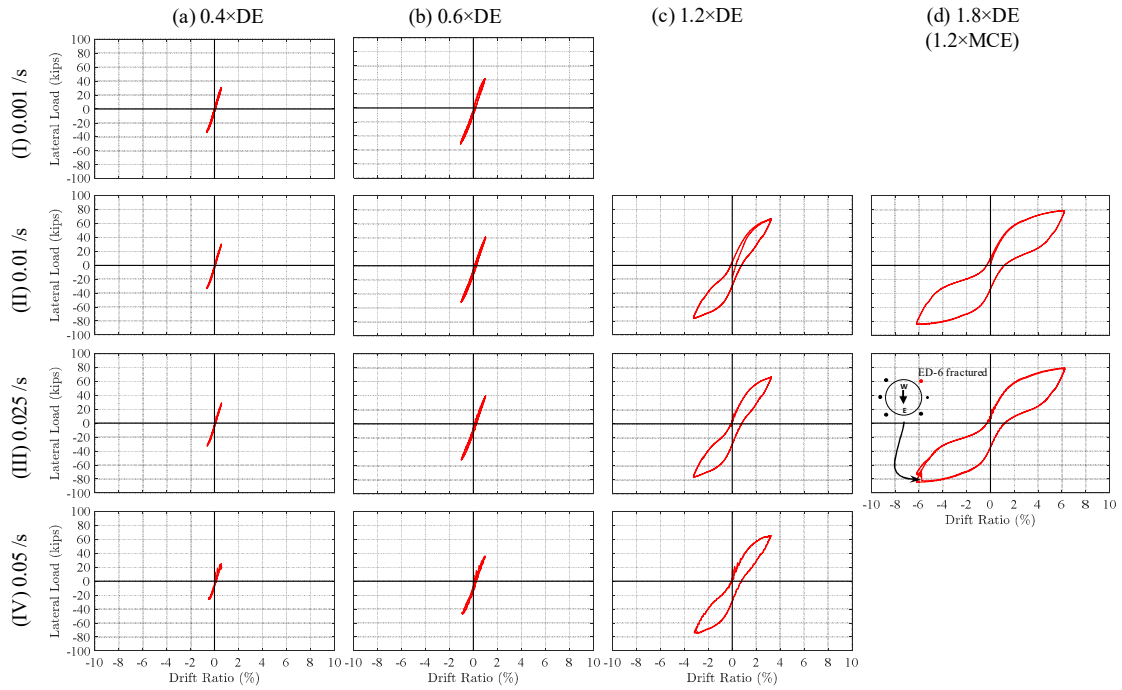


Figure 7.81. Lateral load vs. drift ratio hysteresis curve for the PUE-2 column at different hazard levels and loading rates.

Table 7.18. Summary of peak lateral strength in positive and negative direction at various hazard levels and loading rates: PUED-2 specimen, Phase 2.3.

Hazard Level	0.001 /sec		0.01 /sec		0.025 /sec		0.05 /sec	
	F_{peak}^+	F_{peak}^-	F_{peak}^+	F_{peak}^-	F_{peak}^+	F_{peak}^-	F_{peak}^+	F_{peak}^-
0.4×DE	30.1	-33.2	29.9	-33.5	28.5	-32.2	22.3	-25.6
0.6×DE	41.7	-51.2	41.1	-51.8	40.1	-51.4	35.7	-46.5
1.2×DE	-	-	66.7	-76.1	66.5	-76.1	65.2	-74.0
1.8×DE (1.2×MCE)	-	-	78.6	-84.5	79.1	-84.5	-	-

7.12.3.3.5. Phase 2.4

After removing all the ED links except for ED-3 and ED-7, the specimen was further loaded up to 8” and 10” peak lateral displacement. Because of the location of these links, the response of this system is, in an approximate sense, representative of the response of rocking columns with a bi-layered PU segment at the bottom without ED links (Figure 7.2(c)). As it will be shown later (see Figure 7.97), the response of this column is also similar to the response of rocking columns with a solid PU segment at the bottom without ED links (Figure 7.2(b)).

The lateral load vs. drift ratio hysteretic response of the PUED-2 specimen up to the peak displacement of 8” (7.39% drift ratio) at 1.08 in/sec (0.01 /sec) and 2.71 in/sec (0.025/sec) loading rates is shown in Figure 7.82. Forces have been corrected for the inclination of the vertical actuators in the deformed configuration. A stable response without any softening is observed. As shown, the specimen exhibited practically identical response at 1.08 in/sec (0.01 /sec) and 2.71 in/sec (0.025/sec) loading rates.

Minor hysteresis was observed in the response. Clear nonlinear response was observed in the curves which is attributed to the nonlinear response of the PU material and central RC core in the vicinity of the PU-to-foundation interface. Column peak lateral strength was 58 kips and -57.4 kips, in the positive and negative direction, respectively, observed at 8" (7.39% drift ratio) peak displacement.

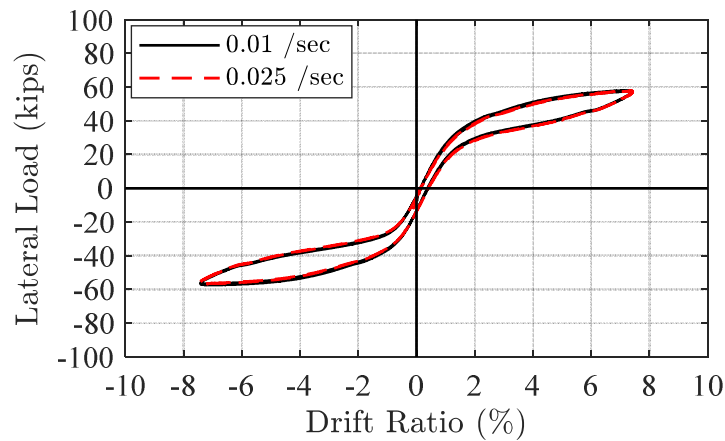


Figure 7.82. Lateral load vs. drift ratio hysteresis curve for the PUED-2 column up to 8" (7.39% drift ratio) lateral displacement at various loading rates.

Lateral load vs. drift ratio hysteretic response of the PUED-2 specimen up to the peak displacement of 10" (9.24% drift ratio) at 1.08 in/sec (0.01 /sec) loading rate is shown in Figure 7.83. A stable response without any softening was observed over the first two cycles with a peak lateral strength of 58.7 kips and -56.7 kips, in the positive and negative direction, respectively, observed at 10" (9.24% drift ratio) peak displacement. Since multiple vertical cracks were observed in the PU on the east and northeast side during the previous cycles (Figure 7.70), the specimen was not tested at a higher rate due to concerns

for potential instability. However, the performance of the system at this damaged state was assessed by repeating the loading cycle with the peak displacement of 10” (9.24% drift ratio) for the third time. As mentioned in Section 7.12.3.1, extensive damage occurred in the PU material on the east side in the form of complete fracture in a large area (Figure 7.71), which was reflected in hysteresis response as a strength degradation initiating at about -2.2% drift ratio with the maximum occurred at -9.24% drift ratio. The observed strength at -9.24% drift ratio was -44.0 kips in the third cycle, which compared to the corresponding value in the previous two cycles (-56.7 kips), corresponds to a 12.7 kip drop (equivalent to a 24.8% drop).

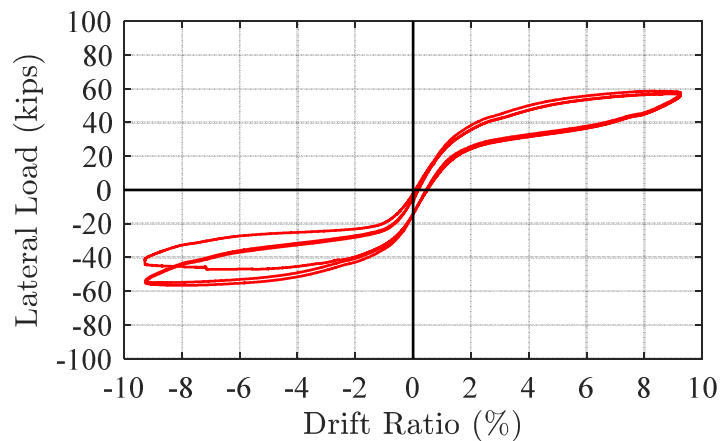


Figure 7.83. Lateral load vs. drift ratio hysteresis curve for the PUE-2.4 column up to 10 in. (Phase 2.4) lateral displacement (9.24% drift ratio) at 0.01 /sec loading rates.

The hysteretic response of the PUED-2 column with two ED links up to 10” peak lateral displacement is compared to the hysteretic response of the RC rocking column in Figure 7.84. The PUED-2 column clearly shows lower lateral strength compared to the RC rocking column up to about +3% drift ratio, beyond which due to the significant softening occurred in the RC rocking column, the PUED-2 column outperforms the RC rocking column in the positive direction.

The elastic stiffness of the PUED-2 column with two ED links is much lower than the RC rocking column as shown in Figure 7.84(b).

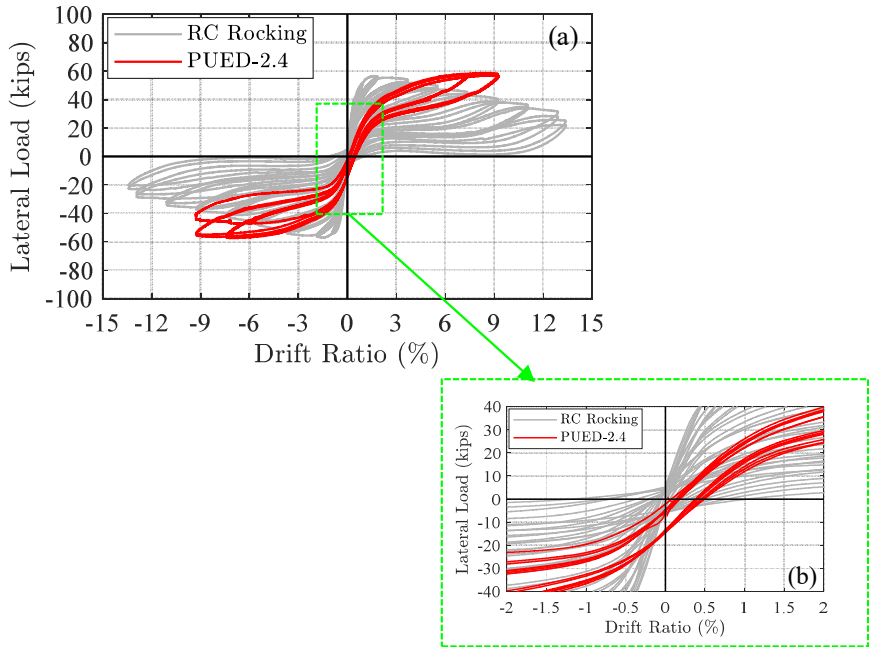


Figure 7.84. Lateral load vs. drift ratio hysteresis curve: PUED-2.4 with two ED links vs. RC rocking column.

7.12.3.4. Post-tensioning Load History

The variation of the PT load with the lateral drift ratio is shown in Figure 7.85(a). The initial PT load level for each loading phase is shown with the dashed red line. Due to the opening at the rocking interface (PU-to-foundation interface), the PT load increases as the column is loaded from the rest position (zero displacement) to the peak displacement in positive or negative direction.

The post-tensioning load at the end of each set of cycles versus the corresponding peak drift ratio is shown in Figure 7.85 (b) for different loading phases. No loss was observed in PT load up to the end of the phase 2-3. The PT load measured at the end of the cycles with 8" and 10" peak lateral displacement was 426 kips and 415.5 kips, which corresponds to a total loss of 0.3% and 2.8 % relative to the initial PT load (427 kips). The maximum observed PT load in the tendon during the entire loading history was 558.7 kips which was below the nominal yield load (632.7 kips), defined using the nominal yield strength of the mono strands (243 ksi).

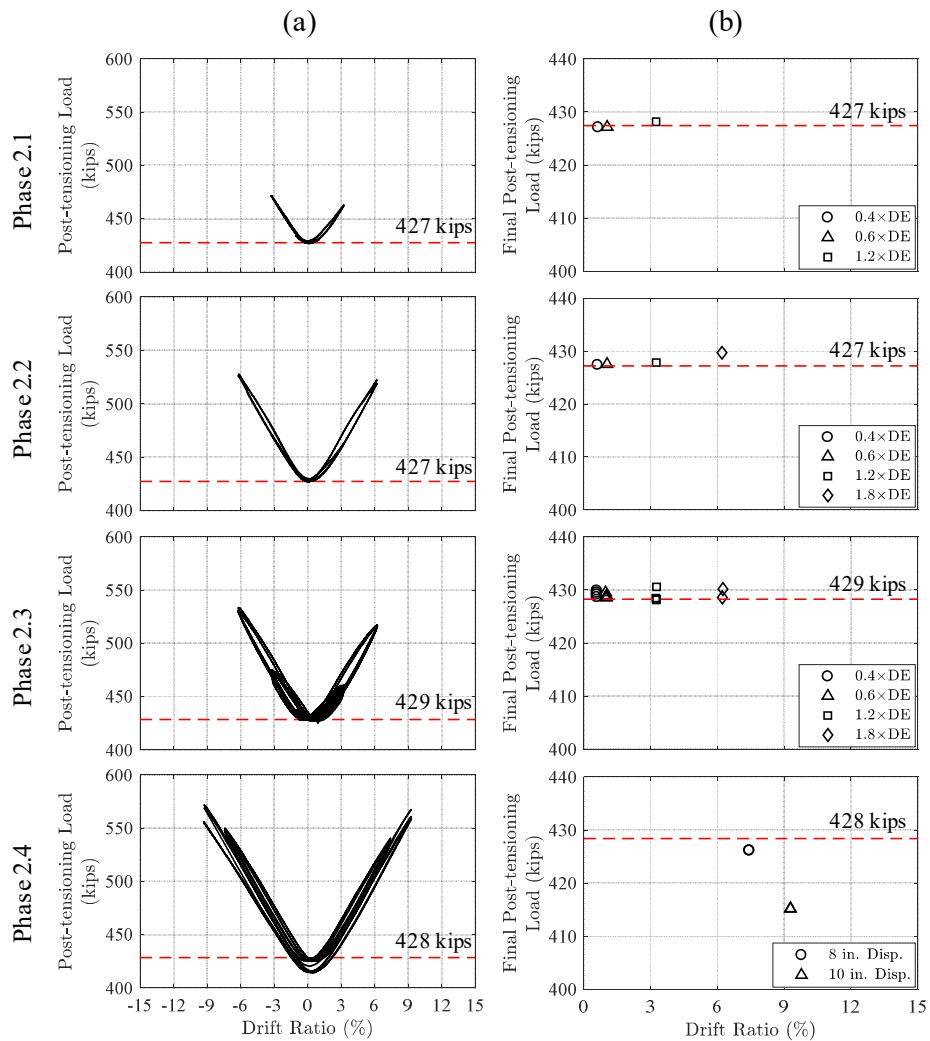


Figure 7.85. PUE-2 column: (a) post-tensioning load vs. peak drift ratio; (b) post-tensioning load at the end of each cycle vs. peak drift ratio.

7.12.3.5. Curvature

The average curvature was computed over a gage length of 15.625" (height of the bi-layered PU segment) using the data from the string potentiometers attached to the foundation on the east and west side of the specimen (Figure 7.14). The string

potentiometers were located at 2.4” from the column face. The average curvature was calculated using the procedure explained in Section 7.12.1.5.

The computed average curvature over the height of the bi-layered PU segment for various drift ratios is compared to that of the RC rocking and PUED-1 columns in Figure 7.86. It can be seen that at the same drift ratio, the curvature at the base rocking interface is approximately the same in all system. The curvature at the top PU interface was not measured. However, since the rocking mechanism at top interface of the bi-layered PU segment was locked by the central steel pipe, no opening was observed at the top PU-to-RC element interface during the test. Thus, the measured lateral displacement at the loading center was only due to the rotation of the column about its compression toe at the PU-foundation interface.

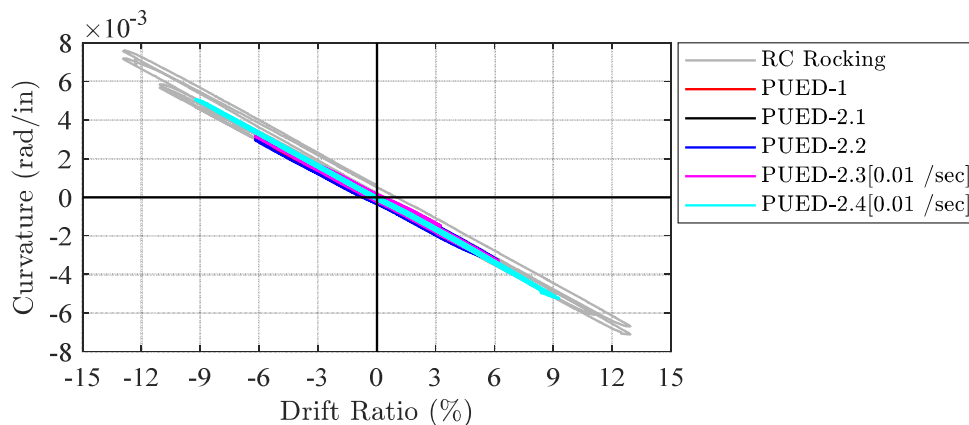


Figure 7.86. Curvature at the base of the bi-layered PU segment vs. drift ratio: PUED-2 vs. PUED-1 and RC rocking column.

7.12.3.6. Energy Dissipation and Equivalent Viscous Damping

The CDE and equivalent viscous damping versus drift ratio (calculated as described previously in Section 7.12.1.6) for the PUED-2, PUED-1, and RC rocking columns are compared in Figure 7.87(a) and (b), respectively. The CDE and, accordingly, the equivalent viscous damping ratio increased with the drift ratio in PUED-2 column (Figure 7.87 (a) and (b) and Table 7.20). Moreover, it can be seen that the energy dissipation capacity of the PUED-2 column in Phase 2.1 and 2.2 of the loading sequence is comparable to that of the PUED-1 column. The energy dissipation capacity of the PUED-2 column decreased by removing two fractured ED links in Phase 2.3, however, it still provides higher energy dissipation capacity compared to the RC rocking column, especially at drift ratios exceeding 1%. The energy dissipation capacity of the PUED-2 column further decreased in Phase 2.4, where all other ED links except for two links (ED-3 and ED-7) were removed from the setup. In this case, the energy dissipation of the PUED column is slightly less than the RC rocking column.

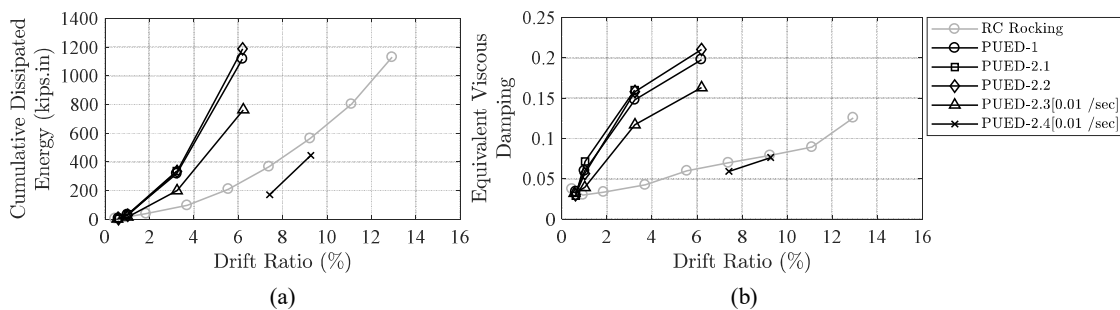


Figure 7.87. PUED-2 column vs. RC rocking column: (a) cumulative dissipated energy; (b) equivalent viscous damping.

7.12.3.7. Self-centering Efficiency

A comparison of the self-centering capabilities of PUED-2, PUED-1, and RC rocking column is presented in Figure 7.63 in terms of RSE (Figure 7.63(a)) and residual drift ratios (at each loading cycle) (Figure 7.63(b)) vs. the peak drift ratio of the cycle. The values of RSE and average RDR for all specimens corresponding to various hazard levels are summarized in Table 7.21 and Table 7.22. As shown, the re-centering capability of the PUED-2 column in all test phases decreases with the peak drift ratio, as reflected in Figure 7.88(a) and (b), yet RSE always remains above 70%. Compared to PUED-1 column, the PUED-2 column showed smaller RSE (larger residual deformation) in Phase 2.1 and 2.2 at various hazard levels ($0.4 \times DE$, $0.6 \times DE$, and $1.2 \times DE$). After removing two fractured ED links (ED-1 and ED-5) at the end of Phase 2.2, a large portion of the residual deformation in the system was recovered, resulting to a final RDR of 0.28%, which compared to the RDR before removing the fractured ED links (1.8%), corresponds to 85% recovery.

After the recovery, in Phase 2.3 of the test, the PUED-2 column outperformed the PUED-1 column by showing higher RSE (lower residual deformation), while compared to the RC rocking column, it showed smaller RSE (larger residual deformation). However, upon removing the other four ED links (ED-2, ED-4, ED-6, and ED-8) at the end of Phase 3, all the residual deformation in the system fully recovered, resulting to a final RDR of 0% (full re-centering).

After the second recovery, in Phase 2.4 of the test, the re-centering performance of the PUED-2 column further improved and was comparable to the RC rocking column.

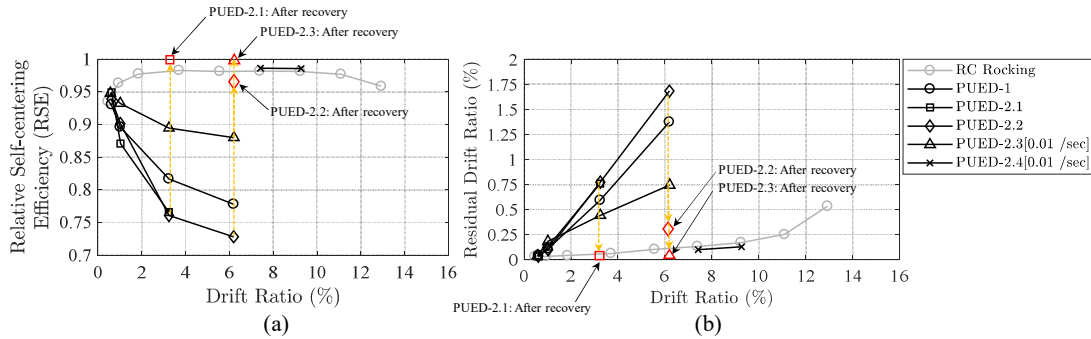


Figure 7.88. PUED-2 column vs. PUED-1 and RC rocking columns: (a) relative self-centering efficiency (RSE); (b) residual drift ratio.

7.12.3.8. Deformation of ED Link

The normalized axial deformation ($\Delta L/L_0$, where ΔL is the axial deformation and L_0 is the gage length ($\sim 12''$)) of ED links versus drift ratio for all ED links is shown for the PUED-2 specimen in Figure 7.89 for Phases 2.1 and 2.2, and in Figure 7.90 and Figure 7.91 for Phases 2.3 and 2.4, respectively. Similar to the observations made for the PUED-1 specimen, the links with the maximum distance from the neutral axis, i.e. ED-1 and ED-5, experienced the maximum deformation, which was comparable to deformation observed in PUED-1. In all ED links, the measured tensile deformation was larger than the compressive deformation due to the larger distance of the ED links from the neutral axis in tension than compression.

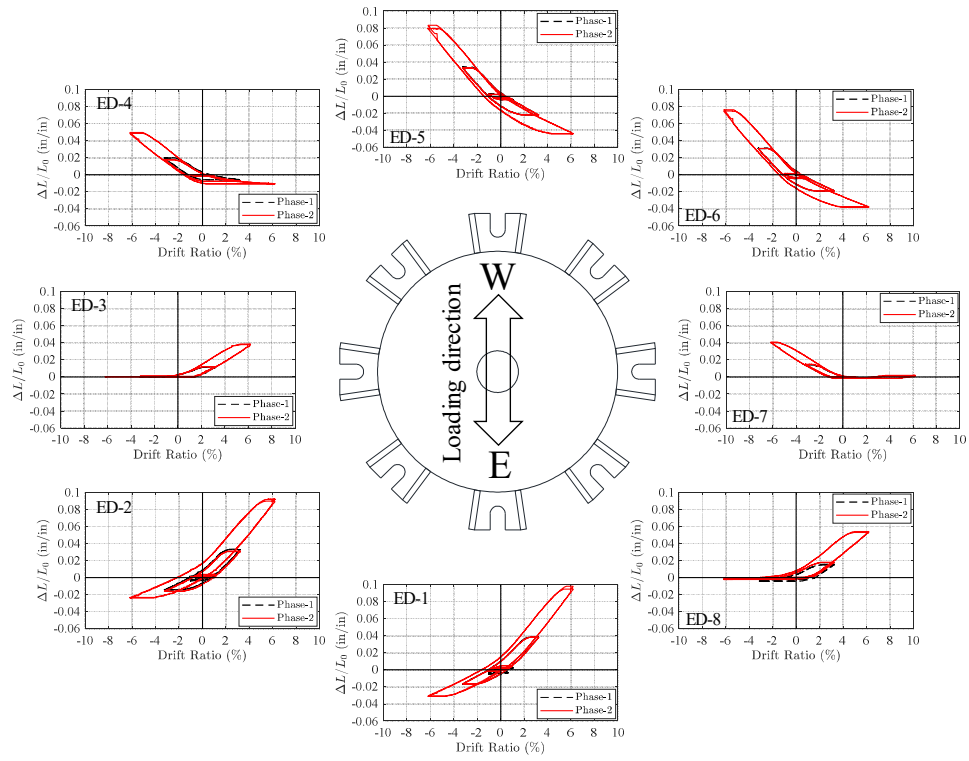


Figure 7.89. Normalized axial deformation in ED links versus drift ratio: PUED-2, Phase 2.1 and 2.2.

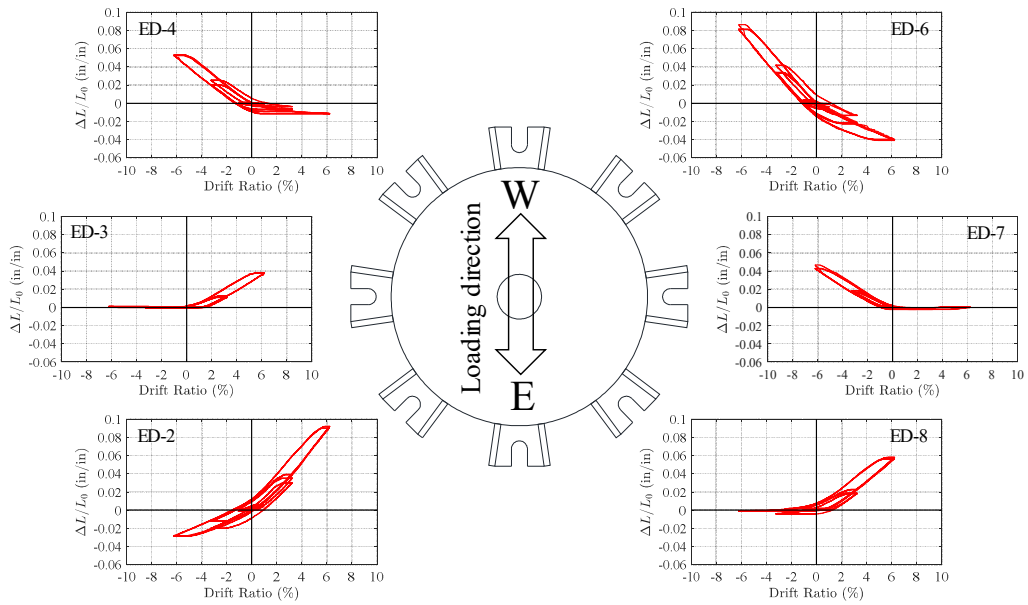


Figure 7.90. Normalized axial deformation in ED links versus drift ratio: PUED-2, Phase 2.3.

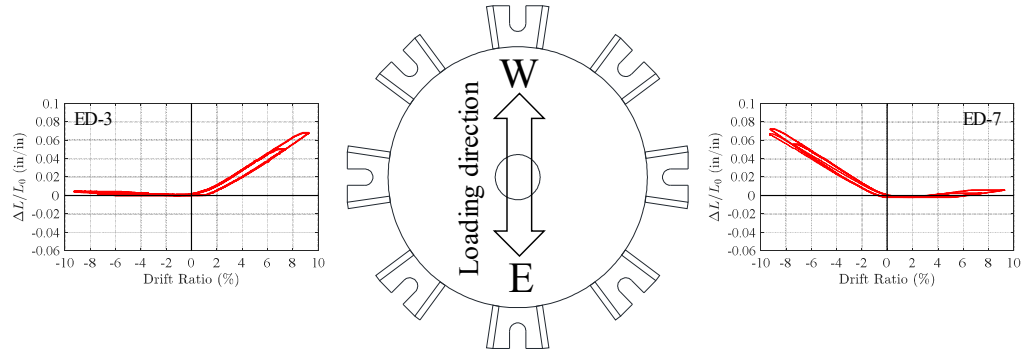


Figure 7.91. Normalized axial deformation in ED links versus drift ratio: PUED-2, Phase 2.4.

7.12.4. PU Specimen

The observed response of the rocking column with a solid PU segment at the bottom (Figure 7.2 (b)), under the loading sequence presented in Table 7.13, is described at each step and supported with photo illustrations. The specimen was pulled to the west (positive direction) and pushed to the east (negative direction). The test started with pulling the specimen.

It should be noted that the minor damage of the grout on the surface of the foundation block and the spalling of the RC element at the interface of the steel collar with the concrete cover from the previous test was fixed by patching the damaged areas with the same non-shrink grout compliant with ASTM C-1107 that can achieve up to 14 ksi compression strength for plastic consistency at 28 days.

7.12.4.1. Observations

7.12.4.1.1. Amplitude 1 – 0.4×DE: ±0.92 in. (±0.85% drift ratio)

No damage was observed.

7.12.4.1.2. Amplitude 2 – 0.6×DE: ±1.65 in. (±1.52% drift ratio)

No damage was observed.

7.12.4.1.3. Amplitude 3 – $1.2 \times DE$: ± 4.79 in. ($\pm 4.42\%$ drift ratio)

At the loading rate of 0.11 in/sec (0.001 drift ratio/sec), minor damage was observed at the PU-foundation interface in the form of grout delamination on west side (Figure 7.92(a)).

At the loading rate of 5.41 in/sec (0.05 drift ratio/sec), a single hairline crack was observed in the concrete cover on the west side at about 4" above the steel collar-concrete joint (Figure 7.92(b)).

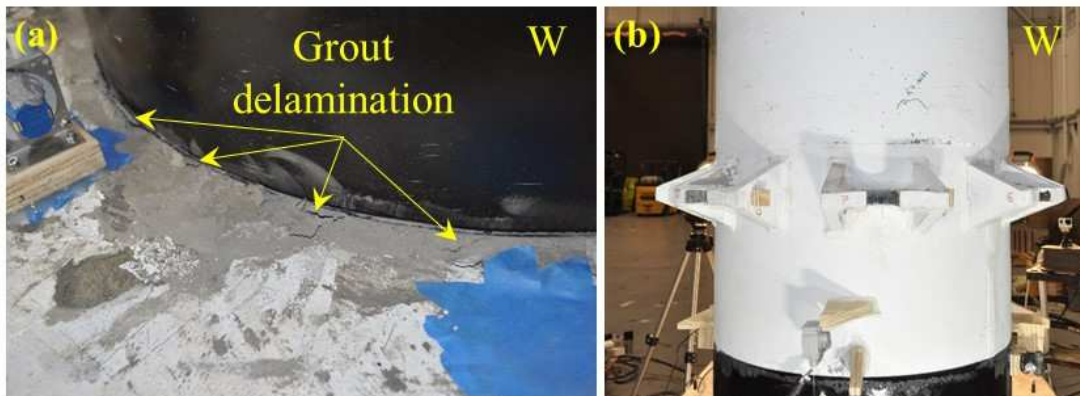


Figure 7.92. Damage state in PU column at $1.2 \times DE$: (a) grout delamination at the loading rate of 0.11 in/sec; (b) crack in concrete at the loading rate of 5.41 in/sec.

7.12.4.1.4. Amplitude 4 – $1.8 \times DE$ ($1.2 \times MCE$): ± 9.17 in. ($\pm 8.47\%$ drift ratio)

At the loading rate of 0.11 in/sec (0.001 drift ratio/sec), a gap was observed at the PU-to-foundation interface on both east and west side at the end of the test. A normal weight letter size paper with three folds was fitted in the gap to provide an idea of the gap

size (height and depth) (Figure 7.93). Moreover, more hairline cracks were observed in the concrete cover extending up to about 5" above the steel collar-to-concrete cover joint on both the east and the west side (Figure 7.94).

At the loading rate of 1.08 in/sec (0.01 drift ratio/sec), the depth of the gap at the PU-to-foundation interface was increased on both east and west sides as shown in Figure 7.95(a) and (b), where the same paper sheet with three folds was fitted further inside the gap. Moreover, one more hairline crack was observed in the concrete cover on the east side at about 4" above the steel collar-to-concrete cover joint (Figure 7.95(c)).

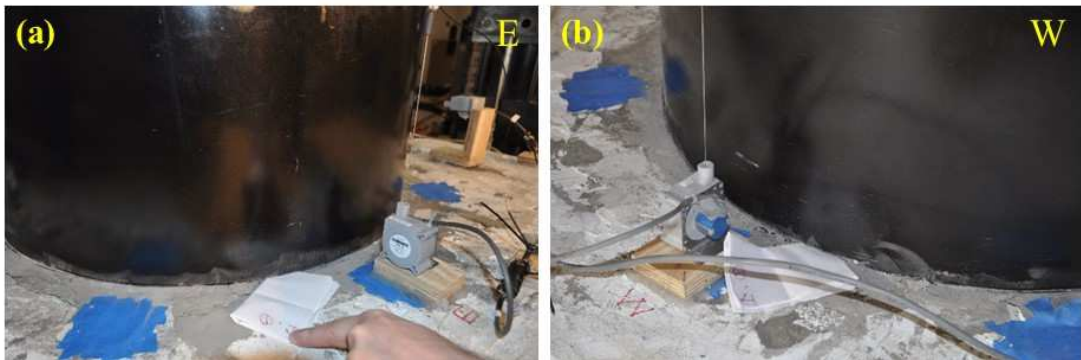


Figure 7.93. PU column at 1.8×DE (1.2×MCE) at the loading rate of 0.11 in/sec: gap at the PU-foundation interface.

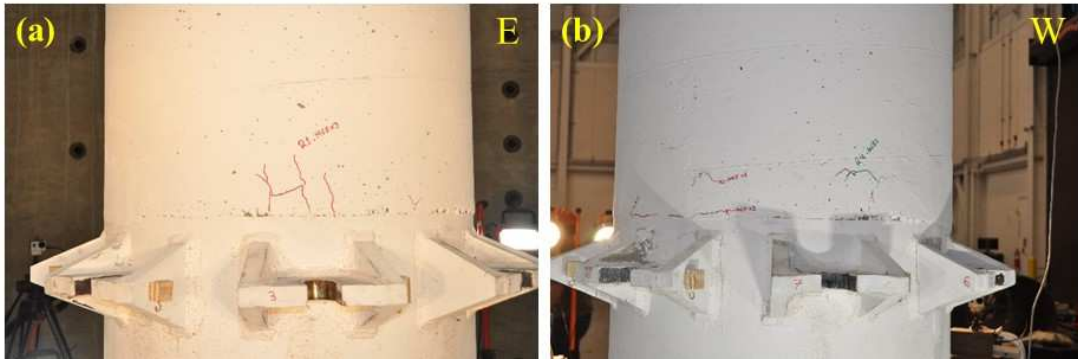


Figure 7.94. PU column at 1.8×DE (1.2×MCE) at the loading rate of 0.11 in/sec: crack in cover concrete.



Figure 7.95. PU column at 1.8×DE (1.2×MCE) at the loading rate of 1.08 in/sec: (a) and (b): gap size increased on east and west sides; (c) crack in cover concrete.

7.12.4.2. Lateral Load-Displacement Response

The lateral load vs. drift ratio hysteretic response of the PU column at selected hazard levels (0.4×DE, 0.6×DE, 1.2×DE, and 1.8×DE (1.2×MCE)) and loading rates (drift ratio rates: 0.001/sec, 0.01/sec, 0.025/sec, and 0.05/sec) is shown in Figure 7.96. Forces have been corrected for the inclination of the vertical actuators in the deformed configuration.

It should be noted that the tests at loading rates of 0.025 /sec and 0.05 /sec for displacement amplitude corresponding to 1.8×DE (1.2×MCE) hazard level were not completed due to malfunction of one of the vertical actuators during the last test.

For the loading cycles corresponding to 0.6×DE, 1.2×DE, and 1.8×DE (1.2×MCE) hazard levels, the specimen showed slightly higher strength (up to about 4.5 kips) in the positive direction (pull loading direction) compared to the negative direction (push direction), while the opposite was observed in loading cycles corresponding to the 0.4×DE hazard level (Table 7.19).

Overall, no significant rate effect was observed in the response of the system at various hazard levels up to the maximum achieved loading rate of 5.41 in/sec. This was further verified by comparing the peak lateral strength in pull and push direction for various hazard levels at different loading rates (Table 7.19). The peak strength either increased or decreased slightly with the loading rate. The reduction in the peak strength with the loading rate is attributed to the incapability of the lateral actuator in capturing the target peak displacements at 0.025 /sec and 0.05 /sec loading rates. At the loading rate of 0.001 /sec, minor softening was observed for drift ratios exceeding approximately 7.0%, as shown in Figure 7.96(d)-(I). However, no softening was observed in the response at the loading rate of 0.01 /sec, up to the peak drift ratio of 8.47%.

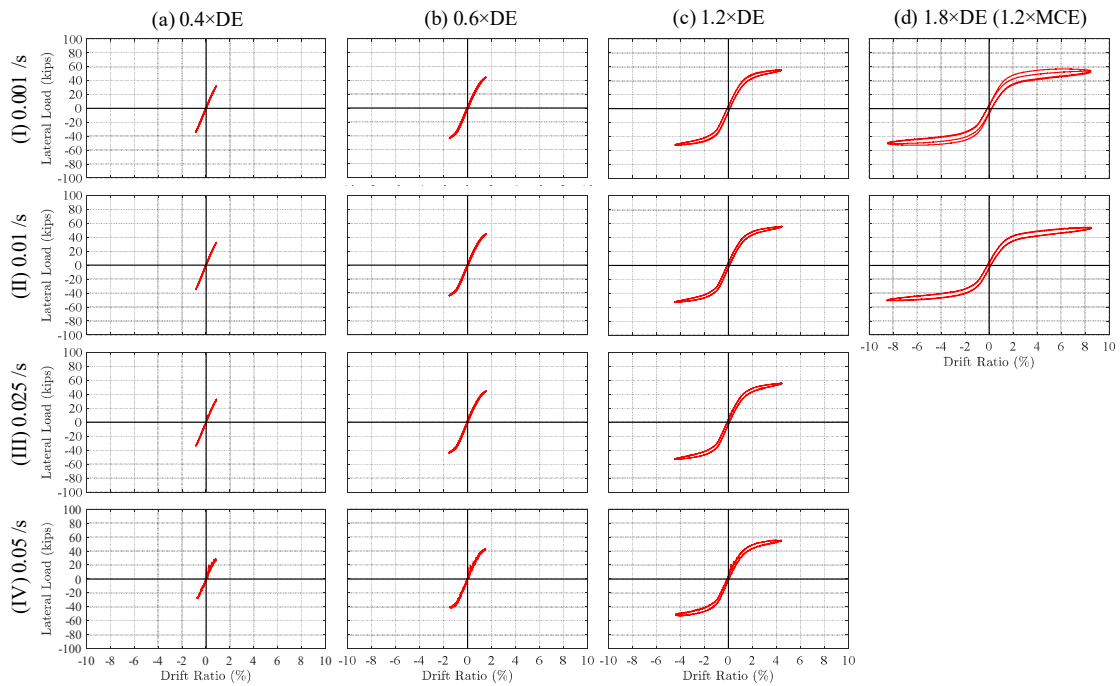


Figure 7.96. Lateral load vs. drift ratio hysteresis curve for the PU column at different hazard levels and loading rates.

Table 7.19. Summary of peak lateral strength in positive and negative direction at various hazard levels and loading rates: PU specimen.

Hazard Level	0.001 /sec		0.01 /sec		0.025 /sec		0.05 /sec	
	F_{peak}^+	F_{peak}^-	F_{peak}^+	F_{peak}^-	F_{peak}^+	F_{peak}^-	F_{peak}^+	F_{peak}^-
0.4xDE	32.5	-34.0	32.9	-34.5	33.1	-33.8	29.6	-27.7
0.6xDE	44.8	-43.7	45.2	-43.9	45.1	-43.8	43.3	-42.0
1.2xDE	55.7	-52.5	55.9	-52.7	56.0	-52.9	55.8	-53.7
1.8xDE (1.2xMCE)	57.0	-52.5	54.5	-50.9	-	-	-	-

The hysteretic response of the PU column is compared to the PUED-2 observed in Phase 2.4 of loading (i.e. specimen PUED-2.4, which is comparable to the PU column, because it only include links ED-3 and ED-7), PUED-1 (as the representative of the

response of a PUED column with bi-layered PU segment), and RC rocking column in Figure 7.97. It is observed that the elastic lateral stiffness of the PU column (with solid PU segment) is comparable to that of the PUED-2.4 column with bi-layered PU segment and two ED links (ED-3 and ED-7). Specifically, the lateral strength of the PU column (with solid PU segment) is comparable to that of the PUED-2.4 column up to about 4% drift ratio. At drift ratios exceeding 4%, the PUED-2.4 column shows higher strength compared to PU column, which is attributed to the contribution of the two central links (ED-3 and ED-7), which becomes significant at large drift ratios. It can further be deduced that the lateral response of rocking columns with the bi-layered or solid PU segments are similar, which was the initial objective of the bi-layered segment design.

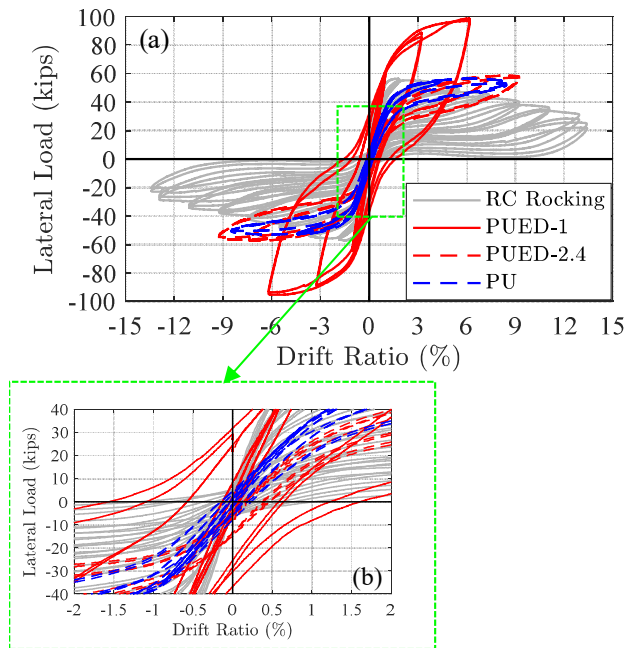


Figure 7.97. Lateral load vs. drift ratio hysteresis curve: PU column vs. PUED-2.4 column with two ED links, PUED-1, and RC rocking column.

7.12.4.3. Post-tensioning Load History

The variation of the PT load with the peak drift ratio for the PU column is shown in Figure 7.98(a) for all hazard levels and all rates. The initial PT load level (after applying the gravity load) is shown with the dashed red line. Due to the opening at the rocking interface (PU-to-foundation interface), the PT load increases as the column is loaded from the rest position (zero displacement) to the peak displacement in positive or negative direction.

The post-tensioning load at the end of each set of cycles versus the corresponding peak drift ratio is shown in Figure 7.99. No loss was observed in PT load up to the peak

drift ratio corresponding to $1.2 \times DE$ hazard level. The PT load measured at the end of the cycles corresponding to $1.8 \times DE$ ($1.2 \times MCE$) hazard level was 414.8 kips, which corresponds to a total loss of 3.4% relative to the initial PT load (429 kips). The maximum observed PT load in the tendon during the entire loading history was 569.2 kips which was below the nominal yield load (632.7 kips), defined using the nominal yield strength of strands (243 ksi).

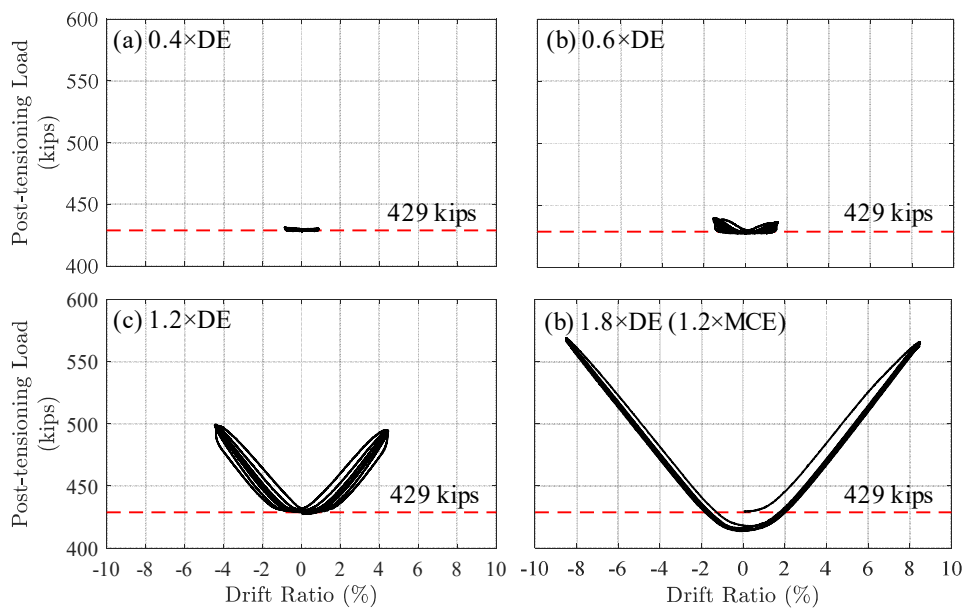


Figure 7.98. Post-tensioning load vs. peak drift ratio for PU column at the hazard levels.

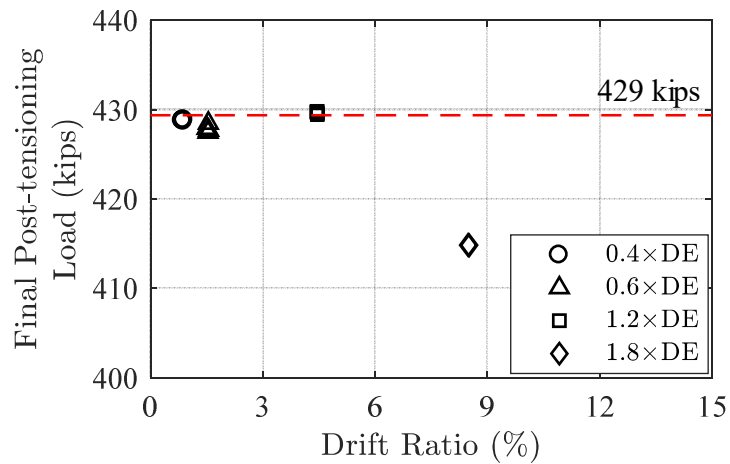


Figure 7.99. Post-tensioning load at the end of each cycle vs. peak drift ratio for PU column at various hazard levels.

7.12.4.4. Curvature

The average curvature at the bottom and top PU segment interface was computed over a gage length of 15.625” (height of the solid PU segment) and 10”, respectively, using the data from the string potentiometers attached to the foundation on the bottom and steel collar on top, on the east and west side of the specimen (Figure 7.16). The string potentiometers were located at 2.4” from the column. The average curvature was calculated using the procedure explained in Section 7.12.1.5.

The computed average curvature at the top and bottom interface of the PU segment vs. drift ratio is shown in Figure 7.100(a). The curvature at the top PU interface was due to rocking at that interface due to the small gap (~1/8”) between the central steel pipe in the top RC segment and the wall of the central hole in the PU segment. Thus, the measured

lateral displacement at the loading center was not only due to the rotation of the column about its compression toe at the PU-foundation interface, but also due to the rotation about the top of the PU segment.

A comparison of the computed average curvature at the base rocking interface vs. drift ratio for the RC rocking, PUED-1, and PUED-2 (Phase 4) columns is presented in Figure 7.100(b). It can be seen that at the same drift ratio, the curvature at the base rocking interface is higher in PU column compared to other systems, specifically the PUED columns, which shows the contribution of ED links in reducing the demand on the PU segment.

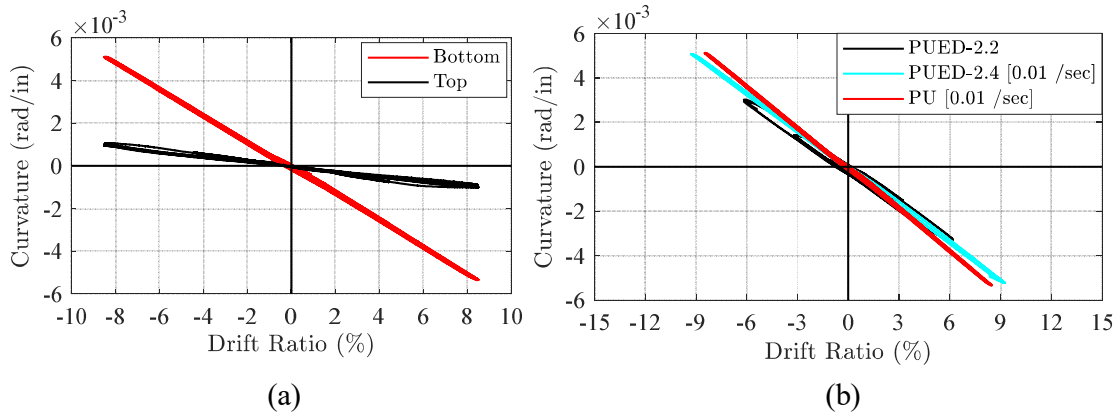


Figure 7.100. (a) Curvature at the top and bottom interface of the PU segment vs. drift ratio; (b) curvature at the bottom PU interface: PU column vs. PUED-2.2 and PUED-2.4.

7.12.4.5. Energy Dissipation and Equivalent Viscous Damping

The CDE and equivalent viscous damping versus drift ratio (calculated as described previously in Section 7.12.1.6) for all columns are compared in Figure 7.101(a) and (b), respectively. Similar to other columns, the CDE and, accordingly, the equivalent viscous damping ratio increased with the drift ratio in PU column (Figure 7.101(a) and (b) and Table 7.20). However, among all column systems, the PU column provides the lowest energy dissipation capacity (and equivalent viscous damping), mostly behaving as an elastic (or visco-elastic) system, exhibiting no (observable) damage and minor energy dissipation, mostly provided by the PU material.

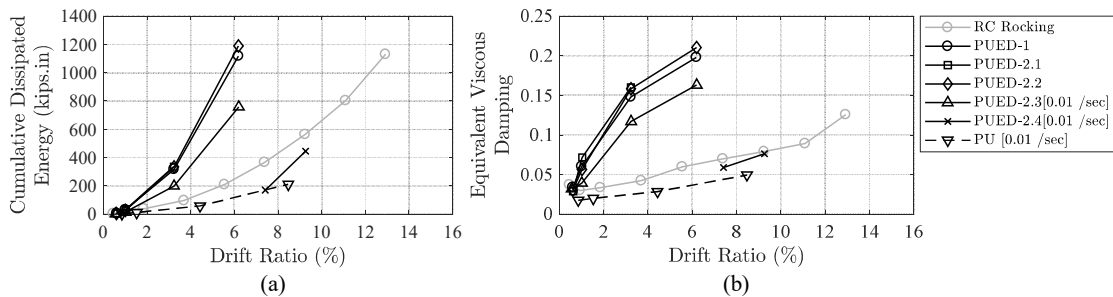


Figure 7.101. PU column vs. PUED and RC rocking columns: (a) cumulative dissipated energy; (b) equivalent viscous damping.

7.12.4.6. Self-centering Efficiency

A comparison of the re-centering capacity of all columns is presented in Figure 7.102 in terms of RSE (Figure 7.102(a)) and residual drift ratio (at each loading cycle) (Figure 7.102(b)) vs. the peak drift ratio of the cycle. The values of RSE and average RDR

for all columns corresponding to various hazard levels are summarized in Table 7.21 and Table 7.22, respectively. As shown, the re-centering capacity of the PU column increased with the peak drift ratio, as reflected in the RSE (Figure 7.102(a)) increasing and the residual drift ratio (Figure 7.102(b)) decreasing with peak drift ratio. Compared to PUED-1 and PUED-2 columns, the PU column showed higher RSE (smaller residual deformation) in all hazard levels. The re-centering capacity of the PU column was comparable to that of the RC rocking column.

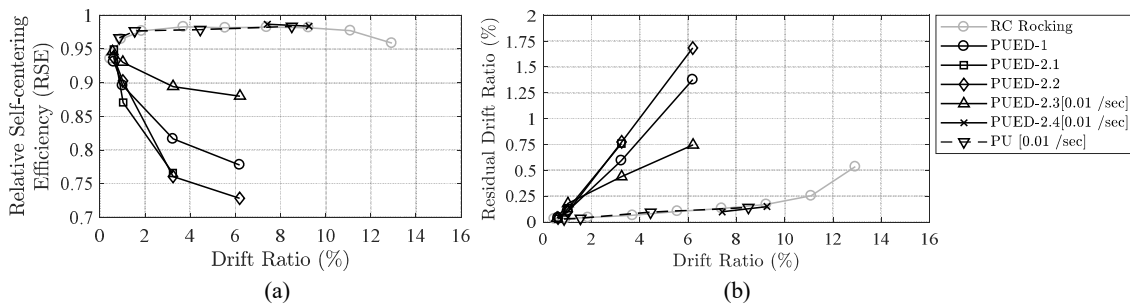


Figure 7.102. PU column vs. PUED and RC rocking columns: (a) relative self-centering efficiency (RSE); (b) residual drift ratio.

Table 7.20. Equivalent viscous damping at various hazard levels for all specimens.

Specimen	Equivalent Viscous Damping			
	0.4×DE	0.6×DE	DE	MCE
RC rocking	0.035	0.031	0.037	0.061
PUED-1	0.034	0.060	0.117	0.173
PUED-2.1	0.029	0.072	0.130	-
PUED-2.2	0.030	0.057	0.123	0.184
PUED-2.3	0.032	0.039	0.090	0.140
PU	0.018	0.018	0.023	0.030

Table 7.21. Relative self-centering efficiency (RSE) at various hazard levels for all specimens.

Specimen	RSE			
	0.4×DE	0.6×DE	DE	MCE
RC rocking	0.94	0.97	0.98	0.98
PUED-1	0.93	0.89	0.84	0.79
PUED-2.1	0.95	0.87	0.80	-
PUED-2.2	0.94	0.90	0.81	0.74
PUED-2.3	0.95	0.93	0.91	0.89
PU	0.97	0.98	0.98	0.98

Table 7.22. Average residual drift ratio (RDR) at various hazard levels for all specimens.

Specimen	RDR (%)			
	0.4×DE	0.6×DE	DE	MCE
RC rocking	0.031	0.035	0.051	0.107
PUED-1	0.045	0.107	0.420	0.980
PUED-2.1	0.031	0.130	0.540	-
PUED-2.2	0.038	0.100	0.540	1.230
PUED-2.3	0.035	0.179	0.350	0.590
PU	0.028	0.035	0.075	0.115

7.13. Summary and Findings

In this section, the performance of bridge columns with polyurethane DR segments compared to the performance of a conventional reinforced (RC) rocking column was assessed via quasi-static cyclic tests. The test specimens included a conventional RC rocking column, a column with PU end segment with bi-layered axisymmetric section and energy dissipation (ED) links (PUED column), and a column with a solid PU end segment (PU column). First, the specimens were post-tensioned monostrand-by-monostrand using a hydraulic jack. Then, the vertical gravity load was applied by the two vertical actuators. Displacement-controlled sinusoidal reversed cyclic loading was subsequently applied with increasing amplitude ultimately reached a drift ratio of approximately 13.4%, 9.2%, and 8.5% in the RC column, PUED column, and PU column, respectively. To evaluate the re-centering capacity of the system upon release of the ED links, all the ED links were released and retightened in the PUED column after being subjected up to a lateral drift ratio of 3.2%. Subsequently, displacement-controlled sinusoidal reversed cyclic loading was applied, which consisted of symmetric cycles at amplitudes corresponding to various hazard levels including $0.4 \times DE$, $0.6 \times DE$, $1.2 \times DE$, and $1.8 \times DE$ ($1.2 \times MCE$). Each set included two cycles of the same amplitude. For each hazard level, the loading was applied at various rates including 0.1, 1.08, 2.71, and 5.41 in/sec corresponding to a drift rate of 0.001, 0.01, 0.025, and 0.05 /sec. The PU column was subjected to sets of symmetric cycles at amplitudes corresponding to various hazard levels including $0.4 \times DE$, $0.6 \times DE$, $1.2 \times DE$, and $1.8 \times DE$ ($1.2 \times MCE$). Each set included two

cycles of the same amplitude. The loading was applied at various rates including 0.1, 1.08, 2.71, and 5.41 in/sec corresponding to a drift rate of 0.001, 0.01, 0.025, and 0.05 /sec, respectively. The major findings of this study are:

- The RC rocking column exhibited a stable response up to about 3% lateral drift ratio (corresponding approximately to the lateral displacement demand at $1.2 \times DE$ hazard level), followed by significant softening in the form of stiffness and strength degradation for drift ratios exceeding 3% with an increasing rate with the drift ratio. The PT load at the end of each set of cycles decreases with the peak drift ratio, for drift ratios beyond 3.7%, due to column shortening as a result of concrete crushing in the vicinity of the rocking interface. The re-centering capacity of the system was maintained up to about 13% drift ratio, at which the maximum average residual drift ratio was about 0.57%.
- The PUED column showed a stable response without any softening up to 6.2% drift ratio, corresponding to the $1.8 \times DE$ ($1.2 \times MCE$) hazard level. Minor loss was observed in PT load at the end of each set of cycles. The first ED link fracture occurred at about 6.2% drift ratio due to low-cycle fatigue, as the specimen was subjected to several loading cycles at various amplitudes in the previous loading steps.

- Almost all of the residual deformations of the PUED column were recovered upon releasing/removing of the ED links. The average residual deformations at a peak drift ratio corresponding to the $1.2 \times DE$ hazard level was about 0.82% (in PUED-2 column) which upon releasing the ED links, the system fully recovered. The average residual drift ratio at the $1.8 \times DE$ ($1.2 \times MCE$) hazard level was about 1.8%, a large portion of which was recovered, after removing two fractured ED links (ED-1 and ED-5), resulting in a final average RDR of 0.28%. Compared to the average RDR before removing the fractured ED links (1.8%), this RDR corresponds to an 85% recovery.
- No significant rate effect was observed in the response of the PUED column system at various hazard levels up to the maximum achieved loading rate of 5.41 in/sec.
- The PU column showed a stable response without any softening up to about 8.2% drift ratio, corresponding to $1.8 \times DE$ ($1.2 \times MCE$) hazard level. No loss was observed in PT load up to the peak drift ratio corresponding to $1.2 \times DE$ hazard level. The PT load loss measured at the end of the cycles corresponding to $1.8 \times DE$ ($1.2 \times MCE$) hazard level was 3.4% relative to the initial PT load.

- The re-centering capacity of the PU column was maintained up to the peak lateral drift ratio of 8.2% corresponding to 1.8×DE (1.2×MCE) hazard level at which the maximum average residual drift ratio was about 0.15%. The re-centering capacity of the PU column was found comparable with that of the RC rocking column.
- Unexpected asymmetric damage occurred in the PU sleeve of the bi-layered axisymmetric segment over the loading cycle with the peak displacement of 10” (9.24% drift ratio) at the loading rate of 1.08 in/sec (0.01 drift ratio/sec). The damage was in the form of multiple vertical cracks in the PU on the east and northeast side over the first two repeated loading cycles. Subsequently, in the third loading cycle, the damage occurred on the east side only, in the form of complete fracture over a large area, and detachment of a piece of the PU material.
- A larger clearance (~1/4”) is recommended for the slotted hole of the mounting eye on the steel collar to ensure ED links can be easily installed/removed (if needed).

8. VALIDATION OF THE NUMERICAL MODEL WITH TEST DATA

8.1. Scope and Objectives

A key to thoroughly assessing the performance of a newly developed system from various aspects is a robust numerical model capable of predicting the response of the system under various loading conditions (e.g. quasi-static cyclic loading with increasing amplitude, dynamic loading in the form of input motions scaled to various hazard levels). This section is primarily aimed at validating the performance of the numerical modeling approach employed in Section 6.3 for seismic performance assessment of various column systems (i.e. RC rocking, PUEd, and PU columns). To this end, the response predicted prior to tests (called *blind prediction* herein) by numerical models of test specimens developed following the approach presented in Section 6.3 is compared to a selection of test results presented in Section 7. Based on the observations on the comparison of the predicted response by the original model with test results, the model was further refined to address some of the discrepancies observed between the blind prediction and test results.

8.2. Pre-test Blind Prediction

8.2.1. Finite Element Modeling

All column models were generated using the open-source structural analysis software OpenSees (McKenna and Fenves 2001) following the scheme presented in Section 6.3 and the schematic representation (with the PUEd column representing the

most general case) shown in Figure 8.1. For a more realistic simulation of the PT system length and the location of bottom anchorage, the model was updated by including the foundation block using an elastic beam-column element (Figure 8.1).

Furthermore, the model was updated by including an elastic beam-column element extending from the center of the deck to the top of the post-tensioning block. The material model parameters were updated based on the final design of the column systems. The cover concrete had an unconfined compressive strength of 8 ksi. For the core concrete based on the material and geometric properties and the transverse reinforcement (Figure 7.5), the confined-to-unconfined compressive strength ratio, K , was defined as 1.35 for the rocking column sections, respectively (Mander et al. 1988). The strain at the peak compressive strength, ϵ_{co} , was taken as 0.0023 for unconfined concrete, and 0.0063 for confined concrete (Mander et al. 1988), respectively. The ultimate/crushing strain, ϵ_{cu} , was taken as 0.0064 (Karthik and Mander 2010) and 0.02 (Paulay and Priestley 1992) for unconfined and confined concrete, respectively. The residual strength at the ultimate strain was defined as $0.2Kf'_c$ (for the unconfined concrete, $K = 1$) based on the Kent and Park model (Scott et al. 1982). The concrete cover and core of all column systems was modeled using the Kent and Park model (Scott et al. 1982) available in OpenSees as *Concrete01*.

The PT tendon (comprised of 12×0.6 in. strands) was modeled by a single co-rotational truss element with a diameter of 1.82 in., resulting to a cross-section area equivalent to that of 12×0.6 in. strands, with material response given by the model of Menegotto and Pinto (1973). The PT system was designed to remain elastic over all

loading sequences, therefore, the yield strength of the steel material was set to a relatively large value (350 ksi compared to the nominal value of 245 ksi) so that the PT system would remain elastic. The elastic modulus of the PT system steel material was set to 28000 ksi (DYWIDAG-Systems International 2018). The initial post-tensioning load in the PT bar was applied in the form of initial strain. An automated iterative procedure was implemented to adjust the value of this strain accounting for immediate losses due to elastic shortening, so that the target post-tensioning load is achieved with acceptable accuracy.

The steel material of the ED links, which conformed to ASTM A36 (ASTM A36/A36M-19 2019), was modeled using the Menegotto-Pinto model with the reduction factor described earlier (see Section 6.3 using the expected yield strength, f_{ye} , of 43.2 ksi, i.e. 1.2 times the nominal yield strength, f_y (36 ksi). The strain hardening ratio was taken as 1.5% of the initial elastic modulus. The residual value of the reduction factor was $R_{min} = 0.001$ with $\epsilon_{f1} = 20\%$ and $\epsilon_{f2} = 21\%$ (Figure 5.1(b)). For a more realistic representation of the end boundary conditions of the ED links, the connection of the ED links to the steel collar and the foundation was fixed as oppose to pin connection used in Section 6.3.

The PU material behavior was simulated using the advanced visco-elastic softening visco-plastic material model presented in Section 5.4. As shown in Section 7.10.4, the compressive response of the PU samples taken from one of the PU batches used in casting PU segments was comparable to that of the PU material tested in SMTL at CU Boulder which was used to calibrate the parameters of the advanced uniaxial

material model. Given that, the same calibrated model parameters obtained in Section 5.4.4.2 were used for the PU material.

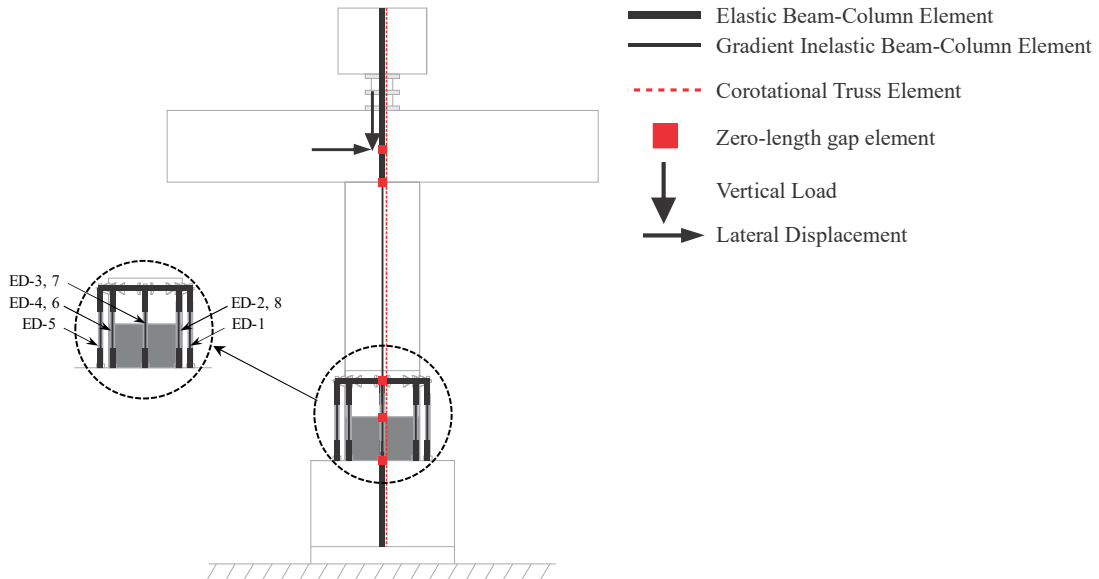


Figure 8.1. Schematic representation of the FE model of the PUED specimen.

8.2.2. Simulation Results

8.2.2.1. RC Rocking Column

The predicted lateral load versus drift ratio and post-tensioning load versus drift ratio response of the RC rocking column is compared with the test results in Figure 8.2(a) and (b), respectively. Overall, the predicted force vs. drift ratio response is in good agreement with the response obtained from the test. The predicted peak lateral strength in the negative (push) direction (-59.6 kips) matched quite well with test data (-59.2 kips), but was overestimated in the positive direction (59.6 kips) with an error of 9.8% relative

to the test data (54.3 kips). It is worth noting that the higher difference between the predicted and measured peak lateral load in the positive (pull) direction was attributed to the fact that the specimen showed slightly higher strength (about 5.6 kips) in the negative (push) loading direction compared to the positive (pull) direction, while the response predicted by the model was symmetric.

The initial elastic stiffness of the system was overestimated by the model with a relative error of 145%. This difference could have resulted from the mechanical properties of the grout material at the base rocking interface which was not accounted for in the model, or because the dry concrete-to-concrete connection at the bottom does not achieve perfect contact resulting in lower stiffness. The post peak softening response of the specimen was underestimated by the model by up to about 9% drift ratio in both the positive (pull) and negative (push) directions.

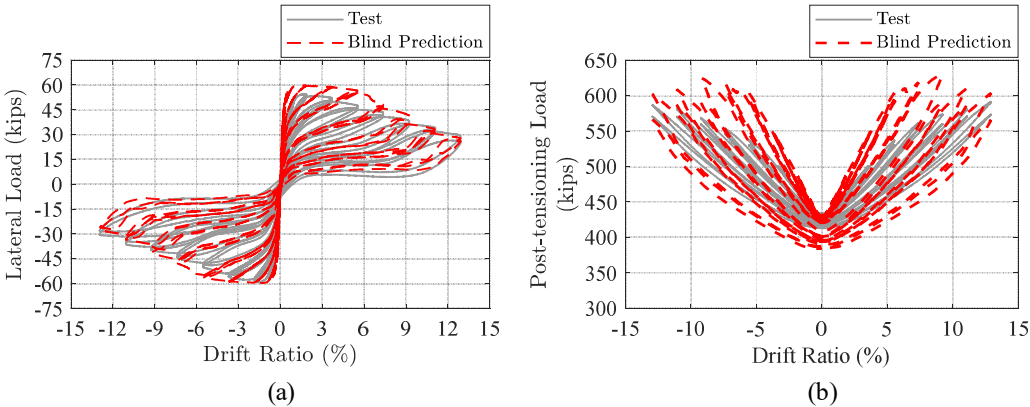


Figure 8.2. Comparison of experimental and predicted response of RC rocking column from the original model: (a) lateral load vs. drift ratio; (b) post-tensioning load vs. drift ratio.

The peak PT load in the positive (pull) and negative (push) direction over each set of cycles was overestimated by the model with the maximum relative error of 12.5% occurring at a 5.5% drift ratio (Figure 8.3(a)). The PT loss over each set of cycles was overestimated by the model (Figure 8.3(b)); The measured and predicted PT load at the end of the loading sequence was 409.3 kips and 384 kips, which corresponds to a total loss of 5.6% and 10.7% relative to the initial PT load (434 kips) , respectively.

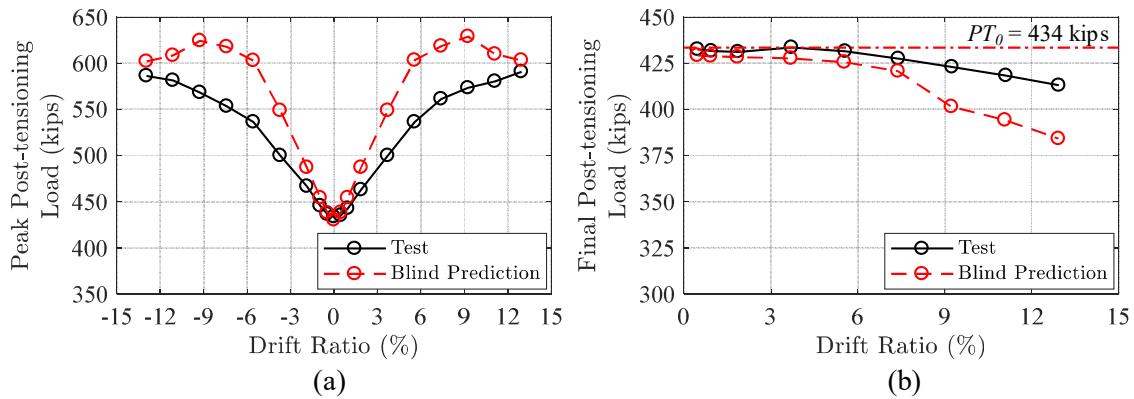


Figure 8.3. Comparison of experimental and predicted response of RC rocking column from the original model: (a) peak post-tensioning load vs. drift ratio; (b) final post-tensioning load vs. drift ratio.

In the test, the specimen sustained an average residual drift ratio increased from 0.03% to 0.53% as the peak drift ratio increased from 0.46% to 12.93%. However, the predicted average residual drift ratio was essentially zero up to the peak drift ratio of 11% and 0.2% at the peak drift ratio of 12.93% (Figure 8.4(a)). The equivalent viscous damping

was underestimated by the model with the minimum and maximum relative error of 40% and 80% at 9.2% and 0.46% peak drift ratio, respectively (Figure 8.4(b)).

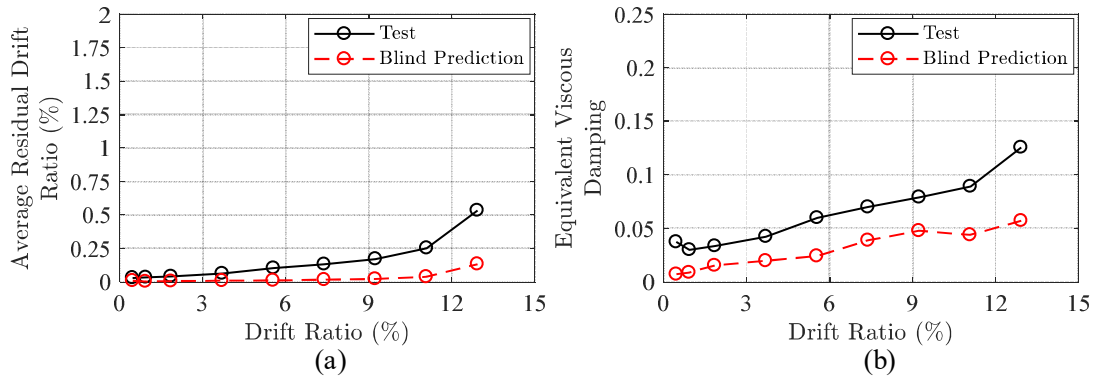


Figure 8.4. Comparison of experimental and predicted response of RC rocking column from the original model: (a) average residual drift ratio vs. drift ratio; (b) equivalent viscous damping vs. drift ratio.

8.2.2.2. PU-enhanced Column with Energy-dissipation Links

The predicted lateral load versus drift ratio and post-tensioning load versus drift ratio response of the PUED-2 column in Phase 2.2, Phase 2.3 (at 0.01 /sec strain rate), and Phase 2.4 (at 0.01 /sec strain rate) is compared with the test results in Figure 8.5(a) and (b), respectively. Overall, the predicted force vs. drift ratio response was in good agreement with the measured response in the test.

In Phase 2.2, the column peak lateral strength was overestimated at the $0.4 \times DE$ level in both the positive (pull) and negative (push) direction with a relative error of 39.8% and 36.1%, respectively (Table 8.1). At higher hazard levels ($0.6 \times DE$, $1.2 \times DE$, and

1.8×DE (1.2×MCE)), the difference between the predicted and measured peak lateral strength was within 10% (Table 8.1). Since the low-cycle fatigue was not accounted for in the steel material model, the low-cycle fatigue failure of the ED links observed in the test during the second pull and second push loading cycle at 6.19% drift ratio (Figure 7.80) was not predicted by the model.

In Phase 2.3, the column peak lateral strength was overestimated by the model at the 0.4×DE level in both the positive (pull) and negative (push) direction by 58.1% and 43.2%, respectively (Table 8.2). At higher hazard levels (0.6×DE, 1.2×DE, and 1.8×DE (1.2×MCE)), the difference between the predicted and measured peak lateral strength was within 10%, except for the peak lateral strength in positive direction at 0.6×DE level which was overestimated by 32.9% (Table 8.2).

In phase 2-4, the predicted column peak lateral strength was in good agreement with measured test data with a relative error within 16% (Table 8.3).

The higher predicted column lateral strength at 0.4×DE hazard level is attributed to the higher initial elastic stiffness of the model compared to the test; The initial elastic stiffness of the system in phase 2-2 and phase 2-3 was overestimated with a relative error of 162% and 164%, respectively. Similar to the RC rocking column, it is believed that the initial stiffness of the test specimen was primarily controlled by the mechanical properties of the grout material at the base rocking interface which was not accounted for in the model.

The predicted post peak hardening response of the specimen was in good agreement with test results in both positive (pull) and negative (push) directions in all three phases.

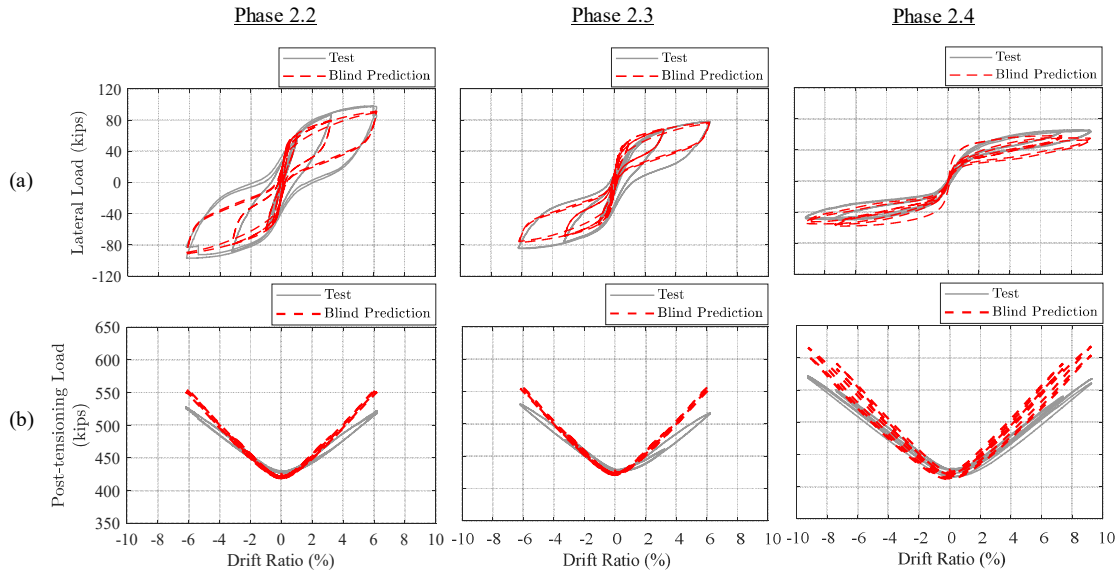


Figure 8.5. Comparison of experimental and predicted response of PUED-2 column from the original model: (a) lateral load vs. drift ratio; (b) post-tensioning load vs. drift ratio.

Table 8.1. Comparison of experimental and predicted peak lateral strength for PUED-2 column in Phase 2.2 from the original model in positive and negative direction at various hazard levels.

Hazard Level	Peak Drift Ratio (%)	F_{peak}^+			F_{peak}^-		
		Test (kips)	Model (kips)	Error (%)	Test (kips)	Model (kips)	Error (%)
0.4×DE	0.60	39.3	55.0	39.8	-40.7	-55.4	36.1
0.6×DE	1.02	56.8	62.6	10.2	-60.9	-62.5	2.7
1.2×DE	3.23	87.4	80.0	8.5	-88.7	-79.8	10.1
1.8×DE (1.2×MCE)	6.19	98.3	91.6	6.8	-97.2	-91.6	5.8

Table 8.2. Comparison of experimental and predicted peak lateral strength for PUED-2 column in Phase 2.3 from the original model in positive and negative direction at various hazard levels.

Hazard Level	Peak Drift Ratio (%)	F_{peak}^+			F_{peak}^-		
		Test (kips)	Model (kips)	Error (%)	Test (kips)	Model (kips)	Error (%)
0.4×DE	0.60	29.9	47.3	58.1	-33.5	-47.9	43.2
0.6×DE	1.02	41.1	54.6	32.9	-51.8	-54.6	5.3
1.2×DE	3.23	66.7	69.0	3.5	-76.1	-68.8	9.6
1.8×DE (1.2×MCE)	6.19	78.6	77.3	1.7	-84.5	-77.2	8.6

Table 8.3. Comparison of experimental and predicted peak lateral strength for PUED-2 column in Phase 2.4 from the original model in positive and negative direction at various peak drift ratios.

Peak Drift Ratio (%)	F_{peak}^+			F_{peak}^-		
	Test (kips)	Model (kips)	Error (%)	Test (kips)	Model (kips)	Error (%)
7.39	65.3	58.3	10.7	-50.2	-58.2	15.9
9.24	65.9	55.4	15.9	-49.5	-55.2	11.6

The peak PT load in the positive (pull) and negative (push) direction over each set of cycles was overestimated by the model in Phase 2.2, Phase 2.3, and Phase 2.3 with the maximum relative error of 6.4%, 8.2%, and 9.4% occurred at 6.2%, 6.2%, and 7.4% drift ratio, respectively (Figure 8.6(a)). The predicted PT load at the end of the loading sequence of all three phases was in good agreement with the corresponding measured values with a relative error within 2.5% (Figure 8.6(b)).

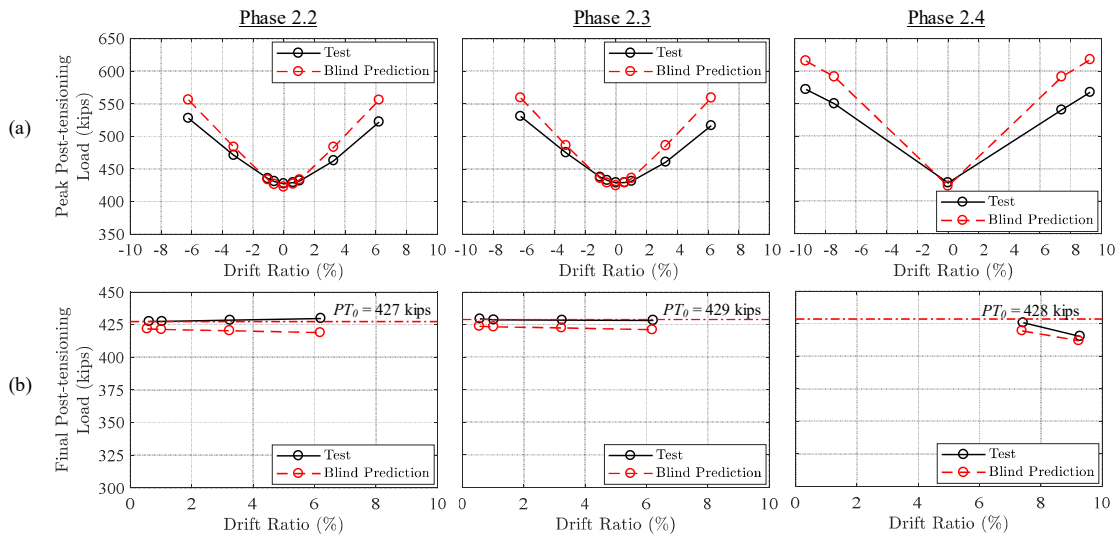


Figure 8.6. Comparison of experimental and predicted response of PUED-2 column from the original model: (a) peak post-tensioning load vs. drift ratio; (b) final post-tensioning load vs. drift ratio.

The predicted average residual drift ratio in Phase 2.2 was in good agreement with test data at the $0.4 \times DE$ and $0.6 \times DE$ hazard levels and was underestimated by 72% and 80% at $1.2 \times DE$ and $1.8 \times DE$ ($1.2 \times MCE$), respectively (Figure 8.7(a)). In Phase 2.3, the

predicted average residual drift ratio was in good agreement with the test data at the DE hazard levels and was underestimated by 60%, 73%, and 77% at the $0.6\times DE$, $1.2\times DE$ and $1.8\times DE$ ($1.2\times MCE$) hazard levels, respectively (Figure 8.7(a)). In Phase 2.4, the average residual drift ratio was underestimated by 59% and 78%, at the peak drift ratio of 7.4% and 9.24%, respectively (Figure 8.7(a)).

The equivalent viscous damping was overestimated in Phase 2.2 at the $0.4\times DE$ and $0.6\times DE$ hazard levels by 196% and 94%, respectively, while it was underestimated at the $1.2\times DE$ and $1.8\times DE$ ($1.2\times MCE$) by 13% and 32%, respectively (Figure 8.7(b)). In Phase 2.3, the equivalent viscous damping was overestimated at $0.4\times DE$ and $0.6\times DE$ hazard levels by 98% and 92%, respectively, while it was underestimated at $1.2\times DE$ and $1.8\times DE$ ($1.2\times MCE$) hazard levels by 13% and 30%, respectively (Figure 8.7(b)). In Phase 2.4, the equivalent viscous damping was in good agreement with the test data at the peak drift ratio of 7.4% and was underestimated by 21% at the peak drift ratio of 9.24% (Figure 8.7(b)).

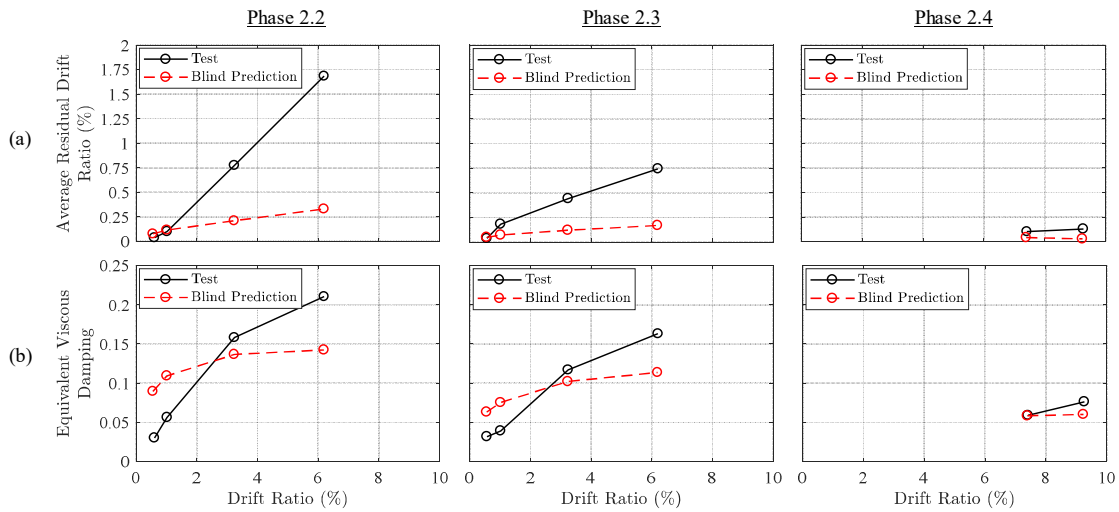


Figure 8.7. Comparison of experimental and predicted response of PUED-2 column from the original model: (a) average residual drift ratio vs. drift ratio; (b) equivalent viscous damping vs. drift ratio.

8.2.2.3. PU-enhanced Column

The predicted lateral load versus drift ratio and post-tensioning load versus drift ratio response of the PU column at the drift ratio rate of 0.001 /sec is compared with the test results in Figure 8.8(a) and (b), respectively. Overall, the predicted force vs. drift ratio response was in good agreement with the measured response in the test.

The column peak lateral strength was in good agreement with the test data at all hazard levels in both the positive (pull) and negative (push) direction with a relative error within 10% and 3.1%, respectively (Table 8.4). It is worth noting that the higher error in the positive (pull) direction was attributed to the fact that the specimen showed slightly higher strength (up to about 4.5 kips) in the positive (pull) direction compared to the negative (push) direction, while the predicted response was symmetric.

Unlike the RC rocking and PUED-2 column, the initial elastic stiffness of the column with the solid PU segment at the bottom was in good agreement with the test data, with a relative error of 24%. This is because, the initial stiffness of this test specimen was primarily controlled by the PU material at the base rocking interface, which at the presence of the gravity and PT loads, achieved a more uniform contact with the foundation surface, which was in agreement with the assumptions of the model. The predicted post peak response of the specimen was in good agreement with the test results.

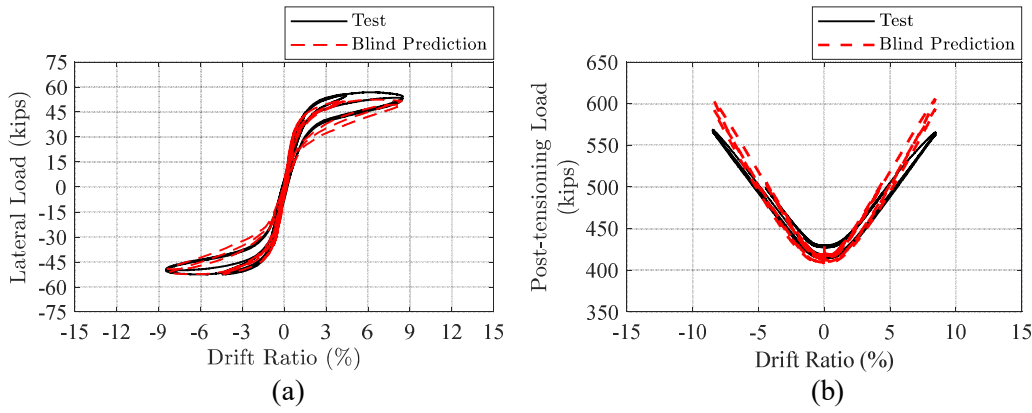


Figure 8.8. Comparison of experimental and predicted response of PU column from the original model: (a) lateral load vs. drift ratio; (b) post-tensioning load vs. drift ratio.

Table 8.4. Comparison of experimental and predicted peak lateral strength for PU column from the original model in positive and negative direction at various hazard levels.

Hazard Level	Peak Drift Ratio (%)	F_{peak}^+			F_{peak}^-		
		Test (kips)	Model (kips)	Error (%)	Test (kips)	Model (kips)	Error (%)
0.4×DE	0.85	32.5	35.7	9.9	-34.0	-35.0	3.1
0.6×DE	1.52	44.8	43.7	2.3	-43.7	-43.7	0.0
1.2×DE	4.42	55.7	52.2	6.2	-52.5	-52.3	0.3
1.8×DE (1.2×MCE)	8.47	56.9	52.4	8.0	-52.5	-52.3	0.3

The peak PT load in positive (pull) and negative (push) direction over each set of cycles was overestimated by the model with the maximum relative error of 7% occurring at 8.47% drift ratio (Figure 8.9(a)). The predicted PT load at the end of each set of cycles was in good agreement with test data with a relative error within 3.5% (Figure 8.9(b)).

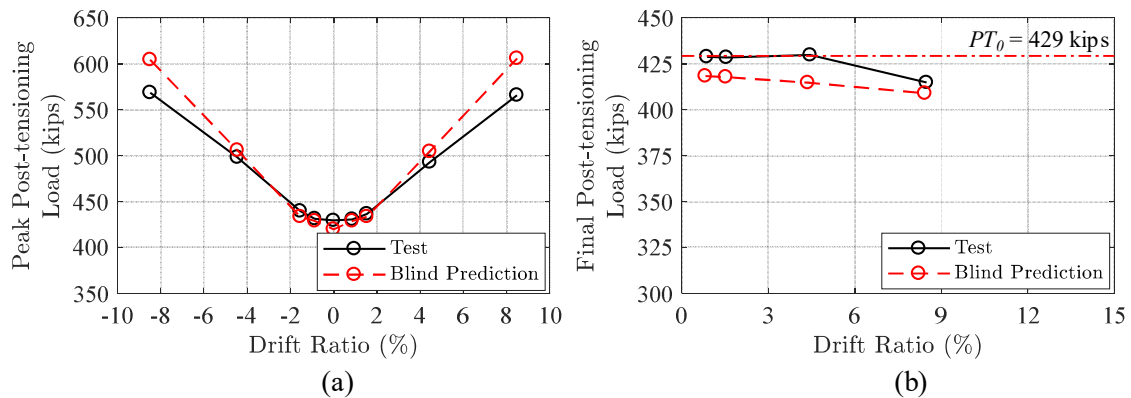


Figure 8.9. Comparison of experimental and predicted response of PU column from the original model: (a) peak post-tensioning load vs. drift ratio; (b) final post-tensioning load vs. drift ratio.

The predicted average residual drift ratio was underestimated with a relative error of 14%, 26%, 35%, and 43% at the $0.4\times DE$, $0.6\times DE$, $1.2\times DE$, and $1.8\times DE$ ($1.2\times MCE$) hazard levels, respectively (Figure 8.10(a)). The equivalent viscous damping was underestimated with a relative error of 31%, 31%, 27%, and 16% at $0.4\times DE$, $0.6\times DE$, $1.2\times DE$, and $1.8\times DE$ ($1.2\times MCE$) hazard levels, respectively (Figure 8.10(b)).

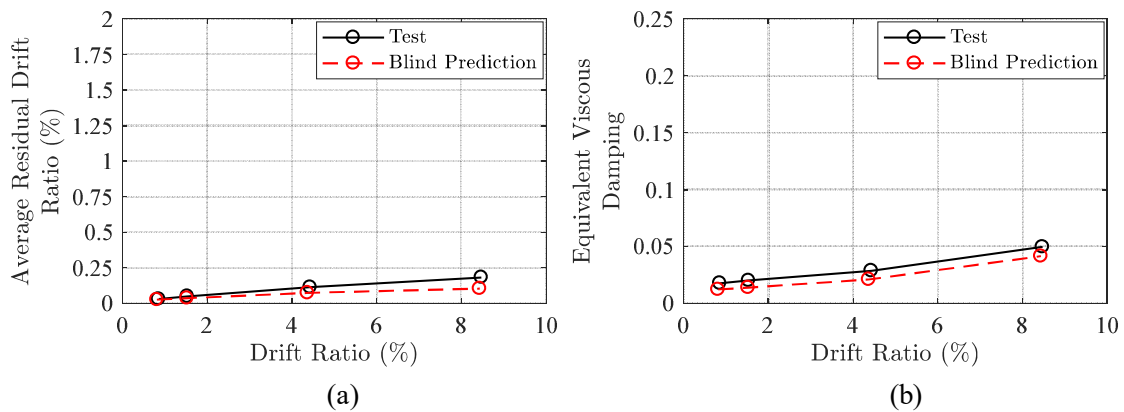


Figure 8.10. Comparison of experimental and predicted response of PU column from the original model: (a) average residual drift ratio vs. drift ratio; (b) equivalent viscous damping vs. drift ratio.

8.3. Post-test Validation

Based on the comparison of the predicted response obtained from the original model developed prior to the execution of the testing program with test results from the testing program, the major discrepancies between the predicted and measured responses are summarized as:

- The initial elastic stiffness was overestimated for all specimens, especially for the RC rocking and PUED columns. As mentioned earlier in Section 8.2.2.1 and 8.2.2.2, this discrepancy may have resulted from the grout material at the base rocking interface which was not accounted for in the model, or because the dry concrete-to-concrete connection at the bottom does not achieve perfect contact, thus, resulting in lower stiffness.
- The model was not able to predict the low-cycle failure of the ED links, since the low-cycle fatigue was not accounted for in the steel material model.
- The peak posttensioning load over each set of cycles was overestimated for all specimens, particularly at larger drift ratios. Moreover, the residual PT load at the end of each set of cycles was underestimated for all specimens, which corresponds to overestimation of the PT load loss over each set of cycles. The difference between the predicted and measured PT load was mainly attributed to the simplifying assumptions made in modelling the PT system as explained in Section 8.2.1.
- The residual drift ratio was underestimated for all specimens, especially for the RC rocking and PUED columns. The underlying source of this discrepancy has remained unclear and is still under investigation.

- The equivalent viscous damping was underestimated for all specimens, in most loading sequences. The underlying source of this discrepancy has remained unclear and is still under investigation.

To further improve the performance of the model, the sensitivity of the predicted response to various modeling parameters was investigated through a preliminary parametric study. Based on the sensitivity analysis results, the model was refined as explained in the following section, followed by the comparison of the response predicted by the revised model with the test data.

8.3.1. Revised Finite Element Model

Based on the preliminary sensitivity analysis results, it was found that:

- The PT load response is highly sensitive to the equivalent diameter of the PT tendon which was originally taken as 1.82 in., resulting to a cross-section area equivalent to that of 12×0.6 in. strands. According to the parametric study results, it was found that an equivalent tendon diameter of 1.5 in. provides a better agreement between the predicted and measured PT load response compared to the original model.
- Moreover, it was found that an unconfined concrete compressive strength of 7 ksi provides a better prediction of the RC rocking column's response. It is worth noting that the test concrete cylinders which were cast from each concrete batch were cured under a controlled humidity (100%) and temperature

(72 °F), while the test specimen was kept in the lab area at the same temperature and lower humidity (~40%). Given that, a lower compressive strength is expected for the concrete in the test specimen compared to the compression cylinders.

- The predicted response for the PUED column, particularly at larger drift ratios, could be further improved by taking the expected yield strength of the ED link steel material as 1.5 times the minimum yield strength, i.e. considering a larger overstrength.
- The initial PT load was increased by 4 kips and 5 kips in PUED and PU columns, respectively, to account for the PT loss due to the vertical load.

8.3.2. Simulation Results

8.3.2.1. RC Rocking Column

The lateral load and post-tensioning load versus drift ratio response of the RC rocking column predicted by the revised model is compared with the test results in Figure 8.11(a) and (b), respectively. The predicted peak lateral strength in the negative (push) direction (-57.7 kips) matched quite well with test data (-59.2 kips) with a relative error of 2.6%, and was overestimated in the positive direction (57.7 kips) with an error of 6.3% relative to the test data (54.3 kips). As mentioned earlier, the higher difference between the predicted and measured peak lateral load in the positive (pull) direction was attributed to the fact that the specimen showed slightly higher strength (about 5.6 kips) in the

negative (push) loading direction compared to the positive (pull) direction, while the response predicted by the model was symmetric. The post peak softening response of the specimen was in good agreement with test results in both positive (pull) and negative (push) directions.

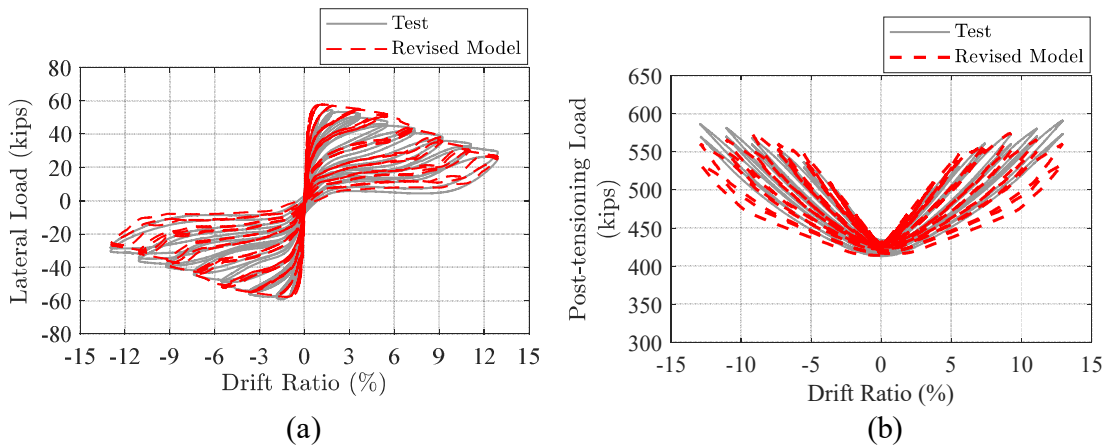


Figure 8.11. Comparison of experimental and predicted response of RC rocking column from the revised model: (a) lateral load vs. drift ratio; (b) post-tensioning load vs. drift ratio.

The predicted peak PT load in positive (pull) and negative (push) direction over each set of cycles was in good agreement with the test results up to about 9% peak drift ratio, while it was underestimated by the model at higher peak drift ratios with the relative error within 5% (Figure 8.12(a)). The measured and predicted PT load at the end of each set of cycles was in good agreement with the test results, with the relative error being within 1%.

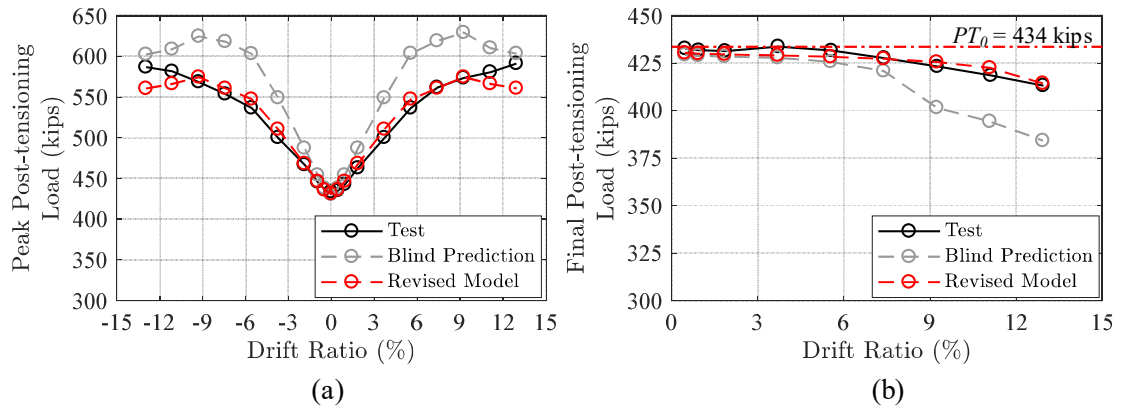


Figure 8.12. Comparison of experimental and predicted response of RC rocking column from the original and revised model: (a) peak post-tensioning load vs. drift ratio; (b) final post-tensioning load vs. drift ratio.

The average residual drift ratio predicted by the revised model was comparable to the blind prediction and was essentially zero up to the peak drift ratio of 11% and 0.33% at the peak drift ratio of 12.93% (Figure 8.13(a)). The equivalent viscous damping predicted by the revised model was approximately the same as the blind prediction. Indeed, the revised model underestimated the equivalent viscous damping with the minimum and maximum relative error of 40% and 80% at 9.2% and 0.46% peak drift ratio, respectively (Figure 8.13(b)).

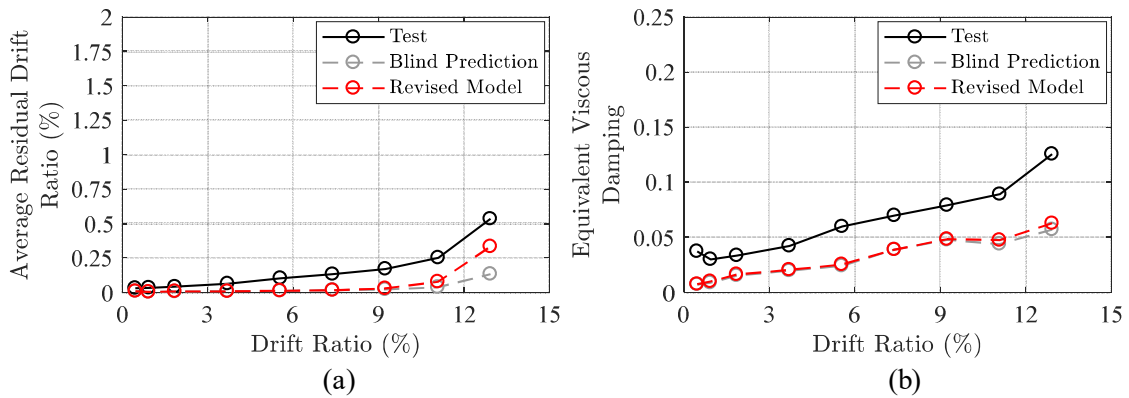


Figure 8.13. Comparison of experimental and predicted response of RC rocking column from the original and revised model: (a) average residual drift ratio vs. drift ratio; (b) equivalent viscous damping vs. drift ratio.

8.3.2.2. PU-enhanced Column with Energy-dissipation Links

The lateral load and post-tensioning load versus drift ratio response of the PUED-2 column in Phase 2.2, Phase 2.3 (at 0.01 /sec strain rate), and Phase 2.4 (at 0.01 /sec strain rate) predicted by the revised model is compared with the test results in Figure 8.14(a) and (b), respectively.

In Phase 2.2 and Phase 2.3, the column peak lateral strength was overestimated by the revised model and was higher than the blind prediction in $0.4 \times DE$ and $0.6 \times DE$ hazard levels in both positive (pull) and negative (push) direction (Table 8.5 and Table 8.6). However, at higher hazard levels ($1.2 \times DE$ and $1.8 \times DE$ ($1.2 \times MCE$)), the revised model provided a better prediction of the column peak lateral strength compared to the blind prediction with a relative error within 2.8% and 9.3% in Phase 2.2 and Phase 2.3, respectively (Table 8.5 and Table 8.6).

In Phase 2.4 where six ED links were removed from the system (see Section 7.12.3), the predicted column peak lateral strength by the revised model was in good agreement with measured test data with a relative error within 19% (Table 8.7).

The predicted post peak hardening response of the specimen was in good agreement with test results in both positive (pull) and negative (push) directions in all three phases.

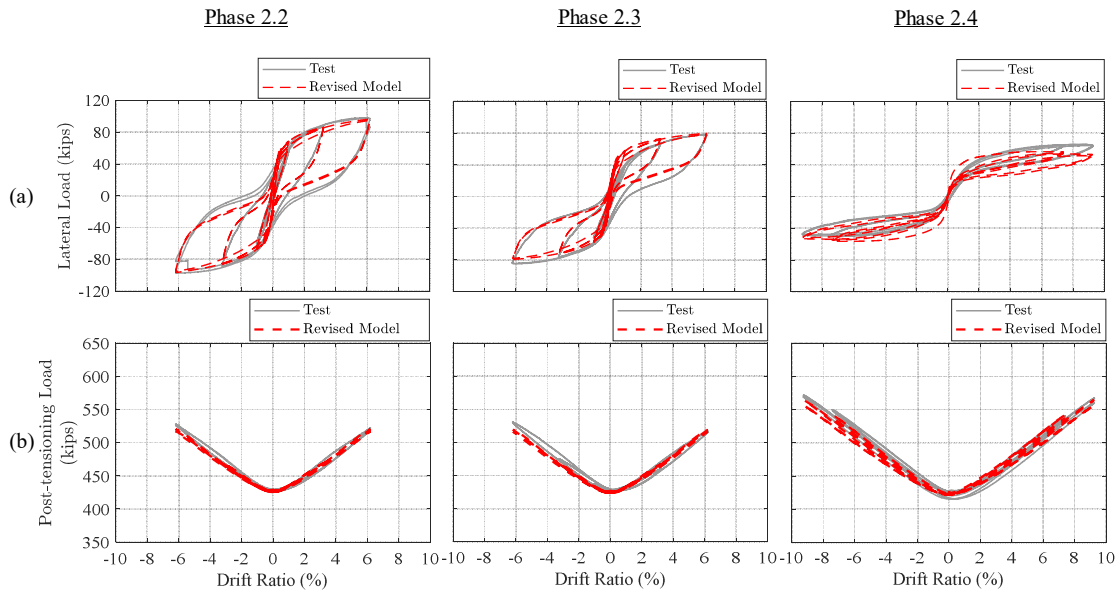


Figure 8.14. Comparison of experimental and predicted response of PUED-2 column from the revised model: (a) lateral load vs. drift ratio; (b) post-tensioning load vs. drift ratio.

Table 8.5. Comparison of experimental and predicted peak lateral strength for PUED-2 column in Phase 2.2 from the revised model (1) in positive and negative direction at various hazard levels.

Hazard Level	Peak Drift Ratio (%)	F_{peak}^+			F_{peak}^-		
		Test (kips)	Model (kips)	Error (%)	Test (kips)	Model (kips)	Error (%)
0.4×DE	0.60	39.3	61.5	56.3	-40.7	-61.8	51.8
0.6×DE	1.02	56.8	69.0	21.5	-60.9	-68.6	12.7
1.2×DE	3.23	87.4	86.6	0.9	-88.7	-86.2	2.8
1.8×DE (1.2×MCE)	6.19	98.3	96.7	1.6	-97.2	-96.6	0.6

Table 8.6. Comparison of experimental and predicted peak lateral strength for PUED-2 column in Phase 2.3 from the revised model (1) in positive and negative direction at various hazard levels.

Hazard Level	Peak Drift Ratio (%)	F_{peak}^+			F_{peak}^-		
		Test (kips)	Model (kips)	Error (%)	Test (kips)	Model (kips)	Error (%)
0.4×DE	0.60	29.9	51.1	70.8	-33.5	-51.7	54.4
0.6×DE	1.02	41.1	58.4	42.0	-51.8	-58.1	12.2
1.2×DE	3.23	66.7	72.9	9.3	-76.1	-72.5	4.7
1.8×DE (1.2×MCE)	6.19	78.6	79.6	1.3	-84.5	-79.5	5.9

Table 8.7. Comparison of experimental and predicted peak lateral strength for PUED-2 column in Phase 2.4 from the revised model (1) in positive and negative direction at various peak drift ratios.

Peak Drift Ratio (%)	F_{peak}^+			F_{peak}^-		
	Test (kips)	Model (kips)	Error (%)	Test (kips)	Model (kips)	Error (%)
7.39	65.3	56.7	13.2	-50.2	-56.4	12.2
9.24	65.9	53.7	18.5	-49.5	-53.7	8.4

Although the low-cycle fatigue was not accounted for in the steel material model, the ED link fracture was simulated by further revising the model (revised model 2) by taking $\varepsilon_{f1} = 10.5\%$ and $\varepsilon_{f2} = 11\%$ (Figure 5.1(b)), i.e. smaller than the values predicted through monotonic tensile testing. As shown in Figure 8.15, the ED link fracture is predicted to occur during the first pull and push loading cycle at 6.19% drift ratio, while the ED link failure occurred in the second pull and push loading cycle at 6.19% drift ratio during the test. The difference in the predicted failure cycle and the observed ED link failure cycle during the test was attributed to the fact that the low-cycle fatigue was not accounted for in the steel material model.

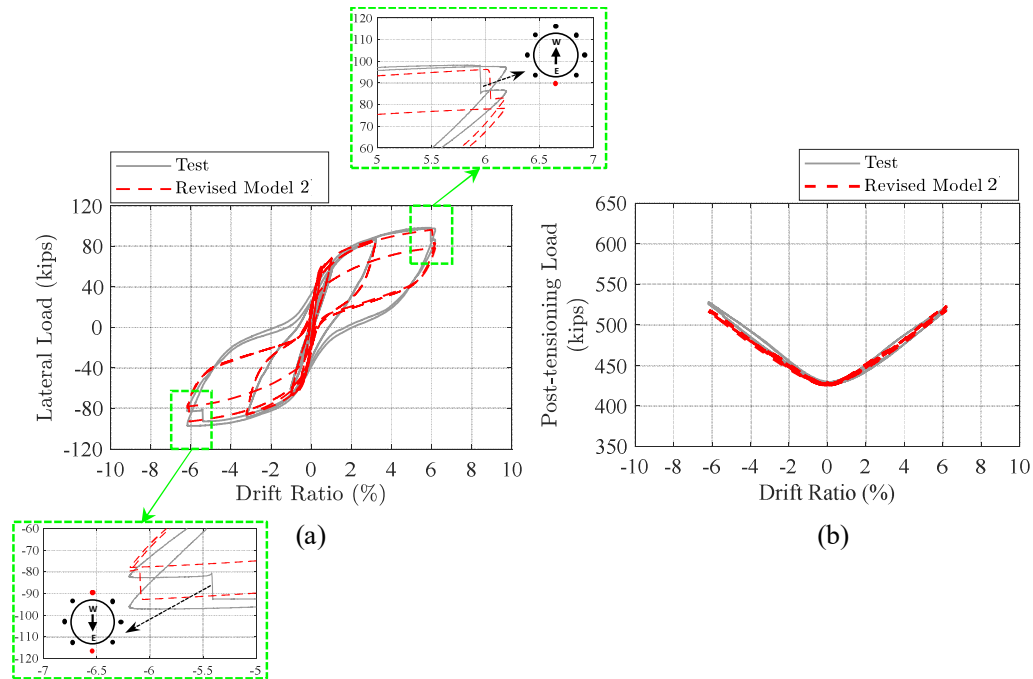


Figure 8.15. Comparison of experimental and predicted response of RC rocking column from the revised model 2: (a) lateral load vs. drift ratio; (b) post-tensioning load vs. drift ratio.

The peak PT load in positive (pull) and negative (push) direction over each set of cycles predicted by the revised models was in good agreement with test results in all three phases, with the relative error being within 2% (Figure 8.16(a)). The measured and predicted PT load at the end of each set cycles was in good agreement with test results with a relative error within 2% (Figure 8.16(b)).

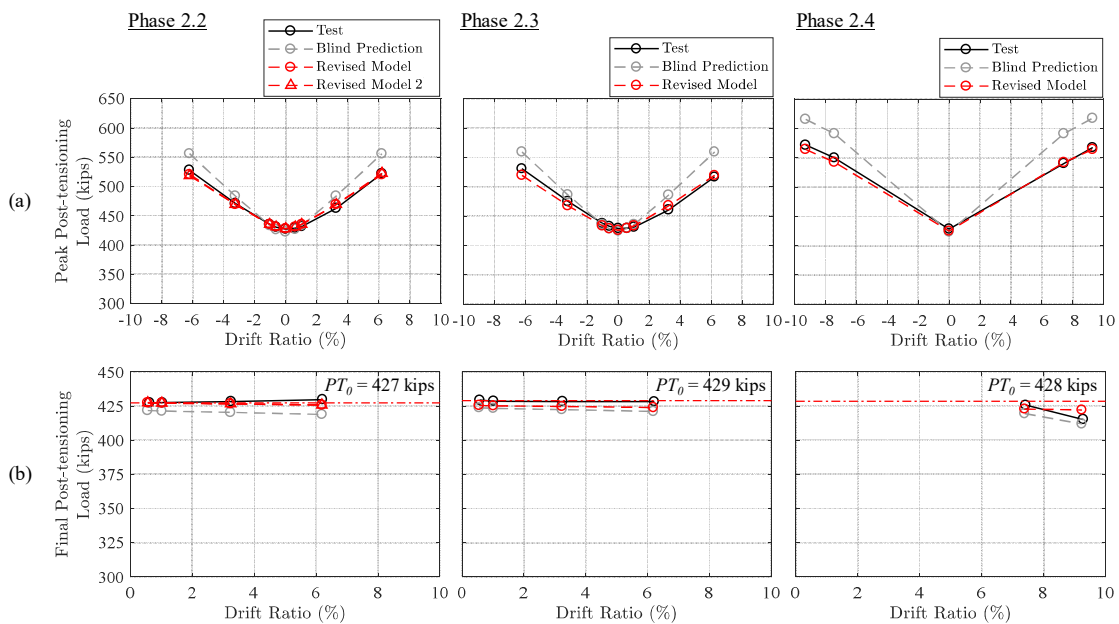


Figure 8.16. Comparison of experimental and predicted response of PUED-2 column from the original and revised models: (a) peak post-tensioning load vs. drift ratio; (b) final post-tensioning load vs. drift ratio.

In Phase 2.2 and 2.3, the average residual drift ratio predicted by the revised models was identical to the blind prediction at the 0.4×DE and 0.6×DE hazard levels, while it was predicted to be slightly larger at the 1.2×DE and 1.8×DE (1.2×MCE) hazard

levels by the revised model compared to the blind prediction (Figure 8.17(a)). The average residual drift ratio in Phase 2.2 was underestimated by the revised model by 58% and 68% at the $1.2\times DE$ and $1.8\times DE$ ($1.2\times MCE$) hazard levels, respectively (Figure 8.17(a)). Compared to the revised model, a new revised model (named Revised Model 2) in which the ED link failure was simulated, predicted a lower average residual drift ratio at $1.8\times DE$ ($1.2\times MCE$) level, where the ED link failure occurred. The measured average residual drift ratio in the test was not affected by ED link failure. This is attributed to the fact that in the test, the fractured ED links still contributed in the response through the interaction of the link and confining tube and through bearing at the failure interface in compression. However, in the model a fractured link does not contribute in the response since both stiffness and strength drop to zero upon fracture. In Phase 2.3 and 2.4, the average residual drift ratio predicted by the revised models was comparable to the blind prediction (Figure 8.17(a)).

The equivalent viscous damping predicted by the revised models was lower than the blind prediction at the $0.4\times DE$ hazard level in Phases 2.2 and 2.3 (Figure 8.17(b)). This is attributed to the higher expected yield strength of the ED link steel material in the revised models compared to the original model, which delayed the yielding of the ED links. In Phases 2.2 and 2.3, the equivalent viscous damping predicted by the revised models at the $0.6\times DE$ hazard level was comparable to the blind prediction, while it was predicted slightly higher at the $1.2\times DE$ and $1.8\times DE$ ($1.2\times MCE$) hazard levels. In Phase

2.4, the equivalent viscous damping predicted by the revised models was comparable to the blind prediction.

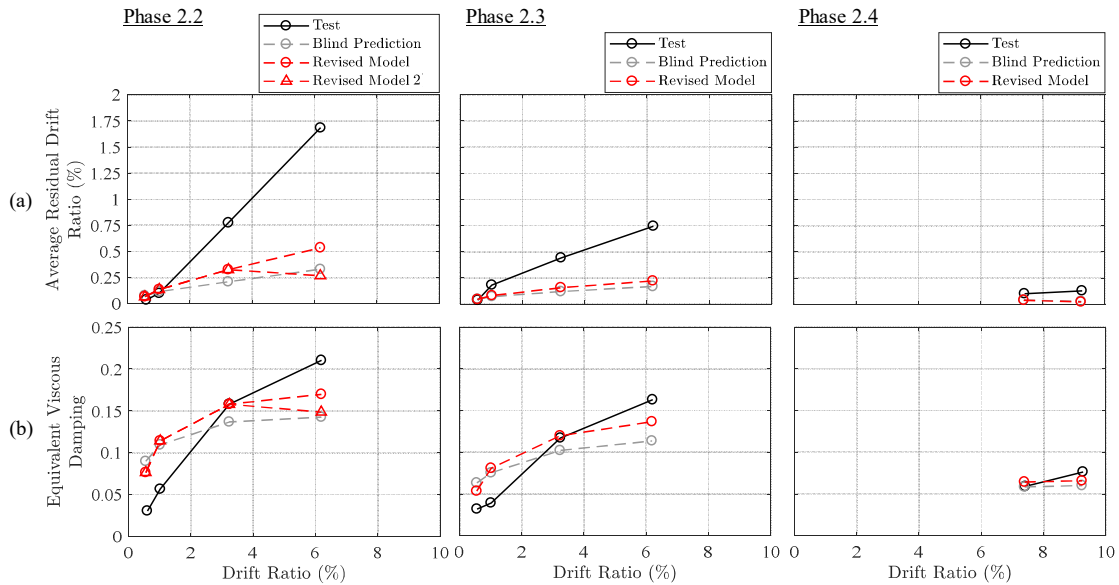


Figure 8.17. Comparison of experimental and predicted response of PUED-2 column from the original and revised model: (a) average residual drift ratio vs. drift ratio; (b) equivalent viscous damping vs. drift ratio.

8.3.2.3. PU-enhanced Column

The lateral load versus and post-tensioning load versus drift ratio response of the PU-enhanced column (without ED links) at the drift ratio rate of 0.001 /sec predicted by the revised model is compared with the test results in Figure 8.18(a) and (b), respectively.

The column peak lateral strength was in good agreement with the test data at all hazard levels in both positive (pull) and negative (push) direction with a relative error within 11.5% and 4%, respectively (Table 8.8). It is worth noting that the higher error in

the positive (pull) direction was attributed to the fact that the specimen showed slightly higher strength (up to about 4.5 kips) in the pull loading direction (positive direction) compared to the push direction (negative direction), while the predicted response was symmetric. The predicted post peak hardening response of the specimen was in good agreement with test results in both positive (pull) and negative (push) directions.

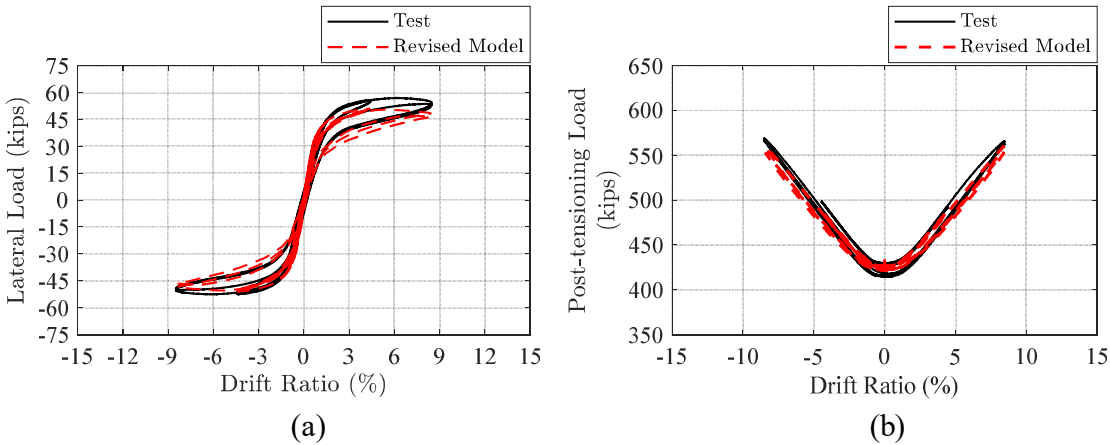


Figure 8.18. Comparison of experimental and predicted response of PU column from the revised model (1): (a) lateral load vs. drift ratio; (b) post-tensioning load vs. drift ratio.

Table 8.8. Comparison of experimental and predicted peak lateral strength for PU column from the revised model in positive and negative direction at various hazard levels.

Hazard Level	Peak Drift Ratio (%)	F_{peak}^+			F_{peak}^-		
		Test (kips)	Model (kips)	Error (%)	Test (kips)	Model (kips)	Error (%)
0.4×DE	0.85	32.5	35.9	10.6	-34.0	-35.2	3.6
0.6×DE	1.52	44.8	43.9	1.9	-43.7	-43.9	0.4
1.2×DE	4.42	55.7	51.0	8.5	-52.5	-51.0	2.8
1.8×DE (1.2×MCE)	8.47	56.9	50.4	11.5	-52.5	-50.4	4.0

The peak PT load in positive (pull) and negative (push) direction over each set of cycles predicted by the revised model was in good agreement with test results with the relative error being within 2% (Figure 8.19(a)). The measured and predicted PT load at the end of each set cycles was in good agreement with test results with a relative error within 1.7% (Figure 8.19(b)).

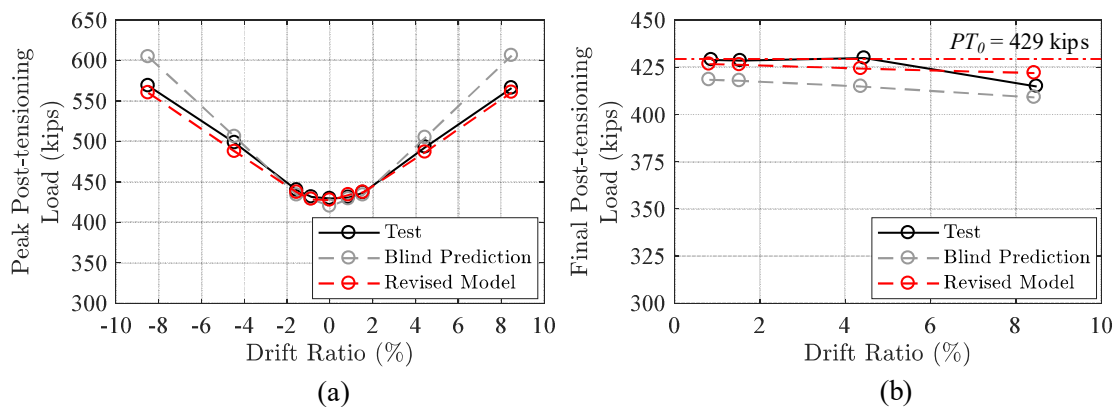


Figure 8.19. Comparison of experimental and predicted response of PU column from the original and revised model: (a) peak post-tensioning load vs. drift ratio; (b) final post-tensioning load vs. drift ratio.

The average residual drift ratio (Figure 8.20(a)) and equivalent viscous damping (Figure 8.20(b)) predicted by the revised model was approximately the same as the blind prediction.

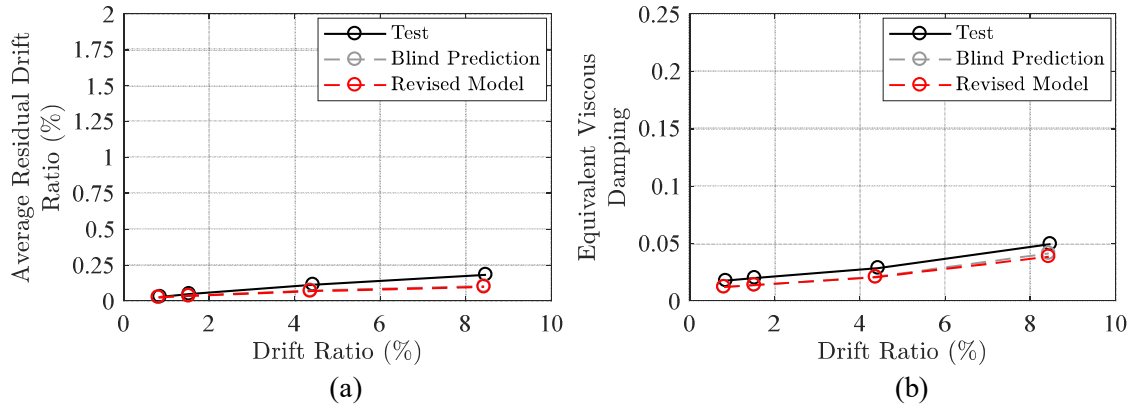


Figure 8.20. Comparison of experimental and predicted response of PU column from the original and revised model: (a) average residual drift ratio vs. drift ratio; (b) equivalent viscous damping vs. drift ratio.

8.4. Summary and Findings

In this section, the response predicted prior to tests (called *blind prediction* herein) through numerical models of test specimens developed following the approach presented in Section 6.3 was validated through comparison with a selection of test results presented in Section 7. Based on the comparison of the predicted response from the original model with the test results, the model was further refined to address some of the discrepancies observed between the blind prediction and test results. The general findings from the validation of the numerical model are:

- The post-tensioning response of all column systems was sensitive to the cross-sectional and geometric properties of the element used to simulate the tendon. Specifically, the PT load response was more sensitive to the equivalent diameter of the PT tendon consisted of multiple monostrands. It was found that a better prediction of the PT load response could be achieved in all specimens by using an equivalent tendon diameter 17% smaller than the original calculated value. This could imply that there is some additional unaccounted flexibility in the system, which could be driven by the anchorage (Sideris et al. 2014a).
- The models underestimated the residual drift ratio and energy dissipation capacity (represented by equivalent viscous damping) for all column designs, and particularly for the RC rocking and PUED-2 column. To further improve such prediction capabilities, the model should be further investigated with a focus on including the contribution of the grout material at the base rocking interface, interaction of the ED links with the confining tube, and material model parameters of concrete and ED links steel material.
- The models overestimated the initial elastic stiffness for all column system, especially for the RC rocking and PUED-2 column. To further improve such prediction capabilities, the model should be further investigated through a parametric study with a focus on including the contribution of the grout material at the column-to-foundation rocking interface.

9. SUMMARY, CONCLUSIONS, AND RECOMMENDATIONS FOR FUTURE RESEARCH

9.1. Summary

In this dissertation, the concept of seismically resilient bridge columns with polyurethane (PU) damage-resistant (DR) joints and replaceable energy dissipating (ED) links, also termed PU-enhanced rocking column with Energy Dissipation (ED) links, is proposed. The proposed system introduces the component of explicit damage control and combines it with the concept of accelerated low cost post-earthquake retrofit/repair in the design of bridges for moderate to high seismicity regions; hence, expanding the focus of the bridge engineering community from ABC to ABC&AR, where AR stands for “accelerated retrofit/repair”. PU-enhanced rocking columns with ED links offer: (i) explicit damage control through PU damage-resistant end segments (ii) self-centering through internal unbonded post-tensioning, (iii) energy dissipation and flexural stiffness/strength through external replaceable ED links. The replaceability of ED links offers low cost rapid post-earthquake retrofit without operation disruptions.

Initially, the concept of the PU-enhanced rocking columns with ED links is introduced. The mechanics of the PU-enhanced rocking columns with ED links under a constant vertical load, post-tensioning load, and monotonically increasing lateral load, were then studied, leading to a simplified analytical model to compute discrete points of the pushover curve. Furthermore, these mechanics are integrated within a capacity

spectrum design methodology, which is used to assess and compare the performance of the proposed column system with various designs in terms of peak displacement demands.

The properties of selected polyurethanes (PU) with various compositions that have been found to be potentially suitable for structural applications was characterized in a three-phase experimental program. In Phase 1, cylindrical samples of three different types of elastomers available from BASF (2016) as Elastocore (ECore), Elastocast (ECast), and Elastoshore (EShore) were subjected to uniaxial compression at a crush rate of 0.05 in/min. According to the findings of Phase 1 of the testing program, among the three PU materials considered in this study, EShore was found unsuitable for the proposed application, primarily due to its low mechanical properties. Given that, the second phase was aimed at further investigation of the response of the remaining two selected PUs, ECore and ECast, via uniaxial compression strain-controlled half-cycle tests under a constant engineering strain rate. In Phase 3, an extensive set of uniaxial tests were conducted to further characterize the main features of two selected polyurethanes (PUs) studied in Phase 2 accounting for environmental conditions (e.g. temperature), loading conditions (e.g. cyclic vs. monotonic loading, loading path and rate), and long term effects (e.g. relaxation and creep). The wide variety of the selected tests allows for decoupling different features of the response (e.g. rate-dependent and rate-independent parts), which further allows for a systematic calibration of the numerical constitutive model proposed later in this study. Besides, the variety of the tests allows for further verification of the calibrated numerical model.

The performance of the proposed column design was assessed through three-dimensional finite element analysis. To this end, an elasto-visco-plastic model including sets of parallel networks was assembled using the material library of the *PolyUMod* software by Bergstrom (2012) and calibrated to the material test data obtained in Phase 2 of the material testing program. A UMAT subroutine was generated for the calibrated constitutive model that was implemented in ABAQUS. A bridge column with a PU (ECast) segment of various geometries and various ED link properties was subjected to monotonic and cyclic pushover loading at various loading rates and amplitudes. The performance of the proposed column design was assessed in terms of strength, stiffness, ductility capacity, energy dissipation properties, self-centering capabilities, damage resistance. The numerical study was conducted using the general-purpose finite element software ABAQUS (SIMULIA 2013).

Two uniaxial visco-elastic/plastic constitutive models were developed capable of capturing the salient response features of the selected PU materials, such as rate dependency, hysteresis and damage (softening), and long term effects (creep, relaxation, and recovery). The proposed models are computationally efficient and suitable for structural engineering applications, which include numerous analyses with several ground motions. The developed constitutive models are implemented in the OpenSEES structural analysis software (McKenna and Fenves 2001), which is widely used for the nonlinear dynamic analysis of structures in various structural engineering applications.

The seismic performance of the proposed column system was assessed through numerical analysis utilizing the OpenSEES structural analysis software (McKenna and Fenves 2001). Specifically, the monotonic and cyclic response of the proposed column design was investigated with respect to the properties of the ED links and compared with the response of a reference conventional reinforced concrete (RC) monolithic column and an RC rocking column. Moreover, the seismic performance of the proposed column design was investigated through incremental dynamic analyses with a suite of far-field ground motions, allowing for a comprehensive quantitative comparison against the reference conventional RC monolithic column and the RC rocking column via fragility analysis considering various damage states.

The performance of the proposed column system and the proposed replacement strategy for ED links was evaluated through large scale (~1:2.5) testing of bridge column systems with various designs including the proposed PU-enhanced column system with/without ED links as well as a conventional reinforced concrete (RC) rocking column. Specifically, the test specimens included a conventional RC rocking column, a column with PU end segment with bi-layered axisymmetric section and energy dissipation (ED) links (PUED column), and a column with a solid PU end segment (PU column). First, the specimens were post-tensioned using a monostrand hydraulic jack. Then, the vertical gravity load of was applied by the two vertical actuators. Displacement-controlled sinusoidal reversed cyclic loading was subsequently applied with increasing amplitude ultimately reaching a drift ratio of approximately 13.4%, 9.2%, and 8.5% in the RC

column, PUED column, and PU column, respectively. To evaluate the re-centering capacity of the system upon releasing the ED links, all the ED links of the PUED column were released after being subjected up to a lateral drift ratio of 3.2% and re-tightened. This process allowed nearly complete self-centering. Subsequently, displacement-controlled sinusoidal reversed cyclic loading was applied, consisted of symmetric cycles at amplitudes corresponding to various hazard levels, including the $0.4 \times DE$, $0.6 \times DE$, $1.2 \times DE$, and $1.8 \times DE$ ($1.2 \times MCE$) hazards. Each set included two cycles of the same amplitude. For each hazard level, the loading was applied at various drift ratio rates including 0.1, 1.08, 2.71, and 5.41 in/sec corresponding to a drift rate of 0.001, 0.01, 0.025, and 0.05 /sec. The PU column was subjected to sets of symmetric cycles at amplitudes corresponding to various hazard levels including the $0.4 \times DE$, $0.6 \times DE$, $1.2 \times DE$, and $1.8 \times DE$ ($1.2 \times MCE$) hazard levels. Each set included two cycles of the same amplitude. The loading was applied at various rates including 0.1, 1.08, 2.71, and 5.41 in/sec corresponding to a drift ratio rate of 0.001, 0.01, 0.025, and 0.05 /sec, respectively.

Finally, the performance of the numerical models of the test specimens developed in the OpenSEES structural analysis software was validated via comparison to the test data. Recommendations were made to further improve the capability of the models to predict the response observed in the quasi-static cyclic tests.

9.2. Major Conclusions

Major findings of this study are summarized in this section. Specific findings of various parts of this study are listed at the end of the corresponding sections. Major findings of this study are:

- The PU-enhanced rocking column with ED links is a viable option for expanding the ABC methods to ABC&AR, where AR stands for “accelerated retrofit/repair, in precast concrete segmental bridge construction in regions of moderate or high seismicity.
- The large-scale experimental study validated the computationally predicted response of the post-tensioned segmental PU-enhanced columns with ED links; thus, further validated the developed mechanics and design/analysis methodologies. The validated response features primarily included a high ductility capacity associated with the damage in the replaceable ED links and the minor or no damage in other components of the system, and the high re-centering capacity of the system upon releasing/removing the ED links.
- The PU material characterization program led to the following findings:
 - The selected PUs can sustain large strains (up to ~50% in compression and ~15% in tension) with minor or no damage.
 - The selected PUs exhibit strain-rate dependent properties in the elastic and inelastic range, highly nonlinear equilibrium hysteresis with a

Bauschinger-type reverse yielding, and damage/softening with tension-compression coupling. Moreover, it was found that the response of the selected PUs is highly temperature dependent; the mechanical properties (stiffness and strength) decreased with temperature in both ECore and ECast.

- The selected PUs showed a strain recovery capacity upon load removal after experiencing large compressive strains (10% in ECast and 20% in ECore). Moreover, the rate of recovery increased with the (applied) loading rate.
- According to the three-dimensional finite element analysis of bridge column with PU (ECast) segment with various geometries and various ED link properties using the general-purpose finite element code ABAQUS SIMULIA 2013, it was found that:
 - PU-enhanced rocking columns with ED links can provide low damage, large deformation capacity and rapid retrofit capabilities. In the absence of ED links, columns with PU end segments provide moderate stiffness and strength, low energy dissipation capacity and large self-centering capabilities. Incorporation of ED links increases the stiffness, strength and energy dissipations capabilities of the proposed column designs. Stiffness,

strength and residual deformations increase with Λ_C (i.e., the contribution of ED links).

- Because of the large elastic deformation capacity and the visco-plastic properties of the selected PU, permanent deformations are small. Specifically, the large elastic deformability permits large deformations without damage, while the visco-plastic properties limit the contribution of the plastic strains in the total strains. As a result, removal of the ED links after large induced lateral drift ratios ($\sim 13\%$), eliminated all column residual deformations ($RSE > 99.5\%$) indicating that the PU segments remained nearly undamaged.
- Rate effects on the peak strength of the column were found to be small, because only a small portion of the PU segment is actually subjected to large strains, for which strain rate effects are significant. However, the residual deformations significantly decreased with the loading rate, indicating that locally induced plastic strains were alleviated, because of the viscous contributions during plastic traveling.
- The geometric properties of the PU segment – height, h_j , and diameter, D_j – strongly affect the observed damage, and lateral stiffness and strength of the column. Specifically, the lateral stiffness and strength increase with D_j/D_c , where D_c is the column diameter. However, the lateral stiffness

decreases with h_j/D_c , while the lateral strength only slightly increases with h_j/D_c . On the other hand, the PU segment height should satisfy $h_j/D_c \geq 1$ to ensure that rocking will occur at the bottom joint, while the PU segment diameter should be small enough ($D_j/D_c = 0.8$ to 0.9), so that large (concentrated) stresses are solely transferred to the confined concrete core.

- From the seismic performance assessment of the PU-enhanced rocking columns with ED links through numerical models developed in the OpenSEES structural analysis software (McKenna and Fenves 2001), it was found that:
 - Columns with PU segments were capable of accommodating large deformations with minor or repairable damage. Specifically, the studied column designs accommodated lateral drift ratios up to 5% without damage and lateral drift ratios up to 15% with damage at the ED links, which are easily replaceable, and minor yielding at the post-tensioning rebar. Moreover, columns with PU segments demonstrated mild post-peak strength deterioration, contrary to rocking RC columns which demonstrated rapid post-peak deterioration, particularly at large drift ratios ($> 5\%$).
 - Columns with PU segments and ED links exhibited much higher median capacity against post-event demolition, which increased with the contribution of the ED links, becoming up to 125% larger (for $\lambda_c = 0.5$)

than that of the conventional cast-in-place column. Similarly, the capacity against structural collapse increased by 17% (for $\lambda_C = 0.5$) with respect to the median capacity of the conventional RC column.

- The performance of the RC rocking column was found to be sensitive on the selection of the intensity measure, IM. Two intensity measures were considered: (i) the 5% damped spectral acceleration at the mean of the fundamental periods of all column designs, and (ii) the 5% damped spectral acceleration at the individual fundamental period of each column design. The second/alternative IM resulted in the RC rocking column is shown to outperform the RC monolithic column against the DS of system demolition/replacement, and also outperform the PU column (without ED links) against the DSs of system demolition/replacement and PT bar yielding and rupture. All other findings were found to be independent of the selected IM, at least from a qualitative perspective.
- Columns with PU segments and ED links demonstrated major resistance against structural damage, in terms of: (i) concrete spalling and crushing, because concrete in the vicinity of the bottom joint has been replaced by PU, and (ii) post-tensioning bar yielding and fracture. Specifically, the median capacity against yielding and fracture increased by 94% and 100% respectively, with respect to that of the rocking RC column (with respect

to the first IM) or by 206% and 138% respectively, with respect to that of the PU column (with respect to the second IM).

- Peak strains in PU decreased with the contribution of ED links, further showing the capability of ED links to prevent damage in other components of the column.
- The general findings from the validation of the numerical model are:
 - Overall, the response (e.g. force vs. drift ratio, PT load vs. peak drift ratio) predicted for all test specimens by the model developed prior to the tests was in reasonable agreement with the response obtained from the test, but also demonstrated deficiencies which were addressed through a revised model
 - The post-tensioning response of all column systems was found sensitive to the cross-sectional and geometric properties of the element used to simulate the tendon. Specifically, the PT load response was more sensitive to the equivalent diameter of the PT tendon consisted of multiple monostrands. It was found that a better prediction of the PT load response could be achieved in all specimens by using an equivalent tendon diameter that is 17% smaller than the original calculated value.
 - Both the original and the revised models underestimated the residual drift ratio and energy dissipation capacity (represented by equivalent viscous

damping) for all column system, especially for the RC rocking and PUED-2 column. To further improve the model in this regard, the model should be further investigated with a focus on including the contribution of the grout material at the base rocking interface, interaction of the ED links with the confining tube, and material model parameters of concrete and ED links steel material.

- The models overestimated the initial elastic stiffness for all column system, especially for the RC rocking and PUED-2 column. To further improve the model in this regard, a parametric study with a focus on including the contribution of the grout material at the base rocking interface should be conducted.

9.3. Original Contribution

The most important original technical contribution made by this study are:

- Introduction and Development of the Concept of Seismically Resilient Post-tensioned Segmental Bridge Columns with Polyurethane Damage-Resistant (DR) Joints And Replaceable Energy Dissipating (ED) Links, which is the major contribution of this study. Segmental precast concrete bridge superstructures have long been used as a means of accelerating construction. Over the past two decades, research efforts have developed and investigated several seismically resistant column connection details. Although the

aforementioned column designs combine construction rapidity with improved seismic performance (compared to monolithic systems), they still sustain considerable concrete damage at the rocking joints under large seismic hazards, which reduces their ultimate strength, ductility capacity and self-centering capabilities, and often requires major post-earthquake repairs, which can be costly. In this study, a new generation of bridge column systems is proposed, which introduces the component of explicit damage control and combines it with the concept of accelerated low cost post-earthquake retrofit/repair. This concept, which is applicable to bridges in moderate and high seismicity regions, expands the focus of the bridge engineering community from ABC to ABC&AR, where AR stands for “accelerated retrofit/repair”. Specifically, the contributions associated with the concept of PU-enhanced columns with ED links are:

1. Explicit damage control in bridge column systems through PU damage-resistant end segments. Specifically, because PU is a highly deformable material compared to concrete, large induced deformations on the column system can be accommodated with limited or no permanent damage. As a result, during strong earthquakes, all damage will be concentrated at target replaceable elements, i.e. ED links, preventing damage from propagating to the column length.

2. Validation of the concept of accelerated low cost post-earthquake retrofit/repair in the design of bridges for moderate to high seismicity regions. Specifically, in the proposed system, supplemental energy dissipation and the required flexural stiffness and strength is provided by external energy dissipating links. The replaceability of ED links offers low cost rapid post-earthquake retrofit without operation disruptions.
3. Development of the mechanics of the proposed system, and formulation of a simplified analytical model to describe the response of the post-tensioned PU-enhanced columns with ED links under a constant vertical load and monotonically increasing lateral load. This model could be used to provide a basis for the design of the proposed system.
4. Development of the geometric and material details (e.g. geometric and material details of the PU segment, geometry of the ED links) for the PU-enhanced columns with ED links.
5. Characterization of mechanical properties of the PU materials selected for the proposed application. Specifically, the mechanical properties of selected PUs with various compositions potentially suitable for structural applications was characterized via a comprehensive three-

phase experimental program accounting for environmental conditions (e.g. temperature), loading conditions (e.g. cyclic vs. monotonic loading, loading path and rate), and long term effects (e.g. relaxation and creep).

6. Development of a three-dimensional elasto-visco-plastic constitutive material model capable of capturing major response features of selected PU materials using the material library of the *PolyUMod* software by Bergstrom (2012). The developed model was added to the material library of the general purpose finite element package, ABAQUS (SIMULIA 2013).
 7. Large scale testing of PU-enhanced rocking columns with ED links. In particular, the performance of the proposed column system and the proposed replacement strategy for ED links was evaluated through large scale (~1:2.5) testing of bridge column systems with various designs including the proposed column system as well as a conventional reinforced concrete (RC) rocking column.
- Development of Novel Uniaxial Viscoelastic Softening Viscoplastic Models for PU Materials Suitable for Structural applications. The majority of the existing models in the literature are three-dimensional, computationally expensive, and tailored to specific polymers. This often makes them unsuitable

for structural engineering applications, which include numerous analyses with several ground motions. This challenge was addressed by developing novel uniaxial visco-elastic/plastic constitutive models capable of capturing the salient response features of the selected polyurethanes, such as rate dependency, hysteresis and damage (softening), and long term effects (creep, relaxation, and recovery).

- Development of Validated Numerical Models of PU-enhanced Columns with ED links. Numerical models of the proposed column system were generated using the open-source structural analysis software OpenSEES (McKenna and Fenves 2001). The performance of the numerical models was validated via comparison with the test data. Recommendations were made to further improve the capability of the models to predict the response observed in the quasi-static cyclic tests.

9.4. Recommendations for Future Research

According to the findings of this study, future research could pursue some of the following areas:

- Seismic performance evaluation of the PU-enhanced columns with ED links under dynamic loading conditions, seismic hazards and ground motion inputs. Investigation of seismic performance of the proposed system through dynamic tests is a key factor in further development of PU-enhanced columns with ED

links. In the seismic tests, attention should be paid to further validate the major response characteristics (i.e., deformation and energy dissipation capacity, re-centering capabilities and control of seismic forces), the effects of several parameters, including the seismic hazard level, the asynchronous base excitation (or multiple-support excitation), the site-to-source motion characteristics (i.e., far-field vs. near-fault motions), and the bi-axial versus tri-axial base excitation, on the response of the proposed system.

- Performance assessment of various bridge systems incorporating PU-enhanced column segments with ED links. Future research should consider investigating the seismic performance of multiple bridge systems obtained by variation of span number (single or multiple) and column bent type (single or multiple). The study should be conducted through detailed experimental and computational modeling and extensive seismic response simulations.
- Development of performance-based seismic design methodologies for PU-enhanced columns with ED links. The development of performance-based seismic design methods is a key factor in supporting the application of PU-enhanced columns with ED links in bridge systems in regions with moderate or high seismicity. Future research should consider developing reliable performance-based design methods with the objective of optimal use of advantageous response features of the proposed system (e.g. high energy

dissipation capacity, explicit damage control, and re-centering, accelerated retrofit) into a design framework that could result in an efficient system design.

Further future research initiatives may also include:

- Investigation of the long-term creep/relaxation effects on the response of PU material under constant axial load. Future research should address the long term effects on the performance of the proposed system over a periods of time longer than 5 days (i.e. the duration of creep tests in this study), both in terms of material mechanical testing and constitutive modeling.
- Investigation of the optimal design of ED links. The performance of the proposed column system highly depends on the performance of ED links as the replaceable sacrificial elements that provide energy dissipation and flexural stiffness/strength. Investigation of the effect of various design parameters of ED links (e.g. number of links, connection details, geometric details of the yielding length, and material properties of the links) on the seismic performance of the proposed system is a key factor in achieving an optimal seismic performance. Investigation of the performance of ED links made of innovative materials, such as PUs and shape memory alloys (e.g. Nickel-titanium). ED links made of shape memory alloys can contribute to the overall self-centering capabilities of the system.

- Investigation of damage mechanisms/sources in PU segments. In the first phase of material testing program, it was shown that the selected PUs, specifically ECast, could sustain compressive strains up to ~50% with no damage. However, unexpected asymmetric damage occurred in the PU sleeve in Phase 2.4 of the large scale testing of the PUEd column in the form of cracks at about 9.2% lateral drift ratio, followed by fracture in the subsequent cycle at the same amplitude. Future research should consider investigating the source of such unexpected damages in PU-enhanced segments and proposing preventive solutions, which is essential to support the reliability of damage-resistant feature of the proposed system.
- Development of replaceable fusing joint setups and connection details in PU-enhanced segments with bi-layered axisymmetric sections. PU-enhanced segments, although are designed to sustain minor or no damage up to the target seismic hazard level, may experience damage in various forms (e.g. permanent plastic deformations, fracture) at larger seismic hazards (e.g. 3×MCE seismic hazard level). Given that, future research should consider developing replaceable fusing joints (i.e. PU sleeve) setups and post-earthquake rapid replacement strategies without disassembly of the entire system and while the bridge remains in service.
- Investigation of the effects of superstructure-to-substructure and superstructure-to-abutment connectivity on the seismic performance of PU-

enhanced columns with ED links. In common practice, the superstructure-to-substructure and superstructure-to-abutment connection is either monolithic (integral bent caps) or simply supported by bearing pads (non-integral bent caps). The performance of PU-enhanced columns with ED links and the replacement of the fusing elements (e.g. ED links and PU sleeve) in bridges employing each of these connection types should be investigated through large scale tests and numerical modeling with the objective of achieving the optimal seismic performance.

- Including the mechanical-temperature coupling effects in the PU constitutive material model. Future research should consider further improving the proposed uniaxial visco-elastic/plastic constitutive models by including the mechanical-temperature coupling effects. Given that the mechanical properties of polymers are highly temperature dependent; such models are a key tool for performance assessment of the proposed system under various environmental condition (e.g. temperature).

REFERENCES

- AASHTO LRFD Bridge Design Specifications (2014). "AASHTO LRFD Bridge Design Specifications, 7th Edition." American Association of State Highway and Transportation Officials (AASHTO), 444 North Capitol Street, NW, Suite 249, Washington, DC 20001.
- Abdelkarim, O. I., ElGawady, M. A., Ghenni, A., Anumolu, S., Abdulazeez, M. (2016). "Seismic Performance of Innovative Hollow-Core FRP–Concrete–Steel Bridge Columns." *Journal of Bridge Engineering*, 22(2): 04016120.
- Addiego, F., Dahoun, A., G'Sell, C., Hiver, J. (2006). "Volume variation process of high-density polyethylene during tensile and creep tests." *Oil & Gas Science and Technology-Revue de l'IFP*, 61(6): 715-724.
- Adhikari, G., Petrini, L., Calvi, G. M. (2010). "Application of direct displacement based design to long span bridges." *Bulletin of Earthquake Engineering*, 8(4): 897-919.
- Amin, A., Alam, M., Okui, Y. (2002). "An improved hyperelasticity relation in modeling viscoelasticity response of natural and high damping rubbers in compression: experiments, parameter identification and numerical verification." *Mechanics of Materials*, 34(2): 75-95.
- Anand, L., Gurtin, M. E. (2003). "A theory of amorphous solids undergoing large deformations, with application to polymeric glasses." *International Journal of Solids and Structures*, 40(6): 1465-1487.
- Anand, L., Ames, N. (2006). "On modeling the micro-indentation response of an amorphous polymer." *International Journal of Plasticity*, 22(6): 1123-1170.
- Armstrong, P. J. (1966). "A mathematical representation of the multiaxial Bauschinger effect." *CEBG Report RD/B/N, 731*.
- Arruda, E. M., Boyce, M. C. (1993). "A three-dimensional constitutive model for the large stretch behavior of rubber elastic materials." *Journal of the Mechanics and Physics of Solids*, 41(2): 389-412.
- ASCE's Report Card for America's Infrastructure (2017). "Report Card for America's Infrastructure, Transportation - Bridges." American Society of Civil Engineers.
- ASTM-D695 (2010). "Standard Test Method for Compressive Properties of Rigid Plastics." ASTM International, West Conshohocken, PA.

- ASTM A36/A36M-19 (2019). "Standard Specification for Carbon Structural Steel." ASTM International, West Conshohocken, PA.
- ASTM A416/A416M-18 (2018). "Standard Specification for Low-Relaxation, Seven-Wire Steel Strand for Prestressed Concrete." ASTM International, West Conshohocken, PA.
- ASTM A572/A572M-15 (2015). "Standard Specification for High-Strength Low-Alloy Columbium-Vanadium Structural Steel." ASTM International, West Conshohocken, PA.
- ASTM A615/A615M-18e1 (2018). "Standard Specification for Deformed and Plain Carbon-Steel Bars for Concrete Reinforcement." ASTM International, West Conshohocken, PA.
- ASTM A706/A706M-16 (2016). "Standard Specification for Low-Alloy Steel Deformed and Plain Bars for Concrete Reinforcement." ASTM International, West Conshohocken, PA.
- ASTM D695 (2010). "Standard Test Method for Compressive Properties of Rigid Plastics." ASTM International, West Conshohocken, PA.
- Bagley, R. L., Torvik, P. (1983). "A theoretical basis for the application of fractional calculus to viscoelasticity." *Journal of Rheology*, 27(3): 201-210.
- Baker, J. W. (2015). "Efficient analytical fragility function fitting using dynamic structural analysis." *Earthquake Spectra*, 31(1): 579-599.
- Barbosa, A. R., Link, T., Trejo, D. (2015). "Seismic performance of high-strength steel RC bridge columns." *Journal of Bridge Engineering*, 21(2): 04015044.
- Bardenhagen, S. G., Stout, M. G., Gray, G. T. (1997). "Three-dimensional, finite deformation, viscoplastic constitutive models for polymeric materials." *Mechanics of Materials*, 25(4): 235-253.
- BASF (1993). "Sandwich Plate System." <<http://www.performance-materials.basf.us/products/view/family/sandwichplatesystem>>. (Accessed in 2019).
- BASF (2016). <<https://www.basf.com/us/en.html>>. (Accessed in February, 2014).

- Bažant, Z. P., Yu, Q., Li, G.-H. (2012). "Excessive long-time deflections of prestressed box girders. I: Record-span bridge in Palau and other paradigms." *Journal of Structural Engineering*, 138(6): 676-686.
- Bergstrom, J., Bischoff, J. (2010). "An advanced thermomechanical constitutive model for UHMWPE." *The International Journal of Structural Changes in Solids*, 2(1): 31-39.
- Bergström, J., Boyce, M. (1998). "Constitutive modeling of the large strain time-dependent behavior of elastomers." *Journal of the Mechanics and Physics of Solids*, 46(5): 931-954.
- Bergström, J., Boyce, M. (2000). "Large strain time-dependent behavior of filled elastomers." *Mechanics of Materials*, 32(11): 627-644.
- Bergström, J., Hilbert, L. (2005). "A constitutive model for predicting the large deformation thermomechanical behavior of fluoropolymers." *Mechanics of Materials*, 37(8): 899-913.
- Bergstrom, J. S. (2012). "PolyUMod: A Library for Advanced User Materials." Veryst Engineering, LLC, Needham, Mass, USA.
- Bergstrom, J. S. (2015). *Mechanics of solid polymers: Theory and computational modeling*, William Andrew. ISBN 0323322964.
- Billington, S. L., Yoon, J. (2004). "Cyclic response of unbonded posttensioned precast columns with ductile fiber-reinforced concrete." *Journal of Bridge Engineering*, 9(4): 353-363.
- Boyce, M. C., Parks, D. M., Argon, A. S. (1988). "Large inelastic deformation of glassy polymers. Part I: rate dependent constitutive model." *Mechanics of Materials*, 7(1): 15-33.
- Brenes, F. J., Wood, S. L., Kreger, M. E. (2006). "Anchorage requirements for grouted vertical-duct connectors in precast bent cap systems." FHWA/TX-06/0-4176-1, Center for Transportation Research, Univ. of Texas, Austin, TX,
- CALTRANS (2006). "Caltrans Seismic Design Criteria - Version 1.4." California Dept. of Transportation, Division of Engineering Services,, Sacramento,CA.
- Calvi, G., Kingsley, G. (1995). "Displacement-based seismic design of multi-degree-of-freedom bridge structures." *Earthquake Engineering & Structural Dynamics*, 24(9): 1247-1266.

- Cardone, D., Dolce, M., Palermo, G. (2009). "Direct displacement-based design of seismically isolated bridges." *Bulletin of Earthquake Engineering*, 7(2): 391-410.
- CEB-FIP Model Code (2010). *Comité Euro-International du Béton, Federation Internationale de la Précontrainte, CEB-FIP Model Code 2010*, Lausanne, Switzerland. ISBN 978-2-88394-095-6.
- Chopra, A. K., Goel, R. K. (2001). "Direct displacement-based design: use of inelastic vs. elastic design spectra." *Earthquake Spectra*, 17(1): 47-64.
- Chou, C. C., Chen, Y. C. (2006). "Cyclic tests of post-tensioned precast CFT segmental bridge columns with unbonded strands." *Earthquake Engineering & Structural Dynamics*, 35(2): 159-175.
- Christensen, R. (2012). *Theory of viscoelasticity: an introduction*, Elsevier. ISBN 0323161820.
- Cohen, A. (1991). "A Padé approximant to the inverse Langevin function." *Rheologica Acta*, 30(3): 270-273.
- Colak, O. U. (2005). "Modeling deformation behavior of polymers with viscoplasticity theory based on overstress." *International Journal of Plasticity*, 21(1): 145-160.
- Colak, O. U. (2008). "Kinematic hardening rules for modeling uniaxial and multiaxial ratcheting." *Materials & Design*, 29(8): 1575-1581.
- Correlated Solutions (2017). "Correlated Solutions." <https://www.correlatedsolutions.com/vic-2d/>. (Accessed in 2017).
- Davis, P. M. (2011). "Unbonded pre-tensioned columns for bridges in seismic regions." Ph.D. Dissertation, University of Washington.
- Davis, P. M., Janes, T. M., Haraldsson, O. S., Eberhard, M. O., Stanton, J. F. (2017). "Unbonded pretensioned columns for accelerated bridge construction in seismic regions." *Journal of Bridge Engineering*, 22(5): 04017003.
- De Almeida, O., Lagattu, F., Brillaud, J. (2008). "Analysis by a 3D DIC technique of volumetric deformation gradients: Application to polypropylene/EPR/talc composites." *Composites Part A: Applied Science and Manufacturing*, 39(8): 1210-1217.
- Diani, J., Fayolle, B., Gilormini, P. (2009). "A review on the Mullins effect." *European Polymer Journal*, 45(3): 601-612.

- Drozdov, A., Lejre, A.-L. H. (2009). "Viscoelasticity, viscoplasticity, and creep failure of polypropylene/clay nanocomposites." *Composites Science and Technology*, 69(15): 2596-2603.
- Drozdov, A. D. (1998). "A model for the nonlinear viscoelastic response in polymers at finite strains." *International Journal of Solids and Structures*, 35(18): 2315-2347.
- Dwairi, H., Kowalsky, M. (2006). "Implementation of inelastic displacement patterns in direct displacement-based design of continuous bridge structures." *Earthquake Spectra*, 22(3): 631-662.
- DYWIDAG-Systems International (2018). "DYWIDAG Post-Tensioning Systems Multistrand Systems Bar Systems Repair and Strengthening." <https://www.dsiamerica.com/fileadmin/downloads/dsi-america/dsi-usa-dywidag-bonded-post-tensioning-systems-us.pdf>. (Accessed in 2018).
- ElGawady, M. A., Dawood, H. M. (2012). "Analysis of Segmental Piers consisted of Concrete Filled FRP tubes." *Engineering Structures*, 38: 142-152.
- Eligehausen, R., Popov, E., Bertero, V. (1983). "Local Bond Stress-Slip Relationships of Deformed Bars under Generalized Excitations." UCB/EERC 83-23, University of California, Berkeley, CA
- European Committee for Standardisation (CEN) (1994). "Eurocode 8: Design Provisions for Earthquake Resistance of Structures." CEN, Brussels, Belgium.
- Fang, Q.-Z., Wang, T., Li, H.-M. (2006). "Large tensile deformation behavior of PC/ABS alloy." *Polymer*, 47(14): 5174-5181.
- Fauster, E., Schalk, P., O'Leary, P. L. "Evaluation and calibration methods for the application of a video-extensometer to tensile testing of polymer materials." *Proc., Machine Vision Applications in Industrial Inspection XIII*, International Society for Optics and Photonics, 187-198.
- Federal Emergency Management Agency (2009). "Quantification of Building Seismic Performance Factors." FEMA P695, Federal Emergency Management Agency (FEMA), Washington, D.C.
- Filiatrault, A., Tremblay, R., Christopoulos, C., Folz, B., Pettinga, D. (2013). *Elements of Earthquake Engineering and Structural Dynamics*, 3rd Edition, Presses Internationales Polytechnique, Montreal, Canada. ISBN 2553016492.

- Findley, W., Onaran, K. (1968). "Product form of kernel functions for nonlinear viscoelasticity of PVC under constant rate stressing." *Transactions of the Society of Rheology*, 12(2): 217-242.
- Finnsson, G. (2013). *Unbonded pre-tensioned bridge columns with hybrid fiber-reinforced concrete shells*, University of Washington. ISBN 1303110970.
- Fortunelli, A., Ortiz, M. (2007). "Constitutive model for plasticity in an amorphous polycarbonate." *Physical Review E*, 76(4): 041806.
- Green, A. E., Rivlin, R. S. (1957). "The mechanics of non-linear materials with memory." *Archive for Rational Mechanics and Analysis*, 1(1): 1-21.
- Guerrini, G., Restrepo, J. I., Massari, M., Vervelidis, A. (2014). "Seismic behavior of posttensioned self-centering precast concrete dual-shell steel columns." *Journal of Structural Engineering*, 141(4): 04014115.
- Haber, Z. B., Saiidi, M. S., Sanders, D. H. (2014). "Seismic performance of precast columns with mechanically spliced column-footing connections." *ACI Structural Journal*, 111(3): 639.
- Halary, J.-L., Lauprêtre, F., Monnerie, L. (2011). *Polymer materials: macroscopic properties and molecular interpretations*, Wiley, Hoboken, N.J. ISBN 047092201X;9780470922019;.
- Haraldsson, O. S., Pang, J. B. K., Stanton, J. F., Eberhard, M. O. (2009). "A Precast Concrete Bridge Bent for Seismic Regions." *Proceedings of the Special International Workshop on Seismic Connection Details for Segmental Bridge Construction - Technical Report MCEER-09-0012*, Seattle, Washington, July 22-24, Multidisciplinary Center for Earthquake Engineering Research, Buffalo, NY, U.S.A.
- Haraldsson, O. S., Janes, T. M., Eberhard, M. O., Stanton, J. F. (2013). "Seismic Resistance of Socket Connection between Footing and Precast Column." *Journal of Bridge Engineering*, 18(9): 910-919.
- Harris, H. G., Sabnis, G. M. (1999). *Structural modeling and experimental techniques*, CRC press. ISBN 1420049585.
- Hasan, O., Boyce, M. (1995). "A constitutive model for the nonlinear viscoelastic viscoplastic behavior of glassy polymers." *Polymer Engineering & Science*, 35(4): 331-344.

- Hasan, O. A. (1994). "An experimental and analytical investigation of the thermomechanical properties of glassy polymers." Ph.D. Dissertation, Massachusetts Institute of Technology.
<<https://dspace.mit.edu/handle/1721.1/12222>>.
- Haupt, P., Lion, A. (1995). "Experimental identification and mathematical modeling of viscoplastic material behavior." *Continuum Mechanics and Thermodynamics*, 7(1): 73-96.
- Haward, R., Thackray, G. "The use of a mathematical model to describe isothermal stress-strain curves in glassy thermoplastics." *Proc., Proceedings of the Royal Society of London A: Mathematical, Physical and Engineering Sciences*, The Royal Society, 453-472.
- Heinrich, G., Kaliske, M. (1997). "Theoretical and numerical formulation of a molecular based constitutive tube-model of rubber elasticity." *Computational and Theoretical Polymer Science*, 7(3-4): 227-241.
- Hewes, J. (2007). "Seismic tests on precast segmental concrete columns with unbonded tendons." *Bridge Structures*, 3(3-4): 215-227.
- Hewes, J. T., Priestley, M. N. (2002). "Seismic design and performance of precast concrete segmental bridge columns." Report No. SSRP-2001/25, Department of Structural Engineering, University of California, San Diego, La Jolla, California 92093-0085
- Ho, K., Krempl, E. (2002). "Extension of the viscoplasticity theory based on overstress (VBO) to capture non-standard rate dependence in solids." *International Journal of Plasticity*, 18(7): 851-872.
- Ichikawa, S., Matsuzaki, H., Moustafa, A., ElGawady, M. A., Kawashima, K. (2016). "Seismic-Resistant Bridge Columns with Ultrahigh-Performance Concrete Segments." *Journal of Bridge Engineering*, 21(9): 04016049.
- Japan Road Association (2006). "Specifications for Highway Bridges." Japan Road Association, Japan.
- Jerabek, M., Major, Z., Lang, R. W. (2010). "Strain determination of polymeric materials using digital image correlation." *Polymer Testing*, 29(3): 407-416.
- Johnson, M. A., Beatty, M. F. (1995). "The Mullins effect in equibiaxial extension and its influence on the inflation of a balloon." *International Journal of Engineering Science*, 33(2): 223-245.

- Karthik, M. M., Mander, J. B. (2010). "Stress-block parameters for unconfined and confined concrete based on a unified stress-strain model." *Journal of Structural Engineering*, 137(2): 270-273.
- Kästner, M., Obst, M., Brummund, J., Thielsch, K., Ulbricht, V. (2012). "Inelastic material behavior of polymers—Experimental characterization, formulation and implementation of a material model." *Mechanics of Materials*, 52: 40-57.
- Kaviani, P., Zareian, F., Taciroglu, E. (2014). "Performance-Based Seismic Assessment of Skewed Bridges." *PEER 2014/01*
- Kelly, J. M. (1993). *Earthquake-resistant design with rubber*, First Edition, Springer-Verlag, London
- Khan, A. S., Lopez-Pamies, O. (2002). "Time and temperature dependent response and relaxation of a soft polymer." *International Journal of Plasticity*, 18(10): 1359-1372.
- Kontou, E., Spathis, G. (2014). "Viscoplastic response and creep failure time prediction of polymers based on the transient network model." *Mechanics of Time-Dependent Materials*, 18(2): 373-386.
- Kontou, E. (2016). "Lower and higher strain regime modeling of cyclic viscoplastic response of an amorphous glassy polymer." *International Journal of Solids and Structures*, 97: 489-495.
- Kowalsky, M. J., Priestley, M. N., Macrae, G. A. (1995). "Displacement-based design of RC bridge columns in seismic regions." *Earthquake Engineering & Structural Dynamics*, 24(12): 1623-1643.
- Kowalsky, M. J. (2002). "A displacement-based approach for the seismic design of continuous concrete bridges." *Earthquake Engineering & Structural Dynamics*, 31(3): 719-747.
- Krempf, E. (1996). "A small strain viscoplasticity theory based on overstress." *Unified Constitutive Laws of Plastic Deformation*, A. S. Krausz, and K. Krausz, eds., Academic Press, San Diego, CA, 281-318.
- Krempf, E., Ho, K. (2000). "An overstress model for solid polymer deformation behavior applied to Nylon 66." *Time Dependent and Nonlinear Effects in Polymers and Composites*, R. Schapery, and C. Sun, eds., ASTM International, West Conshohocken, PA, 118-137.

- Lee, J., Fenves, G. L. (1998a). "Plastic-Damage Model for Cyclic Loading of Concrete Structures." *Journal of Engineering Mechanics*, 124(8): 892-900.
<[http://dx.doi.org/10.1061/\(ASCE\)0733-9399\(1998\)124:8\(892\)](http://dx.doi.org/10.1061/(ASCE)0733-9399(1998)124:8(892))>.
- Lee, J., Fenves, G. L. (1998b). "A plastic-damage concrete model for earthquake analysis of dams." *Earthquake Engineering & Structural Dynamics*, 27(9): 937-956.
- Lee, W. K., Billington, S. L. (2009). "Modeling residual displacements of concrete bridge columns under earthquake loads using fiber elements." *Journal of Bridge Engineering*, 15(3): 240-249.
- Lehman, D. E., Roeder, C. W. (2012). "Foundation connections for circular concrete-filled tubes." *Journal of Constructional Steel Research*, 78: 212-225.
- Li, J., Mayau, D., Lagarrigue, V. (2008). "A constitutive model dealing with damage due to cavity growth and the Mullins effect in rubber-like materials under triaxial loading." *Journal of the Mechanics and Physics of Solids*, 56(3): 953-973.
- Lion, A. (1996). "A constitutive model for carbon black filled rubber: experimental investigations and mathematical representation." *Continuum Mechanics and Thermodynamics*, 8(3): 153-169.
- Lubliner, J., Oliver, J., Oller, S., Oñate, E. (1989). "A plastic-damage model for concrete." *International Journal of Solids and Structures*, 25(3): 299-326, DOI: 10.1016/0020-7683(89)90050-4.
<<http://www.sciencedirect.com/science/article/pii/0020768389900504>>.
- Luco, N., Cornell, C. A. (2000). "Effects of connection fractures on SMRF seismic drift demands." *Journal of Structural Engineering*, 126(1): 127-136.
- Mackie, K. R., Stojadinović, B. (2005). "Fragility basis for California highway overpass bridge seismic decision making." PEER Report 2005/02, Pacific Earthquake Engineering Research Center, College of Engineering, University of California, Berkeley, CA
- Mander, J. B., Priestley, M. J., Park, R. (1988). "Theoretical stress-strain model for confined concrete." *Journal of Structural Engineering*, 114(8): 1804-1826.
- Mander, J. B., Cheng, C.-T. (1997). "Seismic design of bridge piers based on damage avoidance design (NCEER-97-0014)." National Center for Earthquake Engineering Research, Buffalo, NY,

- Marriott, D. (2009). "The Development of High-Performance Post-Tensioned Rocking Systems for the Seismic Design of Structures." Ph.D. Dissertation, University of Canterbury, Christchurch, NZ.
- Marriott, D., Pampanin, S., Palermo, A. (2009). "Quasi-static and pseudo-dynamic testing of unbonded post-tensioned rocking bridge piers with external replaceable dissipaters." *Earthquake Engineering & Structural Dynamics*, 38(3): 331-354.
- Mars, W., Fatemi, A. (2004). "Observations of the constitutive response and characterization of filled natural rubber under monotonic and cyclic multiaxial stress states." *Journal of Engineering Materials and Technology*, 126(1): 19-28.
- MATLAB (2016). "MATLAB", Version, The MathWorks, Inc., Natick, Massachusetts, United States.
- Matsumoto, E. E., Waggoner, M. C., Kreger, M. E., Vogel, J., Wolf, L. (2008). "Development of a Precast Concrete Bent-Cap System." *PCI Journal*, 53(3): 74-99.
- Mazzolani, F., Piluso, V. (1997). "A simple approach for evaluating performance levels of moment-resisting steel frames." *Seismic Design Methodologies for the Next Generation of Codes*. Rotterdam: AA Balkema: 241-252.
- McGuirt, C. W., Lianis, G. (1970). "Constitutive equations for viscoelastic solids under finite uniaxial and biaxial deformations." *Transactions of the Society of Rheology*, 14(2): 117-134.
- McKenna, F., Fenves, G. L. (2001). "The OpenSees command language manual." University of California, Berkeley, CA
- Medhekar, M., Kennedy, D. (2000). "Displacement-based seismic design of buildings—application." *Engineering Structures*, 22(3): 210-221.
- Mehrsoroush, A. (2014). *Experimental and analytical seismic studies of bridge piers with innovative pipe pin column-footing connections and precast cap beams*, University of Nevada, Reno. ISBN 1321498543.
- Menegotto, M., Pinto, P. "Method of analysis for cyclically loaded reinforced concrete frames including changes in geometry and non-elastic behavior of elements under combined normal forces and bending moment." *Proc., Symposium on the Resistance and Ultimate Deformability of Structures Acted on by Well Defined Repeated Loads*, International Association for Bridge and Structural Engineering, 15-22.

- Moehle, J. (1992). "Displacement-based design of RC structures subjected to earthquakes." *Earthquake Spectra*, 8(3): 403-428.
- Mokha, A., Constantinou, M., Reinhorn, A. (1990). "Teflon bearings in base isolation I: Testing." *Journal of Structural Engineering*, 116(2): 438-454.
- Morgen, B., Kurama, Y. (2004). "A friction damper for post-tensioned precast concrete beam-to-column joints." *PCI J*, 49(4): 112-133.
- Motaref, S., Saiidi, M. S., Sanders, D. (2013). "Shake table studies of energy-dissipating segmental bridge columns." *Journal of Bridge Engineering*, 19(2): 186-199.
- Moustafa, A., ElGawady, M. A. (2017). "Seismic Behavior of a Damage-Resistant Segmental Bridge Column with External Energy Dissipaters." *Transportation Research Board 96th Annual Meeting*, Washington DC, United States, Transportation Research Board
- Moustafa, A., Gheni, A., ElGawady, M. A. (2017). "Shaking-Table Testing of High Energy-Dissipating Rubberized Concrete Columns." *Journal of Bridge Engineering*, 22(8): 04017042.
- Müller, S., Kästner, M., Brummund, J., Ulbricht, V. (2011). "A nonlinear fractional viscoelastic material model for polymers." *Computational Materials Science*, 50(10): 2938-2949.
- Mullins, L. (1948). "Effect of stretching on the properties of rubber." *Rubber Chemistry and Technology*, 21(2): 281-300.
- Nakashoji, B. A. (2014). "Seismic performance of square nickel-titanium reinforced ECC columns with headed couplers." M.Sc. Thesis, Civil and Environmental Engineering, University of Nevada, Reno. <<http://hdl.handle.net/11714/2943>>.
- Németh, I., Schleinzer, G., Ogden, R. W., Holzapfel, G. A. "On the modelling of amplitude and frequency-dependent properties in rubberlike solids." *Proc., Constitutive Models for Rubber-Proceedings-*, Balkema, 285.
- Nikoukalam, M., Sideris, P. (2016a). "Experimental Performance Assessment of Nearly Full-Scale Reinforced Concrete Columns with Partially Debonded Longitudinal Reinforcement." *Journal of Structural Engineering*: 04016218.
- Nikoukalam, M., Sideris, P. (2017). "Resilient Bridge Rocking Columns with Polyurethane Damage-Resistant End Segments and Replaceable Energy-Dissipating Links." *Journal of Bridge Engineering*, 22(10): 04017064.

- Nikoukalam, M. T., Sideris, P. (2016b). "Low-Damage Posttensioned Segmental Bridge Columns with Flexible End Joints for Seismic Accelerated Bridge Construction." *Transportation Research Record*, 2592(1): 151-161.
- Ogden, R. W. (2013). *Non-Linear Elastic Deformations*, Dover Publications. ISBN 9780486318714.
- Ou, Y.-C., Chiewanichakorn, M., Aref, A. J., Lee, G. C. (2007). "Seismic Performance of Segmental Precast Unbonded Posttensioned Concrete Bridge Columns." *Journal of Structural Engineering*, 133(11): 1636-1647.
- Ou, Y.-C., Wang, P.-H., Tsai, M.-S., Chang, K.-C., Lee, G. C. (2009). "Large-scale experimental study of precast segmental unbonded posttensioned concrete bridge columns for seismic regions." *Journal of Structural Engineering*, 136(3): 255-264.
- Ou, Y.-C., Oktavianus, Y., Tsai, M.-S. (2013). "An emulative precast segmental concrete bridge column for seismic regions." *Earthquake Spectra*, 29(4): 1441-1457.
- Ou, Y. C., Tsai, M. S., Chang, K. C., Lee, G. C. (2010). "Cyclic behavior of precast segmental concrete bridge columns with high performance or conventional steel reinforcing bars as energy dissipation bars." *Earthquake Engineering & Structural Dynamics*, 39(11): 1181-1198.
- Pan, B., Xie, H., Wang, Z., Qian, K., Wang, Z. (2008). "Study on subset size selection in digital image correlation for speckle patterns." *Optics Express*, 16(10): 7037-7048.
- Pang, J. B., Eberhard, M. O., Stanton, J. F. (2010). "Large-Bar Connection for Precast Bridge Bents in Seismic Regions." *Journal of Bridge Engineering*, 15(3): 231-239.
- Pantelides, C. P., Ameli, M. J., Parks, J. E., Brown, D. N. (2014). "Seismic Evaluation of Grouted Splice Sleeve Connections for Precast RC Bridge Piers in ABC." UT-14.09, Department of Civil and Environmental Engineering, University of Utah, Salt Lake City, Utah
- Parsons, E., Boyce, M., Parks, D. (2004). "An experimental investigation of the large-strain tensile behavior of neat and rubber-toughened polycarbonate." *Polymer*, 45(8): 2665-2684.

- Parsons, E., Boyce, M., Parks, D., Weinberg, M. (2005). "Three-dimensional large-strain tensile deformation of neat and calcium carbonate-filled high-density polyethylene." *Polymer*, 46(7): 2257-2265.
- Paulay, T., Priestley, M. (1992). "Seismic design of concrete and masonry structures." *John Wiley and Sons. New York.*
- Perzyna, P. (1966). "Fundamental problems in viscoplasticity." *Advances in Applied Mechanics*, Elsevier, 243-377.
- Pinho, R., Casarotti, C., Antoniou, S. (2007). "A comparison of single-run pushover analysis techniques for seismic assessment of bridges." *Earthquake Engineering & Structural Dynamics*, 36(10): 1347-1362.
- Priestley, M. (1996). "Displacement-based seismic assessment of existing reinforced concrete buildings." *Bull NZ Soc Earthq Eng*, 29(4): 256-272.
- Qi, H., Boyce, M. (2004). "Constitutive model for stretch-induced softening of the stress–stretch behavior of elastomeric materials." *Journal of the Mechanics and Physics of Solids*, 52(10): 2187-2205.
- Qi, H., Boyce, M. (2005). "Stress–strain behavior of thermoplastic polyurethanes." *Mechanics of Materials*, 37(8): 817-839.
- Reese, S., Govindjee, S. (1998). "A theory of finite viscoelasticity and numerical aspects." *International Journal of Solids and Structures*, 35(26-27): 3455-3482.
- Restrepo, J. I., Tobolski, M. J., Matsumoto, E. E. (2011). "NCHRP Report 681: Development of a Precast Bent Cap System for Seismic Regions." NCHRP 12-74, National Cooperative Highway Research Program (NCHRP), Transportation Research Board of National Academies,
- Roeder, C. W., Stanton, J. F. (1983). "Elastomeric bearings: State-of-the-art." *Journal of Structural Engineering*, 109(12): 2853-2871.
- Roh, H., Reinhorn, A. M. (2010). "Hysteretic Behavior of Precast Segmental Bridge Piers with Superelastic Shape Memory Alloy Bars." *Engineering Structures*, 32(10): 3394-3403, DOI: <http://dx.doi.org/10.1016/j.engstruct.2010.07.013>.
<<http://www.sciencedirect.com/science/article/pii/S0141029610002695>>.
- Rubin, M. (1994). "Plasticity theory formulated in terms of physically based microstructural variables—Part I. Theory." *International Journal of Solids and Structures*, 31(19): 2615-2634.

- Salehi, M., Sideris, P., Liel, A. B. (2017). "Numerical Simulation of Hybrid Sliding-Rocking Columns Subjected to Earthquake Excitation." *Journal of Structural Engineering*, 143(11): 04017149.
- Salehi, M., Sideris, P. (2017). "Refined Gradient Inelastic Flexibility-Based Formulation for Members Subjected to Arbitrary Loading." *Journal of Engineering Mechanics (Accepted)*.
- Schreier, H., Orteu, J.-J., Sutton, M. A. (2009). *Image correlation for shape, motion and deformation measurements: Basic concepts, theory and applications*, Springer US, Boston, MA. ISBN 978-0-387-78747-3.
- Scott, B., Park, R., Priestley, M. "Stress-strain behavior of concrete confined by overlapping hoops at low and high strain rates." *Proc., ACI Journal Proceedings*, ACI.
- Sideris, P. (2012). "Seismic Analysis and Design of Precast Concrete Segmental Bridges." Ph.D. Dissertation, Department of Civil, Structural and Environmental Engineering, State University of New York at Buffalo, Buffalo, NY, U.S.A. <<https://search-proquest-com.gate.lib.buffalo.edu/docview/1114474220?accountid=14169>>.
- Sideris, P., Aref, A. J., Filiatrault, A. (2014a). "Effects of anchorage hardware on the cyclic tensile response of unbonded monostrands." *PCI J*, 59(3): 60-77.
- Sideris, P., Aref, A. J., Filiatrault, A. (2014b). "Large-scale Seismic Testing of a Hybrid Sliding-Rocking Post-Tensioned Segmental Bridge System." *Journal of Structural Engineering*, 140(6): 04014025, DOI: 10.1061/(ASCE)ST.1943-541X.0000961.
- Sideris, P., Aref, A. J., Filiatrault, A. (2015). "Experimental Seismic Performance of a Hybrid Sliding-Rocking Bridge for Various Specimen Configurations and Seismic Loading Conditions." *Journal of Bridge Engineering*, 20(11): 04015009, DOI: [http://dx.doi.org/10.1061/\(ASCE\)BE.1943-5592.0000742#sthash.c4Q1JXLu.dpuf](http://dx.doi.org/10.1061/(ASCE)BE.1943-5592.0000742#sthash.c4Q1JXLu.dpuf).
- Sideris, P., Salehi, M. (2016). "A Gradient-Inelastic Flexibility-based Frame Element Formulation." *Journal of Engineering Mechanics*, 142(7): 04016039, DOI: 10.1061/(ASCE)EM.1943-7889.0001083.
- SIMULIA (2013). "Abaqus analysis user's manual, Version 6.13." SIMULIA, The Dassault Systèmes, Realistic Simulation, USA.

- Smart, J., Williams, J. (1972). "A comparison of single-integral non-linear viscoelasticity theories." *Journal of the Mechanics and Physics of Solids*, 20(5): 313-324.
- Standards New Zealand (2006). "Concrete Structures Standard: Part 1-The Design of Concrete Structures (NZS 3101-1)." Standards New Zealand, New Zealand, Wellington.
- Steuck, K. P., Eberhard, M. O., Stanton, J. F. (2009). "Anchorage of large-diameter reinforcing bars in ducts." *ACI Structural Journal*, 106(4): 506.
- Structural Technologies (2016). <<https://www.vsl.net/>>. (Accessed in April, 2017).
- Tanaka, F., Edwards, S. (1992). "Viscoelastic properties of physically crosslinked networks. 1. Transient network theory." *Macromolecules*, 25(5): 1516-1523.
- Tazarv, M., Saiid Saiidi, M. (2015). "Low-damage precast columns for accelerated bridge construction in high seismic zones." *Journal of Bridge Engineering*, 21(3): 04015056.
- Tazarv, M., Saiidi, M. S. (2015). "UHPC-filled duct connections for accelerated bridge construction of RC columns in high seismic zones." *Engineering Structures*, 99: 413-422.
- Tazarv, M., Saiidi, M. S. (2016). "Seismic design of bridge columns incorporating mechanical bar splices in plastic hinge regions." *Engineering Structures*, 124: 507-520.
- Thonstad, T., Mantawy, I. M., Stanton, J. F., Eberhard, M. O., Sanders, D. H. (2016). "Shaking table performance of a new bridge system with pretensioned rocking columns." *Journal of Bridge Engineering*, 21(4): 04015079.
- Trono, W., Jen, G., Panagiotou, M., Schoettler, M., Ostertag, C. P. (2014). "Seismic response of a damage-resistant recentering posttensioned-HYFRC bridge column." *Journal of Bridge Engineering*, 20(7): 04014096.
- Tschoegl, N. W. (2012). *The phenomenological theory of linear viscoelastic behavior: an introduction*, Springer Science & Business Media. ISBN 3642736025.
- U.S. Seismic Design Maps (2018). "U.S. Seismic Design Maps." United States Geological Survey (USGS), <<https://earthquake.usgs.gov/hazards/designmaps/usdesign.php>>. (Accessed in 2018).

- Vamvatsikos, D., Cornell, C. A. (2002). "Incremental dynamic analysis." *Earthquake Engineering & Structural Dynamics*, 31(3): 491-514.
- Varela, S., Saiidi, M. (2014). "Dynamic performance of novel bridge columns with superelastic CuAlMn shape memory alloy and ECC." *Int. J. Bridge Eng*, 2(3): 29-58.
- Varela, S., Saiidi, M. S. (2017). "Experimental Study on Seismically Resilient 2-Span Bridge Models Designed for Disassembly." *Journal of Earthquake Engineering*, (just-accepted).
- Wang, J. C., Ou, Y. C., Chang, K. C., Lee, G. C. (2008). "Large-scale seismic tests of tall concrete bridge columns with precast segmental construction." *Earthquake Engineering & Structural Dynamics*, 37(12): 1449-1465.
- Ward, I. M., Sweeney, J. (2004). *An introduction to the mechanical properties of solid polymers*, Wiley, Hoboken, NJ. ISBN 0471496251;9780471496250;9780471496267;047149626X;.
- White, S., Palermo, A. (2016). "Quasi-static testing of posttensioned nonemulative column-footing connections for bridge piers." *Journal of Bridge Engineering*, 21(6): 04016025.
- Yamashita, R., Sanders, D. H. (2009). "Seismic Performance of Precast Unbonded Prestressed Concrete Columns." *ACI Structural Journal*, 106(6): 821-830.
- Zhao, J., Sritharan, S. (2007). "Modeling of strain penetration effects in fiber-based analysis of reinforced concrete structures." *ACI structural journal*, 104(2): 133.

APPENDIX A

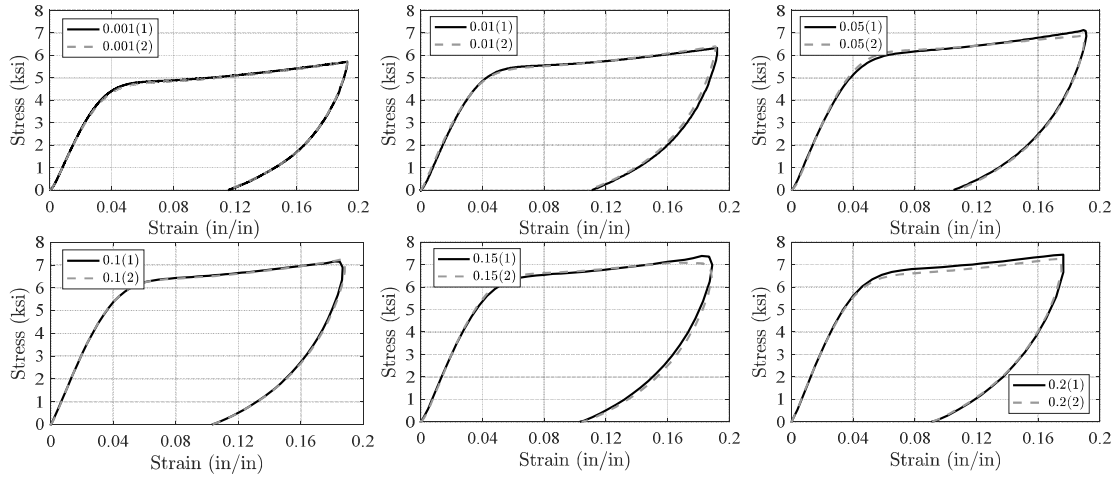


Figure A.1. Reproducibility of ECore response: Monotonic compression test at various strain rates.

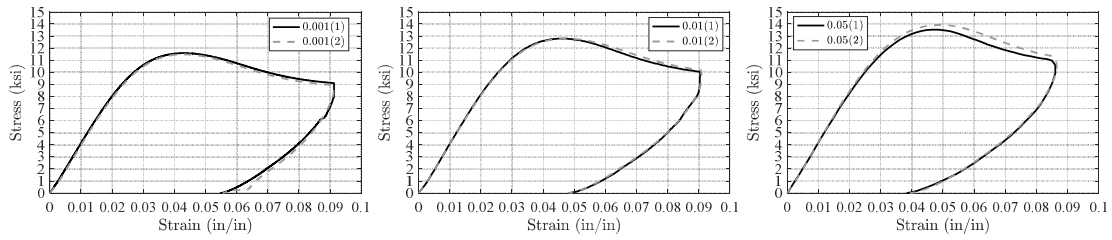


Figure A.2. Reproducibility of ECast response: Monotonic compression test at various strain rates.

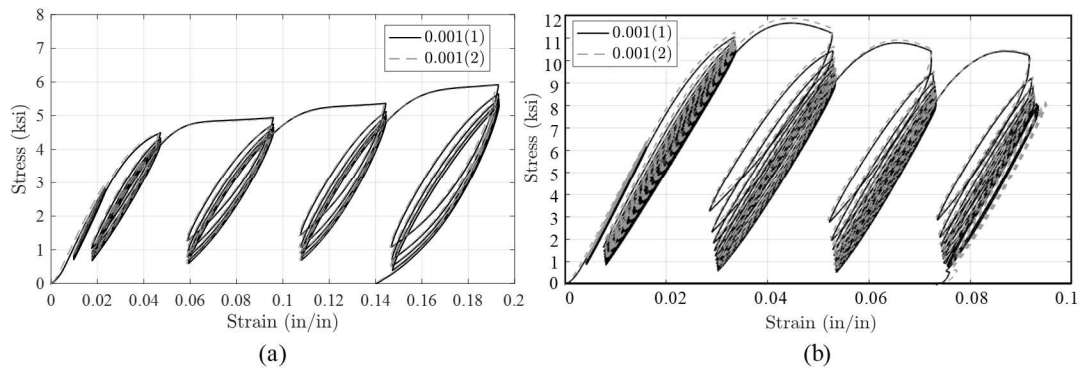


Figure A.3. Reproducibility of cyclic compression-only response at 0.001 /s strain rate: (a) ECore, (b) ECast.

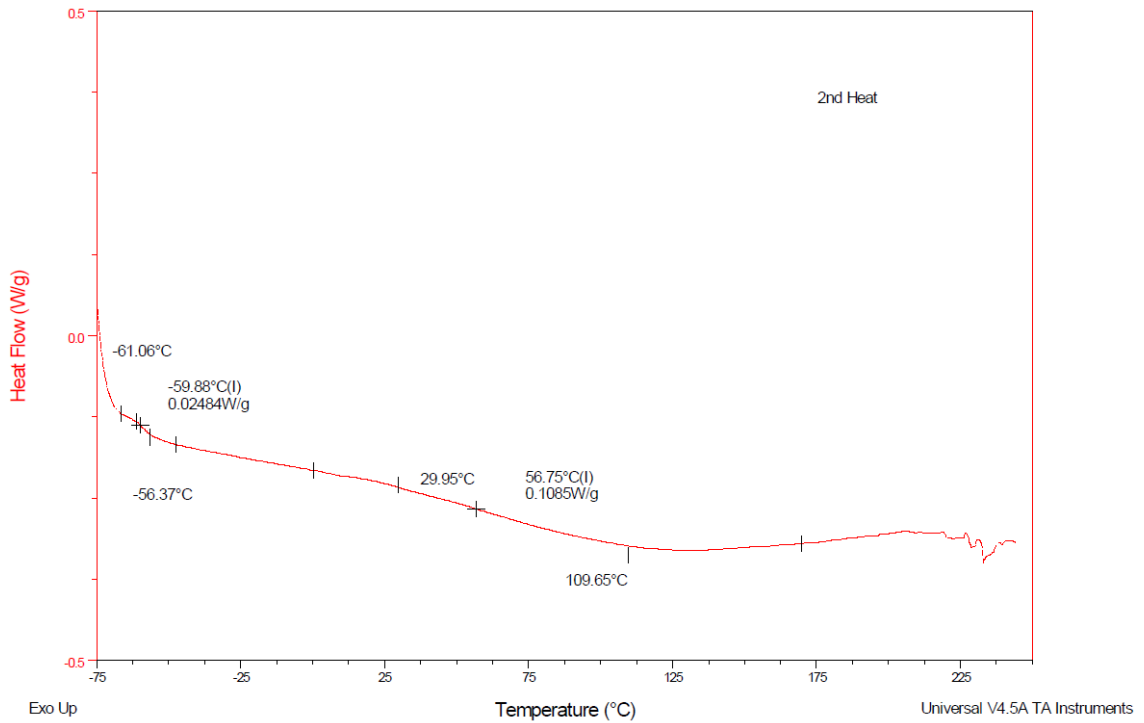


Figure A.4. Heat flow versus temperature for ECore.

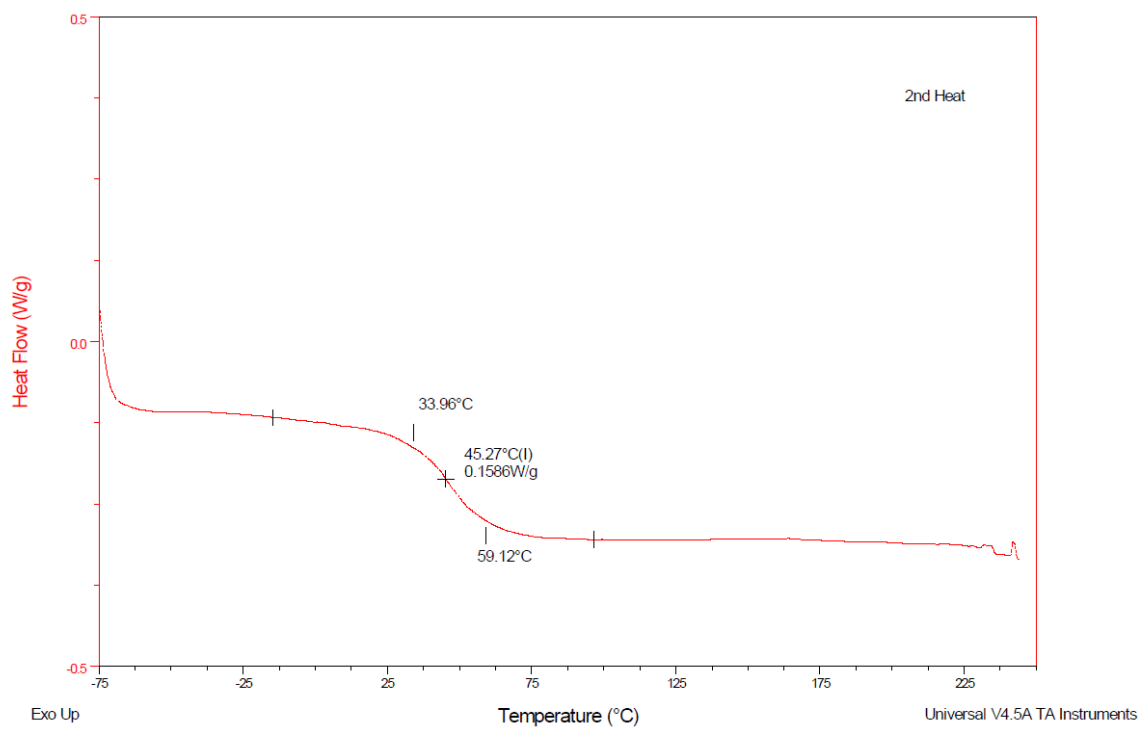


Figure A.5. Heat flow versus temperature for ECast.

APPENDIX B

CAD Drawings of Specimens

GENERAL STRUCTURAL NOTES

CONCRETE

- Concrete 28 days nominal strength should be as:
f_c= 8000 psi (for all uses unless otherwise noted)
- Clear concrete cover shall be 1" or $\frac{1}{2}$ " as noted.
- The required product dimension tolerance is $\frac{1}{8}$ ".

REINFORCING STEEL

- Reinforcing steel shall conform to ASTM 615 Gr. 60.
- All bars are deformed, unless otherwise noted.
- All dimensions are provided in inches, unless otherwise specified
- A minimum length of 7 ft of reinforcement for all diameters listed in the tables shall be added to the total amount. This will be used for testing the bars in the lab to verify the strength.
- The required product dimension tolerance is $\frac{1}{4}$ ".

ED LINKS ASSEMBLY

- The steel material for ED link assembly parts shall be as follows:

<u>Part ID</u>	<u>Grade</u>
GROOVED ROD	ASTM A36
COVER TUBE	ASTM A515 Grade 5
1 1/2 COUPLING NUT	ASTM A563 Grade A
ANCHOR ROD	ASTM A449 Type 1
ANCHOR WASHER	ASTM A572 Grade 50
1 1/2 A563 NUT	ASTM A563 Grade A
1 1/2 F436 WASHER	ASTM F436 Type 1

- The required product dimension tolerance is $\frac{1}{8}$ ".

STEEL COLLAR ASSEMBLY

- The steel material for steel collar assembly parts shall be as follows:

<u>Part ID</u>	<u>Grade</u>
Collar (steel tube)	ASTM A572 Grade 50
Mounting eye plates (Plate 1 and 2)	ASTM A572 Grade 50
Welding electrode	E70XX or E80XX
Headed stud	f _{y,min} = 51000 psi, Elongation (% in 2") > 20%

- The required product dimension tolerance is $\frac{1}{8}$ ".

LOAD CELLS

- The steel material for the load cell parts shall be as follows:

<u>Part ID</u>	<u>Grade</u>
Load cell body (steel tube)	ASTM A572 Grade 50
End plates	ASTM A572 Grade 50

- The required product dimension tolerance is $\frac{1}{8}$ ".

POST-TENSIONING STRANDS

- The post tensioning strands shall be Grade 270 seven-wire low relaxation strands compliant with ASTM A416 with nominal diameter of 0.6", minimum yield strength f_y=243 ksi, and tensile strength f_u= 270 ksi.

Abbreviations

BL: Bi-Layered
 ED Link: Energy Dissipation Link
 ID: Inside Diameter
 NTS: Not To Scale
 OD: Outside Diameter
 PT: Post-tensioning
 PU: Polyurethane
 RC: Reinforced Concrete
 RC-SC: Reinforced Concrete with Steel Collar
 TH.: Thickness



PROJECT: Rocking Column With PU Segment & ED Links Testing	
SHEET TITLE: General Notes and Abbreviations	DRAWN BY: Mohammad T. Nikoukalam
SCALE: NTS	APPROVED BY: Dr.P.Sideris
DATE: 05/05/2018	SHEET NO.: S-0

Figure B.1. General notes and abbreviations.

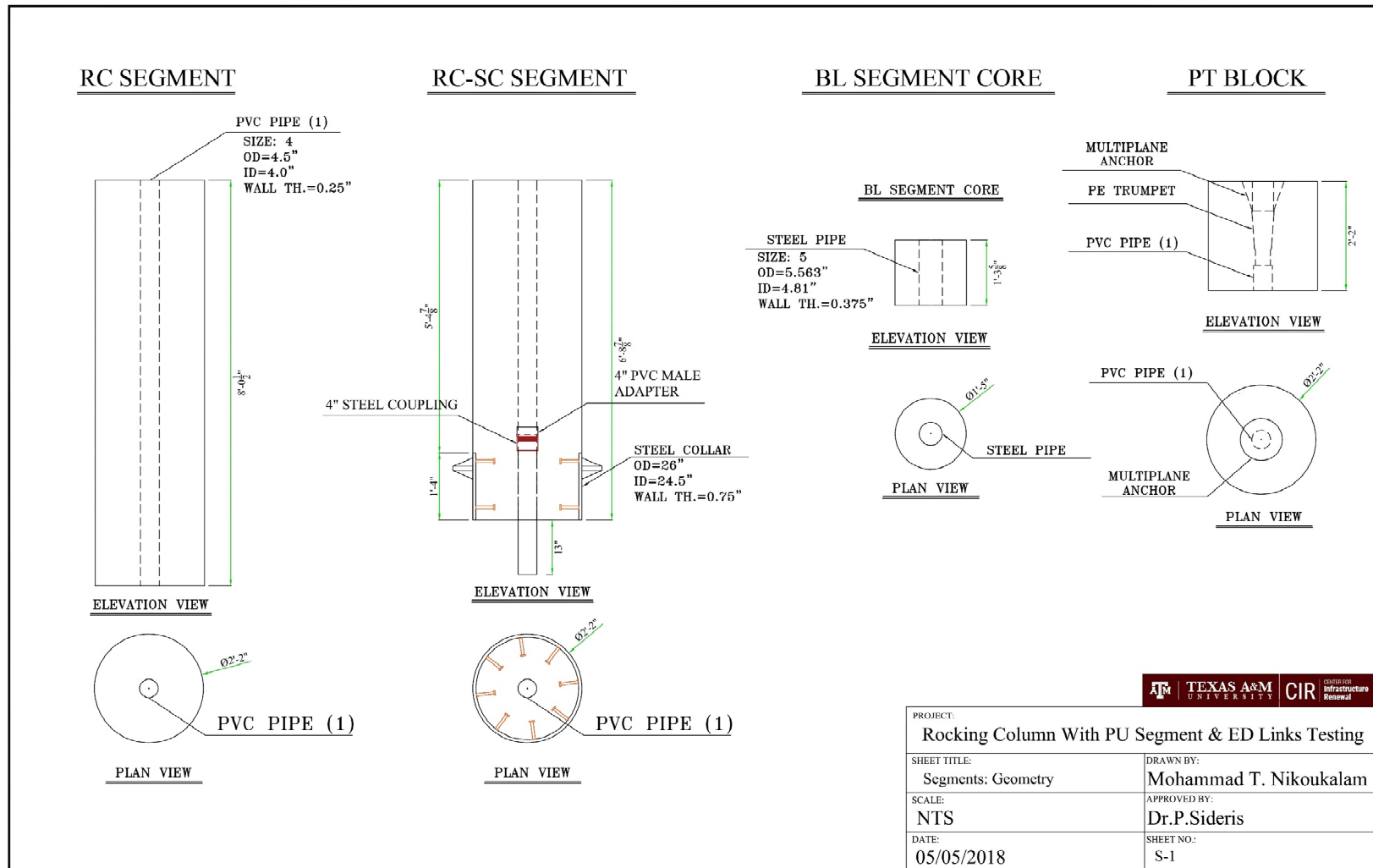


Figure B.2. Geometry details: RC segments.

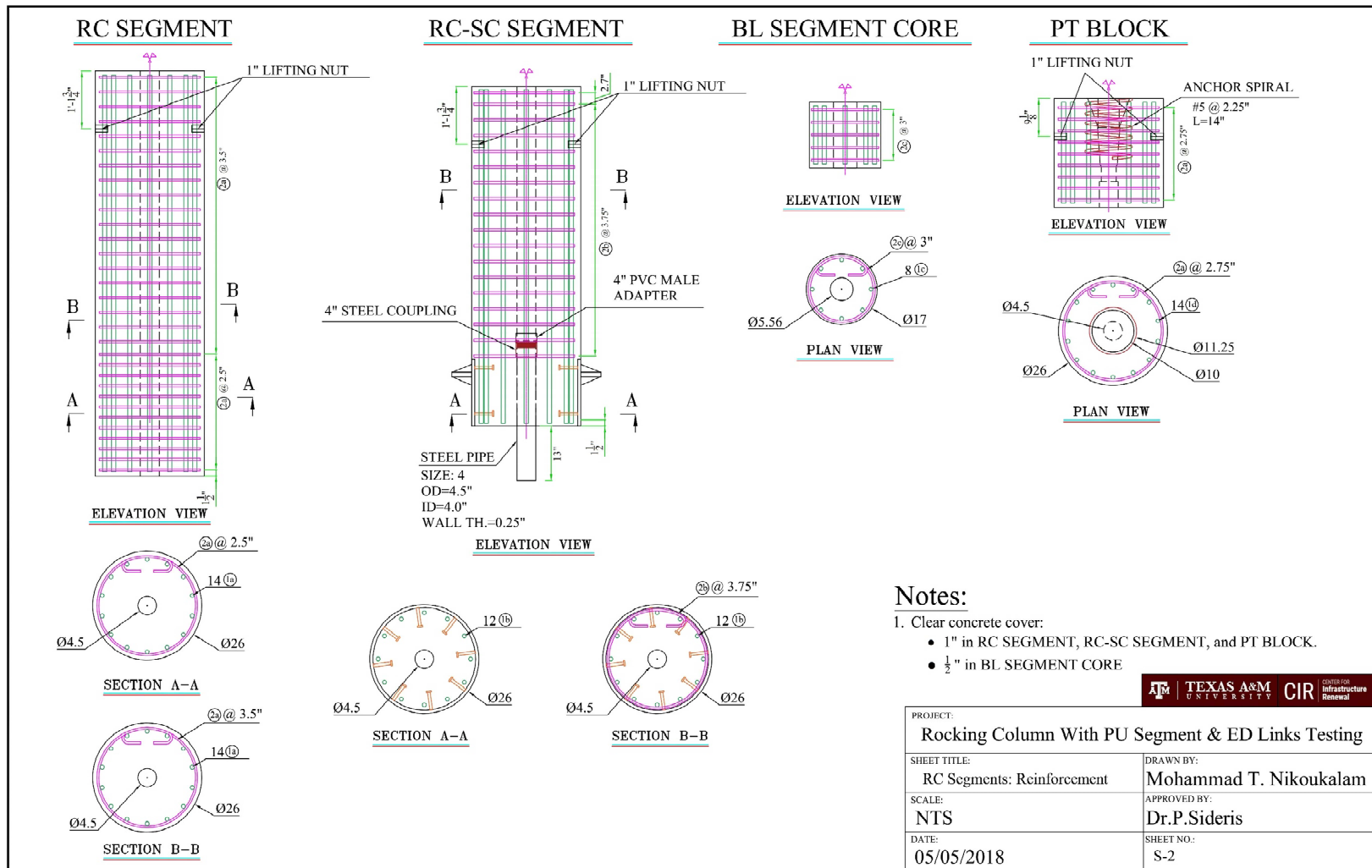


Figure B.3. Reinforcement layout: RC segments.

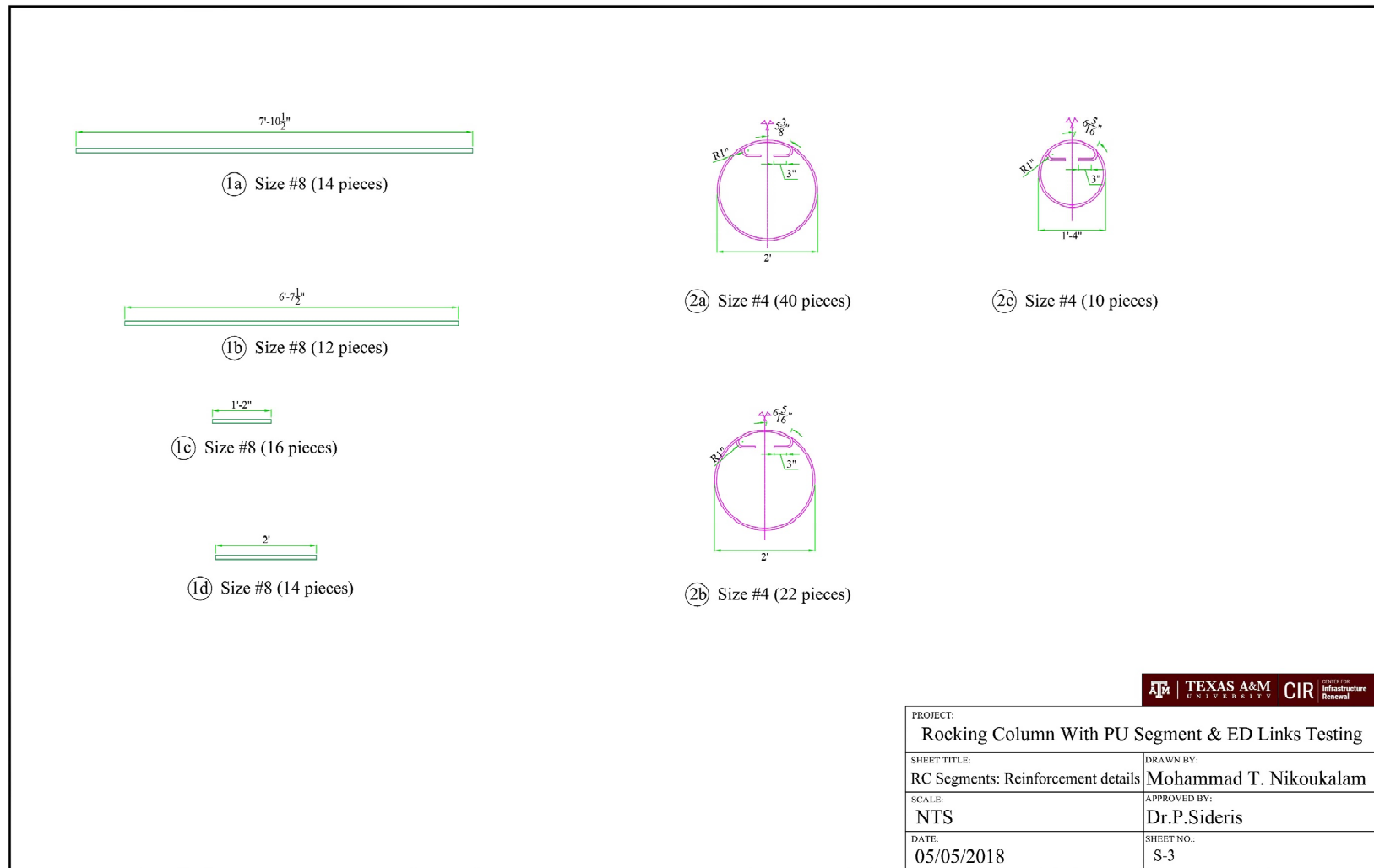


Figure B.4. Details of reinforcement: RC segments.

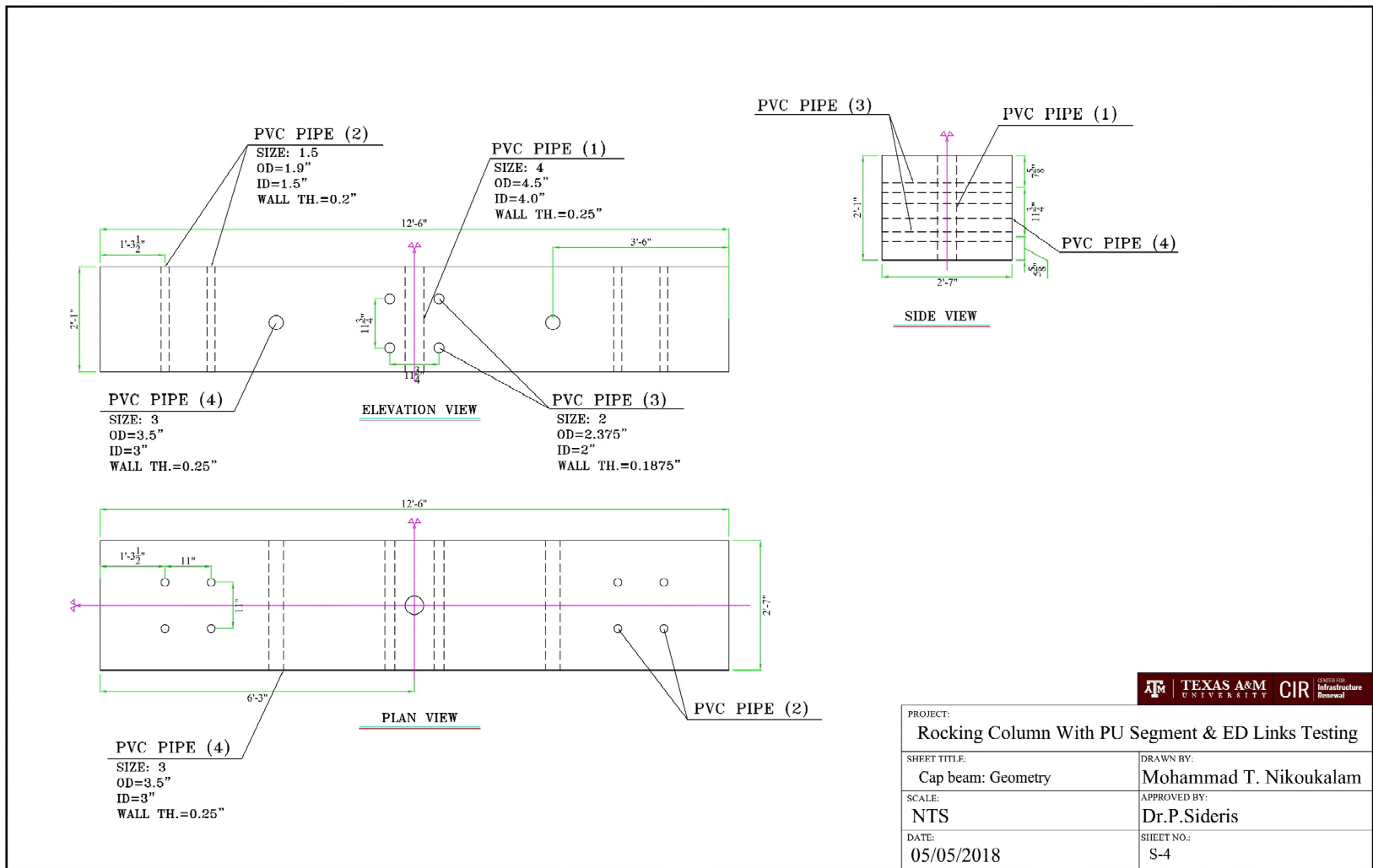


Figure B.5. Geometry details: cap beam.

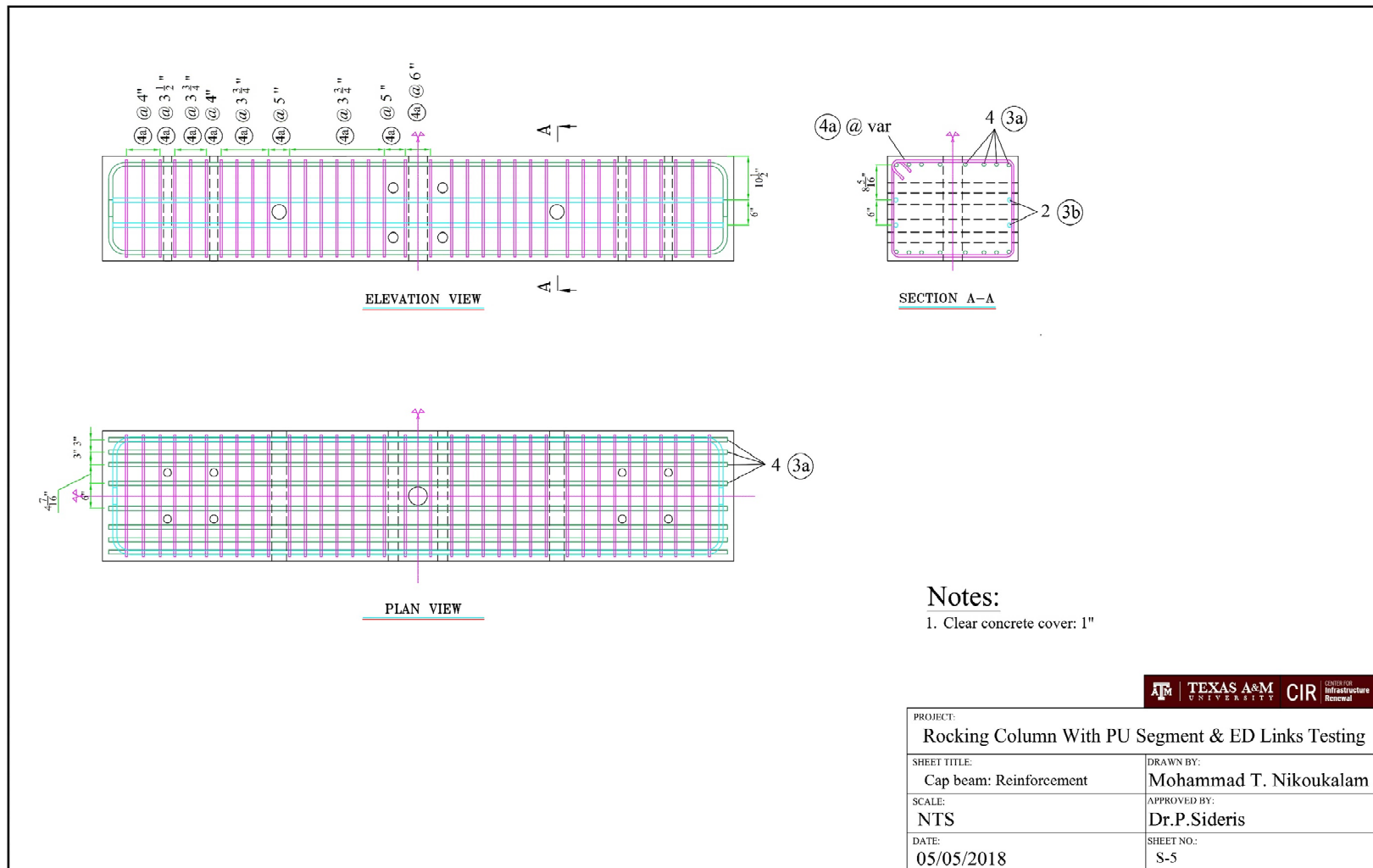


Figure B.6. Reinforcement layout: cap beam.

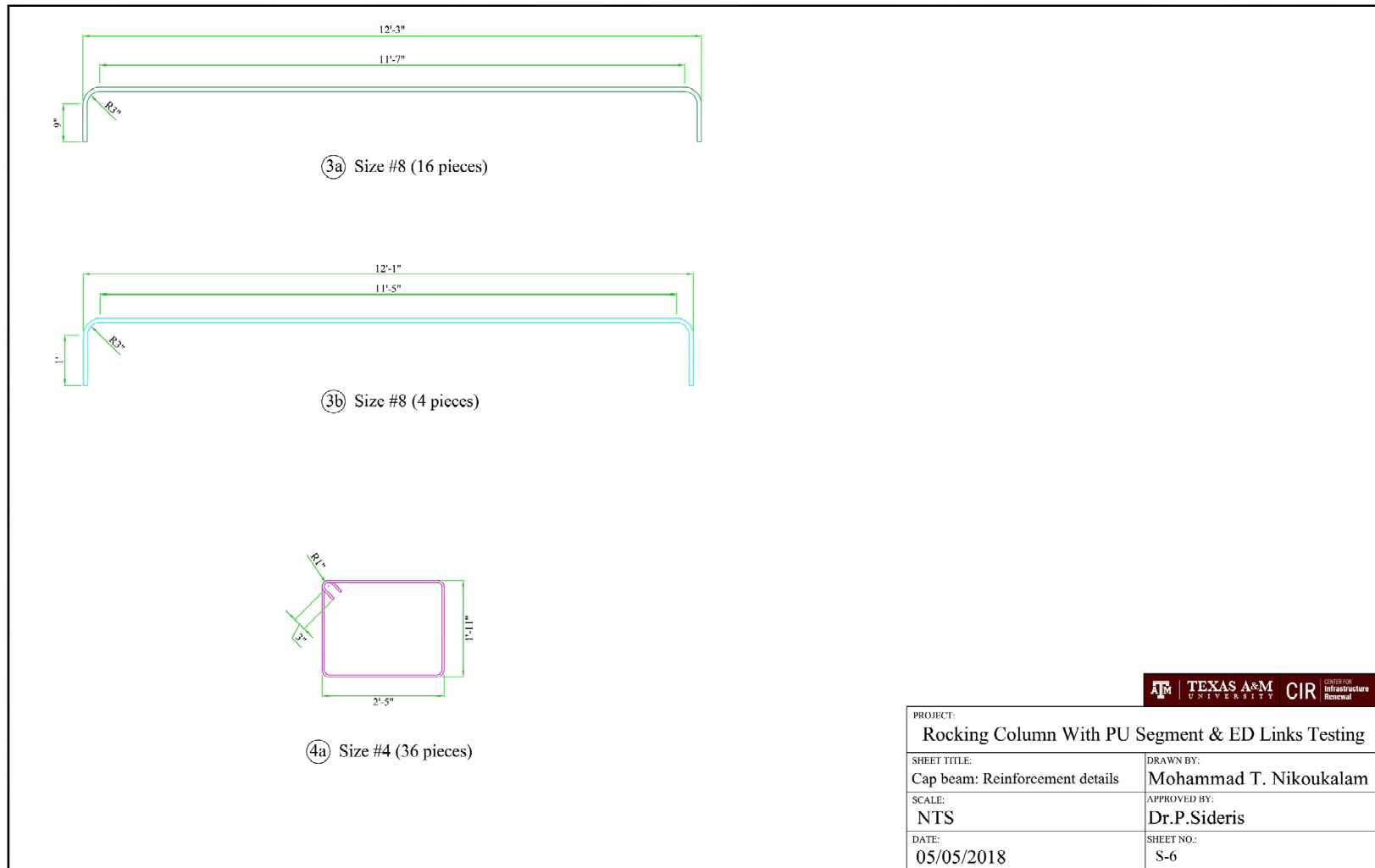


Figure B.7. Details of reinforcement: cap beam.

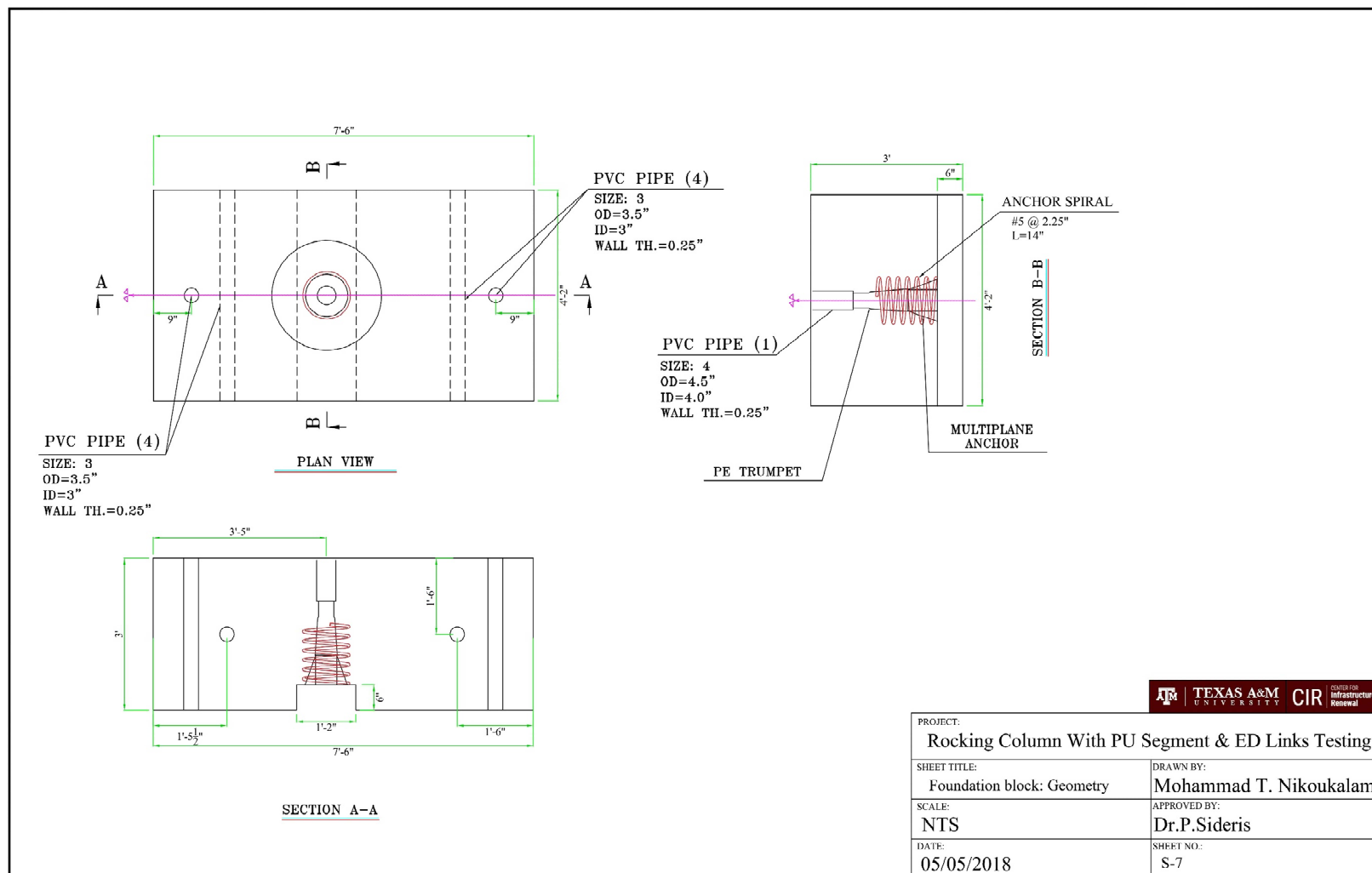


Figure B.8. Geometry details: foundation block.

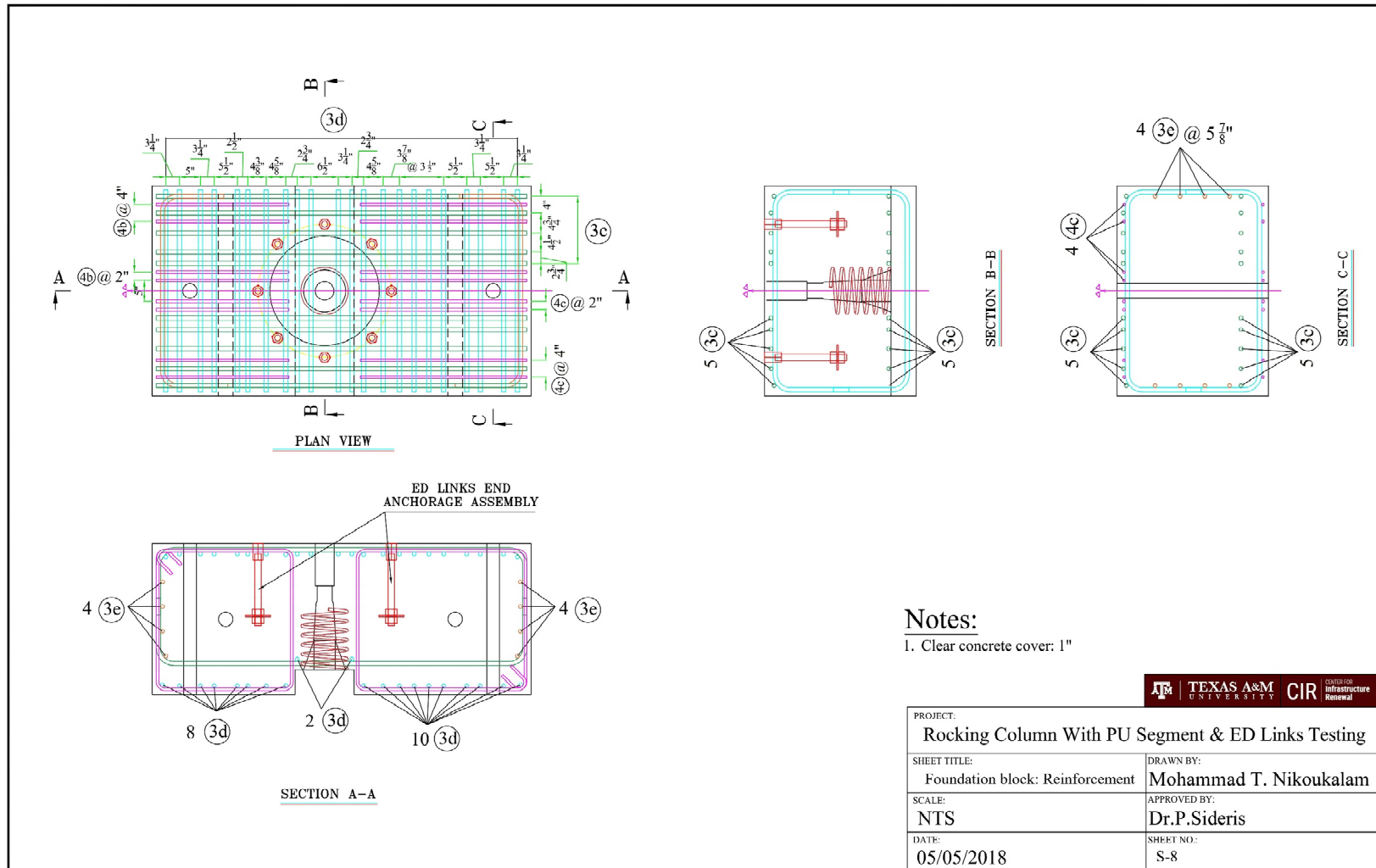


Figure B.9. Reinforcement layout: foundation block.

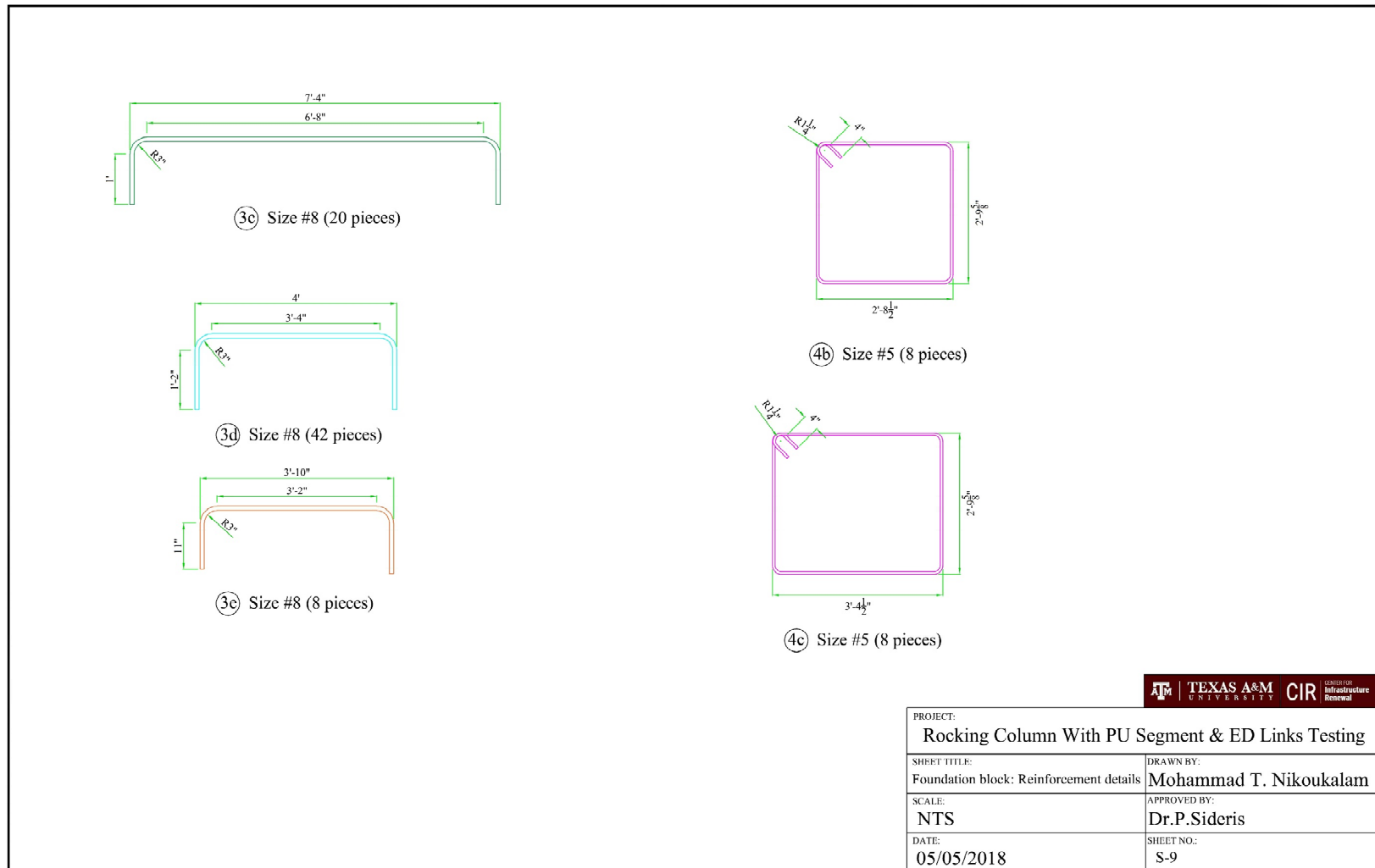


Figure B.10. Details of reinforcement: foundation block.

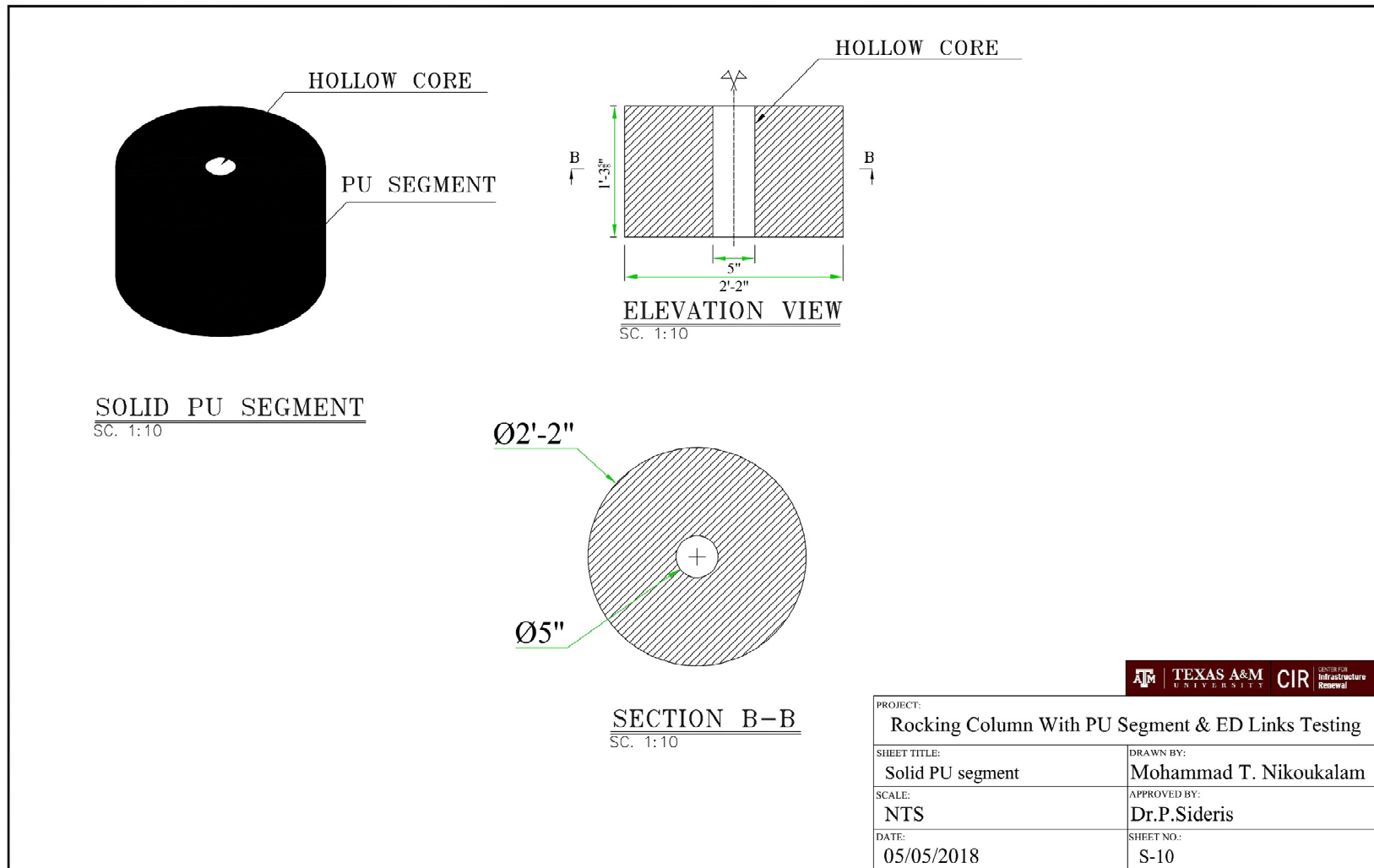


Figure B.11. Details of solid PU segment.

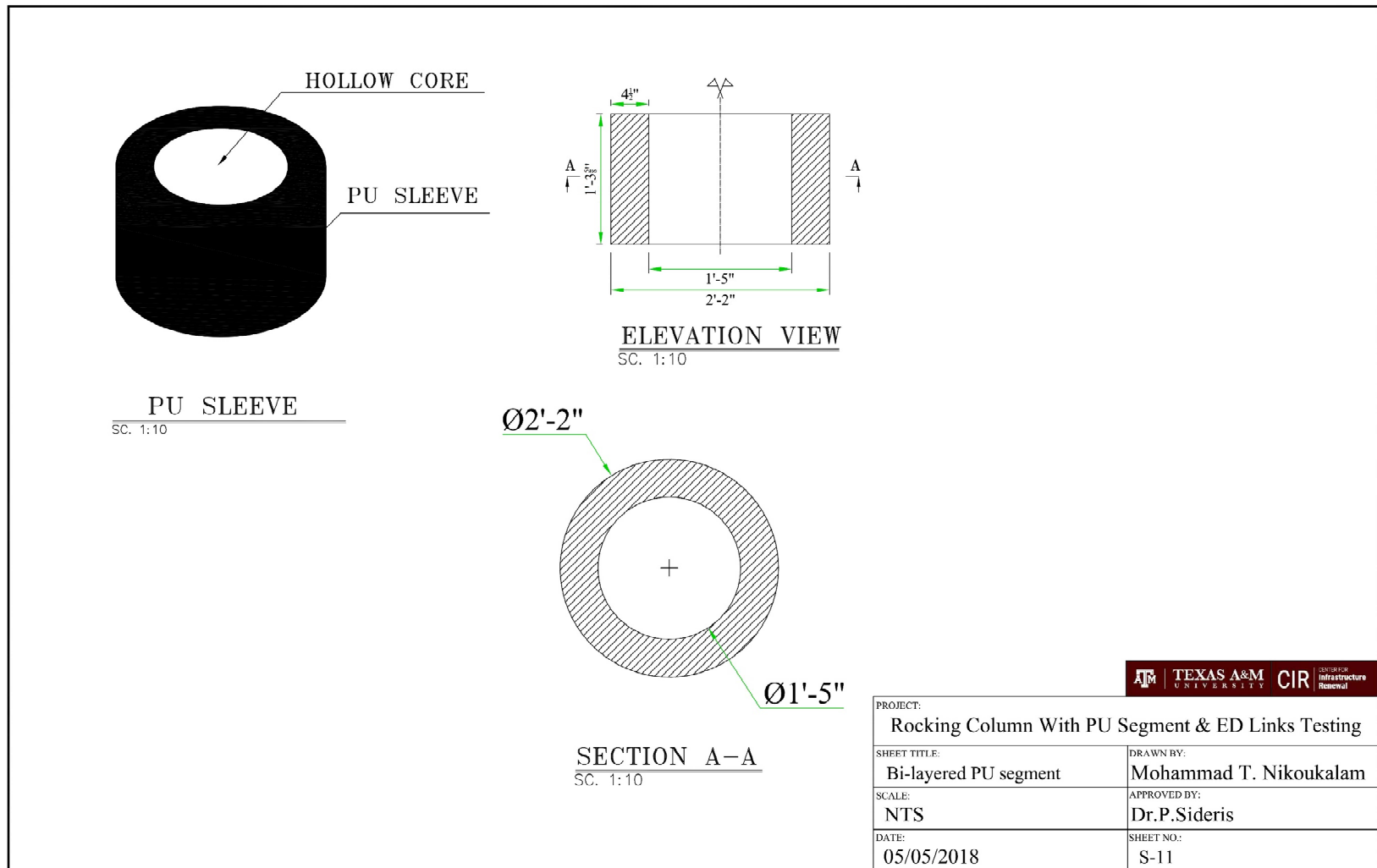
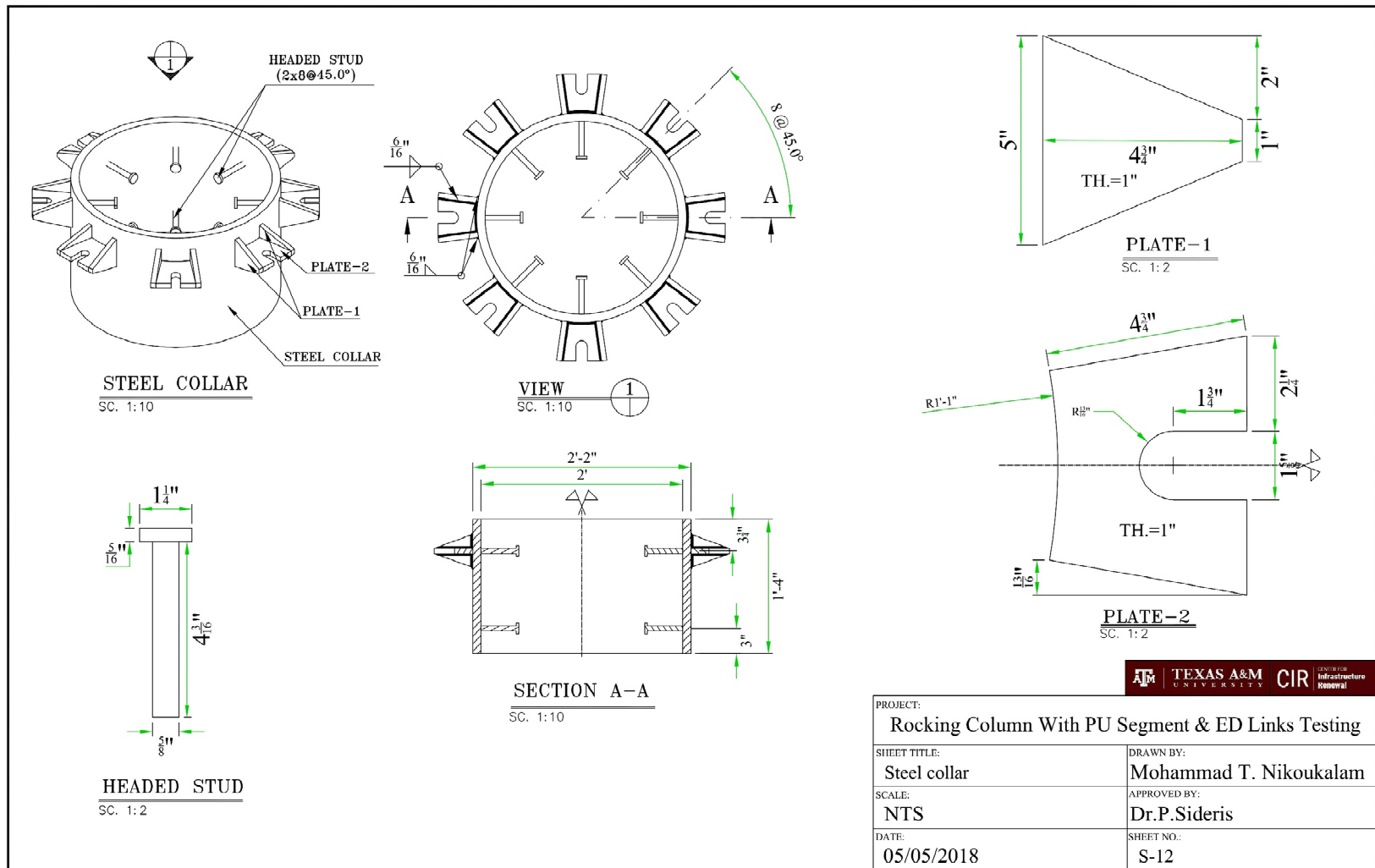


Figure B.12. Details of PU sleeve.



PROJECT: Rocking Column With PU Segment & ED Links Testing	
SHEET TITLE: Steel collar	DRAWN BY: Mohammad T. Nikoukalam
SCALE: NTS	APPROVED BY: Dr.P.Sideris
DATE: 05/05/2018	SHEET NO.: S-12

Figure B.13. Details of steel collar.

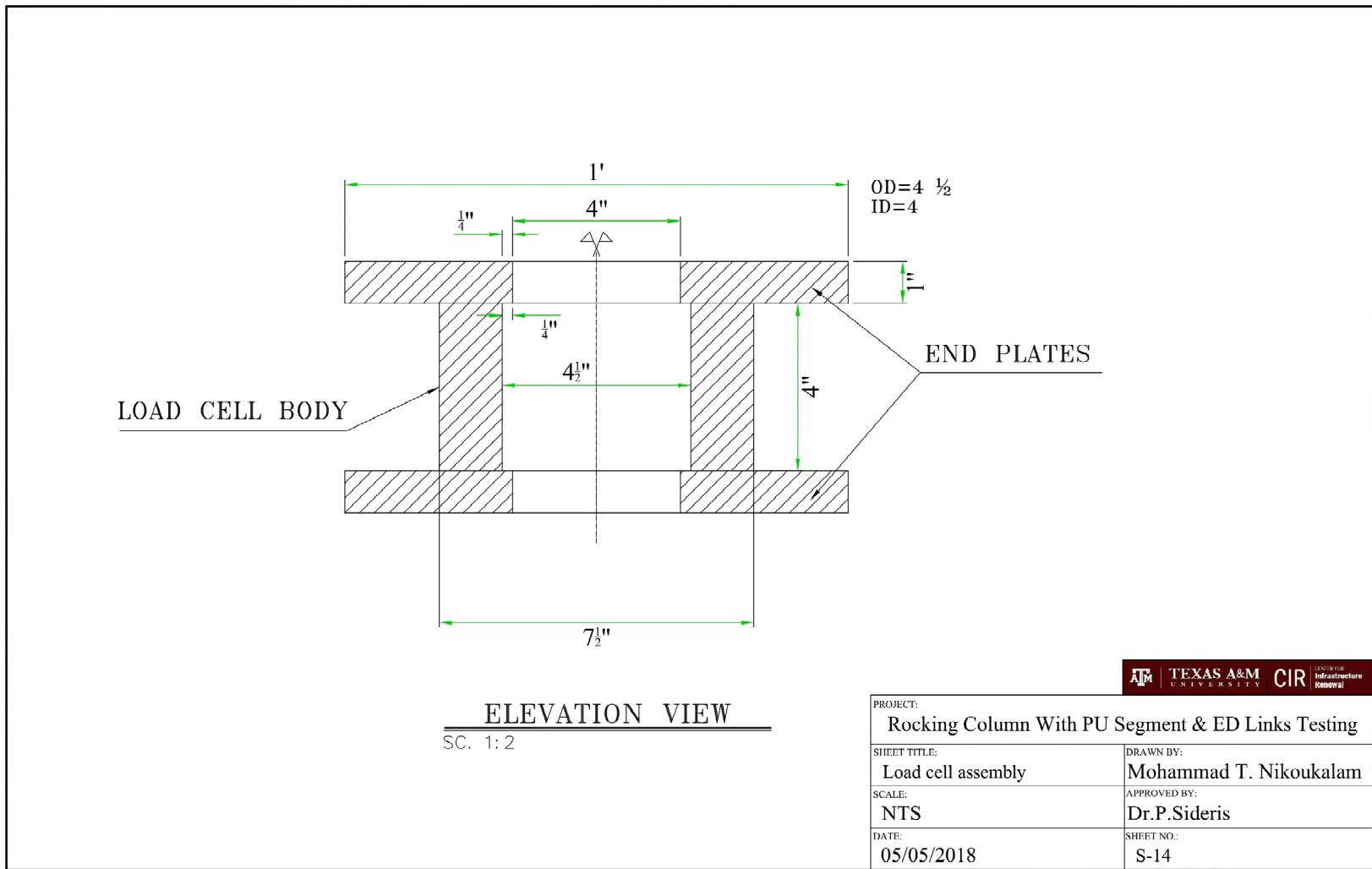


Figure B.15. Details of load cell assembly.

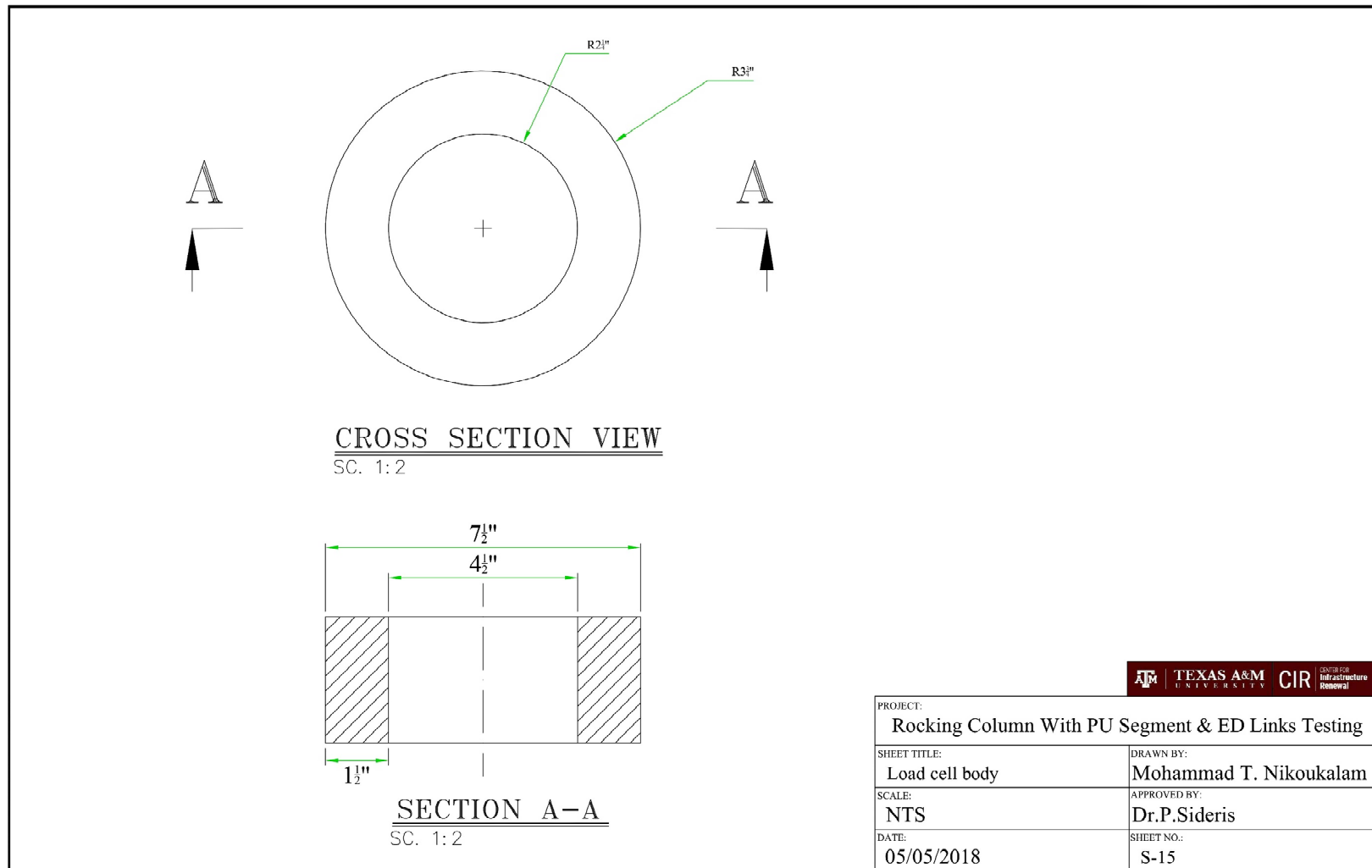


Figure B.16. Details of load cell body.

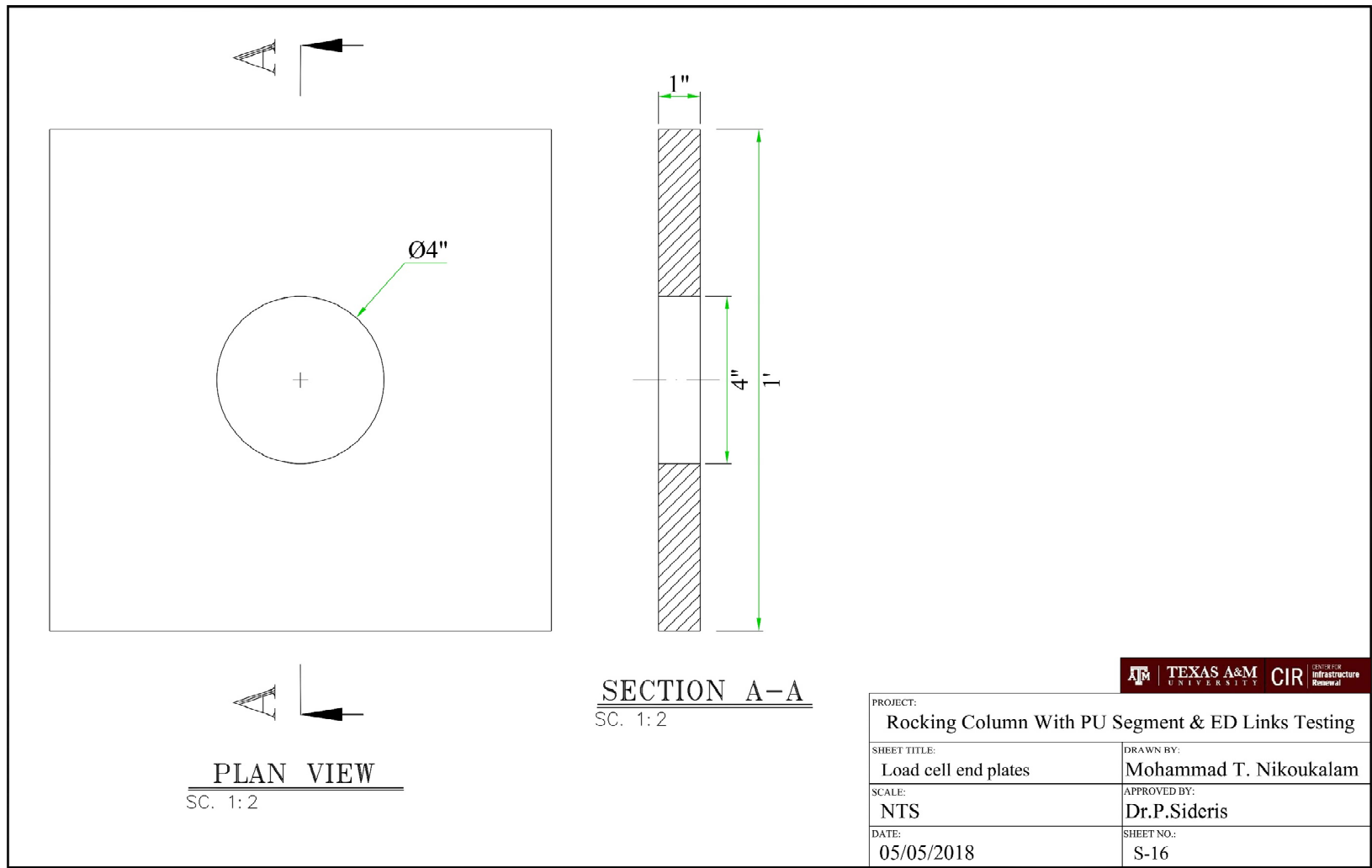


Figure B.17. Details of load cell end plates.